

# Synthese und Reaktivität von trigonalen Imido-Komplexen der späten Übergangsmetalle

Kumulative Dissertationsschrift

zur Erlangung des akademischen Grades eines

Doktors der Naturwissenschaften

(Dr. rer. nat.)

dem Fachbereich Chemie

der Philipps-Universität Marburg

vorgelegt von

**Alexander Reckziegel, M.Sc.**

(geboren am 11.12.1992 in Schwalmstadt)

Erstgutachter: Dr. Gunnar Werncke

Zweitgutachter: Prof. Dr. Crispin Lichtenberg

Marburg / Lahn 2023

Hochschulkenziffer 1180





# Synthese und Reaktivität von trigonalen Imido-Komplexen der späten Übergangsmetalle

Kumulative Dissertationsschrift

zur Erlangung des akademischen Grades eines

Doktors der Naturwissenschaften

(Dr. rer. nat.)

dem Fachbereich Chemie

der Philipps-Universität Marburg

vorgelegt von

**Alexander Reckziegel, M.Sc.**

(geboren am 11.12.1992 in Schwalmstadt)

Erstgutachter: Dr. Gunnar Werncke

Zweitgutachter: Prof. Dr. Crispin Lichtenberg

Marburg / Lahn 2023

Hochschulkenziffer 1180

Diese Arbeit wurde in der Zeit von April 2018 bis März 2023 unter der Leitung von Dr. Gunnar C. Werncke am Fachbereich Chemie der Philipps-Universität Marburg angefertigt.

Erstgutachter: Dr. Gunnar C. Werncke

Zweitgutachter: Prof. Dr. Crispin Lichtenberg

Annahme der Dissertation:

Tag der Disputation:

## Erklärung

Ich erkläre, dass eine Promotion noch an keiner anderen Hochschule als der an der Philipps-Universität Marburg, Fachbereich Chemie, versucht wurde.

Ich versichere, dass meine Dissertation mit dem Titel:

### **„Synthese und Reaktivität von trigonalen Imido-Komplexen der späten Übergangsmetalle“**

Selbst und ohne fremde Hilfe verfasst, nicht andere als die in ihr angegebenen Quellen oder Hilfsmittel benutzt, alle vollständig oder sinngemäß übernommenen Zitate als solche gekennzeichnet, sowie die Dissertation in der vorliegenden oder einer ähnlichen Form noch bei keiner anderen in- und ausländischen Hochschule anlässlich eines Promotionsgesuchs oder zu anderen Prüfungszwecken eingereicht habe.

---

Datum, Ort

---

Alexander Reckziegel

*-Meiner Familie gewidmet-*

*"Es ist eine gefährliche Sache, aus deiner Tür hinauszugehen. Du betrittst die Straße, und wenn du nicht auf deine Füße aufpasst, kann man nicht wissen, wohin sie dich tragen."*

aus *Der Herr der Ringe: Die Gefährten*, J.R.R. Tolkien

# Inhaltsverzeichnis

<b>1</b>	<b>Einleitung</b>	<b>1</b>
1.1	Einleitende Worte . . . . .	1
1.2	Nitren-Transfer-Reaktionen . . . . .	2
1.3	Bindungssituation von Imido-Übergangsmetall-Komplexen . . . . .	3
1.4	Synthese und Eigenschaften von Imido-Übergangsmetall-Komplexen . . . . .	5
1.5	Vorstufen zur Darstellung von Imido-Komplexen . . . . .	20
1.5.1	Monovalente zweifach-koordinierte Übergangsmetall-Komplexe . . . . .	22
1.6	Vorarbeiten . . . . .	24
<b>2</b>	<b>Zielsetzung und Motivation</b>	<b>26</b>
<b>3</b>	<b>Kumulativer Teil</b>	<b>27</b>
3.1	C–H bond activation by an Imido Cobalt(III) and the Resulting Amido Cobalt(II) Complex . . . . .	28
3.2	High-Spin Imido Cobalt Complexes with Imidyl Radical Character . . . . .	36
3.3	On the Synthesis of a T-shaped Imido Nickel Complex and Trigonal Amido Nickel Complexes . . . . .	44
3.4	Intricate Road to Linear Anionic Nickel(I) Hexamethyldisilazanide $[\text{Ni}(\text{N}(\text{SiMe}_3)_2)_2]^-$ . . . . .	54
3.5	Hydrogen Atom Abstraction by Trigonal Imido Cobalt Complexes – Impact of structure onto reactivity . . . . .	67
3.6	Between imide, imidyl and nitrene – an imido iron complex in two oxidation states . . . . .	77
<b>4</b>	<b>Unveröffentlichte Ergebnisse</b>	<b>87</b>
4.1	Weiterführende Untersuchungen zum Reaktionsverhalten von trigonalen Imido-Cobalt-Komplexen . . . . .	87
4.2	Darstellung von Imido-Nickel-Komplexen . . . . .	96
<b>5</b>	<b>Zusammenfassung</b>	<b>101</b>
5.1	Zusammenfassung in deutscher Sprache . . . . .	101
5.2	English Summary . . . . .	105
<b>6</b>	<b>Anhang</b>	<b>113</b>
6.1	Publikationsliste . . . . .	113
6.2	Wissenschaftlicher Lebenslauf . . . . .	114
6.3	Danksagung . . . . .	115
6.4	Allgemeine Analytik und Arbeitstechniken . . . . .	117
6.5	Synthese der beschriebenen Cobalt-Komplexe . . . . .	118
6.6	Synthese von Imido-Nickel-Komplexen . . . . .	121
6.7	NMR Spektren . . . . .	122
6.8	Kristallographischer Anhang . . . . .	126
6.9	Elektronische Zusatzinformationen . . . . .	136
6.9.1	C–H bond activation by an Imido Cobalt(III) and the Resulting Amido Cobalt(II) Complex . . . . .	136
6.9.2	High-Spin Imido Cobalt Complexes with Imidyl Radical Character . . . . .	176

6.9.3	On the Synthesis of a T-shaped Imido Nickel Complex and Trigonal Amido Nickel Complexes . . . . .	222
6.9.4	Intricate Road to Linear Anionic Nickel(I) Hexamethyldisilazanide $[\text{Ni}(\text{N}(\text{SiMe}_3)_2)]^-$ . . . . .	237
6.9.5	Hydrogen Atom Abstraction by Trigonal Imido Cobalt Complexes – Impact of structure onto reactivity . . . . .	264
6.9.6	Between imide, imidyl and nitrene – an imido iron complex in two oxidation states . . . . .	340

## Abkürzungsverzeichnis

°C	Grad Celsius
12K4	1,4,7,10-Tetraoxacyclododecan
18K6	1,4,7,10,13,16-Hexaoxacyclooctadecan
Ada	Adamantyl-
crypt.222	4,7,13,16,21,24-Hexaoxa-1,10-diazabicyclo[8.8.8]hexacosan
Dipp	2,6-Di- <i>iso</i> -propylphenyl-
DMAP	4-(Dimethylamino)pyridin
dme	1,2-Dimethoxyethan
Dmp	2,6-Di-Mesitylphenyl-
dppm	Bis(diphenylphosphino)methan
eq.	Äquivalent
ESR	Elektronenspinresonanz
Et <sub>2</sub> O	Diethylether
g	Gramm
HMDSO	Hexamethyldisiloxan
Hz	Hertz
<i>i</i> Pr	<i>iso</i> -Propyl-
IPr	1,3-Bis(2,6-di <i>isopropylphenyl</i> )-1,3-dihydro-2H-imidazol-2-ylidene
IR	Infrarot
K	Kelvin
KZ	Koordinationszahl
Me	Methyl-
Mes	2,4,6-Trimethylphenyl-
mg	Milligramm
mL	Milliliter
N(Dipp)SiMe <sub>3</sub>	(2,6-Di- <i>iso</i> -propyl)-phenyl-(trimethyl)silylamid
NHC	<i>N</i> -Heterocyclisches Carben
NMR	<i>nuclear magnetic resonance</i>
Ph	Phenyl-
ppm	<i>parts per milion</i>
RT	Raumtemperatur
SQUID	<i>superconducting quantum interference device</i>
THF	Tetrahydrofuran
TMS	Tetramethylsilan
TMS-	Trimethylsilyl-
Tripp	2,4,6-Tri- <i>iso</i> -propylphenyl
vgl.	Vergleiche



# 1 Einleitung

## 1.1 Einleitende Worte

Die Synthese von funktionalisierten, organischen Substraten ist für die chemische Industrie und auch darüber hinaus die Grundlage für verschiedenste Anwendungen. Dabei ist die Suche nach einem effizienteren Zugang, sowie auch eine Optimierung der Reaktionsprozesse, eine Fragestellung, die von allgemeiner Bedeutung ist.

Die durch Übergangsmetall-Komplexe vermittelte Übertragung von Nitren-Fragmenten hebt sich hier durch eine ökonomische Atombilanz sowie meist moderaten Reaktionsbedingungen hervor. Eine Optimierung der verwendeten Katalysatoren setzt ein vollständiges Verständnis des Reaktionsmechanismus voraus, was die Bindungssituation des intermediär gebildeten Imido-Komplexes einschließt.

In dieser Arbeit wurden reaktive Imido-Komplexe, ausgehend von linear koordinierten Metall(I)-Komplexen, als Modellsystem für diese reaktiven Intermediate untersucht. Dabei standen die elektronische Struktur und deren Einfluss auf die Bindungssituation und das Reaktionsverhalten im Fokus.

In Kapitel 1.3 wird ein Einblick in die komplexe Bindungssituation von Imido-Übergangsmetall-Komplexen gegeben. Kapitel 1.4 zeigt die bisherigen Ergebnisse zur Synthese und Reaktivität von Imido-Übergangsmetall-Komplexen ( $M = \text{Fe} - \text{Ni}$ ). Dabei werden auch die Arbeiten, die zeitgleich zu dieser Arbeit veröffentlicht wurden, behandelt. Die, als Vorstufen verwendeten, linear koordinierten Metall(I)-Komplexe zeigen ein hohes Potential, weshalb deren Entwicklung und Eigenschaften in Kapitel 1.5 beschrieben.

## 1.2 Nitren-Transfer-Reaktionen

Erste Untersuchungen zu Nitren-Transfer-Reaktionen mit C–H-Bindungen wurden in der Gruppe von GELLMAN bereits in den 1980er Jahren durchgeführt. Die Wahl des Katalysators fiel auf ein Derivat des Cytochrom P-450, welches bereits eine hohe Reaktivität zu Oxo-Transfer Reaktionen zeigte.[1–3]

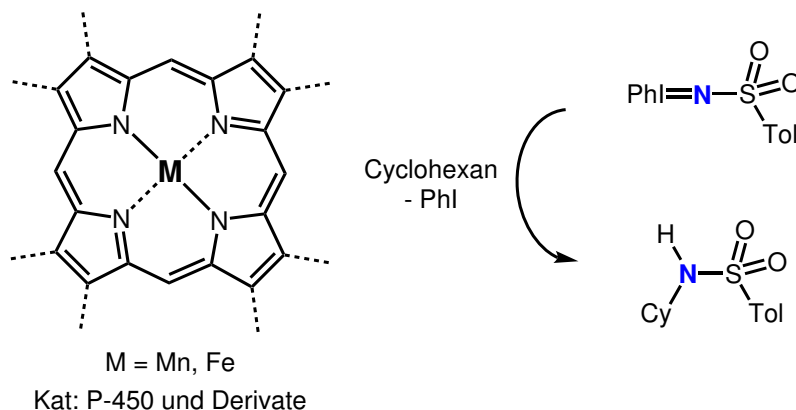


Abb. 1: Schematische Darstellung der C–H-Aminierung am Beispiel von Cyclohexan und des katalytisch eingesetzten, aktiven Metall-Komplexes.[1–3]

Auf diesem Weg konnte sowohl eine intra- als auch eine intermolekulare C–H Aminierung beobachtet werden, was den Grundstein für die Forschung auf diesem Gebiet legte. Die Bildung von Imido-Übergangsmetall-Komplexen als reaktives Intermediat wurde bereits früh vermutet, ein struktureller Beweis blieb zunächst jedoch aus.[1–3]

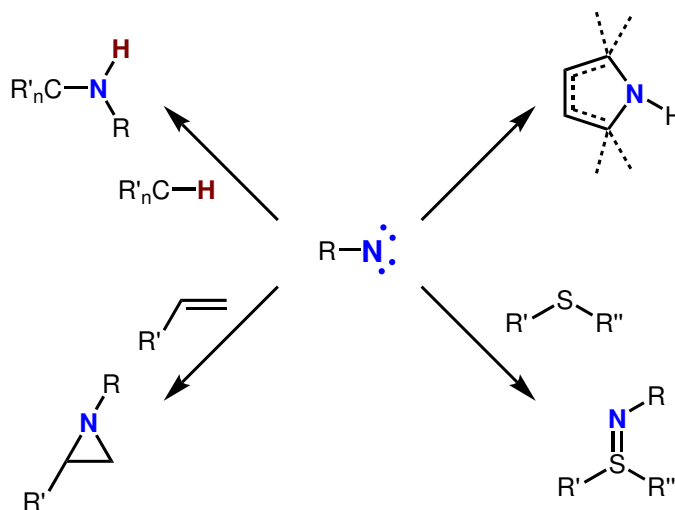


Abb. 2: Schematische Darstellung von bekannten Nitren-Transfer-Reaktionen.[4–10]

In den folgenden Jahrzehnten konnte eine hohe regio- und chemoselektive Reaktivität zur Aminierung von (un)funktionalisierten C–H-Bindungen gezeigt werden. Weiterhin konnten Übertragungen auf Doppelbindungen oder Sulfane beobachtet werden. Die mechanistischen Hypothesen und die Bildung des Zwischenprodukts basierten weiterhin nur auf den Beobachtungen der gebildeten Produkte.[4–10]

### 1.3 Bindungssituation von Imido-Übergangsmetall-Komplexen

Die Bindungssituation der aktiven Imido-Übergangsmetall-Komplexe ist für eine vollständige Aufklärung des Reaktionsmechanismus von großem Interesse. Da zunächst weder eine strukturelle noch spektroskopische Untersuchung der reaktiven Intermediate möglich war, orientierten sich erste Erklärungen an bekannten Komplexen mit Ligand-Metall-Mehrfachbindungen (Oxo-, Nitrido-, Hydrazido-, Alkylden-, Alkyldin-Komplexe, vgl. Abb. 3).[11]

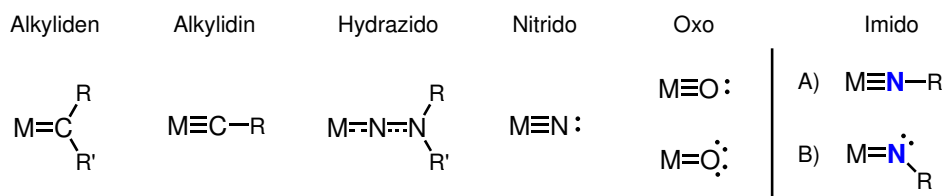


Abb. 3: Vereinfachte Darstellung von Ligand-Metall-Mehrfachbindungen und die daraus abgeleitete Bindungssituation in Imido-Übergangsmetall-Komplexen.[11]

Bereits früh war klar, dass vor allem das verwendete Übergangsmetall, dessen Oxidationsstufe, sowie das Ligandenrückgrat einen signifikanten Einfluss auf die Bindungssituation haben. Dabei wurde, in Anlehnung an terminale Nitrido-Komplexe, zunächst von der Bildung einer  $\sigma$ - und zwei  $\pi$ -Bindungen ausgegangen. Letztere wurden dabei als Wechselwirkung zwischen den besetzten p-Orbitalen des Imido-Stickstoff-Atoms und unbesetzten d-Orbitalen des Übergangsmetall-Ions betrachtet. Dies hat eine lineare Anordnung des Imido-Liganden zur Folge und wurde so bei bekannten, unreaktiven Imido-Komplexen mit frühen Übergangsmetall-Ionen beobachtet (vgl. Abb. 3 **A**).[12, 13]

Für späte Übergangsmetall-Komplexe konnte eine gewinkelte Anordnung des Liganden beobachtet werden, was die Lokalisierung eines p-Orbitals am Imido-Stickstoff-Atom vermuten lässt. Dies kann auf eine mangelnde Wechselwirkung mit freien d-Orbitalen des Übergangsmetall-Ions, durch dessen hohe d-Elektronen-Konfiguration, unpassende Symmetrie, oder konkurrierende  $\pi$ -Bindungen mit dem Ligandenrückgrat, zurückgeführt werden (vgl. Abb. 3 **B**).[12, 13]

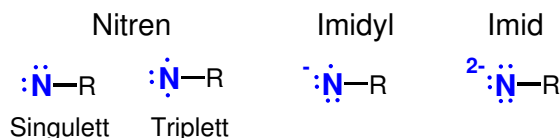


Abb. 4: Verschiedene elektronische Strukturen des Imido-Liganden.[14]

Eine immer größere Zahl an isolierten, teils reaktiven Imido-Komplexen zeigte eine große Komplexität der Bindungssituation, die das zuvor gezeigte System nicht eindeutig beschreiben konnte. Dies führte zu einer großen Zahl an verschiedenen, teils konträr verwendeten Bezeichnungen für die beobachteten Komplexe. Die Gruppe um MUNZ beschrieb kürzlich eine einheitliche Nomenklatur für die verschiedenen Bindungstypen, die im Folgenden beschrieben und für den Rest dieser Arbeit angewendet wird.[14]

Neben dem dianionischen Bindungsmodus (Imid), wurde ein monoanionischer Ligand mit einem Stickstoff zentrierten Radikal (Imidyl) oder eine schwache dative Wechselwirkung eines neutralen Nitren-Fragmentes (Nitren) mit dem Übergangsmetall-Ion beobachtet (vgl. Abb. 4).[14]

Bei Betrachtung der Orbital-Wechselwirkung für frühe Übergangsmetall-Komplexe ist eine große energetische Differenz zwischen den Orbitalen des Liganden und dem Übergangsmetall-Ion beobachtet worden. Dies hat eine klassische ionische Donor-Akzeptor-Wechselwirkung zur Folge (vgl. Abb. 5 **A**). Die Energie der Valenzorbitale wird hin zu späten Übergangsmetall-Ionen abgesenkt, was einen kovalenteren Charakter der Imido-Metall-Bindung zu Folge hat. Weiterhin wird die formale Bindungsordnung durch die Besetzung von antibindenden Orbitalen herabgesetzt (vgl. Abb. 5 **B**). Wenn die Energie der Orbitale des Liganden die der d-Orbitale überschreitet wird ein invertiertes Ligandenfeld erhalten. Durch die Liganden zentrierten Orbitale kann hier ein Nitren-, oder ein Imidyl-Komplex, erhalten werden (Abb. 5 **C**).[12–14]

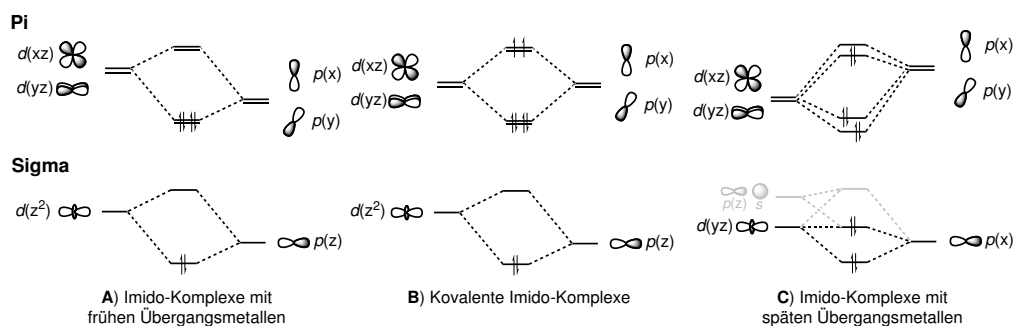


Abb. 5: Idealisierte Orbital Wechselwirkungen in Imido-Übergangsmetall-Komplexen. Nichtbindende Orbitale sind aus Gründen der Übersichtlichkeit nicht abgebildet.[14]

Eine genaue Analyse der Bindungssituation benötigt häufig eine Zusammenarbeit aus spektroskopischen Methoden und quantenchemischen Berechnungen. Da in vielen Fällen keine genauere Aussage über die Bindungssituation getroffen werden konnte, wird im Folgenden der Begriff „Imido“, als Oberbegriff für alle Bindungssituationen verwendet.

## 1.4 Synthese und Eigenschaften von Imido-Übergangsmetall-Komplexen

Die Verwendung von niedrig koordinierten Übergangsmetall-Komplexen als Präkursor für die Synthese von reaktiven Imido-Übergangsmetall-Komplexen wird seit Beginn des 21. Jahrhunderts untersucht.

### Synthese und Reaktivität von Imido-Eisen-Komplexe

Die erste Isolation von Imido-Eisen-Komplexen war in der Gruppe um PETERS durch Verwendung eines tripodalen Phosphine-Liganden möglich. Der erhaltene Adamantyl-Imido- **1** und Aryl-Imido-Komplex **2** zeigen eine lineare Koordination des Liganden. Dies kann auf den hohen sterischen Anspruch des Co-Liganden zurückgeführt werden.[15, 16]

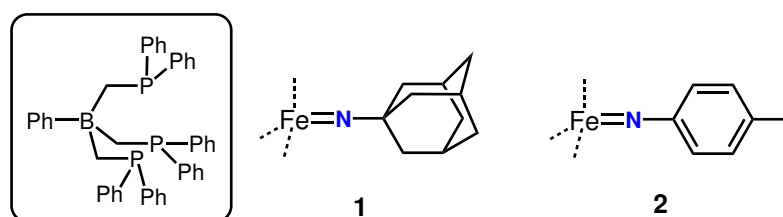


Abb. 6: Tetraedrische Imido-Eisen-Komplexe der Gruppe um PETERS **1/2**. [15, 16]

Untersuchungen zur elektronischen Struktur zeigten in beiden Fällen eine *low-spin* Konfiguration. Der Aryl-Imido-Komplex **2** zeigte weiterhin einen Nitren-Transfer auf Kohlenstoffmonoxid (CO) unter Bildung von 4-Toluylenisocyanat und eines Carbonyl-Eisen-Komplexes.[16]

Das  $\beta$ -Ketiminato-Ligandensystem (NacNac) zeigte hier weitere Erfolge. Der Arbeitsgruppe um HOLLAND war es möglich, den trigonalen Imido-Eisen-Komplex **3**, durch Umsetzung einer Eisen(I)-Vorstufe **4** mit Adamantylazid zu isolieren (vgl. Abb. 7).

Durch Zugabe von *p*-(*tert*-Butyl)-Pyridin konnte spektroskopisch die Bildung des tetragonalen Komplexes **5** beobachtet werden. Dieser zeigt eine hohe Reaktivität gegenüber intra- und intermolekularen H-Atom-Abstraktionen. Durch Quantenchemische Untersuchungen konnte zum einen die Änderung des Spin-Grundzustandes von  $S = 3/2$  (**3**) zu  $S = 5/2$  (**5**), sowie eine geringe Aufweitung und Abwinklung der Fe-N<sub>Imido</sub>-Bindung, bestimmt werden.[17–20]

Bei der Verwendung eines Überschusses von Adamantylazid konnte die Bildung des Hexazen-Komplexes **6** in Abwesenheit des Pyridins, und die Bildung des Tetrazen-Komplexes **7** in dessen Anwesenheit beobachtet werden. Im letzteren Fall verläuft die Reaktion über die Bildung von **5**, während in Erstem keine Bildung eines Imido-Komplexes stattfindet. Eine Verwendung dieses Systems in katalytischen Prozessen war somit nicht möglich.[21, 22]

Eine kinetische Untersuchung der H-Atom-Transfer-Reaktionen der beiden Komplexe bestätigte die deutlich höhere Reaktivität des Pyridin-Adduktes **5**. Als Grund wurde hier die Schwächung der Imido-Eisen-Bindung sowie die höhere Stabilität des gebildeten Adduktes des Amido-Komplexes genannt. Die Untersuchungen wurden durch die gezeigten Nebenreaktionen mit Adamantylazid eingeschränkt.[20]

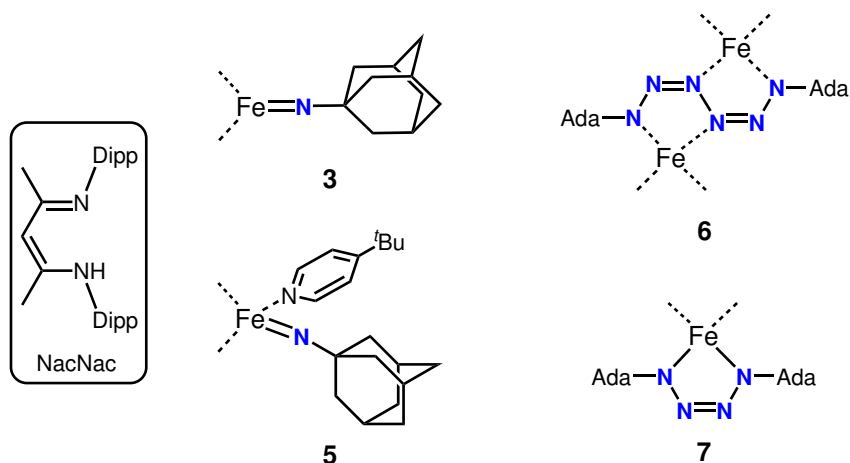


Abb. 7: Struktur der in der Gruppe von HOLLAND dargestellten Imido-Eisen-Komplexe **3** und **5** sowie des erhaltenen Hexazen- **6** und Tetrazen-Komplexes **7** mit NacNac-Ligandensystem.[17–22]

Eine Variation im Rückgrat des verwendeten Co-Liganden ermöglichte Nitren-Transfer-Reaktionen gegenüber nukleophilen Substraten (CO, CN<sup>t</sup>Bu, PMe<sub>3</sub>), wobei der Imido-Komplex **8** nur als reaktives Intermediate beobachtet wurde (vgl. Abb. 8). Gleichzeitig wurden keinerlei H-Atom-Transfer-Reaktivitäten beobachtet, was die Sensibilität des Imido-Liganden auf geringfügige Änderungen des Ligandensystems sehr gut verdeutlicht.[23]

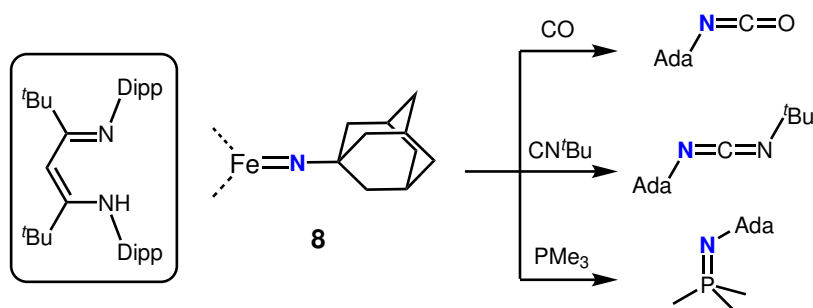


Abb. 8: Nitren-Transfer-Reaktivität des Imido-Eisen-Komplex **8** auf elektronenreiche Substrate.[23]

Weiterhin wurde die Variation der flankierenden Aryl-Substituenten des NacNac-Liganden untersucht, da hier ein direkter Einfluss auf die Bindungstasche des Imido-Liganden genommen werden kann (vgl. Abb. 9).

Bei der Verwendung der sterisch anspruchsvolleren Terphenyl-Gruppen, konnte eine erhöhte Reaktivität des dargestellten Adamantyl-Imido-Komplexes **9** in H-Atom-Transfer Reaktionen beobachtet werden. Der strukturelle Vergleich zu **3** zeigte hier eine gewinkelte Anordnung des Imido-Liganden, was eine geringe Abschirmung des Imido-Stickstoff-Atoms zur Folge hatte. Die weiterhin beobachtete, höhere Reaktivität des Alkyl-Imido-Komplexes **9** im Vergleich zu einem Komplex mit Aryl-Substituent **10**, ließ einen Zusammenhang der H-Atom-Transfer Reaktivität mit der Basizität des Imido-Liganden vermuten.[24]

Als Erweiterung des NacNac-Ligandensystems, wandte sich die Gruppe um BETLEY den Dipyrromethen-Liganden (vgl. Abb. 10 **A**) zu. Dabei lag der Fokus der

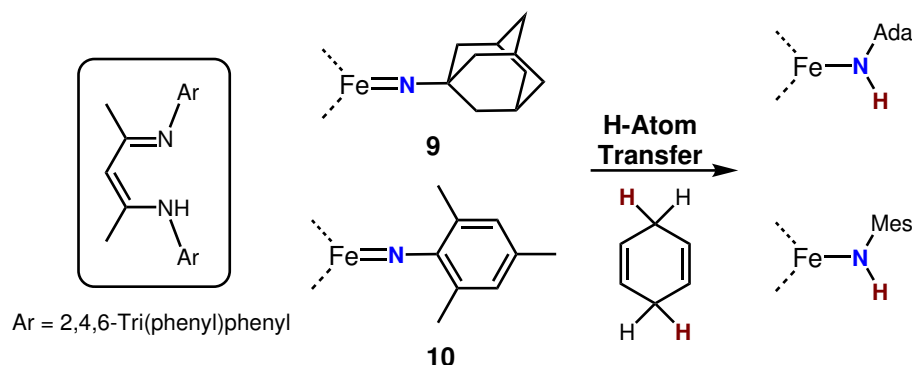


Abb. 9: Vergleich der H-Atom-Transfer Reaktivität von Alkyl- **9** und Aryl-Imido-Eisen-Komplexen **10**.<sup>[24]</sup>

Arbeit zum einen auf der Aufklärung der Bindungssituation von reaktiven Imido-Komplexen, zum anderen auf einer Anwendung als Katalysator.

Bereits erste Umsetzungen eines Eisen(II)-Komplexes mit Adamantylazid zeigten die intramolekulare Insertion in eine C–H-Bindung des Ligandenrückgrates unter Bildung von **11**. Weitere Reaktionen des Komplexes wurden durch eine Koordination der gebildeten Amino-Gruppe an das Übergangsmetall-Ion verhindert.<sup>[25]</sup>

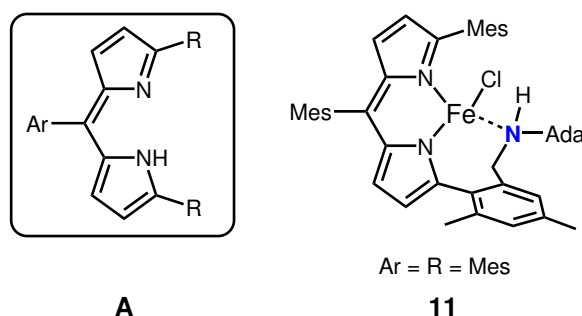


Abb. 10: Struktur des Dipyrromethen-Liganden (**A**) und des, durch intramolekulare C–H Aminierung des Imido-Liganden, erhaltenen Komplexes **11**.<sup>[25]</sup>

Um die beobachtete intramolekulare C–H-Aminierung zu unterbinden, wurden Substitutionen an dem Ligandensystem durchgeführt. Durch Einführung von Adamantyl-Gruppen konnte so der Eisen(II)-Komplex **12** dargestellt werden (vgl. Abb. 11). Dieser Komplex zeigt bei der Umsetzung mit Adamantylazid eine katalytische C–H-Aminierung von benzylicchen C–H-Bindungen sowie die Aziridierung von Styrol (vgl. Abb. 11).

Bei der Verwendung von weiteren Substraten mit C–C-Doppelbindungen, konnte interessanterweise eine Aminierung unter Umlagerung der Doppelbindung an Stelle einer Aziridierung beobachtet werden.<sup>[27]</sup>

Für beide Reaktionen wurde die Bildung eines Imido-Komplexes als reaktives Intermediat vermutet, wobei dessen Isolierung nicht möglich war. Untersuchungen zum Mechanismus der Aminierung konnten zeigen, dass eine radikalische H-Atom-Abstraktion durch den Imido-Eisen-Komplex der geschwindigkeitsbestimmende Schritt der Reaktion ist.

Um die reaktiven Imido-Komplexe zu isolieren, wurden weiterhin Reaktionen mit arylischen Aziden durchgeführt. Bei der Umsetzung des mit 2,4,6-Triphenylphenyl-

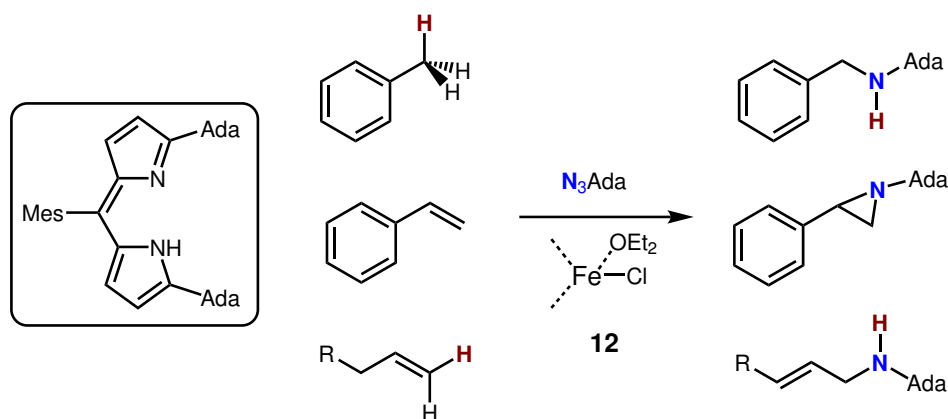


Abb. 11: Motiv des von BETLEY beschriebenen Eisen(II)-Komplexes **12** und Übersicht über dessen katalytische Aktivität.[26, 27]

substituierten Komplexes mit Phenylazid konnte eine Dimerisierung des Imido-Komplexes **13** unter Bildung einer C–N-Bindung beobachtet werden (vgl. Abb. 12). Durch Blockieren der *para*-Position mit einer *tert*-Butylgruppe, konnte die Kupplung verhindert und der terminale Imido-Eisen-Komplex **14** erhalten werden.

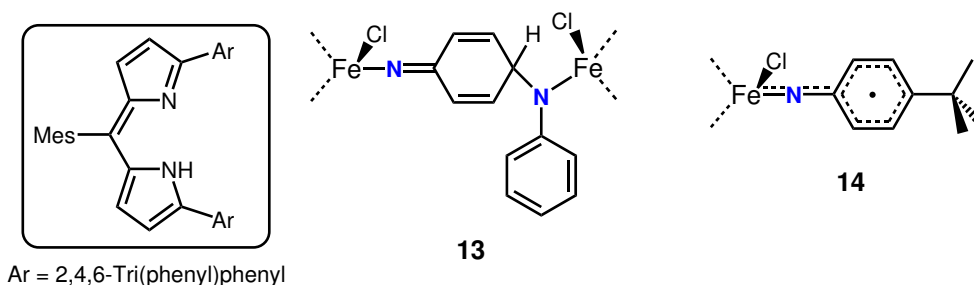


Abb. 12: Strukturen des dimerisierten Imido-Eisen- **13** und terminalen Imidyl-Eisen-Komplexes **14**. [26]

Untersuchungen zur elektronischen Struktur mittels Mößbauer Spektroskopie deuteten hier auf ein Eisen(III)-Zentrum, und damit auf den ersten isolierten Imidyl-Eisen-Komplex, hin. Beide Komplexe zeigen weiterhin eine Reaktivität zu C–H-Aminierungen für benzyliche C–H-Bindungen, was für **13** eine reversible Dimerisierung voraussetzt.[26]

Durch die Funktionalisierung im Rückgrat des Dipyrromethen-Liganden können dessen elektronische Eigenschaften, und damit die des Zentralatoms eines Komplexes, beeinflusst werden. So konnte durch Einführung eines teilweise chlorierten, aromatischen Substituenten der Eisen-Katalysator **15** für eine C–H-Aminierung unter Zyklisierung dargestellt werden (vgl. Abb. 13).[28]

Mechanistische Untersuchungen zeigten einen H-Atom-Transfer, gefolgt von einer Radikal-Rekombination für benzyliche Substrate, während für stärkere C–H-Bindungen eine direkte Insertion vermutet wurde. Weiterführend konnte eine diastereoselektive Zyklisierung untersucht werden, wobei hier der Austausch des Chlorido-Liganden gegen eine Phenolat-Gruppe, eine Erhöhung der Selektivität zur Folge hatte.[28, 29]

Weitere Versuche, die Bindungssituation der Imido-Eisen-Komplexe aufzuklären, führten zu Isolation des terminalen Komplexes **16** (vgl. Abb. 14). Die elektro-



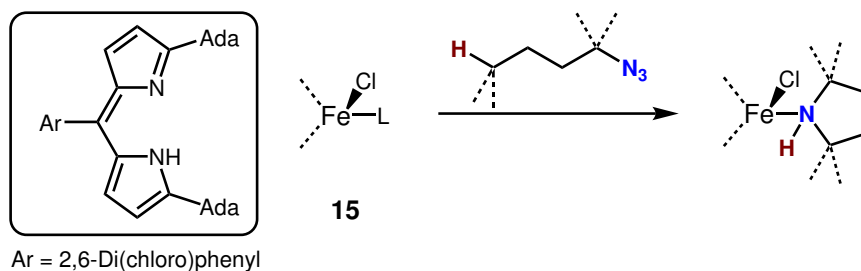


Abb. 13: Katalytische C–H-Aminierung unter Zyklisierung durch den gezeigten Eisen(II)-Komplex **15**. [28, 29]

nische Struktur von **16** wurde durch Mössbauer Spektroskopie und magnetische Messungen untersucht und weist auf einen Imidyl-Eisen(III)-Komplex hin. Untersuchungen des Reaktionsverhaltens zeigten einen H-Atom-Transfer von 1,4-CHD oder eine Aktivierung einer *iso*-Propylgruppe des Dipp-Substituenten. Aus diesem Grund wurde der Eisen(II)-Komplex mit dem sterisch weniger anspruchsvollen 3,5-Bis(Trifluormethyl)phenylazid umgesetzt, wodurch der verbrückende Imido-Komplex **17** erhalten wurde.

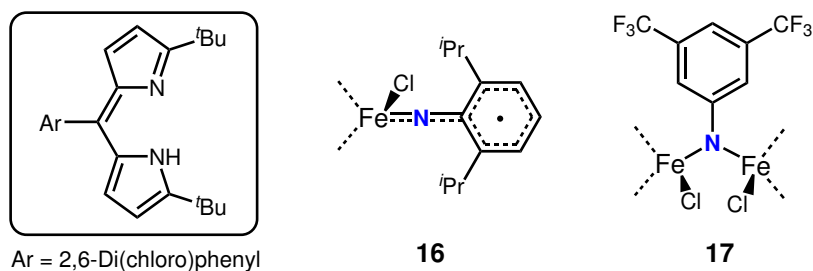


Abb. 14: Struktur des beschriebenen terminalen Imidyl-Eisen- **16** und verbrückenden Imido-Eisen-Komplexes **17**. [30]

Weitere Untersuchungen wiesen hier auf die Bildung eines terminalen Imido-Komplexes in Lösung hin. Dieser zeigt eine hohe Reaktivität zu H-Atom-Transfer, Aziridierungs-, sowie C–H-Aminierungs-Reaktionen. Eine Untersuchung der strukturellen und elektronischen Eigenschaften war auf Grund der Dimerisierung nicht möglich. [30]

Um den Einfluss der Oxidationsstufe des Zentral-Atoms auf die Reaktivität der Imido-Komplexe zu veranschaulichen, wurde die Reduktion der Dipyrromethen-Eisen(II)-Komplexe untersucht (vgl. Abb. 15).

Durch Umsetzung mit  $KC_8$  konnte der Chlorido-Ligand reaktiv abgespalten und im Fall des Aryl-substituierten Komplexes der Eisen(I)-Komplex **18** erhalten werden. Die Koordinationssphäre des Eisen-Ions wird dabei durch Wechselwirkungen mit den *ortho*-Phenyl-Gruppen des Liganden abgesättigt.

Durch dessen Umsetzung mit Adamantyl- und Mesityl-Azid, konnten die trigonalen Imido-Eisen(III)-Komplexe **19** und **20** erhalten werden. Spektroskopische Untersuchungen und quantenchemische Berechnungen zeigten in beiden Fällen einen Sextett-Grundzustand. Weiterhin konnte ein H-Atom-Transfer von 1,4-CHD beobachtet werden, wobei der Adamantyl-Komplex **19** darüber hinaus die C–H-Aminierung von Toluol durchführen kann. [31]

Um schließlich den Einfluss der Bindungssituation des Imido-Liganden auf die Reak-

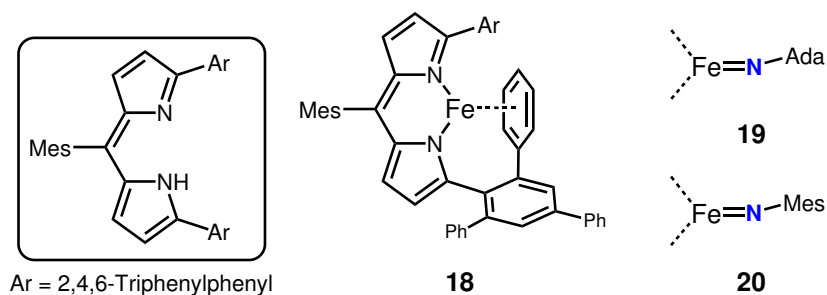


Abb. 15: Struktur des Metall(I)-Komplexes **18**, sowie des Adamantyl-Imido- **19** und Mesityl-Imido-Komplexes **20**. [31]

tivität für C–H-Aminierungen zu untersuchen, wurde der Imidyl-Eisen(III)-Komplex **14** und der Imido-Eisen(III)-Komplex **19** gewählt (vgl. Abb. 16).

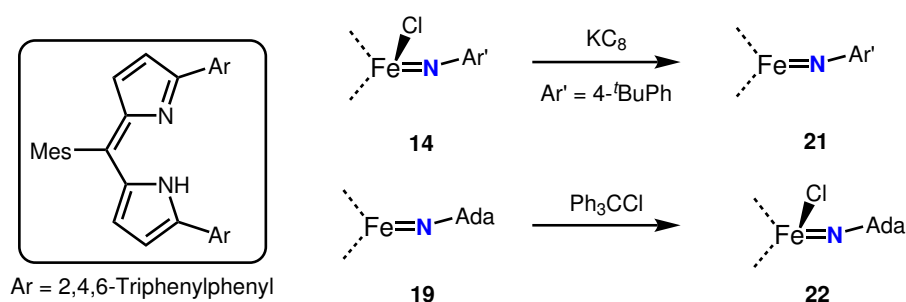


Abb. 16: Reduktion des Imidyl-Eisen(III)-Komplexes **14** unter Bildung des Imido-Eisen(III)-Komplexes **21** und Oxidation des Imido-Eisen **19** unter Bildung des Imidyl-Eisen(III)-Komplexes **22**. [31]

Durch Reduktion, bzw. Oxidation, konnte der entsprechenden Imido- oder Imidyl-Komplex dargestellt werden. Bei Vergleich der C–H-Aminierung von Toluol durch die diversen Komplexe, konnte eine höhere Reaktivität der Imidyl-Komplexe (**14/22**) festgestellt werden. Weiterhin zeigten die Adamantyl-Komplexe eine höhere Reaktivität, als die Aryl-Derivate, was auf eine Delokalisierung der Spin-, bzw. Elektronendichte auf das aromatische System, zurückgeführt wurde. [31, 32]

Weitere Untersuchungen zu H-Atom-Transfer-Reaktion von Imido-Eisen-Komplexen wurden in der Gruppe um SMITH durchgeführt (vgl. Abb. 17).

Durch Reduktion des Imido-Eisen(III)-Komplexes **23** in Anwesenheit von 18c6 konnte der anionische Imido-Komplex **24** erhalten werden. Dieser zeigte zunächst einen nukleophilen Charakter des Imido-Liganden durch eine Guanidierung von Di-*iso*-propylcarbodiimid. Weiterhin konnte die H-Atom-Abstraktion von 1,4-CHD beschrieben werden. Um den Einfluss des Kations auf das Reaktionsverhalten zu untersuchen, wurde die Reduktion von **23** mit verschiedenen Alkalimetallen durchgeführt. Die erhaltenen Komplexe (M = Li: **25**, Na: **26**, K: **27**) zeigten eine Aufweitung der Imido-Metall-Bindung mit Abnahme des Ionenradius des Kations (**25** > **26** > **27**), und auch im Vergleich zu dem ionischen Komplex **24**. Dazu korreliert eine Zunahme der Basizität des Imido-Liganden. Die Umsetzung mit 1,4-CHD zeigt eine starke Abnahme der Reaktivität, bis hin zu einer vollständigen Hemmung im Fall von **25** für die formal neutralen Komplexe. Dies wird auf die Blockierung des Imido-Stickstoff-Atoms durch die LEWIS-Aziden Alkalimetall-Kationen zurückgeführt. [33, 34]

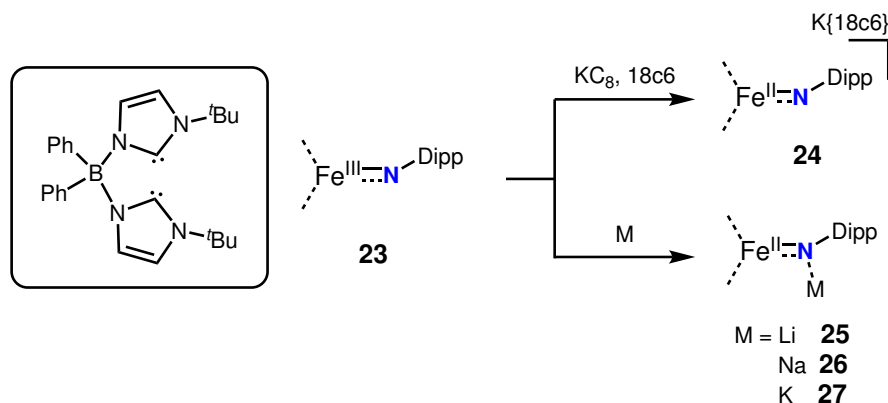


Abb. 17: Struktur des Imido-Eisen(III)-Komplexes (**23**), Reduktion dessen durch verschiedene Alkalimetalle und Struktur der erhaltenen Imido-Eisen(II)-Komplexe.[33, 34]

Kürzlich berichtete die Arbeitsgruppe um LIN von der Synthese eines trigonalen Imido-Komplexes, ausgehend von dem zweifach koordinierten Eisen(II)-Komplex **28** (vgl. Abb. 18).

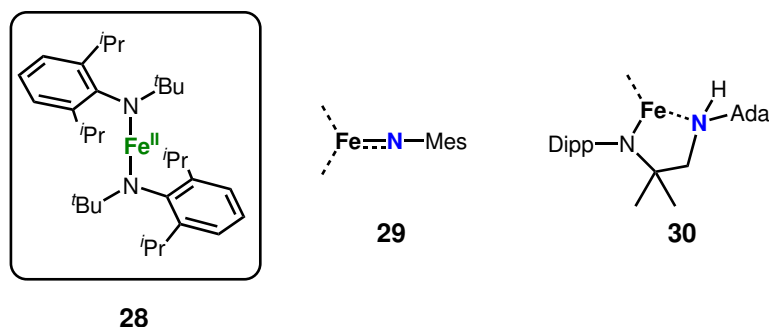


Abb. 18: Struktur des zweifachkoordinierten Eisen(II)- **28**, des trigonalen Imidyl-Eisen(III)-Komplexes **29**, sowie des Insertionsproduktes des Adamantyl-Imido-Komplexes **30**.[35]

Die Umsetzung mit Mesitylazid führte zur Isolation des trigonalen Imido-Eisen-Komplexes **29**. Die Struktur des Komplexes zeigte eine ungewöhnlich lange Imido-Metall-Bindung (Fe–N: 1,761(1) Å), sowie eine Änderungen der Bindungslängen im aromatischen Ring auf. Durch weitere spektroskopische und quantenchemische Untersuchungen konnte ein Imidyl-Charakter des Liganden nachgewiesen werden. Die Umsetzung mit Adamantylazid führte zur Isolation des Komplexes **30**, welcher das Produkt einer intramolekularen C–H-Aminierung durch einen transienten Imido-Komplex ist.[35]

## Synthese und Reaktivität von Imido-Cobalt-Komplexen

Erste terminale Imido-Cobalt-Komplexe sind bereits seit Beginn der 2000er Jahre bekannt. Die dargestellten tetraedrischen Komplexe zeigten eine *low-spin* Konfiguration, sowie eine geringe Reaktivität auf (vgl. Abb. 19).

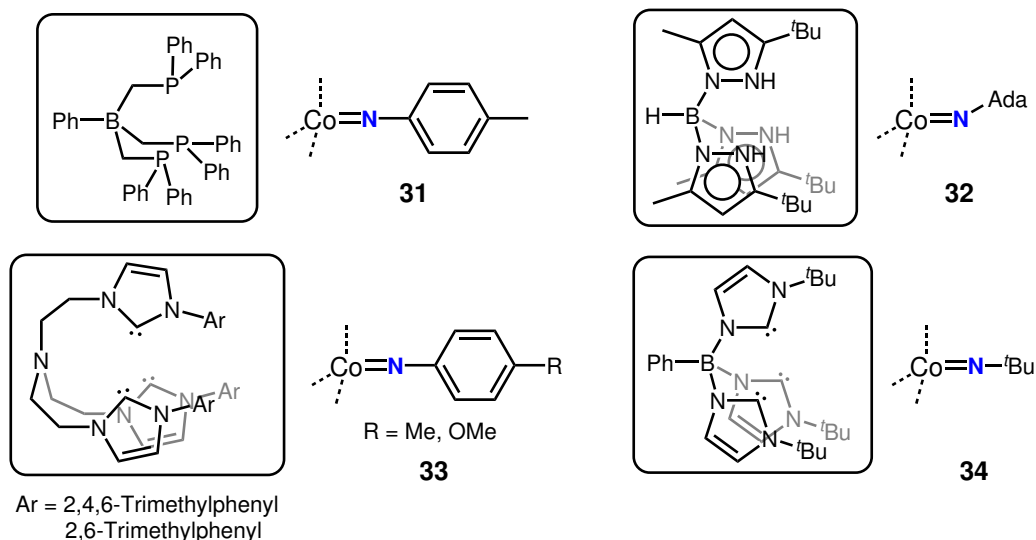


Abb. 19: Tetraedrische Imido-Cobalt-Komplexe der Gruppe um PETERS **31**, THEOPOLD **32**, MEYER **33**, SMITH **34**. [15, 36–39]

Bei erhöhter Temperatur konnte PETERS für **31** einen Nitren-Transfer auf CO unter Bildung eines Isocyanates beobachten, wohingegen der Komplex **32** von THEOPOLD eine intramolekulare C–H-Aminierung zeigt. [15, 36–39] Der in der Gruppe um MEYER dargestellte Komplex **33** zeigte eine Insertion des Nitren-Fragmentes in eine Cobalt-Carben-Bindung des Ligandenrückgrates. [40] Hervorzuheben ist hier die Darstellung des Imido-Cobalt-Komplexes **34**, welcher durch eine H-Atom-Abstraktion aus einem Amido-Komplex erhalten wurde, was dessen geringe Reaktivität verdeutlicht. [41]

Arbeiten der Gruppe um WARREN untersuchten die Verwendung eines Cobalt(I)-NacNac-Komplexes als Vorstufe für die Synthese von Imido-Komplexen (vgl. Abb. 20).

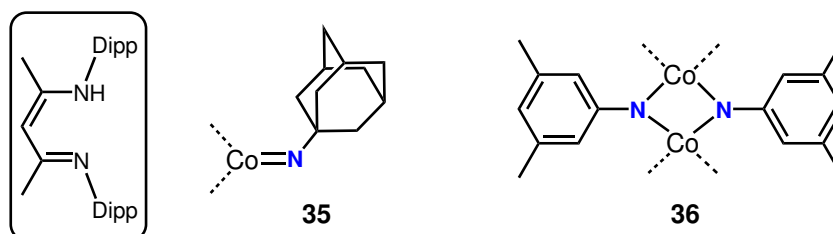


Abb. 20: Struktur des terminale Adamantyl-Imido- **35** und verbrückenden Aryl-Imido-Cobalt-Komplexes **36**. [42]

Der aus der Umsetzung mit Adamantylazid erhaltene Komplex **35** zeigt im Vergleich zu dem Eisen-Derivat **3** eine gewinkelte Anordnung des Imido-Liganden (M–N–Ada: Fe (**3**): 170,4 °; Co (**35**): 161,5 °). Die beobachtete geringe Reaktivität des Komplexes, wird auf die *low-spin* Elektronenkonfiguration und eine daraus resultierende hohe Bindungsordnung in dem 16-Elektronen-Komplex zurückgeführt. Die

Verwendung des sterisch weniger anspruchsvollen 1-Azido-3,5-Dimethylbenzol führte zu einer Dimerisierung unter Bildung des Imido-Komplexes **36**. Das magnetische Moment ( $\mu_{eff}$ ) bei Raumtemperatur von  $8,8 \mu_B$  deutet auf zwei *high-spin* Cobalt-Zentren hin, die keinerlei Wechselwirkung miteinander aufweisen. Untersuchungen zur Reaktivität des verbrückenden Komplexes **36** wurden nicht weiter verfolgt.[42] Äquivalent zu dem zuvor beschriebenen Eisen(I)-Komplex **18** wurde weiterführend die Darstellung von Imido-Cobalt-Komplexen ausgehend von einem zweifach koordinierten Cobalt(I)-Komplex untersucht (vgl. Abb. 21).

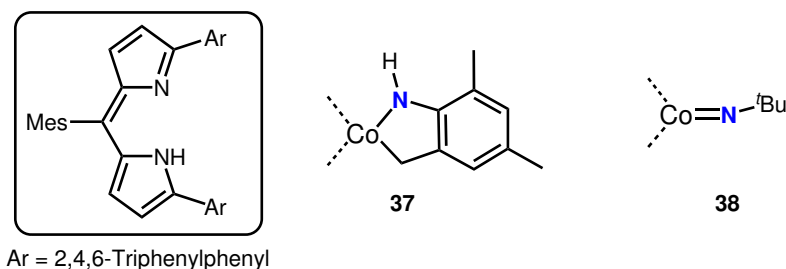


Abb. 21: Struktur des aus der Umsetzung mit Mesitylazid erhaltenen Komplexes **37** und des trigonalen Imido-Cobalt(III)-Komplexes **38**. [43]

Bei der Umsetzung mit Mesitylazid konnte erneut eine intramolekulare H-Atom-Abstraktion von einer *ortho*-Methylgruppe, gefolgt von einer C–Co-Bindungsknüpfung unter Bildung von **37**, beobachtet werden. Die Verwendung von *tert*-Butylazid hingegen ermöglichte die Isolation des trigonalen Imido-Cobalt(III)-Komplexes **38**. Auffällig ist eine nahezu lineare Koordination des Imido-Liganden (Co–N–C:  $177,6^\circ$ ), was durch den hohen sterischen Anspruch des Dipyrromethen-Liganden hervorgerufen werden könnte. Untersuchungen des Reaktionsverhaltens zeigten einen Nitren-Transfer auf  $\text{PMe}_2\text{Ph}$ , während keinerlei H-Atom-Transfer-Reaktivität festgestellt werden konnte. Temperaturabhängige magnetische Messungen von **38** zeigten bei Raumtemperatur einen *spin-crossover* von einem Singulett-Grundzustand in einen angeregten Quintett-Zustand. Entsprechende Untersuchungen für den *in situ* beobachteten Aryl-Imido-Komplex, deuteten auf einen Triplett-Grundzustand des Komplexes hin. Somit konnte hier ein Zusammenhang der elektronischen Struktur von offenschaligen Übergangsmetall-Ionen und der Bindungssituation von Imido-Liganden gezeigt werden.[43]

Um die Koordinationszahl am Zentralatom weiter zu verringern, wurden Cobalt(0)-Komplexe mit sterisch anspruchsvollen N-heterocyclischen Carbenen (IPr) als Vorstufe zur Synthese von Imido-Komplexen untersucht (vgl. Abb. 22).

Der so erhaltene linear koordinierte Imido-Cobalt-Komplex **39** weist einen Quartett-Grundzustand, sowie eine geringe Stabilität bei Raumtemperatur auf. Die Festkörperstruktur zeigt eine Aufweitung der Imido-Cobalt-Bindung (Co–N<sub>Imido</sub>:  $1.691(6) \text{ \AA}$ ), was mit der quantenchemisch bestimmten, erniedrigten Bindungsordnung (MAYER-Bindungsordnung: Co–N<sub>Imido</sub>: 1,55) übereinstimmt. Trotz des hohen sterischen Anspruchs des Imido-Liganden, erfolgte eine Nitren-Übertragung auf Kohlenstoffmonoxid, die Aminierung von Ethen, eine 1,2-Addition mit Silanen und die Deprotonierung von terminalen Alkinen.[44]

Durch Austausch des NHC-Liganden gegen das gesättigte Derivat (SIPr), konnten einzelmolekulartige Eigenschaften in Form einer Barrier für die verlangsamte magnetische Relaxation ( $U_{eff}$ :  $413 \text{ cm}^{-1}$ ) festgestellt werden.[45]

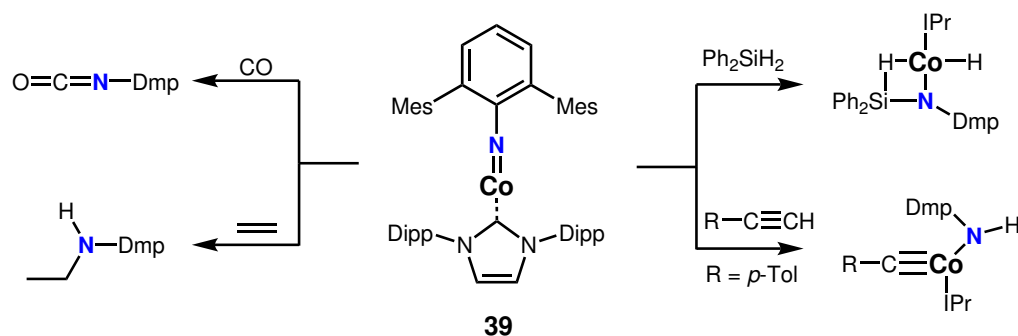


Abb. 22: Struktur und Reaktionsverhalten des linear koordinierten Imido-Cobalt-Komplexes **39**. [44, 45]

Weiter wurde in der Gruppe um MINDIOLA die Umsetzung von Adamantylazid mit einem Cobalt(II)-Komplex mit dreizähligen Chelatliganden untersucht (vgl. Abb. 23). Zunächst konnte die Bildung eines Addukt-Komplexes **40** über das  $\alpha$ -Stickstoff-Atom beobachtet werden.

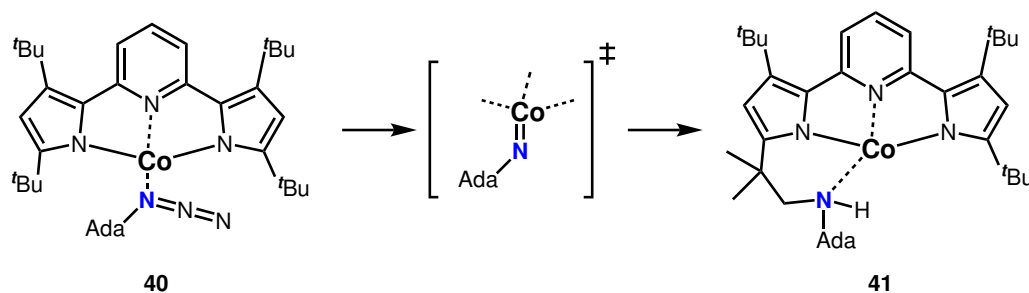


Abb. 23: Struktur des Azido-Komplexes **40** und Produkt der intramolekularen C-H-Aminierung **41**. [46]

Bereits bei Raumtemperatur zeigte sich die Bildung eines intermediären Imido-Komplexes, welcher umgehend eine C-H-Bindung des Chelatliganden unter Bildung von **41** inseriert. Dies verdeutlicht erneut die hohe Reaktivität von Imido-Cobalt-Komplexen. [46]

Die Gruppe um DENG nutzte weiterhin einen tetragonal koordinierten Cobalt(0)-Komplex zur Synthese von Imido-Komplexen (vgl. Abb. 24). Bei der Umsetzung mit Dippazid konnte neben dem tetraedrisch koordinierten Cobalt-Komplex **42** auch die Bildung eines Iminophosphanes beobachtet werden. [47]

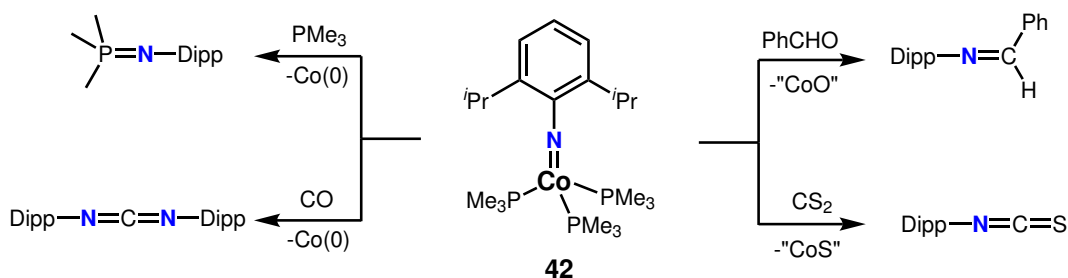


Abb. 24: Struktur und Reaktionsverhalten des tetraedrisch koordinierten Imido-Cobalt-Komplexes **42**. [47]

Die Spektroskopische Analyse der Bindungssituation zeigt klassische Eigenschaften eines Cobalt(II)-Ions. Durch quantenchemische Rechnungen konnte weiterhin ein geringer Imidyl-Charakter beobachtet werden. Untersuchungen zur Reaktivität zeigten ein amphiphiles Verhalten mit Nitren-Transfer-Reaktionen gegenüber Phosphinen sowie Kohlenstoffmonoxid. Weiterhin konnten Austauschreaktionen mit Sauerstoff- und Schwefel-Quellen unter Übertragung des Nitren-Liganden beobachtet werden.[47] Zum Vergleich wurden in der Gruppe um BETLEY die Umsetzung von Cobalt(II)-Komplexen mit Organoaziden untersucht. Hier konnte zunächst eine Koordination über das  $\alpha$ -Stickstoff-Atom des Azides an das Cobalt-Ion unter Bildung von **43** beobachtet werden (vgl. Abb. 25).

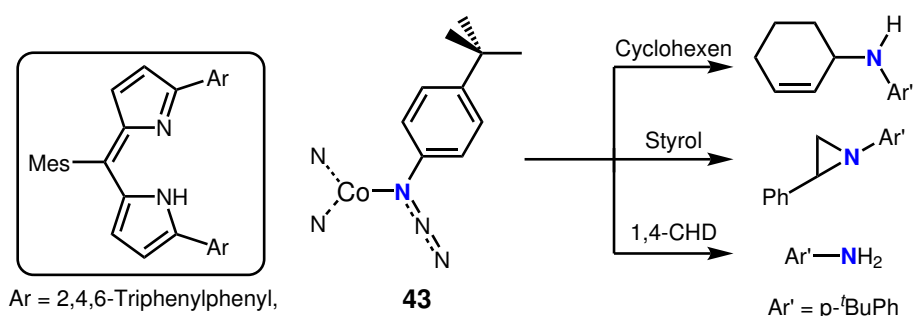


Abb. 25: Struktur und Reaktionsverhalten des Azido-Cobalt-Komplexes **43**. [48]

Für die Verwendung von *para-tert*-Butylphenylazid konnte durch entsprechende Umsetzungen H-Atom-Abstraktionen, C-H-Aminierungen sowie eine Aziridierung gezeigt werden. Die Bildung des Imido-Komplexes, unter Abspaltung von  $N_2$ , konnte dabei auch im Einkristall durch Thermolyse beobachtet werden.[48]

Weiterführend wurden Umsetzungen mit langkettigen aliphatischen Aziden durchgeführt, wobei sowohl die Isolierung von terminalen Imido-Komplexen, als auch eine Zyklisierung durch C-H-Aminierung bei höheren Temperaturen, möglich war (vgl. Abb. 26).

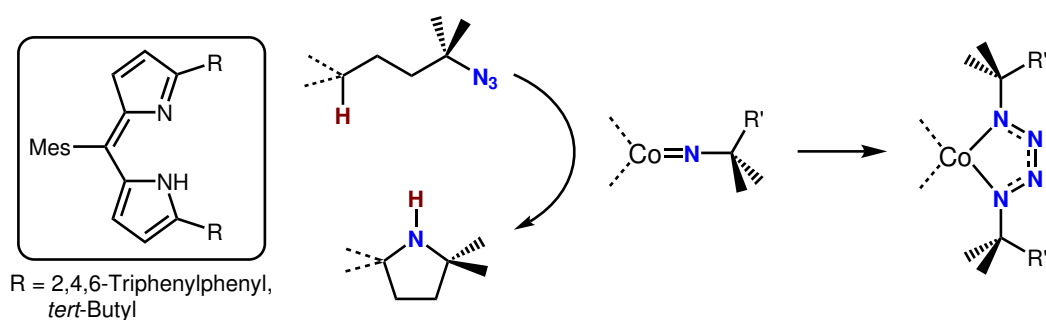


Abb. 26: Zyklisierung von langkettigen Aziden über Imido-Cobalt-Komplexe und Bildung von Tetrazen-Komplexen als Konkurrenzreaktion. [48–50]

Die Reaktion unter katalytischen Bedingungen zeigte die langsame Bildung eines inaktiven Tetrazen-Komplexes, wobei die Zyklisierung bei erhöhten Temperaturen bevorzugt war. Kinetische Untersuchungen ergaben, dass die C-H-Aktivierung der geschwindigkeitsbestimmende Schritt der Reaktion ist. Durch die Zugabe von Pyridin konnte die Bildung des Tetrazen-Komplexes verringert werden, indem die freie Koordinationsstelle des Cobalt-Ions blockiert wurde. Untersuchungen zur elektroni-

schen Struktur ließen für das *in situ* beobachtete Pyridin-Addukt eine höhere Spinmultiplizität des Grundzustandes vermuten, was die höhere Reaktivität erklären könnte. Weiterhin zeigten DFT-Rechnungen, dass der Pyridin-Komplex eine bessere Übereinstimmung mit dem Übergangszustand der H-Atom-Abstraktion zeigt, was die Reaktion weiter begünstigt.[48–50]

Der erste isolierbare, quadratisch planare Imido-Cobalt-Komplex **44**, konnte von der Gruppe um CHIRIK in 2021 dargestellt werden (vgl. Abb. 27). Hier konnte eine nahezu lineare Koordination des Imido-Liganden beobachtet werden, und quantenchemische Rechnungen bestätigten den vermuteten Imidyl-Charakter des Komplexes.[51]

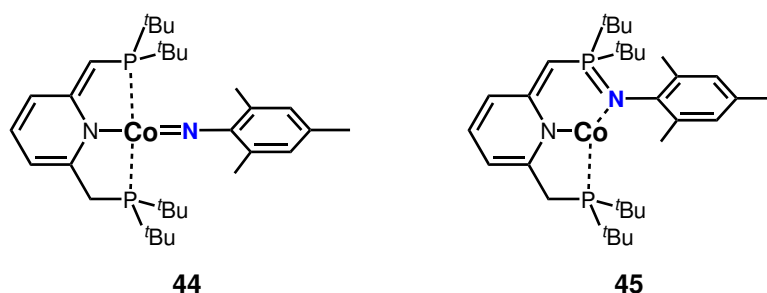


Abb. 27: Struktur des Imidyl-Cobalt-Komplexes **44** und Produkt der Insertion in die Posphor-Cobalt-Bindung **45**. [51]

Bei erhöhter Temperatur konnte die Insertion des Imido-Liganden in eine Metall-Phosphor-Bindung des Co-Liganden unter Bildung von **45** beobachtet werden.[51] Weiterführende Arbeiten in der Gruppe von MEYER an einer Variation des bereits vorgestellten Ligandensystem (vgl. Abb. 19 **33**) erlaubten einen genauen Einblick in die Bindungssituation von verschiedenen Imido-Cobalt-Komplexen (vgl. Abb. 28).[52, 53]

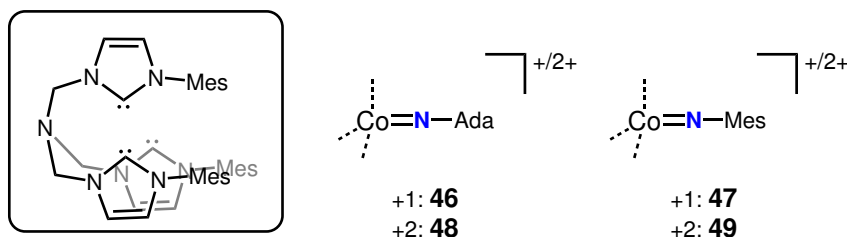


Abb. 28: Struktur der Imido-Cobalt(III)- (R = Ada: **46**, R = Mesityl: **47**) und Imido-Cobalt(IV)-Komplexe (R = Ada: **48**, R = Mesityl: **49**) der Gruppe um MEYER.[52]

Ausgehend von einem Cobalt(I)-Komplex, konnten zwei terminaler Imido-Cobalt(III)-Komplex (R = Ada: **46**, R = Mesityl: **47**) in einer *low-spin* Elektronenkonfiguration erhalten werden. Durch Oxidation konnten diese in Imido-Cobalt(IV)-Komplexe (R = Ada: **48**, R = Mesityl: **49**) überführt werden, die ebenfalls eine *low-spin* Konfiguration aufweist. Neben einer ausführlichen spektroskopischen Untersuchung, wurden verschiedene quantenchemische Modelle zur Beschreibung der Imido-Cobalt-Bindung herangezogen. Diese Kombination zeigte eine klassische Imido-Bindungssituation mit einem hohen Anteil eines Triplett-Nitren-Komplexes für **48**. [52]

Im Vergleich dazu wurde für den oxidierten Mesityl-Imido-Komplex **49** die Besetzung eines antibindenden  $\pi$ -Orbitals und damit eine Imidyl-Bindungssituation



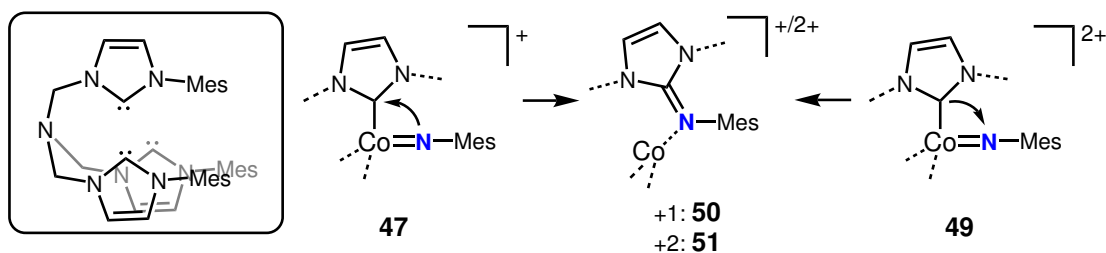


Abb. 29: Konträre Reaktionspfade für die Insertion in die Carben-Cobalt-Bindung und Struktur der gebildeten Produkte **50/51**.<sup>[53]</sup>

beobachtet. Die Isolation eines Imido/Imidyl-Redox-Paares ermöglichte weiterhin einen Vergleich der Reaktivität zu Nitren-Transfer-Reaktionen. Eine Insertion in eine Carben-Metall-Bindung des Ligandenrückgrats konnte in beiden Fällen beobachtet werden. Der Imidyl-Komplex **49** zeigt diese bereits bei tiefen Temperaturen und auch im Festkörper, während der Imido-Komplex **47** unter diesen Bedingungen stabil ist. Mechanistische Untersuchungen deuten hier auf konträre Reaktionsverläufe, in Form eines nukleophilen Angriffes des Imido-Liganden an einen elektrophilen NHC-Ligand hin, während für den Imidyl-Komplex **49** ein nukleophiler Angriff des NHC-Liganden an den Imidyl-Liganden beobachtet wird (vgl. Abb. 29). Somit konnte durch Oxidation eine Umpolung des Reaktionsverhaltens des Imido-Liganden herbeigeführt werden.<sup>[53]</sup>

### Synthese und Reaktivität von Imido-Nickel-Komplexen

Die Darstellung und Reaktivität von Imido-Nickel-Komplexen wurde unter anderem in der Gruppe von HILLHOUSE untersucht. Die Synthese einer Reihe terminaler Imido-Nickel-Komplexe erfolgte sowohl durch Umsetzung eines Nickel(0)-Komplexes mit organischen Aziden, als auch durch Deprotonierung eines Amido-Nickel(II)-Komplexes (vgl. Abb. 30).<sup>[54–59]</sup>

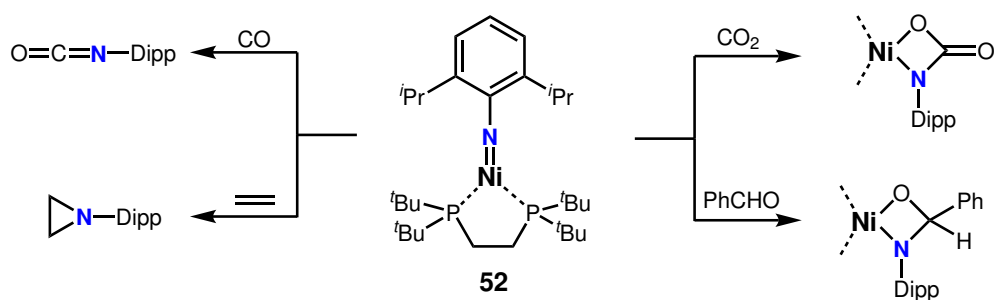


Abb. 30: Struktur und Reaktivität des trigonalen Imido-Nickel(II)-Komplexes **52**.<sup>[60]</sup>

Untersuchungen des Dipp-Imido-Komplexes **52** zeigten neben Aziridierungen und Nitren-Transfer auf CO eine nukleophile Reaktivität mit CO<sub>2</sub> und Aldehyden.<sup>[60]</sup> Weitere Arbeiten mit NacNac-Nickel-Komplexen ermöglichten die Isolation eines terminalen Adamantyl-Imido-Komplexes **53** sowie eines einfach Imido-verbrückenden dinuklearen Komplexes **54** (vgl. Abb. 31).<sup>[42]</sup>

Durch Elektronenspinresonanz-Spektroskopie konnte eine *low-spin* Konfiguration ( $S = 1/2$ ) für **53** bestätigt werden. Weiterhin deutete die beobachtete Aufspaltung des

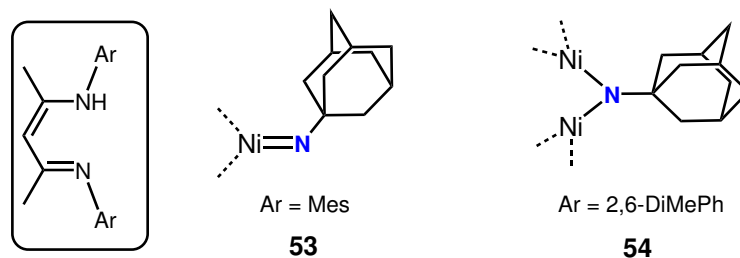


Abb. 31: Struktur des terminale **53** und verbrückenden Adamantyl-Imido-Nickel-Komplexes **54**.<sup>[42]</sup>

Signales zu einem Triplett auf eine starke Wechselwirkung mit einem Stickstoff-Atom ( $^{14}\text{N}$ ,  $I = 1$ ) hin. Mittels quantenchemischen Berechnungen konnte eine hohe Spindichte (57%) auf dem Imido-Stickstoff-Atom bestätigt werden. Aus diesen Gründen wird angedeutet, dass es sich bei dem Komplex um einen radikalischen Imidyl-Komplex handeln könnte. Vergleichbar zu dem beschriebene Eisen-Komplex (vgl. Abb. 7) konnte eine hohe Reaktivität gegenüber Nitren-Transfer-Reaktionen auf elektronenreiche Substrate (CO,  $\text{CN}^t\text{Bu}$ ,  $\text{PMe}_3$ ), aber auch H-Atom Transfer Reaktionen, beobachtet werden.<sup>[61]</sup>

Die Verwendung von Dippazid führt bei der Umsetzung mit einem NacNac-Nickel(I)-Komplex zu einer Dimerisierung über C–C-Bindungsknüpfung (**55**) in *para*-Position (vgl. Abb. 32).<sup>[62]</sup>

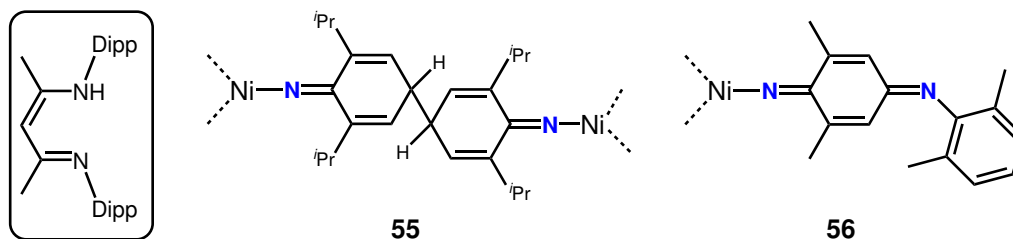


Abb. 32: Produkte der C–C- **55** und C–N-Bindungsknüpfung **56** durch intermediäre Imido-Nickel-Komplexe.<sup>[62]</sup>

Für den Komplex mit Methyl-Gruppen in *ortho*-Position findet eine C–N-Bindungsknüpfung in *para*-Position, unter Abspaltung von elementarem Wasserstoff, statt. Als reaktive Zwischenstufe wird in beiden Fällen ein terminaler Imido-Komplex postuliert, welcher auf Grund einer hohen Lokalisierung von Spindichte auf den aromatischen Liganden die genannten Folgereaktivität zeigt.<sup>[62]</sup>

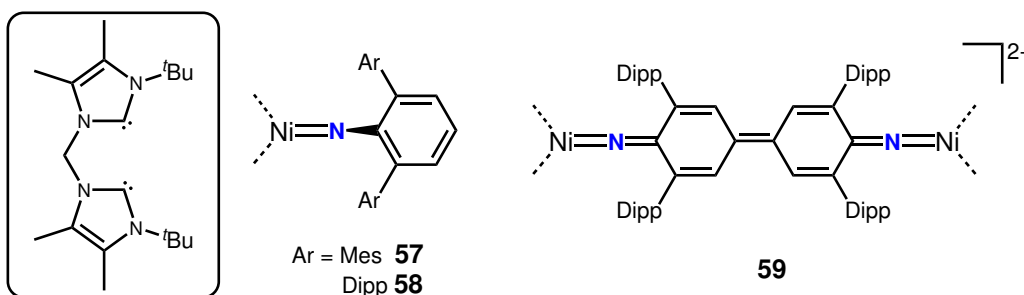


Abb. 33: Struktur der gewinkelten Imido-Nickel-Komplexes **57/58** und des gekoppelten Komplexes **59**.<sup>[63]</sup>

Die Verwendung eines chelatisierenden *N*-heterocyclischen Carben-Nickel(0)-Komplexes ermöglichte HILLHOUSE die Darstellung von stark gewinkelten Imido-Nickel-Komplexen (**57/58**) (vgl. Abb. 33).[63] Versuche, die Komplexe zu oxidieren, führten im Fall von **58** zu einer Dimerisierung über eine C–C-Bindungsknüpfung in *para*-Position und unter Abspaltung von elementarem Wasserstoff (**59**).[63]

In der Gruppe um BETLEY wurde ein Nickel(I)-Komplex mit Dipyrromethen-Liganden zur Synthese von Imido-Nickel-Komplexen genutzt (vgl. Abb. 34).

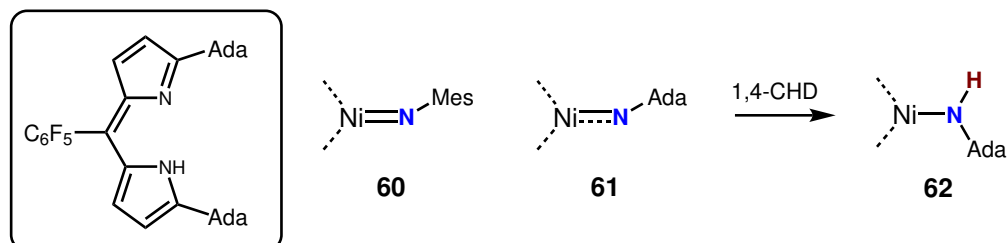


Abb. 34: Struktur des dargestellten Mesityl-Imido- **60** und Adamantyl-Imidyl-Nickel-Komplexes **61** und Bildung des Amido-Nickel-Komplexes **62**. [64]

Eine spektroskopische und quantenchemische Untersuchung zeigte, dass die Bindungssituation des erhaltenen Mesityl-Komplexes **60** zwischen einem klassischen Imido- und einem radikalischen Imidyl-Komplex liegt. Für den Adamantyl-Komplex **61** konnte eine höhere Konzentration der Spindichte auf dem Imido-Stickstoff-Atom beobachtet werden. Außerdem ist dieser Komplex in der Lage, eine H-Atom-Abstraktion von 1,4-CHD unter Bildung des entsprechenden Amido-Komplexes **62** durchzuführen.[64]

Weiterhin konnte gezeigt werden, dass der als Präkursor verwendete Nickel(I)-Komplex als Katalysator für eine C–H Aminierung unter Zyklisierung genutzt werden kann.[65]

Unter Nutzung des chiralen Bisoxazolin-Liganden (BOX) konnte ein weiterer Adamantyl-Imidyl-Komplex **63** dargestellt werden (vgl. Abb. 35).

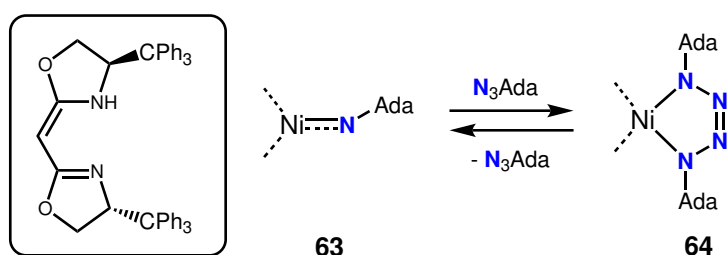


Abb. 35: Struktur des Imidyl-Nickel-Komplexes **63** und reversible Bildung des Tetrazen-Komplexes **64** mit BOX-Liganden.[66]

Auf Grund der reversiblen Bildung eines Tetrazen-Komplexes **64** in Anwesenheit von freiem Adamantylazid, wurde das Reaktionsverhalten nicht weiter untersucht.[66]

Weiterhin ist der Nickel(I)-Komplex auf Grund des chiralen Ligandensystems dazu in der Lage, langkettige aliphatische Azide mit einer hohen Enantioselektivität zu zyklisieren. Die reversible Bildung eines Tetrazen-Liganden kann auch hier als Konkurrenz-Reaktion beobachtet werden, was die Aktivität des Katalysators verringert.[66]

## Zusammenfassung

Die Zahl an isolierbaren, aber dennoch reaktiven Imido-Komplexen der späten Übergangsmetalle hat in den letzten Jahren stark zugenommen und damit einen immer genaueren Einblick in die Imido-Metall-Bindungssituation erlaubt. Die Kombination von spektroskopischen und quantenchemischen Methoden zeigte dabei einen deutlich komplexeren Einfluss des Übergangsmetall-Ions sowie des Ligandenrückgrates auf das Bindungs- und damit auch Reaktionsverhalten der Imido-Komplexe auf.

## 1.5 Vorstufen zur Darstellung von Imido-Komplexen

Die ersten isolierten Imido-Komplexe konnten nur auf Grund sterisch anspruchsvoller Ligandensysteme isoliert werden. Daraus resultierte eine geringe Reaktivität, welche auch in Zusammenhang mit einer *low-spin* Konfiguration der Komplexe gebracht wird. Die zuvor gezeigten Beispiele für reaktive Imido-Übergangsmetall-Komplexe weisen eine geringe Koordinationszahl auf, was in den meisten Fällen mit einer *high-spin* Elektronenkonfiguration einhergeht.

Die Imido-Komplexe werden dabei durch den hohen sterischen Anspruch sowie den chelatisierenden Bindungsmodus des Ligandenrückrates stabilisiert. Letzterer schränkt Folgereaktionen über eine Dissoziation des Co-Liganden ein, allerdings wird die Koordinationsgeometrie des Imido-Komplexes stark durch den Bisswinkel des Chelatliganden beeinflusst. Eine so eingeschränkte Reorganisation des Systems könnte sich negativ auf die Reaktivität der Imido-Komplexe auswirken. Um dies zu verhindern sollen im Folgenden lineare Übergangsmetall-Komplexe mit monodentaten Liganden vorgestellt werden.

### Niedrig koordinierte Übergangsmetall-Komplexe mit monodentaten Liganden

Seit der Definition der Koordinationschemie durch WERNER in den 1890er Jahren prägen oktaedrische (KZ = 6), tetraedrische oder quadratisch planare (KZ = 4) Komplexe das Bild dieser Chemie.[67]

Bereits in den 1960er Jahren wurde durch die Verwendung von verschiedenen Ligandensystemen versucht, Komplexe mit einer geringeren Koordinationszahl darzustellen.[68] In diesem Zusammenhang wurde auch von BÜRGER und WANNGAT erstmals der sterisch anspruchsvollen Hexamethyldisilylamido-Ligand ( $N(SiMe_3)_2$ -Ligand) verwendet (vgl. Abb. 36).

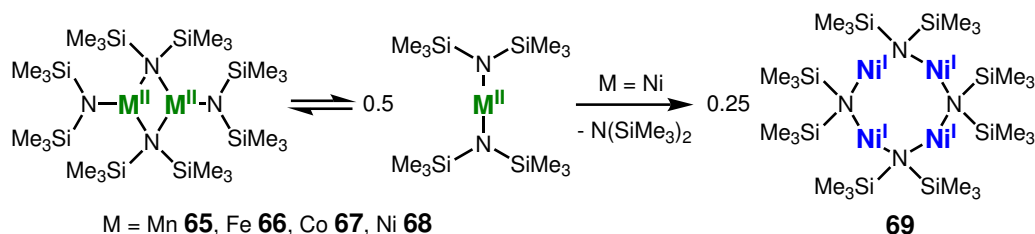


Abb. 36: Struktur der dimeren und monomeren Metall(II)- $N(SiMe_3)_2$ -Komplex (Mn **65**, Fe **66**, Co **67**, Ni **68**) und Zersetzung des Nickel(II)- $N(SiMe_3)_2$ -Komplexes unter Bildung des tetrameren Nickel(I)-Komplexes **69**. [69–72]

Dabei wurde zunächst die Synthese des Mangan(II)- **65**, Cobalt(II)- **67** und Nickel(II)-Komplexes **68** beschrieben, wobei die hohe Empfindlichkeit, vor allem der letzten Verbindung, hervorgehoben wurde.[73, 74]

Die Synthese des entsprechenden Eisen(II)-Komplexes **66** konnte schließlich 1988 von der Gruppe von RYPDAL erstmals durchgeführt werden.[75]

Die Aufklärung der Festkörperstruktur für die genannten Komplexe zeigte die Bildung eines Dimers, wohingegen in der Gasphase dessen monomere Form nachgewiesen werden konnte.[69–71, 75] Untersuchungen des Cobalt-Komplexes in Lösung zeigten ein Gleichgewicht zwischen beiden Formen in unpolaren Lösungsmitteln, während bei Zugabe von LEWIS basischen Lösungsmittel, die Bildung von trigonalen Addukt-Komplexen beobachtet wurde.[76]

Etwa 50 Jahre nach dessen erster Erwähnung, wandte sich die Gruppe um POWER erneut dem instabilen Nickel(II)- $(\text{N}(\text{SiMe}_3)_2)_2$ -Komplex zu. Hier konnte die Zersetzung unter reduktiver Eliminierung eines Amido-Liganden unter Bildung eines Tetrameren Nickel(I)- $\text{N}(\text{SiMe}_3)_2$ -Komplexes **69** als Grund für die hohe Empfindlichkeit identifiziert werden.[72]

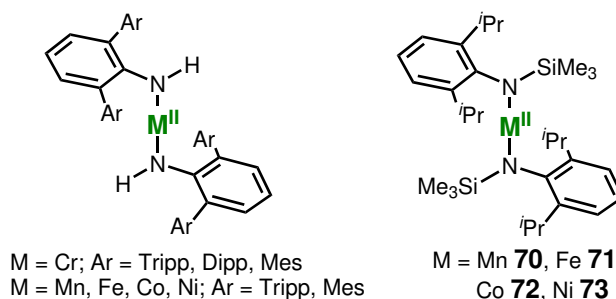


Abb. 37: Struktur der beschriebenen zweifach koordinierten primären Arylamido-Übergangsmetall(II)-Komplexe und Komplexen mit  $\text{N}(\text{Dipp})\text{SiMe}_3$ -Ligandensystem (Mn **70**, Fe **71**, Co **72**, Ni **73**).[77–82]

Die Verwendung von sterisch anspruchsvollen Arylamido-Liganden wurde erstmals durch die Gruppe um POWER untersucht (vgl. Abb. 37). Erste Ergebnisse mit sekundären Amido-Komplexen zeigten eine Wechselwirkung des Übergangsmetall-Ions mit dem *ipso*-Kohlenstoffatom der Aryl-Gruppe, um die mangelnde Koordination auszugleichen.[77–80]

Dies führte zur Entwicklung des  $\text{N}(\text{Dipp})\text{SiMe}_3$ -Ligandensystems, das auf Grund des höheren sterischen Anspruchs der  $\text{SiMe}_3$ -Gruppe die genannte Wechselwirkung verhinderte. Weiterhin konnte gezeigt werden, dass dispersive Wechselwirkungen zwischen den Liganden zur Stabilisierung der dargestellten Komplexe ( $\text{M}(\text{N}(\text{Dipp})\text{SiMe}_3)_2$ ,  $M = \text{Fe } \mathbf{71}, \text{Co } \mathbf{72}, \text{Ni } \mathbf{73}$ ) beitrugen.[81] Trotz des hohen sterischen Anspruches der Liganden, konnte in Lösung die reversible Koordination von verschiedenen LEWIS-Basen an das Zentralatom beobachtet werden. Dies macht die Komplexklasse weiterhin auch für additive Reaktionspfade interessant.[82]

Der entsprechende Mangan-Komplex **70** konnte schließlich von WERNCKE *et. al.* dargestellt werden.[83]

### 1.5.1 Monovalente zweifach-koordinierte Übergangsmetall-Komplexe

Durch die Reduktion der zuvor beschriebenen, zweifach koordinierten Metall(II)-Komplexe, konnte in den frühen 2000er Jahren erstmals monovalente, zweifach koordinierte Übergangsmetall-Komplexe dargestellt werden (vgl. Abb. 38).

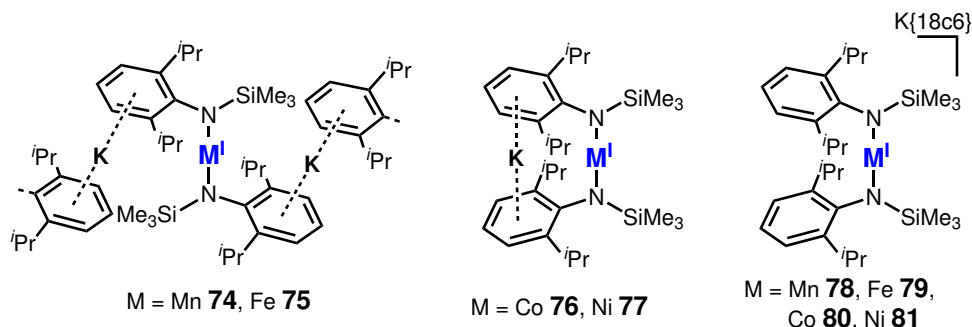


Abb. 38: Struktur der beschriebenen neutralen (Mn **74**, Fe **75**, Co **76**, Ni **77**) und anionischen Metall(I)-Komplexe (Mn **78**, Fe **79**, Co **80**, Ni **81**).[84, 85]

Erste Umsetzungen des Nickel-N(Dipp)SiMe<sub>3</sub>-Komplexes **73** mit KC<sub>8</sub> führten zu der Bildung eines formal neutralen Nickel(I)-Komplexes **77**, wobei das gebildete Kalium-Ion zwischen die Aryl-Ringe der Liganden interkaliert.[84] Die entsprechenden Komplexe mit Mangan- **74**, Eisen- **75** und Cobalt-Zentralatom **76**, konnten schließlich von WERNCKE dargestellt werden. Dabei wurde im Fall des Mangan- und Eisen-Komplexes im Festkörper eine verbrückende Koordination der Kalium-Ionen zwischen den Liganden von zwei Komplex-Ionen beobachtet.[86]

Unter Verwendung von 18-Krone-6, zur Sequestrierung des Kalium-Ions, war POWER die Darstellung von anionischen Metall(I) Komplexen mit dem N(Dipp)SiMe<sub>3</sub>-Ligandensystem (M = Fe **79**, Co **80**, Ni **81**) möglich.[85] Der entsprechende anionische Mangan(I)-Komplex **78** konnte schließlich von WERNCKE dargestellt werden. Im Zuge dessen wurde auch die Reduktion der N(SiMe<sub>3</sub>)<sub>2</sub>-Komplexe (M = Cr – Co) aufgegriffen und konnte, unter Verwendung der zuvor beschriebenen Reaktionsmittel, durchgeführt werden (vgl. Abb. 39).[83]

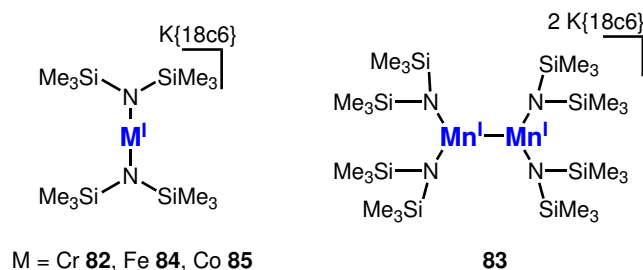


Abb. 39: Struktur der beschriebenen anionischen Metall(I)-Komplexe (Cr **82**, Mn **83**, Fe **84**, Co **85**) mit N(SiMe<sub>3</sub>)<sub>2</sub>-Ligandensystem.[83, 87]

Unabhängig von der Koordinationsumgebung der verwendeten Metall(II)-Vorstufe wurde ein linearer Metall(I)-Komplex (M = Cr **82**, Fe **84**, Co **85**) erhalten. Eine Ausnahme bildete der Mangan-Komplex **86**, da hier eine Dimerisierung unter Ausbildung einer Mn–Mn-Bindung im Festkörper stattfindet.[83, 87]

Die Untersuchung der magnetischen Eigenschaften zeigte eine *high-spin*-Konfiguration der Komplexe, was auf die geringe Koordinationszahl und die geringe Ligandenfeldaufspaltung der Amido-Liganden zurückzuführen ist. Hervorzuheben ist hier der Eisen(I)-Komplex  $K\{18c6\}[Fe(N(SiMe_3)_2)]$  (**84**), der eine Barriere zur magnetischen Relaxation ( $U_{eff} = 43 \text{ cm}^{-1}$ ) aufweist.[83, 87]

Die Reaktivität sowohl der Komplexe, als auch der Derivate mit  $K\{\text{crypt.222}\}$ -Kation, wurde in den letzten Jahren ausgiebig untersucht (vgl. Abb. 40). Dabei konnten die Aktivierung von Halogen-Kohlenstoff-Bindungen, die Ein-Elektronen-Reduktion von verschiedenen Substraten, sowie die Elementaktivierung beschrieben werden.[88–96]

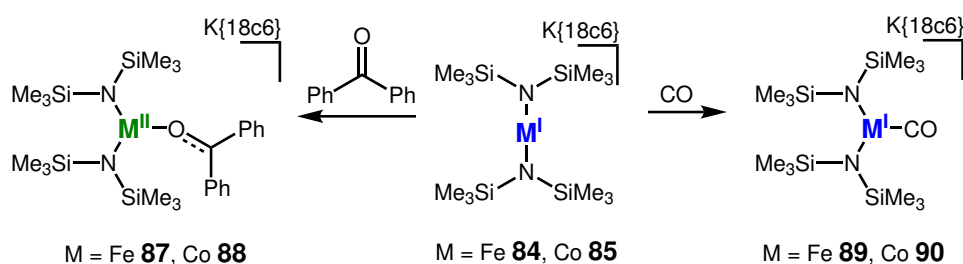


Abb. 40: Reaktivität der linear koordinierten Metall(I)-Komplexe **84/85** am Beispiel der Ein-Elektronen-Reduktion von Benzophenon unter Bildung von Ketyl-Radikal-Komplexen **87/88** (links) und Struktur der *high-spin* Carbonyl-Komplexe **89/90** (rechts). [92, 97]

Weiterhin war es möglich trigonale Carbonyl-Komplexe darzustellen, die trotz des Starkfeld-Liganden CO eine *high-spin* Konfiguration aufweisen.[97]

## 1.6 Vorarbeiten

Im Zuge meiner Masterarbeit habe ich erste Untersuchungen zu Synthese von trigonalen Imido-Übergangsmetall-Komplexen durchgeführt. Dabei wurden die zuvor beschriebenen, linear koordinierten Metall(I)-Komplexe mit Mangan-, Eisen- und Cobalt-Zentralatom als Präkusoren verwendet. Für die Reaktion mit Trimethylsilylazid konnte für die Komplexe mit  $N(\text{SiMe}_3)_2$ -Ligandensystem die Bildung eines trigonalen Komplexes mit terminalen Azido-Liganden beobachtet werden. Als Nebenprodukt wurde der Trisamido-Komplex  $K\{18c6\}[M(\text{N}(\text{SiMe}_3)_2)_3]$  ( $M = \text{Mn}$  **91**,  $\text{Fe}$  **92**,  $\text{Co}$  **93**) erhalten, was auf eine Spaltung von Trimethylsilylazid durch einen intermediären Imido-Komplex hindeutet (vgl. Abb. 41).

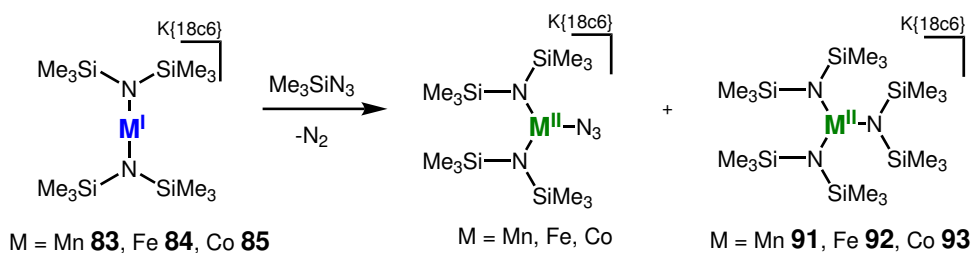


Abb. 41: Bildung von terminalen Azido und Trisamido-Komplexen durch Umsetzung von Metall(I)-Komplexen ( $\text{Mn}$  **83**,  $\text{Fe}$  **84**,  $\text{Co}$  **85**) mit Trimethylsilylazid.

Die entsprechenden Azido Komplexe konnten durch Umsetzung der zweifach koordinierten Metall(II)-Vorstufen ( $M = \text{Mn}$  **65**,  $\text{Fe}$  **66**,  $\text{Co}$  **67**) mit Kaliumazid in Anwesenheit von 18c6 unabhängig dargestellt werden.

Durchgeführte Umsetzungen von Alkylaziden ( $^t\text{BuN}_3$ ,  $\text{AdaN}_3$ ) mit  $K\{18c6\}[\text{Mn}(\text{N}(\text{SiMe}_3)_2)]$  (**83**) zeigten eine unstöchiometrische Umsetzung unter Bildung eines Tetrazen-Liganden (vgl. Abb. 42). Im Fall des sterisch weniger anspruchsvollen *tert*-Butylazid konnte weiterhin die Bildung eines Imido-Liganden sowie der Verlust eines  $\text{N}(\text{SiMe}_3)_2$ -Liganden beobachtet werden.

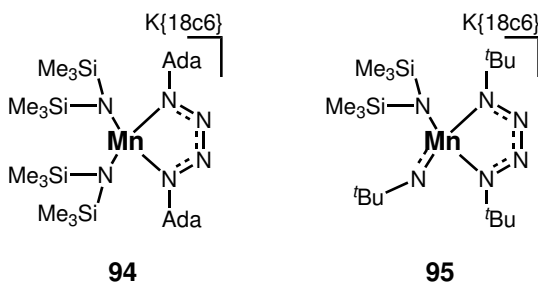


Abb. 42: Struktur der erhaltenen Tetrazen-Mangan-Komplexe mit Adamantyl- **94** und *tert*-Butyl-Substituenten **95**.

Auf Grund von unselektiven Reaktionsverläufen sowie geringen Ausbeuten wurde die Darstellung von Imido-Mangan-Komplexen nicht weiter untersucht.

Im Fall der Eisen-Komplexe wurde, neben dem  $\text{N}(\text{SiMe}_3)_2$ -Ligandensystem auch das sterisch anspruchsvollere  $\text{N}(\text{Dipp})\text{SiMe}_3$ -Ligandensystem untersucht (vgl. Abb. 43). Die Umsetzung mit *tert*-Butylazid hat hier eine intramolekular C–H-Aktivierung einer  $\text{SiMe}_3$ -Gruppe zu Folge.

Die Umsetzung mit Phenylazid führte für beide verwendeten Ligandensysteme zur Bildung der Tetrazen-Komplexe **97** und **98**. Diese weisen eine hohe Stabilität auf



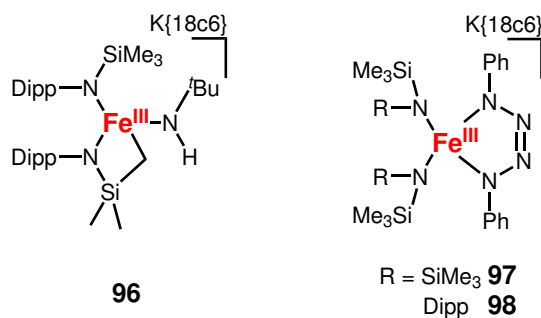


Abb. 43: Struktur des durch C–H-Aktivierung erhaltenen Eisen-Komplexes **96** und der Tetrazen-Komplexe mit N(SiMe<sub>3</sub>)<sub>2</sub>- **97** und N(Dipp)SiMe<sub>3</sub>-Liganden **98**.

und eine Rückbildung der Imido-Komplexe unter reversibler Abspaltung des Organoazides kann somit ausgeschlossen werden.

Die <sup>1</sup>H-NMR spektroskopische Reaktionskontrolle der Umsetzungen von K{18c6}-[Co(N(SiMe<sub>3</sub>)<sub>2</sub>)] (**85**) mit Alkylaziden (*t*BuN<sub>3</sub>, AdaN<sub>3</sub>) zeigten die selektive Bildung des vermuteten Imido-Komplexes, welcher sich jedoch äußerst schnell wieder zersetzt. Die erste strukturelle Untersuchung wurde im Fall des *tert*-Butyl Komplexes **99**, durch Zugabe von 4-DMAP, welches das Kalium-Kation koordinierte und somit die Kristallisation begünstigte, ermöglicht (vgl. Abb. 44).

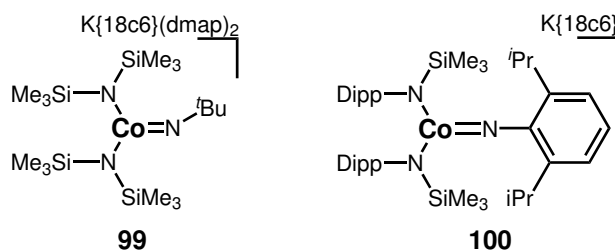


Abb. 44: Struktur der dargestellten trigonalen Alkyl-Imido-Cobalt- **99** und Aryl-Imido-Cobalt-Komplexes **100**.

Im Fall des sterisch anspruchsvolleren N(Dipp)SiMe<sub>3</sub>-Ligandensystems konnte durch Zugabe von 1-Azido-2,6-Di-*iso*-propylbenzol der trigonale Imido Komplex **100** erhalten werden. Die Molekülstruktur im Festkörper zeigte eine ungewöhnlich lange N<sub>Imido</sub>-Co-Bindung (1,751(2) Å), sowie eine lineare Koordination des Liganden (178,8(2) °). Dies ließ einen Imidyl-Charakter des Komplexes vermuten, weshalb erste ESR spektroskopische Untersuchungen durchgeführt wurden, die allerdings noch keine klare Aussage zuließen.

Zusammenfassend zeigte diese Arbeit, dass die Synthese von trigonalen Imido Komplexen für späte Übergangsmetalle, ausgehend von den linear koordinierten Metall(I) Komplexen, möglich ist. Die dargestellten Imido-Cobalt-Komplexe konnten sowohl spektroskopisch, als auch auf ihre Folgereaktivität, im Rahmen der Masterarbeit nicht genauer untersucht werden.

## 2 Zielsetzung und Motivation

Die Aufklärung der Bindungssituation in reaktiven Imido-Komplexen der späten Übergangsstelle ist in den letzten Jahren stark vorangeschritten. Hierbei konnte bisher ein Zusammenhang der Reaktivität mit dem elektronischen Grundzustand beobachtet werden, wobei weitere Faktoren bisher nur wenig untersucht sind. Die zuvor beschriebenen Ergebnisse, die ich in meiner Masterarbeit erarbeiten konnte, zeigten zweifach koordinierte Metall(I)-Komplexe als geeignete Vorstufen zur Synthese von trigonalen Imido-Cobalt-Komplexen.

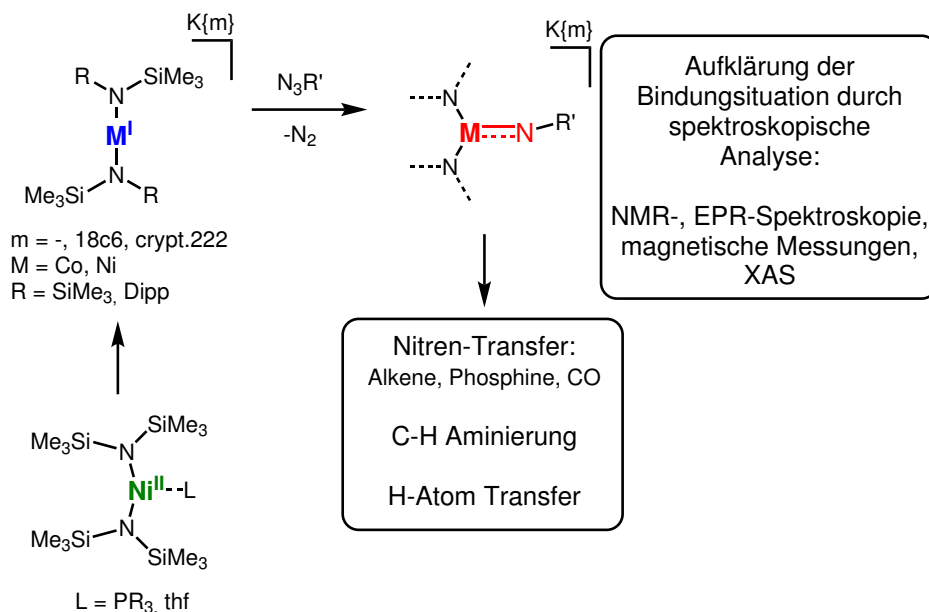


Abb. 45: Übersicht zur Synthese von trigonalen Imido-Übergangsmetall Komplexen, sowie zu einem Nickel(I)-Komplex.

Im Zuge dieser Arbeit sollten umfangreiche Einblicke in die Chemie trigonaler Imido-Cobalt-Komplexe erhalten werden. Hierbei finden lineare Cobalt(I)-Silylamide (namentlich **80** und **85**), welche aufgrund ihres schwachen Ligandenfeldes einen *high-spin*-Charakter der Imido-Verbindungen begünstigen sollen, Verwendung. Aufbauend dazu sollen entsprechende Untersuchungen für Nickel durchgeführt werden. Dabei gilt es für das bis dato unbekanntes  $[\text{Ni}(\text{N}(\text{SiMe}_3)_2)_2]$  einen synthetischen Zugang zu entwickeln.

Aufbauend auf erhaltenen Imido-Metall-Komplexen sollten deren elektronische Eigenschaften und Bindungsverhältnisse eingehend aufgeklärt werden. Diese gilt es dieses ins Verhältnis zur Reaktivität zu setzen, um eventuelle Korrelation zwischen Struktur, elektronischen Eigenschaften und Reaktivität aufzudecken.

### 3 Kumulativer Teil

Das Forschungsprojekt meiner Dissertation hat vier publizierte sowie eine eingereichte Arbeit als Erstautor hervorgebracht. Die durchgeführten Arbeiten befassen sich mit der Synthese und Reaktivität von trigonalen Imido-Komplexen mit Cobalt- und Nickel-Zentralatom sowie der Synthese geeigneter Vorstufen. Eine Beteiligung an einer thematisch auf meinen Arbeiten aufbauend Publikation hinsichtlich der ESR spektroskopischen Untersuchungen zu Imido-Eisen-Komplexen, ist der Vollständigkeit halber ebenfalls aufgeführt.

### 3.1 C–H bond activation by an Imido Cobalt(III) and the Resulting Amido Cobalt(II) Complex

A. Reckziegel, C. Pietzonka, F. Kraus, C.G. Werncke

*Angew. Chem. Int. Ed.* **2020**, *59*, 8527-8531.

DOI: 10.1002/anie.201914718

<https://onlinelibrary.wiley.com/doi/full/10.1002/anie.201914718>

#### Abstract

The 3d-metal mediated nitrene transfer is under intense scrutiny due to its potential as an atom economic and ecologically benign way for the directed amination of (un)functionalised C–H bonds. Here we present the isolation and characterisation of a rare, trigonal imido cobalt(III) complex, which bears a rather long cobalt-imido bond.

#### Zusammenfassung

Durch Umsetzung des quasi-linearen Cobalt(I) Komplexes  $\text{K}\{\text{crypt.222}\}[\text{Co}(\text{N}(\text{SiMe}_3)_2)_2]$  (**101**) mit *tert*-Butylazid konnte, unter Abspaltung von  $\text{N}_2$ , der trigonale Imido-Cobalt(III)-Komplex  $\text{K}\{\text{crypt.222}\}[\text{Co}(\text{N}(\text{SiMe}_3)_2)_2\text{N}^t\text{Bu}]$  (**102**) dargestellt werden.

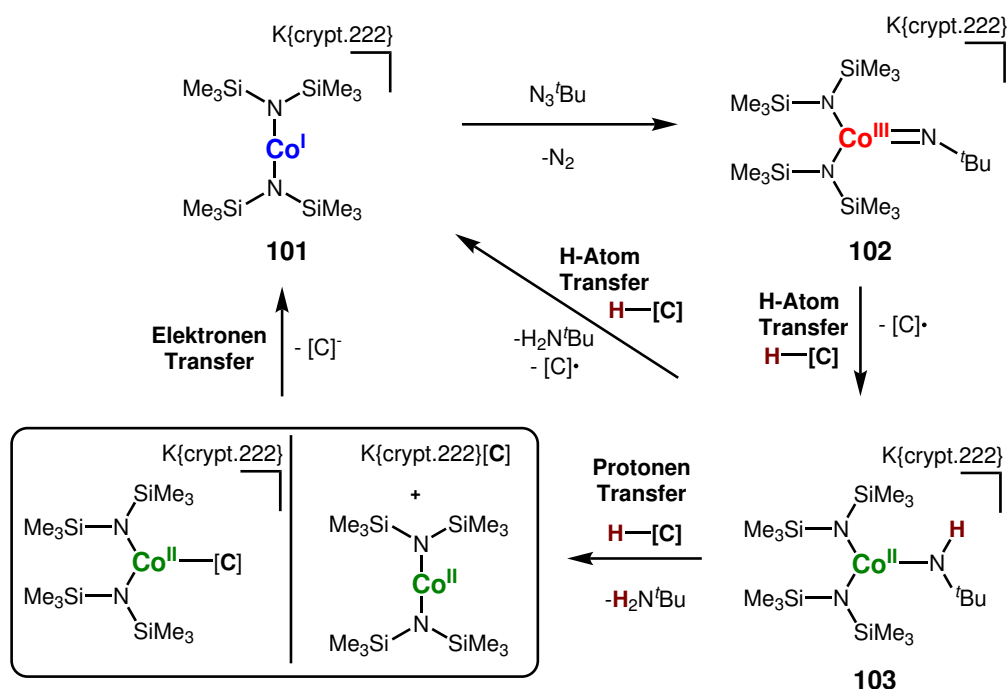


Abb. 46: Darstellung und H-Atom-Transfer-Reaktivität des trigonalen Imido-Cobalt(III)-Komplexes **102** und divergente C–H-Aktivierung des daraus resultierenden Amido-Cobalt(II)-Komplexes **103**.

Dieser weist im Vergleich zu bekannten Imido-Cobalt-Komplexen (1,60-1,69 Å) eine hohe Cobalt– $\text{N}_{\text{Imido}}$ -Bindungslänge von 1,707(1) Å auf. Weiterhin konnte eine gewinkelte Anordnung des Liganden ( $\text{Co}-\text{N}_{\text{Imido}}-\text{C}$ :  $160,8(1)^\circ$ ) beobachtet werden, was

einen gute Zugänglichkeit des Imido-Liganden für Substrate vermuten lässt. Das im Festkörper bestimmte magnetische Moment von  $3,52 \mu_B$  ( $\mu_{s.o.}$  ( $S = 1$ ):  $2,83 \mu_B$ ) deutet auf eine *intermediate-spin* Konfiguration hin. Eine selektive Folgereaktion von **102**, die mittels  $^1\text{H-NMR}$ -Spektroskopie verfolgt wurde, zeigt die Aktivierung von C–H-Bindungen.

Durch Umsetzung von **102** mit 1,4-Cyclohexadien konnte dies unter Bildung des trigonale Amido-Cobalt(II)-Komplexes  $\text{K}\{\text{crypt.222}\}[\text{Co}(\text{N}(\text{SiMe}_3)_2)_2\text{NH}^t\text{Bu}]$  (**103**) bestätigt werden.

**102** ist in der Lage C–H-Bindungen bis zu einer Bindungsstärke von  $94 \text{ kcalmol}^{-1}$  homolytisch zu spalten. Eingehende kinetische Untersuchungen mittels zeitabhängiger UV–Vis-Spektroskopie zeigten einen Zusammenhang der Reaktionskonstanten mit der Bindungsdissoziationsenthalpie (BDE) der C–H-Bindung des eingesetzten Substrates. Durch Verwendung von teilweise deuteriertem 9,10-Dihydroanthracen konnte ein kinetischer Isotopen-Effekt von  $\text{KIE}_{\text{H/D}} = 6,5(2)$ , sowie durch temperaturabhängige Messungen mit 1,4-Cyclohexadien die Aktivierungsenthalpie von  $\Delta H^\ddagger = 19(3) \text{ KJmol}^{-1}$ , bestimmt werden. Die beobachteten Zusammenhänge deuteten auf eine Beteiligung der C–H-Bindung am geschwindigkeitsbestimmenden Schritt und einen radikalischen H-Atom-Transfer-Mechanismus für die untersuchten Substrate hin. In Abhängigkeit des verwendeten Substrates konnte, durch  $^1\text{H-NMR}$  spektroskopische Reaktionskontrolle die Rückbildung des Cobalt(I)-Komplexes **101** beobachtet werden. Eingehende Untersuchungen an **103** diesbezüglich zeigten in Abhängigkeit der Bindungsstärke sowie der Azidität der beteiligten C–H-Bindungen der Substrate, entweder einen direkten H-Atom-Transfer oder eine Deprotonierung mit anschließendem Elektronen-Transfer vom Substrat-Anion zum Cobalt-Komplex. Dies ermöglichte eine katalytische Reaktion von *tert*-Butlyazid zu *tert*-Butylamin durch zwei H-Atom-Transfer-Reaktionen.

Zusammenfassend wurde in der Publikation die Charakterisierung eines seltenen *intermediate-spin* Cobalt(III)-Komplexes vorgestellt. Diese hoch reaktive Verbindung ist in der Lage eine intermolekulare H-Atom-Abstraktion von C–H-Bindungen durchzuführen, was hier erstmalig für Imido-Cobalt-Komplexe gezeigt werden konnte. Der dabei resultierende Amid-Komplex ist wiederum in der Lage, formale H-Atom-Abstraktionen durchzuführen, was für Amido-Cobalt-Komplexe bislang nicht beobachtet wurde.

### Beiträge der Autoren

Die gezeigten Verbindungen wurden von mir dargestellt und mittels  $^1\text{H-NMR}$ -, UV-Vis- und IR-Spektroskopie charakterisiert. Die Messung des magnetischen Momentes nach der EVANS-Methode wurde durch die Serviceabteilung NMR-Spektroskopie der Philipps-Universität Marburg an einem Bruker AV III 500 durchgeführt und von mir ausgewertet.

Zur Bestimmung der Struktur im Festkörper wurden Röntgenbeugungsexperimente am Einkristall durch die Serviceabteilung Kristallstrukturanalyse der Philipps Universität Marburg oder von *Dr. Gunnar Werncke* an einem Bruker D8 Quest durchgeführt. Ich habe die Strukturen aus den erhaltenen Daten gelöst und verfeinert.

Die Bestimmung der Reinheit erfolgte mittels CHN-Elementaranalytik durch die Serviceabteilung Elementaranalytik der Philipps-Universität Marburg.

Für die kinetischen Untersuchungen wurden zeitabhängige UV-Vis Messungen an

einem Specord S600 der Firma Jena von mir durchgeführt und ausgewertet.

Zur Bestimmung der magnetischen Eigenschaften der Festkörper wurden Messungen an einem PPMS-Gerät von LOT/QD von *Clemens Pietzonka* und *Prof. Dr. Florian Kraus* an der Philipps-Universität Marburg durchgeführt und ausgewertet.

Die Elektronenspinresonanz-Experimente wurde von *Beatrice Battistella* aus der Arbeitsgruppe von *K. Ray* an der Humboldt-Universität zu Berlin durchgeführt und von mir ausgewertet.

Das Manuskript habe ich in Zusammenarbeit mit *Dr. Gunnar Werncke* und in Absprache mit allen Co-Autoren verfasst.

**Homogeneous Catalysis**

# C–H Bond Activation by an Imido Cobalt(III) and the Resulting Amido Cobalt(II) Complex

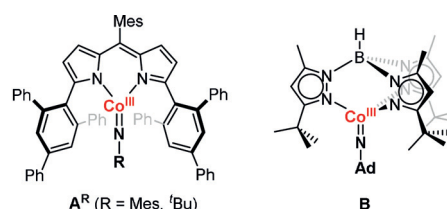
Alexander Reckziegel, Clemens Pietzonka, Florian Kraus, and C. Gunnar Werncke\*

**Abstract:** The 3d-metal mediated nitrene transfer is under intense scrutiny due to its potential as an atom economic and ecologically benign way for the directed amination of (un)functionalised C–H bonds. Here we present the isolation and characterisation of a rare, trigonal imido cobalt(III) complex, which bears a rather long cobalt–imido bond. It can cleanly cleave strong C–H bonds with a bond dissociation energy of up to 92 kcal mol<sup>-1</sup> in an intermolecular fashion, unprecedented for imido cobalt complexes. This resulted in the amido cobalt(II) complex [Co(hmds)<sub>2</sub>(NH<sup>t</sup>Bu)]<sup>-</sup>. Kinetic studies on this reaction revealed an H atom transfer mechanism. Remarkably, the cobalt(II) amide itself is capable of mediating H atom abstraction or stepwise proton/electron transfer depending on the substrate. A cobalt-mediated catalytic application for substrate dehydrogenation using an organo azide is presented.

Imido metal complexes of the late 3d-transition metals are of fundamental interest as they feature a multiply bonded [N–R] functionality that can be potentially transferred to unreactive substrates. As such they are key intermediates in the metal-catalyzed aziridation of olefins and amination of substrates bearing (un-)functionalized C–H bonds.<sup>[1]</sup> An important factor that determines their reactivity is the electronic situation of the imido-bound metal ion, which is influenced by its coordination number, electronic spin, and oxidation state. Whereas imido iron complexes have been studied in detail,<sup>[2,3]</sup> less is known about isolable heavier 3d-metal imido complexes of cobalt to copper. This can be rationalized by a weaker, more reactive metal–nitrogen double bond of late 3d-transition metals, which is due among other things to a higher d-electron count and reduced ligand-to-metal back-bonding.<sup>[4]</sup> This is reminiscent of observations in metal–oxido chemistry, where terminal late transition metal oxido complexes are inherently labile for the same reasons. Therefore, isolable imido complexes of copper,<sup>[5]</sup> nickel,<sup>[6]</sup> and cobalt<sup>[3,7–19]</sup> are scarce and knowledge on the structure, electronic situation and their reactivity is limited.

How to cite: *Angew. Chem. Int. Ed.* **2020**, *59*, 8527–8531  
 International Edition: doi.org/10.1002/anie.201914718  
 German Edition: doi.org/10.1002/ange.201914718

For example, isolable imido cobalt complexes showed a variety of observable oxidation states (+II to +V), however no clear correlation with respect to their reactivity, such as H-atom transfer, has emerged.<sup>[3,7–20]</sup> High-spin complexes are generally ascribed a higher reactivity, whereas low-spin complexes are found to be more stable. This can be reasoned by reduced back-bonding into the partially filled d-orbitals in the case of high-spin complexes. Indeed, nearly all isolable cobalt complexes are found in a low-spin state. Only two imido cobalt systems with higher spin states at room or near room-temperature are known (Scheme 1).<sup>[9,13]</sup> To acquire an imido metal complex in a higher spin state the use of weak-field ancillary ligands, which support the metal–nitrogen multiple bond, is thought to be beneficial. This was showcased by King et al. using a bidentate pyrromethane ligand (Scheme 1, left).<sup>[9]</sup> Respective imido cobalt complexes could perform the intramolecular C–H activation and amination of the ancillary or imido ligand (e.g. benzylic positions), the latter even on a catalytic scale when using an appropriate organo azide.<sup>[21]</sup> However, no intermolecular C–H bond activation by imido cobalt complexes has been observed so far. Further, the knowledge on the behavior of the cobalt amides, which inevitably result from the initial H atom abstraction, towards these substrates beyond deprotonation is absent in the literature. However, knowledge thereof is crucial to fully understand (catalytic) nitrene transfer.



**Scheme 1.** Paramagnetic imido cobalt(III) complexes (Ad = adamantyl).

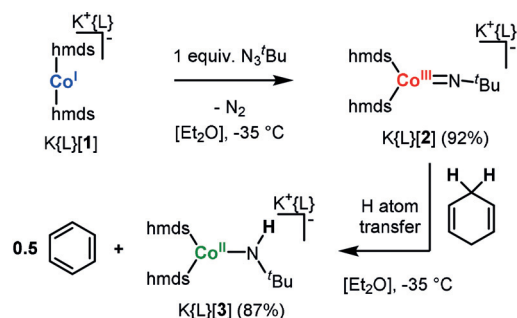
We recently reported on the synthesis of two-coordinate metal(I) complexes such as [Co<sup>I</sup>(hmds)<sub>2</sub>]<sup>-</sup>, [1]<sup>-</sup>, (hmds = -N(SiMe<sub>3</sub>)<sub>2</sub>), which exhibit a very weak ligand field.<sup>[22]</sup> Given the lack of chelating and highly encumbering ligands that enforce a given coordination sphere we hypothesized the use of [1]<sup>-</sup> as an entry into reactive yet isolable imido higher spin cobalt complexes. In this study we present the isolation of a paramagnetic cobalt(III) imide bearing a rather long Co–N imide bond, its unprecedentedly potent intermolecular H atom abstraction capability as well as the multifaceted reactivity of the resulting cobalt(II) amide towards C–H bonds.

[\*] A. Reckziegel, C. Pietzonka, Prof. Dr. F. Kraus, Dr. C. G. Werncke  
 Fachbereich 15/Chemie, Philipps-Universität Marburg  
 Hans-Meerwein-Straße 4, 35043 Marburg (Germany)  
 E-mail: gunnar.werncke@chemie.uni-marburg.de

Supporting information and the ORCID identification number(s) for the author(s) of this article can be found under:  
<https://doi.org/10.1002/anie.201914718>.

© 2020 The Authors. Published by Wiley-VCH Verlag GmbH & Co. KGaA. This is an open access article under the terms of the Creative Commons Attribution Non-Commercial License, which permits use, distribution and reproduction in any medium, provided the original work is properly cited, and is not used for commercial purposes.

Reaction of  $K\{L\}[1]$  ( $L = \text{crypt.222}$ ) with *tert*-butyl azide (Scheme 2) led to the formation of the imido cobalt complex  $K\{L\}[2]$  (Figure 1). In the crystal structure the complex anion  $[2]^-$  exhibits a cobalt ion surrounded by two hm<sub>ds</sub> ligands and the *N*Bu unit in a distorted trigonal-planar fashion. The Co–N<sub>imido</sub> bond length is 1.7067(12) Å, which is slightly longer than those for other reported imido cobalt complexes (1.60–1.69 Å). In the case of  $[2]^-$  this is attributed to the anionic charge and the higher spin state of the complex.<sup>[3,7–19]</sup> The Co–N–C<sub>tBu</sub> angle is slightly bent (160.78(12)°).



**Scheme 2.** Synthesis of  $K\{L\}[2]$  ( $L = \text{crypt.222}$ ;  $\text{hm}_{\text{ds}} = \text{N}(\text{SiMe}_3)_2$ ) and its H atom abstraction ability, which leads to  $K\{L\}[3]$  (shown for 1,4-cyclohexadiene).

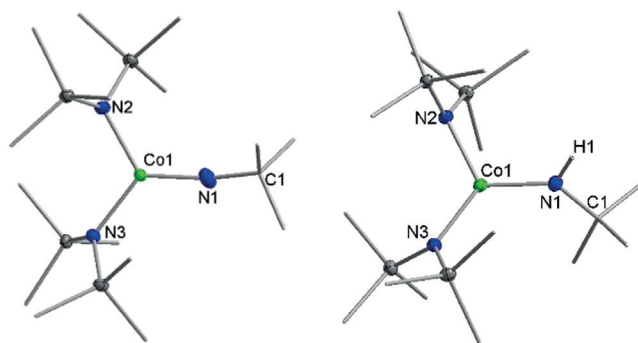


**Figure 1.** Sections of the crystal structures of  $K\{L\}[2]$  (left) and  $K\{L\}[3]$  (right). Cations and unnecessary H atoms are omitted for clarity.

$^1\text{H}$  NMR spectroscopic examination in  $[\text{D}_8]\text{THF}$  showed two paramagnetically shifted signals at  $-2.68$  and  $32.8$  ppm for the hm<sub>ds</sub> and the *t*Bu group, respectively. The paramagnetic nature of  $K\{L\}[2]$  was confirmed in solution ( $\mu_{\text{eff}} = 3.75 \mu_{\text{B}}$ , Evans method) as well as in solid state by VT-dc susceptibility measurements ( $\mu_{\text{eff}} = 3.52 \mu_{\text{B}}$  at 300 K), which suggested a triplet configuration ( $S = 1$ ) as the electronic ground state. These values are similar to those for the imido cobalt(III) complex  $\mathbf{A}^{\text{Mes}}$  ( $\mu_{\text{eff}} = 3.68 \mu_{\text{B}}$ , Scheme 1)<sup>[9]</sup> for which a triplet ground state was proposed, too, and slightly above values found for other low-coordinate cobalt(III) complexes (e.g.  $[\text{Co}^{\text{III}}(\text{SAr})_4]^{-[23]}$ ). X-Band perpendicular-mode EPR measurements at 12 K gave no useful signal, expected for an integer spin system.

Surprisingly,  $K\{L\}[2]$  showed no reactivity in nitrene transfer reactions (e.g. to phosphines or alkenes), contrasting the behavior of most imido cobalt complexes. We then

analyzed the reactivity of  $K\{L\}[2]$  in H atom abstraction (HAA) (Scheme 2). When  $K\{L\}[2]$  was treated with 1,4-cyclohexadiene (1,4-CHD) in  $[\text{D}_8]\text{THF}$ ,  $^1\text{H}$  NMR spectroscopic examination revealed the full conversion of  $K\{L\}[2]$ , formation of benzene and new paramagnetic signals at 76.2 and  $-15.5$  ppm. Layering the reaction mixture with pentane gave the formal H atom abstraction (HAA) product  $K\{L\}-[\text{Co}(\text{hm}_{\text{ds}})_2(\text{HN}^t\text{Bu})]$ ,  $K\{L\}[3]$ , which in the crystal structure exhibits a three-coordinate cobalt ion with a clearly bent *tert*-butyl amide unit ( $134.79(10)^\circ$ ). The Co–N1 bond length of 1.8832(12) Å is in line with a cobalt amide single bond.<sup>[24]</sup> The Co–N<sub>hm<sub>ds</sub></sub> bonds in complex  $[3]^-$  are elongated by about 0.05 Å in comparison with those in complex  $[2]^-$ , indicative of a lower oxidation state of the metal ion in complex  $[3]^-$ . The magnetic moment of complex  $[3]^-$  in solution is  $\mu_{\text{eff}} = 4.58 \mu_{\text{B}}$ , in the range expected for a high-spin cobalt(II) complex ( $4.3\text{--}5.3 \mu_{\text{B}}$ ).

Given the unprecedented intermolecular HAA by an isolable imido cobalt complex, we were interested in the HAA potential of  $K\{L\}[2]$ .  $K\{L\}[2]$  reacted rapidly with stoichiometric amounts of substrates bearing rather weak C–H bonds (9,10-dihydroanthracene (9,10-DHA), xanthene (XAN), indene (IND), 9-fluorene (9-FLU),  $\text{Ph}_2\text{CH}_2$ ,  $\text{Ph}_3\text{CH}$ , and ethylbenzene (EtPh); bond dissociation energies  $\text{BDE} < 85 \text{ kcal mol}^{-1}$ )<sup>[25]</sup> at ambient conditions in  $[\text{D}_8]\text{THF}$ , leading to the formation of  $K\{L\}[3]$ . As in situ analysis of reactions with substrates bearing stronger C–H bonds was limited by the concurrent reaction of the imide with  $[\text{D}_8]\text{THF}$ , respective substrate transformations (including used solvents) were performed either under neat conditions or in 1,2-DFB ( $t_{1/2(\text{DFB})} = 2.5$  h) and subsequently analyzed by  $^1\text{H}$  NMR spectroscopy.  $K\{L\}[2]$  reacted at room temperature rapidly with pure THF ( $92.1 \pm 1.6 \text{ kcal mol}^{-1}$ )<sup>[25]</sup> and  $\text{Et}_2\text{O}$  ( $91.7 \text{ kcal mol}^{-1}$ )<sup>[26]</sup> giving  $K\{L\}[3]$  as the main product. For toluene ( $88.0 \pm 1 \text{ kcal mol}^{-1}$ )<sup>[25]</sup> and ethylbenzene ( $85.4 \text{ kcal mol}^{-1}$ )<sup>[25]</sup> the selective formation of  $K\{L\}[3]$  was observed over the course of 12 h. Kinetic studies on these reactions by UV/Vis spectroscopy showed substrate conversion with pseudo first-order kinetics with respect to the imido cobalt complex  $[2]^-$ .

The observed reaction rates correlated well with the BDE of the involved C–H bond(s) (Figure 2 and S27) but not their acidity. The use of partially deuterated  $[\text{D}_4]9,10\text{-DHA}$  revealed a kinetic isotope effect of  $\text{KIE}_{\text{H/D}} = 6.5(2)$ . This is lower than the semi-classical limit at that temperature ( $\approx 13$ ), pointing to a non-linear C $\cdots$ H $\cdots$ N trajectory. An Eyring analysis of the temperature dependence of the rate constants of the reaction of complex  $[2]^-$  with 1,4-CHD in the range of  $-70^\circ\text{C}$  to  $-30^\circ\text{C}$  gave a rather small activation enthalpy ( $\Delta H^\ddagger = 19(3) \text{ kJ mol}^{-1}$ ). The  $\Delta H^\ddagger$  value is similar to the one for H atom abstraction of C–H or O–H bonds by metal-oxido or -hydroxido complexes.<sup>[27]</sup> Overall, these findings clearly indicate the partition of the C–H bond cleavage in the rate-determining step and suggest an H atom transfer mechanism.

As during the reaction of substrates with  $K\{L\}[2]$  follow-up reactions could be observed, the reaction of the resulting cobalt amide complex  $[3]^-$  was examined more closely by  $^1\text{H}$  NMR spectroscopy and X-ray diffraction analysis of the reaction products. For fluorene and indene simple deprotonation of the substrate by the amide  $[3]^-$  occurred



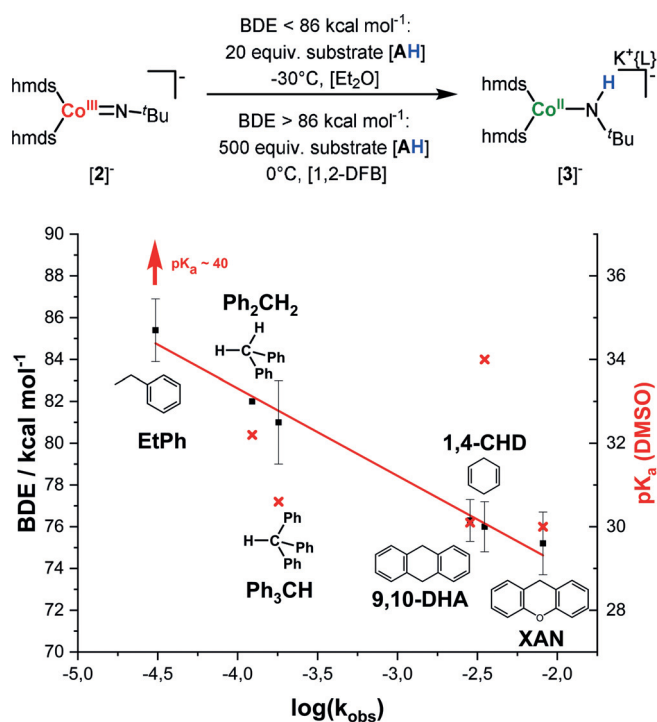
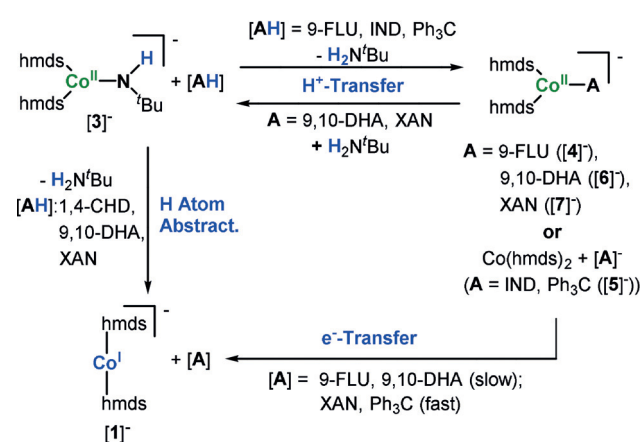


**Figure 2.** Correlation between the reaction constants  $k_{\text{obs}}$  and the C–H BDE (■) (and their acidity (red x)) for different substrates (shown for BDE < 85 kcal mol<sup>-1</sup>) for their reaction with [2]<sup>-</sup>.

(Scheme 3). This gave either the cobalt(II) fluorenyl compound K{L}[Co(hm<sub>2</sub>s)<sub>2</sub>(9-FLU)], K{L}[4] (Figure 3, left), or a mixture of the indenyl anion and Co(hm<sub>2</sub>s)<sub>2</sub>. The organo cobalt complex [4]<sup>-</sup> is rather stable. Only upon heating (60 °C, 1 h) were marginal amounts of complex [1]<sup>-</sup>, the result of a formal homolytic Co–C cleavage, detected. For the reaction of triphenyl methane with [3]<sup>-</sup> in 1,2-DFB, immediate formation of [1]<sup>-</sup> and 'BuNH<sub>2</sub> was observed. Intriguingly, the same reaction in THF led to the formation of mainly Co(hm<sub>2</sub>s)<sub>2</sub> and the precipitation of K{L}[CPh<sub>3</sub>], K{L}[5], due to its low solubility in this solvent. When Co(hm<sub>2</sub>s)<sub>2</sub> was then subjected to the methanide anion in 1,2-DFB, the rapid formation of [1]<sup>-</sup> and the Gomberg dimer was observed,



**Scheme 3.** H atom transfer reactivity of [3]<sup>-</sup> as well as the behavior of resulting Co(hm<sub>2</sub>s)<sub>2</sub>/substrate anion complexes.

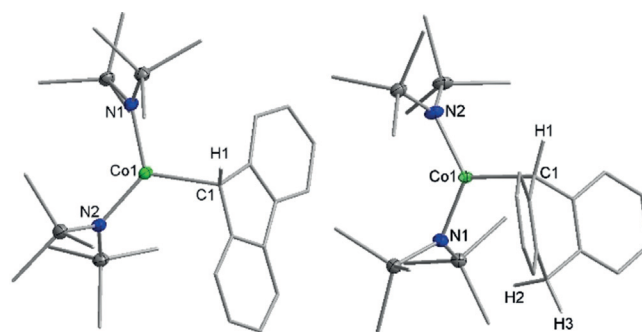


**Figure 3.** Sections of the crystal structure of K{L}[4] (left) and K{L}[6] (right). Cations and unnecessary H atoms are omitted.

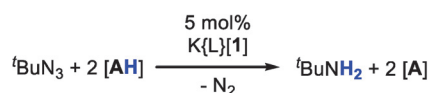
which overall implied a stepwise proton/electron transfer for Ph<sub>3</sub>CH in its reaction with the cobalt amide. Remarkably, the reaction of Ph<sub>3</sub>CH with [3]<sup>-</sup> proceeded significantly faster than the analogous reaction with the imide [2]<sup>-</sup>. For 9,10-DHA, and slower for 1,4-CHD and xanthene, the reaction with complex [3]<sup>-</sup> led to the formation of the starting cobalt(I) complex [1]<sup>-</sup>, *tert*-butyl amine, and the respective dehydrogenation product. Thereby these reactions were slower than the analogous ones with the imide [2]<sup>-</sup>. For xanthene an additional set of paramagnetic signals was observed, pointing to parallel substrate deprotonation. To elucidate a possible stepwise PT/ET process for these substrates, Co(hm<sub>2</sub>s)<sub>2</sub>(thf) was treated with crypt.222 and K(9,10-DHA) or K(XAN), which gave the organometallic complexes (K{L}[Co(hm<sub>2</sub>s)<sub>2</sub>(9,10-DHA)], K{L}[6] (Figure 3, right) and (K{L}[Co(hm<sub>2</sub>s)<sub>2</sub>(XAN)], K{L}[7] (Figure S43, see the Supporting Information). These complexes underwent only moderate homolytic Co–C bond cleavage and complex [1]<sup>-</sup> formation. When [6]<sup>-</sup> and [7]<sup>-</sup> were subjected to 'BuNH<sub>2</sub>, the immediate deprotonation of the amine under formation of [3]<sup>-</sup> and 9,10-DHA or xanthene occurred. Thereby, the deprotonation of the amine was not fully achieved in the case of [7]<sup>-</sup>. This pointed to a readily adjusted equilibrium between the cobalt amide and the cobalt substrate complexes. In view of this equilibrium and the comparison of the speed of homolytic Co–C cleavage by [7]<sup>-</sup> with the reaction of the amide [3]<sup>-</sup> with xanthene, a stepwise PT/ET mechanism can be assumed for this substrate. In contrast, for 9,10-DHA such a pathway is not plausible, as the substrate conversion by the cobalt amide [3]<sup>-</sup> was much quicker than the formation of [1]<sup>-</sup> from complex [6]<sup>-</sup>. Therefore, a direct H atom transfer is hypothesized for this substrate. Such a mechanism is also likely for the reaction of the amide [3]<sup>-</sup> with 1,4-CHD ( $\text{pK}_{\text{a}} \approx 34$ ).

These C–H atom abstraction reactions by [3]<sup>-</sup> are, besides being unprecedented for external substrates in the case of an *amido* cobalt complex, striking for several reasons: a) The amide [3]<sup>-</sup> can deprotonate substrates bearing slightly acidic C–H bonds which potentially poses an unproductive pathway for catalytic nitrene transfer into C–H bonds. This can be followed by reduction of the cobalt(II) complex by the formed substrate anion, which overall constitutes a stepwise proton/electron transfer. c) The formal H atom transfer can also occur in a synchronous fashion. This behavior resembles

the H atom abstraction behavior of a copper or a rhodium aminyl radical complex.<sup>[28]</sup> The reaction trichotomy can be loosely correlated to an interplay between the BDE and  $pK_a$  values of the C–H bond of the substrate. Thereby a very low  $pK_a$  value ( $<22$ ) of the C–H bond leads to simple protonation, whereas a moderate  $pK_a$  value and a higher C–H BDE lead to a stepwise PT/ET. In contrast, for a higher C–H  $pK_a$  and moderate BDE values of the substrate a direct HAT pathway is seemingly preferred. The divergent behavior of amide  $[3]^-$  is reminiscent of related terminal metal hydroxido complexes, which—besides deprotonation—can also facilitate H atom abstraction of C–H bonds.<sup>[29]</sup> Next, we wanted to assess the N–H bond strength of the amide  $[3]^-$ . In view of the rather slow reaction of  $[2]^-$  with  $PH_3C-H$ ,  $[3]^-$  was treated with a fivefold excess of the trityl radical (Gomberg dimer). This led to the detection of small amounts of  $PH_3C-H$ ; which, however, could not be quantified due to subsequent reactions. Together with the results of the substrate scope of  $[2]^-$ , this implies a N–H bond strength range of approximately 85–90 kcal mol<sup>-1</sup> for  $[3]^-$ .

Lastly, we probed selected transformations in a catalytic setting. With 5 mol % of  $K[L][2]$ , H atom transfer from 9,10-DHA to *tert*-butyl azide is observed (49% conversion, 24 h, 25 °C; Table 1). However, examination of the reaction mixture showed decomposition of the employed cobalt complex, although the system remained partially catalytically active. For xanthene, catalytic dehydrogenation was possible but also gave unidentified side products, possibly resulting from C–N bond formation processes. In the case of liquid 1,4-CHD and indene, the catalysis could also be performed under neat conditions.

**Table 1:** Catalytic dehydrogenation of substrates by  $K[L][1]$  using *tert*-butyl azide.



Substrate [AH]	Solvent	t [h]	Conversion [%] (azide)	Yield [%] (amine)
9,10-DHA	[D <sub>8</sub> ]THF	24	49	49
1,4-CHD	/	36	99	99
XAN	[D <sub>8</sub> ]THF	36	61	31
IND	/	36	72	72

In conclusion, we have presented the synthesis, isolation and characterization of a rare paramagnetic imido cobalt(III) complex by reaction of a two-coordinate cobalt(I) complex with *tert*-butyl azide. The complex exhibits a rather long Co–N<sub>imido</sub> bond and facilitates the rapid intermolecular H atom abstraction from C–H bonds with a BDE of up to 92 kcal mol<sup>-1</sup> under formation of a cobalt(II) amido complex. Kinetic and mechanistic studies implicated an H atom transfer mechanism. Remarkably, the formed cobalt(II) amide could also abstract an H atom from the substrate, which gave free *tert*-butyl amine and regenerated the cobalt(I) complex  $[1]^-$ . Depending on the substrate, the formal H atom abstraction

occurred via a concerted or a stepwise proton/electron transfer mechanism. A first catalytic study showed the possibility of employing complex  $[1]^-$  as a precatalyst for substrate dehydrogenation using *tert*-butyl azide as the H atom acceptor.

## Acknowledgements

We thank the DFG (WE 5627/4-1) for financial support and Dr. O. Burghaus (Philipps University Marburg), Prof. Dr. K. Ray and B. Battistella (Humboldt University Berlin) for EPR measurements.

**Keywords:** amido cobalt complex · catalysis · C–H activation · H atom transfer · imido cobalt complex

- a) Y. Park, Y. Kim, S. Chang, *Chem. Rev.* **2017**, *117*, 9247; b) D. N. Zalatan, J. Du Bois in *Topics in Current Chemistry*, Vol. 292 (Eds.: J.-Q. Yu, L. Ackermann), Springer, Berlin, **2010**, pp. 347–378; c) H. Lu, X. P. Zhang, *Chem. Soc. Rev.* **2011**, *40*, 1899; d) F. Collet, R. H. Dodd, P. Dauban, *Chem. Commun.* **2009**, 5061; e) V. Bagchi, A. Kalra, P. Das, P. Paraskevopoulou, S. Gorla, L. Ai, Q. Wang, S. Mohapatra, A. Choudhury, Z. Sun, et al., *ACS Catal.* **2018**, *8*, 9183; f) P. F. Kuijpers, J. I. van der Lugt, S. Schneider, B. de Bruin, *Chem. Eur. J.* **2017**, *23*, 13819; g) J. F. Berry, *Comments Inorg. Chem.* **2009**, *30*, 28.
- a) L. Wang, L. Hu, H. Zhang, H. Chen, L. Deng, *J. Am. Chem. Soc.* **2015**, *137*, 14196; b) R. E. Cowley, N. J. DeYonker, N. A. Eckert, T. R. Cundari, S. DeBeer, E. Bill, X. Ottenwaelder, C. Flaschenriem, P. L. Holland, *Inorg. Chem.* **2010**, *49*, 6172; c) M. J. T. Wilding, D. A. Iovan, A. T. Wrobel, J. T. Lukens, S. N. MacMillan, K. M. Lancaster, T. A. Betley, *J. Am. Chem. Soc.* **2017**, *139*, 14757; d) M. J. T. Wilding, D. A. Iovan, T. A. Betley, *J. Am. Chem. Soc.* **2017**, *139*, 12043; e) K. Searles, S. Fortier, M. M. Khusniyarov, P. J. Carroll, J. Sutter, K. Meyer, D. J. Mindiola, K. G. Caulton, *Angew. Chem. Int. Ed.* **2014**, *53*, 14139; *Angew. Chem.* **2014**, *126*, 14363; f) S. C. Bart, E. Lobkovsky, E. Bill, P. J. Chirik, *J. Am. Chem. Soc.* **2006**, *128*, 5302; g) J. J. Scepaniak, J. A. Young, R. P. Bontchev, J. M. Smith, *Angew. Chem. Int. Ed.* **2009**, *48*, 3158; *Angew. Chem.* **2009**, *121*, 3204; h) A. C. Bowman, C. Milsman, E. Bill, Z. R. Turner, E. Lobkovsky, S. DeBeer, K. Wieghardt, P. J. Chirik, *J. Am. Chem. Soc.* **2011**, *133*, 17353; i) C. C. Lu, C. T. Saouma, M. W. Day, J. C. Peters, *J. Am. Chem. Soc.* **2007**, *129*, 4; j) S. Kuppusswamy, T. M. Powers, B. M. Johnson, M. W. Bezpalko, C. K. Brozek, B. M. Foxman, L. A. Berben, C. M. Thomas, *Inorg. Chem.* **2013**, *52*, 4802; k) C. M. Thomas, N. P. Mankad, J. C. Peters, *J. Am. Chem. Soc.* **2006**, *128*, 4956; l) M.-E. Moret, J. C. Peters, *Angew. Chem. Int. Ed.* **2011**, *50*, 2063; *Angew. Chem.* **2011**, *123*, 2111; m) I. Nieto, F. Ding, R. P. Bontchev, H. Wang, J. M. Smith, *J. Am. Chem. Soc.* **2008**, *130*, 2716.
- T. A. Betley, J. C. Peters, *J. Am. Chem. Soc.* **2003**, *125*, 10782.
- K. Ray, F. Heims, F. F. Pfaff, *Eur. J. Inorg. Chem.* **2013**, 3784.
- a) A. G. Bakhoda, Q. Jiang, J. A. Bertke, T. R. Cundari, T. H. Warren, *Angew. Chem. Int. Ed.* **2017**, *56*, 6426; *Angew. Chem.* **2017**, *129*, 6526; b) K. M. Carsch, I. M. DiMucci, D. A. Iovan, A. Li, S.-L. Zheng, C. J. Titus, S. J. Lee, K. D. Irwin, D. Nordlund, K. M. Lancaster, et al., *Science* **2019**, *365*, 1138.
- a) V. M. Iluc, A. J. M. Miller, J. S. Anderson, M. J. Monreal, M. P. Mehn, G. L. Hillhouse, *J. Am. Chem. Soc.* **2011**, *133*, 13055; b) E. Kogut, H. L. Wiencko, L. Zhang, D. E. Cordeau, T. H. Warren, *J. Am. Chem. Soc.* **2005**, *127*, 11248; c) D. J. Mindiola,

- G. L. Hillhouse, *J. Am. Chem. Soc.* **2001**, *123*, 4623; d) R. Waterman, G. L. Hillhouse, *J. Am. Chem. Soc.* **2008**, *130*, 12628; e) N. D. Harrold, G. L. Hillhouse, *Chem. Sci.* **2013**, *4*, 4011; f) C. A. Laskowski, A. J. M. Miller, G. L. Hillhouse, T. R. Cundari, *J. Am. Chem. Soc.* **2011**, *133*, 771; g) V. M. Iluc, G. L. Hillhouse, *J. Am. Chem. Soc.* **2010**, *132*, 15148; h) Y. Dong, J. T. Lukens, R. M. Clarke, S.-L. Zheng, K. M. Lancaster, T. A. Betley, *Chem. Sci.* **2020**, *123*, 4623.
- [7] X. Hu, K. Meyer, *J. Am. Chem. Soc.* **2004**, *126*, 16322.  
[8] L. Zhang, Y. Liu, L. Deng, *J. Am. Chem. Soc.* **2014**, *136*, 15525.  
[9] E. R. King, G. T. Sazama, T. A. Betley, *J. Am. Chem. Soc.* **2012**, *134*, 17858.  
[10] X.-N. Yao, J.-Z. Du, Y.-Q. Zhang, X.-B. Leng, M.-W. Yang, S.-D. Jiang, Z.-X. Wang, Z.-W. Ouyang, L. Deng, B.-W. Wang, et al., *J. Am. Chem. Soc.* **2017**, *139*, 373.  
[11] J. Du, L. Wang, M. Xie, L. Deng, *Angew. Chem. Int. Ed.* **2015**, *54*, 12640; *Angew. Chem.* **2015**, *127*, 12831.  
[12] Y. Liu, J. Du, L. Deng, *Inorg. Chem.* **2017**, *56*, 8278.  
[13] D. T. Shay, G. P. A. Yap, L. N. Zakharov, A. L. Rheingold, K. H. Theopold, *Angew. Chem. Int. Ed.* **2005**, *44*, 1508; *Angew. Chem.* **2005**, *117*, 1532.  
[14] X. Dai, P. Kapoor, T. H. Warren, *J. Am. Chem. Soc.* **2004**, *126*, 4798.  
[15] B. Wu, R. Hernández Sánchez, M. W. Bezpalko, B. M. Foxman, C. M. Thomas, *Inorg. Chem.* **2014**, *53*, 10021.  
[16] D. M. Jenkins, T. A. Betley, J. C. Peters, *J. Am. Chem. Soc.* **2002**, *124*, 11238.  
[17] C. Jones, C. Schulten, R. P. Rose, A. Stasch, S. Aldridge, W. D. Woodul, K. S. Murray, B. Moubaraki, M. Brynda, G. La Macchia, et al., *Angew. Chem. Int. Ed.* **2009**, *48*, 7406; *Angew. Chem.* **2009**, *121*, 7542.  
[18] M. P. Mehn, S. D. Brown, D. M. Jenkins, J. C. Peters, L. Que, *Inorg. Chem.* **2006**, *45*, 7417.  
[19] R. E. Cowley, R. P. Bontchev, J. Sorrell, O. Sarracino, Y. Feng, H. Wang, J. M. Smith, *J. Am. Chem. Soc.* **2007**, *129*, 2424.  
[20] L. Hu, H. Chen, *ACS Catal.* **2017**, *7*, 285.  
[21] D. A. Iovan, M. J. T. Wilding, Y. Baek, E. T. Hennessy, T. A. Betley, *Angew. Chem. Int. Ed.* **2017**, *56*, 15599; *Angew. Chem.* **2017**, *129*, 15805.  
[22] a) C. G. Werncke, P. C. Bunting, C. Duhayon, J. R. Long, S. Bontemps, S. Sabo-Etienne, *Angew. Chem. Int. Ed.* **2015**, *54*, 245; *Angew. Chem.* **2015**, *127*, 247; b) C. G. Werncke, E. Suturina, P. C. Bunting, L. Vendier, J. R. Long, M. Atanasov, F. Neese, S. Sabo-Etienne, S. Bontemps, *Chem. Eur. J.* **2016**, *22*, 1668.  
[23] P. O. Lagaditis, B. Schluschaß, S. Demeshko, C. Würtele, S. Schneider, *Inorg. Chem.* **2016**, *55*, 4529.  
[24] a) A. Massard, P. Braunstein, A. A. Danopoulos, S. Choua, P. Rabu, *Organometallics* **2015**, *34*, 2429; b) C. B. Hansen, R. F. Jordan, G. L. Hillhouse, *Inorg. Chem.* **2015**, *54*, 4603.  
[25] X.-S. Xue, P. Ji, B. Zhou, J.-P. Cheng, *Chem. Rev.* **2017**, *117*, 8622.  
[26] T. J. Burkey, M. Majewski, D. Griller, *J. Am. Chem. Soc.* **1986**, *108*, 2218.  
[27] a) D. Wang, L. Que, *Chem. Commun.* **2013**, *49*, 10682; b) K. Gardner, J. Mayer, *Science* **1995**, *269*, 1849; c) H. Gao, J. T. Groves, *J. Am. Chem. Soc.* **2017**, *139*, 3938.  
[28] a) N. P. Mankad, W. E. Antholine, R. K. Szilagyi, J. C. Peters, *J. Am. Chem. Soc.* **2009**, *131*, 3878; b) T. Büttner, J. Geier, G. Frison, J. Harmer, C. Calle, A. Schweiger, H. Schönberg, H. Grützmacher, *Science* **2005**, *307*, 235.  
[29] a) Z. Chen, G. Yin, *Chem. Soc. Rev.* **2015**, *44*, 1083; b) P. J. Donoghue, J. Tehranchi, C. J. Cramer, R. Sarangi, E. I. Solomon, W. B. Tolman, *J. Am. Chem. Soc.* **2011**, *133*, 17602.

Manuscript received: November 18, 2019

Accepted manuscript online: March 2, 2020

Version of record online: March 27, 2020

## 3.2 High-Spin Imido Cobalt Complexes with Imidyl Radical Character

A. Reckziegel, M. Kour, B. Battistella, S. Mebs, K. Beuthert, R. Berger, C.G. Wernerke

*Angew. Chem. Int. Ed.* **2021**, *60*, 15367-15380.

DOI: 10.1002/anie.202103841

<https://onlinelibrary.wiley.com/doi/full/10.1002/anie.202103841>

### Abstract

We report on the synthesis of a variety of trigonal imido cobalt complexes  $[\text{Co}(\text{NAr})\text{L}_2]^-$ , ( $\text{L}=\text{N}(\text{Dipp})\text{SiMe}_3$ ),  $\text{Dipp}=2,6\text{-di-}i\text{so-propylphenyl}$ ) with very long  $\text{Co-NAr}$  bonds of around 1.75 Å. Their electronic structure was interrogated using a variety of physical and spectroscopic methods such as EPR or X-Ray absorption spectroscopy which leads to their description as highly unusual imidyl cobalt complexes. Computational analyses corroborate these findings and further reveal that the high-spin state is responsible for the imidyl character. Exchange of the Dipp substituent on the imide by the smaller mesityl function (2,4,6-trimethylphenyl) effectuates the unexpected  $\text{Me}_3\text{Si}$  shift from the ancillary ligand set to the imidyl nitrogen, revealing a highly reactive, nucleophilic character of the imidyl unit.

### Zusammenfassung

Aufbauend auf den Ergebnissen der vorherigen Publikation wurde das sterisch anspruchsvollere  $\text{N}(\text{Dipp})\text{SiMe}_3$ -Ligandensystem zur Synthese von trigonalen *Aryl*-Imido-Cobalt-Komplexen genutzt.

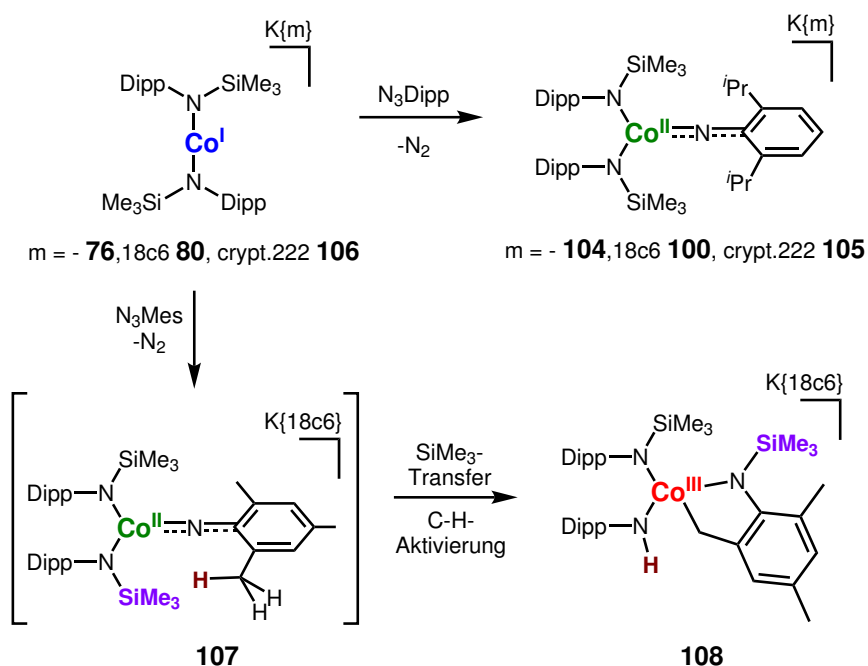


Abb. 47: Synthese und Reaktivität der trigonalen Aryl-Imidyl-Cobalt-Komplexe  $\text{K}\{m\}[\text{Co}(\text{N}(\text{Dipp})\text{SiMe}_3)_2\text{NDipp}]$  ( $m = -104; 18c6: 100; \text{crypt.222}: 105$ ).

Die Umsetzung der Cobalt(I)-Komplexe  $K\{m\}[Co(N(Dipp)SiMe_3)_2]$  ( $m = -$  **76**, **18c6** **80**, crypt.222 **106**) mit dem sterisch anspruchsvollen Dippazid, führte unter Abspaltung von  $N_2$  zur Bildung der trigonalen Imido-Komplexe  $K\{m\}[Co(N(Dipp)SiMe_3)_2NDipp]$  ( $m = -$  **104**; **18c6**: **100**; crypt.222: **105**).

Die Struktur des salzseparierten Komplexes  $K\{18c6\}[Co(N(Dipp)SiMe_3)_2NDipp]$  (**100**) im Festkörper zeigte eine deutliche Aufweitung der  $N_{Imido}$ -Cobalt-Bindung (1,751(2) Å) und eine nahezu lineare Koordination des Imido-Liganden (Co- $N_{Imido}$ -C: 178,8(2)°). Das magnetische Moment ( $\mu_{eff}$ ), bestimmt in Lösung (4,90  $\mu_B$ ) und im Festkörper (4,64  $\mu_B$ ), deutet auf einen Quintet-Grundzustand hin. ESR spektroskopische Untersuchungen weisen auf das Vorliegen eines organischen Radikals mit starker Kopplung zu einem Cobalt-Atom, und ein *high-spin* Cobalt(II)-Ion hin. Mittels Röntgenabsorptionsspektroskopie (XAS) konnte eine Oxidationsstufe von +2 für das Cobalt-Ion bestimmt werden. Damit ließ sich diese Verbindung, im Gegensatz zu dem zuvor beschriebenen Imido-Cobalt(III)-Komplex **102**, als Imidyl-Cobalt-Komplex auffassen.

Quantenchemische Berechnungen bestätigten diese Formulierung, wobei eine ausgedehnte Delokalisierung der Radikaldichte auf den aromatischen Ring berechnet wurde, was im Einklang mit den ESR spektroskopischen Untersuchungen steht. Weiterhin zeigten die Rechnungen, dass eine solche Delokalisierung für einen Triplett-Intermediat nicht zu erwarten ist.

Untersuchungen zur H-Atom-Transfer-Reaktivität des Imidyl-Komplexes **100** zeigten eine geringe Aktivität, was auf den hohen sterischen Anspruch des Ligandensystems zurückgeführt wurde. Weiterhin konnte ein Ligandenaustausch der gebildeten Amido-Cobalt(II)-Komplexe beobachtet werden, was weitere mechanistische und kinetische Untersuchungen verhinderte.

Die Umsetzung des sterisch weniger anspruchsvollen Mesitylazid mit dem anionischen Cobalt(I) Komplex  $K\{18c6\}[Co(N(Dipp)SiMe_3)_2]$  (**80**) führte zur intermediären Bildung eines Mesityl-Imido-Komplexes **107**. Dieser ist instabil und reagiert unter  $SiMe_3$ -Gruppen Übertragung von einem Coliganden auf die Imidofunktion. Die anschließende intramolekulare C-H-Aktivierung des so erzeugten Dipp-Imido-Komplexes hat die Bildung des Komplexes **108** zur Folge.

Zusammenfassend konnte in dieser Publikation der erste Imidyl-Cobalt-Komplex dargestellt und sowohl spektroskopisch als auch quantenchemische eindeutig als solcher identifiziert werden.

### Beiträge der Autoren

Alle gezeigten Verbindungen wurden von mir dargestellt und mittels  $^1H$ -NMR-, UV-Vis- und IR-Spektroskopie charakterisiert. Die Messung des magnetischen Momentes nach der EVANS-Methode wurde durch die Serviceabteilung NMR-Spektroskopie der Philipps-Universität Marburg an einem Bruker AV III 500 durchgeführt und von mir ausgewertet.

Zur Bestimmung der Struktur im Festkörper wurden Röntgenbeugungsexperimente am Einkristall durch die Serviceabteilung Kristallstrukturanalyse der Philipps Universität Marburg oder von *Dr. Gunnar Werncke* an einem Bruker D8 Quest durchgeführt. Die erhaltenen Daten wurde von mir gelöst und verfeinert.

Die Bestimmung der Reinheit erfolgte mittels CHN-Elementaranalytik durch die Serviceabteilung Elementaranalytik der Philipps-Universität Marburg.

Die Elektronenspinresonanz-Experimente wurden von *Beatrice Battistella* aus der

Arbeitsgruppe von *K. Ray* an der Humboldt-Universität zu Berlin durchgeführt. Die Auswertung und Simulation der erhaltenen Daten erfolgte durch mich.

Röntgenabsorptionspektroskopische Messungen wurden durch *Dr. Stefan Mebs* an der Röntgenquelle BESSY II des Helmholtz Zentrums in Berlin durchgeführt. Die Auswertung der erhaltenen Daten wurde von *Dr. Stefan Mebs* übernommen.

Quantenchemische Berechnungen wurden von *Dr. Manjinder Kour*, *Katrin Beuthert* und *Prof. Dr. Robert Berger* unter Verwendung von TURBOMOLE (v7.40.) durchgeführt.

Das Manuskript habe ich in Zusammenarbeit mit *Dr. Gunnar Werncke* und in Absprache mit allen Co-Autoren verfasst.



## Coordination Chemistry

## High-Spin Imido Cobalt Complexes with Imidyl Radical Character\*\*

Alexander Reckziegel, Manjinder Kour, Beatrice Battistella, Stefan Mebs, Katrin Beuthert, Robert Berger, and C. Gunnar Werncke\*

**Abstract:** We report on the synthesis of a variety of trigonal imido cobalt complexes  $[\text{Co}(\text{NAryl})\text{L}_2]^-$ , ( $\text{L} = \text{N}(\text{Dipp})\text{SiMe}_3$ ,  $\text{Dipp} = 2,6\text{-diisopropylphenyl}$ ) with very long  $\text{Co}-\text{N}_{\text{Aryl}}$  bonds of around 1.75 Å. Their electronic structure was interrogated using a variety of physical and spectroscopic methods such as EPR or X-Ray absorption spectroscopy which leads to their description as highly unusual imidyl cobalt complexes. Computational analyses corroborate these findings and further reveal that the high-spin state is responsible for the imidyl character. Exchange of the Dipp substituent on the imide by the smaller mesityl function (2,4,6-trimethylphenyl) effectuates the unexpected  $\text{Me}_3\text{Si}$  shift from the ancillary ligand set to the imidyl nitrogen, revealing a highly reactive, nucleophilic character of the imidyl unit.

Late 3d transition-metal imido complexes are of fundamental interest in coordination chemistry, as the metal-bound nitrene unit  $[\text{NR}]$  can be potentially transferred to unreactive substrates. This is increasingly employed for the catalytic amination of unfunctionalized C–H bonds or the aziridation of olefines.<sup>[1–12]</sup> Despite the resulting high demand for understanding late 3d-transition metal imido species, comprehensive knowledge about the electronic and structural factors that contribute to their properties and bond activation

How to cite: *Angew. Chem. Int. Ed.* **2021**, *60*, 15376–15380  
International Edition: doi.org/10.1002/anie.202103841  
German Edition: doi.org/10.1002/ange.202103841

reactivity is still lacking. Whereas most isolable imido metal complexes are found in a low-spin state, those with higher spin-states tend to be more reactive.<sup>[13–52]</sup>

In recent years substantial advances were made concerning more unusual bond situations of the  $[\text{MNR}]$  unit in higher spin states via structural and spectroscopic identification of singular examples of iron<sup>[28]</sup> and nickel imidyl complexes (also referred to as metal iminyl species)<sup>[29]</sup> or a nitrene copper compound<sup>[32]</sup> (Figure 1) using ancillary weak field ligands.

Herein we report on the synthesis of trigonal arylimido cobalt complexes, which contain very long  $\text{Co}-\text{N}_{\text{imide}}$  bonds of 1.75 Å. The use of a variety of analytical techniques reveals these compounds are best described as high-spin imidyl complexes, unprecedented for cobalt. Computational analyses corroborate these findings and clearly show the spin-state-dependent imidyl/imide interplay with the high-spin state evoking the radical imidyl character. Reduction of steric demand of the imide substituent results in an unexpected intramolecular shift of a  $\text{Me}_3\text{Si}$  unit from a silylamide ligand and reveals a nucleophilic character of the imidyl nitrogen.

The linear cobalt(I) silylamides  $\text{K}[\text{18c6}][\text{CoL}_2]$ ,  $\text{K}[\text{18c6}][\text{1}]$ , ( $\text{L} = \text{N}(\text{Dipp})\text{SiMe}_3$ )<sup>[53]</sup> or its derivative  $\text{K}[\text{crypt.222}][\text{1}]$  that contain weak field silylamide ligands<sup>[30,53,54]</sup> and exhibit magnetically free cobalt(I) ion behavior were reacted with

[\*] A. Reckziegel, Dr. M. Kour, K. Beuthert, Prof. Dr. R. Berger, Dr. C. G. Werncke  
Department of Chemistry  
Philipps-University Marburg  
Hans-Meerwein-Strasse 4, 35032 Marburg (Germany)  
E-mail: gunnar.werncke@chemie.uni-marburg.de

B. Battistella  
Institute of Chemistry  
Humboldt-Universität zu Berlin  
Brook-Taylor-Strasse 2, 12489 Berlin (Germany)

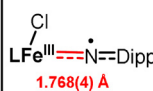
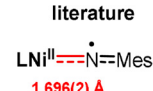
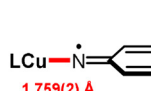
Dr. S. Mebs  
Department of Physics  
Freie Universität zu Berlin  
Arnimallee 14, 14195 Berlin (Germany)

[\*\*] A previous version of this manuscript has been deposited on a preprint server (<https://doi.org/10.26434/chemrxiv.14128709.v1>).

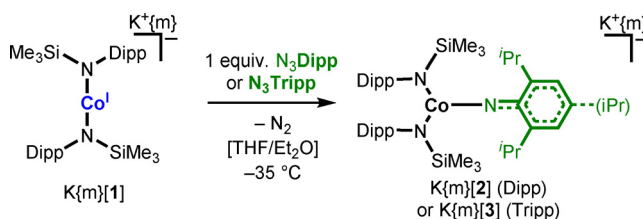
Supporting information (synthetic procedures, magnetic measurements, <sup>1</sup>H NMR, EPR, XANES/EXAFS spectra, computational details with xyz-coordinates, and crystallographic data) and the ORCID identification number(s) for the author(s) of this article can be found under:

<https://doi.org/10.1002/anie.202103841>.

© 2021 The Authors. Angewandte Chemie International Edition published by Wiley-VCH GmbH. This is an open access article under the terms of the Creative Commons Attribution Non-Commercial License, which permits use, distribution and reproduction in any medium, provided the original work is properly cited and is not used for commercial purposes.

Imide $[\text{NR}]^{2-}$	Imidyl $[\text{NR}]^-$	Nitrene $[\text{NR}]^0$
$\text{M}\equiv\text{N}-\text{R}$	$\text{M}=\ddot{\text{N}}-\text{R}$	$\text{M}-\ddot{\text{N}}-\text{R}$ (triplet)
or	or	or
$\text{M}=\ddot{\text{N}}-\text{R}$	$\text{M}-\ddot{\text{N}}-\text{R}$	$\text{M}-\ddot{\text{N}}-\text{R}$ (singlet)
literature		
		
1.768(4) Å	1.696(2) Å	1.759(2) Å
Fe <sup>III</sup> imidyl, <i>JACS</i> <b>2011</b>	Ni <sup>II</sup> imidyl, <i>Chem. Sci.</i> <b>2020</b>	Cu <sup>I</sup> triplet nitrene <i>Science</i> <b>2019</b>

**Figure 1.** Top: Simplified description of the different bonding modes of  $[\text{MNR}]$  units. Bottom: Bond lengths of known low-coordinated nitrene/imidyl complexes (Mes: 2,4,6-trimethylphenyl).



**Scheme 1.** Synthesis of  $\text{K}^{\{m\}}[\text{2}]$  ( $m = \text{none}$ , crypt.222, 18c6) and  $\text{K}^{\{m\}}[\text{3}]$  ( $m = \text{none}$ , 18c6) starting from  $\text{K}^{\{m\}}[\text{1}]$  (Tripp = 2,4,6-triisopropylphenyl).

Dipp-N<sub>3</sub> or Tripp-N<sub>3</sub> (Scheme 1) at –35 °C in Et<sub>2</sub>O/THF. This resulted in an immediate color change from green to dark brown and concomitant N<sub>2</sub> evolution. Isolation yielded dark yellow crystals of K{m}[2] (Dipp; m=crypt, 18c6) K{crypt.222}[2] and K{18c6}[3] (Tripp). In solid state, the complex anions of all compounds exhibit similar structural metrics (Figure 2), for which the K{18c6}[2] is chosen as a representative for discussion. The complex anion shows a trigonally coordinated cobalt ion with a Co–N<sub>imide</sub> bond length of 1.751(2) Å. This is by at least 0.05 Å longer than in all other known aryl imido cobalt complexes (Co–N<sub>imide</sub> from 1.61 Å–1.70 Å).<sup>[13,14,16,23–25,34]</sup>

It resembles those of the known 3d-metal imidyl/nitrene compounds (Figure 1) and a matrix-isolated fluoronitroid cobalt species (Co–N 1.77 Å), for which imidyl/nitrene character was discussed.<sup>[12]</sup> Given these comparably long C–N<sub>imide</sub> bonds found for complexes [2]<sup>–</sup> and [3]<sup>–</sup> we were curious if this was connected to the unique anionic character of these imido complexes,<sup>[46]</sup> as nearly all comparable 3d-metal imido complexes are either neutral or cationic. Thus, the overall neutral cobalt(I) complex K[1]<sup>[55]</sup> was reacted with Dipp-N<sub>3</sub> and Tripp-N<sub>3</sub> which gave the respective complexes K[2] and K[3]. X-Ray analysis revealed (Figure 2) an

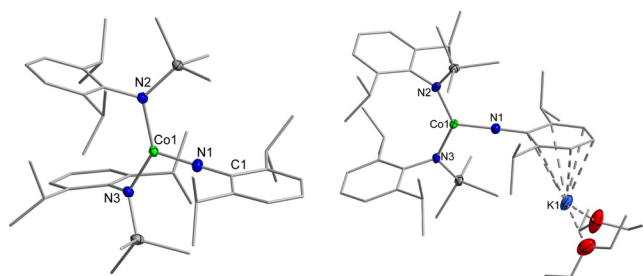


**Figure 2.** Molecular structure of K{18c6}[2] (left) and K[2] (right) in the solid state.<sup>[58]</sup> The K{18c6} cation, solvent molecules as well as H atoms are omitted for clarity. Selected bond lengths (Å) and angles (°): K{18c6}[2]: Co1–N1: 1.751(2); Co1–N2: 1.935(2); Co1–N3: 1.932(2); N1–C1: 1.347(2); Co1–N3–C31: 178.8(2); K[2]: Co1–N1 1.750(3); Co1–N2 1.916(2); Co1–N3 1.920(2); N1–C1 1.338(4); Co1–N1–C1 174.9(3).

intriguing direct potassium interaction, as cation coordination to imide metal units (such as Sc<sup>3+</sup>) is suggested as an important factor in modulating their properties, although direct structural evidence is lacking.<sup>[56,57]</sup> However, in the presented case no impact on the central arylimido cobalt unit was perceived (K[2]: Co–N<sub>imide</sub> 1.750(3) Å, K[3] Co–N<sub>imide</sub> 1.754(2) Å). Determination of the magnetic moment in solution by the Evans method gave  $\mu_{\text{eff}}=4.65 \mu_{\text{B}}$  (K{crypt.222}[2]) and  $\mu_{\text{eff}}=4.90 \mu_{\text{B}}$  (K{18c6}[2]). This is in approximate agreement with susceptibility measurements on K{18c6}[2] in solid state ( $\mu_{\text{eff}}=4.64 \mu_{\text{B}}$  at 300 K) revealing a linear  $1/\chi$  vs.  $T$  slope with no apparent spin-crossover (Figure 3a). The magnetic susceptibility at room temperature is higher than that of the related intermediate spin imido cobalt(III) complex [Co(N<sup>t</sup>Bu)(N(SiMe<sub>3</sub>)<sub>2</sub>)<sub>2</sub>]<sup>–</sup> (3.52  $\mu_{\text{B}}$ ),<sup>[30]</sup> (as well as of any other paramagnetic imido cobalt(III) complex<sup>[16,31,35]</sup>) and approaches the spin-only value of 4.92  $\mu_{\text{B}}$  of a quintet state. X-band EPR spectroscopy of K{18c6}[2] (d<sub>10</sub>-MeTHF, 8 K) gave decisive insights as it showed a broad signal at around  $g_1=5.0$  and a sharper signal at  $g_2=2.05$ , which is split due to the presence of hyperfine coupling (Figure 3b). These features could be modeled as a cobalt(II) ion bound to an organic radical anion (see Figure S27), where the high-field signal (Figure 3b, inset) represents the imide-based radical with moderate coupling to cobalt, the imide nitrogen and one hydrogen atom (presumably H<sub>para</sub>;  $A(^1\text{H})=6.8 \text{ G}$ ,  $A(^{59}\text{Co})=4.3 \text{ G}$ ,  $A(^{14}\text{N})=5.0 \text{ G}$ ). For more direct insight into the oxidation state of the metal, X-ray absorption spectroscopy (XAS) was employed (Figure 3c). For that we examined the pre-edge and edge regions of the Co 1s→3d\* transition of K{18c6}[2] as well as K[2] and the trigonal cobalt(II) amide K{crypt.222}[4] (high-spin Co<sup>II</sup>, synthesis see below) for comparison (solid state or frozen Me–THF solution). XANES shows similar edge positions for all compounds as well as a considerable pre-edge feature. In some cases a shoulder is observed in the edge rise, which, together with a shallow or even lacking edge maximum, is indicative of a low local coordination symmetry for all complexes. This is supported by EXAFS data which also gives congruent features in solid and solution state. Using cobalt oxides as references XANES suggests an oxidation

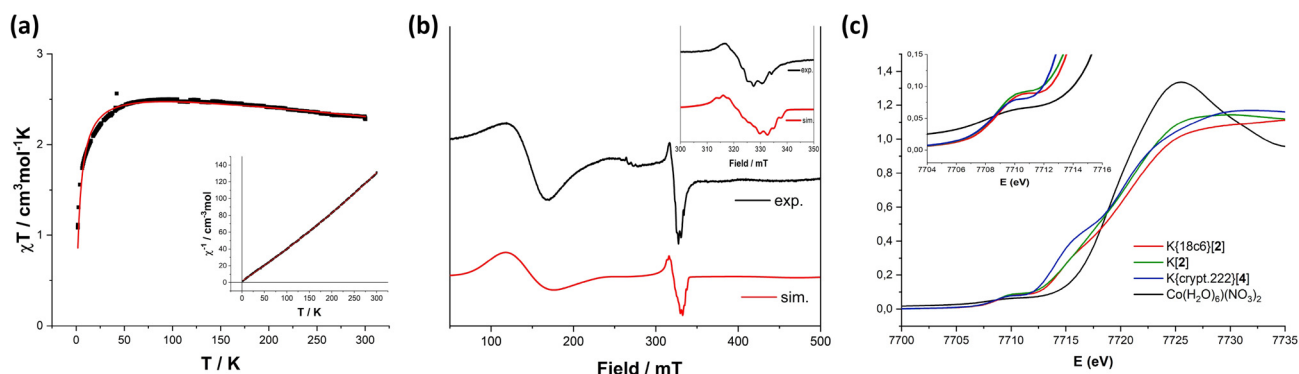


**Figure 3.** a) Variable-temperature susceptibility of K{18c6}[2] collected at 1 T, with  $\chi_{\text{M}}T=2.33 \text{ cm}^3 \text{ mol}^{-1} \text{ K}$  (300 K) and  $n_{\text{eff}}=4.635(4) \mu_{\text{B}}$ . Inset: Reciprocal molar magnetic susceptibility ( $\chi^{-1}$ ) for compound K{18c6}[2]. b) X-Band EPR spectra of K{18c6}[2] in frozen Me–THF solution at 8 K (black) and simulated spectrum (red). K{18c6}[2]:  $S_1=3/2$ ,  $g_{11}=5.0$ ,  $g_{12}=1.4$ ;  $S_2=1/2$ ,  $g_{21}=2.9$ ,  $g_{22}=2.05$ ,  $A_{22}(^1\text{H})=6.8 \text{ G}$ ,  $A_{22}(^14\text{N})=5.0 \text{ G}$ ,  $A_{22}(^{59}\text{Co})=4.3 \text{ G}$ . Hyperfine splitting for signal  $g_{22}=2.05$ . c) Solid-state X-ray absorption spectroscopy (XANES): K{18c6}[2] (red), K[2] (green), K{crypt.222}[4] (blue), Co<sup>II</sup> reference Co(H<sub>2</sub>O)<sub>6</sub>(NO<sub>3</sub>)<sub>2</sub> (black). Inset: Pre K-edge absorption.



state of +2.0 for  $[2]^-$  (and  $K[2]$ ). This is only slightly higher than the corresponding cobalt(II) amide  $[4]^-$  (+1.7) and overall supports a non-innocent character of the imido/imidyl unit.

For further understanding of the experimental findings we turned to computational analysis of the seminal  $K\{18c6\}[2]$ . All electronic structures in their various possible spin states (high-, intermediate- and low-spin) were studied through dispersion-corrected density functional theory (DFT-D3) whereas various density functionals including the generalized gradient approximation (GGA) functionals BLYP and BP; hybrid functional B3-LYP; meta-hybrid functional M06; and the meta-GGA functional M06-L were used for determining the electronic energy differences between different spin states. For all functionals the high-spin state was found to be the most stable for  $[2]^-$  with the intermediate spin slightly higher in energy ( $7 \text{ kJ mol}^{-1}$  to  $38 \text{ kJ mol}^{-1}$ ) and an unfavored low-spin configuration ( $67 \text{ kJ mol}^{-1}$  to  $157 \text{ kJ mol}^{-1}$ ). The differences of the computed spin states of  $[2]^-$  are visualized best using the Co–N<sub>imide</sub> bond which is shortened significantly from 1.75 Å (high-spin), 1.72 Å (intermediate-spin) to 1.67 Å (low-spin; Table 1), whereas the high-spin case represents best the experimental structural features. The analysis of the bond order, a valuable tool for considering contributions made by occupied levels, gives for the high-spin configuration a Wiberg Bond Index (WBI) of 0.79 for the cobalt imidyl bond (Co1–N1), and thus reflects a single-bond character. When going to lower spin states the WBI successively increases (intermediate spin: 1.02, low spin: 1.48) and, together with the shortening of the Co–N<sub>imide</sub> bonds, leads to a more double-bond character. The N–C<sub>aryl</sub> bond lengths, sometimes used as an indicator for the electronic structure of a metal-bound aryl imide,<sup>[28]</sup> are more or less unaffected by the spin state in the present case.

In comparison with the lower spin states, slightly higher Mulliken atomic charges on the cobalt ion in the high-spin state could be observed, which indicates a moderately decreased covalent character of the Co–N<sub>imide</sub> bond (Table 2). The spin density plot, obtained from population analysis of high-spin  $[2]^-$ , shows not only the involvement of the aryl imido unit but also further contributions from the ancillary ligand set (Figure 4, left). The SOMO is mainly localized on the cobalt atom as well as on the imide nitrogen (Figure 4, right). Additional unpaired spin density is found at the *ortho* and *para* positions of the aromatic ring, which reflects well the situation derived from EPR spectroscopy.

**Table 1:** Comparison of selected bond lengths and angles of  $[2]^-$  calculated at the level of DFT-D3/M06-L with the experimental values.<sup>[a]</sup>

Bond lengths [Å] and angles [°]	Experimental values	Calculated		
		h.s.	i.s.	l.s.
$r(\text{Co1-N1})$	1.751	1.758	1.723	1.673
$r(\text{Co1-N2})$	1.935	1.951	1.928	1.858
$r(\text{Co1-N3})$	1.932	1.954	1.924	1.977
$r(\text{N1-C1})$	1.347	1.332	1.337	1.352
$\alpha(\text{Co1-N1-C1})$	178.8	172.39	172.53	162.76

[a] h.s. = high-spin, i.s. = intermediate-spin, l.s. = low-spin.

**Table 2:** Mulliken atomic charges and spin densities on the selected atoms of complex  $[2]^-$  at the level of DFT-D3/M06-L.

Atom	Mulliken atomic charges (spin density)		
	h.s.	i.s.	l.s.
Co1	0.767 (2.620)	0.720 (1.975)	0.688
N1	−0.650 (0.814)	−0.657 (−0.029)	−0.649
N2	−0.963 (0.133)	−0.940 (0.086)	−0.905
N3	−0.968 (0.128)	−0.945 (0.065)	−0.923

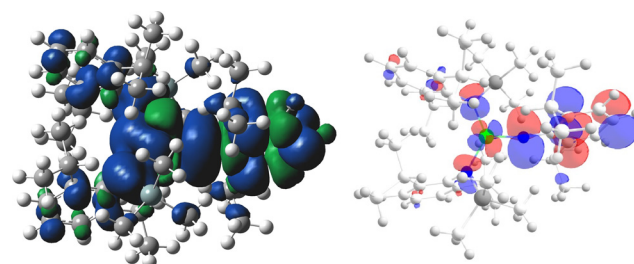
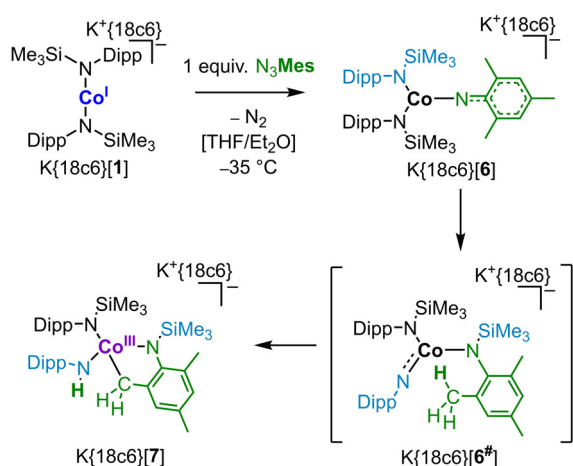


**Figure 4.** Left: Total spin density distribution of the complex  $[2]^-$  in high-spin state. An isosurface value of 0.003 a.u. is chosen. Right: SOMO of complex  $[2]^-$  (calculated with DFT-D3 using the density functional M06-L).

SOMO–1, SOMO–2, SOMO–3 and HOMO are of mixed character with unpaired spin density on the supporting aryl imido ligands as well (see SI). In comparison, for the intermediate-spin state the unpaired spin density is located almost exclusively on the cobalt ion (Table 2). Together with the increased WBI of 1.02 it gives the triplet state a distinct imide character. Overall, calculated electronic and structural parameters of high-spin  $[2]^-$  are in accord with the experimental findings and thus validate the description of  $[2]^-$  as an imidyl complex. This further shows that only in case of the high-spin state the imidyl radical character is present.

Having the first authenticated imidyl cobalt complexes in hand we examined their H atom abstraction capability. Reaction of  $K\{18c6\}[2]$  with 1,4-cyclohexadiene (1,4-CHD, BDE:  $76 \pm 2 \text{ kcal mol}^{-1}$ ) showed clean but slow formation of benzene and the cobalt(II) amide  $K\{18c6\}[\text{CoL}_2(\text{NHDipp})]$ ,  $K\{18c6\}[4]$ , which subsequently undergoes amide ligand scrambling to complex  $\{18c6\}[\text{CoL}(\text{NHDipp})_2]$ ,  $K\{18c6\}[5]$ . To reduce steric factors concerning the observed moderate reactivity of  $[2]^-$ , Mes–N<sub>3</sub> (Mes = 2,4,6-trimethylphenyl) was reacted with  $[1]^-$ . This gave the mesitylimido cobalt complex  $K\{18c6\}[2]$  (Scheme 2), which also has an enlarged Co–N<sub>imide</sub> bond (1.752(2) Å).  $K\{18c6\}[6]$  is highly reactive and could not be isolated in pure form as it facilitates intramolecular C–H bond activation of one of the Me<sub>iPr</sub> groups. It led to the alkyl/amido cobalt(III) complex  $K\{18c6\}[3]$ , which co-crystallized in varying ratios (Figure 5). Closer inspection of the molecular structure of  $K\{18c6\}[7]$  showed that the mesityl nitrogen is now carrying a Me<sub>3</sub>Si unit which originates from the –N(Dipp)SiMe<sub>3</sub> ligand set. This likely occurs starting from  $[6]^-$  with a Me<sub>3</sub>Si shift from the silylamide ligand to the mesityl



**Scheme 2.** Synthesis of  $[6]^-$  and formation of  $[7]^-$  by  $\text{Me}_3\text{Si}$ -group shift followed by intramolecular C–H activation by the transient cobalt imide  $[6]^-$ .

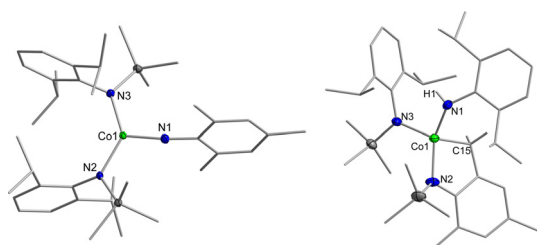


**Figure 5.** Molecular structure of  $\text{K}\{18\text{c}6\}[6]$  and  $\text{K}\{18\text{c}6\}[7]$  in the solid state.<sup>[58]</sup> The  $\text{K}\{18\text{c}6\}$  cation, solvent molecules as well as extraneous H atoms are omitted for clarity. Selected bond length (Å) and angles (°):  $\text{K}\{18\text{c}6\}[6]$ : Co1–N1 1.752(2); Co1–N2 1.931(1); Co1–N3 1.927(1); N1–C1 1.344(2); Co1–N1–C1 168.9(1);  $\text{K}\{18\text{c}6\}[7]$ : Co1–N1 1.897(3); Co1–N2 1.953(3); Co1–N3 1.977(3); Co1–C15 1.960(4).

imide unit which gives the transient cobalt complex  $[\text{CoL}(\text{NDipp})(\text{N}(\text{Mes})\text{SiMe}_3)]^-$  ( $[6]^-$ ). It points to a nucleophilic imide nitrogen in  $[6]^-$  that contrasts the general electrophilic behavior of late 3d-transition metal imides.<sup>[17,28,32,34,42–47]</sup>

Subsequently, intramolecular C–H bond activation in  $[6]^-$  leads to the highly labile organocobalt complex  $\text{K}\{18\text{c}6\}[7]$ . Intramolecular C–H bond activation is usually an unwanted phenomenon for late 3d-metal imido complexes and mainly occurs under insertion of the  $[\text{NR}]$  unit into a C–H bond of the imide substituent or the ancillary ligand set.<sup>[33,41]</sup> However, the formation of a metal–carbon bond was only observed for a mesityl imido cobalt(III) complex<sup>[16]</sup> and a transient aryl imido iron(II) complex.<sup>[36]</sup> There, a recombination of the formed carbon radical with the metal center and not the imide nitrogen was proposed. This is also plausible in the presented case, although a formal addition of the C–H bond along the Co–N unit or a deprotonation mechanism cannot be excluded. Overall, the experimental observations hint to a high reactivity of the imidyl cobalt(II) function and may explain its elusive character.<sup>[15,16,27,35]</sup>

We herein reported the synthesis and characterization of a variety of anionic and formally neutral trigonal arylimido cobalt complexes. They all exhibit by far the longest reported

Co–N<sub>imide</sub> bonds of around 1.75 Å. Comprehensive examination of the physical and spectroscopic properties led to their description as high-spin imidyl cobalt complexes. This is corroborated by computational analysis which connects the imidyl character to the complexes' high-spin state. With the smaller mesityl azide a mesitylimido cobalt complex was observed which underwent an unusual  $\text{Me}_3\text{Si}$ -group shift from the ancillary amide ligand set to the imidyl nitrogen. Overall, this study underscores the impact of the spin state on the central Co–N<sub>imide</sub> bond, and reveals a nucleophilic and highly reactive character of the cobalt imidyl unit.

## Acknowledgement

Funding by the Deutsche Forschungsgemeinschaft (DFG) is gratefully acknowledged: grant WE 5627/4-1 (C.G.W.). M.K. and R.B. thank the Center for Scientific Computing (CSC) Frankfurt for computer time and R. K. Bansal and M. Holthausen for discussion. Open access funding enabled and organized by Projekt DEAL.

## Conflict of interest

The authors declare no conflict of interest.

**Keywords:** C–H bond activation · cobalt · imido · quantum chemical calculations · spectroscopy

- [1] J. Y. Park, Y. Kim, D. Y. Bae, Y. H. Rhee, J. Park, *Organometallics* **2017**, *36*, 3471.
- [2] H. Lu, X. P. Zhang, *Chem. Soc. Rev.* **2011**, *40*, 1899.
- [3] F. Collet, R. H. Dodd, P. Dauban, *Chem. Commun.* **2009**, 5061.
- [4] V. Bagchi, A. Kalra, P. Das, P. Paraskevopoulou, S. Gorla, L. Ai, Q. Wang, S. Mohapatra, A. Choudhury, Z. Sun, T. R. Cundari, P. Stavropoulos, *ACS Catal.* **2018**, *8*, 9183.
- [5] P. F. Kuijpers, J. I. van der Vlugt, S. Schneider, B. de Bruin, *Chem. Eur. J.* **2017**, *23*, 13819.
- [6] D. N. Zalatan, J. Du Bois in *Metal-Catalyzed Oxidations of C–H to C–N Bonds*, 2009, (Eds.: JQ. Yu, Z. Shi), Springer, Berlin, Heidelberg, **2009**, pp. 347–378.
- [7] Y. Dong, C. J. Lund, G. J. Porter, R. M. Clarke, S.-L. Zheng, T. R. Cundari, T. A. Betley, *J. Am. Chem. Soc.* **2021**, *143*, 817.
- [8] R. Breslow, S. H. Gellman, *J. Am. Chem. Soc.* **1983**, *105*, 6728.
- [9] R. Breslow, S. H. Gellman, *J. Chem. Soc. Chem. Commun.* **1982**, 1400.
- [10] M. M. Díaz-Requejo, T. R. Belderráin, M. C. Nicasio, S. Trofimenko, P. J. Pérez, *J. Am. Chem. Soc.* **2003**, *125*, 12078.
- [11] D. Hazelard, P.-A. Nocquet, P. Compain, *Org. Chem. Front.* **2017**, *4*, 2500.
- [12] T. Stüker, T. Hohmann, H. Beckers, S. Riedel, *Angew. Chem. Int. Ed.* **2020**, *59*, 23174; *Angew. Chem.* **2020**, *132*, 23374.
- [13] T. A. Betley, J. C. Peters, *J. Am. Chem. Soc.* **2003**, *125*, 10782.
- [14] X. Hu, K. Meyer, *J. Am. Chem. Soc.* **2004**, *126*, 16322.
- [15] L. Zhang, Y. Liu, L. Deng, *J. Am. Chem. Soc.* **2014**, *136*, 15525.
- [16] E. R. King, G. T. Sazama, T. A. Betley, *J. Am. Chem. Soc.* **2012**, *134*, 17858.
- [17] J. Du, L. Wang, M. Xie, L. Deng, *Angew. Chem. Int. Ed.* **2015**, *54*, 12640; *Angew. Chem.* **2015**, *127*, 12831.
- [18] B. Wu, R. Hernández Sánchez, M. W. Bezpalko, B. M. Foxman, C. M. Thomas, *Inorg. Chem.* **2014**, *53*, 10021.

- [19] R. E. Cowley, R. P. Bontchev, J. Sorrell, O. Sarracino, Y. Feng, H. Wang, J. M. Smith, *J. Am. Chem. Soc.* **2007**, *129*, 2424.
- [20] Y. Liu, L. Deng, *J. Am. Chem. Soc.* **2017**, *139*, 1798.
- [21] J. J. Scepianiak, J. A. Young, R. P. Bontchev, J. M. Smith, *Angew. Chem. Int. Ed.* **2009**, *48*, 3158; *Angew. Chem.* **2009**, *121*, 3204.
- [22] D. T. Shay, G. P. A. Yap, L. N. Zakharov, A. L. Rheingold, K. H. Theopold, *Angew. Chem. Int. Ed.* **2006**, *45*, 7870; *Angew. Chem.* **2006**, *118*, 8034.
- [23] X. Dai, P. Kapoor, T. H. Warren, *J. Am. Chem. Soc.* **2004**, *126*, 4798.
- [24] D. M. Jenkins, T. A. Betley, J. C. Peters, *J. Am. Chem. Soc.* **2002**, *124*, 11238.
- [25] C. Jones, C. Schulten, R. P. Rose, A. Stasch, S. Aldridge, W. D. Woodul, K. S. Murray, B. Moubarak, M. Brynda, G. La Macchia, L. Gagliardi, *Angew. Chem. Int. Ed.* **2009**, *48*, 7406; *Angew. Chem.* **2009**, *121*, 7542.
- [26] M. P. Mehn, S. D. Brown, D. M. Jenkins, J. C. Peters, L. Que, *Inorg. Chem.* **2006**, *45*, 7417.
- [27] S. Thyagarajan, D. T. Shay, C. D. Incarvito, A. L. Rheingold, K. H. Theopold, *J. Am. Chem. Soc.* **2003**, *125*, 4440.
- [28] D. A. Iovan, T. A. Betley, *J. Am. Chem. Soc.* **2016**, *138*, 1983.
- [29] Y. Dong, J. T. Lukens, R. M. Clarke, S.-L. Zheng, K. M. Lancaster, T. A. Betley, *Chem. Sci.* **2020**, *123*, 4623.
- [30] A. Reckziegel, C. Pietzonka, F. Kraus, C. G. Werncke, *Angew. Chem. Int. Ed.* **2020**, *59*, 8527; *Angew. Chem.* **2020**, *132*, 8605.
- [31] Y. Baek, T. A. Betley, *J. Am. Chem. Soc.* **2019**, *141*, 7797.
- [32] K. M. Carsch, I. M. DiMucci, D. A. Iovan, A. Li, S.-L. Zheng, C. J. Titus, S. J. Lee, K. D. Irwin, D. Nordlund, K. M. Lancaster, T. A. Betley, *Science* **2019**, *365*, 1138.
- [33] Y. Baek, E. T. Hennessy, T. A. Betley, *J. Am. Chem. Soc.* **2019**, *42*, 16944.
- [34] Y. Liu, J. Du, L. Deng, *Inorg. Chem.* **2017**, *56*, 8278.
- [35] D. T. Shay, G. P. A. Yap, L. N. Zakharov, A. L. Rheingold, K. H. Theopold, *Angew. Chem. Int. Ed.* **2005**, *44*, 1508; *Angew. Chem.* **2005**, *117*, 1532.
- [36] J. Cheng, J. Liu, X. Leng, T. Lohmiller, A. Schnegg, E. Bill, S. Ye, L. Deng, *Inorg. Chem.* **2019**, *58*, 7634.
- [37] T. R. Cundari, *J. Am. Chem. Soc.* **1992**, *114*, 7879.
- [38] A. I. Olivos Suarez, V. Lyaskovskyy, J. N. H. Reek, J. I. van der Vlugt, B. de Bruin, *Angew. Chem. Int. Ed.* **2013**, *52*, 12510; *Angew. Chem.* **2013**, *125*, 12740.
- [39] K. Ray, F. Heims, F. F. Pfaff, *Eur. J. Inorg. Chem.* **2013**, 3784.
- [40] R. Eikey, *Coord. Chem. Rev.* **2003**, *243*, 83.
- [41] J. F. Berry, *Comments Inorg. Chem.* **2009**, *30*, 28.
- [42] E. R. King, E. T. Hennessy, T. A. Betley, *J. Am. Chem. Soc.* **2011**, *133*, 4917.
- [43] M. J. T. Wilding, D. A. Iovan, A. T. Wrobel, J. T. Lukens, S. N. MacMillan, K. M. Lancaster, T. A. Betley, *J. Am. Chem. Soc.* **2017**, *139*, 14757.
- [44] E. T. Hennessy, R. Y. Liu, D. A. Iovan, R. A. Duncan, T. A. Betley, *Chem. Sci.* **2014**, *5*, 1526.
- [45] E. Kogut, H. L. Wiencko, L. Zhang, D. E. Cordeau, T. H. Warren, *J. Am. Chem. Soc.* **2005**, *127*, 11248.
- [46] J. Xiao, L. Deng, *Dalton Trans.* **2013**, *42*, 5607.
- [47] C. A. Laskowski, A. J. M. Miller, G. L. Hillhouse, T. R. Cundari, *J. Am. Chem. Soc.* **2011**, *133*, 771.
- [48] L. N. Grant, M. E. Carroll, P. J. Carroll, D. J. Mindiola, *Inorg. Chem.* **2016**, *55*, 7997.
- [49] D. J. Mindiola, G. L. Hillhouse, *J. Am. Chem. Soc.* **2001**, *123*, 4623.
- [50] D. J. Mindiola, G. L. Hillhouse, *Chem. Commun.* **2002**, 1840.
- [51] R. Waterman, G. L. Hillhouse, *J. Am. Chem. Soc.* **2003**, *125*, 13350.
- [52] N. D. Harrold, G. L. Hillhouse, *Chem. Sci.* **2013**, *4*, 4011.
- [53] C.-Y. Lin, J. C. Fettinger, F. Grandjean, G. J. Long, P. P. Power, *Inorg. Chem.* **2014**, *53*, 9400.
- [54] C. G. Werncke, E. Suturina, P. C. Bunting, L. Vendier, J. R. Long, M. Atanasov, F. Neese, S. Sabo-Etienne, S. Bontemps, *Chem. Eur. J.* **2016**, *22*, 1668.
- [55] R. Weller, I. Müller, C. Duhayon, S. Sabo-Etienne, S. Bontemps, C. G. Werncke, *Dalton Trans.* **2021**, *50*, 4890.
- [56] S. Kundu, E. Miceli, E. Farquhar, F. F. Pfaff, U. Kuhlmann, P. Hildebrandt, B. Braun, C. Greco, K. Ray, *J. Am. Chem. Soc.* **2012**, *134*, 14710.
- [57] I. Monte-Pérez, S. Kundu, K. Ray, *Z. Anorg. Allg. Chem.* **2015**, *641*, 78.
- [58] Deposition Numbers 2056475 (K{crypt.222}[1]), 2056468 (K{18c6}[2]), 2056470 (K{crypt.222}[2]), 2056477 (K[2]), 2056474 (K{18c6}[3]), 2056465 (K[3]), 2056469 (K{18c6}[4]), 2056472 (K{crypt.222}[4]), 2056477 (K[4]), 2056471 (K{18c6}[5]), 2056473 (K{crypt.222}[5]), 2056476 (K{18c6}[6]), and 2056467 (K{18c6}[7]) contain the supplementary crystallographic data for this paper. These data are provided free of charge by the joint Cambridge Crystallographic Data Centre and Fachinformationszentrum Karlsruhe Access Structures service [www.ccdc.cam.ac.uk/structures](http://www.ccdc.cam.ac.uk/structures).

Manuscript received: March 17, 2021  
Revised manuscript received: May 10, 2021  
Accepted manuscript online: May 11, 2021  
Version of record online: June 9, 2021

### 3.3 On the Synthesis of a T-shaped Imido Nickel Complex and Trigonal Amido Nickel Complexes

A. Reckziegel, B. Battistella, C.G. Werncke

*Eur. J. Inorg. Chem.* **2022**, e202101102.

DOI: 10.1002/ejic.202101102

<https://chemistry-europe.onlinelibrary.wiley.com/doi/10.1002/ejic.202101102?af=R>

#### Abstract

The synthesis of a T-shaped imido nickel complex is reported, obtained by the reaction of phenyl azide with the linear nickel(I) silylamide complex K18-crown-6[NiL<sub>2</sub>] (L=N(Dipp)SiMe<sub>3</sub>; Dipp=2,6-*diisopropylphenyl*). In addition, an unusual shift of a SiMe<sub>3</sub> unit from an ancillary ligand to a putative [Ni=NPh] complex is observed. Examination of the resulting [Ni=NDipp] complex for its electronic properties leads to its description as a low-spin nickel(III) imide and revealed only limited activity with respect to H-atom abstraction from C–H bonds or nitrene. Attempts to obtain information about the general features of trigonal nickel(II) amide products, that would result from such a H-atom abstraction reaction, via reaction of linear nickel(II) silylamide [NiL<sub>2</sub>] with alkali metal salts of primary amides revealed the reduction to the linear nickel(I) complex K18-crown-6[NiL<sub>2</sub>]. The same is observed for alkoxides, secondary amides or benzyl. Reaction of the organic salts with the anionic nickel(II) complex NBu<sub>4</sub>[NiBrL<sub>2</sub>] under salt elimination also give the linear nickel(I) complex. Partial formation of an otherwise stable T-shaped nickel(II) can be observed only for the electron-poor diphenyl amide. This implicates that reduction of the starting nickel(II) complexes by different organic alkali metal salts likely does not occur via a homolytic Ni-R bond cleavage but a direct SET process from the unligated substrate to the nickel(II) ion.

#### Zusammenfassung

Durch die Umsetzung von Phenylazid mit dem linearen Nickel(I)-Komplex K{18c6}[Ni(N(Dipp)SiMe<sub>3</sub>)<sub>2</sub>] (**81**) wurde der trigonale Imido-Nickel-Komplex K{18c6}[Ni(NDipp)(N(Dipp)SiMe<sub>3</sub>)(N(Ph)SiMe<sub>3</sub>)] (**109**) erhalten. Dieser wurde durch die Übertragung einer SiMe<sub>3</sub>-Gruppe von einem N(Dipp)SiMe<sub>3</sub>-Liganden auf den zunächst gebildeten Phenyl-Imido-Liganden gebildet.

Die Struktur im Festkörper zeigt eine Ni–N<sub>Imido</sub>-Bindungslänge von 1,702(2) Å. Dies weist deutlich von dem zuvor beschriebenen *high-spin* Imidyl-Cobalt-Komplex **100** (Cobalt–N<sub>Imido</sub>: 1,751(2) Å) ab, ist aber geringfügig länger ist, als bekannte trigonale Imido-Nickel-Komplexe. Weiterhin ist eine starke Verzerrung um das Nickel-Ion zu einer T-förmigen Koordination, mit einem der N(Dipp)SiMe<sub>3</sub>-Liganden in der äquatorialen Position, zu beobachten. Die bevorzugte T-förmige Koordination des Nickel(III)-Ions ist vermutlich die Triebkraft für die beobachtete Umlagerung der SiMe<sub>3</sub>-Gruppe.

Das, durch die EVANS-Methode in Lösung bestimmte, magnetische Moment (1,95 μ<sub>B</sub>) und das aufgenommene ESR-Spektrum weisen auf das Vorliegen eines *low-spin* Nickel(III)-Komplexes hin. Die Untersuchung des Reaktionsverhaltens von

**109** zeigte nur eine geringe Affinität zu H-Atom-Transfer-Reaktionen, wobei eine Isolierung des erwarteten Amido-Komplexes nicht möglich war.

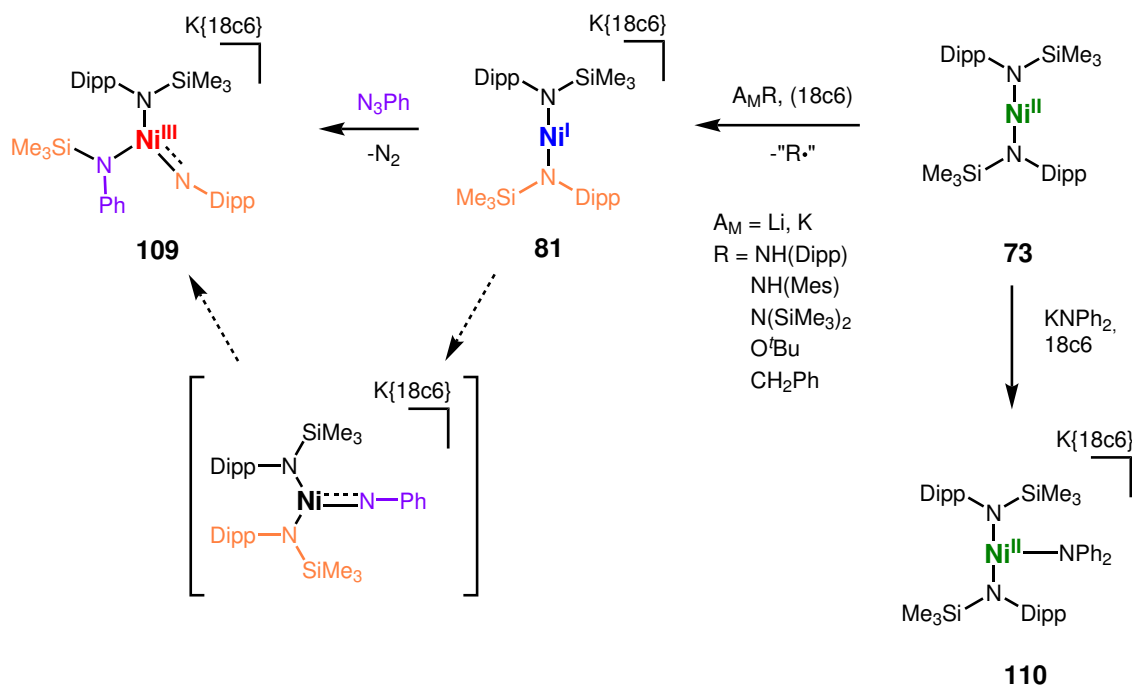


Abb. 48: Darstellung und Bildung des trigonalen Imido-Nickel-Komplexes **109** und Reduktion des linearen Nickel(II)-Komplexes (**73**) durch Alkalimetall Organylverbindungen.

Um das Reaktionsverhalten von trigonalen Amido-Nickel-Komplexen zu untersuchen, wurde versucht, diese durch Umsetzung von Kaliumamiden (KNHDipp, KNH-Mes) mit  $\text{Ni(N(Dipp)SiMe}_3)_2$  (**73**) in Gegenwart von 18c6 darzustellen. Die Reaktionskontrolle mittels  $^1\text{H-NMR}$ -Spektroskopie zeigte hier und für weitere Alkalimetall-Verbindungen (Li/ $\text{KN(SiMe}_3)_2$ ,  $\text{KO}^t\text{Bu}$ ,  $\text{KCH}_2\text{Ph}$ ), die Reduktion des Nickel(II)-Komplexes unter Bildung von  $A_M\{m\}[\text{Ni(N(Dipp)SiMe}_3)_2]$  ( $A_M = \text{Li, K}$ ;  $m = \text{thf}_4, 18\text{c6}$ ). Die Verwendung des elektronenarmen Kaliumdiphenylamides ermöglichte die Isolierung des trigonalen Amido Komplexes  $\text{K}\{18\text{c6}\}[\text{Ni(N(Dipp)SiMe}_3)_2\text{NPh}_2]$  (**110**). Untersuchungen über  $^1\text{H-NMR}$ -Spektroskopie zeigen, dass **110** stabil gegenüber der des Reduktiven Zerfalls ist, während bei dessen *in-situ* Darstellung ein geringer Anteil an **81** zu beobachtet ist. Dies deutet auf eine Reduktion des linearen Nickel(II)-Komplexes **73** durch eine direkte Ein-Elektronen-Übertragung der anionischen Substrate, statt durch eine homolytische Substrat-Nickel-Bindungsspaltung in einem zwischenzeitlich gebildeten trigonalen Komplex, hin.

Zusammenfassend konnte der Imido-Nickel-Komplex **109** mit einer T-förmigen Koordinationsgeometrie dargestellt und charakterisiert werden. Weiterhin wurde die Ein-Elektronen-Reduktion von  $\text{Ni(N(Dipp)(SiMe}_3)_2)$  durch verschiedene organische Salze der Alkalimetalle beschrieben.

### Beiträge der Autoren

Die gezeigten Verbindungen wurde von mir dargestellt und mittels  $^1\text{H-NMR}$ -, UV-Vis- und IR-Spektroskopie charakterisiert. Die Messung des magnetischen Momentes

nach der EVANS-Methode wurde durch die Serviceabteilung NMR-Spektroskopie der Philipps-Universität Marburg an einem Bruker AV III 500 durchgeführt und von mir ausgewertet.

Zur Bestimmung der Struktur im Festkörper, wurden Röntgenbeugungsexperimente am Einkristall durch die Serviceabteilung Kristallstrukturanalyse der Philipps Universität Marburg oder von *Dr. Gunnar Werncke* an einem Bruker D8 Quest durchgeführt. Ich habe die Strukturen aus den erhaltenen Daten gelöst und verfeinert.

Die Bestimmung der Reinheit erfolgte mittels CHN-Elementaranalytik durch die Serviceabteilung Elementaranalytik der Philipps-Universität Marburg.

Die Elektronenspinresonanz-Experimente wurde von *Beatrice Battistella* aus der Arbeitsgruppe von *K. Ray* an der Humboldt-Universität zu Berlin durchgeführt. Die Simulationen der erhaltenen Daten wurde von mir durchgeführt.

Das Manuskript habe ich in Zusammenarbeit mit *Dr. Gunnar Werncke* und in Absprache mit allen Co-Autoren verfasst.



## VIP Very Important Paper

## On the Synthesis of a T-Shaped Imido Nickel Complex and Trigonal Amido Nickel Complexes

Alexander Reckziegel,<sup>[a]</sup> Beatrice Battistella,<sup>[b]</sup> and C. Gunnar Werncke<sup>\*[a]</sup>

The synthesis of a T-shaped imido nickel complex is reported, obtained by the reaction of phenyl azide with the linear nickel(I) silylamide complex  $K\{18\text{-crown-}6\}[\text{NiL}_2]$  ( $\text{L}=\text{N}(\text{Dipp})\text{SiMe}_3$ ;  $\text{Dipp}=2,6\text{-diisopropylphenyl}$ ). In addition, an unusual shift of a  $\text{SiMe}_3$  unit from an ancillary ligand to a putative  $[\text{Ni}=\text{NPh}]$  complex is observed. Examination of the resulting  $[\text{Ni}=\text{NDipp}]$  complex for its electronic properties leads to its description as a low-spin nickel(III) imide and revealed only limited activity with respect to H-atom abstraction from C–H bonds or nitrene. Attempts to obtain information about the general features of trigonal nickel(II) amide products, that would result from such a H-atom abstraction reaction, via reaction of linear nickel(II)

silylamide  $[\text{NiL}_2]$  with alkali metal salts of primary amides revealed the reduction to the linear nickel(I) complex  $K\{18\text{-crown-}6\}[\text{NiL}_2]$ . The same is observed for alkoxides, secondary amides or benzyl. Reaction of the organic salts with the anionic nickel(II) complex  $\text{NBu}_4[\text{NiBrL}_2]$  under salt elimination also give the linear nickel(I) complex. Partial formation of an otherwise stable T-shaped nickel(II) can be observed only for the electron-poor diphenyl amide. This implicates that reduction of the starting nickel(II) complexes by different organic alkali metal salts likely does not occur via a homolytic Ni–R bond cleavage but a direct SET process from the unligated substrate to the nickel(II) ion.

## Introduction

The catalytic amination of unreactive C–H bonds by highly reactive imido complexes of late 3d-transition metals is increasingly shown to be of synthetic use for the formation of secondary amines.<sup>[1–10]</sup> A comprehensive insight into the properties of the imido metal bond, as well as the factors that contribute to its behavior, is thus crucial to control its reactivity. Despite an increasing number of isolable complexes, the electronic and structural factors that govern their reactivity are still not well understood. Most known isolable imido complexes are of low-spin character, which however mitigates its reactivity. As such the amount of the more reactive complexes in higher spin-states is still limited.<sup>[11–17]</sup> Thereby it shows that more intriguing bonding situations in such imido metal complexes, that deviates from the classic description as an  $[\text{NR}]^{2-}$  unit bound to a  $\text{M}^{n+2}$  ion, are increasingly found.<sup>[18,19]</sup> These encompass for iron,<sup>[11]</sup> cobalt<sup>[20,21]</sup> and nickel<sup>[16,22,23]</sup> very few

examples of complexes with a metal bound imidyl  $[\text{NR}]^-$  unit as well as an isolated and putative copper(I) nitrene species.<sup>[24]</sup>

Taking a closer look at nickel, only a small number of isolable, structurally identified imido nickel complexes are known, all in a low-coordinate environment (coordination number  $\leq 3$ ). Their isolation relied either on the use of neutral donor ligands, namely NHC's or chelating phosphines<sup>[25–29]</sup> or chelating monoanionic N-donor ligands (Figure 1).<sup>[22,30]</sup> Most of these compounds are found in a low-spin state. Remarkable exceptions constitute pyrromethane (pyrro) and related bisoxazoline (box) ligated, trigonal imido nickel complexes from Betley for which experimental evidence leads to its description as nickel(II) imidyl species (Figure 1F).<sup>[31]</sup> Here it was attributed to the presence of the weak ligand field imposed by the ancillary ligands, which overall favors higher spin-states. These

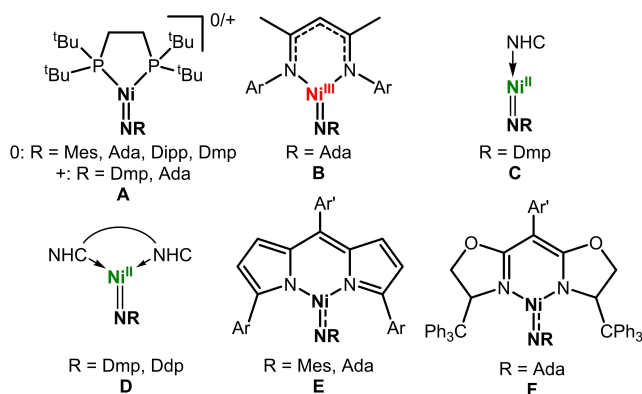


**Figure 1.** Overview of known, low-coordinate imido nickel complexes. A,<sup>[26,28,32,33]</sup> (Ada = adamantyl-, Dmp = 2,6-dimesitylphenyl), B,<sup>[30]</sup> C,<sup>[34]</sup> D<sup>[35]</sup> (Ddp = 2,6-bis(2,6-diisopropyl)phenyl), E,<sup>[22]</sup> and F.<sup>[31]</sup>

[a] A. Reckziegel, Dr. C. G. Werncke  
Department of Chemistry  
Philipps-University Marburg  
Hans-Meerwein-Straße 4, 35032, Marburg, Germany  
E-mail: gunnar.werncke@chemie.uni-marburg.de

[b] B. Battistella  
Institute of Chemistry  
Humboldt-University Berlin  
Brook-Taylor-Strasse 2, 12489, Berlin, Germany

Supporting information for this article is available on the WWW under <https://doi.org/10.1002/ejic.202101102>

Part of the "YourJIC Talents" Special Collection.

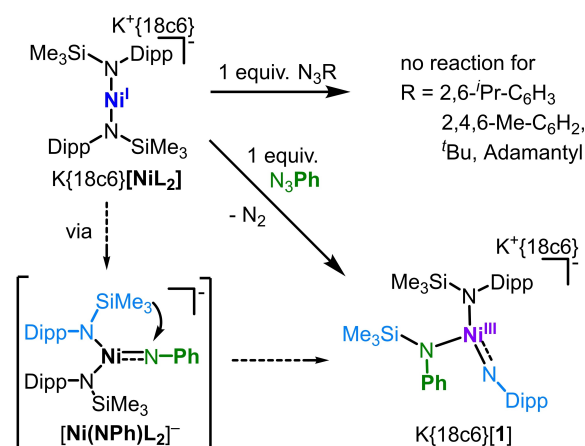
© 2022 The Authors. European Journal of Inorganic Chemistry published by Wiley-VCH GmbH. This is an open access article under the terms of the Creative Commons Attribution Non-Commercial License, which permits use, distribution and reproduction in any medium, provided the original work is properly cited and is not used for commercial purposes.

complexes are capable of catalytic inter- as well as intramolecular C–H amination.

Recently, we contributed to the few examples of imido complexes of the late 3d-transition metals in higher spin states: The trigonal intermediate-spin alkyl imido cobalt(III) complex  $[\text{Co}(\text{N}^t\text{Bu})(\text{N}(\text{SiMe}_3)_2)_2]^-$  proved as exceptionally potent in C–H bond abstraction.<sup>[17]</sup> The related high-spin arylimido cobalt complex  $[\text{Co}(\text{NDipp})\text{L}_2]$  (L=N(Dipp)SiMe<sub>3</sub>, Dipp=2,6-diisopropylphenyl) exhibited radical imidyl character of the imide ligand, whereas steric protection was needed to allow for its isolation.<sup>[36]</sup> We were thus curious if these findings would translate to the heavier neighbor nickel, where a more covalent, thus more reactive metal-imide bond might be expected.<sup>[18,19]</sup>

## Results and Discussion

With this in mind, we thought of the linear nickel(I) silylamido complex  $\text{K}\{18\text{c}6\}[\text{NiL}_2]$  (18c6=18-crown-6) as a suitable entry for low-coordinate imido nickel complexes. Surprisingly, for its treatment with different alkyl- and aryl azides ( $\text{N}_3\text{R}$ : R=<sup>t</sup>Bu, adamantyl, Mes=2,4,6-Me-C<sub>6</sub>H<sub>2</sub>, Dipp) no reaction occurred. We attributed this to the, compared to cobalt, lower reduction potential of the linear nickel(I) complex as well less accessible metal ion due to contraction of the metal amide bond.<sup>[37,38]</sup> As such, only reaction of  $\text{K}\{18\text{c}6\}[\text{NiL}_2]$  with the smallest aromatic azide,  $\text{PhN}_3$ , led to formation of the nickel imide  $\text{K}\{18\text{c}6\}[\text{1}]$  (34%, dark yellow, Scheme 1), as evidenced by X-ray diffraction analysis on suitable crystals (Figure 2). Closer inspection also showed that a shift of a SiMe<sub>3</sub> function from an ancillary silylamide ligand to the phenyl nitrogen occurred. This can be explained by formation of the putative phenyl imido complex  $[\text{Ni}(\text{NPh})\text{L}_2]^-$  (Scheme 1) with a nucleophilic imide function that then facilitates the SiMe<sub>3</sub> shift. This unusual phenomenon was already observed indirectly by us in case of cobalt, whereas the respective rearranged imido complex corresponding to  $[\text{1}]^-$  proved to be too reactive for identification due to intramolecular C–H bond activation.<sup>[36]</sup> The formation of  $[\text{1}]^-$  thus corroborates in hindsight that the SiMe<sub>3</sub> shift precedes C–H activation. In solid state the Ni1–N1 bond length of  $[\text{1}]^-$  amounts to 1.702(2) Å with a Ni1–N1–C1 bond angle of 164.8(2)°. The metal imide bond length is shorter than in the



Scheme 1. Synthesis of  $\text{K}\{18\text{c}6\}[\text{1}]$  by reaction of  $\text{K}\{18\text{c}6\}[\text{NiL}_2]$  with  $\text{N}_3\text{Ph}$ .

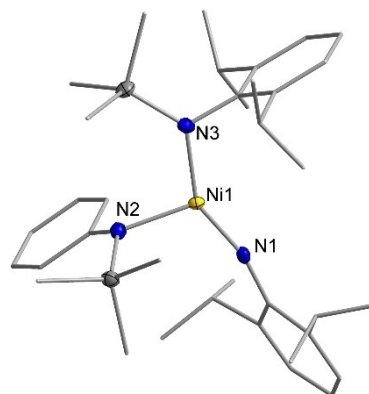


Figure 2. Molecular structure of  $\text{K}\{18\text{c}6\}[\text{1}]$  in the solid state. The  $\text{K}\{18\text{c}6\}$  cation, solvent molecules as well as H atoms are omitted for clarity. Selected bond length (Å) and angles (°): Ni1–N1: 1.702(2); Ni1–N2: 1.957(2); Ni1–N3: 1.898(2); N1–C1: 1.359(4); Ni1–N1–C1: 164.8(2); N1–Ni1–N2: 112.0(1); N1–Ni1–N3: 146.6(1); N2–Ni1–N3: 101.4(1).

related high-spin cobalt complex ( $\text{Co}-\text{N}_{\text{imidyl}}$ : 1.751(2) Å) with imidyl character but similar to the intermediate-spin cobalt complex ( $\text{Co}-\text{N}_{\text{imide}}$ : 1.7067(12) Å). Similar Ni–N bond lengths were observed for diphosphine nickel(II) aryl imido complexes  $[\text{LNi}(\text{NR})]^{+0}$  described by the group of Hillhouse (Figure 1A), whereas a decrease of the Ni– $\text{N}_{\text{imide}}$  bond lengths is observed for the respective Ni(III) complexes (e.g. for  $[\text{LNi}(\text{N}(\text{Dmp}))]$ : 1.697(2) Å;  $[\text{LNi}(\text{N}(\text{Dmp}))]^+$ : 1.674(3) Å, 2,6-dimesityl-C<sub>6</sub>H<sub>3</sub>).<sup>[28,33]</sup>

The group of Betley reported a bond length of 1.696(2) Å for an arylimido complex showing imidyl like character.<sup>[16]</sup> The N1–C1 bond in  $[\text{1}]^-$  amounts to 1.359(4) Å, that is at the upper end of known aryl imido nickel complexes, making a imidyl like bonding situation however unlikely.<sup>[16,19,26,28,32,35]</sup> The geometry around nickel is best described as T-shaped with the newly formed  $-\text{N}(\text{Ph})\text{SiMe}_3$  ligand in the equatorial position. Its Ni1–N2 bond length amounts to 1.957(2) Å which is substantially longer than the one of the silyl amide (1.898(2) Å) that is positioned trans to the imide. It is thus tempting to regard  $[\text{1}]^-$  as an amide adduct of the linear nickel imide  $[\text{Ni}(\text{NDipp})\text{L}]$ . Most mentioned three-coordinate imido nickel complexes (Figure 1)



Gunnar Werncke studied chemistry at the Humboldt-University Berlin, Germany, where he also obtained his PhD under the guidance of Prof. Christian Limberg. After finishing in 2012, he joined the group of Dr. S. Sabo-Etienne at the Laboratoire de Chimie de Coordination in Toulouse, France. In late 2015, he started his independent career and is Fellow of the Emmy-Noether-Programme of the German Research Council (DFG) since 2016. His research focuses on low-valent, linear 3d-transition metal complexes and their use in bond activation as well as in stabilization of unusual main-group fragments. (Photography Jochen Mogk)

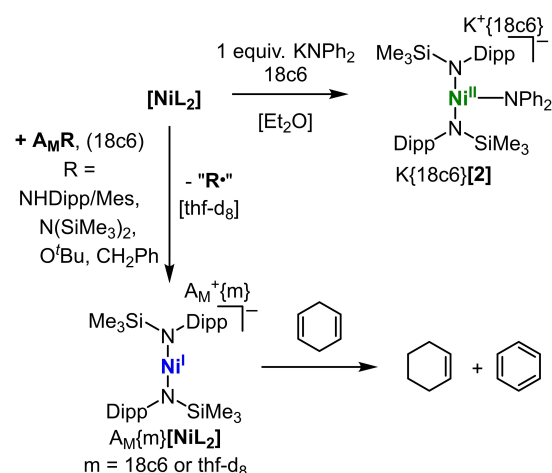


show only slight distortion from a trigonal planar coordination, as exemplified by the nickel(III) imide (Figure 1B) by the group of Warren.<sup>[30]</sup> As a T-shaped geometry of three-coordinate complexes is not unusual for electron rich d-metals<sup>[39–43]</sup> this speaks to steric constraints in those complexes. The geometry of [1]<sup>−</sup> resembles thus more the T-shaped nickel(III) methyl complex [Ni(Me)L<sub>2</sub>], where the methyl group adopts the equatorial position.<sup>[44]</sup> The preference of a T-shaped geometry is the likely driving force for the silyl shift and formation of K{18c6}[1], as it allows for release of steric strain and positioning of the imide ligand in axial position. The <sup>1</sup>H-NMR spectrum of K{18c6}[1] does not show any signals in the range of +200 to −200 ppm belonging to its complex anion. Its magnetic moment amounts to  $\mu_{\text{eff}} = 1.95 \mu_{\text{B}}$  as determined by Evans method in solution<sup>[45]</sup> which is close to the spin-only value of an  $S = 1/2$  system ( $\mu_{\text{s.o.}} = 1.73 \mu_{\text{B}}$ ). Together with a rhombic signal in the X-Band EPR spectrum ( $g_{11} = 2.6$ ,  $g_{12} = 2.2$ ,  $g_{13} = 2.0$ ; see ESI), that would not be in agreement with the alternate description as an antiferromagnetically coupled nickel(II) imidyl, it leads to a formulation of [1]<sup>−</sup> as a low-spin nickel(III) imide.

Examination of the reactivity of [1] showed that it is incapable of nitrene transfer to electron rich substrates (tricyclohexyl phosphine, styrene and phenyl isocyanate), an already observed behavior of related imido cobalt silylamido complexes.<sup>[17,36]</sup> Further, only a low H atom abstraction (HAA) capability is observed as exemplified by using 1,4-cyclohexadiene (CHD) as substrate. In the presented case we tentatively attribute it to the low-spin state of the nickel imide, given the otherwise fairly accessible imide function. A presumably formed nickel(II) amide formed from HAA by [1]<sup>−</sup> could thereby not be isolated from the reaction mixture.

Before the background that the trigonal primary amide carrying cobalt(II) silylamido complex [Co(NH<sup>t</sup>Bu)(NR<sub>2</sub>)<sub>2</sub>]<sup>−</sup> (R=SiMe<sub>3</sub>) was active in H-atom abstraction from suitable substrates under formation of the linear cobalt(I) complex [Co(NR<sub>2</sub>)<sub>2</sub>]<sup>−</sup>,<sup>[17,37]</sup> we were nonetheless interested in the behavior of related amide nickel species. Interestingly, addition of the potassium salts KR<sup>1</sup> (R<sup>1</sup>=NHDipp, NHMes) to the linear nickel(II) complex [NiL<sub>2</sub>]<sup>−</sup> in the presence of 18c6 in thf revealed the linear nickel(I) starting complex K{18c6}[NiL<sub>2</sub>]<sup>−</sup> as the main product by its isolation as well as by *in-situ* <sup>1</sup>H-NMR spectroscopy (Scheme 2). Only very minor paramagnetic signals could be observed that might be attributable to a transient species bearing of the type K{18c6}[Ni(R<sup>1</sup>)L<sub>2</sub>].

The use of LiNHDipp in C<sub>6</sub>D<sub>6</sub> – to examine the effect of lacking counter cation separation – showed by <sup>1</sup>H NMR spectroscopy the slow disappearance of [NiL<sub>2</sub>]<sup>−</sup>, with no dominant signature of a new paramagnetic species and also no signs of [NiL<sub>2</sub>]<sup>−</sup>. As such we contemplated on the exchange of amide ligands and subsequent decomposition, or intramolecular deprotonation.<sup>[47]</sup> In contrast, performing the same reaction in thf-d<sub>8</sub> yielded again [NiL<sub>2</sub>]<sup>−</sup>, showing that cation separation is crucial for the reduction to take place, and that the nature of the alkali metal cation is negligible. For the alkyl amide LiNH<sup>t</sup>Bu similar observations were made. Subsequently, this could also be extended to KN(SiMe<sub>3</sub>)<sub>2</sub> as secondary amide, the alkoxides KO<sup>t</sup>Bu and KOMe, as well as benzyl potassium. In case of the



**Scheme 2.** Reaction of Ni<sup>II</sup>(NDippSiMe<sub>3</sub>)<sub>2</sub>, [NiL<sub>2</sub>] by organic alkali metal salts A<sub>m</sub>R<sup>+</sup> (for A<sub>m</sub>=K, m = 18c6, R=NHDipp, NHMes, N(SiMe<sub>3</sub>)<sub>2</sub>, OtBu, CH<sub>2</sub>Ph; for A<sub>m</sub>=Li, m = thf, R=NHDipp, NH<sup>t</sup>Bu).

latter small amounts 1,2-diphenyl ethane was observed. This hinted to the intermediate presence of the benzyl radical that might be result of direct one-electron reduction of [NiL<sub>2</sub>] via single electron transfer (SET), or homolytic bond cleavage of a transient nickel(II) benzyl complex ([NiL<sub>2</sub>(CH<sub>2</sub>Ph)]<sup>−</sup>). Similar reduction of a palladium(II) complex by homolytic Pd–N bond cleavage of an amido ligand was recently described, as well as the aminyl type behavior of copper or rhodium bound amides.<sup>[48–51]</sup> Alternatively, the role of A<sub>m</sub>R species (e.g. KO<sup>t</sup>Bu) as direct one-electron reductants is widely accepted for organic substrates, which is known to occur via an inner-sphere SET.<sup>[52–54]</sup> A similar mechanism would also be plausible for the reduction of [NiL<sub>2</sub>] whereas its reduction by A<sub>m</sub>R would by-pass the formation of stable adducts of the type [Ni(R)L<sub>2</sub>]<sup>−</sup>.

To elaborate if H atom abstraction processes, e.g. facilitated by a hypothetical [Ni(R)L<sub>2</sub>]<sup>−</sup> adduct, are relevant in the present case we performed the abovementioned addition in the presence of suitable substrates, namely 9,10-dihydroanthracene (DHA) and CHD. Employing DHA, no signs of its H atom abstraction product anthracene were detected. With CHD the formation of not only benzene but also stoichiometric amounts of cyclohexene was observed (Scheme 2). This does not point to a hydrogen transfer to the transient nickel(amide) but a disproportionation reaction, mediated by the in situ formed K{18c6}[NiL<sub>2</sub>]. This type of disproportionation of CHD was already observed in case of the iron(I) complex [Fe(hmds)<sub>2</sub>]<sup>−</sup>,<sup>[55]</sup> and was confirmed by reacting CHD directly with K{18c6}[NiL<sub>2</sub>].

To substantiate the hypothesis of direct SET we also employed the rather electron poor, thus little reducing diphenyl amide KNPh<sub>2</sub>. Its reaction with [NiL<sub>2</sub>] in Et<sub>2</sub>O yielded green crystals of K{18c6}[Ni(NPh<sub>2</sub>)L<sub>2</sub>], K{18c6}[2] (yield 52%, dark green), whose structure was verified using X-ray diffraction analysis (Scheme 2, Figure 3 left).

The central nickel ion is coordinated by the two –N{Dipp}SiMe<sub>3</sub> and the –NPh<sub>2</sub> ligands in a distorted T shape fashion with the silylamide ligands in axial position. The N2–Ni1–N3 angle

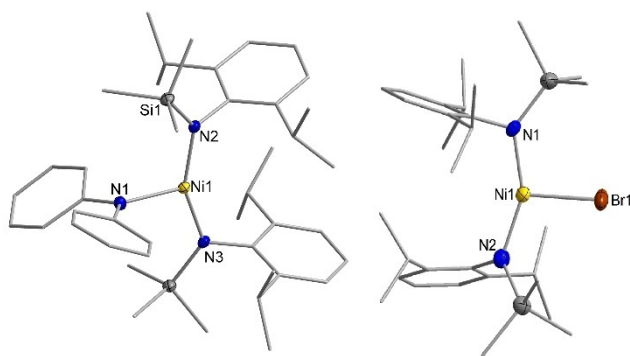


**Figure 3.** Molecular structure of  $K\{18c6\}[2]$  (left) and  ${}^tBu_4N[3]$  (right) in the solid state. The cations, a disorder of one  $SiMe_3$ -group of  $[3]$ , as well as H atoms are omitted for clarity. Selected bond length (Å) and angles ( $^\circ$ ):  $[2]^-$ : Ni1–N1: 2.010(2); Ni1–N2: 1.891(2); Ni1–N3: 1.892(2); N1–Ni1–N2: 104.4(1); N1–Ni1–N3: 104.5(1); N2–Ni1–N3: 151.1(1).  $[3]^-$ : Ni1–N1: 1.854(3); Ni1–N2: 1.897(3); Ni1–Br1: 2.4469(6); N1–Ni1–N2: 149.7(1); N1–Ni1–Br1: 102.8(1); N2–Ni1–Br1: 107.1(1).

between the two ancillary ligands is with  $151.1(1)^\circ$  slightly more bent than in neutral  $[Ni(X)L_2]$  ( $X=MeCN$ , pyridine,  $N'$ -4-dimethyl-aminopyridine) and anionic  $[Ni(Me)L_2]^-$ ,<sup>[38,44,46,56]</sup> that is attributed to the greater steric demand of the diphenyl amide. The Ni– $N_{amide}$  bond to the diphenyl amido ligand (Ni1–N1) is with 2.010(2) Å substantially longer than from nickel to the silylamide ligands (1.89 Å) but is in line with observations made for the few known anionic nickel complexes with diaryl amido ligation.<sup>[57–59]</sup>

In solution  $K\{18c6\}[2]$  shows by proton NMR spectroscopy a distinct paramagnetic signature as well as a solution magnetic moment of  $\mu_{eff}=3.32 \mu_B$ . This corresponds well with an  $S=1$  state of a high-spin nickel(II) ion ( $d^8$ ).  $K\{18c6\}[2]$  is stable in solution with no signs of degradation and  $[NiL_2]^-$  formation. This is in line with observations of the related T-shaped methyl nickel (II) complex  $[Ni(Me)L_2]^-$ .<sup>[38,60]</sup> In contrast, in-situ  ${}^1H$  NMR spectroscopic analysis of the reaction of  $[NiL_2]$  with  $KNPh_2$  spectroscopy showed, besides  $K\{18c6\}[2]$ , substantial amounts of the linear nickel(I) complex  $[NiL_2]^-$  as a side product. This overall implicates that the reaction of  $[NiL_2]$  with  $A_M R$  occurs via a SET mechanism that competes with adduct formation. The reduction of nickel(II) silylamides by alkali metal hexamethyldisilazanes was also observed for synthesis the nickel(I) complex  $[(PPh_3)_2Ni(N(SiMe_3)_2)]$  from the divalent  $[(PPh_3)_2NiCl_2]$  with two equivalents  $Li(N(SiMe_3)_2)$ .<sup>[61]</sup> For the formation of the tetrameric nickel(I) hexamethyldisilazane from the extremely labile  $[Ni\{N(SiMe_3)_2\}_2]^{[62]}$  a homolytic Ni–N bond cleavage was proposed, whereas the trigonal anionic nickel(II) trisamido  $[Ni(N(SiMe_3)_2)_3]^-$  is easily formed and relatively stable.<sup>[60]</sup> The preference of  $[NiL_2]$  reduction over adduct formation is thus likely a combination of its facile reduction ( $E_{1/2}=-1.28$  V vs.  $Fc/Fc^+$ )<sup>[44]</sup> and steric encumbrances that supports a linear geometry. To possibly circumvent the direct reduction, we attempted to introduce the organic ligands via salt elimination reaction starting from the halogenido complex  $NBu_4[NiBrL_2]$ ,  $[3]$  (Figure 3, right). Analogous to the known examples of iron and cobalt,<sup>[63]</sup> it was obtained by reacting  $[NiL_2]$  with  $NBu_4Br$  in THF

as a dark red crystalline material (34% yield). X-ray diffraction analysis on suitable crystals revealed a distorted T-shaped geometry in solid state. The reaction of  $[3]$  with  $KNHDipp$  in  $THF-d_8$  however also revealed a rather quick formation of the nickel(I) complex  $[NiL_2]^-$ , as evidenced by proton NMR spectroscopy. As such an SET to the anionic  $[NiBrL_2]^-$ , either directly or by temporary decoordination of the bromide in solution, is still active. When using  $KNPh_2$ , the formation of  $[2]$  is observed without any sign of reduction to nickel(I). The readily direct reduction of low-coordinate nickel(II) complexes by organic anions that competes with adduct formation or salt metathesis has possible implications for the (re)generation of a monovalent nickel species in a variety of nickel mediated transformations involving anionic nucleophiles such organo lithium reagents or alkoxides as well as nickel halide species resulting from C-halide bond cleavage.<sup>[64–70]</sup>

## Conclusion

We reported the formation of a T-shaped low-spin imido nickel(III) complex by the reaction  $K\{18c6\}[NiL_2]$  ( $L=N-(Dipp)SiMe_3$ ,  $Dipp=2,6$ -diisopropylphenyl) with phenyl azide ( $PhN_3$ ), while more sterically encumbered azides proved unreactive. The resulting nickel imide  $K\{18c6\}[1]$  surprisingly bears a  $[Ni=NDipp]$  imide unit. This can be explained by initial formation of the nickel phenyl imide  $[Ni(NPh)L_2]^-$  that undergoes an intramolecular  $SiMe_3$  shift from the ancillary ligand set to the Dipp imide nitrogen. Comprehensive analysis of  $K\{18c6\}[1]$  leads to its description as a low-spin nickel(III) imide. It is unreactive towards nitrene transfer to electron rich substrates as well as shows only little capabilities for H atom abstraction from external substrates. Attempts for the synthesis of trigonal amido nickel complexes by reacting  $[NiL_2]$  with potassium amides yields readily reduction of the nickel(II) ion under formation of the nickel(I) complex anion  $[NiL_2]^-$ . This can be extended to secondary amides, alkoxides as well as benzyl potassium. We attribute this to a direct single-electron transfer from the organic anion to nickel(II) ion without prior adduct formation. For the electron poor  $KNPh_2$  adduct formation is shown to be preferred giving the stable adduct  $[Ni(NPh)_2L_2]^-$ .

## Experimental Section

### Materials and Methods

All manipulations were carried out in a glovebox under a dry argon atmosphere, unless indicated otherwise. Used solvents were dried by continuous distillation over sodium metal for several days, degassed via three freeze-pump-thaw cycles and stored over molecular sieves 4 Å. Deuterated solvents were used as received, degassed via three freeze-pump cycles and stored over molecular sieves 4 Å. The  ${}^1H$  NMR spectra were recorded on a Bruker AV 500, a Bruker HD 500 or a Bruker HD 300 NMR spectrometer (Bruker Corporation, Billerica, USA). Chemical shifts are reported in ppm relative to the residual proton signals of the solvent (for  ${}^1H$ ) using the MestreNova software package (Mestrelab, Santiago de Compostela, Spain). IR measurements were conducted on a Bruker Alpha

ATR-IR spectrometer (Bruker Corporation, Billerica, USA). Elemental analyses were performed by the "in-house" service of the Chemistry Department of the Philipps University Marburg, Germany using a CHN(S) analyser vario MICRO Cube (Elementar Analysensysteme GmbH, Langenselbold, Germany). EPR spectra were obtained on a Bruker EMXplus (X-band) EPR spectrometer equipped with the Bruker ER4118X-MD5 probehead. The freshly prepared samples were transferred to J-Young quartz EPR tubes and sealed. The solution in the tube was frozen in liquid nitrogen and kept frozen until measured. 18-crown-6, 1,4-cyclohexadiene, 9,10-dihydroanthracene, and tetramethylsilane (TMS) were obtained commercially (Sigma-Aldrich, Acros, Strem, Alfa Aesar) and - if not noted otherwise - used as received. 1,4-cyclohexadiene was degassed, transferred into the glovebox and stored over molecular sieves at  $-35^{\circ}\text{C}$ . 18-crown-6 was sublimed prior use to remove traces of water.  $[\text{NiL}_2]$  and  $\text{K}\{18\text{c}6\}[\text{NiL}_2]^{[71]}$  were prepared according to literature procedures.

**$\text{K}\{18\text{c}6\}[\text{Ni}(\text{NDipp})(\text{N}(\text{Ph})\text{SiMe}_3)\text{L}]$  ( $\text{K}\{18\text{c}6\}[1]$ ).** 144.2 mg (0.17 mmol, 1 equiv.)  $\text{K}\{18\text{c}6\}[\text{NiL}_2]$  and 20 mg (0.17 mmol, 1 equiv.) phenyl azide were separately dissolved in 3 ml, respectively 1 ml,  $\text{Et}_2\text{O}$ , and cooled to  $-35^{\circ}\text{C}$ . Mixing the solutions resulted in an immediate color change from yellow to dark red under concomitant gas evolution (presumably  $\text{N}_2$ ). The solution was layered with 5 ml pentane and stored at  $-35^{\circ}\text{C}$ . After one day, the solution was removed via pipette and the remaining dark yellow crystalline needles were rinsed with  $2 \times 5$  ml pentane. Drying *in vacuo* yielded 53.9 mg (0.06 mmol, 34%)  $\text{K}\{18\text{c}6\}[\text{Ni}(\text{NDipp})(\text{N}(\text{Ph})\text{SiMe}_3)\text{L}]$  ( $\text{K}\{18\text{c}6\}[1]$ ).  **$^1\text{H-NMR}$**  (300 MHz, 300 K,  $\text{thf-d}_8$ ): No signals could be observed in the range of  $+200$  to  $-200$  ppm. **IR** (ATR,  $\text{cm}^{-1}$ ):  $\nu = 3046$  (vw), 2950 (w), 2887 (w), 2863 (w), 1580 (w), 1471 (w), 1452 (w), 1420 (m), 1350 (m), 1313 (m), 1248 (m), 1175 (w), 1102 (vs), 983 (m), 960 (m), 923 (m), 833 (s), 748 (m), 692 (m), 636 (w), 621 (w), 523 (w), 444 (w). **Elemental analysis:** calcd. (%) for  $\text{C}_{48}\text{H}_{81}\text{KN}_3\text{NiO}_6\text{Si}_2$  (950.15 g/mol): C 60.68, H 8.59, N 4.42; found: C 60.15, H 8.252, N 4.92. **magnetic susceptibility:**  $\mu_{\text{eff}} = 1.95 \mu_{\text{B}}$  (Evans,  $\text{thf-d}_8 + 1\%$  TMS),  $\mu_{\text{s.o.}} = 1.73 \mu_{\text{B}}$ .

**$\text{K}\{18\text{c}6\}[\text{Ni}(\text{NPh}_2)\text{L}_2]$  ( $\text{K}\{18\text{c}6\}[2]$ ).** A solution of 50 mg (0.1 mmol, 1 equiv.)  $[\text{NiL}_2]$  in 2 mL  $\text{thf}$  was cooled to  $-30^{\circ}\text{C}$ . A solution of 18.7 mg (0.1 mmol, 1 equiv.)  $\text{KNPh}_2$  and 28.7 mg (0.1 mmol, 1 equiv.) 18c6 in 2 mL  $\text{thf}$  precooled to  $-35^{\circ}\text{C}$  was added. A color change from dark purple to dark green is observed. After 5 min stirring, the solvent is removed *in vacuo* and the residue extracted with  $3 \times 1$  mL diethyl ether. The resulting solution is layered with 3 mL *n*-pentane and stored at  $-35^{\circ}\text{C}$ . After one day, the solution was removed via pipette and the remaining dark green crystalline plates were rinsed with  $2 \times 5$  ml pentane. Drying *in vacuo* yielded 49 mg (0.05 mmol, 52%)  $\text{K}\{18\text{c}6\}[\text{Ni}(\text{NPh}_2)\text{L}_2]$  ( $\text{K}\{18\text{c}6\}[2]$ ).  **$^1\text{H-NMR}$**  (300 MHz, 300 K,  $\text{thf-d}_8$ ): 34.1 (s,  $w_{1/2} = 45.2$  Hz), 30.7 (s,  $w_{1/2} = 28.9$  Hz), 23.53 (s,  $w_{1/2} = 367$  Hz), 5.10 (s,  $w_{1/2} = 22.4$  Hz), 3.60 (s,  $w_{1/2} = 7.4$  Hz, 18c6),  $-5.06$  (s, 42.3 Hz),  $-30.2$  (s, 262 Hz),  $-30.8$  (s, 23.0 Hz),  $-36.0$  (s, 29.8 Hz) ppm. **IR** (ATR,  $\text{cm}^{-1}$ ):  $\nu = 2897$  (w), 2862 (w), 1577 (w), 1474 (m), 1455 (w), 1420 (w), 1350 (w), 1305 (m), 1247 (w), 1233 (m), 1182 (w), 1169 (w), 1101 (vs), 1054 (w), 961 (m), 893 (m), 875 (w), 833 (s), 778 (m), 743 (m), 689 (m), 667 (w), 533 (w), 436 (w). **Elemental analysis:** calcd. (%) for  $\text{C}_{54}\text{H}_{86}\text{KN}_3\text{NiO}_6\text{Si}_2$  (1027.26 g/mol): C 63.14, H 8.44, N 4.09; found: C 61.81, H 8.45, N 4.38. **magnetic susceptibility:**  $\mu_{\text{eff}} = 3.32 \mu_{\text{B}}$  (Evans,  $\text{thf-d}_8 + 1\%$  TMS),  $\mu_{\text{s.o.}} = 2.83 \mu_{\text{B}}$ .

**${}^n\text{Bu}_4\text{N}[\text{Ni}(\text{Br})\text{L}_2]$  ( ${}^n\text{Bu}_4\text{N}[3]$ ).** A solution of 100 mg (0.2 mmol, 1 equiv.)  $[\text{NiL}_2]$  in 2 mL THF added to a suspension 28 mg (0.2 mmol, 1 equiv.)  ${}^n\text{Bu}_4\text{NBr}$  in 2 mL THF. The reaction mixture was stirred for 72 h at ambient temperature. The obtained dark red solution was filtered, and the filtrate was layered with 5 mL *n*-pentane. Storage at  $-35^{\circ}\text{C}$  led to the formation of dark red crystalline plates. The solution was removed via pipette and the remaining solid was

rinsed with  $2 \times 5$  ml pentane. Drying *in vacuo* yielded 65 mg (0.06 mmol, 34%)  ${}^n\text{Bu}_4\text{N}[\text{Ni}(\text{Br})\text{L}_2]$  ( ${}^n\text{Bu}_4\text{N}[3]$ ).  **$^1\text{H-NMR}$**  (300 MHz, 300 K,  $\text{thf-d}_8$ ): 58.0 (s,  $w_{1/2} = 441$  Hz), 52.5 (s,  $w_{1/2} = 228$  Hz), 44.4 (s,  $w_{1/2} = 442$  Hz), 42.3 (s,  $w_{1/2} = 103$  Hz), 35.3 (s,  $w_{1/2} = 251$  Hz), 18.4 (s,  $w_{1/2} = 170$  Hz), 10.2 (s,  $w_{1/2} = 193$  Hz), 6.99 (s,  $w_{1/2} = 128$  Hz),  $-10.4$  (s,  $w_{1/2} = 104$  Hz),  $-36.3$  (s,  $w_{1/2} = 107$  Hz),  $-77.8$  (s,  $w_{1/2} = 257$  Hz) ppm. **IR** (ATR,  $\text{cm}^{-1}$ ):  $\nu = 2957$  (m), 2886 (w), 1460 (w), 1422 (w), 1311 (w), 1233 (m), 1188 (m), 1103 (m), 904 (m), 879 (w), 827 (vs), 780 (m), 747 (m), 733 (m), 675 (s), 632 (m), 533 (m), 440 (w), 420 (w). **Elemental analysis:** calcd. (%) for  $\text{C}_{46}\text{H}_{88}\text{KN}_3\text{NiSi}_2$  (950.15 g/mol): C 62.93, H 10.10, N 4.79; found: C 63.07, H 9.84, N 4.99. **magnetic susceptibility:**  $\mu_{\text{eff}} = 3.47 \mu_{\text{B}}$  (Evans,  $\text{thf-d}_8 + 1\%$  TMS),  $\mu_{\text{s.o.}} = 2.83 \mu_{\text{B}}$ .

**NMR scale reactions:** In a typical NMR scale reaction 15 mg (0.03 mmol, 1 equiv.) of  $[\text{NiL}_2]$  were dissolved in 0.3 mL of the respective solvent ( $\text{thf-d}_8$  or  $\text{C}_6\text{D}_6$ ) and added to a solution of 1 equiv. of the substrate and, if stated 1 equiv. of 18c6, in 0.3 mL of the same solvent.  $^1\text{H-NMR}$  spectra were recorded immediately and after 24 h.

### X-ray diffraction analysis

Data for compounds  $\text{K}\{18\text{c}6\}[1]$  (CCDC 2120264),  $\text{K}\{18\text{c}6\}[2]$  (CCDC 2128458) and  ${}^n\text{Bu}_4\text{N}[3]$  (CCDC 2128459) was collected at 100 K on a Bruker Quest D8 diffractometer (Bruker Corporation, Billerica, USA) using an Incoatec Microfocus Source Mo-K $\alpha$  radiation and equipped with an Oxford Instrument Cooler Device (Oxford Instruments, Abingdon, UK) and Photon 100 detector (CMOS). The structures have been solved using OLEX SHELXT V2014/1<sup>[72]</sup> and refined by means of least-squares procedures on an  $F^2$  with the aid of the program SHELXL-2016/6<sup>[73]</sup> included in the software package WinGX version 1.63.<sup>[74]</sup> The atomic scattering factors were taken from International Tables for X-ray Crystallography.<sup>[75]</sup> All non-hydrogen atoms were refined anisotropically. All hydrogen atoms were refined by using a riding model. Absorption corrections were introduced by using the MULTISCAN and X-Red programs.<sup>[76,77]</sup> Drawings of molecules are performed with the program DIAMOND (Crystal Impact, Bonn, Germany) with 50% probability displacement ellipsoids for non-H atoms. Additional details are given in the Supporting Information.

Deposition Numbers 2120264 (for  $\text{K}\{18\text{c}6\}[1]$ ), 2128458 (for  $\text{K}\{18\text{c}6\}[2]$ ), and 2128459 (for  ${}^n\text{Bu}_4\text{N}[3]$ ) contain the supplementary crystallographic data for this paper. These data are provided free of charge by the joint Cambridge Crystallographic Data Centre and Fachinformationszentrum Karlsruhe Access Structures service [www.ccdc.cam.ac.uk/structures](http://www.ccdc.cam.ac.uk/structures).

### Supporting Information

**Supporting Information** (see footnote on the first page of this article): Spectra and further crystallographic details are available.

### Acknowledgements

We thank the Deutsche Forschungsgemeinschaft (grant WE 5627/4-1 for C. G. W.) and the Philipps-University for financial support. Open Access funding enabled and organized by Projekt DEAL.

## Conflicts of Interest

The authors declare no conflict of interest.

## Data Availability Statement

The data that support the findings of this study are available in the supplementary material of this article.

**Keywords:** Amido ligands · Imido ligands · Nickel · Redox chemistry · Structure elucidation

- [1] Y. Park, Y. Kim, S. Chang, *Chem. Rev.* **2017**, *117*, 9247.
- [2] D. N. Zalatan, J. Du Bois, *Metal-Catalyzed Oxidations of C–H to C–N Bonds*, Springer, Berlin, Heidelberg **2009**, pp. 347–378.
- [3] H. Lu, X. P. Zhang, *Chem. Soc. Rev.* **2011**, *40*, 1899.
- [4] F. Collet, R. H. Dodd, P. Dauban, *Chem. Commun.* **2009**, *34*, 5061.
- [5] V. Bagchi, A. Kalra, P. Das, P. Paraskevopoulou, S. Gorla, L. Ai, Q. Wang, S. Mohapatra, A. Choudhury, Z. Sun, T. R. Cundari, P. Stavropoulos, *ACS Catal.* **2018**, *8*, 9183.
- [6] P. F. Kuijpers, J. I. van der Vlugt, S. Schneider, B. de Bruin, *Chem. Eur. J.* **2017**, *23*, 13819.
- [7] J. F. Berry, *Comment. Inorg. Chem.* **2009**, *30*, 28.
- [8] M. Ju, J. M. Schomaker, *Nat. Rev. Chem.* **2021**, *5*, 580.
- [9] G. Dequiere, V. Pons, P. Dauban, *Angew. Chem. Int. Ed.* **2012**, *51*, 7384.
- [10] L. Degennaro, P. Trincherà, R. Luisi, *Chem. Rev.* **2014**, *114*, 7881.
- [11] D. A. Iovan, T. A. Betley, *J. Am. Chem. Soc.* **2016**, *138*, 1983.
- [12] M. J. T. Wilding, D. A. Iovan, T. A. Betley, *J. Am. Chem. Soc.* **2017**, *139*, 12043.
- [13] M. J. T. Wilding, D. A. Iovan, A. T. Wrobel, J. T. Lukens, S. N. MacMillan, K. M. Lancaster, T. A. Betley, *J. Am. Chem. Soc.* **2017**, *139*, 14757.
- [14] Y. Baek, T. A. Betley, *J. Am. Chem. Soc.* **2019**, *141*, 7797.
- [15] Y. Baek, E. T. Hennessy, T. A. Betley, *J. Am. Chem. Soc.* **2019**, *141*, 16944.
- [16] Y. Dong, J. T. Lukens, R. M. Clarke, S.-L. Zheng, K. M. Lancaster, T. A. Betley, *Chem. Sci.* **2020**, *123*, 4623.
- [17] A. Reckziegel, C. Pietzonka, F. Kraus, C. G. Werncke, *Angew. Chem. Int. Ed.* **2020**, *28*, 8527.
- [18] K. Ray, F. Heims, F. F. Pfaff, *Eur. J. Inorg. Chem.* **2013**, *2013*, 3784.
- [19] A. Grünwald, S. S. Anjana, D. Munz, *Eur. J. Inorg. Chem.* **2021**, *5*, 422.
- [20] Y. Park, S. P. Sempronio, H. Zhong, P. J. Chirik, *Angew. Chem. Int. Ed.* **2021**, *60*, 14376.
- [21] W. Mao, D. Fehn, F. W. Heinemann, A. Scheurer, D. Munz, K. Meyer, *Angew. Chem. Int. Ed.* **2021**, *60*, 16480.
- [22] Y. Dong, R. M. Clarke, G. J. Porter, T. A. Betley, *J. Chem. Soc.* **2020**, *142*, 10996.
- [23] S. Wiese, J. L. McAfee, D. R. Pahls, C. L. McMullin, T. R. Cundari, T. H. Warren, *J. Am. Chem. Soc.* **2012**, *134*, 10114.
- [24] K. M. Carsch, I. M. DiMucci, D. A. Iovan, A. Li, S.-L. Zheng, C. J. Titus, S. J. Lee, K. D. Irwin, D. Nordlund, K. M. Lancaster, T. A. Betley, *Science* **2019**, *365*, 1138.
- [25] D. J. Mendiola, G. L. Hillhouse, *J. Am. Chem. Soc.* **2001**, *123*, 4623.
- [26] R. Waterman, G. L. Hillhouse, *J. Am. Chem. Soc.* **2008**, *130*, 12628.
- [27] C. A. Laskowski, A. J. M. Miller, G. L. Hillhouse, T. R. Cundari, *J. Am. Chem. Soc.* **2011**, *133*, 771.
- [28] V. M. Iluc, A. J. M. Miller, J. S. Anderson, M. J. Monreal, M. P. Mehn, G. L. Hillhouse, *J. Am. Chem. Soc.* **2011**, *133*, 13055.
- [29] C. A. Laskowski, D. J. Bungum, S. M. Baldwin, S. A. Del Ciello, V. M. Iluc, G. L. Hillhouse, *J. Am. Chem. Soc.* **2013**, *135*, 18272.
- [30] E. Kogut, H. L. Wiencko, L. Zhang, D. E. Cordeau, T. H. Warren, *J. Am. Chem. Soc.* **2005**, *127*, 11248.
- [31] Y. Dong, C. J. Lund, G. J. Porter, R. M. Clarke, S.-L. Zheng, T. R. Cundari, T. A. Betley, *J. Am. Chem. Soc.* **2021**, *143*, 817.
- [32] D. J. Mendiola, G. L. Hillhouse, *J. Am. Chem. Soc.* **2001**, *123*, 4623.
- [33] V. M. Iluc, G. L. Hillhouse, *J. Am. Chem. Soc.* **2010**, *132*, 15148.
- [34] C. A. Laskowski, G. R. Morello, C. T. Saouma, T. R. Cundari, G. L. Hillhouse, *Chem. Sci.* **2013**, *4*, 170.
- [35] N. D. Harrold, G. L. Hillhouse, *Chem. Sci.* **2013**, *4*, 4011.
- [36] A. Reckziegel, M. Kour, B. Battistella, S. Mebs, K. Beuthert, R. Berger, C. G. Werncke, *Angew. Chem. Int. Ed.* **2021**, *60*, 15376.
- [37] C. G. Werncke, E. Suturina, P. C. Bunting, L. Vendier, J. R. Long, M. Atanasov, F. Neese, S. Sabo-Etienne, S. Bontemps, *Chem. Eur. J.* **2016**, *22*, 1668.
- [38] M. I. Lipschutz, T. D. Tilley, *Angew. Chem. Int. Ed.* **2014**, *53*, 7290.
- [39] S. Alvarez, J. Cirera, *Angew. Chem. Int. Ed.* **2006**, *45*, 3012.
- [40] M. A. Ortuño, S. Conejero, A. Lledós, *Beilstein J. Org. Chem.* **2013**, *9*, 1352.
- [41] P. Pietrzyk, K. Podolska, Z. Sojka, *Chem. Eur. J.* **2009**, *15*, 11802.
- [42] S. Moncho, G. Ujaque, A. Lledós, P. Espinet, *Chem. Eur. J.* **2008**, *14*, 8986.
- [43] S. Alvarez, *Coord. Chem. Rev.* **1999**, *193–195*, 13.
- [44] M. I. Lipschutz, X. Yang, R. Chatterjee, T. D. Tilley, *J. Am. Chem. Soc.* **2013**, *135*, 15298.
- [45] D. F. Evans, *J. Chem. Soc.* **1959**, 2003.
- [46] M. I. Lipschutz, T. D. Tilley, *Chem. Commun.* **2012**, *48*, 7146.
- [47] L. C. H. Maddock, R. Morton, A. R. Kennedy, E. Hevia, *Chem. Eur. J.* **2021**, *27*, 15180.
- [48] J. Liu, M. M. Bollmeyer, Y. Kim, D. Xiao, S. N. MacMillan, Q. Chen, X. Leng, S. H. Kim, L. Zhao, K. M. Lancaster, L. Deng, *J. Chem. Soc.* **2021**, *143*, 10751.
- [49] N. P. Mankad, W. E. Antholine, R. K. Szilagy, J. C. Peters, *J. Am. Chem. Soc.* **2009**, *131*, 3878.
- [50] T. Büttner, J. Geier, G. Frison, J. Harmer, C. Calle, A. Schweiger, H. Schönberg, H. Grützmaier, *Science* **2005**, *307*, 235.
- [51] E. S. Jang, C. L. McMullin, M. Käß, K. Meyer, T. R. Cundari, T. H. Warren, *J. Am. Chem. Soc.* **2014**, *136*, 10930.
- [52] E. C. Ashby, *Acc. Chem. Res.* **1988**, *21*, 414.
- [53] J. P. Barham, G. Coulthard, K. J. Emery, E. Doni, F. Cumine, G. Nocera, M. P. John, L. E. A. Berlouis, T. McGuire, T. Tuttle, J. A. Murphy, *J. Am. Chem. Soc.* **2016**, *138*, 7402.
- [54] H. Yi, A. Jutand, A. Lei, *Chem. Commun.* **2015**, *51*, 545.
- [55] I. Müller, C. G. Werncke, *Chem. Eur. J.* **2021**, *27*, 4932.
- [56] C.-Y. Lin, J. C. Fetting, P. P. Power, *Inorg. Chem.* **2017**, *56*, 9892.
- [57] C. Yoo, Y. Lee, *Inorg. Chem. Front.* **2016**, *3*, 849.
- [58] C. Yoo, Y. Lee, *Chem. Sci.* **2017**, *8*, 600.
- [59] D. Sahoo, C. Yoo, Y. Lee, *J. Am. Chem. Soc.* **2018**, *140*, 2179.
- [60] A. M. Borys, E. Hevia, *Organometallics* **2021**, *40*, 442.
- [61] W. Lin, T. Bodenstern, V. Mereacre, K. Fink, A. Eichhöfer, *Inorg. Chem.* **2016**, *55*, 2091.
- [62] M. Faust, A. M. Bryan, A. Mansikkamäki, P. Vasko, M. M. Olmstead, H. M. Tuononen, F. E. A. Grandjean, G. J. Long, P. P. Power, *Angew. Chem. Int. Ed.* **2015**, *54*, 12914.
- [63] R. Weller, L. Völlinger, C. G. Werncke, *Eur. J. Inorg. Chem.* **2021**, *2021*, 4383.
- [64] S. Z. Tasker, E. A. Standley, T. F. Jamison, *Nature* **2014**, *509*, 299.
- [65] N. Hazari, P. R. Melvin, M. M. Beromi, *Nat. Chem. Rev.* **2017**, *1*.
- [66] J. B. Diccianni, T. Diao, *Trends Chem.* **2019**, *1*, 830.
- [67] J. Terao, N. Kambe, *Acc. Chem. Res.* **2008**, *41*, 1545.
- [68] G. C. Fu, *ACS Cent. Sci.* **2017**, *3*, 692.
- [69] A. M. Borys, E. Hevia, *Angew. Chem. Int. Ed.* **2021**, *60*, 24659.
- [70] O. Vechorkin, X. Hu, *Angew. Chem. Int. Ed.* **2009**, *48*, 2937.
- [71] C.-Y. Lin, J. C. Fetting, F. Grandjean, G. J. Long, P. P. Power, *Inorg. Chem.* **2014**, *53*, 9400.
- [72] O. V. Dolomanov, L. J. Bourhis, R. J. Gildea, J. A. K. Howard, H. Puschmann, *J. Appl. Crystallogr.* **2009**, *42*, 339.
- [73] G. M. Sheldrick, *Acta Crystallogr. Sect. C* **2015**, *71*, 3.
- [74] L. J. Farrugia, *J. Appl. Crystallogr.* **1999**, *32*, 837.
- [75] W. Schmitz, *Krist. Tech.* **1975**, *10*, K120–K120.
- [76] SADABS-2016/2, *Bruker* **2016**.
- [77] X-R. 1.6.1.0. X-Area, *STOE* **2016**.

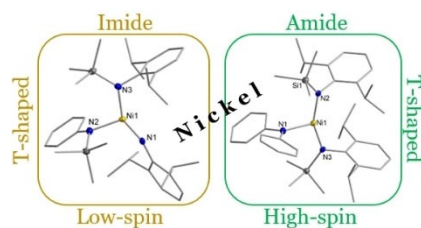
Manuscript received: December 22, 2021

Revised manuscript received: January 13, 2022

Accepted manuscript online: January 14, 2022

## RESEARCH ARTICLE

We describe the synthesis of a stable T-shaped low-spin nickel(III) imide which is subject of intramolecular  $\text{SiMe}_3$ -shift from an amide to the original imide function. Attempts to obtain anionic trigonal nickel(II) amides lead to reduction of the nickel center with the exception of the electron-poor diphenylamide.



A. Reckziegel, B. Battistella, Dr. C. G. Werncke\*

1 – 7

**On the Synthesis of a T-Shaped Imido Nickel Complex and Trigonal Amido Nickel Complexes**



### 3.4 Intricate Road to Linear Anionic Nickel(I) Hexamethyldisilazanide $[\text{Ni}(\text{N}(\text{SiMe}_3)_2)_2]^-$

A. Reckziegel, B. Battistella, A. Schmidt, C.G. Wernecke

*Inorg. Chem.* **2022**, *61*, 7794-7803.

DOI: 10.1021/acs.inorgchem.2c00214

<https://pubs.acs.org/doi/abs/10.1021/acs.inorgchem.2c00214>

#### Abstract

In this report, we present intricate pathways for the synthesis of linear nickel(I) silylamide  $\text{Km}[\text{Ni}(\text{NR}_2)_2]$  ( $\text{NR}_2 = -\text{N}(\text{SiMe}_3)_2$ ). This is achieved first via the reduction of nickel(II) trisamide  $\text{Li}(\text{donor})_4[\text{Ni}(\text{NR}_2)_3]$  ( $\text{Li}(\text{thf})_x[\mathbf{1}]$ ) with  $\text{KC}_8$  in the presence of 18-crown-6 or crypt.222. In due course, the behavior of  $\text{Li}(\text{donor})_4[\text{Ni}(\text{NR}_2)_3]$  as a source of masked two-coordinate nickel(II) hexamethyldisilazanide is explored, leading to the formation of nickel(I) and nickel(II) N-donor adducts, as well as metal-metal-bonded dinickel(I) trisamide  $\text{K}(\text{toluene})[\text{Ni}_2(\text{NR}_2)_3]$  ( $\text{K}(\text{toluene})[\mathbf{5}]$ ). Finally, a convenient and reliable synthesis of  $\text{Km}[\text{Ni}(\text{NR}_2)_2]$  by ligand exchange of phosphines in  $[\text{Ni}(\text{NR}_2)(\text{PPh}_3)_2]$  with  $\text{Km}(\text{NR}_2)$  is presented. This allows for the comprehensive analysis of its electronic properties which reveals a fluxional behavior in solution with tight anion/cation interactions.

#### Zusammenfassung

Durch Umsetzung von drei Äquivalenten  $\text{LiN}(\text{SiMe}_3)_2$  mit Nickel(II)-chlorid in THF, konnte  $\text{Li}(\text{thf})_x[\text{Ni}(\text{N}(\text{SiMe}_3)_2)_3]$  (**111**) als amorpher Feststoff erhalten werden.

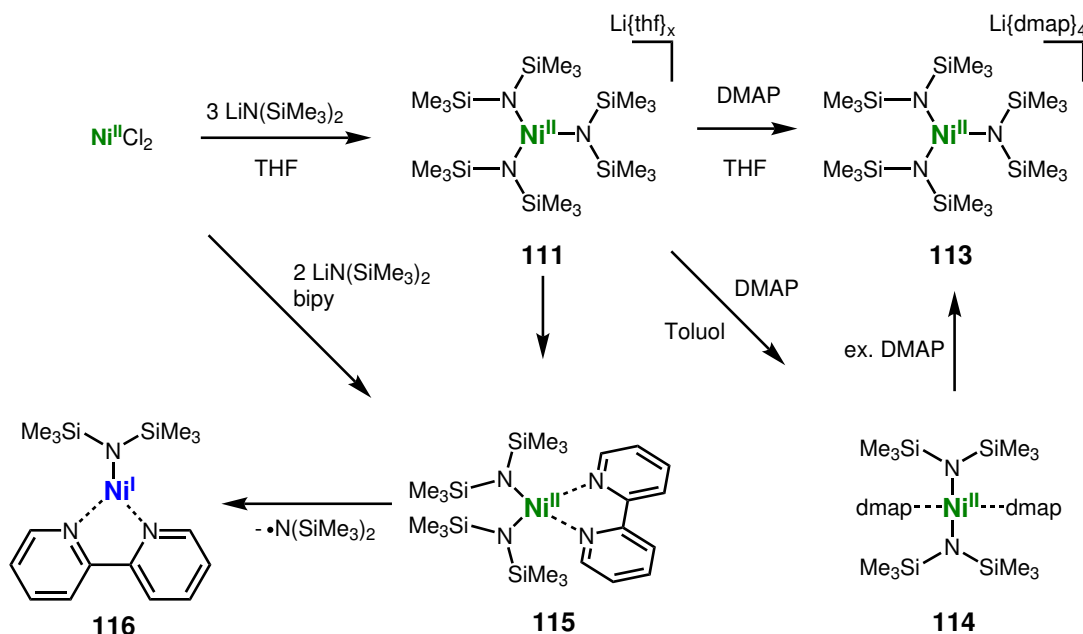


Abb. 49: Synthese und Reaktionsverhalten von  $\text{Li}(\text{thf})_x[\text{Ni}(\text{N}(\text{SiMe}_3)_2)_3]$  (**111**).

Die Charakterisierung erfolgte über  $^1\text{H}$ -NMR- und UV-VIS-Spektroskopie, wobei ein vom Lösungsmittel abhängiges Gleichgewicht mit dem neutralen Nickel(II)-Komplex  $[\text{Ni}(\text{N}(\text{SiMe}_3)_2)_2(\text{thf})]$  (**112**) und  $\text{LiN}(\text{SiMe}_3)_2$  beobachtet wurde.



Um das beobachtete Gleichgewicht weiter zu untersuchen, wurde 4-(Dimethylamino)pyridin (DMAP) als LEWIS-Base zugegeben. In THF konnte auf diese Weise der Trisamido-Komplex  $\text{Li}(\text{dmap})_4[\text{Ni}(\text{N}(\text{SiMe}_3)_2)_3]$  (**113**) isoliert werden. Bei der Verwendung von Toluol als unpolares und nicht koordinierendes Lösungsmittel, konnte die Bildung des neutralen  $[\text{Ni}(\text{N}(\text{SiMe}_3)_2)_2(\text{dmap})_2]$  (**114**) beobachtet werden. Dass bei der Verwendung eines Überschusses von DMAP erneut die Bildung von **113** beobachtet wird, zeigt, dass das Gleichgewicht abhängig von der koordinativen Ab-sättigung des Lithium-Ions ist.

$^1\text{H}$ -NMR spektroskopische Untersuchungen mit 2,2'-Bipyridin als chelatisierenden Liganden, ließen zunächst die Bildung des tetraedrisch koordinierten Komplexes  $[\text{Ni}(\text{N}(\text{SiMe}_3)_2)_2(\text{bipy})]$  (**115**) vermuten. Bei den aus der Reaktion erhaltenen Kristallen handelte es sich um  $[\text{Ni}(\text{N}(\text{SiMe}_3)_2)(\text{bipy})]$  (**116**), welches durch die reduktive Abspaltung eines  $\text{N}(\text{SiMe}_3)_2$ -Liganden gebildet wurde. Dieser Mechanismus der Zersetzung wurde bereits in vorherigen Untersuchungen zu Instabilität von  $\text{Ni}(\text{N}(\text{SiMe}_3)_2)_2(\text{thf})$  beschrieben.[72] Die Synthese von **115** erfolgte über eine alternative Syntheseroute ausgehend von  $\text{NiCl}_2(\text{dme})$ , wobei nur eine geringe Ausbeute beobachtet werden konnte.

Die gezielte Reduktion von  $\text{Li}(\text{thf})_x[\text{Ni}(\text{N}(\text{SiMe}_3)_2)_3]$  (**111**) unter Verwendung von  $\text{KC}_8$  in Toluol führte zur Isolation von wenigen Kristallen der Verbindung  $\text{K}[\text{Ni}_2(\text{N}(\text{SiMe}_3)_2)_3]$  (**117**). Der erhaltene Komplex kann als ein Addukt aus dem erwarteten  $\text{K}[\text{Ni}(\text{N}(\text{SiMe}_3)_2)_2]$  und einem äquivalent  $\text{Ni}(\text{N}(\text{SiMe}_3)_2)$ , was durch reduktive Eliminierung eines  $\text{N}(\text{SiMe}_3)_2$ -Liganden gebildet wurde, betrachtet werden. Das erhaltene Produkt und die geringe Ausbeute lassen auf einen unselektiven Reaktionspfad schließen, weshalb im Folgenden eine Maskierungsreagenz (18c6, crypt.222) für das Kalium-Kation zugegeben wurde.

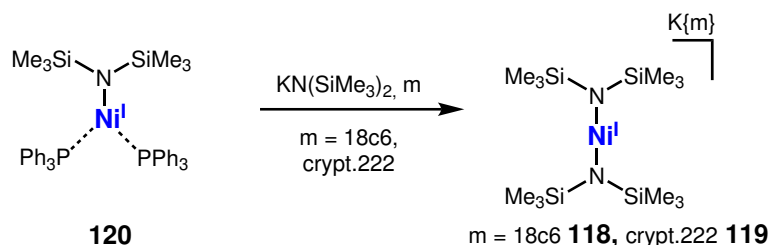


Abb. 50: Alternative Syntheseroute zur Darstellung von  $\text{K}\{m\}[\text{Ni}(\text{N}(\text{SiMe}_3)_2)_2]$  ( $m = 18\text{c}6$ : **118**; crypt.222: **119**).

Auf diesem Weg konnte die Zielverbindung  $\text{K}\{m\}[\text{Ni}(\text{N}(\text{SiMe}_3)_2)_2]$  ( $m = 18\text{c}6$ : **118**; crypt.222: **119**) isoliert werden. Der unbekannte Gehalt an THF im verwendeten Edukt, sowie die Separation des bei der Reduktion entstehenden  $\text{KN}(\text{SiMe}_3)_2$ , erschwerten die Aufreinigung des Produktes auf dieser Syntheseroute.

Aus diesem Grund wurde eine alternative Synthese, ausgehend von dem trigonalen Nickel(I)-Komplex  $\text{Ni}(\text{N}(\text{SiMe}_3)_2)(\text{PPh}_3)_2$  (**120**), untersucht (vgl. Abb. 50). Durch Umsetzung mit  $\text{K}(\text{N}(\text{SiMe}_3)_2)$  in Anwesenheit eines Maskierungsreagenzes (18c6, crypt.222) konnte die linearen Nickel(I)-Komplexe in guten Ausbeuten dargestellt werden.

Im Festkörper konnte eine quasi-lineare Koordination des Nickel-Ions ( $179,6(1)^\circ$ ) beobachtet werden. Das magnetische Moment von  $2,31 \mu_B$  ( $\mu_{s.o.}$  ( $S = 1/2$ ):  $1,73 \mu_B$ ) ist in guter Übereinstimmung mit einem Spinsystem von  $S = 1/2$ . Durch temperaturabhängige  $^1\text{H}$ -NMR-Spektroskopie konnte eine starke Anionen-Kationen-Wechselwir-

kung bei tiefen Temperaturen beobachtet werden. Im ESR-Spektrum der Verbindung sind zwei Signalsätze zu beobachten, was auf die zu zuvor beschriebene Anion-Kation-Wechselwirkung und die daraus resultierende Ausbildung von verschiedenen Konformationen im Festkörper zurückzuführen ist.

Zusammenfassend wurde die Synthese und das Reaktionsverhalten von  $\text{Li}(\text{thf})_x[\text{Ni}(\text{N}(\text{SiMe}_3)_2)_3]$  (**111**) und die Synthese und Eigenschaften der linear koordinierten Zielverbindung  $\text{K}\{m\}[\text{Ni}(\text{N}(\text{SiMe}_3)_2)_2]$  ( $m = 18\text{c}6$ : **118**; crypt.222: **119**) beschrieben.

### Beiträge der Autoren

Die gezeigten Verbindungen wurde von *Andreas Schmidt* im Zuge eines von mir betreuten Vertiefungspraktikums und weiterführend von mir dargestellt und mittels  $^1\text{H}$ -NMR-, UV-Vis- und IR-Spektroskopie charakterisiert. Die Messung des magnetischen Momentes nach der EVANS-Methode wurde durch die Serviceabteilung NMR-Spektroskopie der Philipps-Universität Marburg an einem Bruker AV III 500 durchgeführt und von mir ausgewertet.

Zur Bestimmung der Struktur im Festkörper wurden Röntgenbeugungsexperimente durch die Serviceabteilung Kristallstrukturanalyse der Philipps Universität Marburg oder von *Dr. Gunnar Werncke* an einem Bruker D8 Quest durchgeführt. Ich habe die Strukturen aus den erhaltenen Daten gelöst und verfeinert.

Die Bestimmung der Reinheit erfolgte mittels CHN-Elementaranalytik durch die Serviceabteilung Elementaranalytik der Philipps-Universität Marburg.

Die Elektronenspinresonanz-Experimente wurden von *Beatrice Battistella* aus der Arbeitsgruppe von *K. Ray* an der Humboldt-Universität zu Berlin durchgeführt. Die Simulationen der erhaltenen Daten wurde von mir vorgenommen.

Das Manuskript habe ich in Zusammenarbeit mit *Dr. Gunnar Werncke* und in Absprache mit allen Co-Autoren verfasst.



## Intricate Road to Linear Anionic Nickel(I) Hexamethyldisilazanide $[\text{Ni}(\text{N}(\text{SiMe}_3)_2)_2]^-$

Alexander Reckziegel, Beatrice Battistella, Andreas Schmidt, and C. Gunnar Werncke\*



Cite This: *Inorg. Chem.* 2022, 61, 7794–7803



Read Online

ACCESS |



Metrics & More

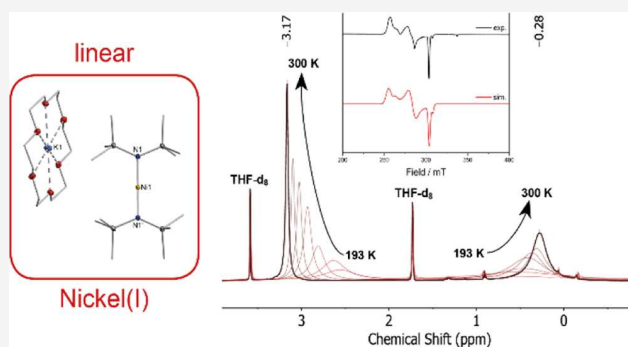


Article Recommendations



Supporting Information

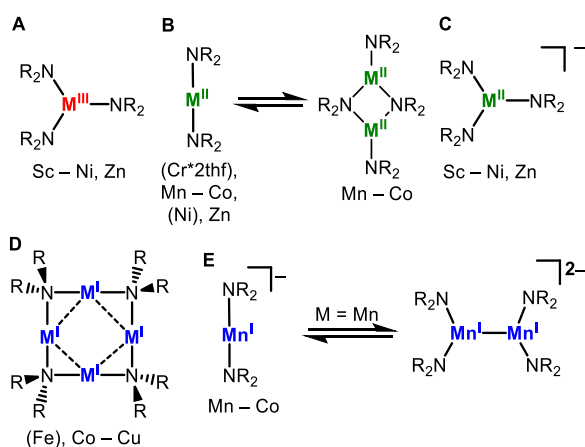
**ABSTRACT:** In this report, we present intricate pathways for the synthesis of linear nickel(I) silylamide  $\text{K}\{m\}[\text{Ni}(\text{NR}_2)_2]$  ( $\text{NR}_2 = -\text{N}(\text{SiMe}_3)_2$ ). This is achieved first via the reduction of nickel(II) trisamide  $\text{Li}(\text{donor})_4[\text{Ni}(\text{NR}_2)_3]$  ( $\text{Li}(\text{thf})_x[1]$ ) with  $\text{KC}_8$  in the presence of 18-crown-6 or crypt.222. In due course, the behavior of  $\text{Li}(\text{donor})_4[\text{Ni}(\text{NR}_2)_3]$  as a source of masked two-coordinate nickel(II) hexamethyldisilazanide is explored, leading to the formation of nickel(I) and nickel(II) N-donor adducts, as well as metal–metal-bonded dinickel(I) trisamide  $\text{K}(\text{toluene})[\text{Ni}_2(\text{NR}_2)_3]$  ( $\text{K}(\text{toluene})[5]$ ). Finally, a convenient and reliable synthesis of  $\text{K}\{m\}[\text{Ni}(\text{NR}_2)_2]$  by ligand exchange of phosphines in  $[\text{Ni}(\text{NR}_2)(\text{PPh}_3)_2]$  with  $\text{K}\{m\}(\text{NR}_2)$  is presented. This allows for the comprehensive analysis of its electronic properties which reveals a fluxional behavior in solution with tight anion/cation interactions.



### INTRODUCTION

Homoleptic 3d-metal hexamethyldisilazanides  $[\text{M}(\text{NR}_2)_n]$  ( $n = 1-3$ ,  $\text{NR}_2 = -\text{N}(\text{SiMe}_3)_2$ ) are widely used in coordination chemistry (Figure 1).<sup>1-9</sup> They are mostly employed as a halide-free source for molecular ligand exchange reactions and precursors in materials and surface science.<sup>10-16</sup> For most 3d-metals (Sc–Co), they can be found in the trivalent state (Figure 1A).<sup>3,4,17-23</sup> Divalent compounds are known from manganese to nickel and zinc (Figure 1B). These are dimeric in the solid state (with the exception of monomeric zinc and

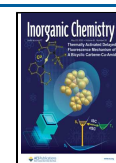
nickel) but mostly monomeric in solution.<sup>2-7,9</sup> Chromium compounds can be only obtained via the formation of square-planar donor adducts.<sup>24</sup> Trigonal anionic metal(II) hexamethyldisilazanides  $[\text{A}^M\{m\}][(\text{M}(\text{NR}_2)_3)]$  ( $\text{A}^M = \text{alkali metal}$ ,  $m = \text{none or chelating O/N-donor ligands such as dimethoxyethane (dme) or 18-crown-6 are also known (Figure 1C)}$ ). They are obtained either via the reduction of a trivalent precursor (Sc,<sup>25</sup> V,<sup>18</sup> and Cr<sup>18</sup>) or  $\text{A}^M\text{NR}_2$  adduct formation with neutral  $[\text{M}(\text{NR}_2)_2]$  (Mn,<sup>2</sup> Fe,<sup>26,27</sup> Co,<sup>20</sup> Ni,<sup>28</sup> and Zn<sup>29</sup>). In case of nickel, the latest and most recent addition to the hexamethyldisilazanide family, the neutral divalent compound, could only be characterized in the solid state as adducts of one thf (trigonal) or two pyridine (2X, square planar) molecules.<sup>5</sup> These compounds are extremely temperature-sensitive and decompose to the tetrameric nickel(I) silylamide  $[\text{Ni}(\mu\text{-NR}_2)]_4$  with a square-planar  $\text{Ni}_4\text{N}_4$  core bearing two-coordinate nickel(I) ions (Figure 1D).<sup>5</sup> This and similar tetranuclear motifs are found for iron,<sup>30</sup> cobalt,<sup>31</sup> and copper,<sup>32</sup> whereas for the latter, higher-valent hexamethyldisilazanides are on the other hand unknown. Overall, the metal silylamides well reflect the overall trend of the relative oxidation state stability of each metal.

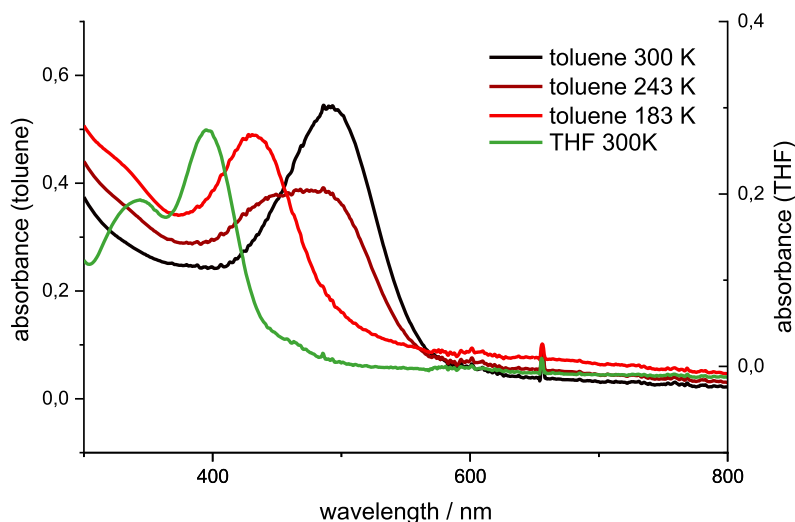
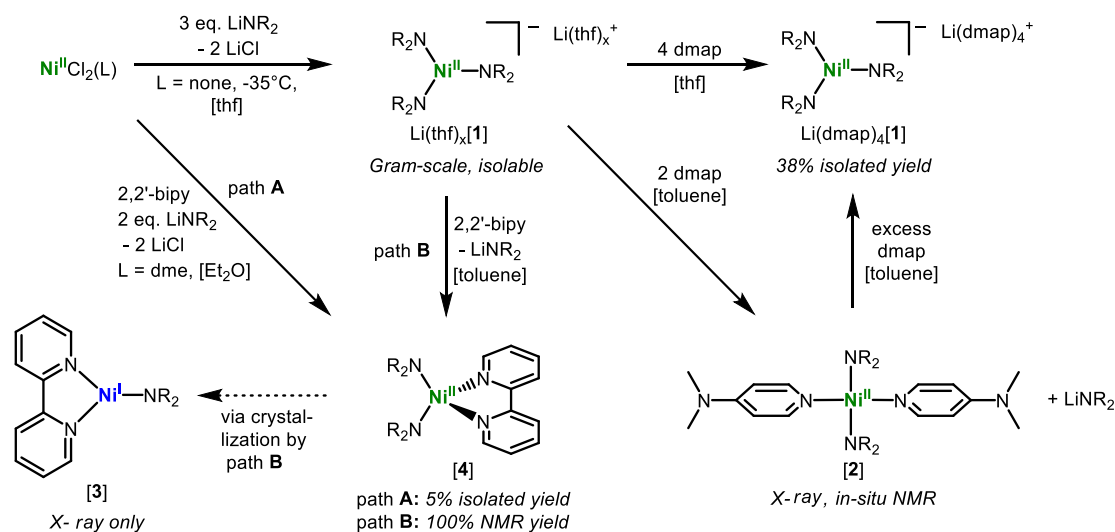


**Figure 1.** Overview of known, homoleptic 3d-metal hexamethyldisilazanides  $[\text{M}(\text{NR}_2)_n]^{(-)}$  ( $n = 1-3$ ;  $\text{R} = \text{SiMe}_3$ ).

Received: January 21, 2022

Published: May 6, 2022



**Scheme 1. Synthesis of the Lithium Tris(hexamethyldisilazanido) Nickelate(II)  $\text{Li}(\text{thf})_x[\text{Ni}(\text{NR}_2)_3]$  ( $\text{R} = \text{SiMe}_3$ ) and Its Chemical Behavior toward Different N-Donor Ligands**


**Figure 2.** Overlay of UV/vis spectra of  $\text{Li}(\text{thf})_x[\text{Ni}(\text{NR}_2)_3]$  in (a)  $\text{thf}$  at 300 K (green) and (b) in toluene at 300 K (black), 243 K (burgundy), and 183 K (red).

In recent years, the chemistry of monovalent 3d-metal hexamethyldisilazanides has been explored beyond tetrameric metal(I) monosilylamides, namely, via the synthesis of the anionic linear complexes  $[\text{M}(\text{NR}_2)_2]^-$  of chromium to cobalt (Figure 1E).<sup>33–35</sup> These are obtained by reduction of the respective divalent precursors with  $\text{KC}_8$  in the presence of 18-crown-6 or crypt.222. They are highly reactive, as expected from the—for these metals—low oxidation state in conjunction with the low-coordinate environment. As such, they have been exploited for a number of different reactivities such as C–F bond cleavage,<sup>36,37</sup> C–C multiple bond transformation,<sup>37–39</sup> reduction,<sup>40,41</sup> and a platform for either low-coordinate  $\pi$ -acceptor adducts (CO or alkynes),<sup>39,40,42</sup> imido,<sup>43</sup> or chalcogenido complexes.<sup>44</sup> Given the multifaceted use of these linear compounds, we were naturally interested in the respective nickel(I) complex, which constitutes the heaviest open-shell linear metal(I) hexamethyldisilazanide. Furthermore, nickel(I) species are increasingly found to play

a crucial role in bond activation processes, such as in C–C cross-coupling.<sup>45–50</sup>

Here, we report on the synthesis of the linear nickel(I) complex  $\text{K}\{\text{m}\}[\text{Ni}(\text{NR}_2)_2]$ . In doing so, the chemical behavior of the nickel(II) hexamethyldisilazanide system is further explored.

## RESULTS AND DISCUSSION

**Synthesis of the Trisamide  $\text{Li}(\text{thf})_x[\text{Ni}(\text{NR}_2)_3]$ .** To achieve the synthesis of the title compound  $\text{K}\{\text{m}\}[\text{Ni}(\text{NR}_2)_2]$  ( $\text{m} = 18\text{-crown-6, crypt.222}$ ), we initially attempted the reduction of divalent  $[\text{Ni}(\text{NR}_2)_2 \cdot \text{thf}]^+$ , mimicking the synthesis of the lighter congeners of chromium to cobalt.<sup>33,34</sup> This approach was however discarded eventually due to the extreme sensitivity and overall unreliable synthesis of the nickel(II) silylamide that precluded stoichiometric considerations. Recently, Borys and Hevia have reported on a more stable yet still highly sensitive  $\text{Na}(\text{pmdeta})_2[\text{Ni}(\text{NR}_2)_3]$ ,<sup>28</sup> ( $N,N,N',N'',N'''$ -pentamethyldiethylenetriamine), whereas a

N-donor is needed for stabilization of the anion via cation separation. Nonetheless, in noncoordinating solvents, this compound dissociates into  $[\text{Ni}(\text{NR}_2)_2]$  and  $\text{NaNR}_2$ . As such, we contemplated such a nickel trisamide as the starting point for the envisioned  $[\text{Ni}(\text{NR}_2)_2]^-$  complex anion by further reduction with  $\text{KC}_8$  in the presence 18-crown-6 or crypt.222. To better separate the liberated alkali metal hexamethyldisilazide, we set out to obtain first  $\text{Li}[\text{Ni}(\text{NR}_2)_3]$ , given the high solubility of  $\text{LiNR}_2$  as the prospective coproduct upon reduction. Accordingly, 3 equiv of  $\text{LiNR}_2$  were added to a precooled ( $-30\text{ }^\circ\text{C}$ ) suspension of  $\text{NiCl}_2$  in thf (Scheme 1).

After stirring for 12 h at ambient temperatures, the solvent was partially removed until a sticky solid was obtained. This was extracted with  $\text{Et}_2\text{O}$  to remove  $\text{LiCl}$ , and the solution was evaporated to give  $\text{Li}(\text{thf})_x[\text{Ni}(\text{NR}_2)_3]$  ( $\text{Li}(\text{thf})_x[\mathbf{1}]$ ) as an amorphous dark-green solid. It is important to note that immediately after all excess of solvent is removed from the emerging solid, a red vapor attributed to  $[\text{Ni}(\text{NR}_2)_2\text{thf}]$  is observed. This can be distilled off at ambient temperatures to give a characteristic dark-red oil and green solid upon freezing with liquid nitrogen. Its identity was corroborated by proton NMR using the reported values.<sup>5</sup> As such  $\text{Li}(\text{thf})_x[\mathbf{1}]$  might be a more convenient starting point for the distillative isolation and/or subsequent use of  $[\text{Ni}(\text{NR}_2)_2\text{thf}]$ . Attempts for the synthesis of the potassium salt  $\text{K}(\text{thf})_x[\mathbf{1}]$  using  $\text{K}(\text{NR}_2)$  and  $\text{NiCl}_2$  gave only intractable brownish solids, whereas for the before-mentioned  $\text{Na}[\text{Ni}(\text{NR}_2)_3]$ , isolation was possible, but degradation upon prolonged drying was reported.<sup>28</sup>

**NMR and UV/Vis Spectroscopy of  $\text{Li}[\text{Ni}(\text{NR}_2)_3]$ .** Similar to  $\text{Na}(\text{pmdeta})_2[\text{Ni}(\text{NR}_2)_3]$ ,<sup>28</sup> a proton NMR spectrum of  $\text{Li}(\text{thf})_x[\mathbf{1}]$  in  $\text{thf}-d_8$  shows a broad signal at  $\delta_{\text{SiMe}_3} = 1.12$  ppm for the  $\text{SiMe}_3$  groups (Figure S1). Equally, in the noncoordinating solvent toluene- $d_8$ , it dissociates into  $[\text{Ni}(\text{NR}_2)_2]$  ( $\delta_{\text{SiMe}_3} = 9.71$  ppm;  $\delta_{\text{thf}} = 4.80, 2.20$  ppm)<sup>5</sup> and  $\text{LiNR}_2$  (Figure S1). In due process, the thf amount in  $\text{Li}(\text{thf})_x[\mathbf{1}]$  could be estimated to  $x = 4.5\text{--}5.5$ , which is slightly higher than the four that are commonly observed for coordination to lithium. The different speciation of  $\text{Li}(\text{thf})_x[\mathbf{1}]$  in thf and toluene was supported by UV/vis spectroscopy. In thf, two broad absorption bands at 340 and 395 nm were observed at 298 K attributed to the trisamide  $[\mathbf{1}]^-$  (Figure 2, green trace). In contrast, in toluene, only one band was observed at ambient temperatures, which is situated at 492 nm (Figure 2, black trace).

Cooling the toluene solution led first to a slight decrease of the principal band, whereas below 240 K, a pronounced drop was observed with the appearance of a new band at 430 nm and a weak shoulder around 330 nm (isosbestic point at 455 nm) (Figures 2 and S12). This double feature resembles that of  $[\mathbf{1}]^-$  and pointed to a related, trigonal nickel(II) species, presumably the thf adduct  $[\text{Ni}(\text{NR}_2)_2(\text{thf})]$ . Accordingly, at higher temperatures, the donor free  $[\text{Ni}(\text{NR}_2)_2]$  would be present, as proposed by Power based on proton NMR spectroscopic studies between 270 and 362 K on  $[\text{Ni}(\text{NR}_2)_2(\text{thf})]$ .<sup>5</sup> However, given that by UV/vis spectroscopy substantial changes only occur below this temperature range proton NMR spectra of  $\text{Li}(\text{thf})_x[\mathbf{1}]$  in toluene were recorded from 300 down to 193 K. Starting from 300 K, the  $\text{SiMe}_3$  signal at  $\delta_{\text{SiMe}_3} = 10.0$  ppm slightly shifts to higher fields upon lowering the temperature to 240 K (240 K:  $\delta_{\text{SiMe}_3} = 8.65$  ppm, Figure S14), in general agreement with the observations made by Power.<sup>5</sup> However, below 240 K, the signal moved into the

opposite direction again (193 K:  $\delta_{\text{SiMe}_3} = 9.11$  ppm). Upon plotting the paramagnetic chemical shifts versus  $1/T$  according to the Curie–Weiss law, two distinct linear regions are visible above and below 240 K (Figure S15). Overall, this implicates that the thf adduct of  $[\text{Ni}(\text{NR}_2)_2]$  is present in toluene only at very low temperatures, whereas the adduct-free form is the dominant species above  $-30\text{ }^\circ\text{C}$ . Moreover, the trisamide  $[\text{Ni}(\text{NR}_2)_3]^-$  is absent at any temperature in toluene. Lastly, in the synthetically relevant solvent  $\text{Et}_2\text{O}$ , the trisamide  $[\text{Ni}(\text{NR}_2)_3]^-$  is predominantly present below  $0\text{ }^\circ\text{C}$ , judging from variable-temperature UV/vis spectroscopy ( $\lambda_{\text{max}} = 400$  nm, Figure S13), whereas a shoulder at 440 nm points to the possible  $\text{Et}_2\text{O}$  adduct  $[\text{Ni}(\text{NR}_2)_2(\text{OEt}_2)]$ . At more elevated temperatures, the equilibrium shifts toward  $[\text{Ni}(\text{NR}_2)_2]$ . Overall, these observations clearly show the influence of the temperature and solvent on the speciation of nickel(II) hexamethyldisilazides and is thus an added complication to the overall sensible synthesis of  $[\text{Ni}(\text{NR}_2)_2]$ .

**Chemical Behavior of  $\text{Li}(\text{thf})_x[\text{Ni}(\text{NR}_2)_3]$ .** Combustion analysis on  $\text{Li}(\text{thf})_x[\mathbf{1}]$ , under consideration of the NMR spectroscopically determined thf content, gave consistently too low carbon and hydrogen values. Furthermore, we did not manage to perform X-ray diffraction (XRD) analysis of  $\text{Li}(\text{thf})_x[\mathbf{1}]$  due to the lack of a crystalline solid. As such, 4-dimethylamino pyridine (dmap) was introduced as a less volatile donor ligand for cation coordination. This yielded green crystalline  $\text{Li}(\text{dmap})_4[\text{Ni}(\text{NR}_2)_3]$  ( $\text{Li}(\text{dmap})_4[\mathbf{1}]$ , Scheme 1), which could be isolated in moderate yields (38%) and was fully characterized. In the solid state, the complex anion is trigonal planar (Figure 3a), with structural

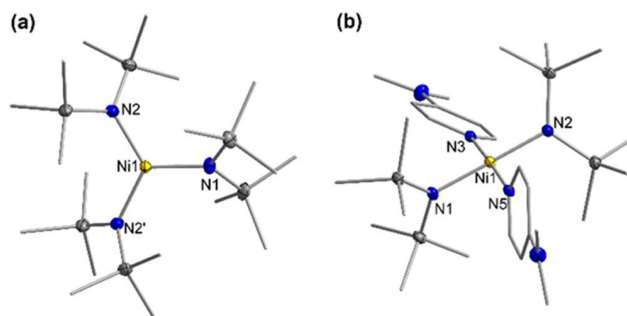


**Figure 3.** Molecular structure of  $\text{Li}(\text{dmap})_4[\mathbf{1}]$  (a) and  $[\mathbf{2}]$  (b) in the solid state. The cation, solvent molecules, and H atoms are omitted for clarity. Selected bond length (Å) and angles (deg):  $\text{Li}(\text{dmap})_4[\mathbf{1}]$ : Ni1–N1 1.933(2), Ni1–N2 1.929(1), N1–Ni1–N2 118.68(3), N2–Ni1–N2' 122.64(7).  $[\mathbf{2}]$ : Ni1–N1 1.950(1), Ni1–N2 1.948(1), Ni1–N3 1.918(2), Ni1–N5 1.916(2), N1–Ni1–N2 179.08(6), N3–Ni1–N5 177.56(6).

metrics resembling those found in  $\text{Na}(\text{pmdeta})_2[\text{Ni}(\text{NR}_2)_3]$ <sup>28</sup> and will thus not be further discussed here. Following the dmap addition to  $\text{Li}(\text{thf})_x[\mathbf{1}]$  in toluene- $d_8$  by proton NMR yielded clean formation of an intermediate species for 2 equiv of dmap ( $\delta_{\text{SiMe}_3} = 4.24$  ppm, Figure S6), which was eventually identified as square-planar *trans*- $[\text{Ni}(\text{NR}_2)_2(\text{dmap})_2]$  ( $[\mathbf{2}]$ ) by XRD analysis (Figure 3b).  $[\mathbf{2}]$  is isostructural to the bis(pyridine) adduct reported by Power<sup>5</sup> and similarly shows low stability in solution, precluding its isolation. The twofold adduct formation speaks to the increased accessibility of the nickel ion in  $[\text{Ni}(\text{NR}_2)_2]$  in comparison to the more bulky

$[\text{Ni}(\text{N}(\text{Dipp})\text{SiMe}_3)_2]$  (Dipp = 2,6-di-isopropylphenyl), which forms only monoadducts.<sup>51–53</sup>

Further addition of dmap to  $\text{Li}(\text{thf})_x[\mathbf{1}]$  shifts the equilibrium from  $[\mathbf{2}]$  back to  $[\text{Ni}(\text{NR}_2)_3]^-$  due to complete sequestration of the lithium cation by dmap. Contrastingly, if 2 equiv of dmap is added to  $\text{Li}(\text{thf})_x[\mathbf{1}]$  in  $\text{thf}-d_8$ , no amide dissociation but only partial displacement of the donor ligands coordinating the lithium cation is observed, as evidenced by X-ray analysis on  $\text{Li}(\text{thf})_2(\text{dmap})_2[\mathbf{1}]$  (see the Supporting Information for solid-state structure). To elaborate more on the impact of the geometry of pyridine coordination to nickel(II) silylamide, we employed the chelate 2,2'-bipyridine (bipy), which precludes trans-orientation of the silylamide ligands, in noncoordinating solvents. Addition of 2,2'-bipyridine to  $\text{Li}(\text{thf})_x[\mathbf{1}]$  in toluene- $d_8$  (Scheme 1) resulted in a color change from green to brownish red and cleanly yielded a complex of the presumed composition  $[\text{Ni}(\text{NR}_2)_2\text{bipy}]$ , judging from its proton NMR signature. The signal belonging to the  $\text{NR}_2$  unit is found at 10.62 ppm with the three signals attributed to the bipyridine ligand at 20.12, 54.90, and 59.51 ppm. Attempts for isolation gave only a few brown crystals, which were surprisingly identified as the trigonal nickel complex  $[\text{Ni}(\text{NR}_2)\text{bipy}]$  ( $\mathbf{3}$ ); Figure 4a). In the

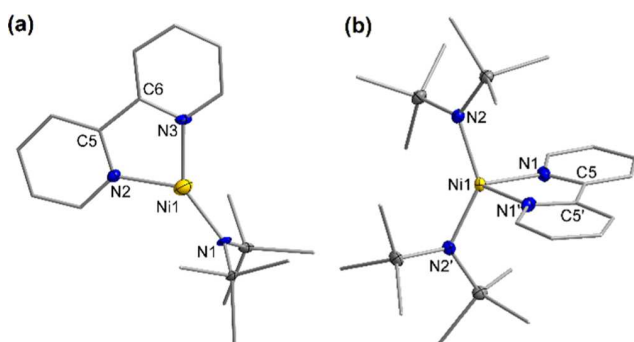


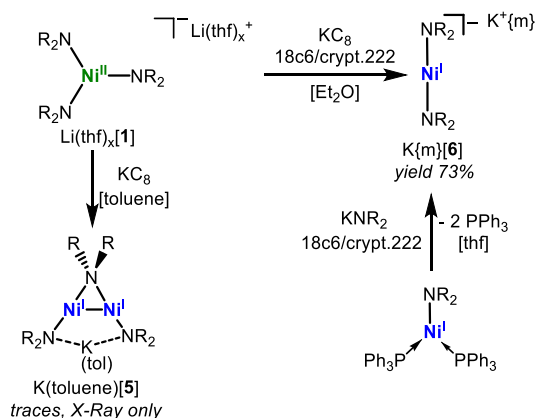
**Figure 4.** Molecular structure of  $\mathbf{3}$  (a) and  $\mathbf{4}$  (b) in the solid state. The cation, solvent molecules, and H atoms are omitted for clarity. Selected bond length (Å) and angles (deg):  $\mathbf{3}$ : Ni1–N1 1.898(3); Ni1–N2 1.949(4), Ni1–N3 1.944(4), C5–C6 1.477(7).  $\mathbf{4}$ : Ni1–N1 2.030(1), Ni1–N2 1.860(1), C5–C5' 1.480(3); N1–Ni1–N1' 79.82(6); N1–Ni1–N2 99.59(4), N2–Ni1–N2' 136.05(6).

solid state, the central nickel ion is coordinated by bipyridine and one amido ligand in a distorted trigonal planar fashion. The central C5–C6 bond length of the bipyridine ligand amounts 1.477(7) Å. Based on this structural feature, it implies the formulation of  $[\text{Ni}(\text{NR}_2)\text{bipy}]$  as a nickel(I) complex with a neutral bipyridine ligand, opposed to the possibility of nickel(II) bound to a bipyridine radical anion.<sup>54–58</sup> Remarkably, structurally known trigonal nickel(I) bipyridine complexes are absent, although they are proposed as key intermediates in nickel-/bipy-catalyzed  $\text{C}(\text{sp}^2)\text{--}\text{C}(\text{sp}^3)$  cross-coupling.<sup>59–62</sup> The only other relatable trigonal nickel polypyridine complex is the three-coordinate neocuproine (cup)-based aryl nickel(I) complex  $[(\text{cup})\text{Ni}(2,4,6\text{-}i\text{Pr}_3\text{-C}_6\text{H}_2)]$ .<sup>63</sup> Metal reduction to nickel(I) in  $[\text{Ni}(\text{NR}_2)\text{bipy}]$  ( $\mathbf{3}$ ) likely stems from the degradation of  $[\text{Ni}(\text{NR}_2)_2]$ , as proposed by Power during the synthesis of  $[\text{Ni}(\mu\text{-NR}_2)_4]$  when no donor ligand is present.<sup>5</sup> Similarly, we recently observed the one-electron reduction of the divalent linear  $[\text{Ni}(\text{N}(\text{Dipp})\text{SiMe}_3)_2]$  using alkali metal salts of organic nucleophiles, for example,  $\text{KO}^t\text{Bu}$  or  $\text{KNR}_2$ .<sup>64</sup> In an attempt

to independently obtain either bipyridine adduct in larger amounts,  $[\text{NiCl}_2(\text{dme})]$  was reacted with 2 equiv of  $\text{LiNR}_2$  in the presence of 1 equiv of 2,2'-bipyridine in  $\text{Et}_2\text{O}$  (Scheme 1). From this, the nickel(II) complex  $[\text{Ni}(\text{NR}_2)_2(\text{bipy})]$  ( $\mathbf{4}$ ) was isolated as dark-orange crystals, albeit in poor yields (5%). The structure of  $\mathbf{4}$  in the solid state shows a distorted tetrahedral surrounding of the nickel ion (Figure 4b). This is in agreement with other 4-coordinate nickel(II) bipy complexes bearing weak-field  $\pi$ -donor ligands (e.g.,  $[\text{Ni}(\text{I})_2(\{4,4'\text{-}t\text{Bu}_2\}\text{bipy})]$ ).<sup>65–68</sup> The  $\text{M--N}_{\text{bipy}}$  bond distances of  $[\text{Ni}(\text{NR}_2)_2\text{bipy}]$  amount to 2.030(1) Å, which fit well into the trend of the analogous complexes  $[\text{M}(\text{NR}_2)_2(\text{bipy})]$  of manganese (2.26 Å), iron (2.18 Å), and cobalt (2.11 Å).<sup>58,69</sup> The  $^1\text{H}$  NMR spectroscopic signature of  $\mathbf{3}$  is identical to that of the species obtained from the reaction of bipy with  $\text{Li}(\text{thf})_x[\mathbf{1}]$ .

**Synthesis and Properties of the Linear  $\text{K}\{\text{m}\}[\text{Ni}(\text{NR}_2)_2]$ .** Having elaborated on the behavior of  $\text{Li}(\text{thf})_x[\mathbf{1}]$ , we pursued its reduction using  $\text{KC}_8$  (Scheme 2). In toluene,

**Scheme 2. Reduction of  $\text{Li}(\text{thf})_x[\text{Ni}(\text{NR}_2)_3]$  ( $\text{Li}(\text{thf})_x[\mathbf{1}]$ ) with  $\text{KC}_8$  with and without a Cation Masking Agent and Synthesis of  $\text{K}\{\text{m}\}[\text{Ni}(\text{NR}_2)_2]$ , ( $\text{K}\{\text{m}\}[\mathbf{6}]$ ) from  $[\text{Ni}(\text{NR}_2)(\text{PPh}_3)_2]$**



this leads to the observation of the dimeric compound  $\text{K}(\text{toluene})[\text{Ni}_2(\text{NR}_2)_3]$ ,  $\text{K}(\text{toluene})[\mathbf{5}]$ , which could however only be crystallographically identified (Figure 5a), despite multiple attempts for further isolation. In the solid state,  $\text{K}(\text{toluene})[\mathbf{5}]$  contains two metal–metal-bonded  $\text{Ni}^{\text{I}}(\text{NR}_2)$  units with a third  $\text{NR}_2$  ligand bridging both metal ions ( $\text{Ni1--Ni1'--Ni1}$  80.24(7)°). The distance between the nickel ions is 2.4416(4) Å, close to the tetrameric  $[\text{Ni}(\mu\text{-NR}_2)_4]$  ( $\text{Ni--Ni}$  2.433 Å) complex described by Power.<sup>5</sup> The potassium ion is situated between both terminal  $\text{NR}_2$  ligands and is saturated by one molecule of toluene.

Disregarding the potassium cation, the anion can be described as a linear  $[\text{Ni}(\text{NR}_2)_2]^-$  ( $\text{N1--Ni1--N2}$  174.74(5)°) that interacts with a  $\text{Ni}(\text{NR}_2)$  fragment with a  $\text{Ni1--Ni1'--N2'}$  angle of 135.29(4)°.  $[\mathbf{5}]^-$  can be seen as an intermediate in the decomposition of  $[\text{Ni}(\text{NR}_2)_2]$  to the tetrameric  $[\text{Ni}(\mu\text{-NR}_2)_4]$ <sup>5</sup> or of the metal–metal-bonded  $[\text{Mn}^{\text{I}}(\text{NR}_2)_2]^-$  dimer (Figure 1F) to amorphous Mn,  $\text{NR}_2^-$  and  $[\text{Mn}(\text{NR}_2)_3]^-$ .<sup>34</sup> Performing the reduction of  $\text{Li}(\text{thf})_x[\mathbf{1}]$  in  $\text{Et}_2\text{O}$  in the presence of 18-crown-6 (18c6) led to the isolation of a yellowish-green product from a pentane-layered  $\text{Et}_2\text{O}$  solution at  $-35$  °C (Scheme 2). XRD analysis on suitable crystals corroborated the presence of the sought-after  $\text{K}\{18\text{c}6\}[\text{Ni}(\text{NR}_2)_2]$  ( $\text{K}\{18\text{c}6\}[\mathbf{6}]$ ; Figure 5b). The complex



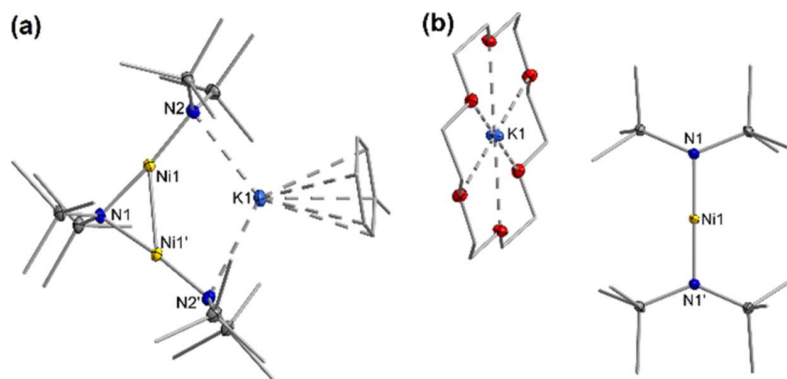


**Figure 5.** Molecular structure of  $K(\text{toluene})[5]$  (a) and  $K\{18\text{c}6\}[6]$  (b) in the solid state. H atoms are omitted for clarity. Selected bond length ( $\text{\AA}$ ) and angles ( $\text{deg}$ ):  $[5]$ : Ni1–Ni1' 2.4416(4), Ni1–N1 1.894(1), Ni1–N2 1.867(1); N1–Ni1–N2 174.74(5), Ni1–Ni1–Ni1' 80.24(7), Ni1–N1–Ni1' 80.24(7).  $[6]$  Ni1–N1 1.866(1); N1–Ni1–N1' 180.

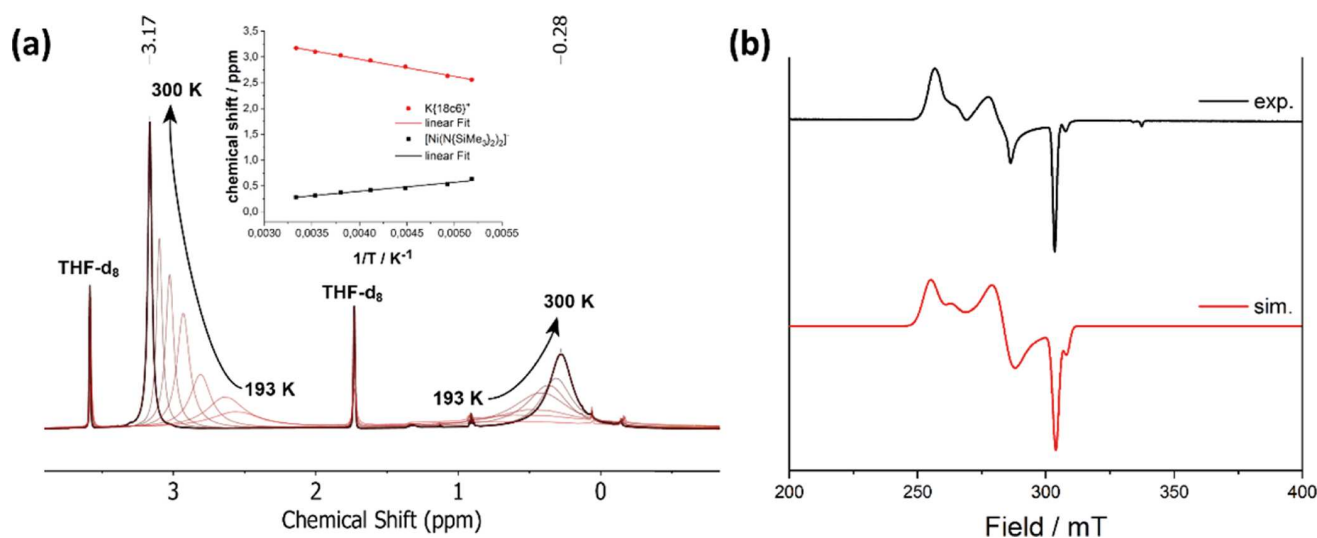


**Figure 6.** (a) Temperature-dependent  $^1\text{H}$  NMR spectra of  $K\{18\text{c}6\}[\text{Ni}(\text{NR}_2)_2]$  ( $K\{18\text{c}6\}[6]$ ) (500 MHz,  $\text{thf-d}_8$ ) from 300 to 193 K; inset: Curie–Weiss plot of the chemical shift vs  $1/T$ . (b) X-band EPR spectrum of  $K\{18\text{c}6\}[\text{Ni}(\text{NR}_2)_2]$  ( $K\{18\text{c}6\}[6]$ ) in frozen Me-thf at 13.3 K.  $S_1 = 1/2$ ,  $g_{11} = 2.62$ ,  $g_{12} = 2.36$ ,  $g_{13} = 2.2$ , weight = 0.8;  $S_2 = 1/2$ ,  $g_{21} = 2.54$ ,  $g_{22} = 2.35$ ,  $g_{23} = 2.17$ , weight = 0.2.

anion exhibits a linear N1–Ni1–N1' axis of  $180^\circ$ , which is attributed to a crystallographic inversion center on the metal atom. The Ni1–N1 bond length amounts to 1.866(1)  $\text{\AA}$  that fits into the trend of ion radius contraction with respect to its lighter congeners (Cr: 2.049(17)  $\text{\AA}$ , Fe: 1.9213(6)  $\text{\AA}$ , and Co: 1.8979(11)  $\text{\AA}$ ).<sup>33,34</sup> The bond lengths in  $[6]^-$  are slightly longer than those of the related, bulkier  $[\text{Ni}(\text{N}(\text{Dipp})\text{SiMe}_3)_2]^-$  (1.85  $\text{\AA}$ ). These differences might be attributed to attractive interligand dispersion interactions in  $[\text{Ni}(\text{N}(\text{Dipp})\text{SiMe}_3)_2]^-$ , as proposed for the divalent counterpart,<sup>51</sup> or to a stronger electrostatic repulsion between the more basic hexamethyldisilazane ligands in  $[6]^-$  with the filled d-orbitals of the nickel(I) ion.<sup>34</sup> Both silylamide ligands in  $K\{18\text{c}6\}[6]$  are slightly twisted with a Si1–N1–N1'–Si torsion angle of  $14.66(8)^\circ$ . Crystallization from a *n*-pentane-layered thf solution of  $K\{18\text{c}6\}[6]$  led to the observation of  $[K\{18\text{c}6\}(\text{thf})_2][6]$  in which two thf molecules coordinate additionally to the  $K\{18\text{c}6\}$  cation at the axial positions. Interestingly, this allows for the observation of the full complex anion within the unit cell, for which a “true” N–Ni–N angle of  $179.59(12)^\circ$  is found with slightly different Ni–N bond lengths of 1.854(2) and 1.863(2)  $\text{\AA}$ . These features align nonetheless well with the symmetry generated for  $K\{18\text{c}6\}[6]$ . The sole difference is

found for the twisting of the ligands with an increased torsion angle of  $26.9(2)^\circ$  in  $[K\{18\text{c}6\}(\text{thf})_2][6]$ . Although  $K\{m\}[\text{Ni}(\text{NR}_2)_2]$  ( $K\{m\}[6]$ ) could now be obtained, the use of the  $\text{Li}(\text{thf})_x[1]$  did not fully eliminate stoichiometric uncertainties due to the ease of  $[\text{Ni}(\text{NR}_2)_2(\text{thf})]$  evaporation and changing thf contents. This sometimes gave rise to the presence of intractable contaminations of  $K\{18\text{c}6\}[\text{Ni}(\text{NR}_2)_3]$  ( $K\{18\text{c}6\}[1]$ ) and additional 18-crown-6 coordination to the potassium cation, which made the isolation of pure  $K\{m\}[\text{Ni}(\text{NR}_2)_2]$  ( $K\{m\}[6]$ ) not sufficiently reliable. Using crypt.222 as a masking agent also did not resolve this general problem, which also occurred when using  $\text{Li}(\text{dmap})_4[1]$ .

As such, we ultimately chose a different approach using the known nickel(I) phosphine adduct  $[\text{Ni}(\text{NR}_2)(\text{PPh}_3)_2]$ . This is obtained by reacting  $[\text{NiCl}_2(\text{PPh}_3)_2]$  with 2 equiv of  $\text{Li}(\text{NR}_2)$ , whereas one  $\text{NR}_2$  ligand acts as a reductant.<sup>70,71</sup> Subsequently, the reaction of  $[\text{Ni}(\text{NR}_2)(\text{PPh}_3)_2]$  with  $\text{KNR}_2$  in the presence of 18c6 or crypt.222 yielded  $K\{m\}[6]$  in good yields and reliable purity under displacement of the phosphine ligands (Scheme 2). Decoordination of the phosphine ligands was thereby expected as the indifference of anionic two-coordinate metal(I) complexes toward donor ligands was already observed for other  $[\text{M}(\text{NR}_2)_2]^-$  complexes.<sup>33,34</sup>  $K\{m\}[6]$  is also

unaffected by 2,2'-bipyridine. This contrasts the behavior of all known lighter  $K\{m\}[M(NR_2)_2]$ , which react readily with bipy to give  $K\{m\}[M(NR_2)_2(\text{bipy})]$  under bipyridine reduction.<sup>58</sup> For  $[6]^-$ , it can be attributed to the comparably little reducing capabilities of linear nickel(I) silylamides ( $E_{1/2}([\text{Ni}(\text{N}(\text{Dipp})\text{-SiMe}_3)_2]^{-/0}) = -1.28 \text{ V vs Fc/Fc}^+$ ).<sup>48</sup> On the other hand, bipyridine reduction is observed for the related nickel mesityl complex  $K\{\text{crypt}\}[M(\text{mesityl})_2(\text{bipy})]$ <sup>55</sup> and likely reflects on the lesser donor strength of silylamides with regards to the mesityl ligands. With an optimized synthesis of pure  $K\{18c6\}[6]$  in hand, we took a closer look into its electronic features in solution. The UV/vis spectrum in  $\text{Et}_2\text{O}$  shows no defined absorption band between 300 and 1000 nm at ambient temperature and upon cooling to  $-100 \text{ }^\circ\text{C}$ . In the proton NMR spectrum,  $K\{18c6\}[6]$  is represented by a broad signal at 0.26 ppm for the  $\text{SiMe}_3$  groups, reflecting a slight paramagnetism. Indeed, the magnetic moment in solution, determined by the method of Evans,<sup>72</sup> amounts to  $2.31 \mu_B$ . These values are marginally higher than those of other linear nickel(I) silylamides<sup>48,73</sup> and correspond to a  $S = 1/2$  system ( $\mu_{s.o.} = 1.73 \mu_B$ ) with substantial orbital contributions to the magnetic moment. Temperature-dependent  $^1\text{H}$  NMR spectroscopy revealed a shift of the signals belonging to the complex anion and the counter  $K\{18c6\}$  cation and substantial line broadening upon cooling (Figure 6a). Plotting the chemical shift versus  $1/T$  gave a linear dependency for both signals, implicating significant ion pairing in solution. The X-band EPR spectrum of  $K\{18c6\}[6]$ , measured in a frozen Me-thf solution at 13.3 K, revealed rhombic signals centered at  $g$  values around 2.62, 2.36, and 2.2 (Figure 6b) that do not correspond to a singular species. The signals could be sufficiently modeled as two  $S = 1/2$  species with  $g_{11} = 2.62$ ,  $g_{12} = 2.36$ , and  $g_{13} = 2.2$  and  $g_{21} = 2.54$ ,  $g_{22} = 2.35$ , and  $g_{23} = 2.17$  in a 0.8–0.2 ratio. As the employed  $K\{m\}[6]$  was pure by other means of analysis, we contemplated on two conformationally and thus EPR spectroscopically different species. Such a behavior is plausible, given the tight cation/anion interactions of  $K\{m\}[6]$  observed by  $^1\text{H}$  NMR spectroscopy. These interactions could lead to distortion from linearity and/or suppression of the rotation of the amide ligands along the principal axis, whereas distinct conformations are locked by freezing of the solution. Corresponding observations were made for the cationic linear nickel(I) complex ( $[\text{Ni}(\text{Mes}_2\text{Im})_2][\text{BF}_4]$ ), whereas differing interactions with the counteranion caused two principal conformations with similar EPR signatures.<sup>74</sup> The importance of the cation/anion interaction becomes clear as X-band EPR measurement of  $K\{\text{crypt}\}[6]$  led to the observation of two slightly different  $S = 1/2$  species (see the Supporting Information for spectra) with  $g_{11} = 2.40$ ,  $g_{12} = 2.35$ , and  $g_{13} = 2.20$  and  $g_{21} = 2.61$ ,  $g_{22} = 2.38$ , and  $g_{23} = 1.98$  (ratio 0.35:0.65). These observations point toward a geometric flexibility of the complex anion and thus underscores the unique nature of anionic linear metal(I) hexamethyldisilazanides that adopt a linear geometry despite the absence of a sterically highly encumbered metal center.

## CONCLUSIONS

In conclusion, we reported on the synthesis and properties of linear nickel(I) silyl amide  $K\{m\}[\text{Ni}(\text{NR}_2)_2]$  ( $m = 18c6$ , crypt.222;  $\text{NR}_2 = \text{N}(\text{SiMe}_3)_2$ ), which is the heaviest open-shell example of this class of compounds. Along the way, we were able to isolate the trisamido complex  $\text{Li}(\text{thf})_x[\text{Ni}(\text{NR}_2)_3]$  ( $x = 4.5\text{--}5.5$ ), which disproportionates in unpolar solvents, leading

to the nickel(II) hexamethyldisilazanide  $[\text{Ni}(\text{NR}_2)_2]$  under the liberation of  $\text{LiNR}_2$ . The reaction of  $\text{Li}(\text{thf})_x[\text{Ni}(\text{NR}_2)_3]$  with dimethylaminopyridine (dmap) led first led first to *trans*- $[\text{Ni}(\text{NR}_2)_2(\text{dmap})_2]$  and, with an excess of dmap, again to salt-separated  $\text{Li}(\text{dmap})_4[\text{Ni}(\text{NR}_2)_3]$ . The use of 2,2'-bipyridine as a donor ligand yielded the tetrahedral  $[\text{Ni}(\text{NR}_2)_2(2,2'\text{-bipy})]$ , which degraded into the trigonal nickel(I) complex  $[\text{Ni}(\text{NR}_2)(2,2'\text{-bipy})]$ . Reduction of  $\text{Li}(\text{thf})_x[\text{Ni}(\text{NR}_2)_3]$  with  $\text{KC}_8$  led to the observation of the dinuclear nickel(I) complex  $[\text{K}(\text{toluene})\text{Ni}_2[\text{NR}_2)_3]$ , whereas in the presence of 18-crown-6 or crypt.222, the linear complex  $K\{m\}[\text{Ni}(\text{NR}_2)_2]$  was obtained. An optimized, reliable synthesis method for  $K\{m\}[\text{Ni}(\text{NR}_2)_2]$  was further developed by displacement of the phosphine ligands in the monovalent  $[\text{Ni}(\text{PPh}_3)_2(\text{NR}_2)]$  with  $K\{m\}[\text{NR}_2]$ . The linear nickel(I) complex  $[\text{Ni}(\text{NR}_2)_2]^-$  was subsequently examined for its physical properties, leading to its description as a  $S = 1/2$  system with pronounced axial anisotropy, as well as strong anion/cation interaction. Its chemical behavior is under current scrutiny in our lab.

## EXPERIMENTAL SECTION

**General Considerations.** All manipulations were carried out in a glovebox or using Schlenk-type techniques under a dry argon atmosphere. The used solvents were dried by continuous distillation over sodium metal for several days, degassed via three freeze–pump cycles, and stored over molecular sieves 4 Å. The  $^1\text{H}$  NMR spectra were recorded using a Bruker AV III 500 or Bruker AV II 300 NMR spectrometer. Chemical shifts are reported in parts per million relative to the residual proton signals (for  $^1\text{H}$ ) or relative to the signal of the solvent itself ( $^{13}\text{C}$ ).  $w_{1/2}$  is the line width of a signal at half its maximum intensity. The integrals of the broad signals of the silylamide units were obtained directly or by peak fitting (in case of overlapping signals) using the MestreNova software package. IR measurements were conducted using a Bruker Alpha ATR-IR spectrometer. Elemental analysis was performed by the “in-house” service of the Chemistry Department of the Philipps University Marburg, Germany, using a CHN(S) analyzer vario MICRO Cube (Elementar). The UV/vis measurements were recorded using an Analytik Jena Specord S600 using WinASPECT software and an UNISOKU CoolSpeK Cryostat. The diamagnetic correction was performed using the pascal constants and the experimentally determined value of the polyurethane sample holder. The solution magnetic susceptibilities were determined by the Evans method.<sup>72</sup> Anhydrous  $\text{NiCl}_2$ , *n*-butyl lithium (2.5 M in hexane), 4-dimethylaminopyridine (dmap), 2,2'-bipyridine (bipy),  $\text{KNR}_2$ ,  $\text{PPh}_3$ , 18-crown-6, crypt.222, and tetramethylsilane were obtained commercially (Sigma-Aldrich, Acros, Strem, Alfa Aesar) and—if not noted otherwise—used as received. 18-crown-6 (18c6) was sublimed prior to the use to remove traces of water.  $[\text{Ni}(\text{NR}_2)(\text{PPh}_3)_2]$ <sup>71</sup> and  $[\text{NiCl}_2(\text{dme})]^{75}$  (dme = dimethoxyethane) were prepared according to the literature procedures. Caution: all mentioned compounds are highly oxygen- and moisture-sensitive and should be handled with care.

$\text{Li}(\text{thf})_x[\text{Ni}(\text{NR}_2)_3]$  ( $\text{Li}(\text{thf})_x[1]$ ). 1.55 g of  $\text{LiNR}_2$  (9 mmol, 3 equiv) were dissolved in 15 mL of thf, and the solution precooled to  $-30 \text{ }^\circ\text{C}$ . 400 mg of  $\text{NiCl}_2$  (3 mmol, 1 equiv) were added as a solid, and the reaction mixture was stirred at room temperature (RT) over 12 h. The solvent of the resulting dark-green solution was partially removed under reduced pressure, resulting in a green sticky solid. The residue was extracted using  $3 \times 5 \text{ mL}$  of  $\text{Et}_2\text{O}$ . The filtrate was cooled to  $0 \text{ }^\circ\text{C}$ , and the solvent was removed under reduced pressure.  $\text{Li}(\text{thf})_x[\text{Ni}(\text{NR}_2)_3]$  ( $\text{Li}(\text{thf})_x[1]$ ) was obtained as a dark-green solid (1.63 g). The amount of thf left in the product was determined by  $^1\text{H}$  NMR spectroscopy in toluene- $d_8$  to  $x = 4.5\text{--}5$ .  $^1\text{H}$  NMR: (thf- $d_8$ , 298 K, ppm, 300 MHz):  $\delta$  1.12 (54H,  $w_{1/2} = 123 \text{ Hz}$ ,  $[\text{Ni}(\text{N}(\text{SiMe}_3)_2)_3]^-$ ); (toluene- $d_8$ , 298 K, ppm, 300 MHz):  $\delta$  9.71 (36H,  $\text{Ni}(\text{N}(\text{SiMe}_3)_2)_2\text{thf}$ ), 4.80 (4 H,  $\text{Ni}(\text{NR}_2)_2\text{thf}$ ), 2.20 (4 H,  $\text{Ni}(\text{NR}_2)_2\text{thf}$ ),

0.30 (18 H, Li(N(SiMe<sub>3</sub>)<sub>2</sub>)). IR (ATR, cm<sup>-1</sup>):  $\nu$  2946 (vw), 1235 (w), 1041 (w), 976 (w), 827 (w), 776 (w), 749 (w), 665 (w), 418 (w), 407 (w). UV/vis: in toluene:  $\lambda_{\text{max}}$  (300 K) = 490 nm ( $\epsilon$  = 16,000 L m<sup>-1</sup> mol<sup>-1</sup>),  $\lambda_{\text{max}}$  (180 K) = 430 nm ( $\epsilon$  = 14,000 L m<sup>-1</sup> mol<sup>-1</sup>); in thf:  $\lambda_{\text{max}}$  (300 K) = 340 nm ( $\epsilon$  = 5600 L m<sup>-1</sup> mol<sup>-1</sup>), 395 nm ( $\epsilon$  = 8000 L m<sup>-1</sup> mol<sup>-1</sup>).

**Li(dmap)<sub>4</sub>[Ni(NR<sub>2</sub>)<sub>3</sub>] (Li(dmap)<sub>4</sub>[1]).** 200 mg of Li{thf}<sub>x</sub>[Ni(NR<sub>2</sub>)<sub>3</sub>] (0.3 mmol, 1 equiv) were dissolved in 3 mL of thf, and 90 mg of dmap (0.8 mmol, 4 equiv) dissolved in 2 mL of thf were added at ambient temperature. The yellowish-green solution was stirred for 2 h, and the solvent was removed under reduced pressure. The residue was dissolved in Et<sub>2</sub>O, and the yellowish-green solution was layered with *n*-pentane. Storage at -30 °C led to the precipitation of a green solid. The supernatant solution was removed, and the residue was washed with precooled 3 × 1 mL *n*-pentane prior to drying under reduced pressure. The obtained solid was recrystallized three times in the same manner, leading to the formation of bright-green plates. Li(dmap)<sub>4</sub>[1] was obtained as a bright-green solid (80 mg, 0.1 mmol, 38%). <sup>1</sup>H NMR (thf-*d*<sub>8</sub>, 298 K, ppm, 300 MHz):  $\delta$  8.12 (8H, *w*<sub>1/2</sub> = 23.3 Hz, CH<sub>Ar</sub>), 6.58 (8H, *w*<sub>1/2</sub> = 12.1 Hz, CH<sub>Ar</sub>), 2.98 (36H, *w*<sub>1/2</sub> = 4.10 Hz, CH<sub>3</sub>), 1.18 (54H, *w*<sub>1/2</sub> = 122 Hz, [Ni(N(SiMe<sub>3</sub>)<sub>2</sub>)<sub>3</sub>]). IR (ATR, cm<sup>-1</sup>):  $\nu$  2942 (w), 2893 (w), 1606 (m), 1527 (w), 1445 (w), 1383 (w), 1227 (w), 1109 (w), 1000 (w), 988 (w), 971 (m), 949 (w), 856 (w), 827 (m), 805 (m), 776 (w), 745 (w), 706 (w), 656 (w), 615 (w), 609 (w), 531 (w), 434 (w), 403 (w). Elemental analysis: calcd (%) for C<sub>46</sub>H<sub>94</sub>Li<sub>11</sub>Ni<sub>3</sub>Si<sub>6</sub> (1035.48 g/mol): C, 53.36; H, 9.15; N, 14.88. Found: C, 53.48; H, 8.85; N, 14.81. Magnetic susceptibility:  $\mu_{\text{eff}}$  = 3.32  $\mu_{\text{B}}$  (Evans, thf-*d*<sub>8</sub> + 1% Si(CH<sub>3</sub>)<sub>4</sub>),  $\mu_{\text{s.o.}}$  (*S* = 1) = 2.83  $\mu_{\text{B}}$ .

**[Ni(NR<sub>2</sub>)<sub>2</sub>(dmap)<sub>2</sub>] ([2]).** 500 mg of Li{thf}<sub>x</sub>[Ni(NR<sub>2</sub>)<sub>3</sub>] (0.5 mmol, 1 equiv) were dissolved in 5 mL of precooled toluene (-30 °C), and 125 mg of dmap (1 mmol, 2 equiv) dissolved in 5 mL of precooled toluene were added. The solvent of the resulting dark-yellow solution was removed under reduced pressure after 15 min. The residue was extracted using 3 × 5 mL of precooled *n*-pentane. The filtrate was concentrated under reduced pressure and stored at -30 °C. Few crystals suitable for XRD could be obtained after 1 day. <sup>1</sup>H NMR: (toluene-*d*<sub>8</sub>, 298 K, ppm, 300 MHz):  $\delta$  4.24 (36 H, Ni(N(SiMe<sub>3</sub>)<sub>2</sub>)<sub>2</sub>), no observable signals for the dmap protons. IR (ATR, cm<sup>-1</sup>):  $\nu$  2942 (w), 1612 (m), 1530 (m), 1443 (w), 1381 (w), 1249 (m), 1235 (m), 1217 (m), 1025 (w), 984 (s), 951 (w), 860 (m), 823 (s), 807 (s), 782 (m), 745 (m), 710 (w), 658 (m), 609 (w), 531 (w). UV/vis (toluene, 300 K):  $\lambda_{\text{max}}$  = 415 nm ( $\epsilon$  = 1300 L m<sup>-1</sup> mol<sup>-1</sup>).

**[Ni(NR<sub>2</sub>)<sub>2</sub>(bipy)] ([3]).** 100 mg of Li(thf)<sub>x</sub>[Ni(NR<sub>2</sub>)<sub>3</sub>] and 28.5 mg 2,2'-bipy were dissolved in 5 mL of toluene and stirred for 1 h at RT. The reaction mixture was filtered, and the filtrate was concentrated under reduced pressure. Storage at -30 °C led to the formation of few dark-brown crystals suitable for XRD.

**[Ni(NR<sub>2</sub>)<sub>2</sub>(bipy)] ([4]).** 650 mg of [NiCl<sub>2</sub>(dme)] (3 mmol, 1 equiv) and 466 mg of 2,2'-bipyridine (3 mmol, 1 equiv) were suspended in 5 mL of Et<sub>2</sub>O, and a solution of 1 g of LiNR<sub>2</sub> (6 mmol, 2 equiv) in 5 mL of Et<sub>2</sub>O was added. The reaction mixture was stirred over 12 h. The reaction mixture was filtered, and the solvent was removed under reduced pressure. The residue was extracted using 3 × 5 mL of *n*-pentane. The filtrate was concentrated under reduced pressure, and storage at -35 °C led to the formation of dark-orange crystals. The supernatant solution was removed by filtration, and the residue was dried under reduced pressure. [Ni(NR<sub>2</sub>)<sub>2</sub>(2,2'-bipy)] ([4]) was obtained as a dark crystalline solid (78 mg, 0.15 mol, 5%). <sup>1</sup>H NMR: (thf-*d*<sub>8</sub>, 298 K, ppm, 300 MHz):  $\delta$  61.38 (2 H, *bipy*), 56.73 (2 H, *bipy*), 21.48 (2 H, *bipy*), 9.74 (36H, Ni(N(SiMe<sub>3</sub>)<sub>2</sub>)<sub>2</sub>bipy); (toluene-*d*<sub>8</sub>, 298 K, ppm, 300 MHz):  $\delta$  59.51 (2 H, *bipy*), 54.90 (2 H, *bipy*), 20.12 (2 H, *bipy*), 10.62 (36 H, Ni(N(SiMe<sub>3</sub>)<sub>2</sub>)<sub>2</sub>bipy). IR (ATR, cm<sup>-1</sup>):  $\nu$  2942 (w), 2889 (w), 1464 (w), 1439 (w), 1425 (w), 1389 (w), 1235 (w), 1184 (w), 1151 (w), 996 (m), 930 (w), 893 (w), 869 (s), 817 (s), 786 (s), 755 (m), 710 (w), 661 (m), 609 (w), 574 (w), 566 (w), 549 (w), 520 (w), 420 (w). Elemental analysis: calcd (%) for C<sub>22</sub>H<sub>44</sub>N<sub>4</sub>NiSi<sub>4</sub> (535.66 g/mol): C, 49.33; H, 8.28; N, 10.46. Found: C, 49.96; H, 7.79; N, 10.65. UV/vis (toluene, 300 K):  $\lambda_{\text{max}}$  = 400 nm ( $\epsilon$  = 1900 L m<sup>-1</sup> mol<sup>-1</sup>).

**K(toluene)[Ni<sub>2</sub>(NR<sub>2</sub>)<sub>3</sub>] (K(toluene)[5]).** 400 mg of Li{thf}<sub>x</sub>[Ni(NR<sub>2</sub>)<sub>3</sub>] was dissolved in 5 mL of toluene. 62 mg of KC<sub>8</sub> was added as a solid, and the reaction mixture was stirred for 1 h at RT. After filtration, the filtrate was concentrated under reduced pressure. Storage at -30 °C led to the formation of few dark-orange crystals suitable for XRD.

**K{18c6}[Ni(NR<sub>2</sub>)<sub>2</sub>] (K{18c6}[6]).** 500 mg of [Ni(NR<sub>2</sub>)(PPh<sub>3</sub>)<sub>2</sub>] (0.7 mmol, 1 equiv) were dissolved in 5 mL of thf, and the solution was precooled to -30 °C. A solution of 134 mg of KNR<sub>2</sub> (0.7 mmol, 1 equiv) and 160 mg of 18-crown-6 (0.7 mmol, 0.9 equiv) in 3 mL of thf was added, and the reaction mixture was stirred at RT over 12 h. The solvent was removed in vacuo, and the residue was extracted with 3 × 3 mL of Et<sub>2</sub>O. Layering of the solution with 10 mL of *n*-pentane led to the formation of a yellow crystalline solid. The supernatant solution was removed by filtration, and the residue was washed with 3 × 2 mL of *n*-pentane. Drying under reduced pressure afforded K{18c6}[6] as a pale-yellow crystalline solid (338 mg, 0.5 mol, 73%). <sup>1</sup>H NMR (thf-*d*<sub>8</sub>, 298 K, ppm, 300 MHz):  $\delta$  3.35 (24 H, *w*<sub>1/2</sub> = 13.4 Hz 18c6), 0.25 (36H, *w*<sub>1/2</sub> = 100.4 Hz, [Ni(N(SiMe<sub>3</sub>)<sub>2</sub>)<sub>2</sub>]). IR (ATR, cm<sup>-1</sup>):  $\nu$  2940 (w), 2887 (m), 1472 (w), 1454 (w), 1432 (w), 1351 (m), 1283 (w), 1245 (m), 1230 (s), 1130 (vs), 1032 (s), 963 (s), 858 (m), 820 (vs), 775 (m), 738 (m), 697 (w), 657 (s), 608 (m), 531 (w), 468 (w), 435 (w), 411 (w). Elemental analysis: calcd (%) for C<sub>24</sub>H<sub>60</sub>KN<sub>2</sub>NiO<sub>6</sub>Si<sub>2</sub> (682.88 g/mol): C, 42.41; H, 8.86; N, 4.10. Found: C, 42.01; H, 8.605; N, 4.14. Magnetic susceptibility:  $\mu_{\text{eff}}$  = 2.31  $\mu_{\text{B}}$  (Evans, thf-*d*<sub>8</sub> + 1% Si(CH<sub>3</sub>)<sub>4</sub>),  $\mu_{\text{s.o.}}$  = 1.73  $\mu_{\text{B}}$ .

**K{crypt}[Ni(NR<sub>2</sub>)<sub>2</sub>] (K{crypt}[6]).** 500 mg of [Ni(NR<sub>2</sub>)(PPh<sub>3</sub>)<sub>2</sub>] (0.7 mmol, 1 equiv) were dissolved in 5 mL of thf, and the solution was precooled to -30 °C. A solution of 134 mg of KNR<sub>2</sub> (0.7 mmol, 1 equiv) and 227 mg of crypt.222 (0.7 mmol, 0.9 equiv) in 3 mL of thf was added, and the reaction mixture was allowed to warm to RT and stirred for 12 h. The solvent was removed in vacuo, and the residue was extracted with 3 × 3 mL of Et<sub>2</sub>O. Layering of the solution with 10 mL of *n*-pentane led to the formation of an orange crystalline solid. The supernatant solution was removed by filtration, and the residue was washed using 3 × 2 mL of *n*-pentane. Drying under reduced pressure afforded K{crypt}[6] as a pale-yellow crystalline solid (390 mg, 0.5 mol, 73%). <sup>1</sup>H NMR (thf-*d*<sub>8</sub>, 298 K, ppm, 300 MHz):  $\delta$  3.31 (24 H, *w*<sub>1/2</sub> = 15.1 Hz, crypt), 2.34 (14 H, *w*<sub>1/2</sub> = 13.1 Hz, crypt), 0.24 (36H, *w*<sub>1/2</sub> = 108.1 Hz, [Ni(N(SiMe<sub>3</sub>)<sub>2</sub>)<sub>2</sub>]). IR (ATR, cm<sup>-1</sup>):  $\nu$  2952 (w), 2940 (w), 2880 (w), 2810 (w), 1352 (w), 1297 (w), 1258 (w), 1243 (w), 1229 (m), 1130 (w), 1076 (m), 1029 (m), 951 (m), 932 (w), 860 (w), 819 (m), 774 (w), 743 (w), 661 (w), 650 (w). Elemental analysis: calcd (%) for C<sub>30</sub>H<sub>72</sub>KN<sub>4</sub>NiO<sub>6</sub>Si<sub>4</sub> (795.06 g/mol): C, 45.32; H, 9.13; N, 7.05. Found: C, 45.78; H, 8.75; N, 6.93. Magnetic susceptibility:  $\mu_{\text{eff}}$  = 2.30  $\mu_{\text{B}}$  (Evans, thf-*d*<sub>8</sub> + 1% Si(CH<sub>3</sub>)<sub>4</sub>),  $\mu_{\text{s.o.}}$  = 1.73  $\mu_{\text{B}}$ .

Data for Li(thf)<sub>2</sub>(dmap)<sub>2</sub>[1] (CCDC 2141857), Li(dmap)<sub>4</sub>[1] (CCDC 2141859), [2] (CCDC 2141856), [3] (CCDC 2141853), [4] (CCDC 2141854), K(toluene)[5] (CCDC 2141860), K{18c6}[6] (CCDC 2141858), [K{18c6}(thf)<sub>2</sub>][6] (CCDC 2141861), and K{crypt}[6] (CCDC 2141855) were collected at 100 K using a Bruker Quest D8 diffractometer using a graphite-monochromated Mo K $\alpha$  radiation and equipped with an Oxford Instrument The structures were solved using either OLEX SHELXT V2014/1<sup>76</sup> and refined by means of least-squares procedures on F<sup>2</sup> with the aid of the program SHELXL-2016/6<sup>77</sup> included in the software package WinGX version 1.63<sup>78</sup> or CRYSTALS.<sup>79</sup> The atomic scattering factors were taken from International Tables for X-Ray Crystallography.<sup>80</sup> All non-hydrogen atoms were refined anisotropically. All hydrogens atoms were refined by using a riding model. Absorption corrections were introduced by using the MULTISCAN program.<sup>81</sup> Drawings of molecules were created using the programs DIAMOND and POV-Ray with 50% probability displacement ellipsoids for non-H atoms. Depiction of H atoms is omitted for clarity.



## ■ ASSOCIATED CONTENT

### SI Supporting Information

The Supporting Information is available free of charge at <https://pubs.acs.org/doi/10.1021/acs.inorgchem.2c00214>.

<sup>1</sup>H NMR, UV/vis, and X-band EPR spectra and crystallographic details (PDF)

### Accession Codes

CCDC 2141853–2141861 contain the supplementary crystallographic data for this paper. These data can be obtained free of charge via [www.ccdc.cam.ac.uk/data\\_request/cif](http://www.ccdc.cam.ac.uk/data_request/cif), or by emailing [data\\_request@ccdc.cam.ac.uk](mailto:data_request@ccdc.cam.ac.uk), or by contacting The Cambridge Crystallographic Data Centre, 12 Union Road, Cambridge CB2 1EZ, UK; fax: +44 1223 336033.

## ■ AUTHOR INFORMATION

### Corresponding Author

C. Gunnar Werncke – Department of Chemistry, Philipps University Marburg, D-35037 Marburg, Germany;  
orcid.org/0000-0002-9963-8391;  
Email: [gunnar.werncke@chemie.uni-marburg.de](mailto:gunnar.werncke@chemie.uni-marburg.de)

### Authors

Alexander Reckziegel – Department of Chemistry, Philipps University Marburg, D-35037 Marburg, Germany  
Beatrice Battistella – Institute of Chemistry, Humboldt-University Berlin, D-12489 Berlin, Germany  
Andreas Schmidt – Department of Chemistry, Philipps University Marburg, D-35037 Marburg, Germany;  
orcid.org/0000-0001-9979-774X

Complete contact information is available at:  
<https://pubs.acs.org/10.1021/acs.inorgchem.2c00214>

### Author Contributions

The manuscript was written through contributions of all authors. All authors have given approval to the final version of the manuscript.

### Notes

The authors declare no competing financial interest.

## ■ ACKNOWLEDGMENTS

We would like to thank the Deutsche Forschungsgemeinschaft (DFG, grant WE 5627/4-1 to C.G.W.) for funding.

## ■ REFERENCES

- Lappert, M.; Protchenko, A.; Power, P.; Seeber, A. *Metal Amide Chemistry*; John Wiley & Sons, Ltd, 2008.
- Murray, B. D.; Power, P. P. Three-coordinate metal amides of manganese(II) and cobalt(II): Synthesis and x-ray structure of the first tris(silylamide) of manganese and the x-ray crystal structures of  $[M_2N(SiMe_3)_2]_4$  (M = Mn, Co). *Inorg. Chem.* **1984**, *23*, 4584–4588.
- Bürger, H.; Wannagat, U. Silylamido-Derivate von Eisen und Kobalt. *Monatsh. Chem.* **1963**, *94*, 1007–1012.
- Bürger, H.; Wannagat, U. Silylamido-Verbindungen von Chrom, Mangan, Nickel und Kupfer. *Monatsh. Chem.* **1964**, *95*, 1099–1102.
- Faust, M.; Bryan, A. M.; Mansikkamäki, A.; Vasko, P.; Olmstead, M. M.; Tuononen, H. M.; Grandjean, F.; Long, G. J.; Power, P. P. The Instability of  $Ni\{N(SiMe_3)_2\}_2$ : A Fifty Year Old Transition Metal Silylamide Mystery. *Angew. Chem., Int. Ed.* **2015**, *54*, 12914–12917.
- Power, P. P. Stable two-coordinate, open-shell ( $d^1-d^9$ ) transition metal complexes. *Chem. Rev.* **2012**, *112*, 3482–3507.
- Power, P. P.; Ruhlandt-Senge, K.; Shoner, S. C. Synthesis and characterization of the isoelectronic  $d_{10}$  species bis[is-

(methylphenylsilyl)amido]cuprate(1-) and -zinc. *Inorg. Chem.* **1991**, *30*, 5013–5015.

(8) Aleya, E. C.; Bradley, D. C.; Copperthwaite, R. G. Three-coordinate transition metal compounds. Part I. The preparation and characterization of tris(bis(trimethylsilylamido)-derivatives of scandium, titanium, vanadium, chromium, and iron. *J. Chem. Soc., Dalton Trans.* **1972**, 1580.

(9) Andersen, R. A.; Faegri, K.; Green, J. C.; Haaland, A.; Lappert, M. F.; Leung, W. P.; Rypdal, K. Synthesis of bis[bis(trimethylsilyl)amido]iron(II). Structure and bonding in  $M\{N(SiMe_3)_2\}_2$  (M = manganese, iron, cobalt): Two-coordinate transition-metal amides. *Inorg. Chem.* **1988**, *27*, 1782–1786.

(10) Dumestre, F.; Chaudret, B.; Amiens, C.; Renaud, P.; Fejes, P. Superlattices of Iron Nanocubes Synthesized from  $Fe\{N(SiMe_3)_2\}_2$ . *Science* **2004**, *303*, 821–823.

(11) Desvaux, C.; Amiens, C.; Fejes, P.; Renaud, P.; Respaud, M.; Lecante, P.; Snoeck, E.; Chaudret, B. Multimillimetre-large superlattices of air-stable iron–cobalt nanoparticles. *Nat. Mater.* **2005**, *4*, 750–753.

(12) Conley, M. P.; Delley, M. F.; Siddiqi, G.; Lapadula, G.; Norsic, S.; Monteil, V.; Safonova, O. V.; Copéret, C. Polymerization of Ethylene by Silica-Supported Dinuclear  $Cr^{III}$  Sites through an Initiation Step Involving CH Bond Activation. *Angew. Chem., Int. Ed.* **2014**, *53*, 1872–1876.

(13) Margeat, O.; Amiens, C.; Chaudret, B.; Lecante, P.; Benfield, R. E. Chemical Control of Structural and Magnetic Properties of Cobalt Nanoparticles. *Chem. Mater.* **2005**, *17*, 107–111.

(14) Deschner, T.; Törnroos, K. W.; Anwander, R. Iron Silylamide-Grafted Periodic Mesoporous Silica. *Inorg. Chem.* **2011**, *50*, 7217–7228.

(15) Baxter, D. V.; Chisholm, M. H.; Gama, G. J.; Hector, A. L.; Parkin, I. P. Low pressure chemical vapor deposition of metallic films of iron, manganese, cobalt, copper, germanium and tin employing bis(trimethyl)silylamido complexes,  $M\{N(SiMe_3)_2\}_n$ . *Chem. Vap. Depos.* **1995**, *1*, 49–51.

(16) Suh, S.; Hoffman, D. M.; Atagi, L. M.; Smith, D. C. Atmospheric-Pressure MOCVD of Films Containing Zinc Silicate. *Chem. Vap. Depos.* **2001**, *7*, 81–84.

(17) Ellison, J. J.; Power, P. P.; Shoner, S. C. First examples of three-coordinate manganese(III) and cobalt(III): synthesis and characterization of the complexes  $M\{N(SiMe_3)_2\}_3$  (M = Mn or Co). *J. Am. Chem. Soc.* **1989**, *111*, 8044–8046.

(18) Wagner, C. L.; Phan, N. A.; Fettingner, J. C.; Berben, L. A.; Power, P. P. New Characterization of  $V\{N(SiMe_3)_2\}_3$ : Reductions of Tris[bis(trimethylsilyl)amido]vanadium(III) and -chromium(III) To Afford the Reduced Metal(II) Anions  $[M\{N(SiMe_3)_2\}_3]^-$  (M = V and Cr). *Inorg. Chem.* **2019**, *58*, 6095–6101.

(19) Bradley, D. C.; Copperthwaite, R. G.; Extine, M. W.; Reichert, W. W.; Chisholm, M. H. Transition Metal Complexes of Bis-(Trimethyl-silyl)Amine (1,1,1,3,3,3-Hexamethyldisilazane). In *Inorganic Syntheses*; Douglas, B. E., Ed.; John Wiley & Sons, Inc, 1978; pp 112–120.

(20) Putzer, M. A.; Neumüller, B.; Dehnicke, K.; Magull, J. Synthese und Kristallstrukturen der Amido-Komplexe  $[Na(12-Krone-4)_2][M\{N(SiMe_3)_2\}_3]$  mit M = Mn, Fe und Co. *Chem. Ber.* **1996**, *129*, 715–719.

(21) Ghotra, J. S.; Hursthouse, M. B.; Welch, A. J. Three-coordinate scandium(III) and europium(III); crystal and molecular structures of their tris(hexamethyldisilylamido)s. *J. Chem. Soc., Chem. Commun.* **1973**, 669.

(22) Putzer, M. A.; Magull, J.; Goesmann, H.; Neumüller, B.; Dehnicke, K. Synthese, Eigenschaften und Kristallstrukturen der Titan(III)-Amido-Komplexe  $Ti\{N(SiMe_3)_2\}_3$ ,  $[TiCl_2\{N(SiMe_3)_2\}-(THF)_2]$  und  $[Na(12-Krone-4)_2][TiCl_2\{N(SiMe_3)_2\}_3]$ . *Chem. Ber.* **1996**, *129*, 1401–1405.

(23) Hursthouse, M. B.; Rodesiler, P. F. Crystal and molecular structure of tris(hexamethyldisilylamido)iron(III). *J. Chem. Soc., Dalton Trans.* **1972**, 2100.



- (24) Bradley, D. C.; Hursthouse, M. B.; Newing, C. W.; Welch, A. J. Square planar and tetrahedral chromium(II) complexes; crystal structure determinations. *J. Chem. Soc., Chem. Commun.* **1972**, 567.
- (25) Woen, D. H.; Chen, G. P.; Ziller, J. W.; Boyle, T. J.; Furche, F.; Evans, W. J. Solution Synthesis, Structure, and CO<sub>2</sub> Reduction Reactivity of a Scandium(II) Complex, {Sc[N(SiMe<sub>3</sub>)<sub>2</sub>]<sub>3</sub>}<sup>-</sup>. *Angew. Chem., Int. Ed.* **2017**, *56*, 2050–2053.
- (26) König, S. N.; Schneider, D.; Maichle-Mössmer, C.; Day, B. M.; Layfield, R. A.; Anwender, R. Divalent Transition Metal Silylamide Ate Complexes. *Eur. J. Inorg. Chem.* **2014**, 4302–4309.
- (27) Maddock, L. C. H.; Cadenbach, T.; Kennedy, A. R.; Borilovic, I.; Aromí, G.; Hevia, E. Accessing sodium ferrate complexes containing neutral and anionic N-heterocyclic carbene ligands: structural, synthetic, and magnetic insights. *Inorg. Chem.* **2015**, *54*, 9201–9210.
- (28) Borys, A. M.; Hevia, E. Beyond Ni{N(SiMe<sub>3</sub>)<sub>2</sub>}: Synthesis of a Stable Solvated Sodium Tris-Amido Nickelate. *Organometallics* **2021**, *40*, 442–447.
- (29) Putzer, M. A.; Neumüller, B.; Dehnicke, K. Synthese und Kristallstrukturen der Zinkate [Na(12-Krone-4)<sub>2</sub>][Zn{N(SiMe<sub>3</sub>)<sub>2</sub>}]<sub>3</sub> und [Na(12-Krone-4)<sub>2</sub>][Zn(CC-Ph)<sub>3</sub>(THF)][Zn(CC-Ph)<sub>3</sub>]. *Z. Anorg. Allg. Chem.* **1997**, *623*, 539–544.
- (30) Gieshoff, T. N.; Chakraborty, U.; Villa, M.; Jacobi von Wangelin, A. Alkene Hydrogenations by Soluble Iron Nanocluster Catalysts. *Angew. Chem., Int. Ed.* **2017**, *56*, 3585–3589.
- (31) Ohki, Y.; Shimizu, Y.; Araake, R.; Tada, M.; Sameera, W. M. C.; Ito, J.-I.; Nishiyama, H. Co<sub>6</sub>H<sub>8</sub>(P<sup>i</sup>Pr<sub>3</sub>)<sub>6</sub>: A Cobalt Octahedron with Face-Capping Hydrides. *Angew. Chem., Int. Ed.* **2016**, *55*, 15821–15825.
- (32) James, A. M.; Laxman, R. K.; Fronczek, F. R.; Maverick, A. W. Phosphorescence and Structure of a Tetrameric Copper(I)–Amide Cluster. *Inorg. Chem.* **1998**, *37*, 3785–3791.
- (33) Werncke, C. G.; Bunting, P. C.; Duhayon, C.; Long, J. R.; Bontemps, S.; Sabo-Etienne, S. Two-coordinate iron(I) complex Fe{N(SiMe<sub>3</sub>)<sub>2</sub>}: Synthesis, properties, and redox activity. *Angew. Chem.* **2015**, *54*, 245–248.
- (34) Werncke, C. G.; Suturina, E.; Bunting, P. C.; Vendier, L.; Long, J. R.; Atanasov, M.; Neese, F.; Sabo-Etienne, S.; Bontemps, S. Homoleptic Two-Coordinate Silylamido Complexes of Chromium(I), Manganese(I), and Cobalt(I). *Chem.—Eur. J.* **2016**, *22*, 1668–1674.
- (35) Weller, R.; Völlinger, L.; Werncke, C. G. On the Synthesis and Reduction of Trigonal Halido Bis(silylamido) Metalates of Chromium to Cobalt. *Eur. J. Inorg. Chem.* **2021**, 4383–4392.
- (36) Werncke, C. G.; Pfeiffer, J.; Müller, I.; Vendier, L.; Sabo-Etienne, S.; Bontemps, S. C-Halide bond cleavage by a two-coordinate iron(I) complex. *Dalton Trans.* **2019**, 48, 1757–1765.
- (37) Müller, I.; Werncke, C. G. Reductive Coupling of (Fluoro)pyridines by Linear 3d-Metal(I) Silylamides of Cr-Co: A Tale of C-C Bond Formation, C-F Bond Cleavage and a Pyridyl Radical Anion. *Chem.—Eur. J.* **2021**, *27*, 4932–4938.
- (38) Werncke, C. G.; Müller, I. The ambiguous behaviour of diphosphines towards the quasilinear iron(i) complex Fe(N(SiMe<sub>3</sub>)<sub>2</sub>)<sub>2</sub><sup>-</sup> - between inertness, P-C bond cleavage and C-C double bond isomerisation. *Chem. Commun.* **2020**, 56, 2268–2271.
- (39) Weller, R.; Müller, I.; Werncke, C. G. Catalytic 1,3-H Atom Shift of a Terminal Benzylic Alkyne by Iron and Alkali Metal Silylamides – Switching between Allene and Internal Alkyne. *Eur. J. Inorg. Chem.* **2022**, 365.
- (40) Müller, I.; Munz, D.; Werncke, C. G. Reactions of Alkynes with Quasi-Linear 3d Metal(I) Silylamides of Chromium to Cobalt: A Comparative Study. *Inorg. Chem.* **2020**, *59*, 9521–9537.
- (41) Sieg, G.; Pessemeche, Q.; Reith, S.; Yelin, S.; Limberg, C.; Munz, D.; Werncke, C. G. Cobalt and Iron Stabilized Ketyl, Ketiminy and Aldiminy Radical Anions. *Chem.—Eur. J.* **2021**, *27*, 16760.
- (42) Schneider, C.; Guggolz, L.; Werncke, C. G. High-spin carbonyl complexes of iron(I) and cobalt(I). *Dalton Trans.* **2022**, 51, 179.
- (43) Reckziegel, A.; Pietzonka, C.; Kraus, F.; Werncke, C. G. C-H Bond Activation by an Imido Cobalt(III) and the Resulting Amido Cobalt(II) Complex. *Angew. Chem., Int. Ed.* **2020**, *59*, 8527.
- (44) Schneider, C.; Groß, S. J.; Demeshko, S.; Bontemps, S.; Meyer, F.; Werncke, C. G. Synthesis and characterisation of a very low-coordinate diferrous [2Fe-2S]<sup>0</sup> unit. *Chem. Commun.* **2021**, 57, 10751.
- (45) Kalvet, I.; Guo, Q.; Tizzard, G. J.; Schoenebeck, F. When Weaker Can Be Tougher: The Role of Oxidation State (I) in P- vs N-Ligand-Derived Ni-Catalyzed Trifluoromethylthiolation of Aryl Halides. *ACS Catal.* **2017**, *7*, 2126–2132.
- (46) Diccianni, J.; Lin, Q.; Diao, T. Mechanisms of Nickel-Catalyzed Coupling Reactions and Applications in Alkene Functionalization. *Acc. Chem. Res.* **2020**, *53*, 906–919.
- (47) Lin, C.-Y.; Power, P. P. Complexes of Ni(I): a “rare” oxidation state of growing importance. *Chem. Soc. Rev.* **2017**, *46*, 5347–5399.
- (48) Lipschutz, M. I.; Yang, X.; Chatterjee, R.; Tilley, T. D. A structurally rigid bis(amido) ligand framework in low-coordinate Ni(I), Ni(II), and Ni(III) analogues provides access to a Ni(III) methyl complex via oxidative addition. *J. Am. Chem. Soc.* **2013**, *135*, 15298–15301.
- (49) Lipschutz, M. I.; Tilley, T. D. Useful Method for the Preparation of Low-Coordinate Nickel(I) Complexes via Transformations of the Ni(I) Bis(amido) Complex K{Ni[N(SiMe<sub>3</sub>)-(2,6-<sup>i</sup>Pr<sub>2</sub>-C<sub>6</sub>H<sub>3</sub>)<sub>2</sub>]}<sub>2</sub>. *Organometallics* **2014**, *33*, 5566–5570.
- (50) Lipschutz, M. I.; Tilley, T. D. Carbon-carbon cross-coupling reactions catalyzed by a two-coordinate nickel(II)-bis(amido) complex via observable Ni(I), Ni(II), and Ni(III) intermediates. *Angew. Chem., Int. Ed.* **2014**, *53*, 7290–7294.
- (51) Lin, C.-Y.; Guo, J.-D.; Fettinger, J. C.; Nagase, S.; Grandjean, F.; Long, G. J.; Chilton, N. F.; Power, P. P. Dispersion force stabilized two-coordinate transition metal-amido complexes of the -N(SiMe<sub>3</sub>)-Dipp (Dipp = C<sub>6</sub>H<sub>3</sub>-2,6-<sup>i</sup>Pr<sub>2</sub>) ligand: Structural, spectroscopic, magnetic, and computational studies. *Inorg. Chem.* **2013**, *52*, 13584–13593.
- (52) Lin, C.-Y.; Fettinger, J. C.; Power, P. P. Reversible Complexation of Lewis Bases to Low-Coordinate Fe(II), Co(II), and Ni(II) Amides: Influence of the Metal, Donor Ligand, and Amide Substituent on Binding Constants. *Inorg. Chem.* **2017**, *56*, 9892–9902.
- (53) Lipschutz, M. I.; Tilley, T. D. Synthesis and reactivity of a conveniently prepared two-coordinate bis(amido) nickel(II) complex. *Chem. Commun.* **2012**, 48, 7146–7148.
- (54) Wolff, C.; Gottschlich, A.; England, J.; Wiegardt, K.; Saak, W.; Haase, D.; Beckhaus, R. Molecular and Electronic Structures of Mononuclear and Dinuclear Titanium Complexes Containing π-Radical Anions of 2,2'-Bipyridine and 1,10-Phenanthroline: An Experimental and DFT Computational Study. *Inorg. Chem.* **2015**, *54*, 4811–4820.
- (55) Irwin, M.; Doyle, L. R.; Krämer, T.; Herchel, R.; McGrady, J. E.; Goicoechea, J. M. A homologous series of first-row transition-metal complexes of 2,2'-bipyridine and their ligand radical derivatives: trends in structure, magnetism, and bonding. *Inorg. Chem.* **2012**, *51*, 12301–12312.
- (56) Irwin, M.; Jenkins, R. K.; Denning, M. S.; Krämer, T.; Grandjean, F.; Long, G. J.; Herchel, R.; McGrady, J. E.; Goicoechea, J. M. Experimental and computational study of the structural and electronic properties of Fe(II)(2,2'-bipyridine)(mes)<sub>2</sub> and Fe(II)-(2,2'-bipyridine)(mes)<sub>2</sub>, a complex containing a 2,2'-bipyridyl radical anion. *Inorg. Chem.* **2010**, *49*, 6160–6171.
- (57) Scarborough, C. C.; Wiegardt, K. Electronic structure of 2,2'-bipyridine organotransition-metal complexes. Establishing the ligand oxidation level by density functional theoretical calculations. *Inorg. Chem.* **2011**, *50*, 9773–9793.
- (58) Müller, I.; Schneider, C.; Pietzonka, C.; Kraus, F.; Werncke, C. G. Reduction of 2,2'-Bipyridine by Quasi-Linear 3d-Metal(I) Silylamides—A Structural and Spectroscopic Study. *Inorganics* **2019**, *7*, 117.
- (59) Weix, D. J. Methods and Mechanisms for Cross-Electrophile Coupling of Csp(2) Halides with Alkyl Electrophiles. *Acc. Chem. Res.* **2015**, *48*, 1767–1775.
- (60) Cornella, J.; Edwards, J. T.; Qin, T.; Kawamura, S.; Wang, J.; Pan, C.-M.; Gianatassio, R.; Schmidt, M.; Eastgate, M. D.; Baran, P. S.

Practical Ni-Catalyzed Aryl-Alkyl Cross-Coupling of Secondary Redox-Active Esters. *J. Am. Chem. Soc.* **2016**, *138*, 2174–2177.

(61) Tellis, J. C.; Kelly, C. B.; Primer, D. N.; Jouffroy, M.; Patel, N. R.; Molander, G. A. Single-Electron Transmetalation via Photoredox/Nickel Dual Catalysis: Unlocking a New Paradigm for sp(3)-sp(2) Cross-Coupling. *Acc. Chem. Res.* **2016**, *49*, 1429–1439.

(62) Shen, Y.; Gu, Y.; Martin, R. sp<sup>3</sup> C-H Arylation and Alkylation Enabled by the Synergy of Triplet Excited Ketones and Nickel Catalysts. *J. Am. Chem. Soc.* **2018**, *140*, 12200–12209.

(63) Mohadjer Beromi, M.; Brudvig, G. W.; Hazari, N.; Lant, H. M. C.; Mercado, B. Q. Synthesis and Reactivity of Paramagnetic Nickel Polypyridyl Complexes Relevant to C(sp<sup>2</sup>)-C(sp<sup>3</sup>) Coupling Reactions. *Angew. Chem., Int. Ed.* **2019**, *58*, 6094–6098.

(64) Reckziegel, A.; Battistella, B.; Werncke, C. G. On the Synthesis of a T-Shaped Imido Nickel Complex and Trigonal Amido Nickel Complexes. *Eur. J. Inorg. Chem.* **2022**, No. e202101102.

(65) Biswas, S.; Weix, D. J. Mechanism and selectivity in nickel-catalyzed cross-electrophile coupling of aryl halides with alkyl halides. *J. Am. Chem. Soc.* **2013**, *135*, 16192–16197.

(66) Benson, E. E.; Rheingold, A. L.; Kubiak, C. P. Synthesis and characterization of 6,6'-(2,4,6-triisopropylphenyl)-2,2'-bipyridine (tripbipy) and its complexes of the late first row transition metals. *Inorg. Chem.* **2010**, *49*, 1458–1464.

(67) Serrano, E.; Martin, R. Nickel-Catalyzed Reductive Amidation of Unactivated Alkyl Bromides. *Angew. Chem., Int. Ed.* **2016**, *55*, 11207–11211.

(68) Marshall, W. J.; Grushin, V. V. Activation of chlorobenzene with Ni(0) N,N-chelates — A remarkably profound effect of a minuscule change in ligand structure. *Can. J. Chem.* **2005**, *83*, 640–645.

(69) Margraf, G.; Schödel, F.; Sängler, I.; Bolte, M.; Wagner, M.; Lerner, H.-W. Eine elektrochemische und strukturelle Studie an den Eisensilylamiden Fe[N(SiMe<sub>3</sub>)<sub>2</sub>]<sub>2</sub> und Fe[N(SiMe<sub>3</sub>)<sub>2</sub>]<sub>3</sub> / An Electrochemical and Structural Study of the Iron Silylamides Fe[N(SiMe<sub>3</sub>-2)]<sub>2</sub> and Fe[N(SiMe<sub>3</sub>)<sub>2</sub>]<sub>3</sub>. *Z. Naturforsch.* **2012**, *67*, 549.

(70) Bradley, D. C.; Hursthouse, M. B.; Smallwood, R. J.; Welch, A. J. Three-co-ordinated complexes of cobalt(II) and nickel(I) containing bis-trimethylsilylamino- and triphenylphosphine-ligands. *Chem. Commun.* **1972**, 872.

(71) Lin, W.; Bodenstern, T.; Mereacre, V.; Fink, K.; Eichhöfer, A. Field-Induced Slow Magnetic Relaxation in the Ni(I) Complexes NiCl(PPh<sub>3</sub>)<sub>2</sub>·C<sub>4</sub>H<sub>8</sub>O and Ni(N(SiMe<sub>3</sub>)<sub>2</sub>)(PPh<sub>3</sub>)<sub>2</sub>. *Inorg. Chem.* **2016**, *55*, 2091–2100.

(72) Evans, D. F. 400. The determination of the paramagnetic susceptibility of substances in solution by nuclear magnetic resonance. *J. Chem. Soc.* **1959**, 2003.

(73) Lin, C.-Y.; Fettinger, J. C.; Grandjean, F.; Long, G. J.; Power, P. P. Synthesis, structure, and magnetic and electrochemical properties of quasi-linear and linear iron(I), cobalt(I), and nickel(I) amido complexes. *Inorg. Chem.* **2014**, *53*, 9400–9406.

(74) Kuntze-Fechner, M. W.; Verplancke, H.; Tendra, L.; Diefenbach, M.; Kruppenacher, I.; Braunschweig, H.; Marder, T. B.; Holthausen, M. C.; Radius, U. Coligand role in the NHC nickel catalyzed C-F bond activation: investigations on the insertion of bis(NHC) nickel into the C-F bond of hexafluorobenzene. *Chem. Sci.* **2020**, *11*, 11009–11023.

(75) Kermagoret, A.; Braunstein, P. Mono- and Dinuclear Nickel Complexes with Phosphino-, Phosphinito-, and Phosphonitopyridine Ligands: Synthesis, Structures, and Catalytic Oligomerization of Ethylene. *Organometallics* **2008**, *27*, 88–99.

(76) Sheldrick, G. M. SHELXT - integrated space-group and crystal-structure determination. *Acta Crystallogr., Sect. A: Found. Adv.* **2015**, *71*, 3–8.

(77) Sheldrick, G. M. Crystal structure refinement with SHELXL. *Acta Crystallogr., Sect. C: Struct. Chem.* **2015**, *71*, 3–8.

(78) Farrugia, L. J. WinGX suite for small-molecule single-crystal crystallography. *J. Appl. Crystallogr.* **1999**, *32*, 837–838.

(79) Betteridge, P. W.; Carruthers, J. R.; Cooper, R. I.; Prout, K.; Watkin, D. J. CRYSTALS version 12: software for guided crystal structure analysis. *J. Appl. Crystallogr.* **2003**, *36*, 1487.

(80) Schmitz, W. International Tables for X-ray Crystallography, vol. IV (Ergänzungsband). Herausgegeben von der International Union of Crystallography. The Kynoch Press, Birmingham, England, 1974, 366 Seiten einschließlich Tabellen und Sachwortverzeichnis. *Krist. Tech.* **1975**, *10*, K120.

(81) Bruker SADABS-2016/2; Bruker, 2016.

## Recommended by ACS

### 16-Electron Nickel(0)-Olefin Complexes in Low-Temperature C(sp<sup>2</sup>)-C(sp<sup>3</sup>) Kumada Cross-Couplings

Sigrid Lutz, Josep Cornella, *et al.*

MARCH 26, 2021  
ORGANOMETALLICS

READ 

### Extreme g-Tensor Anisotropy and Its Insensitivity to Structural Distortions in a Family of Linear Two-Coordinate Ni(I) Bis-N-heterocyclic Carbene Complexes

William J. M. Blackaby, Michael K. Whittlesey, *et al.*

JANUARY 10, 2022  
INORGANIC CHEMISTRY

READ 

### Nickel(I) Aryl Species: Synthesis, Properties, and Catalytic Activity

Megan Mohadjer Beromi, Brandon Q. Mercado, *et al.*

FEBRUARY 13, 2018  
ACS CATALYSIS

READ 

### Ni(NIXANTPHOS)-Catalyzed Mono-Arylation of Toluenes with Aryl Chlorides and Bromides

Hui Jiang, Patrick J. Walsh, *et al.*

MARCH 06, 2019  
ORGANIC LETTERS

READ 

Get More Suggestions >

### 3.5 Hydrogen Atom Abstraction by Trigonal Imido Cobalt Complexes – Impact of structure onto reactivity

A. Reckziegel, B. Battistella, C. Millidoni, K. Ray, C.G. Wernecke

*manuscript in preparation*

#### Abstract

The first series of isolable, reactive imido cobalt complexes, bearing alkyl and aryl imido substituents, and their behaviour in H atom abstraction is reported. The HAT reactivity is connected to changes of the Co–N–R bond angle, and to a lesser extent to the Co–N bond lengths, when transitionening to the corresponding amido complexes.

#### Zusammenfassung

Um die H-Atom-Transfer-Reaktivität von trigonalen Imido-Cobalt-Komplexe weiter zu untersuchen, wurde eine Reihe von Alkyl- und Arylaziden mit dem linear koordinierten Cobalt(I)-Komplex **101** umgesetzt.

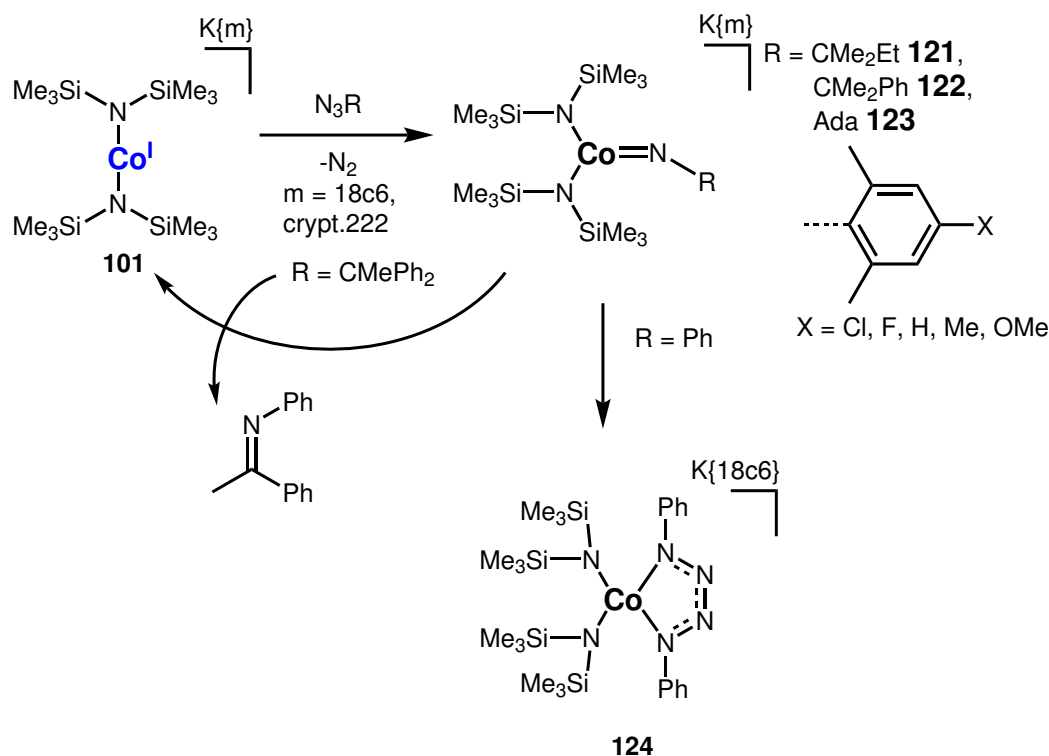


Abb. 51: Umsetzung des linear koordinierten Cobalt(I)-Komplexes **101** mit organischen Aziden.

Die erhaltenen Alkyl-Imido-Komplexe mit CMe<sub>2</sub>Et (**121**), CMe<sub>2</sub>Ph (**122**) und Adamantyl-Substituent (**123**), zeigten eine große Varianz in ihrer Imido-Cobalt-Bindungslänge (1,673(2) – 1,758(8) Å), sowie dem Bindungswinkel des Liganden (145,5(8) – 167,6(1)°) auf. Die spektroskopischen Daten und bestimmten magnetischen Momente (3,22 – 3,85 μ<sub>B</sub>) deuten auf eine *intermediate-spin* Konfiguration, vergleichbar

zu dem beschriebene *tert*-Butyl-Imido-Komplex **102**, hin. Für  $\text{N}_3\text{CMePh}_2$  konnte die katalytische Bildung des Ketimines  $(\text{Ph})\text{NC}(\text{Me})\text{Ph}$  beobachtet werden. Dies geschieht vermutlich über die Verschiebung einer Phenylgruppe innerhalb eines Imido-Komplexes, und ist ein für freie Nitrene unter erhöhten Temperaturen bekanntes Phänomen.

Die Umsetzung des Cobalt(I)-Komplexes mit Phenylazid hatte die Bildung eines Tetrazen-Komplexes (**124**) zur Folge, welcher aus einer Reaktion von  $\text{Ph}_3\text{N}$  mit einem transienten Phenyl-Imido-Komplexes herrührt. Der auf gleiche Weise erhaltene Mesityl-Imido-Komplex (**125**) zeigte eine zu dem zuvor beschriebenen Imidyl-Komplex (**100**) ähnliche Bindungssituation ( $\text{Co}-\text{N}_{\text{Imido}}$ : 1,751(2) Å). Um den elektronischen Einfluss des Substituenten zu untersuchen, wurden anschließend die *para*-Position des Arylsubstituenten, unter Verwendung der entsprechenden Organoazide, variiert. Die Bindungssituation der erhaltene Imido-Cobalt-Komplexe ( $\text{Co}-\text{N}_{\text{Imido}}$ : 1,710(3) – 1,776(2) Å), sowie die experimentell bestimmten magnetischen Momente (4,46 – 4,94  $\mu_B$ ), deuten auf eine *high-spin* Konfiguration hin.

Alle beschriebenen Imido-Komplexes zeigen einen H-Atom-Transfer gegenüber C–H-Bindungen, wobei hier bereits eine generell geringere Reaktivität der Aryl-Komplexe zum Vorschein kommt. Die aus dieser Reaktion erhaltenen trigonalen Amido-Komplexe mit Alkyl-Substituenten zeigen in ihren strukturellen und spektroskopischen Eigenschaften gute Übereinstimmung mit dem *tert*-Butyl-Amido-Komplex **103**. Im Fall der Aryl-Komplexe ist, wie zu erwarten, eine leichte Aufweitung der Amido-Cobalt-Bindung zu beobachten. Weiterhin konnte hier die Bildung des Tris-amido-Komplexes  $\text{K}\{\text{crypt.222}\}[\text{Co}(\text{N}(\text{SiMe}_3)_2)_3]$  (**93**) beobachtet werden, was auf eine Ligandenaustausch-Reaktion für diese Komplexe hindeutet.

Versuche, die Stärke der gebildeten N–H-Bindungen in den Amido-Komplexen experimentell zu bestimmen, erwiesen sich als uneindeutig. Die elektrochemische Untersuchung zeigte eine irreversible Oxidation der Alkyl-Amido-Komplexe (-0,7 – -1,2 V vs.  $\text{Fc}/\text{Fc}^+$ ). Ein vermuteter Zersetzungsmechanismus ist die intramolekulare Deprotonierung des gebildeten, neutralen Amido-Cobalt(III)-Komplexes. Für die Alkyl-Imido-Komplexe konnte keine Reduktion, stattdessen eine reversible Oxidation (-1,2 – -1,4 V vs  $\text{Fc}/\text{Fc}^+$ ) beobachtet werden. Die gezielte Protonierung der Imido-Komplexe oder Deprotonierung der Amido-Komplexe hatte unselektive Reaktionsverläufe zu Folge.

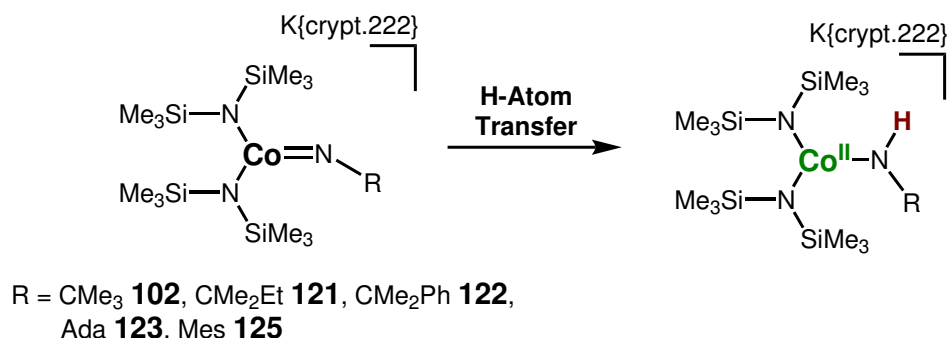


Abb. 52: H-Atom-Transfer Reaktivität der dargestellten trigonalen Imido-Cobalt-Komplexe unter Bildung der trigonalen Amido-Cobalt-Komplexe.

Um die H-Atom-Transfer-Reaktion besser zu verstehen wurden umfangreiche kinetische Untersuchungen durchgeführt. Da die  $^1\text{H}$ -NMR-Reaktionskontrolle bereits

Nebenreaktionen für die Aryl-Imido-Komplexe mit elektronenziehenden Substituenten ( $X = \text{H}, \text{F}, \text{Cl}$ ) zeigt, wurden diese nicht weiter untersucht. Durch zeitaufgelöste UV-VIS-Spektroskopie wurde die Reaktionskonstanten für die Umsetzung mit verschiedenen organischen Substraten (XAN, CHD, DHA) in einer Reaktion *pseudo*-erster Ordnung bestimmt. Dies zeigte eine deutlich höhere Reaktivität für den Adamantyl-Imido-Cobalt-Komplex **123**, selbst im Vergleich zu dem reaktiven *tert*-Butyl-Komplex **102**. Die dargestellte Reihe von Imido-Komplexen erlaubt erstmal einen Zusammenhang zwischen dem Reaktionsverhalten und der Struktur des Komplexes zu untersuchen. Dieser konnte bei Betrachtung der Änderung des Imido-Amido-Cobalt-Bindungswinkels gefunden werden. Eine geringe Änderung ist hier mit einer höheren Reaktivität verknüpft, was auf einen geringeren Energieaufwand zur Reorganisation des Systems zurückzuführen ist.

Zusammenfassend konnte eine Reihe von reaktiven Imido-Cobalt-Komplexen dargestellt werden, die erstmalig einen Struktur/Reaktivität-Zusammenhang für Imido-Metall-Komplexe der späten 3d-Metalle erlaubt.

### Beiträge der Autoren

Die gezeigten Verbindungen wurden von *Christina Millidoni* im Zuge eines von mir betreuten Vertiefungspraktikums und weiterführend von mir dargestellt und mittels  $^1\text{H-NMR}$ -, UV-Vis- und IR-Spektroskopie charakterisiert. Die Messung des magnetischen Momentes nach der EVANS-Methode wurde durch die Serviceabteilung NMR-Spektroskopie der Philipps-Universität Marburg an einem Bruker AV III 500 durchgeführt und von mir ausgewertet.

Zur Bestimmung der Struktur im Festkörper wurden Röntgenbeugungsexperimente am Einkristall durch die Serviceabteilung Kristallstrukturanalyse der Philipps Universität Marburg oder von *Dr. Gunnar Werncke* an einem Bruker D8 Quest durchgeführt. Ich habe die Strukturen aus den erhaltenen Daten gelöst und verfeinert.

Die Bestimmung der Reinheit erfolgte mittels CHN-Elementaranalytik durch die Serviceabteilung Elementaranalytik der Philipps-Universität Marburg.

Für die kinetischen Untersuchungen wurden zeitabhängige UV-Vis Messungen an einem Specord S600 der Firma Jena von mir durchgeführt und ausgewertet.

Die Elektronenspinresonanz-Experimente wurden von *Beatrice Battistella* aus der Arbeitsgruppe von *K. Ray* an der Humboldt-Universität zu Berlin durchgeführt und von mir ausgewertet.

Das Manuskript habe ich in Zusammenarbeit mit *Dr. Gunnar Werncke* und in Absprache mit allen Co-Autoren verfasst.

# Hydrogen Atom Abstraction by Trigonal Imido Cobalt Complexes – Impact of structure onto reactivity

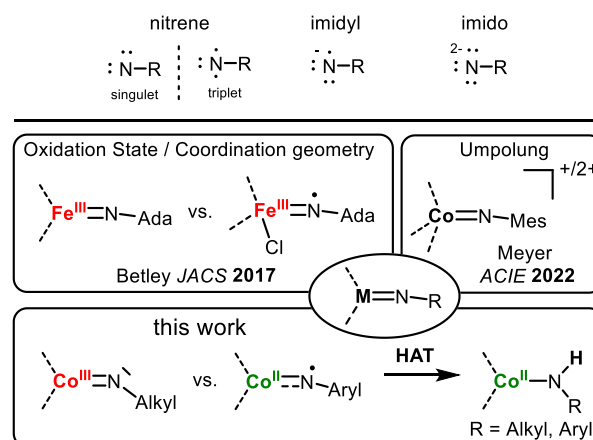
A. Reckziegel,<sup>[a]</sup> B. Battistella,<sup>[b]</sup> C. Millidoni,<sup>[a]</sup> K. Ray,<sup>[b]</sup> C. G. Werncke\*<sup>[a]</sup>

**Abstract:** A series of trigonal imido cobalt complexes based on  $[\text{Co}(\text{NCMe}_3)(\text{hmds})_2]^-$  and capable of hydrogen atom transfer reactions were synthesized. Spectroscopic examination revealed an intermediate spin configuration for alkyl complexes, while aryl complexes inherent a high spin state. Kinetic studies towards hydrogen atom abstraction revealed a correlation of the reactivity with the change of the bond angle.

## Introduction

The 3d-metal catalyzed amination of (un)-functionalized C–H bonds yields potential as an atom economic and environmentally benign approach entry to secondary amines.<sup>[1–4]</sup> Despite its increasing application in organic synthesis<sup>[5–8]</sup> the nature of the nitrene transferring  $[\text{MNR}]$  intermediate, as well as the factors that drive its reactivity, are only partially understood. Most isolable imido chemistry are found in a low-spin state, yet show marginal C–H bond activation reactivity.<sup>[9–12]</sup> In recent years an increasing number of more reactive complexes were isolated in which more unusual bond situations of the  $[\text{MNR}]$  unit are present. Here the imido ligand deviates from the classic formation of an anionic imide ligand  $\text{NR}^{2-}$  and is better described as either an imidyl ( $\text{NR}^-$ ) or a nitrene  $[\text{NR}^0]$ . Few imidyl type complexes could be authenticated for iron, cobalt and nickel, with the even rarer metal bound nitrene were substantiated for copper. This allows for first indications of the benefit of higher-spin states and increased imidyl/nitrene character of the imido unit. Betley could show that oxidation of an iron(III) imide to an iron(III) imidyl results in a substantial increase in intermolecule HAT reactivity. It was attributed to the increase in spin density on and electron deficiency of the abstracting nitrogen atom. Similarly,  $1e^-$  oxidation of a low-spin cobalt(III) imide was also N-centered, resulting in an increase of an intramolecular reactivity. Besides oxidation induced changes in the electronic structure, first insights of the impact of the N-substituent could also be gained. Here it showed that aromatic ligands effectuate a decrease in reactivity due to a delocalisation of unpaired spin density onto the aromatic ring.<sup>[13,14]</sup>

Despite these advances a nuanced picture of the different influences onto the HAT and amination reactivity of imido metal complexes is still lacking. This can be mainly attributed to the ongoing difficulties in isolation of reactive yet stable imido metal complexes.



**Scheme 1.** Bonding situation in imido complexes and studies towards the influence of the oxidation state onto the bonding situation as well as the reactivity.

Recently we reported on the intermediate-spin cobalt(III) complex  $[\text{Co}(\text{NCMe}_3)(\text{hmds})_2]$  ( $\text{hmds} = \text{N}(\text{SiMe}_3)_2$ ) (**1**) which is highly proficient in H atom abstraction reactivity.<sup>[15]</sup> A related arylimido cobalt complex ( $[\text{Co}(\text{NDipp})(\text{N}(\text{Dipp})\text{SiMe}_3)_2]$ ; Dipp = 2,6-diisopropylphenyl) was identified as a high-spin cobalt(II) imidyl complex with partial spin delocalization onto the aromatic unit.<sup>[16]</sup> It was however unreactive due to the steric encumbrance imposed by the silylamide ligand set as well as the imido substituent.

Herein we now report on a family of isostructural imido cobalt complexes of the type  $[\text{Co}(\text{NR})(\text{hmds})_2]^-$ , bearing different alkyl and aryl imido substituents. All *alkyl* imidos display a large variety of Co–N bond lengths and Co–N–R angles, which are interconnected, and are found in an *intermediate-spin* state. In contrast, *high-spin aryl* imidos exhibit a more uniform, comparably long Co–N bond and a near-linear Co–N–R unit. Subsequent screening towards H atom abstraction from C–H bonds, together with the isolation of resulting cobalt(II) amides  $[\text{Co}(\text{N}(\text{H})\text{R})(\text{hmds})_2]^-$ , ultimately allowed for the first time for a comprehensive structure-reactivity relationship a given reactive imido metal system. Hereby the reactivity correlates best with lesser structural changes of the Co–N–R unit when transitioning from the imide to the corresponding imide.

## Results:

### Synthesis and solid state structures of imido metal complexes

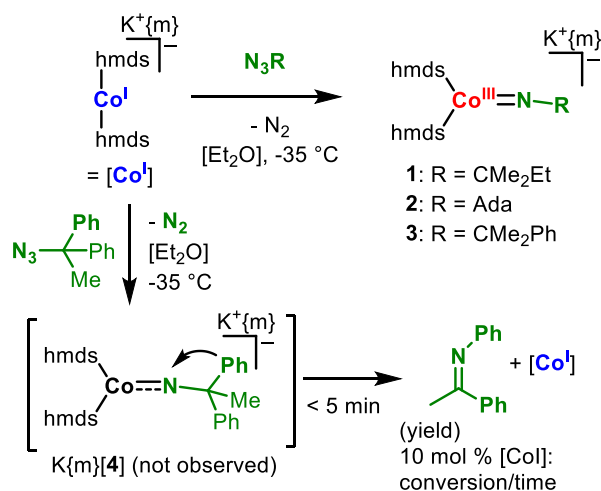
Following the synthesis of the known tert-butyl derivative  $[\text{Co}(\text{N}(\text{CMe}_3)(\text{hmds})_2)]^{15}$  the linear cobalt(I) complex ( $\text{K}\{\text{cypt.222}\}[\text{Co}(\text{hmds})_2]$ ) was reacted with different organic azides  $\text{N}_3\text{R}$  with varying alkyl ( $\text{R} = \text{CMe}_2\text{Et}$  (Amyl), adamantyl (Ada),  $\text{CMe}_2\text{Ph}$ ,  $\text{CMePh}_2$ ) as well as aryl substituents ( $\text{R} = \text{Dipp}$ , Ph, 2,4-dimethylphenyl groups with varying para substituents  $\text{X} = \text{H}$ , Me, OMe, Cl, F) in  $\text{Et}_2\text{O}$  at  $-30^\circ\text{C}$ . This generally resulted in gas evolution ( $\text{N}_2$ ) and color change from pale green to dark red for alkyl imides and dark green for the aryl derivatives. Upon rapid

[a] A. Reckziegel, C. Millidoni, Dr. C. G. Werncke  
Fachbereich 15/Chemie  
Philipps-Universität Marburg  
Hans-Meerwein-Straße 4, D-35043, Marburg, Germany  
E-mail: [gunnar.werncke@chemie.uni-marburg.de](mailto:gunnar.werncke@chemie.uni-marburg.de)

[b] B. Battistella, K. Ray  
Institute für Chemie  
Humboldt-Universität zu Berlin  
Brook-Taylor-Strasse 2, D-12489 Berlin, Germany



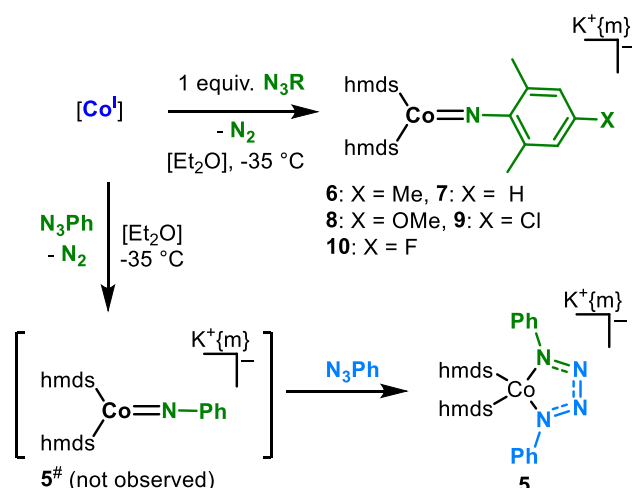
layering of the filtrated reaction solution with pentane and storage at  $-35^{\circ}\text{C}$  allowed for product isolation.



**Scheme 2.** Formation of trigonal alkyl imido cobalt complexes  $[\text{K}\{\text{L}\}[\text{Co}(\text{NR})(\text{hmds})_2]$  ( $\text{L} = \text{crypt.222}$ ;  $\text{hmds} = -\text{N}(\text{SiMe}_3)_2$ ) and the ketimine  $\text{PhN}=\text{C}(\text{Me})\text{Ph}$ .

For the alkyl imidos this yielded the terminal imido complexes  $\text{K}\{\text{crypt}\}[\text{Co}(\text{NR})(\text{hmds})_2]$  with  $\text{R} = \text{CMe}_2\text{Et}$  (**1**),  $\text{Ada}$  (**2**) and  $\text{CMe}_2\text{Ph}$  (**3**) (**Scheme 2**). For  $\text{R} = \text{CMePh}_2$  the  $^1\text{H-NMR}$  reaction control revealed the formation of *N*-phenylacetophenone ketimine ( $\text{PhN}=\text{C}(\text{Me})\text{Ph}$ ) as well as the starting cobalt(I) complex  $[\text{Co}^I]$ . 1,2-aryl migration is known for aryl substituted tertiary alkyl azides under thermolysis as well as UV light irradiation amongst other via a discrete nitrene intermediate.<sup>[17,18]</sup> As such we postulate on the initial formation of the imido complex  $[\text{K}\{\text{crypt}\}[\text{Co}(\text{N}(\text{CMePh}_2)(\text{hmds})_2)]^-$  (**[4]**), 1,2-aryl migration and decoordination of the imine. The 1,2 aryl migration could also be performed catalytically under ambient conditions using 10 mol%  $[\text{Co}^I]$  (ambient temperature, 4h). Metal catalysed 1,2-aryl migration was reported only recently yet needed more forcing conditions (10 mol% iron precatalyst,  $80^{\circ}\text{C}$ , 8 h).<sup>[19]</sup> Lowering the catalyst loading led to reduced conversion, likely due to blocking of  $[\text{Co}^I]$  by the increasing excess of imine, as shown for reaction of *N*-methylidiphenylketimine ( $\text{Ph}_2\text{C}=\text{NMe}$ ) with  $[\text{Co}^I]$ .<sup>[20]</sup>

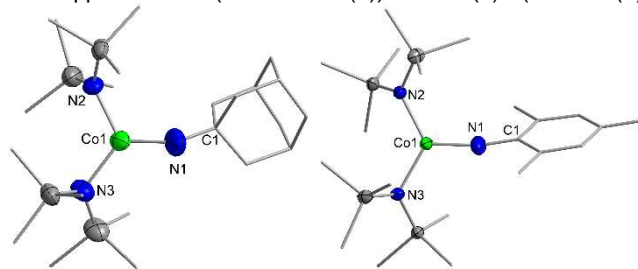
In case of aryl azides, we initially employed  $\text{Dipp-N}_3$ ,  $\text{Mes-N}_3$  as well as  $\text{Ph-N}_3$  (**Scheme 3**). For the smallest azide  $\text{PhN}_3$  the formation of the cobalt tetrazene (**5**), presumably via a [3+2] dipolar addition of a second  $\text{PhN}_3$  to the putative phenylimido complex  $[\text{Co}(\text{NPh})(\text{hmds})_2]^-$ , is observed. For the bulkier substituents only for  $\text{R} = \text{Mes}$  the respective imido complex could be isolated (**6**), whereas for the more encumbered  $\text{DippN}_3$  the partial and slow formation of an imido complex could only be assumed from *in-situ*  $^1\text{H-NMR}$  spectroscopy. The isolation of the mesityl derivative **6** prompted us to elaborate on electronic effects via variation of the para substituent. Indeed, respective compounds were obtained for  $\text{R} = \text{H}$  (**7**),  $\text{OMe}$  (**8**),  $\text{Cl}$  (**9**),  $\text{F}$  (**10**).



**Scheme 3.** Formation of trigonal aryl imido cobalt complexes  $[\text{K}\{\text{m}\}[\text{Co}(\text{NR})(\text{hmds})_2]$  ( $\text{m} = \text{crypt.222}$ ;  $\text{hmds} = -\text{N}(\text{SiMe}_3)_2$ ) as well as the tetrazene cobalt complex (**5**;  $\text{m} = 18\text{c6}$ ).

All aryl and alkyl complexes were obtained in moderate to excellent yields (34 – 92%), and exhibit a trigonal planar geometry around the cobalt atom with similar  $\text{Co}-\text{N}_{\text{SiMe}_3}$  (1.91–1.94 Å),  $\text{N}_{\text{SiMe}_3}-\text{Co}-\text{N}_{\text{SiMe}_3}$  ( $112-123^{\circ}$ ),  $\text{N}_{\text{imido}}-\text{Co}-\text{N}_{\text{SiMe}_3}$  ( $115-125^{\circ}$ ) bond lengths and angles. The most prominent differences arise from the  $\text{Co}-\text{N}_{\text{imido}}$  bond lengths and  $\text{Co}-\text{N}_{\text{imido}}-\text{R}$  bond angles of all imido compounds, which are given in in **Table 1**.

The alkyl imido complexes exhibit a large variation of the cobalt imido bond length  $\text{Co}-\text{N}_{\text{imido}}$  ranging from 1.673(2) Å ( $\text{R} = \text{CMe}_2\text{Et}$ ) to 1.758(8) Å ( $\text{R} = \text{Ada}$ ). The latter are rather long and comparable to that of previously<sup>[16,21]</sup> or herein reported aromatic imido cobalt complexes (vide infra), that all bear a silylamide ligand set. Interestingly the increase in  $\text{Co}-\text{N}_{\text{imido}}$  bond length correlates with a pronounced bending of the  $\text{C}-\text{N}_{\text{imido}}-\text{R}$  angle from approx.  $166.3^{\circ}$  ( $\text{R} = \text{CMe}_2\text{Et}$  (**1**)) to  $145.5(8)^{\circ}$  ( $\text{R} = \text{ada}$  (**2**)).



**Scheme 4.** Molecular structure of **2** (left) and **6** (right) in the solid state. The  $\text{K}\{\text{crypt.222}\}$  cation, solvent molecules as well as H atoms are omitted for clarity. Selected bond lengths (Å) and angles ( $^{\circ}$ ):

In solution all imido complexes show only a limited stability in ( $\text{THF-d}_8$ ), and decompose within minutes ( $\text{R} = \text{Ada}$  (**2**)) to several hours to the respective cobalt(II) amides stemming from HAA from the used solvent. Using the inert 1,2-difluorobenzene (DFB) allowed for the identification of decomposition products via single crystal diffraction analysis in case of (**2**) and the original complex **1**.

**Table 1.** Important structural and electronic parameters of mentioned cobalt imido and amido complexes. The cation is  $\text{K}\{\text{crypt.222}\}$ .

R	Imide [Co(hmnds) <sub>2</sub> NR] <sup>-</sup>				Amide [Co(hmnds) <sub>2</sub> NHR] <sup>-</sup>		
	Co1-N1 (Å)	Co1-N1-C1 (°)	μ <sub>eff</sub> (μ <sub>B</sub> )	δ <sub>SiMe<sub>3</sub></sub> (ppm)	Co1-N1 (Å)	Co1-N1-C1 (°)	δ <sub>SiMe<sub>3</sub></sub> (ppm)
CMe <sub>2</sub> Et ( <b>1</b> )	1.673(2)	166.3(3)	3.22	-2.68	1.880(3)	136.3(3)	-15.5
Ada ( <b>2</b> )	1.758(8)	145.5(8)	3.85	-2.78	1.899(2)	131.9(2)	-15.2
CMe <sub>2</sub> Ph ( <b>3</b> )	1.691(1)	167.6(1)	3.66	-2.68	1.898(2)	135.1(2)	-17.7
CMe <sub>3</sub> <sup>[15]</sup> ( <b>1</b> )	1.706(1)	160.8(1)	3.75	-2.68	1.883(1)	134.8(1)	-15.5
Mes ( <b>6</b> )	1.751(2)	169.1(2)	4.51	-9.05	1.935(2)	139.3(2)	-12.8
2,6-dimethyl ( <b>7</b> )	1.776(2)	163.2(2)	4.72	-10.2	1.920(2)	139.7(2)	-13.0
4-OMe ( <b>8</b> )	1.724(3) 1.710(3)	176.3(2) 167.2(3)	4.46	-6.83	1.921(1)	139.7(1)	-12.9
4-Cl ( <b>9</b> )	1.753(4)	164.2(3)	4.61	-10.2	1.944(3)	142.0(3)	-13.2
4-F ( <b>10</b> )	1.751(8)	172.6(9)	4.94	-9.09	1.940(2)	139.9(2)	-13.1

In case of the former, HAA from the crypt counter ion by **2** and subsequent scavenging of the organic cation radical by a second molecule of **2** yields in a cobalt(II) complex in which the crypt cation is connected to the imide N-nitrogen at the  $\alpha$ -position of the cations amine position (see figures S19). In case of [Co(NCMe<sub>3</sub>)(hmnds)<sub>2</sub>]<sup>-</sup> the connection occurs via the  $\beta$ -position, but is also followed by C–O cleavage of one arm of the cryptand by deprotonation of the parallelly formed cobalt(II) amide [Co(N(H)CMe<sub>3</sub>)(hmnds)<sup>-</sup> (**IH**). The internal C–H bond activation emphasizes the pronounced reactivity of the herein presented alkyl imido cobalt complexes, reveals the intrinsic limitations of this system, yet also points to the possibility of steering the C–N bond formation via cation stabilisation of the organic radical.

#### Solution state spectroscopic and magnetic features:

To gain insights into the electronic situation of the isolable imido complexes, magnetic measurements in solution (EVANS method) were performed. It gave for alkyl imidos values of (μ<sub>eff</sub> (**1**) = 3.22 μ<sub>B</sub>, μ<sub>eff</sub> (**3**) = 3.66), which are similar to that of **I** (μ<sub>eff</sub> = 3.75 μ<sub>B</sub>) for which an intermediate spin configuration (S = 1) was determined.<sup>[15,16]</sup> For **2** the value could only be approximated by *in situ* synthesis using a concentration of 50 mM to mitigate effects of its rapid decomposition (μ<sub>eff</sub> (**2**) = 3.85 μ<sub>B</sub>). The magnetic moment of the aryl imido complexes (μ<sub>eff</sub>: (**6**): 4.51 μ<sub>B</sub>, (**7**) 4.72 μ<sub>B</sub>, (**8**): 4.46 μ<sub>B</sub>, (**9**): 4.61 μ<sub>B</sub>, (**10**): 4.94 μ<sub>B</sub>), as determined by the EVANS method, are close to the value observed for the cobalt(II) imidyl complex (Co(L<sub>2</sub>)NDipp: μ<sub>eff</sub>: 4.90 μ<sub>B</sub>)<sup>[16]</sup>, and indicate a *high spin* configuration. No signals could be observed in the X-band EPR spectra for the alkyl imido complexes even at 10 K, which is expected for a S = 1 system. Measurements of the aromatic imide **6** gave unresolved absorption between g = 7 and g = 1.5. These could not be satisfactorily modelled, yet indicate a partial cobalt(II) character. No unequivocal signal belonging to the supposed imidyl radical ligand was detected, as observed for the cobalt(II) imidyl complex [Co(NDipp)(L<sub>2</sub>)]<sup>-</sup>.<sup>[16]</sup> This speaks to a stronger, unresolvable radical-cobalt interaction for the presented aryl imido complexes than in the related seminal imidyl cobalt(II) complex [Co(NDipp)(L<sub>2</sub>)]<sup>-</sup>.<sup>[22]</sup>

The <sup>1</sup>H-NMR spectra of the alkyl imido complexes show signals belonging to the SiMe<sub>3</sub> groups at around -3 ppm (CMe<sub>2</sub>Et **1**: -2.68 ppm, Ada **2**: -2.80 ppm, NCMe<sub>2</sub>Ph **3**: -2.68 ppm), in line with (**1**: -2.68 ppm)<sup>[15]</sup>. Further paramagnetically shifted signals are found for the protons belonging to the imide substituent. The <sup>1</sup>H-NMR signal of the hmnds ligands of the aryl complexes are found between 6.83 (**8**) and 10.2 ppm (**7/9**). It is high-field shifted in comparison to the alkyl derivatives and closer to the signal of the corresponding cobalt(II) amide complexes (13–18 ppm, *vide infra*). Together with substantially shifted signals for the aryl substituents (200–500 ppm), it implicates a partial cobalt(II) character as well as additional spin density on the aromatic ring. The UV-Vis spectra of the alkyl imido complexes show two absorption bands at around 540 and 850 cm<sup>-1</sup>, which is in good resemblance to **I**.<sup>[15]</sup> The aromatic imido complexes exhibit a distinctly different signature at around 680 cm<sup>-1</sup>, whose position resembles that of the respective cobalt(II) amido complexes (*vide infra*) and is attributed to d–d transitions. Taken these observations together, these results show that the herein presented aryl imido complexes, as described best as *high-spin* cobalt(II) imidyl complexes, as found for the seminal [Co(NDipp)(N{Dipp})SiMe<sub>3</sub>]<sup>-</sup><sup>[16]</sup>, with however comparably stronger interaction of the divalent cobalt ion with organic radical. The alkyl imidos are *intermediate-spin* cobalt(III) imides.

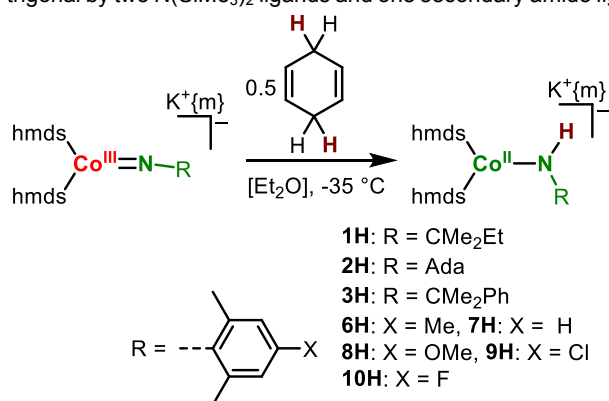
#### Amide formation by HAA

To substantiate the hydrogen atom abstraction (HAT) reactivity of the imido complexes from external substrates, initial reactions with 1,4-cyclohexadiene were carried out (**Scheme 5**). A colour change of the reaction solution to green was observed within minutes (R = alkyl) or several hours (R = aryl), which pointed to a general HAT reactivity of the imidos complexes. Following the reactions by <sup>1</sup>H NMR spectroscopy revealed a clean transformation for the alkyl imido complexes. In case of the aryl imido complexes only for electron donating substituents (Me, OMe) the reaction is well behaved. In the other cases further, mostly unidentified species were observed. In some instances [Co(hmnds)<sub>3</sub>]<sup>-</sup> is detected, which we attribute amide ligand



scrambling of the primary amides with the silylamides as observed for the bulkier  $[\text{CoL}_2(\text{NHAr})]^-$ .<sup>[16]</sup> Attempts to obtain the respective aromatic amides via independent synthesis from KNHMe with  $\text{Co}(\text{hmds})_2$  in the presence of crypt.222 led also to similar observations.

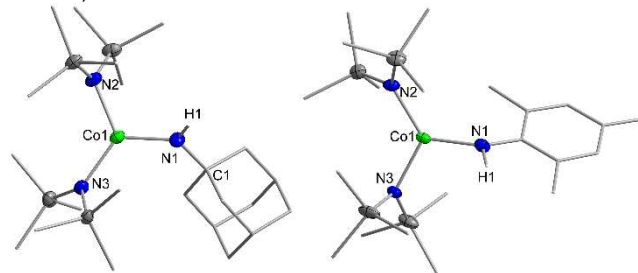
Nonetheless, for all mentioned imido metal complexes the corresponding amido complexes  $\text{K}\{\text{crypt}\}[\text{Co}(\text{NHR})(\text{hmds})_2]$  could be eventually obtained in moderate to good yields (51 – 87%) with varying amount of  $[\text{Co}(\text{hmds})_3]^-$  for the aryl complexes. All compounds presented as green crystals suitable for X-ray diffraction analysis that showed the expected trigonal arrangement. In solid state the cobalt ion is coordinated distorted trigonal by two  $\text{N}(\text{SiMe}_3)_2$  ligands and one secondary amido ligand.



**Scheme 5.** Formation of the trigonal amido complexes via hydrogen atom abstraction by the corresponding imido complexes.

The  $\text{Co}-\text{N}_{\text{amide}}$  bond lengths of the alkyl amido complexes fall in a narrow range of approx. 1.89 Å ( $\text{CMe}_2\text{Et}$  (**1H**): 1.880(3) Å, Ada (**2H**): 1.899(2) Å,  $\text{CMe}_2\text{Ph}$  (**3H**): 1.898(2) Å), in agreement with the seminal  $[\text{Co}(\text{N}(\text{H})\text{CMe}_3)(\text{hmds})_2]^-$  (**1H**): 1.883(1) Å).<sup>[15]</sup> In comparison, the aryl amido complexes show an elongated  $\text{Co}-\text{N}_{\text{amide}}$  bonds of around 1.92–1.94 Å (4-Me (**6H**): 1.935(2) Å, 4-H (**7H**): 1.920(2) Å, 4-OMe (**8H**): 1.921(1) Å, 4-Cl (**9H**): 1.944(3) Å, 4-F (**10H**): 1.940(3) Å) similar to the aryl amido complexes with NDipp( $\text{SiMe}_3$ ) ligand set.<sup>[16]</sup> These observations are in line with the known bond difference between alkyl and aryl amido cobalt complexes.<sup>[15,16,23,24]</sup> The  $\text{Co}-\text{N}-\text{R}$  bond angles of the amido complexes are in the range of 130° to 143°, with the aryl complexes being at the upper end. The  $^1\text{H}$ -NMR spectra gave for alkyl amido complexes a shift of –15 to –18 ppm for the hmds ligands, while the signals of the aryl complexes are at 13 ppm. In this regard we note that the chemical shift differences between aryl imides and amides is comparably small (3 – 6 ppm vs 13 – 15 ppm for the alkyl complexes). Using the  $\text{SiMe}_3$  proton signal as a qualitative handle of the electronic state of cobalt it speaks to a closer electronic relation between aryl imides/amides. This is in line with the previous made assumption of the aryl imido complexes as cobalt(II) imidyls. The magnetic moments amounts to 4.27  $\mu_B$  (**1H**), 4.49  $\mu_B$  (**2H**) and 3.91  $\mu_B$  (**3H**) which are in line with other trigonal high spin cobalt(II) complexes.<sup>[23,24]</sup> As such these aryl imido complexes (R = H, F, Cl) complexes were

excluded from kinetic H atom abstraction studies (see next section).



**Scheme 6.** Molecular structure of **2H** (left) and **6H** (right) in the solid state. The  $\text{K}\{\text{crypt.222}\}$  cation, solvent molecules as well as unnecessary H atoms are omitted for clarity. Selected bond lengths (Å) and angles (°):

### Kinetics of C–H bond activation

With the imido (and amido) cobalt complexes that show different structural metrics and electronic structures in hand, we were curious if and how this would translate in variations of HAT abstraction reactivity.

For that, compounds **1-3** and **6** were examined more closely towards their behaviour towards different substrates (9,10-dihydroanthracene (DHA, BDE = 76.3 kcal mol<sup>-1</sup>, pka = 30.1), 1,4-cyclohexadiene (CHD, BDE = 76.0 kcal mol<sup>-1</sup>, pka ~36), xanthene (XAN, BDE = 75.2 kcal mol<sup>-1</sup>, pka = 30.0)<sup>[25]</sup> using low-temperature UV/vis spectroscopy (20 eq. substrate, –30°C, in  $\text{Et}_2\text{O}$ ). **10** was disregarded as the spectroscopic changes upon H atom abstraction proved insufficient for extraction of reproducible reaction rates. Mapping the observed reaction rates with the BDE of the involved C–H bond showed for all complexes a good correlation with the BDE. It is in line with a more extensive, previous analysis on  $[\text{Co}(\text{NCMe}_3)(\text{hmds})_2]^-$  complex, and speaks for a HAT mechanism for all herein examined complexes. Given the different metrics of the  $[\text{MNR}]$  unit of these complexes, it was thus tempting to correlate these to the observed reaction rates.

For the aliphatic imido complexes, a larger  $k_{\text{obs}}$  can be linearly correlated to an increase of the  $\text{Co}-\text{N}_{\text{imide}}$  bond length as well as bending of  $\text{Co}-\text{N}_{\text{imide}}-\text{R}$  bond angle. Looking at the the isolobal metal-oxo chemistry, these observations can be understood from the intrinsic barriers for HAT that stem from Marcus-type inner-sphere reorganization energies ( $\lambda_i$ ) as well as the thermodynamic driving force.<sup>[26–29]</sup> Accordingly, the closer the imide geometry is to that of the transition state - and by that also to the formed amide - the lower is the reorganisation barrier. As such the structure/reactivity correlation holds also true, when regarding the differences of bond lengths and angles of the respective imide/amide couple. The general benefit of a more bent geometry was already observed in case of a pair of dipyrromethene cobalt imido complexes.<sup>[30]</sup> Here the bending was however enforced by steric constraints, and both complexes show near identical  $\text{Co}-\text{N}$  bond lengths. On the other hand for a nacnac based imido iron complex a strong increase in HAT reactivity was observed upon  $\text{M}-\text{N}$  elongation,<sup>[31]</sup> whereas a sizable impact of  $\text{M}-\text{N}-\text{R}$  bending was ruled out.

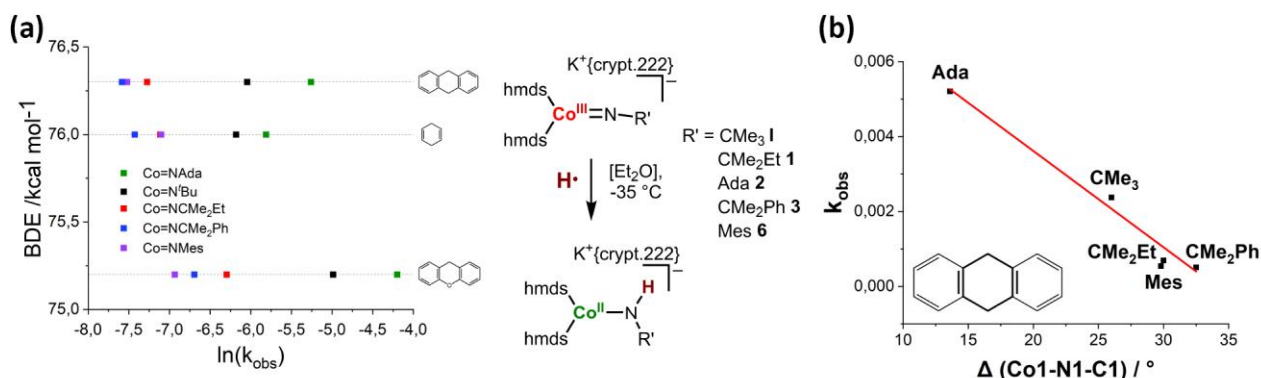
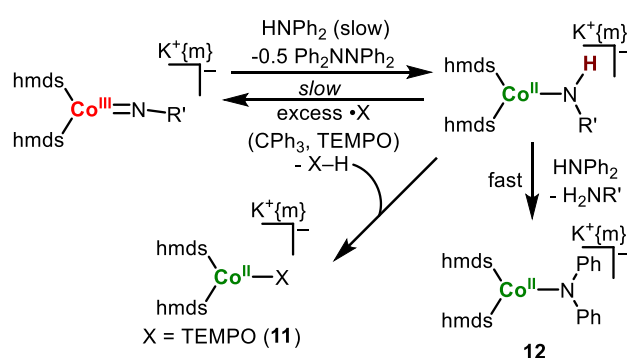


**Figure 1.** Hydrogen atom abstraction reactivity of the trigonal imido cobalt complexes. Correlation of the observed reactions rates ( $k_{\text{obs}}$ ) with the BDE of the respective substrate (a) and with the Co-N<sub>imido</sub> bond angle for 9,10-DHA (b)

Looking at the bond length and moreover angle changes initially it also allowed to understand the comparably low reactivity of the mesityl imido complex **6**. Although it features a very long Co-N<sub>imido</sub> bond, this is counteracted by an elongated Co-N<sub>amide</sub> bond of the corresponding amide ( $d = 0.184 \text{ \AA}$ ). Moreover, the metal-imido function of **8** is rather linear, thus deviating considerably from the bent amide orientation. However, taking the other aromatic imido complexes **7-10** also into account, such a correlation became less obvious. They all show a reduced HAA behaviour despite in part similar metrical changes as some of the slower aliphatic systems. This points for the aromatic imido complexes to further influencing factors, such as delocalisation of unpaired electron density onto the aromatic ring. This was proposed by Betley and Lin for aliphatic and aromatic high-spin imidyl iron complexes, and in their case led to reduced unpaired spin-density on the imidyl-nitrogen<sup>[13,14]</sup> A detrimental effect of delocalisation into the aromatic ring could be retraced in our case on a qualitative level, as transformation of the respective aryl imido complexes is slightly faster with electron donating para-substituents (e.g. OMe) than with electron-withdrawing substituents (e.g. Cl) using proton NMR spectroscopy.

At last we wished to shed light on the possible impact of the formed N-H bond, and by that on the thermodynamic driving forces of the HAA. This was however thwarted by the high reactivity of the involved amides and imides. For example, for the HAA from cobalt(II) amides using TEMPO and the trityl radical Ph<sub>3</sub>C• only in case the latter and its reaction with the comparably little reactive **1H** triphenyl methane was detected. A quantification of any equilibria was not possible because of subsequent deprotonation of triphenyl methane by the formed amide. Similar observations were made using TEMPO, that ultimately yielded in small amounts of the cobalt(II) TEMPO complex K{crypt}[Co(TEMPO)(hmds)<sub>2</sub>] (**11**), stemming from H atom transfer to TEMPO and subsequent deprotonation of formed TEMPO-H by remaining **1H**. Pseudo-self-exchange reactions of imides with different corresponding amides, did not result in any H atom transfer reactions. In view of the otherwise pronounced reactivity of the imido compounds, it speaks to suppression of the HAT by steric factors in this case.



**Scheme 7.** Attempts for interconversion of imido and amido complexes.

Cyclic voltammetric examination of the alkyl amido complexes gave an irreversible cathodic event between  $-1.2 \text{ V}$  (**1H**) and  $-0.7 \text{ V}$  (**3H**), whereas examination of the aryl amides was not possible for due to the abovementioned ligand scrambling. By comparison with the reversible oxidation of the trisamides [Co(hmds)<sub>3</sub>]<sup>-</sup> ( $E_{1/2} = -0.40 \text{ V}$ ) and **12** ( $E_{1/2} = -0.70 \text{ V}$ , see ESI), the irreversibility of the oxidation of **1H** and **1H-3H** is likely attributed to an intramolecular deprotonation of the formed neutral Co(NHR)(hmds)<sub>2</sub>. Attempts for deprotonation of the amides with strong bases such as nBuLi or BnK remained inconclusive, and pointed more to ligand exchange reactions of the amides with the used nucleophiles than deprotonation.

Turning to the imides, protonation of the seminal **1** with rather acidic ammonium salts gave only unselective degradation. Weaker proton sources ( $\text{pK}_a > 20$ ) resulted primarily in HAT reactivity. Most notably, reaction of **1H** with HNPPh<sub>2</sub> (BDE:  $87 \text{ kcal mol}^{-1}$ ;  $\text{pK}_a$  25) gave a mixture of the main product [Co(hmds)<sub>2</sub>(NPh<sub>2</sub>)]<sup>-</sup> (**12**), **1H**, remaining **1** as well as tetraphenylhydrazine. The latter showed that H atom abstraction from N-H bonds by the cobalt imides is also possible, yet is in competition with substrate deprotonation by the formed cobalt(II) amide. Treatment of **1** with H-hmds, that exhibits a similar  $\text{pK}_a$  as HNPPh<sub>2</sub> (**26**)<sup>[32,33]</sup> yet has a higher BDE ( $110 \text{ kcal mol}^{-1}$ )<sup>[34]</sup>, yields no reaction – thus further supporting a BDE driven HAT reactivity of the alkyl imido complexes. Cyclic voltammetric examination of the imides gave no discernible reduction event down to  $-2.5 \text{ V}$  for the alkyl imido complexes. Only in case of the mesityl imido

complex **6** a reduction is perceivable, albeit at very low potentials (−2.7 V), which is however deemed irrelevant for an electron transfer driven substrate oxidation. In contrast, all examined imido complexes show an irreversible oxidation event between −1.2 V (R = CMe<sub>2</sub>Ph) and −1.4 V (R = CMe<sub>2</sub>Et, Ada), with the values following the expectation of the more electron rich nature of alkyl versus aryl substituents. Although this could implicate the basicity of the imido as a driving factor for reactivity, differences in electrochemical potentials did not correlate with the observed reaction rates  $k_{\text{obs}}$ . Hereby it has to be noted, that the low oxidation potentials are similar to that of the related previously reported iron(II) imidyl complex [Fe(NMes)(N(Dipp)SiMe<sub>3</sub>)<sub>2</sub>]<sup>−</sup> (−1.40 V).<sup>[22]</sup> This was identified as a metal(II) imidyl, yet reacted nucleophilic via insertion of the CS<sub>2</sub> into the imido–metal bond.

## Conclusion

Herein we reported on the first library of isolable imido cobalt complexes in higher spin states that are active in H atom abstraction from external substrates. It shows that the trigonal *alkyl* imidos are found only in an intermediate spin state, and exhibit a large range of C–N bond lengths, and described best as cobalt(III) imides. For them an elongation of the Co–N bond correlates with a more bent Co–N–R bond angle. The *aryl* imido complexes on the other hand are found in a high-spin state, bear long Co–N bonds and comparably more linear [CoNR] units, in agreement with an overall cobalt(II) imidyl like situation. All complexes are capable of H atom abstraction that yields the corresponding cobalt(II) amido complexes. Comprehensive H atom abstraction studies on suitable imido complexes reveal for alkyl imido complexes a higher reactivity for smaller changes in the Co–N–R unit upon amide formation. Aryl imido complexes are less reactive, despite their comparably long Co–N imido bond and higher spin state. This is ascribed to a negative impact by partial delocalisation of unpaired spin state onto the aromatic ring, which can be partially modulated by introducing electron withdrawing/donating substituents. Accordingly, an imidyl character and/or high-spin state of an imido complex is not a sufficient predictor, and even a detriment for its HAT reactivity. This study thus underlines the intricacies of the late 3d-metal imido bond, which necessitates the synthesis of larger sets of isostructural species. Elucidation of the nature of the oxidized, formal cobalt(IV) imido complexes [Co(NR)(hmds)<sub>2</sub>]<sup>0</sup> is subject of ongoing studies.

## Acknowledgements

We thank the DFG (WE 5627/4–1) and the Philipps-Universität Marburg for funding.

## Conflicts of interest

The authors declare no conflict of interest.

**Keywords:** Imido cobalt complex • H Atom Transfer • C–H activation • Amido cobalt complex • Catalysis

## References

- [1] P. F. Kuijpers, J. I. van der Vlugt, S. Schneider, B. de Bruin, *Chem. Eur. J.* **2017**, *23*, 13819.
- [2] F. Collet, R. H. Dodd, P. Dauban, *Chem. Commun.* **2009**, 5061.
- [3] H. Lu, X. P. Zhang, *Chem. Soc. Rev.* **2011**, *40*, 1899.
- [4] Y. Park, Y. Kim, S. Chang, *Chem. Rev.* **2017**, *117*, 9247.
- [5] M. Ju, J. M. Schomaker, *Nat Rev Chem* **2021**, *5*, 580.
- [6] X. Nie, C.-X. Ye, S. I. Ivlev, E. Meggers, *Angew. Chem.* **2022**, *61*, e202211971.
- [7] H. Hayashi, T. Uchida, *Eur. J. Org. Chem.* **2020**, *2020*, 909.
- [8] T. R. Roose, D. S. Verdoorn, P. Mampuy, E. Ruijter, B. U. W. Maes, R. V. A. Orru, *Chem. Soc. Rev.* **2022**, *51*, 5842.
- [9] R. Eikey, *Coord. Chem. Rev.* **2003**, *243*, 83.
- [10] K. Ray, F. Heims, F. F. Pfaff, *Eur. J. Inorg. Chem.* **2013**, *2013*, 3784.
- [11] W. Mao, D. Fehn, F. W. Heinemann, A. Scheurer, M. van Gastel, S. A. V. Jannuzzi, S. DeBeer, D. Munz, K. Meyer, *Angew. Chem.* **2022**.
- [12] W. Mao, D. Fehn, F. W. Heinemann, A. Scheurer, D. Munz, K. Meyer, *Angew. Chem.* **2021**, *60*, 16480.
- [13] M. J. T. Wilding, D. A. Iovan, A. T. Wrobel, J. T. Lukens, S. N. MacMillan, K. M. Lancaster, T. A. Betley, *J. Am. Chem. Soc.* **2017**, *139*, 14757.
- [14] P.-C. Yang, K.-P. Yu, C.-T. Hsieh, J. Zou, C.-T. Fang, H.-K. Liu, C.-W. Pao, L. Deng, M.-J. Cheng, C.-Y. Lin, *Chem. Sci.* **2022**, *13*, 9637.
- [15] A. Reckziegel, C. Pietzonka, F. Kraus, C. G. Werncke, *Angew. Chem.* **2020**, 8527.
- [16] A. Reckziegel, M. Kour, B. Battistella, S. Mebs, K. Beuthert, R. Berger, C. G. Werncke, *Angew. Chem.* **2021**, *60*, 15376.
- [17] R. A. Abramovitch, E. P. Kyba, *J. Am. Chem. Soc.* **1974**, *96*, 480.
- [18] E. P. Kyba, R. A. Abramovitch, *J. Am. Chem. Soc.* **1980**, *102*, 735.
- [19] K. Wei, T. Yang, Q. Chen, S. Liang, W. Yu, *Chem. Commun.* **2020**, *56*, 11685.
- [20] G. Sieg, Q. Pessemesse, S. Reith, S. Yelin, C. Limberg, D. Munz, C. G. Werncke, *Chem. Eur. J.* **2021**, *27*, 16760.
- [21] W. Weller, L. Ruppach, A. Shlyaykher, F. Tambornino, C. G. Werncke, *Dalton transactions (Cambridge, England : 2003)* **2021**, *50*, 10947.
- [22] S. Reith, S. Demeshko, B. Battistella, A. Reckziegel, C. Schneider, A. Stoy, C. Lichtenberg, F. Meyer, D. Munz, C. G. Werncke, *Chem. Sci.* **2022**, *103*, 2905.
- [23] A. Massard, P. Braunstein, A. A. Danopoulos, S. Choua, P. Rabu, *Organometallics* **2015**, *34*, 2429.
- [24] C. B. Hansen, R. F. Jordan, G. L. Hillhouse, *Inorg. Chem.* **2015**, *54*, 4603.
- [25] X.-S. Xue, P. Ji, B. Zhou, J.-P. Cheng, *Chem. Rev.* **2017**, *117*, 8622.
- [26] J. P. Roth, J. C. Yoder, T. J. Won, J. M. Mayer, *Science* **2001**, *294*, 2524.
- [27] W. Lai, C. Li, H. Chen, S. Shaik, *Angew. Chem.* **2012**, *51*, 5556.
- [28] J. M. Mayer, *The journal of physical chemistry letters* **2011**, *2*, 1481.
- [29] C. R. Waidmann, X. Zhou, E. A. Tsai, W. Kaminsky, D. A. Hrovat, W. T. Borden, J. M. Mayer, *J. Am. Chem. Soc.* **2009**, *131*, 4729.
- [30] Y. Baek, E. T. Hennessy, T. A. Betley, *J. Am. Chem. Soc.* **2019**, 16944.
- [31] R. E. Cowley, N. A. Eckert, S. Vaddadi, T. M. Figg, T. R. Cundari, P. L. Holland, *J. Am. Chem. Soc.* **2011**, *133*, 9796.

- [32] S. Tabassum, O. Sereda, P. V. G. Reddy, R. Wilhelm, *Org. Biomol. Chem.* **2009**, *7*, 4009.
- [33] F. G. Bordwell, J. C. Branca, D. L. Hughes, W. N. Olmstead, *J. Org. Chem.* **1980**, *45*, 3305.
- [34] Y.-R. Luo, *Comprehensive Handbook of Chemical Bond Energies*, CRC Press, **2007**.

### 3.6 Between imide, imidyl and nitrene – an imido iron complex in two oxidation states

S. Reith, S. Demeskho, B. Battistella, **A. Reckziegel**, C. Schneider, A. Stoy, C. Lichtenberg, F. Meyer, D. Munz, C.G. Werncke

*Chem. Sci* **2022**, *13*, 7907-7913.

DOI: 10.1039/D2SC01088G

<https://pubs.rsc.org/en/content/articlelanding/2022/SC/D2SC01088G>

#### Abstract

Imidyl and nitrene metal species play an important role in the N-functionalisation of unreactive C–H bonds as well as the aziridination of olefines. We report on the synthesis of the trigonal imido iron complexes  $[\text{Fe}(\text{NMes})\text{L}_2]^{0,-}$  ( $\text{L} = -\text{NDippSiMe}_3$ );  $\text{Dipp} = 2,6$ -diisopropyl-phenyl;  $\text{Mes} = (2,4,6\text{-trimethylphenyl})$  via reaction of mesityl azide ( $\text{MesN}_3$ ) with the linear iron precursors  $[\text{FeL}_2]^{0,-}$ . UV-vis-, EPR-,  $^{57}\text{Fe}$  Mössbauer spectroscopy, magnetometry, and computational methods suggest for the reduced form an electronic structure as a ferromagnetically coupled iron(II) imidyl radical, whereas oxidation leads to mixed iron(III) imidyl and electrophilic iron(II) nitrene character. Reactivity studies show that both complexes are capable of H atom abstraction from C–H bonds. Further, the reduced form  $[\text{Fe}(\text{NMes})\text{L}_2]^-$  reacts nucleophilically with  $\text{CS}_2$  by inserting into the imido iron bond, as well as electrophilically with CO under nitrene transfer. The neutral  $[\text{Fe}(\text{NMes})\text{L}_2]$  complex shows enhanced electrophilic behavior as evidenced by nitrene transfer to a phosphine, yet in combination with an overall reduced reactivity.

#### Zusammenfassung

Aufbauend auf den gezeigten Arbeiten zu Cobalt-Komplexen, wurden entsprechende Eisenverbindungen untersucht. Die Umsetzung des quasi-linear koordinierten Eisen(I)-Komplexes  $\text{K}\{\text{crypt.222}\}[\text{Fe}(\text{N}(\text{Dipp})\text{SiMe}_3)_2]$  (**79**) mit Mesitylazid ermöglichte die Isolierung des trigonalen Imido-Eisen-Komplexes **126**.

Die Strukturanalyse mittels Röntgenbeugungsexperimenten am Einkristall weist eine aufgeweitete Imido-Eisen-Bindung ( $\text{Fe-N}_{\text{Imido}}$ : 1,774(2) Å), sowie einen geringen Bindungswinkel ( $173,6(13)^\circ$ ), auf. Für die Bindungssituation konnte durch eine ausführliche Untersuchung der magnetischen Eigenschaften in Kombination mit Mössbauer- und ESR-Spektroskopie, ein signifikanter Imidyl-Charakter nachgewiesen werden.

Untersuchungen zum RedOx-Verhalten zeigten eine reversible Oxidation des Komplexes (-1,4 V vs.  $\text{Fc}/\text{Fc}^+$ ) unter Bildung des neutralen Imido-Eisen-Komplexes **127**. Dieser konnte unabhängig davon durch die Umsetzung des Eisen(II)-Komplexes **71** mit Mesitylazid dargestellt werden, und durch Reduktion in den anionischen Komplex **126** überführt werden. Der Vergleich der Bindungssituation des Imido-Liganden zeigte nur eine geringfügige Änderung ( $\text{Fe-N}_{\text{Imido}}$ : 1,741(2) Å;  $177,5(2)^\circ$ ), während eine deutliche Verkürzung der  $\text{N}(\text{Dipp})\text{SiMe}_3$ -Eisen-Bindungen beobachtet wird. Spektroskopische und quantenchemische Untersuchungen an diesem formalen Imido-Eisen(IV)-Komplex wiesen auf einen Imidyl-Eisen(III)-Komplex mit substantiellen Anteilen einer Nitren-Eisen(II)-Resonanzform hin. Untersuchungen

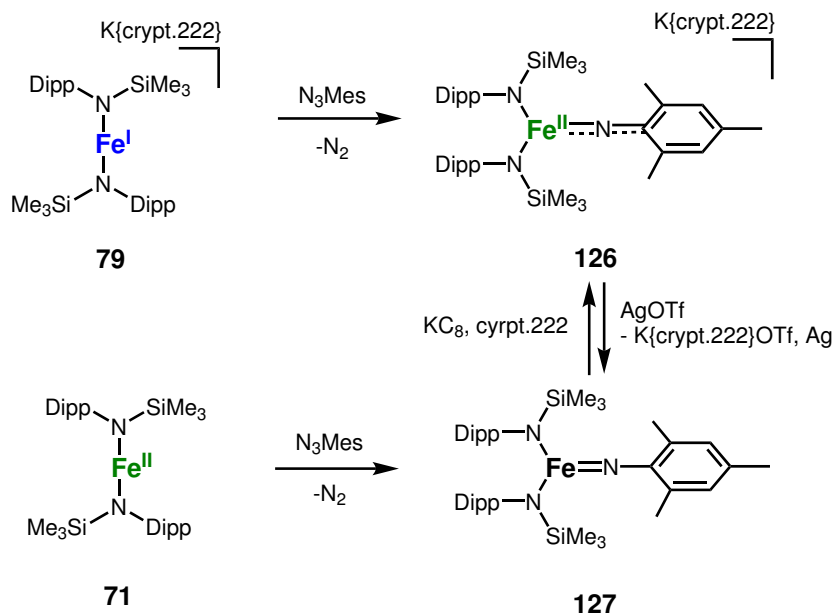


Abb. 53: Darstellung und Struktur des anionischen Imidyl-Eisen(II)- (**126**) und des neutralen Imido-Eisen(IV)-Komplexes (**127**).

zum Reaktionsverhalten der beiden Imido-Eisen-Komplexe zeigten eine H-Atom-Abstraktion von 1,4-CHD, wobei eine Isolierung der vermuteten Amido-Komplexe nicht möglich war. Weiterhin wurde im Fall des anionischen Komplexes **126** die Insertion des elektrophilen  $\text{CS}_2$  in die Imido-Metall-Bindung, sowie ein elektrophiler Angriff des Nitren-Fragmentes auf CO beobachtet. Der neutrale Komplex **127** weist keinerlei Nucleophilie auf, ist jedoch in der Lage, das Nitrenfragment teilweise auf ein Phosphin zu übertragen.

Zusammenfassend konnten zwei Imido-Eisen-Komplexe in unterschiedlichen Oxidationsstufen dargestellt und spektroskopisch charakterisiert werden. So konnte die unterschiedliche Bindungssituation der Imido-Komplexe, bestätigt durch quantenchemische Rechnungen, aufgezeigt werden und anschließend durch eine divergente Reaktivität der Komplexe bestätigt werden.

### Beiträge der Autoren

Die gezeigten Verbindungen wurden von *Sascha Reith* dargestellt und mittels  $^1\text{H}$ -NMR-, UV-Vis- und IR-Spektroskopie charakterisiert. Die Messung des magnetischen Momentes nach der EVANS-Methode wurde durch die Serviceabteilung NMR-Spektroskopie der Philipps-Universität Marburg an einem Bruker AV III 500 durchgeführt und von *Sascha Reith* ausgewertet.

Zur Bestimmung der Struktur im Festkörper wurden Röntgenbeugungsexperimente am Einkristall durch die Serviceabteilung Kristallstrukturanalyse der Philipps Universität Marburg oder von *Dr. Gunnar Werncke* an einem Bruker D8 Quest durchgeführt. *Sascha Reith* hat die Strukturen aus den erhaltenen Daten gelöst und verfeinert.

Die Bestimmung der Reinheit erfolgte mittels CHN-Elementaranalytik durch die Serviceabteilung Elementaranalytik der Philipps-Universität Marburg.

Die Elektronenspinresonanz-Experimente bei Raumtemperatur wurde von *Andreas Stoy* aus der Arbeitsgruppe von *Crispin Lichtenberg* durchgeführt und ausgewertet.

Die Cyclovoltammetrie wurde von *Sascha Reith* und *Christian Schneider* durchgeführt und ausgewertet.

Mössbauer Spektroskopie und magnetische Messungen im Festkörper wurden von *Serhiy Demeshko*, aus der Arbeitsgruppe von *Franc Meyer* an der Georg-August-Universität in Göttingen, durchgeführt und ausgewertet.

Die Elektronenspinresonanz-Experimente bei Helium-Temperatur wurde von *Beatrice Battistella* aus der Arbeitsgruppe von *K. Ray* an der Humboldt-Universität zu Berlin durchgeführt und von mir ausgewertet.

Quantenchemische Berechnungen wurden von *Dominik Munz* durchgeführt.

Das Manuskript hat *Sascha Reith* in Zusammenarbeit mit *Dr. Gunnar Werncke* und in Absprache mit allen Co-Autoren verfasst.



Cite this: *Chem. Sci.*, 2022, 13, 7907

All publication charges for this article have been paid for by the Royal Society of Chemistry

## Between imide, imidyl and nitrene – an imido iron complex in two oxidation states†

Sascha Reith,<sup>a</sup> Serhiy Demeshko,<sup>b</sup> Beatrice Battistella,<sup>c</sup> Alexander Reckziegel,<sup>a</sup> Christian Schneider,<sup>a</sup> Andreas Stoy,<sup>a</sup> Crispin Lichtenberg,<sup>a</sup> Franc Meyer,<sup>b</sup> Dominik Munz<sup>\*de</sup> and C. Gunnar Werncke<sup>id\* a</sup>

Imidyl and nitrene metal species play an important role in the *N*-functionalisation of unreactive C–H bonds as well as the aziridination of olefines. We report on the synthesis of the trigonal imido iron complexes  $[\text{Fe}(\text{NMes})\text{L}_2]^{0,-}$  ( $\text{L} = -\text{N}(\text{Dipp})\text{SiMe}_3$ ;  $\text{Dipp} = 2,6$ -diisopropyl-phenyl;  $\text{Mes} = (2,4,6\text{-trimethylphenyl})$ ) via reaction of mesityl azide ( $\text{MesN}_3$ ) with the linear iron precursors  $[\text{FeL}_2]^{0,-}$ . UV-vis-, EPR-,  $^{57}\text{Fe}$  Mössbauer spectroscopy, magnetometry, and computational methods suggest for the reduced form an electronic structure as a ferromagnetically coupled iron(II) imidyl radical, whereas oxidation leads to mixed iron(III) imidyl and electrophilic iron(III) nitrene character. Reactivity studies show that both complexes are capable of H atom abstraction from C–H bonds. Further, the reduced form  $[\text{Fe}(\text{NMes})\text{L}_2]^-$  reacts nucleophilically with  $\text{CS}_2$  by inserting into the imido iron bond, as well as electrophilically with CO under nitrene transfer. The neutral  $[\text{Fe}(\text{NMes})\text{L}_2]$  complex shows enhanced electrophilic behavior as evidenced by nitrene transfer to a phosphine, yet in combination with an overall reduced reactivity.

Received 21st February 2022

Accepted 28th May 2022

DOI: 10.1039/d2sc01088g

rsc.li/chemical-science

## Introduction

Imido complexes of the late 3d-transition metals play a crucial role in nitrene transfer catalysis.<sup>1,2</sup> As such there is an innate interest in understanding the structural and electronic features of the central imido metal unit to control and predict its reactivity.<sup>3–5</sup> The imido ligand is classically regarded as a dianionic imide  $[\text{NR}]^{2-}$  that forms either a double or triple bond, as it is the case for early transition metals.<sup>2,6</sup> For the 3d-metals, the metal–imido bond becomes more covalent and  $p \rightarrow d$  donation is reduced due to (partially) filled d-orbitals. This may result in intriguing bonding situations, namely metal stabilized imidyl radical  $[\text{NR}]^{\cdot-}$  or even electrophilic nitrene  $[\text{NR}]^0$  ligands, that are highly reactive.<sup>4,5</sup> The former was observed in a few instances for iron,<sup>7,8</sup> cobalt<sup>9,10</sup> and nickel.<sup>11,12</sup> 3d-Metal nitrenes

are mostly known for copper,<sup>13–15</sup> with only two isolated examples.<sup>13,15</sup> Given the overall reactive nature of late 3d-metal imido species, the impact of oxidation state changes onto the imido unit is only partially understood. For low-spin complexes, mostly found for isolable and rather unreactive late 3d-metal imidos, few reports of one-electron oxidation showed contraction of the imido metal bond.<sup>12,16–20</sup> This can be explained by a metal centred oxidation, accompanied with ion radius contraction as well as increased  $p \rightarrow d$  donation and depopulation of *anti*-bonding molecular orbitals.<sup>5,21</sup> Contrastingly, in the only two reports of oxidation of high-valent high-spin 3d-metal imidos M–N bond elongation took place (Fig. 1).<sup>9,22</sup>

This was attributed to a ligand-centred oxidation and spin density increase at the imido ligand, that resulted in an imidyl radical character. For a pseudo-trigonal bipyramidal imido

<sup>a</sup>Philipps-University Marburg, Department of Chemistry, Hans-Meerwein-Str. 4, D-35037 Marburg, Germany. E-mail: gunnar.werncke@chemie.uni-marburg.de

<sup>b</sup>University of Göttingen, Institute of Inorganic Chemistry, Tammannstr. 4, D-37077 Göttingen, Germany

<sup>c</sup>Humboldt-University, Berlin Institute for Chemistry, Brook-Taylor-Str. 2, D-12489 Berlin, Germany

<sup>d</sup>Saarland University, Inorganic Chemistry: Coordination Chemistry, Campus C4.1, D-66123 Saarbrücken, Germany. E-mail: dominik.munz@uni-saarland.de

<sup>e</sup>Friedrich-Alexander University Erlangen-Nürnberg, Inorganic Chemistry, Egerlandstr. 1, D-91058 Erlangen, Germany

† Electronic supplementary information (ESI) available: General, experimental, analytical (NMR, IR, UV/vis,  $^{57}\text{Fe}$  Mössbauer and EPR spectroscopy, SQUID magnetometry, cyclovoltammetry), computational and crystallographic details. CCDC 2130485–2130488. For ESI and crystallographic data in CIF or other electronic format see <https://doi.org/10.1039/d2sc01088g>

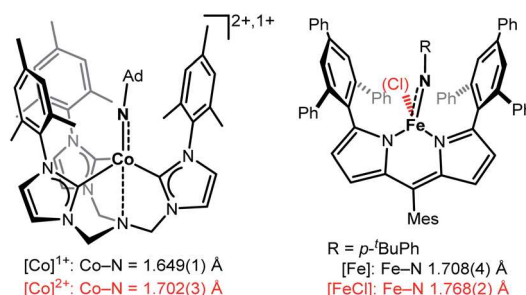


Fig. 1 Examples of imido metal complex oxidation leading to M–N bond lengthening and imidyl character (Ad = adamantyl, Mes = 2,4,6-trimethylphenyl).<sup>7–9</sup>



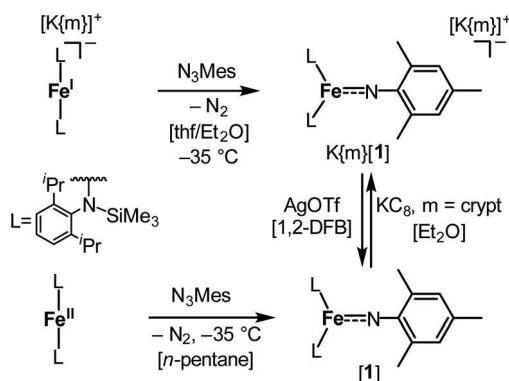


cobalt complex (Fig. 1, left) oxidation led to a switch from the high-spin to the low-spin configuration ( $d^5$ ,  $S = 1/2$ ).<sup>9</sup> For a trigonal planar dipyrromethane (dpm) based imido iron complex (Fig. 1, right) the high-spin state persisted, with an increase of the coordination number.<sup>22</sup>

Building on recent examples of low-coordinate imido cobalt silylamides in higher spin-states<sup>23,24</sup> we report herein the trigonal iron imido complexes  $[\text{Fe}(\text{NMes})\text{L}_2]^{0,-}$  ( $\text{L} = -\text{N}(\text{Dipp})\text{SiMe}_3$ ; Dipp = 2,6-diisopropyl-phenyl; Mes = 2,4,6-trimethyl-phenyl) in the formal oxidation states +III and +IV, which can be interconverted by oxidation/reduction. Detailed spectroscopic and computational analyses reveal the ambiguous electronic structure of both complexes. The anionic  $[\text{Fe}(\text{NMes})\text{L}_2]^-$  is described best as an iron(II) imidyl complex whereas the oxidized neutral  $[\text{Fe}(\text{NMes})\text{L}_2]^0$  shares iron(III) imidyl and iron(II) nitrene character. The electronic ambiguity is reflected best by  $[\text{Fe}(\text{NMes})\text{L}_2]^-$  which shows ambiphilic, *i.e.* combined nucleophilic and electrophilic behaviour, whereas the nucleophilicity is lost upon oxidation to  $[\text{Fe}(\text{NMes})\text{L}_2]^0$ .

## Results and discussion

The imido iron complex  $\text{K}\{m\}[\text{Fe}(\text{NMes})\text{L}_2]$ ,  $\text{K}\{m\}[\mathbf{1}]$  ( $m = \text{crypt.222}$ ), was obtained as a green crystalline solid (yield 86%) by treatment of a solution of the linear iron(I) precursor  $\text{K}\{m\}[\text{FeL}_2]$  in a mixture of thf/Et<sub>2</sub>O (1 : 3) with MesN<sub>3</sub> at  $-40^\circ\text{C}$  (Scheme 1). X-ray diffraction analysis revealed for the complex anion  $[\mathbf{1}]^-$  (Fig. 2) a Fe–N<sub>imidyl</sub> bond length of 1.7744(15) Å and a Fe–N–C<sub>Aryl</sub> bond angle of  $173.6(13)^\circ$ . Usually, imido-iron bond lengths of low-spin complexes range from 1.65 to 1.70 Å.<sup>16–18,25,26</sup> Longer Fe–N<sub>imidyl</sub> bonds are rarely observed, but are found for high-spin iron imidos with<sup>7,8,27</sup> or without<sup>28</sup> imidyl character on the nitrogen atom as well as an anionic iron(II) imide.<sup>20</sup>  $[\mathbf{1}]^-$  shows a short N–C<sub>Aryl</sub> bond of 1.339(2) Å, which is in line with aforementioned high-spin imido iron complexes with C–N double bond character. The observed structural metrics closely resemble the related high-spin imidyl cobalt(II) complex  $[\text{Co}(\text{NDipp})\text{L}_2]^-$  (*e.g.* M–N<sub>imidyl</sub> 1.751(2) Å, N–C<sub>Aryl</sub> 1.347(2) Å),<sup>23</sup> which suggested for  $[\mathbf{1}]^-$  also an iron(II) imidyl-like bonding situation on a structural level.



Scheme 1 Synthesis of complexes  $\text{K}\{m\}[\text{Fe}(\text{NMes})\text{L}_2]$ ,  $\text{K}\{m\}[\mathbf{1}]$  ( $m = \text{crypt.222}$ ), and  $[\text{Fe}(\text{NMes})\text{L}_2]$ ,  $[\mathbf{1}]$ , as well as their interconversion by oxidation and reduction.

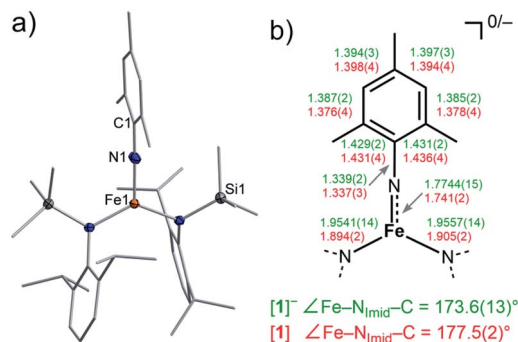


Fig. 2 (a) Solid state structure of  $[\mathbf{1}]$ . The H atoms are omitted for clarity. (b) Selected bond metrics for  $[\mathbf{1}]^-$  (green) and  $[\mathbf{1}]$  (red) [Å].

Given the scarcity of unambiguously identified iron bound imidyl units, namely only tetrahedral iron(III) imidyls of the type  $[(\text{dpm})\text{Fe}(\text{Cl})(\text{NR})]$  from Betley and co-workers (Fig. 1, right),<sup>7,8,22</sup> we sought further insights into the electronic situation of  $[\mathbf{1}]^-$ . Magnetic measurements (SQUID) on solid material yielded an  $\chi_{\text{M}}T$  value of  $4.4 \text{ cm}^3 \text{ mol}^{-1} \text{ K}$  (corresponding to an effective magnetic moment of  $\mu_{\text{eff}} = 5.93 \mu_{\text{B}}$ ) at 210 K (Fig. 3a).

This is close to the spin-only value of a sextet state ( $\mu_{\text{s.o.}} = 5.92 \mu_{\text{B}}$ ) and can be rationalized either by an iron(II) ion ferromagnetically coupled to an imidyl radical anion, or by a high-spin iron(III) imide. Upon cooling, a sharp drop is observed below 20 K, which is attributed to zero-field splitting (simulation of the  $\chi_{\text{M}}T$  data gave  $g = 2.01$ ,  $D = 2.5 \text{ cm}^{-1}$ ; see ESI† for more details).

To assess the oxidation state of the metal in  $[\mathbf{1}]^-$ , zero-field <sup>57</sup>Fe Mössbauer spectroscopy was employed. It revealed a doublet with an isomer shift (IS) of  $\delta = 0.43 \text{ mm s}^{-1}$  (at 80 K) and a large quadrupole splitting (QS) of  $|\Delta E_{\text{Q}}| = 4.18 \text{ mm s}^{-1}$  (Fig. 3b). The IS is similar to that of the related three-coordinate high-spin iron(III) imide  $[(\text{dpm})\text{Fe}(\text{N}\{p\text{-}^t\text{Bu-Ph}\})]$ :  $\delta = 0.44 \text{ mm s}^{-1}$ ,  $|\Delta E_{\text{Q}}| = 0.00 \text{ mm s}^{-1}$ , at 200 K; Fig. 1, right),<sup>8,27,28</sup> but also to that of the anionic iron(II) imide  $[(\text{Ph}_2\text{B}\{^t\text{BuIM}\})_2\text{Fe}(\text{NDipp})]^-$  ( $\delta = 0.46 \text{ mm s}^{-1}$ ,  $|\Delta E_{\text{Q}}| = 1.45 \text{ mm s}^{-1}$ , at 80 K).<sup>20</sup> The IS of  $\text{K}\{m\}[\mathbf{1}]$  ranges between those of the diferric and diferrous silylamide complexes  $[(\text{L}_2\text{Fe})_2(\mu\text{-S})]^{2-,0}$  at 80 K with unambiguous trigonal iron(II) ( $\delta = 0.59 \text{ mm s}^{-1}$ ) and iron(III) ions ( $\delta = 0.29 \text{ mm s}^{-1}$ ).<sup>29</sup> The large QS of  $\text{K}\{m\}[\mathbf{1}]$  is remarkable and would generally point to divalent iron. However, also for a number of planar iron(III) complexes large QS have been reported.<sup>30</sup> Moreover, related (pseudo-)trigonal iron silylamides exhibit substantially larger QS in the ferric compared to the ferrous state (*e.g.*  $[(\text{L}_2\text{Fe})_2(\mu\text{-S})]^{2-,0}$ :  $|\Delta E_{\text{Q}}| = 0.22 \text{ mm s}^{-1}$  ( $\text{Fe}^{2+}$ ),  $3.70 \text{ mm s}^{-1}$  ( $\text{Fe}^{3+}$ ), at 80 K;<sup>29</sup>  $[\text{Fe}(\text{N}(\text{SiMe}_3)_2)_3]^{0,-}$ :  $|\Delta E_{\text{Q}}|$  ( $\text{Fe}^{2+}$ ) =  $0.60 \text{ mm s}^{-1}$  at 3 K,<sup>31</sup>  $|\Delta E_{\text{Q}}|$  ( $\text{Fe}^{3+}$ ) =  $5.12 \text{ mm s}^{-1}$  at 77 K<sup>32</sup>).

X-band EPR spectroscopic examination of  $[\mathbf{1}]^-$  at 13 K yielded an axial signal with  $g_1 = 6.5$ ,  $g_2 = 4.28$ ,  $g_3 = 4.18$  ( $A_1(^{14}\text{N}) = 107 \text{ G}$ ,  $A_2(^{14}\text{N}) = 1.7 \text{ G}$ ,  $A_3(^{14}\text{N}) = 20.5 \text{ G}$ ; see ESI†), the large <sup>14</sup>N hyperfine coupling implicating substantial spin density on nitrogen. This is consistent with substantial imidyl character in  $[\mathbf{1}]^-$ , and also aligns with its structural features.

Next, we wanted to elaborate if we could electrochemically attenuate the electronic situation of  $[\mathbf{1}]^-$ . Cyclic voltammetry



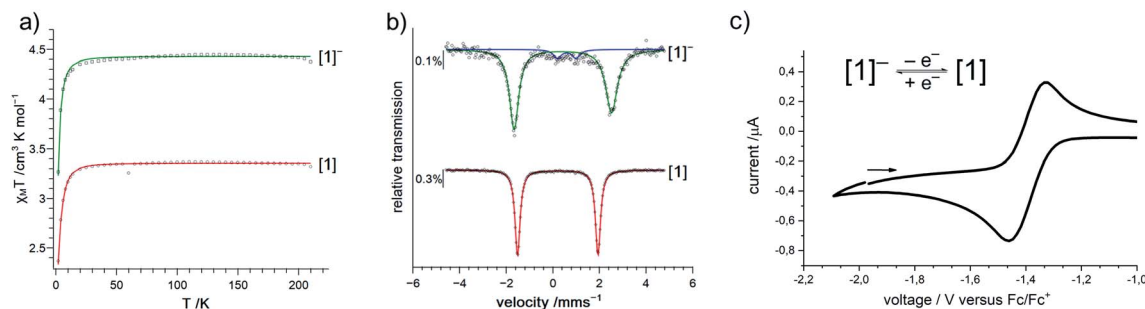


Fig. 3 (a) Variable-temperature magnetic susceptibility of solid  $K(m)[1]$  (green) and  $[1]$  (red) in the range of 2–210 K. (b) Zero-field  $^{57}\text{Fe}$  Mössbauer spectra of solid  $K(m)[1]$  (green) and  $[1]$  (red) at 80 K. Parameters for  $K(m)[1]$ :  $\delta = 0.43 \text{ mm s}^{-1}$ ,  $|\Delta E_Q| = 4.18 \text{ mm s}^{-1}$  (92%);  $[1]$ :  $\delta = 0.21 \text{ mm s}^{-1}$ ,  $|\Delta E_Q| = 3.45 \text{ mm s}^{-1}$ . (c) Cyclic voltammogram of  $K(m)[1]$  ( $500 \text{ mV s}^{-1}$ , thf,  $0.1 \text{ M } n\text{Bu}_4[\text{PF}_6]$ ) vs.  $\text{Fc}/\text{Fc}^+$ .

examination showed a reversible redox event at  $E_{1/2} = -1.4 \text{ V}$  at  $500 \text{ mV s}^{-1}$  (THF, vs.  $\text{Fc}/\text{Fc}^+$ , Fig. 3c), that becomes irreversible upon lowering the scan rate to  $50 \text{ mV}$  (Fig. S24†). The potential is in line with those for the oxidation of imido iron(III) and imido iron(II) species ( $\approx -1.3$  to  $-0.7 \text{ V}$ ).<sup>16,17,33</sup> Gratifyingly, chemical oxidation of  $[1]^-$  in 1,2-difluorobenzene with  $\text{AgOTf}$  ( $\text{OTf}^- = \text{F}_3\text{CSO}_3^-$ ) led to the formation of a new paramagnetic species which we attributed to neutral  $[1]$ .  $[1]$  could not be isolated *via* this pathway due to partial degradation, but was independently synthesized by reacting  $[\text{FeL}_2]$  with  $\text{MesN}_3$  in *n*-pentane (yield 64%, Scheme 1). It can be reduced back to  $[1]^-$  by  $\text{KC}_8$  in the presence of crypt.222, evidencing the possibility of their chemical interconversion. X-ray diffraction analysis of  $[1]$  showed in comparison with  $[1]^-$  that all metal–nitrogen bonds contract upon oxidation with otherwise little changes in the Fe–N–C unit (Fe– $\text{N}_{\text{imide}} 1.741(2) \text{ \AA}$ , Fe– $\text{N}_{\text{imide}}\text{–C}_{\text{Aryl}} 177.5(2)^\circ$ ,  $\text{N}_{\text{imide}}\text{–C}_{\text{Aryl}} 1.337(3) \text{ \AA}$ ; Fig. 2, right), where the contraction of the Fe–N amide bonds was slightly more pronounced. Thus, it was suggestive of at least partial metal based oxidation. This was corroborated by  $^{57}\text{Fe}$  Mössbauer spectroscopy showing an IS of  $\delta = 0.21 \text{ mm s}^{-1}$  for  $[1]$  (vs.  $[1]^-$ :  $0.43 \text{ mm s}^{-1}$ ). It is in line with shorter Fe–ligand bonds and by that with the decrease of the radial extension of the 4s wave function in case of the oxidized species  $[1]$ . Further, a negative correlation of the IS with the Fe oxidation state is usually valid for high spin complexes.<sup>34</sup> The QS for  $[1]$  is with  $|\Delta E_Q| = 3.56 \text{ mm s}^{-1}$  (vs.  $[1]^-$ :  $4.18 \text{ mm s}^{-1}$ ) only slightly reduced, and indicates a similar electron density distribution (electric field gradient) in both complexes. The IS value of  $[1]$  is distinct from those of iron(IV) imides, which are found between  $-0.09$  and  $-0.52 \text{ mm s}^{-1}$ .<sup>26,35</sup> This precludes for  $[1]$  a formulation as an iron(IV) imide. Accordingly, its IS value is closer to those of high-spin iron(III) imides ( $\delta = 0.37\text{--}0.47 \text{ mm s}^{-1}$ ,  $|\Delta E_Q| \approx 0 \text{ mm s}^{-1}$  at 200 K),<sup>8,27,28</sup> a trigonal intermediate-spin iron(III) imide ( $\delta = 0.25 \text{ mm s}^{-1}$ ,  $|\Delta E_Q| = 1.32 \text{ mm s}^{-1}$ , at 200 K)<sup>20</sup> or four-coordinate high-spin iron(III) imidyls (e.g.  $[(\text{dpm})\text{Fe}(\text{N}\{p\text{-}^t\text{Bu-C}_6\text{H}_4\})\text{Cl}] \delta = 0.28 \text{ mm s}^{-1}$ ,  $|\Delta E_Q| = 2.22 \text{ mm s}^{-1}$ , at 90 K).<sup>7,8,22</sup> Solid state SQUID measurements on  $[1]$  (Fig. 3a) gave a  $\chi_M T$  value of  $3.3 \text{ cm}^3 \text{ mol}^{-1} \text{ K}$  ( $\mu_{\text{eff}} = 5.14 \mu_B$ ) at 210 K with  $D = -3.5 \text{ cm}^{-1}$  and  $g = 2.12$ . These values correspond to an overall  $S = 2$  spin ground state that fits with the absence of pronounced X-band EPR features.  $[1]$  and  $[1]^-$  are

thus the first isostructural imido metal complexes in two oxidation states in which both exhibit a high-spin state.

To shed further light on the electronic structures of  $[1]^-$  and  $[1]$ , DFT-(PBE, TPSSH, PBE0) and CASSCF/NEVPT2 calculations were performed.<sup>36</sup> All investigated computational methods afforded good to reasonable agreement with the XRD, Mössbauer-, EPR- and SQUID data (bond lengths and angles,  $\Delta E_Q$ ,  $\delta$ ,  $g$ ,  $A$ ,  $D$ ; Tables S3–S6†). According to the CASSCF calculations, in  $[1]^-$ , six electrons populate the two pairs of  $\pi/\pi^*$ -interactions between the metal and imido ligand (Fig. 4, S43–S45†).

The two unpaired electrons in the antibonding combinations are thereby once metal centred ( $d_{xz}/\pi^*$ ; Fe : N = 0.8 : 0.2; Löwdin population analysis) and once rather located at the

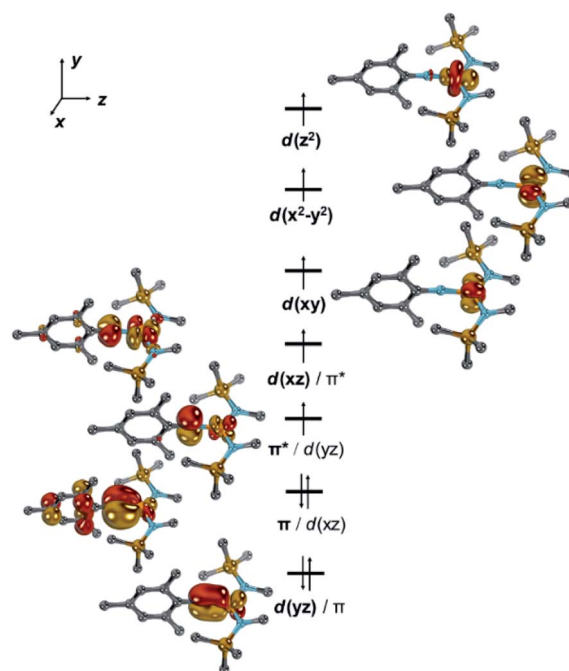


Fig. 4 Electronic structure of  $[1]^-$  by CASSCF(11,9). Dipp groups were truncated by methyl groups, hydrogen atoms are omitted for clarity, one set of bonding and antibonding Dipp-centred  $\pi$ -orbitals is omitted for clarity.



ligand ( $\pi^*/d_{yz}$ ; N : Fe = 0.6 : 0.4). This tentatively gives rise to the electronic structure of an imidyl iron(II) complex for  $[1]^-$ . An oxidation state of iron(+II) is also substantiated by the Löwdin spin density of +0.66 a.u. at the imido nitrogen atom.

Neutral  $[1]$  features a quintet ground state ( $\Delta E_{q/t} = +0.55$  eV;  $\Delta E_{q/sept} = +1.16$  eV). The main configuration ( $c = 0.63$ ) predicts thereby four unpaired electrons in d-orbitals (Fig. 5 and S40–S42†). Further two electrons are paired in the  $d_{xy}$  orbital, which combines with the imido ligand's  $p_x$  orbital (Fe : N = 7 : 3) and to a minor extent with the aromatic mesityl substituent. This gives overall rise to a formal  $d^6$  ( $Fe^{II}$ ) electron configuration of the metal and an electrophilic nitrene-type ligand. However, the second most important configuration ( $c = 0.21$ ) relates to the  $\pi-\pi^*$  transition and thus suggests significant imidyl radical character.<sup>5</sup> This is further corroborated by accumulation of spin density at the imido nitrogen atom ( $-0.21$  a.u.), which is suggestive of considerable antiferromagnetic character. Accordingly, the doubly excited resonance structure is also of relevance ( $c = 0.13$ ), which overall leads to a population of the LUMO by formally  $0.49 e^-$  and a shift of electron density to the ligand. Thus, when going from  $[1]$  to  $[1]^-$  the additional electron populates the antibonding  $\pi^*$  orbital, and weakens the metal-imido bond by formally  $-0.5$ . As such, the calculations highlight the electronic flexibility of the covalent iron-imido ligand interaction where the additional electron is not accepted by either the metal or the ligand, but by both. Since the electron is shared within the  $[FeNR]$  linkage, of course, rather similar Mössbauer spectroscopic features of  $[1]$  and  $[1]^-$  are expected, which aligns well with the experimental (*vide supra*) and

calculated (Table S4†) parameters. It is thus reasonable to consider the imido iron unit in both complexes in its entirety, as proposed for a linear imido cobalt(II) compound.<sup>37</sup> Using the Enemark–Feltham notation for nitrosyl complexes<sup>38</sup> this leads to notations  $\{FeNR\}^8$  for  $[1]$  and  $\{FeNR\}^9$  for  $[1]^-$ , and by that avoids singling out or overemphasizing a particular resonance structure.

Given these computed electronic structures of the “iron(II) imidyl”  $[1]^-$  as well as the “iron(II) nitrene”  $[1]$ , we were curious if and how they would translate to differences in chemical reactivity. Both complexes showed only limited H-atom abstraction capabilities in case of 1,4-cyclohexadiene (after 24 h:  $[1]$ : 39%;  $[1]^-$ : 73%). H atom abstraction from 1-hydroxy-2,2,6,6-tetramethyl-piperidine (TEMPO-H) was observed for  $[1]$  (24 h: 25% TEMPO by X-band EPR spectroscopy), whereas for  $[1]^-$  an ill-defined transformation of the imido complex was detected, without significant formation of TEMPO. These observations can be explained by the steric congestion. Possibly also to the ambivalent electronic nature of both complexes may contribute to the observed differences in reactivity. Reaction products of the H atom abstraction, *e.g.* the corresponding amides, could neither be identified nor isolated. This is attributed to subsequent reaction pathways such as scrambling of the amide ligands, as observed in a related cobalt system.<sup>23</sup> Subjecting  $[1]$  to an excess  $PEt_3$  resulted in initial disappearance of the  $^{31}P$  NMR signal of  $PEt_3$ . This phenomenon pointed to reversible coordination of the phosphine to the paramagnetic metal centre leading to spin polarisation and disappearance of the  $^{31}P$  signal.<sup>39</sup> Addition of a stronger donor (2,2'-bipyridine) to such a reaction mixture after 24 h led immediately to reoccurrence of the  $PEt_3$  signal, and more importantly small amounts of the nitrene transfer product  $MesN=PEt_3$  (Scheme 2). This points to a slightly electrophilic behaviour of  $[1]$ . In contrast,  $[1]^-$  is completely inert towards  $PEt_3$ , as was also observed for the related cobalt complex.<sup>23</sup> On the other hand  $[1]^-$  reacts with CO to give  $MesNCO$  under nitrene transfer, whereas  $[1]$  does not.

Isonitriles ( $tBuNC$ ,  $MesNC$ ) interact with both complexes, however no reaction product could be identified (*i.e.*, the

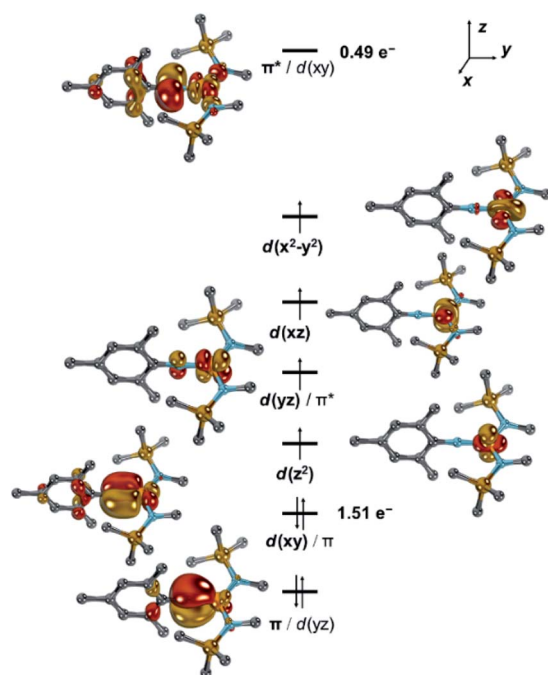
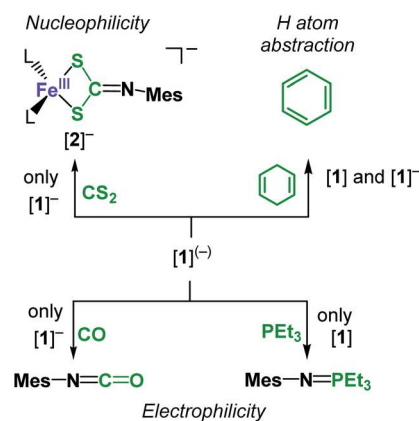


Fig. 5 Electronic structure of  $[1]$  by CASSCF(10,9). Dipp groups were truncated by methyl groups, hydrogen atoms are omitted for clarity, one set of bonding and antibonding Dipp-centred  $\pi$ -orbitals is omitted for clarity.



Scheme 2 Diverging reactivity of  $[1]$  and  $K(m)[1]$  towards nucleophiles, electrophiles, and C–H bonds.



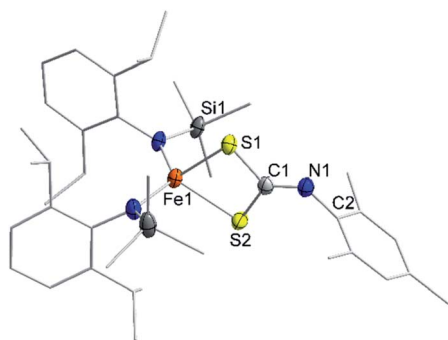


Fig. 6 Solid state structure of  $K(m)[2]$ . The  $K(m)$  cation as well as H atoms are omitted for clarity.

presumed carbodiimide  $RNC=NMe_s$ ). Probing the nucleophilicity using  $CS_2$  as a substrate revealed that  $[1]^-$  is unaffected for a prolonged period of time.  $[1]^-$  on the other hand reacted readily *via* insertion into the imido metal bond resulting in the dithiocarbonimidate complex  $[L_2Fe(\eta^2-S_2C=NMe_s)]^-$ ,  $[2]^-$  (Fig. 6, Scheme 2). The assembly of a dithiocarbonimidate ligand *via* this reaction is remarkable, as in the coordination sphere of a metal it was only achieved by a  $[2 + 2]$  addition of organo isothiocyanates with transient terminal metal sulfides<sup>40</sup> or oxidation of isonitriles with metal persulfides.<sup>41</sup> The formation of  $[2]^-$  resembles the insertion of a carbodiimide into the iron(II) imido bond of the nucleophilic  $[(Ph_2B(^tBuIM)_2)Fe(NDipp)]^-$ . In both cases it likely results from an initial  $[2 + 2]$  cycloaddition of one of the  $C=X$  bonds with the  $M-N$  unit, in resemblance to the reaction of an imido nickel(II) complex with  $CO_2$  or an imido iron(IV) complex with a carbodiimide ( $PhNCNPh$ ).<sup>26,42</sup>  $[2]^-$  exhibits in solution a magnetic moment of  $5.39 \mu_B$  that is close to the spin-value of an  $S = 5/2$  ion ( $\mu_{s.o.} = 5.92 \mu_B$ ). It shows that despite its mostly iron(II) imidyl character  $K\{m\}[1]$  reacts with an electrophile as an iron(III) imide, thus underscoring the electronic flexibility of the imido iron unit.

## Conclusion

Concluding, we describe with  $[Fe(NMe_s)L_2]^{0,-}$  ( $L = -N(Dipp)SiMe_3$ ) a pair of isostructural imido iron complexes in two oxidation states. The electronic structures of the two compounds were comprehensively assessed, amongst others by EPR and  $^{57}Fe$  Mössbauer spectroscopy and magnetometry, and revealed for both complexes a high-spin state. In line with the computational analysis and structural features, the neutral compound shares iron(II) nitrene and iron(III) imidyl character, whereas the reduced form is described best as an iron(II) imidyl. The change of the complexes' oxidation state is thus ligand and metal based, revealing the electronic flexibility of the imido metal bond. The ambiguity of the  $[FeNR]$  unit is reflected best by  $[Fe(NMe_s)L_2]^-$  which shows a nucleophilic and electrophilic behaviour. Upon oxidation to  $[Fe(NMe_s)L_2]^0$  the nucleophilicity is lost in accordance with a shift to a more nitrene-like electronic situation. We foresee these reactivity shifts to be relevant for directing NR group transfer reactivity of metal imidos towards different functionalities in organic substrates.

## Data availability

All experimental procedures, spectral data, and computational data are included in the ESI.† Xyz coordinates may be obtained *via* the ESI,† output files can be obtained by D. M upon request. NMR/EPR/IR/Mössbauer raw data is so far only available upon request to C. G. W.

## Author contributions

S. R. carried out the synthetic work and analytical characterization, including the crystallographic studies. S. D. recorded the SQUID and  $^{57}Fe$  Mössbauer data, and both S. D. and F. M. analyzed the data. B. B., A. R., A. S. and C. L. recorded and analyzed the EPR data. C. S. performed the cyclic voltammetric analysis. D. M. performed the quantum chemical calculations. S. R. and C. G. W. wrote the manuscript with contributions from all authors.

## Conflicts of interest

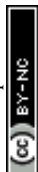
There are no conflicts to declare.

## Acknowledgements

We thank the DFG for funding (grant 5627/4-1 for C. G. W., INST 186/1329-1 FUGG (SQUID magnetometer) for F. M.). D. M. thanks the RRZ Erlangen for computational resources. This project has received funding from the European Research Council (ERC) under the European Union's Horizon 2020 Research and Innovation Program (grant agreement no. 946184 for C. L. and no. 948185 for D. M.).

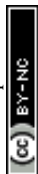
## Notes and references

- (a) P. Müller and C. Fruit, *Chem. Rev.*, 2003, **103**, 2905–2920; (b) L. Zhang and L. Deng, *Chin. Sci. Bull.*, 2012, **57**, 2352–2360; (c) Y. Park, Y. Kim and S. Chang, *Chem. Rev.*, 2017, **117**, 9247–9301; (d) Y. Liu, T. You, H.-X. Wang, Z. Tang, C.-Y. Zhou and C.-M. Che, *Chem. Soc. Rev.*, 2020, **49**, 5310–5358.
- K. Kawakita, Y. Kakiuchi, H. Tsurugi, K. Mashima, B. F. Parker, J. Arnold and I. A. Tonks, *Coord. Chem. Rev.*, 2020, **407**, 213118.
- (a) J. Strähle, *Angew. Chem.*, 1989, **101**, 957; (b) P. F. Kuijpers, J. I. van der Vlugt, S. Schneider and B. de Bruin, *Chem.–Eur. J.*, 2017, **23**, 13819–13829; (c) J. F. Berry, *Comments Inorg. Chem.*, 2009, **30**, 28–66.
- K. Ray, F. Heims and F. F. Pfaff, *Eur. J. Inorg. Chem.*, 2013, **2013**, 3784–3807.
- A. Grünwald, S. S. Anjana and D. Munz, *Eur. J. Inorg. Chem.*, 2021, **2021**, 4147–4166.
- (a) R. A. Eikey and M. M. Abu-Omar, *Coord. Chem. Rev.*, 2003, **243**, 83–124; (b) N. Hazari and P. Mountford, *Acc. Chem. Res.*, 2005, **38**, 839–849; (c) J. L. Martinez, S. A. Lutz, H. Yang, J. Xie, J. Telser, B. M. Hoffman, V. Carta, M. Pink, Y. Losovj and J. M. Smith, *Science*, 2020, **370**, 356–359.





- 7 E. R. King, E. T. Hennessy and T. A. Betley, *J. Am. Chem. Soc.*, 2011, **133**, 4917–4923.
- 8 M. J. T. Wilding, D. A. Iovan, A. T. Wrobel, J. T. Lukens, S. N. MacMillan, K. M. Lancaster and T. A. Betley, *J. Am. Chem. Soc.*, 2017, **139**, 14757–14766.
- 9 W. Mao, D. Fehn, F. W. Heinemann, A. Scheurer, D. Munz and K. Meyer, *Angew. Chem., Int. Ed.*, 2021, **60**, 16480–16486.
- 10 Y. Park, S. P. Semproni, H. Zhong and P. J. Chirik, *Angew. Chem., Int. Ed.*, 2021, **60**, 14376–14380.
- 11 Y. Dong, C. J. Lund, G. J. Porter, R. M. Clarke, S.-L. Zheng, T. R. Cundari and T. A. Betley, *J. Am. Chem. Soc.*, 2021, **143**, 817–829.
- 12 Y. Dong, J. T. Lukens, R. M. Clarke, S.-L. Zheng, K. M. Lancaster and T. A. Betley, *Chem. Sci.*, 2020, **123**, 4623.
- 13 K. M. Carsch, I. M. DiMucci, D. A. Iovan, A. Li, S.-L. Zheng, C. J. Titus, S. J. Lee, K. D. Irwin, D. Nordlund, K. M. Lancaster and T. A. Betley, *Science*, 2019, **365**, 1138–1143.
- 14 (a) A. G. Bakhoda, Q. Jiang, Y. M. Badiei, J. A. Bertke, T. R. Cundari and T. H. Warren, *Angew. Chem., Int. Ed.*, 2019, **58**, 3421–3425; (b) J. Moegling, A. Hoffmann, F. Thomas, N. Orth, P. Liebhäuser, U. Herber, R. Rampmaier, J. Stanek, G. Fink, I. Ivanović-Burmazović and S. Herres-Pawlis, *Angew. Chem., Int. Ed.*, 2018, **57**, 9154–9159; (c) M. J. B. Aguila, Y. M. Badiei and T. H. Warren, *J. Am. Chem. Soc.*, 2013, **135**, 9399–9406; (d) T. Corona, L. Ribas, M. Rovira, E. R. Farquhar, X. Ribas, K. Ray and A. Company, *Angew. Chem., Int. Ed.*, 2016, **55**, 14005–14008; (e) S.-L. Abram, I. Monte-Pérez, F. F. Pfaff, E. R. Farquhar and K. Ray, *Chem. Commun.*, 2014, **50**, 9852–9854.
- 15 F. Dielmann, D. M. Andrada, G. Frenking and G. Bertrand, *J. Am. Chem. Soc.*, 2014, **136**, 3800–3802.
- 16 C. M. Thomas, N. P. Mankad and J. C. Peters, *J. Am. Chem. Soc.*, 2006, **128**, 4956–4957.
- 17 S. D. Brown and J. C. Peters, *J. Am. Chem. Soc.*, 2005, **127**, 1913–1923.
- 18 I. Nieto, F. Ding, R. P. Bontchev, H. Wang and J. M. Smith, *J. Am. Chem. Soc.*, 2008, **130**, 2716–2717.
- 19 (a) L. Zhang, Y. Liu and L. Deng, *J. Am. Chem. Soc.*, 2014, **136**, 15525–15528; (b) Y. Liu, J. Du and L. Deng, *Inorg. Chem.*, 2017, **56**, 8278–8286.
- 20 Y. Gao, V. Carta, M. Pink and J. M. Smith, *J. Am. Chem. Soc.*, 2021, **143**, 5324–5329.
- 21 J. R. Winkler and H. B. Gray, in *Molecular Electronic Structures of Transition Metal Complexes I*, ed. D. M. P. Mingos, P. Day and J. P. Dahl, Springer Berlin Heidelberg, Berlin, Heidelberg, 2012, vol. 142, pp. 17–28.
- 22 D. A. Iovan and T. A. Betley, *J. Am. Chem. Soc.*, 2016, **138**, 1983–1993.
- 23 A. Reckziegel, M. Kour, B. Battistella, S. Mebs, K. Beuthert, R. Berger and C. G. Werncke, *Angew. Chem., Int. Ed.*, 2021, **60**, 15376–15380.
- 24 (a) A. Reckziegel, C. Pietzonka, F. Kraus and C. G. Werncke, *Angew. Chem., Int. Ed.*, 2020, **59**, 8527–8531; (b) R. Weller, L. Ruppach, A. Shlyaykher, F. Tambornino and C. G. Werncke, *Dalton Trans.*, 2021, **50**, 10947–10963.
- 25 (a) A. K. Verma, T. N. Nazif, C. Achim and S. C. Lee, *J. Am. Chem. Soc.*, 2000, **122**, 11013–11014; (b) S. D. Brown, T. A. Betley and J. C. Peters, *J. Am. Chem. Soc.*, 2003, **125**, 322–323; (c) S. C. Bart, E. Lobkovsky, E. Bill and P. J. Chirik, *J. Am. Chem. Soc.*, 2006, **128**, 5302–5303; (d) C. Ni, J. C. Fettinger, G. J. Long, M. Brynda and P. P. Power, *Chem. Commun.*, 2008, 6045; (e) J. J. Scepaniak, J. A. Young, R. P. Bontchev and J. M. Smith, *Angew. Chem., Int. Ed.*, 2009, **48**, 3158–3160; (f) R. E. Cowley, N. J. DeYonker, N. A. Eckert, T. R. Cundari, S. DeBeer, E. Bill, X. Ottenwaelder, C. Flaschenriem and P. L. Holland, *Inorg. Chem.*, 2010, **49**, 6172–6187; (g) H. Zhang, Z. Ouyang, Y. Liu, Q. Zhang, L. Wang and L. Deng, *Angew. Chem., Int. Ed.*, 2014, **53**, 8432–8436; (h) S. Kuppuswamy, T. M. Powers, B. M. Johnson, M. W. Bezpalko, C. K. Brozek, B. M. Foxman, L. A. Berben and C. M. Thomas, *Inorg. Chem.*, 2013, **52**, 4802–4811; (i) B. P. Jacobs, P. T. Wolczanski, Q. Jiang, T. R. Cundari and S. N. MacMillan, *J. Am. Chem. Soc.*, 2017, **139**, 12145–12148.
- 26 L. Wang, L. Hu, H. Zhang, H. Chen and L. Deng, *J. Am. Chem. Soc.*, 2015, **137**, 14196–14207.
- 27 M. J. T. Wilding, D. A. Iovan and T. A. Betley, *J. Am. Chem. Soc.*, 2017, **139**, 12043–12049.
- 28 A. Sridharan, A. C. Brown and D. L. M. Suess, *Angew. Chem., Int. Ed.*, 2021, **60**, 12802–12806.
- 29 C. Schneider, S. Demeshko, F. Meyer and C. G. Werncke, *Chem.–Eur. J.*, 2021, **27**, 6348–6353.
- 30 Y. Sanakis, P. P. Power, A. Stubna and E. Münck, *Inorg. Chem.*, 2002, **41**, 2690–2696.
- 31 A. Eichhöfer, Y. Lan, V. Mereacre, T. Bodenstern and F. Weigend, *Inorg. Chem.*, 2014, **53**, 1962–1974.
- 32 E. C. Alyea, D. C. Bradley, R. G. Copperthwaite, K. D. Sales, B. W. Fitzsimmons and C. E. Johnson, *J. Chem. Soc. D*, 1970, 1715–1716.
- 33 K. E. Aldrich, B. S. Fales, A. K. Singh, R. J. Staples, B. G. Levine, J. McCracken, M. R. Smith and A. L. Odom, *Inorg. Chem.*, 2019, **58**, 11699–11715.
- 34 P. Gütllich, *Mössbauer Spectroscopy and Transition Metal Chemistry. Fundamentals and Applications*, Springer Berlin/Heidelberg, Berlin, Heidelberg, 2011.
- 35 (a) M. R. Anneser, G. R. Elpitiya, J. Townsend, E. J. Johnson, X. B. Powers, J. F. DeJesus, K. D. Vogiatzis and D. M. Jenkins, *Angew. Chem., Int. Ed.*, 2019, **58**, 8115–8118; (b) K. Searles, S. Fortier, M. M. Khusniyarov, P. J. Carroll, J. Sutter, K. Meyer, D. J. Mindiola and K. G. Caulton, *Angew. Chem., Int. Ed.*, 2014, **53**, 14139–14143.
- 36 F. Neese, F. Wennmohs, U. Becker and C. Riplinger, *J. Chem. Phys.*, 2020, **152**, 224108.
- 37 X.-N. Yao, J.-Z. Du, Y.-Q. Zhang, X.-B. Leng, M.-W. Yang, S.-D. Jiang, Z.-X. Wang, Z.-W. Ouyang, L. Deng, B.-W. Wang and S. Gao, *J. Am. Chem. Soc.*, 2017, **139**, 373–380.
- 38 J. H. Enemark and R. D. Feltham, *Coord. Chem. Rev.*, 1974, **13**, 339–406.
- 39 R. Weller, A. Gonzalez, H. Gottschling, C. Hänisch and C. G. Werncke, *Z. Anorg. Allg. Chem.*, 2022, e202100338.
- 40 (a) J. Ahmed, K. Itoh, I. Matsuda, F. Ueda, Y. Ishii and J. A. Ibers, *Inorg. Chem.*, 1977, **16**, 620–624; (b) K.-E. Lee,



- X. Chang, Y.-J. Kim, H. S. Huh and S. W. Lee, *Organometallics*, 2008, **27**, 5566–5570; (c) Y.-J. Kim, H.-T. Jeon, K.-E. Lee and S. W. Lee, *J. Organomet. Chem.*, 2010, **695**, 2258–2263; (d) R. O. Harris, J. Powell, A. Walker and P. V. Yaneff, *J. Organomet. Chem.*, 1977, **141**, 217–229.
- 41 R. D. Adams, B. Captain, O.-S. Kwon and S. Miao, *Inorg. Chem.*, 2003, **42**, 3356–3365.
- 42 D. J. Mindiola, R. Waterman, V. M. Iluc, T. R. Cundari and G. L. Hillhouse, *Inorg. Chem.*, 2014, **53**, 13227–13238.



## 4 Unveröffentlichte Ergebnisse

In diesem Kapitel sind Ergebnisse, die im Rahmen dieser Promotion erhalten und bisher nicht veröffentlicht wurden, zusammengefasst.

### 4.1 Weiterführende Untersuchungen zum Reaktionsverhalten von trigonalen Imido-Cobalt-Komplexen

Der bereits beschriebenen Komplex  $\text{K}\{\text{crypt.222}\}\text{Co}(\text{N}(\text{SiMe}_3)_2)_2\text{N}^t\text{Bu}$  (**102**) weist eine hohe Reaktivität gegenüber H-Atom-Abstraktionen von C-H-Bindungen auf. Im Folgenden wurden weitere Element-Wasserstoff-Bindungen sowie die Reaktivität gegenüber elektro- und nukleophilen Substraten untersucht.

#### H-Atom-Transfer von Element-Wasserstoff-Bindungen

Die Verwendung von zwei Äquivalenten 2,4,6-Tri-*tert*-Butylphenol führte ebenfalls zur Bildung eines trigonalen Phenolat-Komplexes **128**.

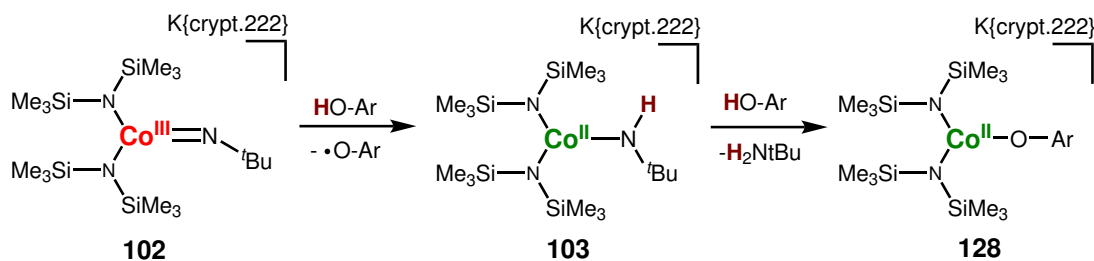


Abb. 54: Reaktion des trigonalen Imido-Cobalt-Komplexes **102** mit 2,4,6-Tri-*tert*-Butylphenol ( $\text{HOAr}$ ) unter Bildung des Amido-Komplexes **103** gefolgt von der Bildung des Phenolat-Komplexes **128**.

Die Bildung dieses Komplexes erfolgt vermutlich über eine H-Atom-Abstraktion des Imido-Komplexes **102**, gefolgt von einer Deprotonierung des Phenoles durch den Amido-Komplex **103** (vgl. Abb. 54). Die gezielte Synthese des Komplexes war durch die Umsetzung des Amido-Komplexes **103** mit dem Phenol möglich, was den gezeigten Syntheseweg bestätigt. Die Festkörperstruktur von **128** konnte durch Röntgenbeugungsexperimente am Einkristall bestimmt werden (vgl. Abb. 55).

Die Struktur weist Fehlordnungen an der *para-tert*-Butyl-Gruppe des Phenolat-Liganden, zwei  $\text{SiMe}_3$ -Gruppen der Amido-Liganden und einem Sauerstoff-Atom des crypt.222 auf, die keinen Einfluss auf die Koordinationsumgebung des Cobalt-Ions haben und aus diesem Grund nicht weiter diskutiert werden. Das Zentralatom ( $\text{Co1}$ ) ist trigonal planar von zwei Amido- und einem Phenolat-Liganden umgeben. Die Bindungslänge ersterer ( $\text{Co-N}_{\text{Amido}}$ : 1,95 Å) ist in guter Übereinstimmung mit anderen beschriebenen trigonalen Cobalt(II)-Komplexen. Die Bindung des Phenolat-Liganden weist eine Länge von 1,894(5) Å auf, was im Bereich der bekannten Phenolat-Cobalt(II)-Bindungen liegt (1,87 – 1,90 Å). Der Ligand zeigt nur eine geringe Abwinklung ( $\text{Co-O-C}$ : 171,0(5)°), was auf den hohen sterischen Anspruch aller Liganden zurückzuführen ist.[98–101]

Das  $^1\text{H-NMR}$ -Spektrum der Verbindung zeigt ein Signal mit einer Verschiebung von -13,9 ppm, welches den  $\text{N}(\text{SiMe}_3)_2$ -Liganden zugeordnet werden kann (vgl. Abb. 82).

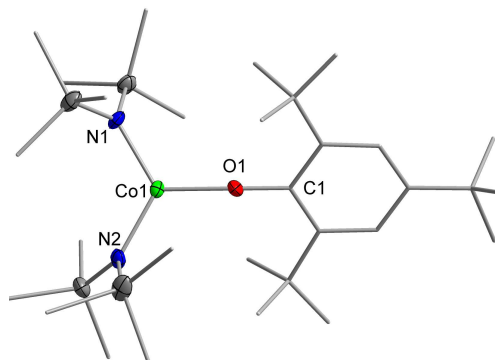


Abb. 55: Molekülstruktur von **128** im Festkörper. Das  $\text{K}\{\text{crypt.222}\}$ -Kation, Wasserstoffatome und Fehlorderungen der Liganden sind aus Gründen der Übersichtlichkeit nicht dargestellt. Kohlenstoff-Atome sind im Wire/Sticks-Modell dargestellt. Die Größe der Ellipsoide entspricht einer Aufenthaltswahrscheinlichkeit von 50 %.

Weiterhin ist das Signal der *ortho-tert*-Butyl-Gruppen (9,52 ppm), sowie der *meta*-H-Atome (40,5 ppm) des Phenolat-Liganden mit einer paramagnetischen Verschiebung zu erkennen. Die Signale des Kryptanden (3,02 - 2,04 ppm) und der *para-tert*-Butyl-Gruppe (1,50 ppm) weisen keine starke Verschiebung auf, was für letztere auf eine schwache Wechselwirkung mit dem paramagnetischen Zentrum hindeutet.

### Umsetzung mit Organoboranen

Neben O–H-Bindungen wurde der H-Atom-Transfer von Boranen untersucht. Die Umsetzung des Imido-Cobalt-Komplexes **102** mit Pinakolboran zeigte dabei keinen selektiven Reaktionsverlauf. Die  $^1\text{H}$ - und  $^{11}\text{B}$ -NMR-Reaktionskontrolle der Umsetzung mit 9-Borabicyclo(3.3.1)nonan (9-BBN) hingegen, zeigte die Bildung des Boramins **129** sowie des linear koordinierten Cobalt(I)-Komplex  $\text{K}\{\text{crypt.222}\}[\text{Co}(\text{N}(\text{SiMe}_3)_2)_2]$  (**101**).

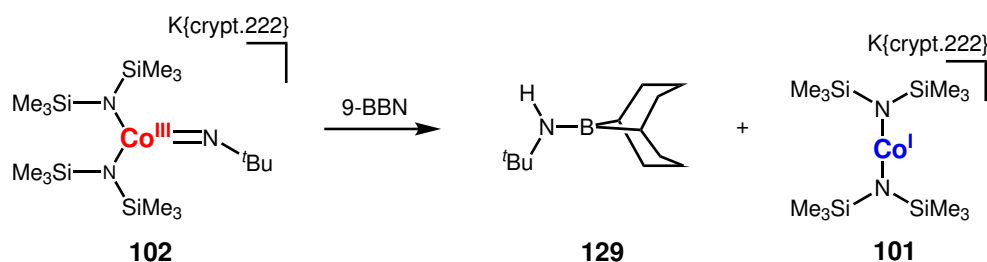


Abb. 56: Bildung des Boramins **129** durch Umsetzung von 9-BBN mit **102**.

Um einen genaueren Einblick in den Reaktionsmechanismus zu erhalten, wurde das Substrat ebenfalls mit dem Amido-Cobalt-Komplex **103** umgesetzt, was zur Bildung des Dihydridoborat-Cobalt-Komplexes  $\text{K}\{\text{crypt.222}\}[\text{Co}(\text{N}(\text{SiMe}_3)_2)_2(\text{H}_2\text{-9-BBN})]$  (**130**) führte. Die Molekülstruktur konnte durch Röntgenbeugungsexperimente am Einkristall bestimmt werden (vgl. Abb. 58).

Das Cobalt-Ion ist verzerrt tetraedrisch von zwei Amido-Liganden und zwei Wasserstoff-Atomen koordiniert. Die Bindungslängen ersterer sind mit 1,95 Å vergleichbar zu den zuvor beschriebenen Cobalt(II)-Komplexen. Der Abstand zwischen dem Cobalt-Ion und dem Bor-Atom des Hydridoborat-Liganden (B1) beträgt 2,21 Å, was



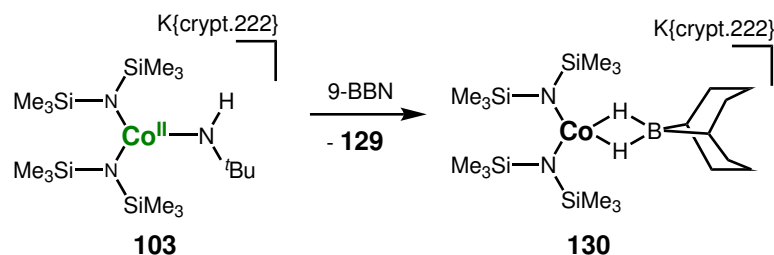


Abb. 57: Bildung des Dihydridoborat-Cobalt-Komplexes **130** durch Umsetzung von 9-BBN mit **103**.

eine geringfügige Aufweitung im Vergleich zu bekannten Cobalt(II)-Komplexen mit Dihydridoborat-Liganden (2,13 - 2,16) zeigt.[102, 103] Die Bildung dieses Komplexes hat vermutlich über einen Hydrido-Komplex der Form  $[\text{Co}(\text{N}(\text{SiMe}_3)_2)_2\text{H}]^-$  und anschließenden Addukt-Bildung mit einem weiteren Äquivalent 9-BBN stattgefunden.

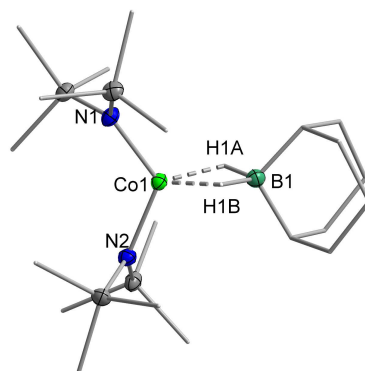


Abb. 58: Molekülstruktur von **130** im Festkörper. Das  $\text{K}\{\text{crypt.222}\}$ -Kation und nicht relevante Wasserstoffatome sind aus Gründen der Übersichtlichkeit nicht dargestellt. Kohlenstoff-Atome sind im Wire/Sticks-Modell und Wasserstoff-Atome als Kugel-Modell dargestellt. Die Größe der Ellipsoide entspricht einer Aufenthaltswahrscheinlichkeit von 50 %.

Das  $^1\text{H}$ -NMR-Spektrum des Komplexes zeigt ein verbreitertes Signal mit einer Verschiebung von 1,52 ppm, was auf Grund des Integrals den  $\text{N}(\text{SiMe}_3)_2$ -Liganden zugeordnet werden kann (vgl. Abb. 83). Eine genaue Zuordnung der weiteren paramagnetischen Signale des Dihydridoborat-Liganden ist nicht möglich. Untersuchungen zur elektronischen Struktur des Übergangsmetall-Ions wurden bisher nicht durchgeführt.

### Untersuchungen zur elektrophilen Reaktivität von Imido-Cobalt-Komplexen

Um die elektronische Struktur des Imido-Liganden besser zu verstehen, wurden sowohl elektrophile, als auch nukleophile Substrate mit **102** umgesetzt. Wie bereits beschrieben, konnte kein Nitren-Transfer auf Alkene oder Phosphine beobachtet werden.[104]

### Umsetzung mit Kohlenstoffmonoxid (CO)

Bei der Reaktion des Imido-Komplexes **102** mit CO wurde die Bildung eines blauen, kristallinen Feststoffes aus der Reaktionslösung beobachtet. Durch Röntgenbeugungsexperimente am Einkristall konnten diese als  $(K\{\text{crypt.222}\})_2[\text{Co}(\text{NCO})_4]$  (**131**) identifiziert werden (vgl. Abb. 59). Die Struktur des Anions stimmt mit dem aus der Literatur bekannten Verbindungen mit anderen Kationen überein.[105] Die Bildung der Isocyanat-Liganden deutet auf eine Zersetzung des Imido-, als auch der Amido-Liganden hin. Die Umsetzung des Amido-Komplexes **103** mit CO hatte erneut die Bildung eines blauen Feststoffes zur Folge. Eine Analyse mittels Röntgenbeugungsexperimenten war hier nicht möglich.

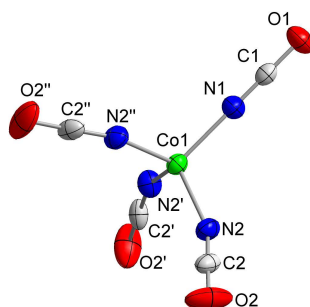


Abb. 59: Molekülstruktur von **131** im Festkörper. Die  $K\{\text{crypt.222}\}$ -Kationen sind aus Gründen der Übersichtlichkeit nicht dargestellt. Kohlenstoff-Atome sind im Wire/Sticks-Modell dargestellt. Die Größe der Ellipsoide entspricht einer Aufenthaltswahrscheinlichkeit von 50 %.

### Bildung von Tetrazen-Komplexen

Die Bildung von Tetrazen-Liganden ist eine bekannte Nebenreaktion in der Synthese von Imido-Komplexen. Diese wurde bei der Synthese von **102** bisher nicht beobachtet, was auf den sterischen Anspruch der *tert*-Butyl-Gruppe zurückzuführen ist. Um die Bildung eines Tetrazen-Liganden zu erzwingen, wurde **102** mit dem sterisch wenig anspruchsvollen und elektronenarmen Phenylazid umgesetzt.

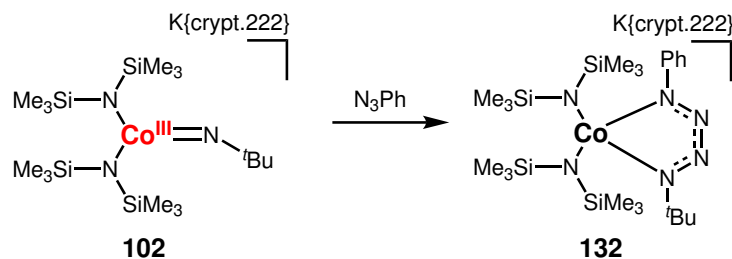


Abb. 60: Bildung des Tetrazen-Komplexes **132** durch Umsetzung des Imido-Cobalt-Komplexes **102** mit Phenylazid.

Bei der Reaktion konnte ein Farbwechsel von dunkelrot zu dunkelgrün beobachtet werden. Die isolierten Kristalle konnten, mittels Röntgenbeugungsexperimenten am Einkristall als der gemischte Tetrazen-Komplex  $K\{\text{crypt.222}\}\text{Co}(\text{N}(\text{SiMe}_3)_2)_2$

(PhN<sup>t</sup>Bu) (**132**) identifiziert werden (vgl. Abb. 61). Hierbei handelt es sich um den ersten Tetrazen-Cobalt-Komplex mit verschiedenen Substituenten. Das Cobalt-Ion ist verzerrt tetraedrisch von zwei Amido- und dem Tetrazen-Liganden koordiniert. Erstere weisen eine Bindungslänge von 1,98 Å auf, was vergleichbar mit den zuvor beschriebenen Amido-Cobalt-Komplexen ist. Die Abstände des Cobalt-Ions zu den Stickstoff-Atomen des Tetrazen-Liganden unterscheiden sich geringfügig, was auf die Unterschiede in der elektronischen Struktur und dem sterischen Anspruch der Substituenten zurückzuführen ist. Die N–N-Bindungen im Tetrazen-Liganden unterscheiden sich nur geringfügig (1,31 – 1,33 Å), was auf einen radikalmonoanionischen Bindungsmodus des Liganden hindeutet.

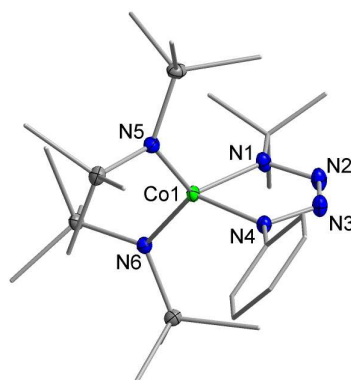


Abb. 61: Molekülstruktur von **132** im Festkörper. Das K{crypt.222}-Kation und Wasserstoffatome sind aus Gründen der Übersichtlichkeit nicht dargestellt. Kohlenstoff-Atome sind im Wire/Sticks-Modell dargestellt. Die Größe der Ellipsoide entspricht einer Aufenthaltswahrscheinlichkeit von 50 %.

Das <sup>1</sup>H-NMR-Spektrum des Komplexes zeigt ein stark verbreitertes Signal mit einer Verschiebung von 0,37 ppm, welches den N(SiMe<sub>3</sub>)<sub>2</sub>-Liganden zugeordnet wird (Abb. 84). Das Signal der *tert*-Butyl-Gruppe kann auf Grund der Integralverhältnisse dem Signal mit einer Verschiebung von 6,59 ppm zugeordnet werden. Für die Signale der Phenyl-Gruppe (65,0, 47,4 und -11,2 ppm) ist auf Grund deren geringen Intensität keine genauere Zuordnung möglich. Das magnetische Moment von 3,29 μ<sub>B</sub> (μ<sub>s.o.</sub> (*S* = 1): 2,83 μ<sub>B</sub>) deutet auf ein System mit einem Gesamtspin von *S* = 1 und könnte damit auf eine antiferromagnetische Kopplung zwischen dem radikalischen Liganden (*S* = 1/2) und einem *high-spin* Cobalt(II)-Ion (*S* = 3/2), was auch durch die Bindungslängen der N(SiMe<sub>3</sub>)<sub>2</sub>-Liganden angedeutet wird.

## Reaktivität gegenüber CO<sub>2</sub>-Derivaten

Um den nukleophilen Charakter des Imido-Liganden nachzuweisen, wurden entsprechende Kohlenstoff-Verbindungen genutzt. Da für CO<sub>2</sub> Nebenreaktionen mit den Amido-Liganden beobachtet wurden, werden im Folgenden verschiedene Derivate betrachtet.

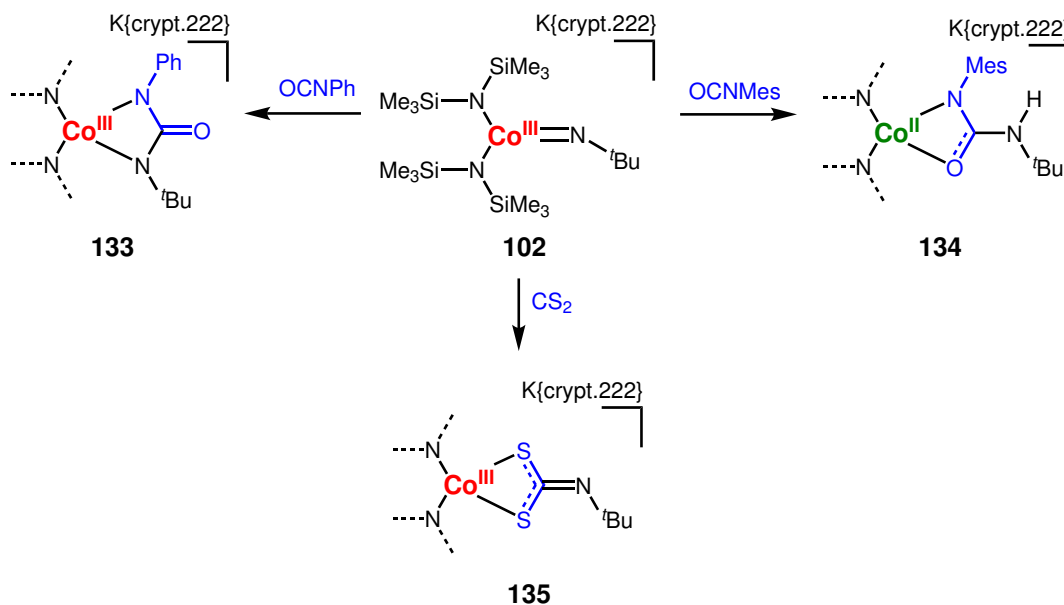


Abb. 62: Umsetzung des trigonalen Imido-Cobalt-Komplexes **102** mit Phenyl- und Mesitylisocyanat, sowie mit CS<sub>2</sub>.

Die Umsetzung mit Phenylisocyanat zeigte eine Farbänderung von dunkelrot zu einem dunklen Violett. Durch die Aufarbeitung konnten entsprechende Kristalle, geeignet für Röntgenbeugungsexperimente am Einkristall, erhalten werden. Die bestimmte Struktur zeigt die Bildung von K{crypt.222}Co(N(SiMe<sub>3</sub>)<sub>2</sub>)<sub>2</sub>(PhN(CO)N<sup>t</sup>Bu) **133** (vgl. Abb. 63). Dieser entsteht vermutlich über eine 2+2-Cycloaddition des Isocyanats an die Co-N<sub>Imido</sub>-Bindung. Die Bindungslängen der Amido-Liganden sind mit 1,93 Å im Bereich der in dieser Arbeit beschriebenen Cobalt(III)-Komplexe mit N(SiMe<sub>3</sub>)<sub>2</sub>-Ligandensystem einzuordnen. Der Abstand des Cobalt-Ions zu dem *tert*-Butyl-substituierten Stickstoff-Atom ist mit 2,0 Å größer als zu dem Phenyl-substituierten Stickstoff-Atom, was auf den unterschiedlichen sterischen Anspruch der Substituenten zurückzuführen ist. Der Abstand zwischen C1 und O1 liegt mit 1,24 Å im Bereich einer C–O-Doppelbindung. Das <sup>1</sup>H-NMR-Spektrum der Verbindung zeigt drei Signale mit einer paramagnetischen Verschiebung sowie einer starken Verbreiterung (vgl. Abb. 85). Auf Grund der Integral-Verhältnisse kann das Signal mit einer Verschiebung von 6,27 ppm vermutlich den N(SiMe<sub>3</sub>)<sub>2</sub>-Liganden, sowie das Signal mit einer Verschiebung von 22,2 ppm der *tert*-Butyl-Gruppe zugeordnet werden. Das Signal mit einer Verschiebung von 115,2 ppm stammt somit von den Protonen der Phenyl-Gruppe. Eine genauere Zuordnung ist auf Grund der geringen Intensität des Signales nicht möglich. Weiterhin ist ein Signal das Komplex-Anion von [Co(N(SiMe<sub>3</sub>)<sub>2</sub>)<sub>3</sub>]<sup>−</sup> (**93**) mit einer Verschiebung von -7,7 ppm zu erkennen, was auf eine partielle Zersetzung hindeutet.

Um den Koordinationsmodus des gezeigten Ureat-Liganden zu untersuchen, wurde das sterisch anspruchsvollere Mesitylisocyanat verwendet. Bei der Umsetzung mit

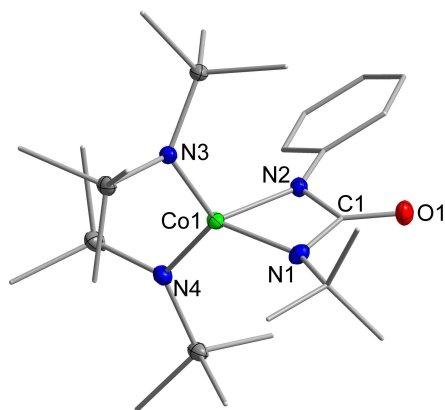


Abb. 63: Molekülstruktur von **133** im Festkörper. Das  $\text{K}\{\text{crypt.222}\}$ -Kation und Wasserstoffatome sind aus Gründen der Übersichtlichkeit nicht dargestellt. Kohlenstoff-Atome sind im Wire/Sticks-Modell dargestellt. Die Größe der Ellipsoide entspricht einer Aufenthaltswahrscheinlichkeit von 50 %.

**102** konnte zunächst ein Farbwechsel zu Violett beobachtet werden. Aus der Reaktionslösung konnten nach wenigen Tagen jedoch grüne Kristalle erhalten werden, die mittels Röntgenbeugungsexperimenten untersucht wurden. Die so erhaltene Struktur zeigt, dass es sich bei der Verbindung um  $\text{K}\{\text{crypt.222}\}\text{Co}(\text{N}(\text{SiMe}_3)_2)_2(\text{MesN}(\text{CO})\text{N}(\text{H})^t\text{Bu})$  **134** handelt (vgl. Abb. 64).

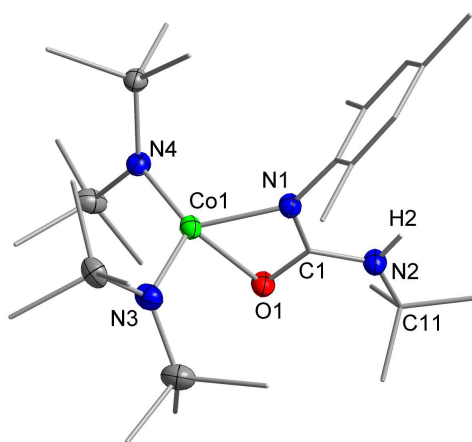


Abb. 64: Molekülstruktur von **134** im Festkörper. Das  $\text{K}\{\text{crypt.222}\}$ -Kation und nicht relevante Wasserstoffatome sind aus Gründen der Übersichtlichkeit nicht dargestellt. Kohlenstoff-Atome sind im Wire/Sticks-Modell dargestellt. Die Größe der Ellipsoide entspricht einer Aufenthaltswahrscheinlichkeit von 50 %.

Das Cobalt-Ion ist verzerrt tetraedrisch von zwei Amido- und einem Ureat-Liganden umgeben. Die Bindungslängen der  $\text{N}(\text{SiMe}_3)_2$ -Liganden zeigen im Vergleich zu **133** eine Aufweitung auf  $1,98 \text{ \AA}$ , was vergleichbar zu den beschriebenen trigonalen Amido-Cobalt-Komplexen ist. Die Koordination des Ureat-Liganden erfolgt über ein Stickstoff- und ein Sauerstoff-Atom und zeigt eine Bindungslänge von  $2,05 \text{ \AA}$  für das Stickstoff-Atoms (N1), was mit dem zuvor beschriebenen Ureat-Liganden übereinstimmt. Der Abstand zu dem Sauerstoff-Atom (O1) deutet mit  $2,20 \text{ \AA}$  auf eine schwächere Wechselwirkung mit dem Cobalt-Ion hin. Die Bindung zwischen dem zentralen

Kohlenstoff-Atom (C1) und dem Sauerstoff-Atom (O1) zeigt im Zusammenhang mit der Sauerstoff-Cobalt-Wechselwirkung eine leichte Aufweitung der Doppelbindung auf 1,27 Å. Der Abstand des abgewandten und koordinierenden Stickstoff-Atoms zu dem zentralen Kohlenstoff-Atom unterscheiden sich nur geringfügig, was auf eine Einbindung hindeutet. Dies könnte über einen H-Atom-Transfer von einem Lösungsmittelmolekül auf N2 erklärt werden. Der Winkel um das Stickstoff-Atom N2 von 125 ° (C1–N2–C11) unterstützt diese Annahme ebenfalls. Da ein direkter Farbwechsel zu dunkelviolett beobachtet wurde, hat vermutlich erst die Bildung des Ureat-Liganden stattgefunden, gefolgt von der Abstraktion eines H-Atoms. Um die Synthese zu optimieren, könnte 1,4-Cyclohexadien als guter H-Atom Donor nach der Bildung des Ureat-Liganden zugegeben werden oder die Umsetzung direkt mit dem Amido-Cobalt-Komplex **103** durchgeführt werden.

Anschließend wurde die Umsetzung von **102** mit CS<sub>2</sub> untersucht. Die Reaktionslösung zeigte nur eine geringe Aufhellung. Die erhaltenen dunkelroten Kristalle konnten mit Röntgenbeugungsexperimenten am Einkristall untersucht werden und zeigten die Bildung von K{crypt.222}Co(N(SiMe<sub>3</sub>)<sub>2</sub>)<sub>2</sub>(S<sub>2</sub>CN<sup>t</sup>Bu) (**135**). Dies zeigt die Bildung eines Dithiocarbamid-Liganden durch Insertion des Substrates in die Imido-Cobalt-Bindung (vgl. Abb. 65).

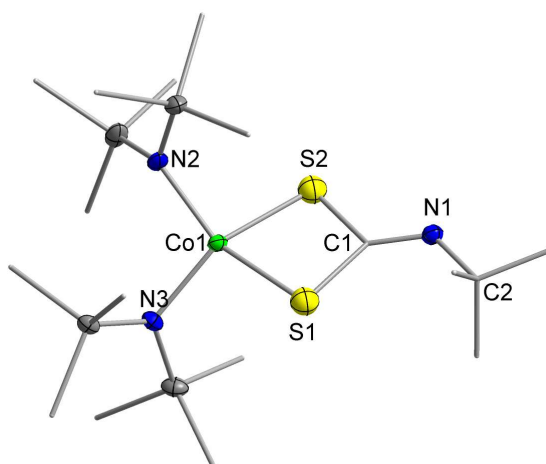


Abb. 65: Molekülstruktur von **135** im Festkörper. Das K{crypt.222}-Kation und nicht relevante Wasserstoffatome sind aus Gründen der Übersichtlichkeit nicht dargestellt. Kohlenstoff-Atome sind im Wire/Sticks-Modell dargestellt. Die Größe der Ellipsoide entspricht einer Aufenthaltswahrscheinlichkeit von 50 %.

Das Zentralatom ist verzerrt tetraedrisch von zwei Amido-Liganden und den beiden Schwefelatomen des Carbamid-Liganden koordiniert. Die Bindungslängen der N(SiMe<sub>3</sub>)<sub>2</sub>-Liganden sind mit 1,93 Å im Bereich der trigonalen Imido-Cobalt-Komplexe und vergleichbar zu **133**. Die Bindungen zwischen den Schwefel-Atomen und dem zentralen Kohlenstoff-Atom sind mit 1,79 Å symmetrisch und im Bereich einer Einfachbindung, was auf einen dianionischen Liganden hindeutet. Der Abstand zwischen dem C1 und N1 ist mit 1,25 Å im Bereich einer Doppelbindung und der Bindungswinkel um N1 (C1–N1–C2) beträgt 122 °. Die Bindungslängen in dem Dithiocarbamid-Liganden sind in guter Übereinstimmung mit dem bereits veröffentlichten Dithiocarbamid-Eisen-Komplex **136**, der im Zuge dieser Arbeit beschrieben werden konnte.[106]

Das  $^1\text{H}$ -NMR-Spektrum von **135** zeigt ein Signal mit einer Verschiebung von -3,15 ppm, welches den  $\text{N}(\text{SiMe}_3)_2$ -Liganden zugeordnet werden kann (vgl. Abb. 86). Das Signal der *tert*-Butyl-Gruppe weist mit 3,84 ppm nur eine geringe Verschiebung auf, was auf eine schwache Wechselwirkung mit dem paramagnetischen Cobalt-Ion hindeutet. Weiterhin zeigen die Signale um 0 ppm eine teilweise Zersetzung des Komplexes in Lösung. Diese Verunreinigungen schlagen sich auch in einer bislang starken Abweichung hinsichtlich der Reinheit mittels Elementaranalyse wieder.

Zusammenfassend konnte über die hohe Reaktivität zu H-Atom-Abstraktionen hinaus, ein ambiphiler Charakter des Imido-Komplexes **102** festgestellt werden. Neben der Bildung des Tetrazen-Komplexes **132** konnte die Addition von elektrophilen Substraten unter Bildung von Ureat-Liganden beobachtet werden.

## 4.2 Darstellung von Imido-Nickel-Komplexen

Nach der erfolgreichen Synthese des linear koordinierten Nickel(I)-Komplexes  $K\{18c6\}[Ni(N(SiMe_3)_2)_2]$  (**118**), wurde dieser als Vorstufe zur Darstellung von trigonalen Imido-Nickel-Komplexen genutzt.

### Umsetzung von $K\{m\}Ni(N(SiMe_3)_2)_2$ mit Alkylaziden

Die Umsetzung des Nickel(I)-Komplexes **118** mit Alkylaziden (*tert*-Butyl, Adamantyl) zeigte einen Farbwechsel zu einem dunklen Orange. Da kein selektiver Reaktionsverlauf beobachtet werden konnte, werden die erhaltenen Ergebnisse hier nicht weiter diskutiert.

Vor dem Hintergrund, dass im Falle von Cobalt die Kristallisation der entsprechenden Imido-Komplexe mit  $K\{\text{crypt.222}\}$ -Kation gelang, wurden auch hier im Folgenden entsprechende Untersuchungen durchgeführt.

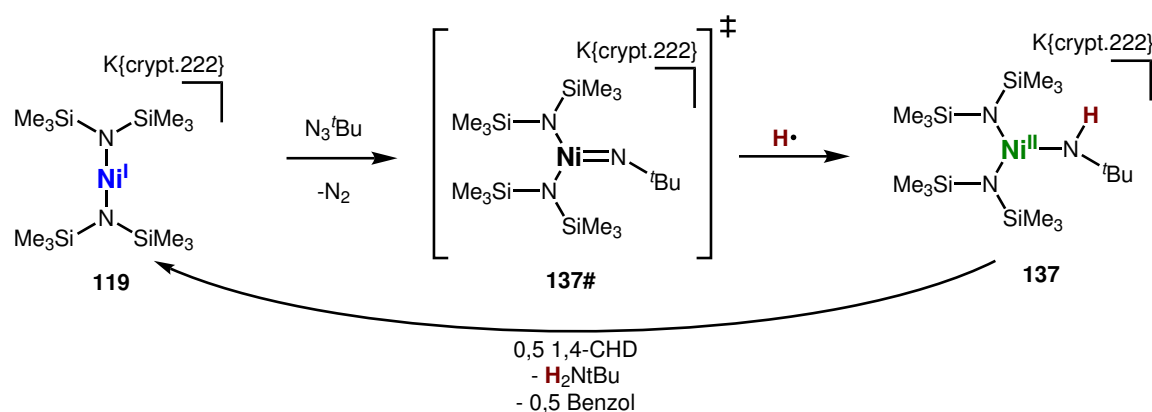


Abb. 66: Bildung des trigonalen Amido-Nickel-Komplexes **137** durch Umsetzung des Nickel(I)-Komplexes **119** mit *tert*-Butylazid.

Die Umsetzung des Nickel(I)-Komplexes **119** mit *tert*-Butylazid resultierte in einer dunkelbraunen Lösung. Im Vergleich zu Synthese des entsprechenden Imido-Cobalt-Komplexes **102**, konnte hier keine sichtbare Gasentwicklung festgestellt werden.

Durch Übersichten der Reaktionslösung (Diethylether) mit *n*-Pentan konnten dunkelorange Kristalle erhalten werden. Die, durch Röntgenbeugungsexperimente, bestimmte Struktur um Festkörper zeigte die Bildung eines trigonal koordinierten Nickel-Komplexes **137** (vgl. Abb. 67).

Die  $N(SiMe_3)_2$ -Liganden weisen eine Bindungslänge von 1,92 Å zum Nickel-Ion auf, was vergleichbar zu dem trigonalen Nickel(II)-Komplex  $Li\{\text{dmap}\}_4Ni(N(SiMe_3)_2)_3$  **113** (1,93 Å) ist.[107] Bei dem dritten Liganden handelt es sich vermutlich um einen sekundären Amido-Liganden, der durch einen H-Atom-Abstraktion von einem Lösungsmittelmolekül durch einen intermediären Imido-Nickel-Komplexes gebildet wurde. Die Bindungslänge von 1,78 Å zeigt eine deutliche Kontraktion im Vergleich zu dem trigonalen Amido-Cobalt-Komplex **103** (1,88 Å), was auf den geringeren Ionenradius des Zentralatoms zurückzuführen ist. Die beobachtete N–Ni-Bindungslänge liegt weiterhin im Bereich, welche für Amido-Nickel-Komplexe beobachtet wird (1,74 – 1,86 Å).[55, 61, 104, 108]

Der Bindungswinkel des Amido-Liganden von 139,0° stimmt gut mit den literaturbekannten Amido-Nickel-Komplexen (Ni–N–C: 132 - 137°) und dem Amido-Cobalt-Komplex **103** (134,8°) überein.[55, 61, 104, 108]



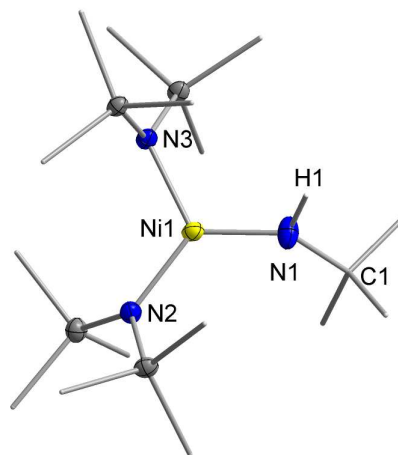


Abb. 67: Molekülstruktur von **137** im Festkörper. Das  $K\{\text{crypt.222}\}$ -Kation und nicht relevante Wasserstoffatome sind aus Gründen der Übersichtlichkeit nicht dargestellt. Kohlenstoff-Atome sind im Wire/Sticks-Modell dargestellt. Die Größe der Ellipsoide entspricht einer Aufenthaltswahrscheinlichkeit von 50 %.

Das  $^1\text{H}$ -NMR-Spektrum der Verbindung zeigt ein Signal mit einer Verschiebung von 23 ppm, welches der *tert*-Butyl-Gruppe des Komplexes zugeordnet werden kann. Das Signal der  $\text{N}(\text{SiMe}_3)_2$ -Liganden weist eine Verschiebung von 1,8 ppm sowie eine starke Verbreiterung auf. Weiterhin wird es teilweise von dem Restsignal des Lösungsmittels überlagert ( $\text{THF-d}_8$ : 1,73 ppm). Ein Vergleich mit dem trigonalen Nickel(II)-Komplex  $[\text{Ni}(\text{N}(\text{SiMe}_3)_2)_3]^-$  (1,12 ppm) zeigte nur eine geringe Abweichung der Signale, was auf eine ähnliche elektronische Struktur schließen lässt.[107] Die Bildung eines Amido-Komplexes deutet hier auf eine hohe Reaktivität des intermediäre gebildeten Imido-Nickel-Komplexes **137#** hin.

Da auch der Amido-Cobalt(II)-Komplex **103** eine Reaktivität gegenüber C–H-Bindungen zeigt, wurden auch hier erste NMR-Experimente zu H-Atom-Transfer-Reaktionen durchgeführt. Die direkte Umsetzung mit 1,4-CHD zeigt die Bildung von Benzol (7,30 ppm), sowie des linear koordinierten Nickel(I)-Komplexes **119** (0,27 ppm). Nach 24 Stunden ist neben einer vollständigen Umsetzung, die Bildung von *tert*-Butylamin (1,06 ppm) zu beobachten (vgl. Abb. 87). Die Umsetzung mit 9,10-Dihydroanthracen zeigt ebenfalls die parallele Bildung des Nickel(I)-Komplexes **119**, wobei die Bildung von Anthracen nicht beobachtet werden kann (vgl. Abb. 88). Letzteres wurde auch in Fall der untersuchten Cobalt-Komplexe beobachtet und kann auf eine schwache Wechselwirkung von Anthracen mit dem gebildeten Metall(I)-Komplex zurückgeführt werden.

### Umsetzung von $K\{m\}\text{Ni}(\text{N}(\text{SiMe}_3)_2)_2$ mit Arylaziden

Für die Darstellung von Aryl-Imido-Komplexen wurden die Nickel(I)-Komplexe (**118/119**) im Anschluss mit Mesitylazid umgesetzt.

Bei der Umsetzung konnte ein Farbwechsel von orange zu grün mit einer begleitenden Gasentwicklung beobachtet werden. Unabhängig vom verwendeten Kation konnten grüne Kristalle erhalten werden, die für Röntgenbeugungsexperimente am Einkristall geeignet sind (vgl. Abb. 69). Erneut ist die Bildung eines trigonalen Nickel-Komplexes zu beobachten. Die beiden  $\text{N}(\text{SiMe}_3)_2$ -Liganden zeigen Bindungslängen

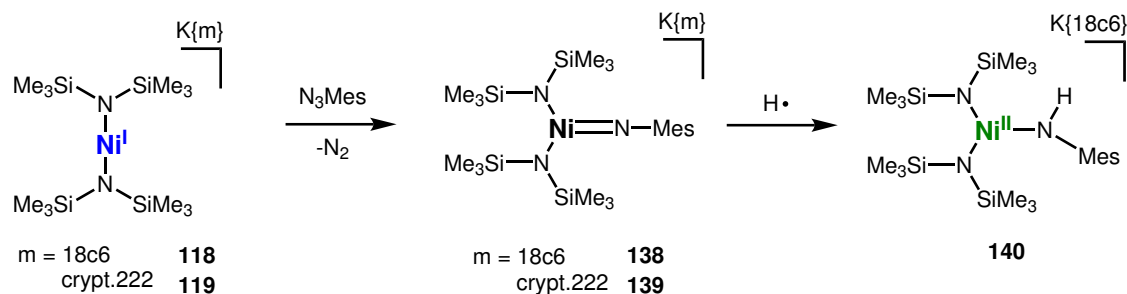


Abb. 68: Darstellung der trigonalen Mesityl-Imido-Komplexe **138** und **139**, sowie H-Atom-Transfer Reaktivität von **138** unter Bildung von **140**.

im Bereich um 1,93 Å, was vergleichbar zu den zuvor beschriebenen Komplexen ist.

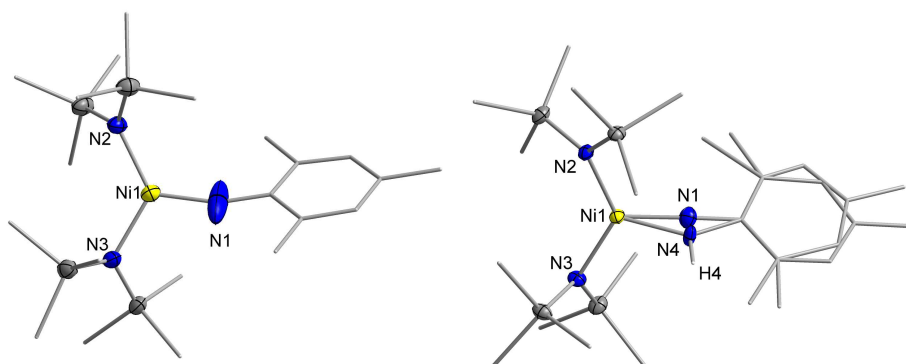


Abb. 69: Molekülstruktur von **139** (links) und des Gemisches aus **138** und **140** (rechts) im Festkörper. Das Kation und nicht relevante Wasserstoffatome sind aus Gründen der Übersichtlichkeit nicht dargestellt. Kohlenstoff-Atome sind im Wire/Sticks-Modell dargestellt. Die Größe der Ellipsoide entspricht einer Aufenthaltswahrscheinlichkeit von 50 %.

Im Fall des Komplexes mit K{crypt.222}-Kation **139** konnte weiterhin ein Imido-Ligand mit einer Bindungslänge von 1,74 Å zum Nickel-Ion beobachtet werden. Dieser ist nur geringfügig kürzer, als der zuvor beschriebene sekundäre Amido-Ligand von **137**, weist allerdings Unterschiede zu vergleichbaren Aryl-Amido-Nickel-Komplexen auf (1,76 - 1,95 Å). Auffällig ist hier vor allem die geringe Abwinkelung des Liganden (162 °), die gegen einen Amido-Liganden spricht (Ni-N<sub>Amido</sub>-C: 128 - 147 °), und ähnlich zu dem Mesityl-Imido-Cobalt-Komplex ist (**125**: 169 °). Aufgrund der starken thermischen Auslenkung des Imido-Stickstoff-Atoms, weist diese allerdings einen hohen Fehler auf.[54, 58, 109–112]

Im Fall des Komplexes mit K{18c6}-Kations ist eine Fehlordnung des vermeintlichen Imido-Liganden zu erkennen. Die Strukturlösung deutet hier auf eine Mischung aus dem Imido- (**138**: 75 %) und dem Amido-Komplex (**140**: 25 %) hin, die cokrystallisiert sind. Im Fall von **139** wurde dies nicht beobachtet, weshalb für Untersuchungen zur elektronischen Struktur nur dieser Komplex herangezogen wurde. Die Bindungssituation des Imido-Liganden (Ni-N<sub>Imido</sub>: 1,74 Å; Ni-N<sub>Imido</sub>-C: 173 °) stimmt gut mit dem zuvor beschriebenen Komplex **139** überein. Der Amido-Komplex zeigt eine Aufweitung der Metall-Stickstoff-Bindung (Ni-N<sub>Amido</sub>: 1,85 Å) sowie eine größere Abwinkelung des Liganden (Ni-N<sub>Amido</sub>-C: 139 °), was mit den literaturbekannten Amido-Nickel-Komplexen übereinstimmt.[54, 58, 109–111]

Die Bildung des Amido-Komplexes deutet erneut auf eine hohe Reaktivität des Imido-Nickel-Komplexes hin.

Untersuchungen der Komplexe mittels  $^1\text{H}$ -NMR-Spektroskopie zeigte im Fall des Komplexes mit K{18c6}-Komplexes **138** nur einen Signalsatz. Ein breites Signal mit einer Verschiebung von 2,42 ppm, was den  $\text{N}(\text{SiMe}_3)_2$ -Liganden zugeordnet werden kann (vgl. Abb. 89 **A**). Weiterhin sind Signale mit einer paramagnetischen Verschiebung zu erkennen, die dem Mesityl-Liganden zuzuordnen sind (93,5, 81,6 und 49,2 ppm), sowie der Zersetzung des Komplexes. Für den Komplex mit K{crypt.222}-Kation (vgl. Abb. 89 **B**) sind die identischen Signale für den Mesityl-Substituenten zu erkennen. Das Signal der  $\text{N}(\text{SiMe}_3)_2$ -Liganden ist mit 2,12 ppm geringfügig verschoben und wird teilweise von einem Signal des Kryptanden überlagert. Ein Vergleich mit dem zuvor beschriebenen, trigonalen Amido-Nickel-Komplex zeigt nur eine geringe Abweichung der Signale für die  $\text{N}(\text{SiMe}_3)_2$ -Liganden (**137**: 1,8 ppm). Dies könnte auf einen Imidyl-Charakter, und somit eine Nickel(II)-Zentralatom, der Imido-Komplexe hindeuten.

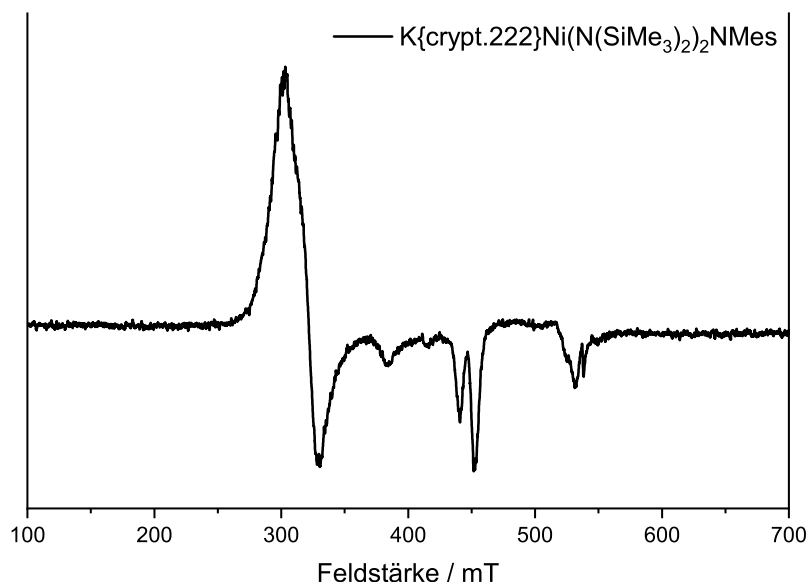


Abb. 70: X-Band ESR-Spektrum (9,35 GHz, 12 K) von K{cyrpt.222}Ni(N(SiMe<sub>3</sub>)<sub>2</sub>)<sub>2</sub>NMes (**139**) in gefrorener Lösung von Methyl-THF.

Um einen Einblick in die elektronische Struktur des Imido-Komplexes **139** zu erlangen, wurde ein ESR-Spektrum der Verbindung aufgenommen. Dieses zeigt auf den ersten Blick ein axiales Signal mit einer durch Elektron-Kern-Wechselwirkung hervorgerufenen Aufspaltung. Diese konnte nicht über eine Kopplung zu einem Nickel- oder Stickstoff-Atom, was für einen Imido- oder Imidyl-Liganden zu erwarten wäre, erklärt werden. Das ESR-Spektrum des linear koordinierten Nickel(I)-Komplexes **118** zeigt zwei Konformere, die aus einer starken Anionen-Kationen-Wechselwirkung resultieren.[107] Dies könnte auch hier der Fall sein, allerdings war auch unter Berücksichtigung mehrerer Komplexe keine zufriedenstellende Simulation des Spektrums möglich.

Um einen genaueren Einblick in die Oxidationsstufe des Nickel-Zentralatoms zu bekommen wurde Röntgen-Nahkanten-Absorptions-Spektroskopie genutzt. Die Proben wurden dabei sowohl im Festkörper, als auch aus einer gefrorenen Lösung von Methyltetrahydrofuran vermessen (vgl. Abb. 71). Neben dem Imido-Komplex **139** wurden hier auch der linear koordinierte Nickel(I)-Komplex  $\text{K}\{\text{crypt.222}\}\text{Ni}(\text{N}(\text{SiMe}_3)_2)_2$  (**119**) und der trigonale Nickel(II)-Komplex  $\text{Li}(\text{dmap})_4[\text{Ni}(\text{N}(\text{SiMe}_3)_2)_3]$  (**113**) untersucht.

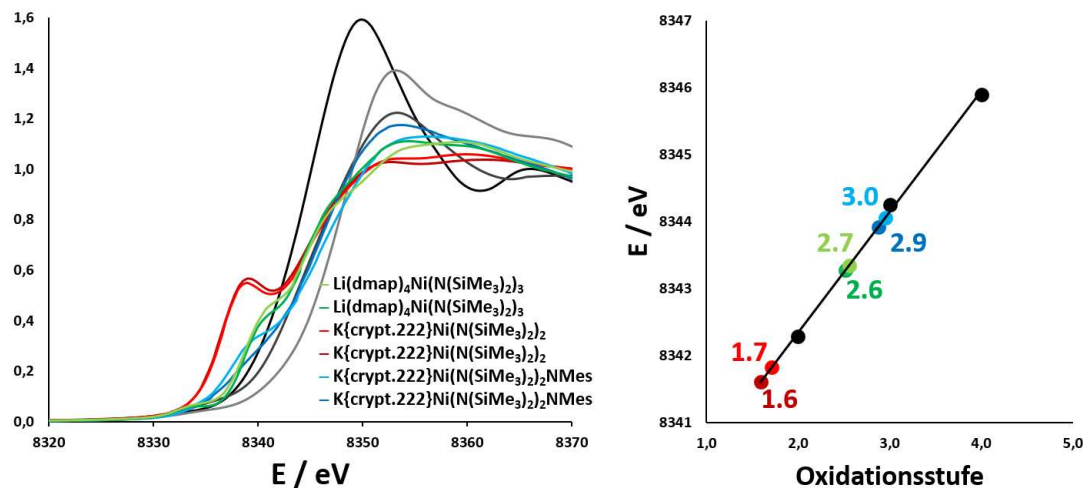


Abb. 71: Röntgen-Nahkanten-Absorptions-Spektroskopie der Nickel-Komplexe  $\text{Li}(\text{dmap})_4[\text{Ni}(\text{N}(\text{SiMe}_3)_2)_3]$  (**113**) (grün),  $\text{K}\{\text{crypt.222}\}\text{Ni}(\text{N}(\text{SiMe}_3)_2)_2$  (**119**) (rot) und  $\text{K}\{\text{crypt.222}\}\text{Ni}(\text{N}(\text{SiMe}_3)_2)_2\text{NMes}$  (**139**) (blau) (links) und daraus bestimmten Oxidationsstufen der Nickel-Ionen (rechts).

Aus der Energie der Absorptionskanten wurde die Oxidationsstufen von 1,7 für **119**, 2,7 für **113** und 3,0 für **139** bestimmt. In den ersten beiden Fällen zeigen sich starke Abweichungen von den erwarteten Werten (**119**: Ni(I); **113**: Ni(II)). Diese können auf die strukturellen Unterschiede zwischen den zur Kalibration verwendeten Nickel-Salzen und den gemessenen Nickel-Komplexen zurückgeführt werden. Aus diesem Grund werden im Folgenden nicht die absoluten Werte, sondern die Differenz der bestimmten Oxidationsstufen betrachtet.

Hier zeigt sich eine gute Übereinstimmung zwischen dem Nickel(I)-Komplex **119** und dem Nickel(II)-Komplex **113**, wobei **139** nur einen geringfügig höheren Wert als **113** zeigt. Dies deutet auf einen Imidyl-Charakter des Komplexes hin, was vergleichbar zu den in dieser Arbeit beschriebenen *Aryl*-Imido-Cobalt-Komplexen ist.

Zusammenfassend konnte der Grundstein für die Untersuchung des Reaktionsverhaltens von trigonalen Imido-Nickel-Komplexen gelegt werden. Zusammen mit den Ergebnissen für Imido-Cobalt-Komplexe bietet sich hier die Möglichkeit den Einfluss des Zentralatoms auf die elektronische Struktur und das Reaktionsverhalten weiter aufzuklären. Die hohe Reaktivität der Komplexe stellt eine Herausforderung für die Isolierung dar, ist gleichzeitig aber auch ein Anreiz für eine genauere Betrachtung dieser Komplexklasse.

## 5 Zusammenfassung

### 5.1 Zusammenfassung in deutscher Sprache

Im Rahmen dieser Doktorarbeit wurden die Synthese und das Reaktionsverhalten von niedrig koordinierten Imido-Komplexen des Cobalts und Nickels untersucht. Als Ausgangsverbindungen wurden zweifach-koordinierte Metall(I)-Komplexe mit sterisch anspruchsvollen Amido-Liganden gewählt.

Durch Umsetzung des quasi-linear koordinierten Cobalt(I)-Komplexes **101** mit *tert*-Butylazid konnte der trigonale Imido-Cobalt(III)-Komplex K{crypt.222}[Co(N(SiMe<sub>3</sub>)<sub>2</sub>)<sub>2</sub>N<sup>*t*</sup>Bu] (**102**) dargestellt werden.

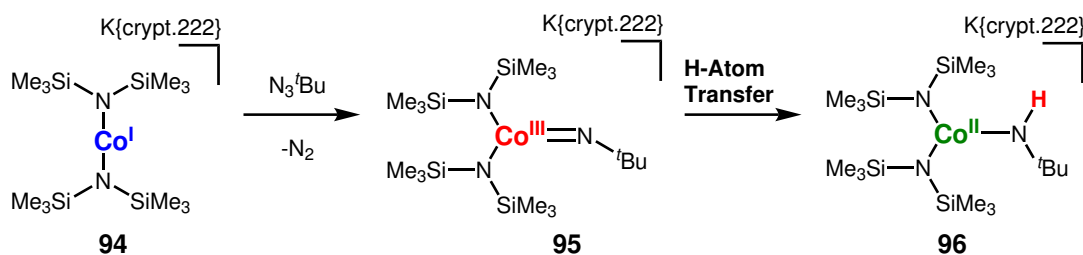


Abb. 72: Darstellung und H-Atom-Transfer-Reaktivität des trigonalen Imido Cobalt(III) Komplexes **102** unter Bildung des trigonalen Amido-Cobalt-Komplexes **103**.

Dieser weist eine vergleichsweise große N<sub>Imido</sub>-Cobalt-Bindungslänge von 1,707(1) Å sowie eine gewinkelte Anordnung des Liganden (Co-N<sub>Imido</sub>-C: 160,8(1)°) auf. Das im Festkörper bestimmte magnetische Moment von 3,52 μ<sub>B</sub> (μ<sub>s.o.</sub> (S = 1): 2,83 μ<sub>B</sub>) deutet auf eine *intermediate-spin* Konfiguration hin. Dieser Komplex zeigt sich als hochreaktiv in der H-Atom-Abstraktion von C-H-Bindungen externer Substrate. Dies wurde bislang für isolierbare Imido-Cobalt-Komplexe nicht beobachtet. In Folge konnte der trigonale Amido-Cobalt(II)-Komplex K{crypt.222}[Co(N(SiMe<sub>3</sub>)<sub>2</sub>)<sub>2</sub>NH<sup>*t*</sup>Bu] (**103**) erhalten werden.

Ausführliche Untersuchungen bezüglich der formalen H-Atom-Abstraktion durch **102** von C-H-Bindungen zeigen eine Korrelation zwischen der Reaktionsrate und der Bindungsdissoziationsenthalpie, und damit eine HAT-Mechanismus. Weiterhin sind Bindungen mit bis zu einer Bindungsstärke von 92 kcal mol<sup>-1</sup> zugänglich. Der gebildete Amido-Cobalt-Komplex **103** ist ebenfalls in der Lage, H-Atom-Abstraktionsreaktionen durchzuführen, was in der Form für Amido-Cobalt-Komplexe auch unbekannt war. In Abhängigkeit der BDE und des pK<sub>a</sub> der beteiligten C-H-Bindung kann dies über einen konzertierten HAT oder einen schrittweisen Protonen-/Elektronentransfer erfolgen.

Anschließende Untersuchungen mit dem sterisch anspruchsvolleren N(Dipp)SiMe<sub>3</sub>-Ligandensystem ermöglichten die Isolation eines trigonalen Imidyl-Komplexes mit einer stark aufgeweiteten Co-N-Bindung (1,751(2) Å) sowie einer linearen Anordnung des Liganden (Co-N<sub>Imido</sub>-C: 178,8(2)°).

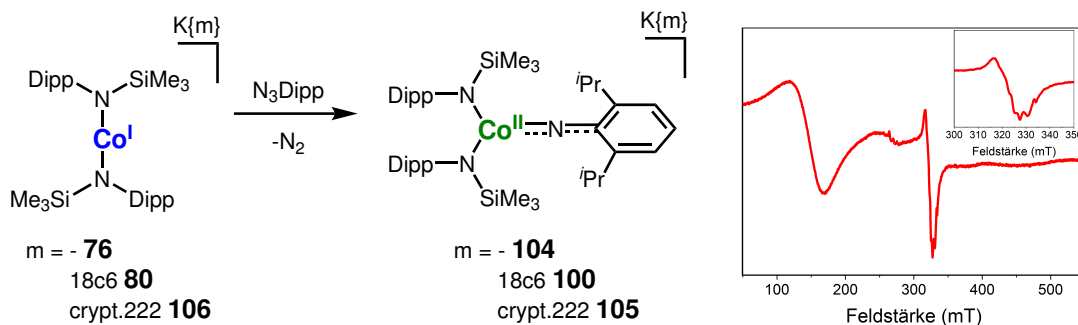


Abb. 73: Links: Synthese und Reaktivität der trigonalem Aryl-Imidyl-Cobalt Komplexe. Rechts: X-Band ESR-Spektrum von **100**.

Dieser, nun im *high-spin*-Zustand vorliegende, Komplex **100** konnte durch umfangreiche spektroskopische Methoden als erstes Beispiel eines Imidyl-Cobalt-Komplexes identifiziert werden. Dabei ist der *high-spin*-Zustand entscheidend für den Imidyl-Charakter, während die elektronische Situation für einen *intermediate*- oder *low-spin*-Komplex dem eines Imido-Cobalt(III)-Komplexes entspricht. Die Verringerung des sterischen Anspruches am Imido-Liganden hatte eine intramolekulare Zersetzung zur Folge, und beschreibt somit die hohe Reaktivität dieser Komplexklasse. Um diese weiter zu untersuchen, wandten wir uns wieder dem weniger sterisch anspruchsvollen N(SiMe<sub>3</sub>)<sub>2</sub>-Ligandensystem zu. Hier konnte nun eine Reihe von reaktiven Alkyl-Imido-Komplexen dargestellt werden, die wie **102** eine *intermediate-spin* Konfiguration aufweisen. Durch Verwendung von *para*-substituierten Mesitylazid-Derivaten wurden die entsprechenden *Aryl*-Imido-Komplexe dargestellt, die strukturell und in ihren magnetischen Eigenschaften Ähnlichkeiten zu dem zuvor beschriebenen Imidyl-Cobalt-Komplex **100** aufweisen.

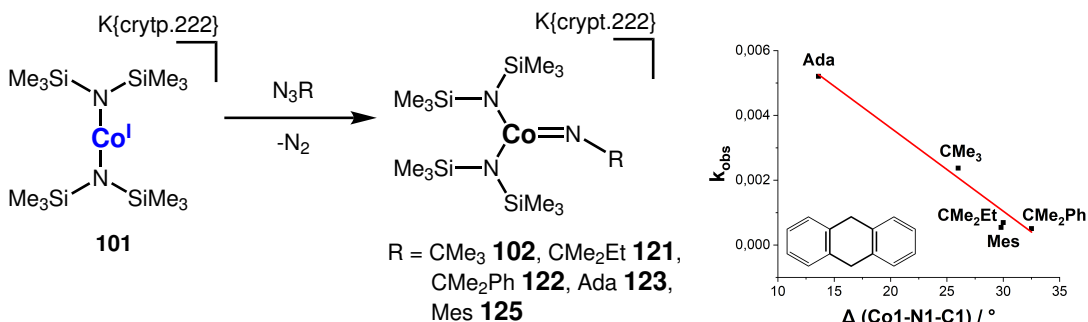


Abb. 74: Links: Synthese der reaktiven Imido-Cobalt-Komplexe. Rechts: Zusammenhang der Reaktionskonstanten ( $k_{obs}$ ) der H-Atom Transfer Reaktion mit DHA und der Änderung des Bindungswinkels zwischen Imido- und Amido-Cobalt-Komplex.

Die Untersuchung zur H-Atom-Transfer-Reaktivität zeigten für die *Alkyl*-Imido-Komplexe eine Korrelation zwischen der Reaktivität und der strukturellen Ähnlichkeit der Imido- und korrespondierenden Amido-Komplexen. Dies bedeutet umso geringer die Änderung der Bindungslänge, bzw. des Bindungswinkels, ausfällt umso größer ist die Reaktivität. Dies gilt nicht für *Aryl*-Imido-Komplexe welche insgesamt eine geringe Reaktivität aufwiesen. Über Variation der *para*-Substituenten wurde hier nur ein geringer Einfluss desselben auf die Reaktivität beobachtet.

Um den Einfluss des Zentralatoms zu untersuchen, wurden die Arbeiten zu Cobalt auf den schwereren Nachbarn Nickel ausgeweitet. Hierbei zeigte sich tenden-

ziell eine zögerlichere Bildung der Imido-Komplexe. So führte die Umsetzung von  $K\{18c6\}[Ni(N(Dipp)SiMe_3)_2]$  (**81**) mit organischen Aziden führte nur im Fall des sterisch wenig anspruchsvollen Phenylazides zur Bildung des trigonalen Imido-Nickel-Komplexes (**109**).

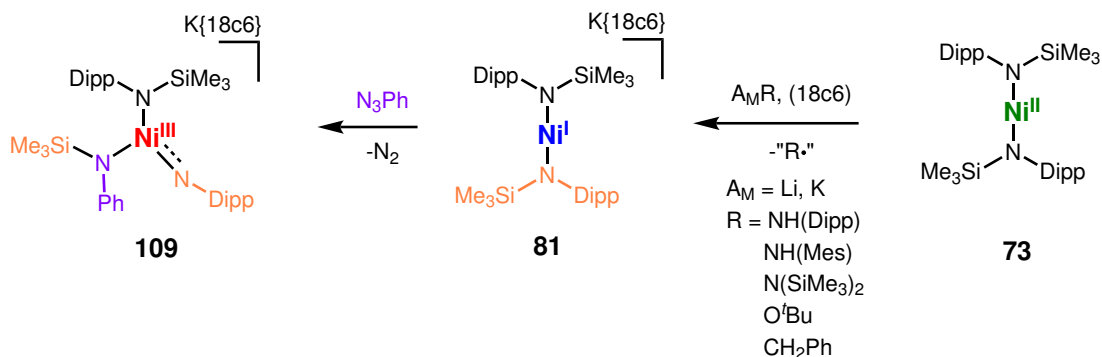


Abb. 75: Darstellung und Bildung des trigonalen Imido-Nickel-Komplexes **109** und Reduktion des linearen Nickel(II) Komplexes (**73**) durch Alkalimetall Organylverbindungen.

Hierbei handelt es sich um das Produkt einer intramolekularen  $SiMe_3$ -Übertragung, welche auf Grund der bevorzugten T-förmigen Koordination des Nickel(III)-Ions stattfindet. Versuche zur Synthese von trigonalen Amido-Nickel-Komplexen durch Umsetzung des Nickel(II)-Komplexes mit sekundären Amiden, zeigten die Reduktion des Nickel-Komplexes durch eine Ein-Elektronen-Übertragung. Dies konnte anschließend auch für Alkoholate und Benzylkalium beobachtet werden.

Im Fall des  $N(SiMe_3)_2$ -Ligandensystems erfolgte erstmals die Synthese des linear koordinierten Metall(I)-Komplex  $K\{18c6\}[Ni(N(SiMe_3)_2)_2]$  (**118**). Aufgrund der literaturbekannten Instabilität von  $Ni(N(SiMe_3)_2)_2$  war eine direkte Reduktion dieser Verbindung, in Analogie zu Cobalt und Eisen, nicht möglich.[72]

Daher wurde  $Li(thf)_x[Ni(N(SiMe_3)_2)_2]$  (**111**) dargestellt, für welches sich in nicht-koordinierenden Lösungsmitteln ein Gleichgewicht mit dem freien  $Ni(N(SiMe_3)_2)_2$  und  $LiN(SiMe_3)_2$  zeigte. Die Synthese des gewünschten linear koordinierten Nickel(I)-Komplexes **118**, war durch die Reduktion dieser Vorstufe in Diethylether möglich, allerdings verhinderte der unbekannt THF-Gehalt eine genaue Einstellung der Stöchiometrie, was die Verunreinigung des Produktes zur Folge hatte.

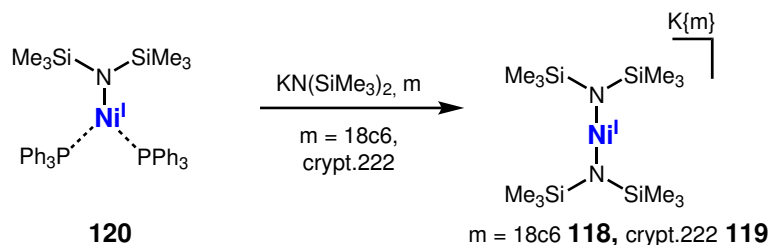


Abb. 76: Alternative Syntheseroute zur Darstellung von  $K\{m\}[Ni(N(SiMe_3)_2)_2]$  ( $m = 18c6$ : **118**;  $crypt.222$ : **119**).

Der zweite Ansatz führte über die Verwendung des Nickel(I)-Komplexes  $Ni(N(SiMe_3)_2)(PPh_3)_2$  (**120**) unter Ligandenaustausch der Phosphane mit einem



zweiten Silylamide zur Bildung des gewünschten Nickel(I)-Komplexes. Auf diesem Syntheseweg konnte eine gute Ausbeute und Reinheit erhalten werden, was eine vollständige Charakterisierung des Komplexes erlaubte. In ersten Untersuchungen zeigte sich dieser Komplex als potentieller Vorläufer zur Darstellung von reaktiven Imido-Nickel-Komplexen.

Insgesamt konnte ich zeigen, dass lineare Metall(I)silylamide als vielseitige Komplexplattformen für die Darstellung von trigonalen Imido-Komplexen in höheren Spinzuständen geeignet sind. Diese erweisen sich als zum Teil hochreaktiv und erlauben tiefe Einblicke in die vielfältige Imido-Metall-Bindungssituation. Die dabei gewonnenen Erkenntnisse sind wegweisend für ein vollständiges Verständnis von Nitren-Transfer-Reaktionen.

## 5.2 English Summary

In this PhD thesis, the synthesis and reaction behavior of low-coordinated imido complexes of cobalt and nickel were investigated. Two-coordinate metal(I) complexes with sterically demanding amido ligands were chosen as starting compounds. By reacting the quasi-linearly coordinated cobalt(I) complex **101** with *tert*-butylazide, the trigonal imido-cobalt(III) complex  $\text{K}\{\text{crypt.222}\}[\text{Co}(\text{N}(\text{SiMe}_3)_2)_2\text{N}^t\text{Bu}]$  (**102**) was prepared.

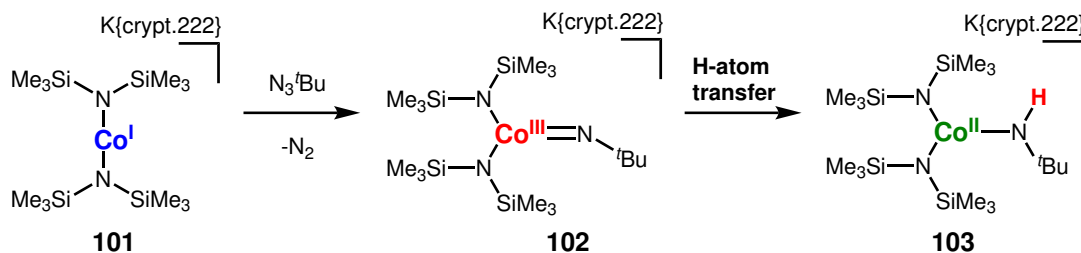


Abb. 77: Preparation and H-atom transfer reactivity of the trigonal imido cobalt(III) complex **102** forming the trigonal amido cobalt complex **103**.

This has a comparatively large  $\text{N}_{\text{Imido}}\text{-Co}$  bond length of 1.707(1) Å and an angled arrangement of the ligand ( $\text{Co-N}_{\text{Imido}}\text{-C}$ : 160.8(1)°). The magnetic moment of 3.52  $\mu_B$  determined in the solid ( $\mu_{s.o.}$  ( $S = 1$ ): 2.83  $\mu_B$ ) indicates an *intermediate-spin* configuration. This complex is shown to be highly reactive in H-atom abstraction from C–H bonds of external substrates. This has not been observed previously for isolable imido cobalt complexes. As a consequence, the trigonal amido-cobalt(II) complex  $\text{K}\{\text{crypt.222}\}[\text{Co}(\text{N}(\text{SiMe}_3)_2)_2\text{NH}^t\text{Bu}]$  (**103**) was obtained.

Detailed studies concerning the formal H-atom abstraction by **102** of C–H bonds show a correlation between the reaction rate and the bond dissociation enthalpy, and thus a HAT mechanism. Furthermore, bonds with bond strengths up to 92 kcal mol<sup>-1</sup> are accessible. The formed amido cobalt complex **103** is also capable of H-atom abstraction reactions, which was also unknown in the form for amido-cobalt complexes. Depending on the BDE and the  $\text{pK}_a$  of the C–H bond involved, this can be done via a concerted HAT or a stepwise proton/electron transfer.

Subsequent studies with the sterically more demanding  $\text{N}(\text{Dipp})\text{SiMe}_3$ -ligand system allowed the isolation of a trigonal imidyl complex with a strongly expanded Co–N bond (1.751(2) Å) as well as a linear arrangement of the ligand ( $\text{Co-N}_{\text{Imido}}\text{-C}$ : 178.8(2)°).

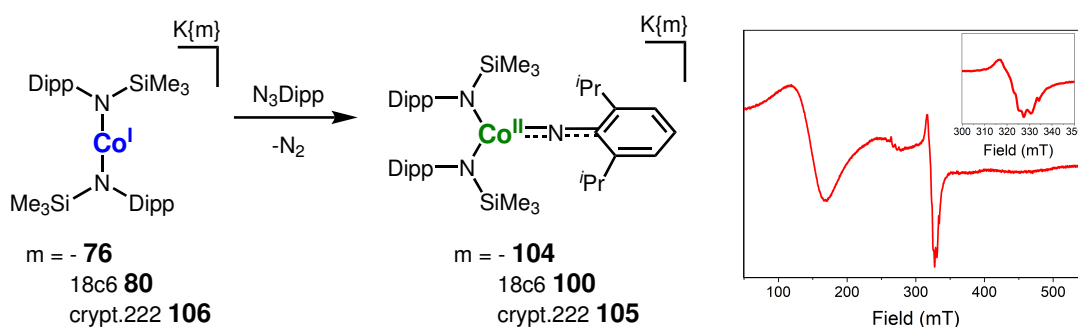


Abb. 78: Left: Synthesis and reactivity of the trigonal aryl-imidyl-cobalt complexes. Right: X-band ESR spectrum of **100**.

The complex **100**, now in the *high-spin* state, was identified by extensive spectroscopic methods as the first example of an imidyl cobalt complex. Here, the *high-spin* state is crucial for the imidyl character, while the electronic situation for an *intermediate* or *low-spin* complex corresponds to that of an imido cobalt(III) complex. The reduction of steric demand on the imido ligand resulted in intramolecular decomposition, and thus describes the high reactivity of this class of complexes. To investigate this further, we turned back to the less sterically demanding  $\text{N}(\text{SiMe}_3)_2$ -ligand system. Here, we were now able to present a series of reactive *alkyl* imido complexes that, like **102**, have an *intermediate-spin* configuration. By using *para*-substituted mesitylazide derivatives, the corresponding *aryl* imido complexes were presented, which structurally and in their magnetic properties show similarities to the previously described imidyl cobalt complex **100**.

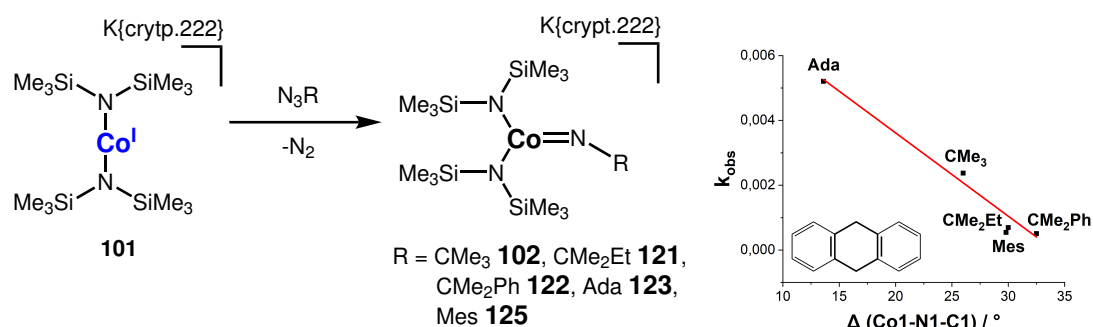


Abb. 79: Left: Synthesis of the reactive imido-cobalt complexes. Right: Correlation of the reaction constants ( $k_{\text{obs}}$ ) of the H-atom transfer reaction with DHA and the change of the bond angle between imido and amido-cobalt complex.

The investigation of the H-atom transfer reactivity showed a correlation between the reactivity and the structural similarity of the imido and corresponding amido complexes for the *alkyl* imido complexes. This means that the smaller the change in bond length, or bond angle, the greater the reactivity. This does not apply to *aryl* imido complexes, which exhibit low reactivity overall. Only a slight influence of the *para* substituent on the reactivity was observed here via variation of the *para* substituent.

To investigate the influence of the central atom, the work on cobalt was extended to its heavier neighbor nickel. This tended to show a more hesitant formation of the imido complexes. Thus, the reaction of  $\text{K}\{18\text{c}6\}[\text{Ni}(\text{N}(\text{Dipp})\text{SiMe}_3)_2]$  (**81**) with organic azides led to the formation of the trigonal imido nickel complex (**109**) only in the case of the sterically less demanding phenyl azide.

This is the product of an intramolecular  $\text{SiMe}_3$  transfer, which occurs due to the preferential T-shaped coordination of the nickel(III) ion. Experiments on the synthesis of trigonal amido nickel complexes by reaction of the nickel(II) complex with secondary amides, showed the reduction of the nickel complex by a one-electron transfer. This was subsequently also observed for alcoholates and benzyl potassium. In the case of the  $\text{N}(\text{SiMe}_3)_2$ -ligand system, the synthesis of the linearly coordinated metal(I) complex  $\text{K}\{18\text{c}6\}[\text{Ni}(\text{N}(\text{SiMe}_3)_2)_2]$  (**118**) was carried out for the first time. Due to the known instability of  $\text{Ni}(\text{N}(\text{SiMe}_3)_2)_2$  in the literature, a direct reduction of this compound, in analogy to cobalt and iron, was not possible.[72]

Therefore,  $\text{Li}(\text{thf})_x[\text{Ni}(\text{N}(\text{SiMe}_3)_2)_2]$  (**111**) was presented, for which equilibrium was shown in non-coordinating solvents with the free  $\text{Ni}(\text{N}(\text{SiMe}_3)_2)_2$  and  $\text{LiN}(\text{SiMe}_3)_2$ .

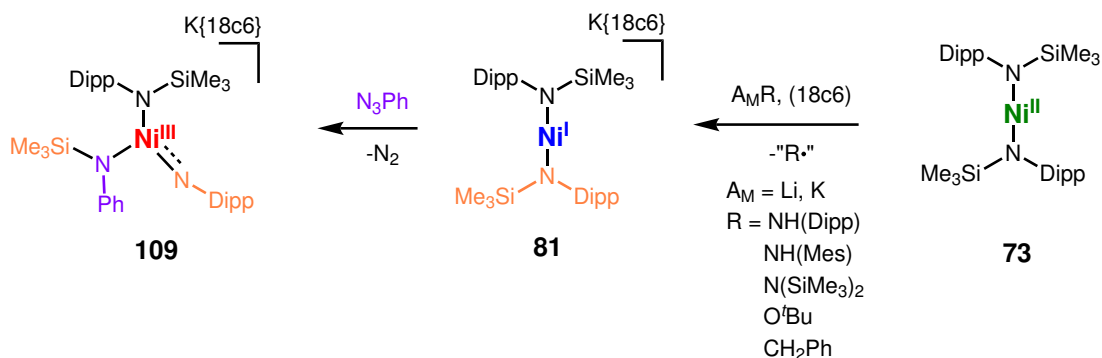


Abb. 80: Preparation and formation of the trigonal imido nickel complex **109** and reduction of the linear nickel(II) complex (**73**) by alkali metal organyl compounds.

Synthesis of the desired linearly coordinated nickel(I) complex **118**, was possible by reducing this precursor in diethyl ether, but the unknown THF content prevented accurate adjustment of the stoichiometry, resulting in contamination of the product.

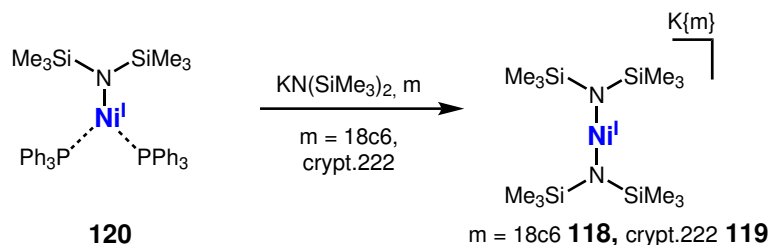


Abb. 81: Alternative synthetic route for the preparation of  $\text{K}\{\text{m}\}[\text{Ni}(\text{N}(\text{SiMe}_3)_2)_2]$  ( $\text{m} = 18\text{c}6$ : **118**;  $\text{crypt.222}$ : **119**).

For the second approach the nickel(I) complex  $\text{Ni}(\text{N}(\text{SiMe}_3)_2)(\text{PPh}_3)_2$  (**120**) was used in an ligand exchange of the phosphanes with a second silylamide to form the desired nickel(I) complex. Good yield and purity were obtained by this synthetic route, which allowed a complete characterization of the complex. Initial studies showed this complex to be a potential precursor for the preparation of reactive imido nickel complexes.

Overall, I was able to show that linear metal(I)silylamides are versatile complex platforms for the preparation of trigonal imido complexes in higher spin states. These prove to be highly reactive in some cases and allow deep insights into the diverse imido metal bonding situation. The insights gained are groundbreaking for a complete understanding of nitrene transfer reactions.

---

## Literatur

- (1) Breslow, R.; Gellman, S. H. *J. Chem. Soc.* **1982**, 1400.
- (2) Breslow, R.; Gellman, S. H. *J. Am. Chem. Soc.* **1983**, *105*, 6728–6729.
- (3) Svastits, E. W.; Dawson, J. H.; Breslow, R.; Gellman, S. H. *J. Am. Chem. Soc.* **1985**, *107*, 6427–6428.
- (4) F. Collet; R. H. Dodd; P. Dauban *Chem. Commun.* **2009**, 5061–5074.
- (5) Lu, H.; Zhang, X. P. *Chem. Soc. Rev.* **2011**, *40*, 1899–1909.
- (6) Park, Y.; Kim, Y.; Chang, S. *Chem. Rev.* **2017**, *117*, 9247–9301.
- (7) Yang, Y.; Arnold, F. H. *Acc. Chem. Res.* **2021**, *54*, 1209–1225.
- (8) Athavale, S. V.; Gao, S.; Liu, Z.; Mallojjala, S. C.; Hirschi, J. S.; Arnold, F. H. *Angew. Chem.* **2021**, *60*, 24864–24869.
- (9) Liu, Z.; Qin, Z.-Y.; Zhu, L.; Athavale, S. V.; Sengupta, A.; Jia, Z.-J.; Garcia-Borràs, M.; Houk, K. N.; Arnold, F. H. *J. Am. Chem. Soc.* **2022**, *144*, 80–85.
- (10) Athavale, S. V.; Gao, S.; Das, A.; Mallojjala, S. C.; Alfonzo, E.; Long, Y.; Hirschi, J. S.; Arnold, F. H. *J. Am. Chem. Soc.* **2022**, *144*, 19097–19105.
- (11) Nugent, W. A.; Mayer, J. M., *Metal-ligand multiple bonds: The chemistry of transition metal complexes containing oxo, nitrido, imido, alkylidene, or alkylidyne ligands*; A Wiley-Interscience publication; Wiley: New York, 1988.
- (12) Eikey, R. *Coord. Chem. Rev.* **2003**, *243*, 83–124.
- (13) Ray, K.; Heims, F.; Pfaff, F. F. *Eur. J. Inorg. Chem.* **2013**, *2013*, 3784–3807.
- (14) Grünwald, A.; Anjana, S. S.; Munz, D. *Eur. J. Inorg. Chem.* **2021**, *5*, 422.
- (15) Betley, T. A.; Peters, J. C. *J. Am. Chem. Soc.* **2003**, *125*, 10782–10783.
- (16) Brown, S. D.; Betley, T. A. *J. Am. Chem. Soc.* **2003**, *125*, 322–323.
- (17) Eckert, N. A.; Vaddadi, S.; Stoian, S.; Lachicotte, R. J.; Cundari, T. R.; Holland, P. L. *Angew. Chem.* **2006**, *45*, 6868–6871.
- (18) Cowley, R. E.; DeYonker, N. J.; Eckert, N. A.; Cundari, T. R.; DeBeer, S.; Bill, E.; Ottenwaelder, X.; Flaschenriem, C.; Holland, P. L. *Inorg. Chem.* **2010**, *49*, 6172–6187.
- (19) Cowley, R. E.; Holland, P. L. *Inorg. Chim. Acta* **2011**, *369*, 40–44.
- (20) Cowley, R. E.; Eckert, N. A.; Vaddadi, S.; Figg, T. M.; Cundari, T. R.; Holland, P. L. *J. Am. Chem. Soc.* **2011**, *133*, 9796–9811.
- (21) Cowley, R. E.; Elhaïk, J.; Eckert, N. A.; Brennessel, W. W.; Bill, E.; Holland, P. L. *J. Am. Chem. Soc.* **2008**, *130*, 6074–6075.
- (22) Cowley, R. E.; Bill, E.; Neese, F.; Brennessel, W. W.; Holland, P. L. *Inorg. Chem.* **2009**, *48*, 4828–4836.
- (23) Cowley, R. E.; Eckert, N. A.; Elhaïk, J.; Holland, P. L. *Chem. Commun.* **2009**, 1760–1762.
- (24) Cowley, R. E.; Holland, P. L. *Inorg. Chem.* **2012**, *51*, 8352–8361.
- (25) King, E. R.; Betley, T. A. *Inorg. Chem.* **2009**, *48*, 2361–2363.

- 
- (26) King, E. R.; Hennessy, E. T.; Betley, T. A. *J. Am. Chem. Soc.* **2011**, *133*, 4917–4923.
- (27) Hennessy, E. T.; Liu, R. Y.; Iovan, D. A.; Duncan, R. A.; Betley, T. A. *Chem. Sci.* **2014**, *5*, 1526–1532.
- (28) Hennessy, E. T.; Betley, T. A. *Science* **2013**, *340*, 591–595.
- (29) Iovan, D. A.; Wilding, M. J. T.; Baek, Y.; Hennessy, E. T.; Betley, T. A. *Angew. Chem.* **2017**, *129*, 15805–15808.
- (30) Iovan, D. A.; Betley, T. A. *J. Am. Chem. Soc.* **2016**, *138*, 1983–1993.
- (31) Wilding, M. J. T.; Iovan, D. A.; Wrobel, A. T.; Lukens, J. T.; MacMillan, S. N.; Lancaster, K. M.; Betley, T. A. *J. Am. Chem. Soc.* **2017**, *139*, 14757–14766.
- (32) Wilding, M. J. T.; Iovan, D. A.; Betley, T. A. *J. Am. Chem. Soc.* **2017**, *139*, 12043–12049.
- (33) Gao, Y.; Carta, V.; Pink, M.; Smith, J. M. *J. Am. Chem. Soc.* **2021**, *143*, 5324–5329.
- (34) Gao, Y.; Pink, M.; Smith, J. M. *J. Am. Chem. Soc.* **2022**, *144*, 1786–1794.
- (35) Yang, P.-C.; Yu, K.-P.; Hsieh, C.-T.; Zou, J.; Fang, C.-T.; Liu, H.-K.; Pao, C.-W.; Deng, L.; Cheng, M.-J.; Lin, C.-Y. *Chem. Sci.* **2022**, *13*, 9637–9643.
- (36) Thyagarajan, S.; Shay, D. T.; Incarvito, C. D.; Rheingold, A. L.; Theopold, K. H. *J. Am. Chem. Soc.* **2003**, *125*, 4440–4441.
- (37) Shay, D. T.; Yap, G. P. A.; Zakharov, L. N.; Rheingold, A. L.; Theopold, K. H. *Angew. Chem.* **2005**, *117*, 1532–1534.
- (38) Shay, D. T.; Yap, G. P. A.; Zakharov, L. N.; Rheingold, A. L.; Theopold, K. H. *Angew. Chem.* **2006**, *45*, 7870.
- (39) Jenkins, D. M.; Betley, T. A.; Peters, J. C. *J. Am. Chem. Soc.* **2002**, *124*, 11238–11239.
- (40) Hu, X.; Meyer, K. *J. Am. Chem. Soc.* **2004**, *126*, 16322–16323.
- (41) Cowley, R. E.; Bontchev, R. P.; Sorrell, J.; Sarracino, O.; Feng, Y.; Wang, H.; Smith, J. M. *J. Am. Chem. Soc.* **2007**, *129*, 2424–2425.
- (42) Dai, X.; Kapoor, P.; Warren, T. H. *J. Am. Chem. Soc.* **2004**, *126*, 4798–4799.
- (43) King, E. R.; Sazama, G. T.; Betley, T. A. *J. Am. Chem. Soc.* **2012**, *134*, 17858–17861.
- (44) Du, J.; Wang, L.; Xie, M.; Deng, L. *Angew. Chem.* **2015**, *54*, 12640–12644.
- (45) Yao, X.-N.; Du, J.-Z.; Zhang, Y.-Q.; Leng, X.-B.; Yang, M.-W.; Jiang, S.-D.; Wang, Z.-X.; Ouyang, Z.-W.; Deng, L.; Wang, B.-W.; Gao, S. *J. Am. Chem. Soc.* **2017**, *139*, 373–380.
- (46) Grant, L. N.; Carroll, M. E.; Carroll, P. J.; Mindiola, D. J. *Inorg. Chem.* **2016**, *55*, 7997–8002.
- (47) Liu, Y.; Du, J.; Deng, L. *Inorg. Chem.* **2017**, *56*, 8278–8286.
- (48) Baek, Y.; Das, A.; Zheng, S.-L.; Reibenspies, J. H.; Powers, D. C.; Betley, T. A. *J. Am. Chem. Soc.* **2020**, *142*, 11232–11243.
-

- 
- (49) Baek, Y.; Hennessy, E. T.; Betley, T. A. *J. Am. Chem. Soc.* **2019**, 16944–16953.
- (50) Baek, Y.; Betley, T. A. *J. Am. Chem. Soc.* **2019**, *141*, 7797–7806.
- (51) Park, Y.; Semproni, S. P.; Zhong, H.; Chirik, P. J. *Angew. Chem.* **2021**, *60*, 14376–14380.
- (52) Mao, W.; Fehn, D.; Heinemann, F. W.; Scheurer, A.; Munz, D.; Meyer, K. *Angew. Chem.* **2021**, *60*, 16480–16486.
- (53) Mao, W.; Fehn, D.; Heinemann, F. W.; Scheurer, A.; van Gastel, M.; Januzzi, S. A. V.; DeBeer, S.; Munz, D.; Meyer, K. *Angew. Chem.* **2022**, DOI: 10.1002/ange.202206848.
- (54) Mindiola, D. J.; Hillhouse, G. L. *J. Am. Chem. Soc.* **2001**, *123*, 4623–4624.
- (55) Iluc, V. M.; Miller, A. J. M.; Anderson, J. S.; Monreal, M. J.; Mehn, M. P.; Hillhouse, G. L. *J. Am. Chem. Soc.* **2011**, *133*, 13055–13063.
- (56) Waterman, R.; Hillhouse, G. L. *J. Am. Chem. Soc.* **2008**, *130*, 12628–12629.
- (57) Cundari, T. R.; Jimenez-Halla, J. O. C.; Morello, G. R.; Vaddadi, S. *J. Am. Chem. Soc.* **2008**, *130*, 13051–13058.
- (58) Iluc, V. M.; Hillhouse, G. L. *J. Am. Chem. Soc.* **2010**, *132*, 15148–15150.
- (59) Mindiola, D. J.; Hillhouse, G. L. *Chem. Commun.* **2002**, 1840.
- (60) Mindiola, D. J.; Waterman, R.; Iluc, V. M.; Cundari, T. R.; Hillhouse, G. L. *Inorg. Chem.* **2014**, *53*, 13227–13238.
- (61) Kogut, E.; Wiencko, H. L.; Zhang, L.; Cordeau, D. E.; Warren, T. H. *J. Am. Chem. Soc.* **2005**, *127*, 11248–11249.
- (62) Bai, G.; Stephan, D. W. *Angew. Chem.* **2007**, *46*, 1856–1859.
- (63) Harrold, N. D.; Hillhouse, G. L. *Chem. Sci.* **2013**, *4*, 4011.
- (64) Dong, Y.; Lukens, J. T.; Clarke, R. M.; Zheng, S.-L.; Lancaster, K. M.; Betley, T. A. *Chem. Sci.* **2020**, *123*, 4623.
- (65) Dong, Y.; Clarke, R. M.; Porter, G. J.; Betley, T. A. *J. Chem. Soc.* **2020**, *142*, 10996–11005.
- (66) Dong, Y.; Lund, C. J.; Porter, G. J.; Clarke, R. M.; Zheng, S.-L.; Cundari, T. R.; Betley, T. A. *J. Am. Chem. Soc.* **2021**, *143*, 817–829.
- (67) Werner, A. **1893**, *3*, 267–330.
- (68) Schmidbaur, H.; Schmidt, M. *J. Am. Chem. Soc.* **1962**, *84*, 3600–3601.
- (69) Bradley, D. C.; Hursthouse, M. B.; Abdul Malik, K. M.; Mäseler, R. *Transition Met. Chem.* **1978**, *3*, 253–254.
- (70) Murray, B. D.; Power, P. P. *Inorg. Chem.* **1984**, *23*, 4584–4588.
- (71) Olmstead, M. M.; Power, P. P.; Shoner, S. C. *Inorg. Chem.* **1991**, *30*, 2547–2551.
- (72) Faust, M.; Bryan, A. M.; Mansikkamäki, A.; Vasko, P.; Olmstead, M. M.; Tuononen, H. M.; Grandjean, F.; Long, G. J.; Power, P. P. *Angew. Chem.* **2015**, *54*, 12914–12917.
- (73) Bürger, H.; Wannagat, U. *Monatsh. Chem.* **1963**, *94*, 1007–1012.
-



- 
- (74) Bürger, H.; Wannagat, U. *Monatsh. Chem.* **1964**, *95*, 1099–1102.
- (75) Andersen, R. A.; Faegri, K.; Green, J. C.; Haaland, A.; Lappert, M. F.; Leung, W. P.; Rypdal, K. *Inorg. Chem.* **1988**, *27*, 1782–1786.
- (76) Bryan, A. M.; Long, G. J.; Grandjean, F.; Power, P. P. *Inorg. Chem.* **2013**, *52*, 12152–12160.
- (77) Merrill, A. W.; Stich, T. A.; Brynda, M.; Yeagle, G. J.; Fettinger, J. C.; de Hont, R.; Reiff, W. M.; Schulz, C. E.; Britt, R. D.; Power, P. P. *J. Am. Chem. Soc.* **2009**, *131*, 12693–12702.
- (78) Ni, C.; Rekken, B.; Fettinger, J. C.; Long, G. J.; Power, P. P. *Dalton Trans.* **2009**, 8349–8355.
- (79) Boynton, J. N.; Merrill, W. A. 3.; Reiff, W. M.; Fettinger, J. C.; Power, P. P. *Inorg. Chem.* **2012**, *51*, 3212–3219.
- (80) Bryan, A. M.; Merrill, W. A.; Reiff, W. M.; Fettinger, J. C.; Power, P. P. *Inorg. Chem.* **2012**, *51*, 3366–3373.
- (81) Lin, C.-Y.; Guo, J.-D.; Fettinger, J. C.; Nagase, S.; Grandjean, F.; Long, G. J.; Chilton, N. F.; Power, P. P. *Inorg. Chem.* **2013**, *52*, 13584–13593.
- (82) Lin, C.-Y.; Fettinger, J. C.; Power, P. P. *Inorg. Chem.* **2017**, *56*, 9892–9902.
- (83) Werncke, C. G.; Suturina, E.; Bunting, P. C.; Vendier, L.; Long, J. R.; Atanasov, M.; Neese, F.; Sabo-Etienne, S.; Bontemps, S. *Chem. Eur. J.* **2016**, *22*, 1668–1674.
- (84) Lipschutz, M. I.; Yang, X.; Chatterjee, R.; Tilley, T. D. *J. Am. Chem. Soc.* **2013**, *135*, 15298–15301.
- (85) Lin, C.-Y.; Fettinger, J. C.; Grandjean, F.; Long, G. J.; Power, P. P. *Inorg. Chem.* **2014**, *53*, 9400–9406.
- (86) Weller, R.; Müller, I.; Duhayon, C.; Sabo-Etienne, S.; Bontemps, S.; Werncke, C. G. *Dalton Trans.* **2021**, *50*, 4890–4903.
- (87) Werncke, C. G.; Bunting, P. C.; Duhayon, C.; Long, J. R.; Bontemps, S.; Sabo-Etienne, S. *Angew. Chem.* **2015**, *54*, 245–248.
- (88) Werncke, C. G.; Pfeiffer, J.; Müller, I.; Vendier, L.; Sabo-Etienne, S.; Bontemps, S. *Dalton Trans.* **2019**, *48*, 1757–1765.
- (89) Müller, I.; Schneider, C.; Pietzonka, C.; Kraus, F.; Werncke, C. G. *Inorganics* **2019**, *7*, 117.
- (90) Müller, I.; Munz, D.; Werncke, C. G. *Inorg. Chem.* **2020**, *59*, 9521–9537.
- (91) Müller, I.; Werncke, C. G. *Chem. Eur. J.* **2021**, *27*, 4932–4938.
- (92) Sieg, G.; Pessemesse, Q.; Reith, S.; Yelin, S.; Limberg, C.; Munz, D.; Werncke, C. G. *Chem. Eur. J.* **2021**, *27*, 16760–16767.
- (93) Sieg, G.; Fischer, M.; Dankert, F.; Siewert, J.-E.; Hering-Junghans, C.; Werncke, C. G. *Chem. Commun.* **2022**, *58*, 9786–9789.
- (94) Sieg, G.; Müller, I.; Weißer, K.; Werncke, G. *Chem. Sci.* **2022**, DOI: 10.1039/D2SC04451J.
- (95) Schneider, C.; Demeshko, S.; Meyer, F.; Werncke, C. G. *Chem. Eur. J.* **2021**, *27*, 6348–6353.
-

- 
- (96) Schneider, C.; Groß, S. J.; Demeshko, S.; Bontemps, S.; Meyer, F.; Werncke, C. G. *Chem. Commun.* **2021**, *57*, 10751–10754.
- (97) Schneider, C.; Guggolz, L.; Werncke, C. G. *Dalton Trans.* **2022**, *2*, 749.
- (98) Lee, H. K.; Lam, C. H.; Li, S. L.; Zhang, Z. Y.; Mak, T. C. *Inorg. Chem.* **2001**, *40*, 4691–4695.
- (99) Ingleson, M. J.; Pink, M.; Fan, H.; Caulton, K. G. *J. Am. Chem. Soc.* **2008**, *130*, 4262–4276.
- (100) Hansen, C. B.; Jordan, R. F.; Hillhouse, G. L. *Inorg. Chem.* **2015**, *54*, 4603–4610.
- (101) Yuan, C.; Xu, X.; Zhang, Y.; Ji, S. *Chin. J. Chem.* **2012**, *30*, 1474–1478.
- (102) Lin, T.-P.; Peters, J. C. *J. Am. Chem. Soc.* **2013**, *135*, 15310–15313.
- (103) Murugesan, S.; Stöger, B.; Weil, M.; Veiros, L. F.; Kirchner, K. *Organometallics* **2015**, *34*, 1364–1372.
- (104) Reckziegel, A.; Pietzonka, C.; Kraus, F.; Werncke, C. G. *Angew. Chem.* **2020**, 8527.
- (105) Peppel, T.; Hinz, A.; Thiele, P.; Geppert–Rybczyńska, M.; Lehmann, J. K.; Köckerling, M. *Eur. J. Inorg. Chem.* **2017**, *2017*, 885–893.
- (106) Reith, S.; Demeshko, S.; Battistella, B.; Reckziegel, A.; Schneider, C.; Stoy, A.; Lichtenberg, C.; Meyer, F.; Munz, D.; Werncke, C. G. *Chem. Sci.* **2022**, *103*, 2905.
- (107) Reckziegel, A.; Battistella, B.; Schmidt, A.; Werncke, C. G. *Inorg. Chem.* **2022**, *61*, 7794–7803.
- (108) Cámpora, J.; Matas, I.; Palma, P.; Álvarez, E.; Graiff, C.; Tiripicchio, A. *Organometallics* **2007**, *26*, 3840–3849.
- (109) Herbert, D. E.; Lara, N. C.; Agapie, T. *Chem. Eur. J.* **2013**, *19*, 16453–16460.
- (110) Kim, J.; Park, K.; Lee, Y. *Inorganica Chimica Acta* **2017**, *460*, 55–62.
- (111) Macaulay, C. M.; Gustafson, S. J.; Fuller, J. T.; Kwon, D.-H.; Ogawa, T.; Ferguson, M. J.; McDonald, R.; Lumsden, M. D.; Bischof, S. M.; Sydora, O. L.; Ess, D. H.; Stradiotto, M.; Turculet, L. *ACS Catal.* **2018**, *8*, 9907–9925.
- (112) Reckziegel, A.; Kour, M.; Battistella, B.; Mebs, S.; Beuthert, K.; Berger, R.; Werncke, C. G. *Angew. Chem.* **2021**, *60*, 15376–15380.
- (113) Evans, D. F. *J. Chem. Soc.* **1959**, 2003.
- (114) Dolomanov, O. V.; Bourhis, L. J.; Gildea, R. J.; Howard, J. A. K.; Puschmann, H. *J. Appl. Crystallogr.* **2009**, *42*, 339–341.
- (115) Kratzert, D.; Holstein, J. J.; Krossing, I. *J. Appl. Crystallogr.* **2015**, *48*, 933–938.
- (116) Sheldrick, G. M. *Acta Cryst. A* **2015**, *71*, 3–8.
- (117) Sheldrick, G. M. *Acta Cryst. C* **2015**, *71*, 3–8.
- (118) Putz, H.; Brandenburg, K. *Diamond: Crystal and Molecular Structure Visualization*, Kreuzherrenstr. 102, 53227 Bonn, Germany, 2018.
-

## 6 Anhang

### 6.1 Publikationsliste

Die in der Arbeit enthaltenen Publikationen sind durch fett gedruckte Titel gekennzeichnet.

**[7] "Hydrogen Atom Abstraction by Trigonal Imido Cobalt Complexes – Impact of structure onto reactivity"**

A. Reckziegel, B. Battistella, C. Millidoni, K. Ray, C.G. Werncke, *manuscript in preparation*.

**[6] "Between Imide, Imidyl and Nitrene – An Imido Iron Complex in Two Oxidation States"**

S. Reith, S. Demeshko, B. Battistella, A. Reckziegel, C. Schneider, A. Stoy, C. Lichtenberg, F. Meyer, D. Munz, C. G. Werncke, *Chem. Sci* **2022**, *13*, 7907-7913.

**[5] "Intricate Road to Linear Anionic Nickel(I) Hexamethyldisilazide  $[\text{Ni}(\text{N}(\text{SiMe}_3)_2)_2]^-$ "**

A. Reckziegel, B. Battistella, A. Schmidt, C.G. Werncke, *Inorg. Chem.* **2022**, *61*, 7794-7803.

**[4] "On the Synthesis of a T-shaped Imido Nickel Complex and Trigonal Amido Nickel Complexes"**

A. Reckziegel, B. Battistella, C.G. Werncke, *Eur. J. Inorg. Chem.* **2022**, e202101102.

**[3] "High-Spin Imido Cobalt Complexes with Imidyl Radical Character"**

A. Reckziegel, M. Kour, B. Battistella, S. Mebs, K. Beuthert, R. Berger, C.G. Werncke, *Angew. Chem. Int. Ed.* **2021**, *60*, 15367-15380.

**[2] "C–H bond activation by an Imido Cobalt(III) and the Resulting Amido Cobalt(II) Complex"**

A. Reckziegel, C. Pietzonka, F. Kraus, C.G. Werncke, *Angew. Chem. Int. Ed.* **2020**, *59*, 8527-8531.

**[1] "Balancing Steric and Electronic Effects in Carbonyl–Phosphine Molybdacarboranes"**

Alasdair P. M. Robertson, Alexander Reckziegel, John J. Jones, Georgina M. Rosair, Alan J. Welch, *Eur. J. Inorg. Chem.* **2017**, 4581-5488.

### 6.3 Danksagung

An dieser Stelle möchte ich mich bei den Personen bedanken, die mich in den letzten Jahren unterstützt haben und mir das Anfertigen meiner Promotionsschrift ermöglicht haben.

Zuallererst bedanke ich mich bei meinem Doktorvater *Dr. Gunnar C. Werncke* für die Unterstützung in den 5 letzten Jahren, vor allem für die Ideen und Anregungen zu diesem Thema. Deine Gelassenheit und Lösungsansätze im Umgang mit Problemen, sowie deine motivierende Art, werde ich stets in guter Erinnerung behalten.

*Prof. Dr. Crispin Lichtenberg* danke ich für die hilsbereite und unkomplizierte Übernahme des Zweitgutachtens.

Vielen Dank auch an *Prof. Dr. Andreas Seubert* und *Prof. Dr. Wolf-Christian Pilgrim* für die Teilnahme an der Prüfungskommission.

Im Folgenden möchte ich mich bei meinen Kooperationspartnern bedanken, die mir unentbehrliche Auswertungen und Messungen für meine Arbeit ermöglicht haben. *Clemens Pietzonka* und *Prof. Dr. Florian Kraus* danke ich für die Durchführung und Auswertung von magnetischen Messungen im Festkörper, *Beatrice Batistella* für die Vorbereitung und Messung einer Vielzahl von ESR-Proben. Danke auch für die Hilfestellungen bei der Auswertung der erhaltenen Daten. *Dr. Stefan Mebs* ermöglichte mir den Zugang zur Röntgenabsorptionsspektroskopie. Quantenchemische Rechnungen wurden dankenswerterweise von *Dr. Manjinder Kour* und *Prof. Dr. Robert Berger* bzw. von *Dominik Munz* durchgeführt.

Weiterhin danke ich *Andreas Schmidt*, *Kevin Dollberg*, *Christina Millidoni* und *Desiree Richter*, die mich im Zuge eines Forschungspraktikums, bzw. einer Bachelorarbeit, bei meiner Arbeit unterstützt haben.

Für das Korrekturlesen dieser Arbeit danke ich *Sascha Reith*, *Andres Gonzales* und *Willfried Pfaff*.

Den aktuellen und ehemaligen Mitarbeiter der Arbeitsgruppe Werncke *Igor Müller*, *Christian Schneider*, *Ruth Weller*, *Grégoire Sieg*, *Sascha Reith* und *Andres Gonzales* möchte ich für die angenehme und freundschaftliche Arbeitsatmosphäre danken. Die hilfreichen Ratschläge und angeregten Diskussionen waren mir eine große Hilfe. Auch den Mitgliedern der Arbeitsgruppen Dehnen, Heine, Tambornino, von Hänisch und Lichtenberg danke ich für die Unterstützung und den fachlichen Austausch.

Den Mitarbeitern der Service-Abteilungen der Philipps-Universität Marburg danke ich für ihre gewissenhafte Arbeit. Besonder Dank gilt dabei *Cornelia Mischke* und *Katinka Grimmeisen* für die Messung zahlreicher NMR-Spektren, *Martina Stucke* und *Heike Mallinger* für die Durchführung der Elementaranalyse, sowie *Michael Marsch*, *Radostan Riedel* und *Dr. Sergei Ivlev* der Abteilung für Kristallstrukturanalyse.

Abschließend möchte ich meiner Familie einen großen Dank aussprechen, die mir

meinen bisherigen Lebensweg und mein Studium ermöglicht haben. Danke, dass ihr mir immer zur Seite steht und mich in jeder Situation hilfreich unterstützt.

## 6.4 Allgemeine Analytik und Arbeitstechniken

Die Darstellung der Edukten wurde unter Verwendung von SCHLENK-Technik in einer Argon-Schutzgasatmosphäre durchgeführt. Die verwendeten Glasgeräte wurden mittels Heißluftfön geheizt und im Vakuum abgekühlt. Zum Erzeugen des Vakuums wurden Drehschieberölpumpen (Fa. Pfeiffer) genutzt. Die Arbeiten mit den Metall(I)-Komplexen wurde in einer Glovebox (Fa. M. Braun) unter Argon-Schutzgasatmosphäre durchgeführt. Die verwendeten Lösungsmittel wurden über elementarem Natrium getrocknet und unter Argon-Schutzgasatmosphäre über Molsieb mit 4 Å Porengröße gelagert.

Die erhaltenen Feststoffe wurden vor Gebrauch *in vacuo* getrocknet, Flüssigkeiten wurden gefriergetrocknet und über Molsieb mit 4 Å Porengröße gelagert.

### Kernresonanzspektroskopie

Die Kernresonanzspektren (NMR) der Verbindungen wurden an den von Fa. BRUKER hergestellten Geräten AV II 300 MHz, AV III HD 250 MHz, AV III HD 300 MHz, AV III 500 MHz oder AV III HD 500 MHz der NMR-Serviceabteilung der Philipps-Universität Marburg gemessen. Sofern nicht anders angegeben, erfolgte die Messung bei Raumtemperatur. Für die <sup>1</sup>H-NMR-Spektren wurde Trimethylsilan ( $\delta$ : 0.00 ppm) als interner Standard verwendet. Die angegebenen Verschiebungen  $\delta$  wurden in ppm relativ zu dem Standard angegeben. Die Kopplung zweier Kerne (A und B) mit dem Kernspin 0.5 über n Bindungen wurde mit der Kopplungskonstante  ${}^nJ_{AB}$  angegeben. Die verschiedenen Signalmultiplizitäten wurden wie folgt abgekürzt:

s = Singulett, d = Duplett, sep = Septett, m = Multipllett.

Die Auswertung der erhaltenen Daten wurde mit dem Programm MESTRENOVA durchgeführt.

### Bestimmung der magnetischen Eigenschaften

Für Messungen des magnetischen Momentes nach der Methode von EVANS wurde deuteriertes Lösungsmittel mit einem Volumenprozent Tetramethylsilan verwendet. Als interner Standard wurde eine Kapillare mit entsprechendem Lösungsmittel verwendet.[113]

### Röntgenstrukturanalyse

Die Röntgenbeugungsexperimente am Einkristall wurden durch die Service Abteilung der Philipps-Universität Marburg oder von *Dr. Gunnar Werncke* an dem Geräten D8 Quest der Fa. BRUKER durchgeführt.

Für die Verarbeitung der erhaltenen Daten wurde die Programme APEX 3/4 (D8 Quest) und Olex2 mit den Implementierungen ShelXL und ShelXT von SHELDRICK verwendet.[114–117] Zum Erstellen der gezeigten Abbildungen wurde DIAMOND 4 verwendet.[118]

### ESR-Spektroskopie

Die Elektronen-Spin-Resonanz-Spektren (ESR) wurden durch *Beatrice Battistella* und *Amanda Opis Basilio* aus der Arbeitsgruppe *K. Ray* an der Humboldt Universität zu Berlin an einem EMXplus (X-Band) ESR-Spektrometer der Firma BRUKER

mit einem ER4118X-MD5 Probenkopf durchgeführt. Die Proben wurden vorbereitet, in einem J. Young Quartz ESR-Röhrchen überführt und direkt in flüssigem Stickstoff eingefroren.

### Röntgen-Absorptions-Spektroskopie (XAS)

Die Röntgen-Absorptions-Spektroskopie wurde im Festkörper und in gefrorener Lösung an der KMC3 *beamline* der Röntgenquelle BESSY am Helmholtz-Zentrum Berlin (HZB) von *Dr. Stefan Mebs* durchgeführt. Die Daten wurden bei 20 K in einem flüssig Helium Kryostaten unter Nutzung eines Silizium-Drift-Detektors (13 Elemente, ultra-low energy resolving) von Canberra aufgenommen. Für jede Verbindung wurden mindestens 25 Spektren gemittelt um das Verhältnis von Signal zu Rauschen zu verbessern. Die Korrektur des Hintergrundes wurde durch eine hauseigenen Software des HZB durchgeführt. Die Probenvorbereitung erfolgte durch *Beatrice Battistella* aus der Arbeitsgruppe *K. Ray* an der Humboldt Universität zu Berlin. Als Lösungsmittel für die Messungen in gefrorener Lösung wurde MeTHF verwendet. Als Standard für die Bestimmung der Oxidationsstufe wurden Nickel(II)-Oxid (NiO), Lithium-Nickel(III)-Dioxid (LiNiO<sub>2</sub>) und Kalium-Nickel(IV)-Dihydrogenperiodat (K<sub>2</sub>Ni(H<sub>2</sub>IO<sub>6</sub>)<sub>2</sub>) genutzt.

## 6.5 Synthese der beschriebenen Cobalt-Komplexe

### Darstellung von K{crypt.222}[Co(N(SiMe<sub>3</sub>)<sub>2</sub>O(<sup>t</sup>Bu<sub>3</sub>)Ar] (**128**)

Eine grünen Lösung von 30 mg K{crypt.222}[Co(N(SiMe<sub>3</sub>)<sub>2</sub>)<sub>2</sub>NH<sup>t</sup>Bu] (**103**) (0,03 mmol, 1 eq.) in 3 mL Et<sub>2</sub>O wurde bei -30 °C zu 9,2 mg 2,4,6-Tri-*tert*-Butylphenol (0,03 mmol, 1 eq.) gegeben. Die erhaltene gelbgrüne Lösung wurde mit 2 mL *n*-Pentan überschichtet und bei -30 °C gelagert. Der erhaltene gelbgrüne Feststoff wurde abfiltriert, mit 3x3 mL *n*-Pentan gewaschen und *in vacuo* getrocknet. Es wurden 21 mg des Produktes (**128**) (0,02 mmol, 65 %) in Form eines gelbgrünen, kristallinen Feststoffes erhalten.

<sup>1</sup>H-NMR (300 MHz, 300 K, THF-d<sub>8</sub>): 40,5 (s, 3H, *m*-Ar), 9,52 (s, 18H, *o*-<sup>t</sup>Bu), 3,04 (s, 12H, crypt.222), 3,01 (s, 12H, crypt.222), 2,04 (s, 12H, crypt.222), 1,50 (s, 9H, *p*-<sup>t</sup>Bu), -13,93 (s, 36H, SiMe<sub>3</sub>) ppm.

### Darstellung von K{crypt.222}[Co(N(SiMe<sub>3</sub>)<sub>2</sub>H<sub>2</sub>-9-BBN] (**130**)

Eine grüne Lösung von 60 mg K{crypt.222}[Co(N(SiMe<sub>3</sub>)<sub>2</sub>)<sub>2</sub>NH<sup>t</sup>Bu] (**103**) (0,1 mmol, 1 eq.) in 3 mL Et<sub>2</sub>O wurde bei -30 °C zu 16,8 mg 9-BBN (0,1 mmol, 1 eq.) gegeben. Die erhaltene gelbgrüne Lösung wurde für 12 Stunden gerührt, mit 2 mL *n*-Pentan überschichtet und bei -30 °C gelagert. Der erhaltene blaugrüne Feststoff wurde abfiltriert, mit 3x3 mL *n*-Pentan gewaschen und *in vacuo* getrocknet. Es wurden 40 mg des Produktes (**130**) (0,04 mmol, 63 %) in Form eines blaugrünen, kristallinen Feststoffes erhalten.

<sup>1</sup>H-NMR (300 MHz, 300 K, THF-d<sub>8</sub>): 82,0 (s), 25,7 (s) 3,31 (s, 12H, crypt.222), 3,27 (s, 12H, crypt.222), 2,28 (s, 12H, crypt.222), 1,52 (s, 36H, SiMe<sub>3</sub>), -4,80 (s), -11,9 (s), -18,0 (s, 36H, SiMe<sub>3</sub>) ppm.

**CHN** Gefunden: C = 49,83; H = 9,31; N = 6,37.  
Berechnet: C = 49,70; H = 9,66; N = 6,10.

### Darstellung von $\text{K}\{\text{crypt.222}\}_2[\text{Co}(\text{NCO})_4]$ (**131**)

Eine rote Lösung von 30 mg  $\text{K}\{\text{crypt.222}\}[\text{Co}(\text{N}(\text{SiMe}_3)_2)_2\text{N}^t\text{Bu}]$  (**102**) (0,1 mmol, 1 eq.) in 3 mL  $\text{Et}_2\text{O}$  wurde mit einer Atmosphäre CO versetzt. Ein Farbwechsel zu grün und schließlich zu blau, gefolgt von der Bildung eines blauen Feststoffes, wurde beobachtet. Der Rückstand wurde in 1,2-Difluorbenzol gelöst und filtriert. Die erhaltene blaue Lösung wurde mit 2 mL *n*-Pentan überschichtet und bei  $-30^\circ\text{C}$  gelagert. Der erhaltene blaue Feststoff wurde abfiltriert, mit 3x3 mL *n*-Pentan gewaschen und *in vacuo* getrocknet. Das Produkt (**131**) wurde als blauer, kristalliner Feststoff erhalten.

### Darstellung von $\text{K}\{\text{crypt.222}\}[\text{Co}(\text{N}(\text{SiMe}_3)_2(\text{PhN}_4^t\text{Bu}))]$ (**132**)

Eine rote Lösung von 45 mg  $\text{K}\{\text{crypt.222}\}[\text{Co}(\text{N}(\text{SiMe}_3)_2)_2\text{N}^t\text{Bu}]$  (**102**) (0,05 mmol, 1 eq.) in 3 mL  $\text{Et}_2\text{O}$  wurde bei  $-30^\circ\text{C}$  zu 6 mg Phenylazid (0,05 mmol, 1 eq.) gegeben. Die erhaltene dunkelgrüne Lösung wurde mit 2 mL *n*-Pentan überschichtet und bei  $-30^\circ\text{C}$  gelagert. Der erhaltene grüne Feststoff wurde abfiltriert, mit 3x3 mL *n*-Pentan gewaschen und *in vacuo* getrocknet. Es wurden 33 mg des Produktes (**132**) (0,03 mmol, 64 %) in Form eines grünen, kristallinen Feststoffes erhalten.

<sup>1</sup>**H-NMR** (300 MHz, 300 K, THF-*d*8): 65,0 (s, *Ph*), 47,4 (s, *Ph*), 6,59 (s, 9H, *t*Bu), 3,66 (s, 12H, crypt.222), 3,47 (s, 12H, crypt.222), 2,75 (s, 12H, crypt.222) ppm, 0,37 (s, 36H, *SiMe*<sub>3</sub>), -11,2 (s, *Ph*).

**EVANS** (500 MHz, 298 K, THF-*d*8 +1% TMS):  $\mu_{eff} = 3,29 \mu_B$ .

**IR** (ATR,  $\text{cm}^{-1}$ )  $\nu$ : 2946 (w), 2885 (w), 1480 (w), 1354 (w), 1260 (w), 1233 (m), 1132 (w), 1099 (s), 1081 (m), 1056 (w), 957 (s), 949 (s), 932 (m), 879 (w), 862 (m), 819 (s), 778 (m), 759 (m), 749 (m), 708 (m), 691 (m), 663 (m), 654 (m), 609 (w), 566 (w), 523 (w)  $\text{cm}^{-1}$ .

**CHN** Gefunden: C = 49,17; H = 8,50; N = 11,02.  
Berechnet: C = 48,75; H = 8,80; N = 11,37.

### Darstellung von $\text{K}\{\text{crypt.222}\}[\text{Co}(\text{N}(\text{SiMe}_3)_2(\text{PhN}(\text{CO})\text{N}^t\text{Bu}))]$ (**133**)

Eine Lösung von 10 mg PhNCO (0,1 mmol, 1 eq.) in 2 mL  $\text{Et}_2\text{O}$  wurde auf  $-30^\circ\text{C}$  vorgekühlt und zu 60 mg  $\text{K}\{\text{crypt.222}\}[\text{Co}(\text{N}(\text{SiMe}_3)_2)_2\text{N}^t\text{Bu}]$  (**102**) (0,1 mmol, 1 eq.) gegeben. Nach vollständigem Lösen des Feststoffes wurde die violette Reaktionslösung sofort filtriert, mit 3 mL *n*-Pentan überschichtet und bei  $-30^\circ\text{C}$  gelagert. Die überstehende Lösung des erhaltenen violetten Feststoffes wurde abfiltriert und dieser mit 3x3 mL *n*-Pentan gewaschen. Nach Trocknen *in vacuo* wurden 53 mg des Produktes (**133**) (0,08 mmol, 78 %) in Form eines violetten, kristallinen Feststoffes



erhalten.

**<sup>1</sup>H-NMR** (300 MHz, 300 K, THF-d<sub>8</sub>): 115,2 (s), 22,2 (s, 9H, *t*Bu), 6,27 (s, 36H, SiMe<sub>3</sub>), 3,62 (s, 12H, crypt.222), 3,58 (s, 12H, crypt.222), 2,58 (s, 12H, crypt.222) ppm.

**IR** (ATR, cm<sup>-1</sup>) v: 2950 (w), 2882 (m), 2817 (w), 2160 (w), 2135 (w), 1593 (s), 1476 (m), 1445 (w), 1352 (m), 1299 (m), 1256 (m), 1235 (s), 1210 (m), 1132 (m), 1101 (s), 1079 (s), 947 (s), 829 (s), 772 (s), 747 (s), 691 (s), 661 (s), 613 (s), 568 (w), 516 (m) cm<sup>-1</sup>.

**CHN** Gefunden: C = 51,50; H = 8,67; N = 8,10.  
Berechnet: C = 51,38; H = 9,11; N = 8,17.

### Darstellung von K{crypt.222}[Co(N(SiMe<sub>3</sub>)<sub>2</sub>(MesN(CO)N(H)*t*Bu)] (134)

Eine Lösung von 11,2 mg MesNCO (0,1 mmol, 1 eq.) in 2 mL Et<sub>2</sub>O wurde auf -30°C vorgekühlt und zu 60 mg K{crypt.222}[Co(N(SiMe<sub>3</sub>)<sub>2</sub>N*t*Bu] (**102**) (0,1 mmol, 1 eq.) gegeben. Nach vollständigem Lösen des Feststoffes, wurde die violette Reaktionslösung sofort filtriert, mit 3 mL *n*-Pentan überschichtet und bei -30°C gelagert. Die überstehende Lösung des erhaltenen grünen Feststoffes wurde abfiltriert und dieser mit 3x3 mL *n*-Pentan gewaschen. Nach Trocknen *in vacuo* wurden 22 mg des Produktes (**134**) (0,1 mmol, 78 %) in Form eines grünen, kristallinen Feststoffes erhalten.

**CHN** Gefunden: C = 51,50; H = 8,67; N = 8,10.  
Berechnet: C = 51,38; H = 9,11; N = 8,17.

### Darstellung von K{crypt.222}[Co(N(SiMe<sub>3</sub>)<sub>2</sub>(S<sub>2</sub>CN*t*Bu)] (135)

Eine Lösung von 4,2 μL CS<sub>2</sub> (0,1 mmol, 1 eq.) in 2 mL Et<sub>2</sub>O wurde auf -30°C vorgekühlt und zu 60 mg K{crypt.222}[Co(N(SiMe<sub>3</sub>)<sub>2</sub>N*t*Bu] (**102**) (0,1 mmol, 1 eq.) gegeben. Nach vollständigem Lösen des Feststoffes, wurde die dunkelrote Reaktionslösung sofort filtriert, mit 3 mL *n*-Pentan überschichtet und bei -30°C gelagert. Die überstehende Lösung des erhaltenen dunkelroten Feststoffes wurde abfiltriert und dieser mit 3x3 mL *n*-Pentan gewaschen. Nach Trocknen *in vacuo* wurden 53 mg des Produktes (**135**) (0,1 mmol, 65 %) in Form eines dunkelroten, kristallinen Feststoffes erhalten.

**<sup>1</sup>H-NMR** (300 MHz, 300 K, THF-d<sub>8</sub>): 3,85 (s, 9H, *t*Bu), 3,10 (s, 12H, crypt.222), 3,05 (s, 12H, crypt.222), 2,06 (s, 12H, crypt.222), -3,15 (s, 36H, SiMe<sub>3</sub>) ppm.

**IR** (ATR, cm<sup>-1</sup>) v: 2957 (m), 2885 (m), 1573 (s), 1354 (m), 1258 (w), 1233 (m), 1132 (m), 1103 (vs), 986 (s), 949 (s), 932 (m), 875(s), 823(s), 776(s), 747(s), 708(m), 691(s), 661(s), 617(m), 422(w) cm<sup>-1</sup>.

**CHN** Gefunden: C = 45,19; H = 8,35; N = 7,31; S = 6,81.  
 Berechnet: C = 44,51; H = 8,86; N = 7,41; S = 6,79.

## 6.6 Synthese von Imido-Nickel-Komplexen

### Darstellung von $\text{K}\{\text{crypt.222}\}[\text{Ni}(\text{N}(\text{SiMe}_3)_2\text{N}(\text{H})^t\text{Bu})]$ (**137**)

Eine gelbe Lösung von 80 mg  $\text{K}\{\text{crypt.222}\}[\text{Ni}(\text{N}(\text{SiMe}_3)_2)_2]$  (**119**) (0,1 mmol, 1 eq.) in 3 mL  $\text{Et}_2\text{O}$  wurde bei  $-30\text{ }^\circ\text{C}$  zu 10 mg *tert*-Butylazid (0,1 mmol, 1 eq.) gegeben. Die erhaltene orange Lösung wurde mit 2 mL *n*-Pentan überschichtet und bei  $-30\text{ }^\circ\text{C}$  gelagert. Der erhaltene orange Feststoff wurde abfiltriert, mit 3x3 mL *n*-Pentan gewaschen und *in vacuo* getrocknet. Es wurden 45 mg des Produktes (**137**) (0,05 mmol, 52 %) in Form eines orangen, kristallinen Feststoffes erhalten.

$^1\text{H-NMR}$  (300 MHz, 300 K,  $\text{THF-d}_8$ ): 23,0 (s,  $\text{N}^t\text{Bu}$ ), 3,57 (s, 24H, crypt.222), 2,56 (s, 12H, crypt.222), 1,80 (s, 36H,  $\text{SiMe}_3$ ) ppm.

### Darstellung von $\text{K}\{\text{18c6}\}[\text{Ni}(\text{N}(\text{SiMe}_3)_2\text{NMe}_3)]$ (**138**)

Eine gelbe Lösung von 42 mg  $\text{K}\{\text{18c6}\}[\text{Ni}(\text{N}(\text{SiMe}_3)_2)_2]$  (**118**) (0,03 mmol, 1 eq.) in 3 mL  $\text{Et}_2\text{O}$  wurde bei  $-30\text{ }^\circ\text{C}$  zu 10 mg Mesitylazid (0,03 mmol, 1 eq.) gegeben. Die erhaltene orange Lösung wurde mit 2 mL *n*-Pentan überschichtet und bei  $-30\text{ }^\circ\text{C}$  gelagert. Der erhaltene grüngelbe Feststoff wurde abfiltriert, mit 3x3 mL *n*-Pentan gewaschen und *in vacuo* getrocknet.

*Es wurde ein Gemisch aus dem Imido-Komplex 138 und dem Amido-Komplex 140 erhalten.*

### Darstellung von $\text{K}\{\text{crypt.222}\}[\text{Ni}(\text{N}(\text{SiMe}_3)_2\text{NMe}_3)]$ (**139**)

Eine gelbe Lösung von 49 mg  $\text{K}\{\text{crypt.222}\}[\text{Ni}(\text{N}(\text{SiMe}_3)_2)_2]$  (**119**) (0,06 mmol, 1 eq.) in 3 mL  $\text{Et}_2\text{O}$  wurde bei  $-30\text{ }^\circ\text{C}$  zu 10 mg Mesitylazid (0,06 mmol, 1 eq.) gegeben. Die erhaltene orange Lösung wurde mit 2 mL *n*-Pentan überschichtet und bei  $-30\text{ }^\circ\text{C}$  gelagert. Der erhaltene grüngelbe Feststoff wurde abfiltriert, mit 3x3 mL *n*-Pentan gewaschen und *in vacuo* getrocknet. Es wurden 37 mg des Produktes (**139**) (0,04 mmol, 68 %) in Form eines grüngelb, kristallinen Feststoffes erhalten.

**CHN** Gefunden: C = 50,96; H = 8,91; N = 7,73.  
 Berechnet: C = 50,46; H = 9,01; N = 7,54.

## 6.7 NMR Spektren

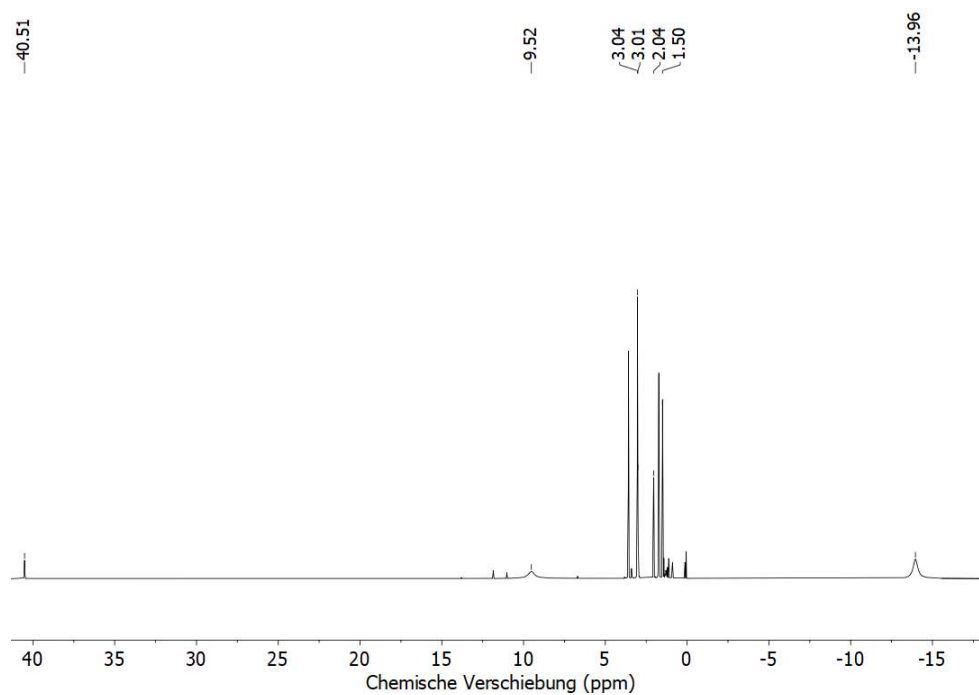


Abb. 82:  $^1\text{H-NMR}$ -Spektren (300 MHz, 300 K,  $\text{THF-d}_8$ ) von  $\text{K}\{\text{crypt.222}\}\text{Co}(\text{N}(\text{SiMe}_3)_2)_2(\text{PhN}_4^t\text{Bu})$  (**128**).

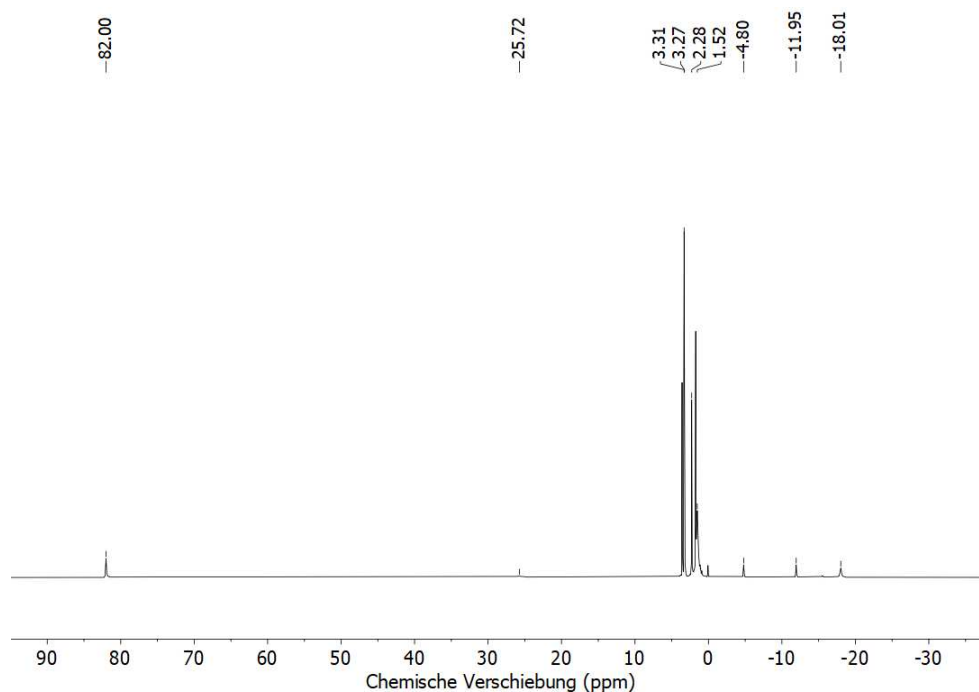


Abb. 83:  $^1\text{H-NMR}$ -Spektren (300 MHz, 300 K,  $\text{THF-d}_8$ ) von  $\text{K}\{\text{crypt.222}\}\text{Co}(\text{N}(\text{SiMe}_3)_2)_2(\text{H}_2\text{-9-BBN})$  (**130**).

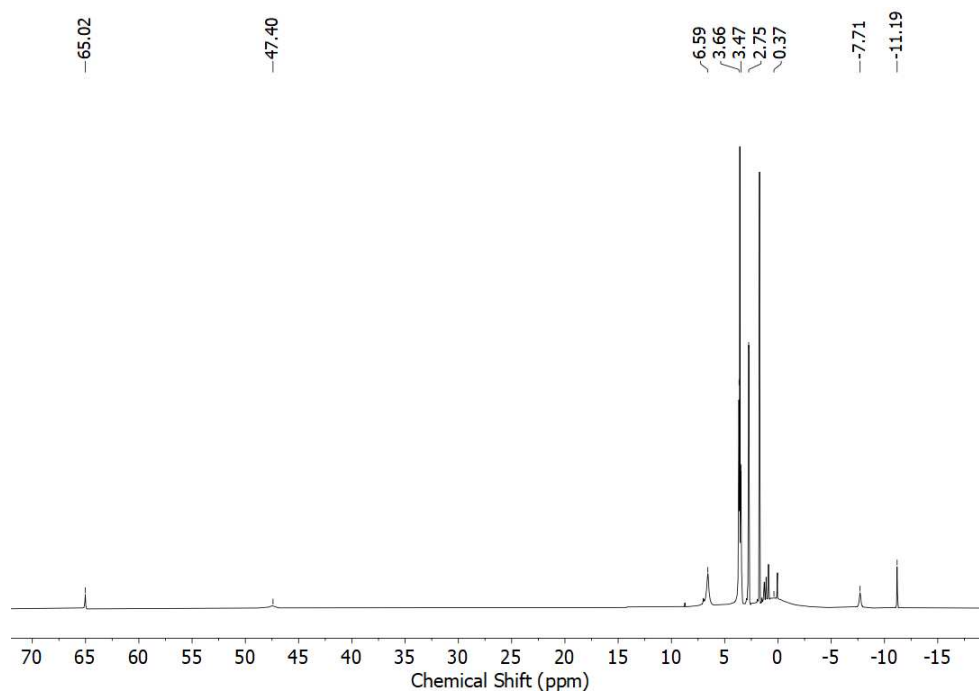


Abb. 84:  $^1\text{H}$ -NMR-Spektren (300 MHz, 300 K, THF- $d_8$ ) von  $\text{K}\{\text{crypt.222}\}\text{Co}(\text{N}(\text{SiMe}_3)_2)(\text{PhN}^t\text{Bu})$  (**132**).

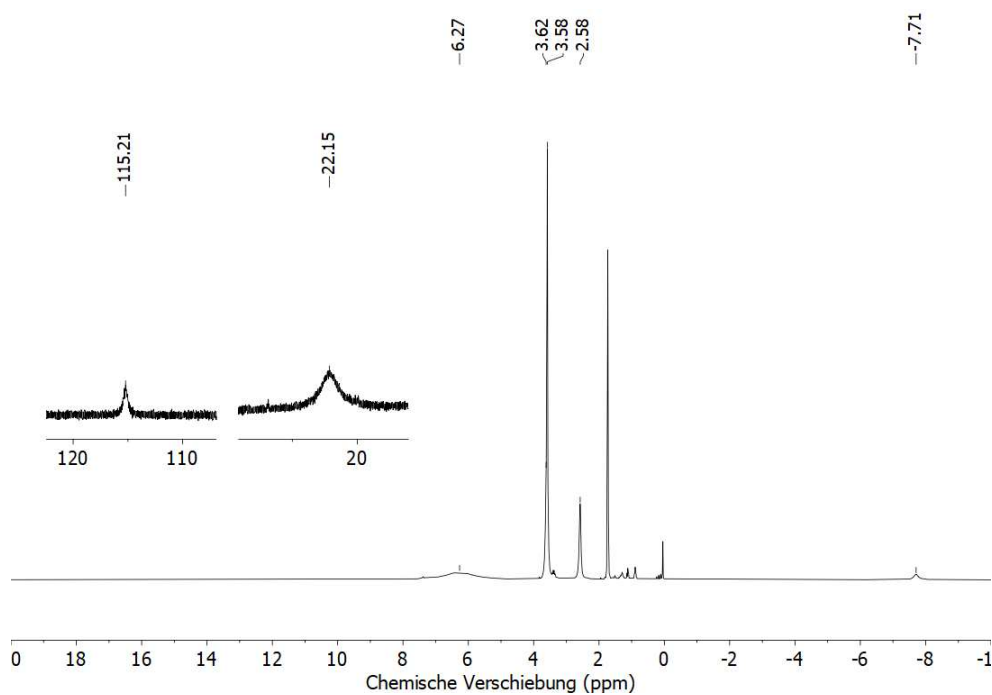


Abb. 85:  $^1\text{H}$ -NMR-Spektren (300 MHz, 300 K, THF- $d_8$ ) von  $\text{K}\{\text{crypt.222}\}\text{Co}(\text{N}(\text{SiMe}_3)_2)(^t\text{BuN}(\text{CO})\text{NPh})$  (**133**).

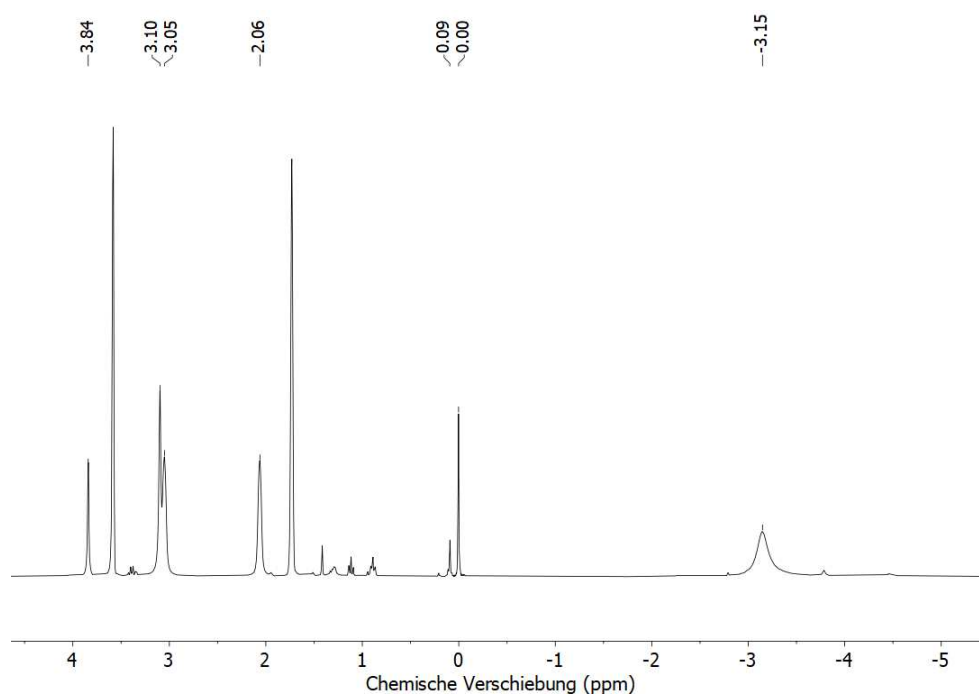


Abb. 86:  $^1\text{H-NMR}$ -Spektren (300 MHz, 300 K,  $\text{THF-d}_8$ ) von  $\text{K}\{\text{crypt.222}\}\text{Co}(\text{N}(\text{SiMe}_3)_2)_2(\text{S}_2\text{CN}^t\text{Bu})$  (**135**).

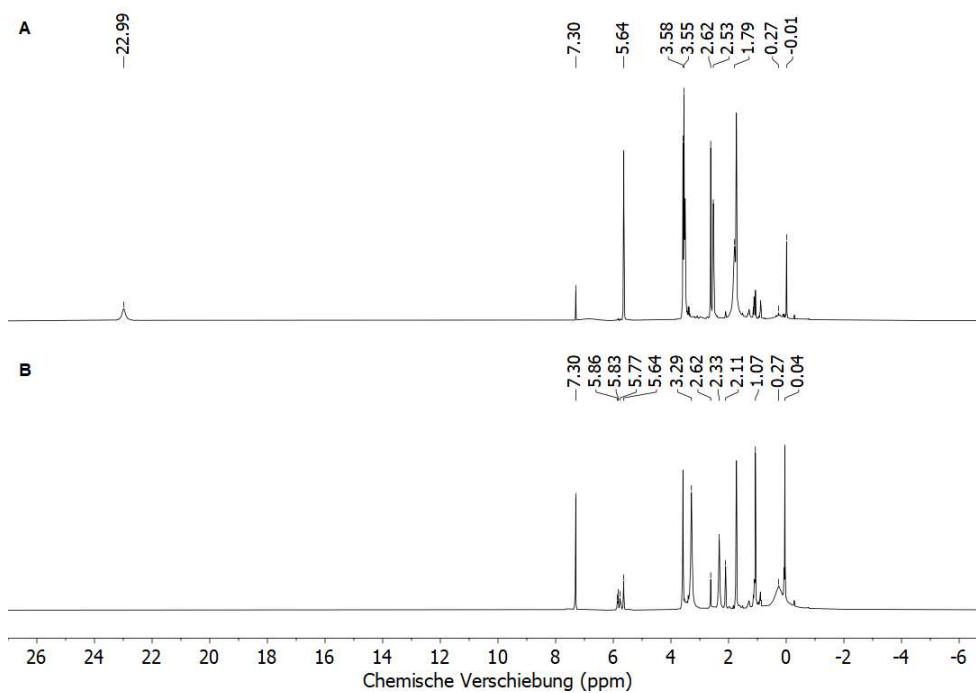


Abb. 87:  $^1\text{H-NMR}$ -Spektren (300 MHz, 300 K,  $\text{THF-d}_8$ ) der Umsetzung von  $\text{K}\{\text{crypt.222}\}\text{Ni}(\text{hmds})_2\text{N}^t\text{Bu}$  (**137**) mit 1,4-Cyclohexadien. (A:  $t = 5$  min; B:  $t = 24$  h).

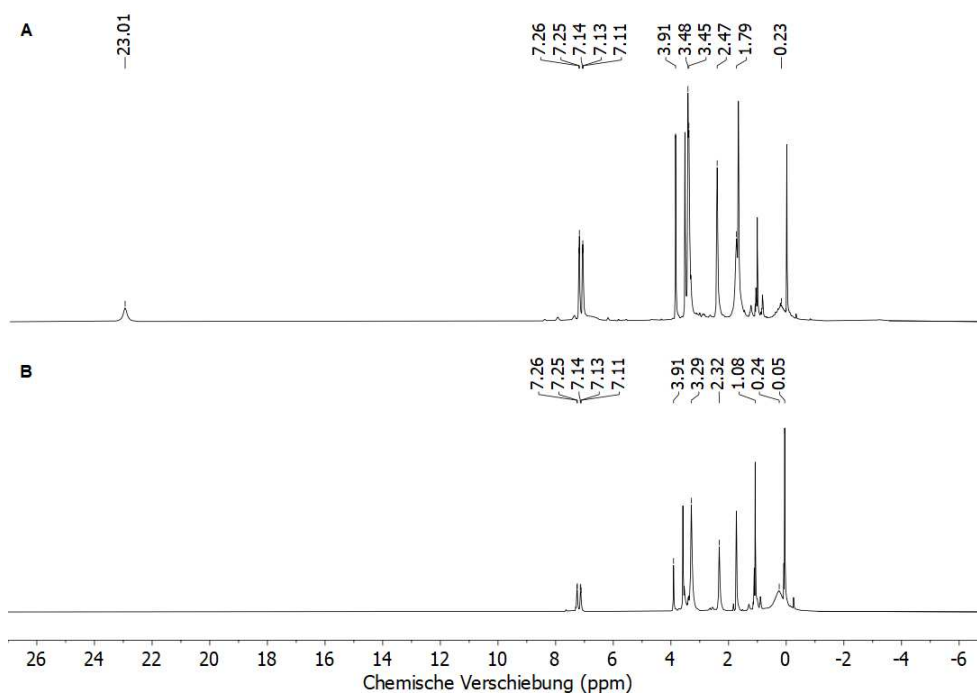


Abb. 88:  $^1\text{H}$ -NMR-Spektren (300 MHz, 300 K,  $\text{THF-d}_8$ ) der Umsetzung von  $\text{K}\{\text{crypt.222}\}\text{Ni}(\text{hmds})_2\text{N}^t\text{Bu}$  (**137**) mit 9,10-Dihydroanthracen. (A:  $t = 5$  min; B:  $t = 24$  h).

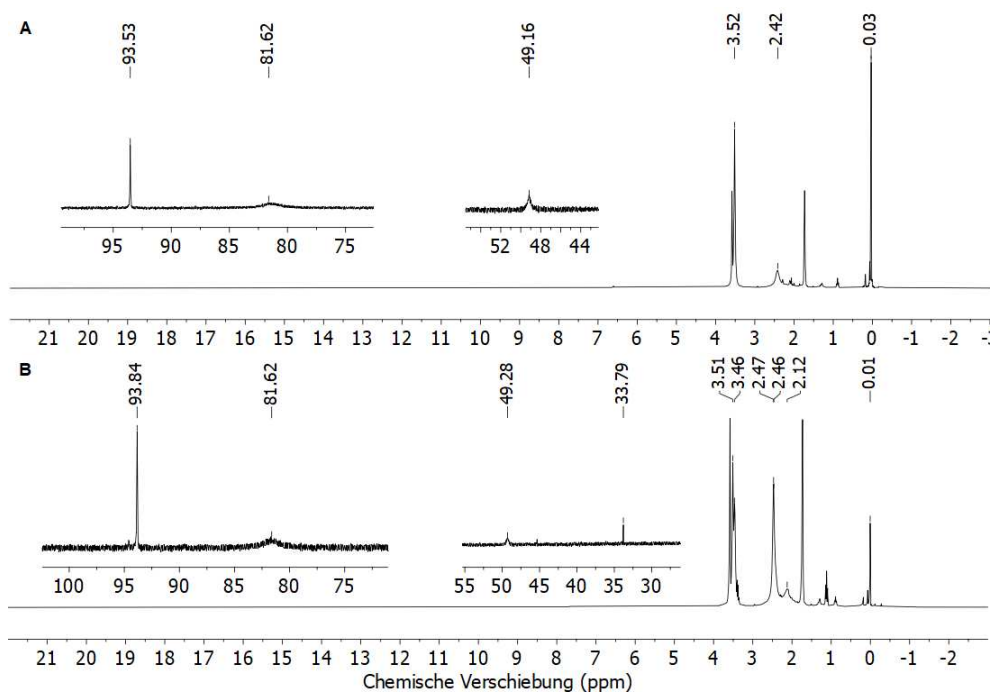


Abb. 89:  $^1\text{H}$ -NMR-Spektren (300 MHz, 300 K,  $\text{THF-d}_8$ ) von  $\text{K}\{18\text{c}6\}\text{Ni}(\text{N}(\text{SiMe}_3)_2)_2\text{NMes}$  (**138**) **A** und von  $\text{K}\{\text{crypt.222}\}\text{Ni}(\text{N}(\text{SiMe}_3)_2)_2\text{NMes}$  (**139**) **B**.

## 6.8 Kristallographischer Anhang

K{crypt.222}Co(N(SiMe<sub>3</sub>)<sub>2</sub>)<sub>2</sub>O<sup>tBu<sub>3</sub></sup>Ph (128)Tab. 1: Kristallographische Daten von **128**

Identification code	GWX066C
Empirical formula	C <sub>50.5</sub> H <sub>107</sub> CoKN <sub>4</sub> O <sub>7</sub> Si <sub>4</sub>
Formula weight / gmol <sup>-1</sup>	1092.78
Temperature / K	100.01
Crystal system	monoclinic
Space group	<i>P</i> 2 <sub>1</sub> / <i>c</i>
<i>a</i> / Å	14.1153(6)
<i>b</i> / Å	22.9799(10)
<i>c</i> / Å	20.5316(9)
$\alpha$ / °	90
$\beta$ / °	108.5600(10)
$\gamma$ / °	90
Volume / Å <sup>3</sup>	6313.4(5)
<i>Z</i>	4
$\rho_{calc}$ / g/cm <sup>3</sup>	1.150
$\mu$ / mm <sup>-1</sup>	0.460
F(000)	2384
Crystal size/ mm <sup>3</sup>	0.316 x 0.215 x 0.166
Radiation	MoK $\alpha$ ( $\lambda$ = 0.71073)
2 $\Theta$ range for data collection/°	4.546 to 52.15
Index ranges	-17 $\leq h \leq$ 17, -28 $\leq k \leq$ 28, -25 $\leq l \leq$ 25
Reflections collected	85086
Independent reflections	124631 [Rint = 0.0644, Rsigma = 0.0384]
Data/restraints/parameters	124631/66/716
Goodness-of-fit on F <sup>2</sup>	1.372
Final R indexes [I $\geq$ 2 $\sigma$ (I)]	R1 = 0.1240, wR2 = 0.2768
Final R indexes [all data]	R1 = 0.1349, wR2 = 0.2807
Largest diff. peak/hole / e Å <sup>-3</sup>	0.94/-0.82

**K{crypt.222}Co(N(SiMe<sub>3</sub>)<sub>2</sub>)<sub>2</sub>(H<sub>2</sub>-9-BBN) (130)**Tab. 2: Kristallographische Daten von **130**

Identification code	GWX146
Empirical formula	C <sub>38</sub> H <sub>87</sub> BCoKN <sub>4</sub> O <sub>6</sub> Si <sub>4</sub>
Formula weight / gmol <sup>-1</sup>	917.31
Temperature / K	100.00
Crystal system	monoclinic
Space group	<i>P</i> 2 <sub>1</sub> / <i>n</i>
a / Å	14.3265(6)
b / Å	22.8000(9)
c / Å	16.9765(7)
α / °	90
β / °	108.794(2)
γ / °	90
Volume / Å <sup>3</sup>	5249.64(4)
Z	4
ρ <sub>calc</sub> / g/cm <sup>3</sup>	1.161
μ / mm <sup>-1</sup>	0.539
F(000)	1992.0
Crystal size/ mm <sup>3</sup>	0.597 x 0.322 x 0.305
Radiation	MoKα (λ = 0.71073)
2θ range for data collection/°	4.38 to 67.526
Index ranges	-21 ≤ <i>h</i> ≤ 21, -35 ≤ <i>k</i> ≤ 35, -25 ≤ <i>l</i> ≤ 26
Reflections collected	198505
Independent reflections	18947 [Rint = 0.0784, Rsigma = 0.0510]
Data/restraints/parameters	18947/0/516
Goodness-of-fit on F <sup>2</sup>	1.112
Final R indexes [I ≥ 2σ (I)]	R1 = 0.0445, wR2 = 0.1324
Final R indexes [all data]	R1 = 0.0714, wR2 = 0.1378
Largest diff. peak/hole / e Å <sup>-3</sup>	1.35/-0.64



**(K{crypt.222})<sub>2</sub>[Co(NCO)<sub>4</sub>] (131)**Tab. 3: Kristallographische Daten von **131**

Identification code	GWX90_0m
Empirical formula	C <sub>40</sub> H <sub>72</sub> CoK <sub>2</sub> N <sub>8</sub> O <sub>16</sub>
Formula weight / gmol <sup>-1</sup>	1058.18
Temperature / K	100.00
Crystal system	hexagonal
Space group	<i>P</i> 6 <sub>3</sub>
a / Å	11.7223(6)
b / Å	11.7223(6)
c / Å	21.8314(16)
α / °	90
β / °	90
γ / °	120
Volume / Å <sup>3</sup>	2607.8(3)
Z	2
ρ <sub>calc</sub> / g/cm <sup>3</sup>	1.348
μ / mm <sup>-1</sup>	0.559
F(000)	1122.0
Crystal size/ mm <sup>3</sup>	0.485 x 0.261 x 0.194
Radiation	MoKα (λ = 0.71073)
2θ range for data collection/°	4.418 to 52.232
Index ranges	-14 ≤ h ≤ 14, -14 ≤ k ≤ 14, -27 ≤ l ≤ 27
Reflections collected	41709
Independent reflections	3468 [Rint = 0.0509, Rsigma = 0.0252]
Data/restraints/parameters	3468/1/203
Goodness-of-fit on F <sup>2</sup>	1.057
Final R indexes [I ≥ 2σ (I)]	R1 = 0.0323, wR2 = 0.0677
Final R indexes [all data]	R1 = 0.0393, wR2 = 0.0703
Largest diff. peak/hole / e Å <sup>-3</sup>	0.33/-0.24
Flack parameter	0.03(2)

**K{crypt.222}Co(N(SiMe<sub>3</sub>)<sub>2</sub>)<sub>2</sub>(PhN<sup>t</sup><sub>4</sub>Bu) (132)**Tab. 4: Kristallographische Daten von **132**

Identification code	XP84_0m
Empirical formula	C <sub>40</sub> H <sub>86</sub> CoKN <sub>8</sub> O <sub>6</sub> Si <sub>4</sub>
Formula weight / gmol <sup>-1</sup>	985.55
Temperature / K	100.00
Crystal system	triclinic
Space group	<i>P</i> $\bar{1}$
a / Å	11.6468(5)
b / Å	15.5575(7)
c / Å	16.3093(8)
$\alpha$ / °	67.380(2)
$\beta$ / °	85.434(2)
$\gamma$ / °	89.829(2)
Volume / Å <sup>3</sup>	2704.9(2)
Z	2
$\rho_{calc}$ / g/cm <sup>3</sup>	1.210
$\mu$ / mm <sup>-1</sup>	0.530
F(000)	1064.0
Crystal size/ mm <sup>3</sup>	0.459 x 0.15 x 0.127
Radiation	MoK $\alpha$ ( $\lambda$ = 0.71073)
2 $\Theta$ range for data collection/°	4.302 to 54.36
Index ranges	-14 $\leq h \leq$ 14, -19 $\leq k \leq$ 19, -20 $\leq l \leq$ 20
Reflections collected	97197
Independent reflections	11990 [Rint = 0.0494, Rsigma = 0.0293]
Data/restraints/parameters	11990/0/556
Goodness-of-fit on F <sup>2</sup>	1.057
Final R indexes [I $\geq$ 2 $\sigma$ (I)]	R1 = 0.0267, wR2 = 0.0682
Final R indexes [all data]	R1 = 0.0332, wR2 = 0.0697
Largest diff. peak/hole / e Å <sup>-3</sup>	0.38/-0.34

**K{crypt.222}Co(N(SiMe<sub>3</sub>)<sub>2</sub>O(<sup>t</sup>Bu<sub>3</sub>)Ar 133**Tab. 5: Kristallographische Daten von **133**

Identification code	XP73_0m
Empirical formula	C <sub>41</sub> H <sub>86</sub> CoKN <sub>6</sub> O <sub>7</sub> Si <sub>4</sub>
Formula weight / gmol <sup>-1</sup>	985.54
Temperature / K	100.00
Crystal system	orthorhombic
Space group	<i>Pbca</i>
a / Å	21.6798(7)
b / Å	20.4857(6)
c / Å	24.7544(9)
α / °	90
β / °	90
γ / °	90
Volume / Å <sup>3</sup>	10994.1(6)
Z	8
ρ <sub>calc</sub> / g/cm <sup>3</sup>	1.191
μ / mm <sup>-1</sup>	0.522
F(000)	4256.0
Crystal size/ mm <sup>3</sup>	0.486 x 0.258 x 0.237
Radiation	MoKα (λ = 0.71073)
2θ range for data collection/°	3.976 to 55.898
Index ranges	-28 ≤ h ≤ 27, -26 ≤ k ≤ 26, -32 ≤ l ≤ 32
Reflections collected	256599
Independent reflections	13193 [Rint = 0.1312, Rsigma = 0.0480]
Data/restraints/parameters	13193/0/556
Goodness-of-fit on F <sup>2</sup>	0.748
Final R indexes [I ≥ 2σ (I)]	R1 = 0.0308, wR2 = 0.1000
Final R indexes [all data]	R1 = 0.0471, wR2 = 0.1065
Largest diff. peak/hole / e Å <sup>-3</sup>	0.91/-0.34

**K{crypt.222}Co(N(SiMe<sub>3</sub>)<sub>2</sub>)<sub>2</sub>(MesN(CO)N(H)<sup>t</sup>Bu) 141**

Tab. 6: Kristallographische Daten von 141

Identification code	GWX175_0m
Empirical formula	C <sub>48</sub> H <sub>103</sub> CoKN <sub>6</sub> O <sub>8</sub> Si <sub>4</sub>
Formula weight / gmol <sup>-1</sup>	1102.75
Temperature / K	100.00
Crystal system	monoclinic
Space group	<i>P</i> 2 <sub>1</sub> / <i>c</i>
<i>a</i> / Å	14.1677(5)
<i>b</i> / Å	12.6550(5)
<i>c</i> / Å	35.994(1)
$\alpha$ / °	90
$\beta$ / °	91.8840
$\gamma$ / °	90
Volume / Å <sup>3</sup>	6450.0(4)
<i>Z</i>	4
$\rho_{calc}$ / g/cm <sup>3</sup>	1.136
$\mu$ / mm <sup>-1</sup>	0.452
F(000)	2396.0
Crystal size/ mm <sup>3</sup>	0.5 x 0.407 x 0.312
Radiation	MoK $\alpha$ ( $\lambda$ = 0.71073)
2 $\Theta$ range for data collection/°	4.316 to 54.262
Index ranges	-18 $\leq h \leq$ 18, -16 $\leq k \leq$ 16, -46 $\leq l \leq$ 46
Reflections collected	112728
Independent reflections	14252 [Rint = 0.0287, Rsigma = 0.0176]
Data/restraints/parameters	14252/0/637
Goodness-of-fit on F <sup>2</sup>	1.119
Final R indexes [I $\geq$ 2 $\sigma$ (I)]	R1 = 0.0461, wR2 = 0.1102
Final R indexes [all data]	R1 = 0.0493, wR2 = 0.1119
Largest diff. peak/hole / e Å <sup>-3</sup>	0.59/-0.46

**K{crypt.222}Co(N(SiMe<sub>3</sub>)<sub>2</sub>)<sub>2</sub>(S<sub>2</sub>CN<sup>t</sup>Bu) (135)**Tab. 7: Kristallographische Daten von **135**

Identification code	SGPX19_0m
Empirical formula	C <sub>35</sub> H <sub>81</sub> CoKN <sub>5</sub> O <sub>6</sub> S <sub>2</sub> Si <sub>4</sub>
Formula weight / gmol <sup>-1</sup>	942.55
Temperature / K	100.00
Crystal system	orthorhombic
Space group	<i>Pbca</i>
a / Å	21.130(3)
b / Å	15.627(2)
c / Å	33.243(4)
α / °	90
β / °	90
γ / °	90
Volume / Å <sup>3</sup>	10977(2)
Z	8
ρ <sub>calc</sub> / g/cm <sup>3</sup>	1.141
μ / mm <sup>-1</sup>	0.591
F(000)	4064.0
Crystal size/ mm <sup>3</sup>	0.47 x 0.363 x 0.19
Radiation	MoKα (λ = 0.71073)
2θ range for data collection/°	4.568 to 52.048
Index ranges	-26 ≤ h ≤ 26, -19 ≤ k ≤ 16, -37 ≤ l ≤ 41
Reflections collected	52480
Independent reflections	10790 [Rint = 0.1111, Rsigma = 0.1099]
Data/restraints/parameters	10790/0/510
Goodness-of-fit on F <sup>2</sup>	1.043
Final R indexes [I ≥ 2σ (I)]	R1 = 0.0734, wR2 = 0.1250
Final R indexes [all data]	R1 = 0.1262, wR2 = 0.1402
Largest diff. peak/hole / e Å <sup>-3</sup>	0.68/-0.45

**K{crypt.222}Ni(N(SiMe<sub>3</sub>)<sub>2</sub>)<sub>2</sub>N(H)<sup>t</sup>Bu (137)**Tab. 8: Kristallographische Daten von **137**

Identification code	XP76_0m
Empirical formula	C <sub>34</sub> H <sub>82</sub> KN <sub>5</sub> NiO <sub>6</sub> Si <sub>4</sub>
Formula weight / gmol <sup>-1</sup>	867.21
Temperature / K	100.00
Crystal system	monoclinic
Space group	<i>P</i> 2 <sub>1</sub> / <i>c</i>
<i>a</i> / Å	10.5762(4)
<i>b</i> / Å	28.2729(11)
<i>c</i> / Å	16.9724(7)
$\alpha$ / °	90
$\beta$ / °	103.832(2)
$\gamma$ / °	90
Volume / Å <sup>3</sup>	4927.9(3)
<i>Z</i>	4
$\rho_{calc}$ / g/cm <sup>3</sup>	1.469
$\mu$ / mm <sup>-1</sup>	0.617
F(000)	1888.0
Crystal size/ mm <sup>3</sup>	0.365 x 0.261 x 0.106
Radiation	MoK $\alpha$ ( $\lambda$ = 0.71073)
2 $\Theta$ range for data collection/°	3.966 to 51.53
Index ranges	-12 $\leq h \leq$ 12, -34 $\leq k \leq$ 34, -20 $\leq l \leq$ 20
Reflections collected	118500
Independent reflections	9400 [Rint = 0.0985, Rsigma = 0.0483]
Data/restraints/parameters	9400/0/479
Goodness-of-fit on F <sup>2</sup>	1.042
Final R indexes [I $\geq$ 2 $\sigma$ (I)]	R1 = 0.0298, wR2 = 0.0668
Final R indexes [all data]	R1 = 0.0531, wR2 = 0.0693
Largest diff. peak/hole / e Å <sup>-3</sup>	0.34/-0.25

**K{18c6}Ni(N(SiMe<sub>3</sub>)<sub>2</sub>)<sub>2</sub>N(H)Mes (138)**Tab. 9: Kristallographische Daten von **138**

Identification code	XP42_0m
Empirical formula	C <sub>37</sub> H <sub>81</sub> KN <sub>3</sub> NiO <sub>7</sub> Si <sub>4</sub>
Formula weight / gmol <sup>-1</sup>	890.21
Temperature / K	99.99
Crystal system	triclinic
Space group	<i>P</i> $\bar{1}$
a / Å	11.9746(7)
b / Å	14.0682(8)
c / Å	15.9339(8)
$\alpha$ / °	85.290(2)
$\beta$ / °	80.518(2)
$\gamma$ / °	75.202(2)
Volume / Å <sup>3</sup>	2557.5(3)
Z	2
$\rho_{calc}$ / g/cm <sup>3</sup>	1.156
$\mu$ / mm <sup>-1</sup>	0.596
F(000)	966.0
Crystal size/ mm <sup>3</sup>	0.457 x 0.238 x 0.154
Radiation	MoK $\alpha$ ( $\lambda$ = 0.71073)
2 $\Theta$ range for data collection/°	4.44 to 57.968
Index ranges	-16 $\leq h \leq$ 16, -19 $\leq k \leq$ 19, -21 $\leq l \leq$ 21
Reflections collected	76389
Independent reflections	13552 [Rint = 0.0443, Rsigma = 0.0360]
Data/restraints/parameters	13552/0/561
Goodness-of-fit on F <sup>2</sup>	1.037
Final R indexes [I $\geq$ 2 $\sigma$ (I)]	R1 = 0.0374, wR2 = 0.0758
Final R indexes [all data]	R1 = 0.0551, wR2 = 0.0815
Largest diff. peak/hole / e Å <sup>-3</sup>	0.40/-0.32

**K{crypt.222}Ni(N(SiMe<sub>3</sub>)<sub>2</sub>)<sub>2</sub>NMes (139)**Tab. 10: Kristallographische Daten von **139**

Identification code	XP79_0m
Empirical formula	C <sub>39</sub> H <sub>82</sub> KN <sub>5</sub> NiO <sub>6</sub> Si <sub>4</sub>
Formula weight / gmol <sup>-1</sup>	927.26
Temperature / K	100.00
Crystal system	triclinic
Space group	<i>P</i> $\bar{1}$
a / Å	12.5602(5)
b / Å	13.1912(6)
c / Å	17.6512(8)
$\alpha$ / °	109.960(2)
$\beta$ / °	93.672(2)
$\gamma$ / °	94.179(2)
Volume / Å <sup>3</sup>	2729.2(2)
Z	2
$\rho_{calc}$ / g/cm <sup>3</sup>	1.128
$\mu$ / mm <sup>-1</sup>	0.561
F(000)	1004.0
Crystal size/ mm <sup>3</sup>	0.136 x 0.091 x 0.075
Radiation	MoK $\alpha$ ( $\lambda = 0.71073$ )
2 $\Theta$ range for data collection/°	3.902 to 52.132
Index ranges	-15 $\leq h \leq$ 15, -16 $\leq k \leq$ 16, -21 $\leq l \leq$ 21
Reflections collected	89591
Independent reflections	10796 [Rint = 0.1069, Rsigma = 0.0815]
Data/restraints/parameters	10796/0/520
Goodness-of-fit on F <sup>2</sup>	1.067
Final R indexes [I $\geq$ 2 $\sigma$ (I)]	R1 = 0.0479, wR2 = 0.1214
Final R indexes [all data]	R1 = 0.0793, wR2 = 0.1364
Largest diff. peak/hole / e Å <sup>-3</sup>	0.48/-0.44



## **6.9 Elektronische Zusatzinformationen**

### **6.9.1 C–H bond activation by an Imido Cobalt(III) and the Resulting Amido Cobalt(II) Complex**

Supporting Information

**C–H Bond Activation by an Imido Cobalt(III) and the Resulting Amido Cobalt(II) Complex**

*Alexander Reckziegel, Clemens Pietzonka, Florian Kraus, and C. Gunnar Werncke\**

anie\_201914718\_sm\_miscellaneous\_information.pdf

## Table of Contents

General considerations .....	3
1. Synthesis of $K\{\text{crypt.222}\}[\text{Co}(\text{hmds})_2]$ ( $K\{\text{crypt.222}\}[1]$ ).....	4
2. Synthesis of $K\{\text{crypt.222}\}[\text{Co}(\text{hmds})_2(\text{N}^t\text{Bu})]$ ( $K\{\text{crypt.222}\}[2]$ ).....	4
3. Synthesis of $K\{\text{crypt.222}\}[\text{Co}(\text{hmds})_2(\text{HN}^t\text{Bu})]$ ( $K\{\text{crypt.222}\}[3]$ ).....	6
4. Synthesis of $K\{\text{crypt.222}\}[\text{Co}(\text{hmds})_2(9\text{-Flu})]$ ( $K\{\text{crypt.222}\}[5]$ ).....	7
5. Synthesis of $K\{\text{crypt.222}\}[\text{Co}(\text{hmds})_2(9,10\text{-DHA})]$ ( $K\{\text{crypt.222}\}[6]$ ).....	8
6. Synthesis of $K\{\text{crypt.222}\}[\text{Co}(\text{hmds})_2(\text{XAN})]$ ( $K\{\text{crypt.222}\}[7]$ ).....	9
7. NMR-scale reactions.....	11
8. Kinetic studies .....	19
9. Catalytic reactions .....	26
10. Magnetic measurements.....	28
11. EPR measurements.....	30
12. X-Ray diffraction analysis and molecular structures .....	31

## General considerations

All manipulations were carried out in a glovebox or using Schlenk-type techniques under a dry argon atmosphere. Used solvents were dried by continuous distillation over sodium metal for several days, degassed via three freeze-pump cycles and stored over molecular sieves 4 Å. [D8]THF was degassed via three freeze-pump cycles and stored over molecular sieves 4 Å. The  $^1\text{H}$  NMR spectra were recorded on a *Bruker AV III 500* or *Bruker AV II 300* NMR spectrometers. Chemical shifts are reported in ppm relative to the residual proton signals of the solvent (for  $^1\text{H}$ ) or relative to the signal of the solvent itself ( $^{13}\text{C}$ ).  $w_{1/2}$  is the line width of a signal at half its maximum intensity. Integrals of the broad signals of the silylamide units were obtained directly or by peak fitting (in case of overlapping signals) using the MestreNova software package. IR measurements were conducted on a *Bruker Alpha ATR-IR* spectrometer. Elemental analysis was performed by the "in-house" service of the Chemistry Department of the Philipps University Marburg, Germany using a CHN(S) analyzer *vario MICRO Cube (Elementar)*. The UV/VIS measurement were recorded on an *Analytik Jena Specord S600* using *WinASPECT* software and an *UNISOKU CoolSpeK Cryostat*. The DC susceptibility measurements were made in the range of 3 K to 300 K by 1 T on a 9 Tesla instrument from LOT / QD. The diamagnetic correction was performed using the pascal constants and the experimentally determined value of the polyurethane sample holder. Solution magnetic susceptibilities were determined by the Evans method.<sup>[i]</sup> n-Butyl lithium (2.5 M in hexane), 18-crown-6, 2.2.2-cryptand, 1,4-cyclohexadiene, 9,10-dihydroanthracen, xanthene, 9-fluorene, indene, triphenylmethane ( $\text{Ph}_3\text{CH}$ ), diphenylmethane ( $\text{Ph}_2\text{CH}_2$ ), ethylbenzene, 1,2-difluorobenzene and tetramethylsilane (TMS) were obtained commercially (Sigma-Aldrich, Acros, Strem, Alfa Aesar) and - if not noted otherwise - used as received. 1,4-cyclohexadiene, ethylbenzene and 1,2-difluorobenzene was degassed, transferred into the glovebox and stored over molecular sieves. 18-crown-6 was sublimed prior use to remove traces of water.  $[\text{Co}\{\text{N}(\text{SiMe}_3)_2\}_2(\text{thf})]^{ii}$ , 9,10-dihydroanthracen- $\text{d}_4$ <sup>iii</sup> and *tert*-butylazide<sup>iv</sup> were prepared according to literature procedures.

## 1. Synthesis of K{crypt.222}[Co(hmds)<sub>2</sub>] (K{crypt.222}[1])

795.4 mg [Co{N(SiMe<sub>3</sub>)<sub>2</sub>}(thf)] (2.00 mmol, 1 equiv.) and 752.9 mg crypt.222 (2.00 mmol, 1 equiv.) were dissolved in 10 mL Et<sub>2</sub>O. Addition of 297.4 mg K<sub>2</sub>C<sub>8</sub> (2.20 mmol, 1.1 equiv.) resulted in an immediate colour change to greenish yellow. After stirring for 5 min, the mixture was filtered, the residue was extracted with 2x3 mL Et<sub>2</sub>O and the combined filtrates were layered with 15 mL pentane. Storing the solution at -35 °C for several days resulted in a light green crystalline solid. The supernatant solution was removed by filtration and the residue washed with 2x5 mL pentane. Drying under reduced pressure afforded K{crypt.222}[1] as a pale-green crystalline solid (1.07 g, 1.3 mmol, 67%). <sup>1</sup>H-NMR ([D<sub>8</sub>]THF, 298 K, ppm, 300 MHz): δ = 3.68 (s, 2.2.2, w<sub>1/2</sub> = 18.5 Hz, 12 H), 3.61 (s, 2.2.2, w<sub>1/2</sub> = 18.5 Hz, 12 H), 2.54 (s, 2.2.2, w<sub>1/2</sub> = 18.5 Hz, 12 H), -4.69 (s, SiMe<sub>3</sub>, w<sub>1/2</sub> = 22.9 Hz, 36 H) ppm. IR (ATR, cm<sup>-1</sup>) v: 2942 (m), 2885 (m), 2816 (m), 1477 (w), 1445 (w), 1354 (m), 1296 (w), 1232 (m), 1133 (m), 1104 (s), 1002 (s), 950 (m), 864 (m), 824 (vs), 775 (m), 750 (m), 659 (m), 608 (w), 523 (w). **Elemental analysis:** calcd. (%) for C<sub>30</sub>H<sub>72</sub>CoKN<sub>4</sub>O<sub>6</sub>Si<sub>4</sub> (795.30 g mol<sup>-1</sup>): C 45.31 H 9.13 N 7.04; found: C 45.15 H 9.11 N 7.07. μ<sub>eff</sub> = 3.41 μ<sub>B</sub> (Evans, [D<sub>8</sub>]THF + 1% Si(CH<sub>3</sub>)<sub>4</sub>, 500 MHz, 298 K, μ<sub>s.o.</sub> = 2.83 μ<sub>B</sub>).

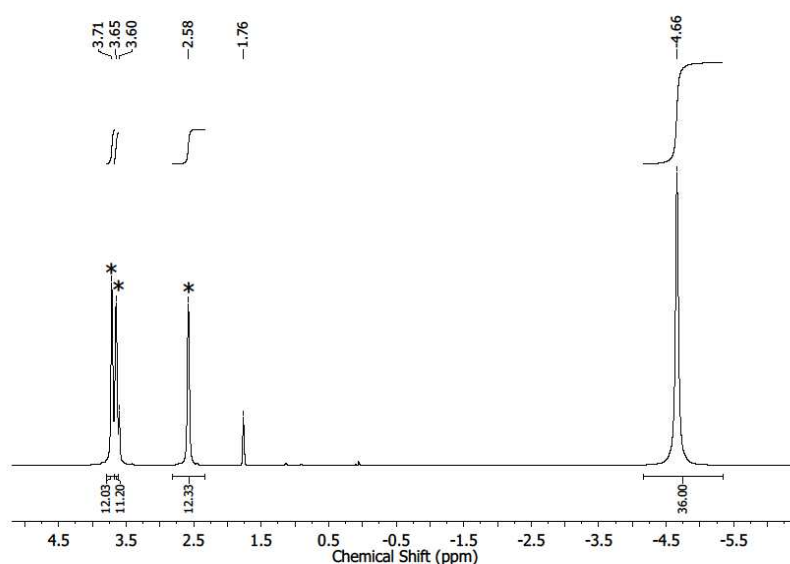


**Figure S1.** <sup>1</sup>H-NMR spectrum of K{crypt.222}[Co(hmds)<sub>2</sub>] (K{crypt.222}[1]) ([D<sub>8</sub>]THF, 298 K, 300 MHz).

## 2. Synthesis of K{crypt.222}[Co(hmds)<sub>2</sub>(N<sup>t</sup>Bu)] (K{crypt.222}[2])

80 mg K{crypt.222}[Co(hmds)<sub>2</sub>] (0.1 mmol, 1 equiv.) was dissolved in 2 mL Et<sub>2</sub>O. Addition of 10 mg N<sub>3</sub><sup>t</sup>Bu (0.1 mmol, 1 equiv.) at -35 °C resulted in an immediate colour change from green to red under concomitant gas evolution. After stirring for 5 minutes, the solution was layered with 3 mL pentane and stored at -35 °C. After one day, the supernatant solution was removed via pipette and the residue was rinsed with 2x3 mL pentane. Drying in *vacuo* afford K{crypt.222}[2] as dark red crystals (80 mg, 0.1 mmol, 92%). <sup>1</sup>H-NMR ([D<sub>8</sub>]THF, 298 K, ppm, 300 MHz): δ = 32.8 (s, N<sup>t</sup>Bu, 9 H), 3.29 (s, crypt.222, 12 H), 3.26 (s, crypt.222, 12 H), 2.28 (s, crypt.222, 12 H), -2.68 (s, SiMe<sub>3</sub>, 36 H) ppm. IR (ATR, cm<sup>-1</sup>) v: 2942 (m), 2885 (m), 2816 (m), 1477 (w), 1445 (w), 1354 (m), 1296 (w), 1232 (m), 1133 (m), 1104 (s), 1002 (s), 950 (m), 864 (m), 824 (vs), 775 (m), 750 (m), 659 (m), 608 (w), 523 (w). **Elemental analysis:** calcd. (%) for C<sub>34</sub>H<sub>81</sub>CoKN<sub>5</sub>O<sub>6</sub>Si<sub>4</sub> (866.42 g mol<sup>-1</sup>): C 47.13 H 9.42 N 8.08; found: C 46.67 H 9.01 N 8.06.

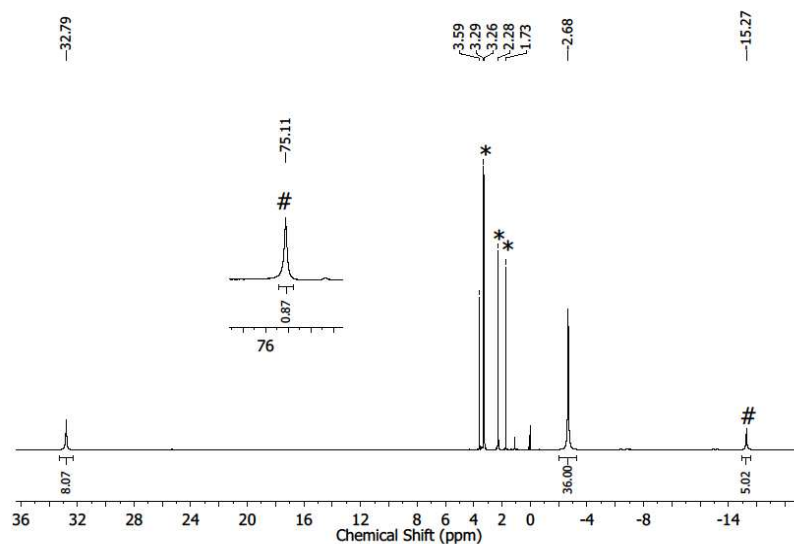


**Figure S2.**  $^1\text{H}$ -NMR spectrum of  $\text{K}\{\text{crypt.222}\}[\text{Co}(\text{hmds})_2(\text{N}^t\text{Bu})]$  ( $\text{K}\{\text{crypt.222}\}\{\mathbf{2}\}$ ) ( $[\text{D}_8]\text{THF}$ , 298 K, 300 MHz). Signals of  $\text{K}\{\text{crypt.222}\}[\text{Co}(\text{hmds})_2(\text{NH}^t\text{Bu})]$  ( $\text{K}\{\text{crypt.222}\}\{\mathbf{3}\}$ ), due to beginning reaction with the solvent, are marked with #.

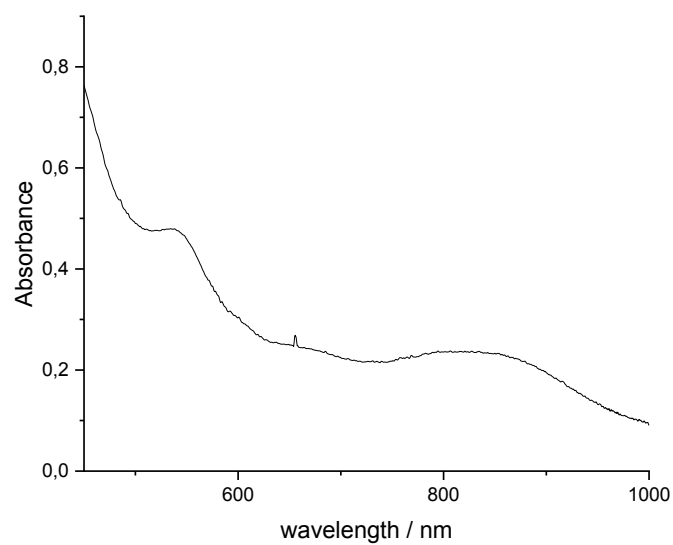


**Figure S3.** UV/VIS-spectrum of  $\text{K}\{\text{crypt.222}\}[\text{Co}(\text{hmds})_2(\text{N}^t\text{Bu})]$  ( $\mathbf{2}$ ) in  $\text{Et}_2\text{O}$  (3 mM).

### 3. Synthesis of K{crypt.222}[Co(hmds)<sub>2</sub>(HN<sup>t</sup>Bu)] (K{crypt.222}[3])

75 mg K{crypt.222}[Co(hmds)<sub>2</sub>(N<sup>t</sup>Bu)] (0.09 mmol, 1 equiv.) was dissolved in 2 mL Et<sub>2</sub>O. Addition of 5  $\mu$ L 1,4-cyclohexadiene (0.09 mmol, 1 equiv.) at RT resulted in a colour change from red to green. After stirring the mixture for 15 min, the mixture was layered with 3 mL pentane and stored at  $-35$  °C. After one day, the supernatant solution was removed via pipette and the residue was rinsed with 2x3 mL pentane. Drying in *vacuo* afford K{crypt.222}[3] as green crystals (65 mg, 0.07 mmol, 87%). **<sup>1</sup>H-NMR** ([D8]THF, 298 K, ppm, 300 MHz):  $\delta$  = 76.1 (s, N<sup>t</sup>Bu, 9 H), 2.90 (s, crypt.222, 12 H), 2.86 (s, crypt.222, 12 H), 1.88 (s, crypt.222, 12 H),  $-15.5$  (s, SiMe<sub>3</sub>, 36 H) ppm. **IR** (ATR, cm<sup>-1</sup>)  $\nu$ : 2942 (m), 2884 (m), 2819 (m), 1477 (w), 1444 (w), 1354 (m), 1295 (w), 1258 (w), 1227 (m), 1133 (m), 1103 (m), 1077 (s), 1037 (s), 1021 (m), 979 (s), 934 (m), 891 (m), 867 (m), 819 (vs), 766 (s), 749, 697 (s), 659 (m), 605 (w), 569 (m), 522 (w), 461 (w), 416 (w). **Elemental analysis**: calcd. (%) for C<sub>34</sub>H<sub>82</sub>CoKN<sub>5</sub>O<sub>6</sub>Si<sub>4</sub> (867.43 g mol<sup>-1</sup>): C 47.08 H 9.53 N 8.07; found: C 46.65 H 9.041 N 7.57.  $\mu_{\text{eff}}$  = 4.58  $\mu_{\text{B}}$  (Evans, [D8]THF + 1% Si(CH<sub>3</sub>)<sub>4</sub>, 500 MHz, 298 K,  $\mu_{\text{s.o.}}$  = 3.87  $\mu_{\text{B}}$ ).

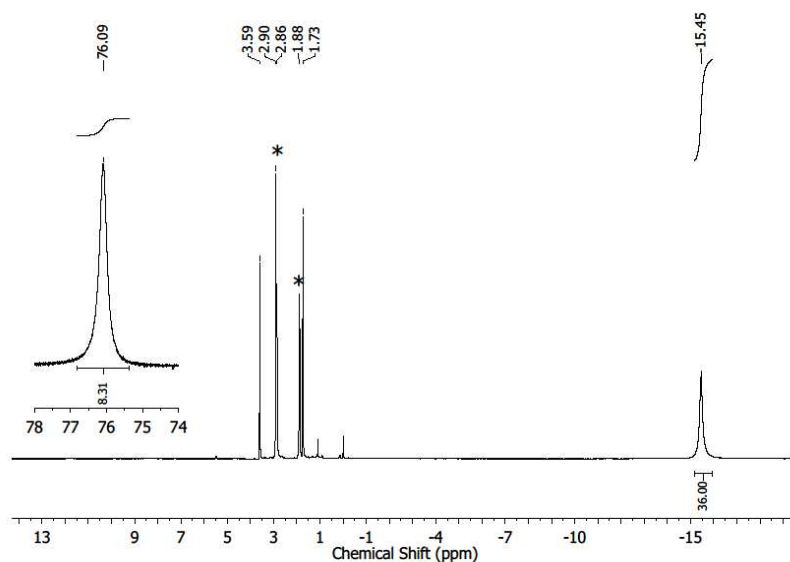


**Figure S4.** <sup>1</sup>H-NMR spectrum of K{crypt.222}[Co(hmds)<sub>2</sub>(NH<sup>t</sup>Bu)] (K{crypt.222}[3]) ([D8]THF, 298 K, 300 MHz).

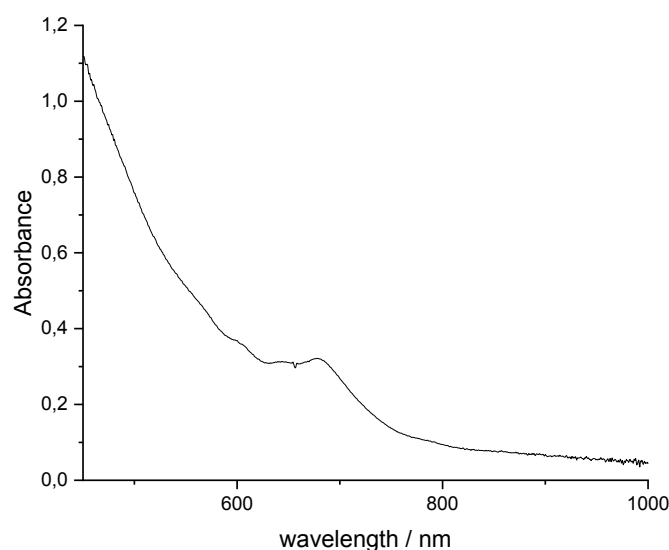


**Figure S5.** UV/VIS-spectrum of  $K\{\text{crypt.222}\}[\text{Co}(\text{hmds})_2(\text{NH}^t\text{Bu})]$  ( $K\{\text{crypt.222}\}[3]$ ) in  $\text{Et}_2\text{O}$  (3mM).

#### 4. Synthesis of $K\{\text{crypt.222}\}[\text{Co}(\text{hmds})_2(9\text{-Flu})]$ ( $K\{\text{crypt.222}\}[5]$ )

20 mg fluorene (0.1 mmol, 1 equiv.) and 45.3 mg crypt.222 (0.1 mmol, 1 equiv.) were dissolved in 2 mL  $\text{Et}_2\text{O}$ . The solution was filtered through 16.3 mg  $\text{KC}_8$  (0.1 mmol, 1.1 equiv.) whereby a colour change to orange was observed. After filtration a solution of 45.7 mg  $[\text{Co}\{\text{N}(\text{SiMe}_3)_2\}_2]$  (0.1 mmol, 1 equiv.) was added, which resulted in a colour change to green. After stirring the mixture for 5 minutes, the mixture was layered with 3 mL pentane and stored at  $-35\text{ }^\circ\text{C}$ . After one day, the supernatant solution was removed using a Pasteur pipette and the remaining yellowish green crystals were rinsed with 2x3 mL pentane. Drying in *vacuo* afforded ( $K\{\text{crypt.222}\}[5]$ ) as green crystals (66 mg, 0.07 mmol, 57%).  **$^1\text{H-NMR}$**  ( $[\text{D}_8]\text{THF}$ , 298 K, ppm, 300 MHz):  $\delta = 43.1$  (s, flu, 2 H), 13.7 (s, flu, 2 H), 5.58 (s, crypt.222, 12 H), 5.35 (s, crypt.222, 12 H), 4.69 (s, crypt.222, 12 H),  $-18.6$  (s,  $\text{SiMe}_3$ , 36 H),  $-43.4$  (s, flu, 2H) ppm. **IR** (ATR,  $\text{cm}^{-1}$ )  $\nu$ : 2942 (m), 2884 (m), 2818 (m), 1587 (w), 1477 (w), 1444 (w), 1429 (w), 1354 (w), 1319 (m), 1295 (m), 1233 (m), 1199 (w), 1133 (m), 1103 (vs), 1077 (m), 1000 (s), 950 (m), 932 (m), 863 (m), 818 (s), 773 (m), 742 (m), 728 (m), 708 (m), 662 (w), 639 (m), 611 (m), 582 (w), 523 (w), 493 (w), 459 (w), 426 (w). **Elemental analysis:** calcd. (%) for  $\text{C}_{43}\text{H}_{81}\text{CoKN}_4\text{O}_6\text{Si}_4$  ( $960.51\text{ g mol}^{-1}$ ): C 53.77 H 8.50 N 5.83; found: C 53.90 H 8.112 N 5.91.  $\mu_{\text{eff}} = 4.55\ \mu_{\text{B}}$  (Evans,  $[\text{D}_8]\text{THF} + 1\% \text{Si}(\text{CH}_3)_4$ , 500 MHz, 298 K,  $\mu_{\text{s.o.}} = 3.87\ \mu_{\text{B}}$ ).



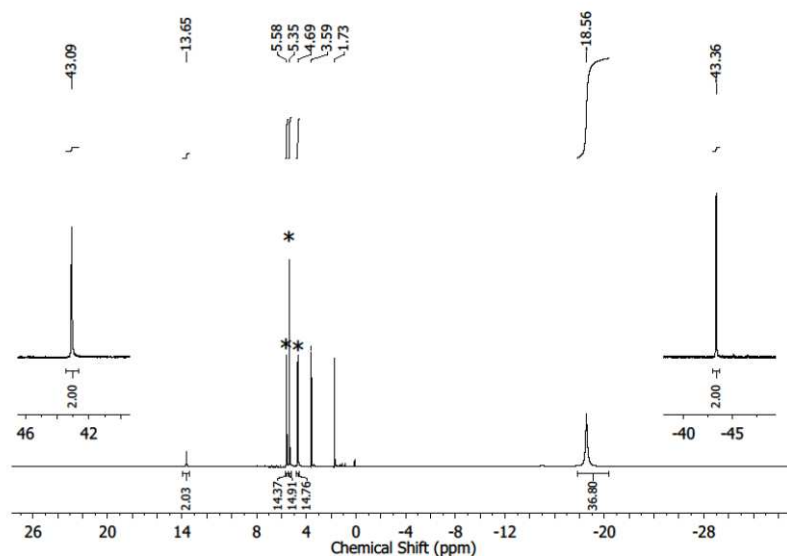


**Figure S6.**  $^1\text{H-NMR}$  spectrum of  $\text{K}\{\text{crypt.222}\}[\text{Co}(\text{hmds})_2(9\text{-Flu})]$  ( $\text{K}\{\text{crypt.222}\}[5]$ ) ( $[\text{D8}]\text{THF}$ , 298 K, 300 MHz).

## 5. Synthesis of $\text{K}\{\text{crypt.222}\}[\text{Co}(\text{hmds})_2(9,10\text{-DHA})]$ ( $\text{K}\{\text{crypt.222}\}[6]$ )

7.1 mg 9,10-dihydroanthracene (0.04 mmol, 1 equiv.) and 15 mg crypt.222 (0.04 mmol, 1 equiv.) were dissolved in 2 mL THF. The solution was added to a suspension of 1.5 mg KH (0.04 mmol, 1 equiv.) in THF, whereby a slow colour change to red was observed. After filtration a solution of 15 mg  $[\text{Co}\{\text{N}(\text{SiMe}_3)_2\}_2]$  (0.04 mmol, 1 equiv.) in THF was added, which resulted in a colour change to yellow. The mixture was layered with 3 mL pentane and stored at  $-35\text{ }^\circ\text{C}$ . After one day, the supernatant solution was removed using a Pasteur pipette and the remaining yellowish crystals were rinsed with 2x3 mL pentane. Drying in *vacuo* afforded ( $\text{K}\{\text{crypt.222}\}[6]$ ) as yellow crystals (21.6 mg, 0.02 mmol, 56%).  $^1\text{H-NMR}$  ( $[\text{D8}]\text{THF}$ , 298 K, ppm, 300 MHz):  $\delta = 69.8$  (s, 1 H), 38.8 (s, 2 H), 20.1 (s, 2 H), 6.51 (s, crypt.222, 12 H), 6.42 (s, crypt.222, 12 H), 5.58 (s, crypt.222, 12 H),  $-24.9$  (s,  $\text{SiMe}_3$ , 36 H),  $-72.61$  (s, 2H) ppm. **IR** (ATR,  $\text{cm}^{-1}$ )  $\nu$ : 2942 (m), 2883 (m), 2814 (m), 1586 (w), 1477 (w), 1445 (w), 1354 (w), 1298 (m), 1247 (m), 1175 (w), 1132 (m), 1102 (vs), 1078 (m), 999 (s), 948 (m), 932 (m), 887 (m), 862 (m), 818 (s), 774 (m), 746 (m), 723 (m), 701 (m), 659 (w), 608 (m), 524 (w), 447 (w), 410 (w). **Elemental analysis:** calcd. (%) for  $\text{C}_{44}\text{H}_{83}\text{CoKN}_4\text{O}_6\text{Si}_4$  ( $974.54\text{ g mol}^{-1}$ ): C 54.23 H 8.58 N 5.75; found: C 54.63 H 8.129 N 6.00.  $\mu_{\text{eff}} = 4.58\ \mu_{\text{B}}$  (Evans,  $[\text{D8}]\text{THF} + 1\% \text{Si}(\text{CH}_3)_4$ , 500 MHz, 298 K,  $\mu_{\text{s.o.}} = 3.87\ \mu_{\text{B}}$ ).

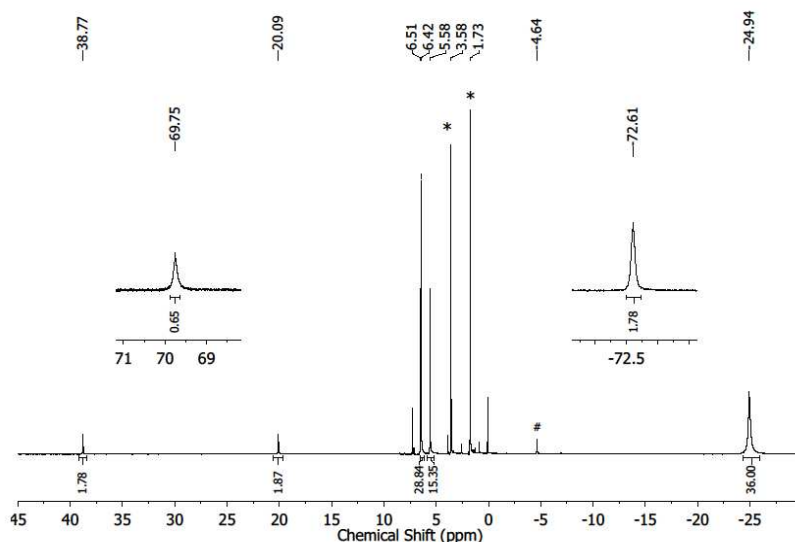


**Figure S7.**  $^1\text{H-NMR}$  spectrum of  $\text{K}\{\text{crypt.222}\}[\text{Co}(\text{hmnds})_2(\text{HA})]$  ( $\text{K}\{\text{crypt.222}\}[6]$ ) ( $[\text{D8}]\text{THF}$ , 298 K, 300 MHz). Signals of  $\text{K}\{\text{crypt.222}\}[\text{Co}(\text{hmnds})_2]$  ( $\text{K}\{\text{crypt.222}\}[1]$ ), due to decomposition, are marked with #.

## 6. Synthesis of $\text{K}\{\text{crypt.222}\}[\text{Co}(\text{hmnds})_2(\text{XAN})]$ ( $\text{K}\{\text{crypt.222}\}[7]$ )

20 mg xanthene (0.1 mmol, 1 equiv.) and 41.2 mg crypt.222 (0.1 mmol, 1 equiv.) were dissolved in 2 mL THF. The solution was added to a suspension of 4.4 mg KH (0.1 mmol, 1 equiv.) in THF, whereby a slow colour change to red was observed. After filtration a solution of 41.2 mg  $[\text{Co}\{\text{N}(\text{SiMe}_3)_2\}_2]$  (0.1 mmol, 1 equiv.) in THF was added, which resulted in a colour change to orange. The mixture was layered with 3 mL pentane and stored at  $-35^\circ\text{C}$ . After one day, the supernatant solution was removed using a Pasteur pipette and the remaining orange crystals were rinsed with 2x3 mL pentane. Drying *in vacuo* afforded  $\text{K}\{\text{crypt.222}\}[7]$  as orange crystals (81 mg, 0.08 mmol, 76%).  $^1\text{H-NMR}$  ( $[\text{D8}]\text{THF}$ , 298 K, ppm, 300 MHz):  $\delta = 52.4$  (s, 2 H), 31.8 (s, 2 H), 5.31 (s, crypt.222, 12 H), 5.21 (s, crypt.222, 12 H), 4.36 (s, crypt.222, 12 H),  $-23.2$  (s,  $\text{SiMe}_3$ , 36 H),  $-49.1$  (s, 1H),  $-64.0$  (s, 2H) ppm. **IR** (ATR,  $\text{cm}^{-1}$ )  $\nu$ : 2940 (m), 2880 (m), 2813 (m), 1580 (w), 1468 (w), 1353 (w), 1328 (m), 1294 (m), 1245 (m), 1203 (w), 1132 (m), 1104 (vs), 1076 (m), 1008 (s), 951 (m), 931 (m), 888 (m), 865 (s), 776 (m), 745 (m), 701 (m), 659 (w), 609 (m), 592 (w), 529 (w), 501 (w), 436 (w). **Elemental analysis**: calcd. (%) for  $\text{C}_{43}\text{H}_{81}\text{CoKN}_4\text{O}_7\text{Si}_4$  ( $976.51\text{g mol}^{-1}$ ): C 52.89 H 8.36 N 5.74; found: C 53.06 H 7.88 N 5.77.  $\mu_{\text{eff}} = 4.34 \mu_{\text{B}}$  (Evans,  $[\text{D8}]\text{THF} + 1\% \text{Si}(\text{CH}_3)_4$ , 500 MHz, 298 K,  $\mu_{\text{s.o.}} = 3.87 \mu_{\text{B}}$ ).

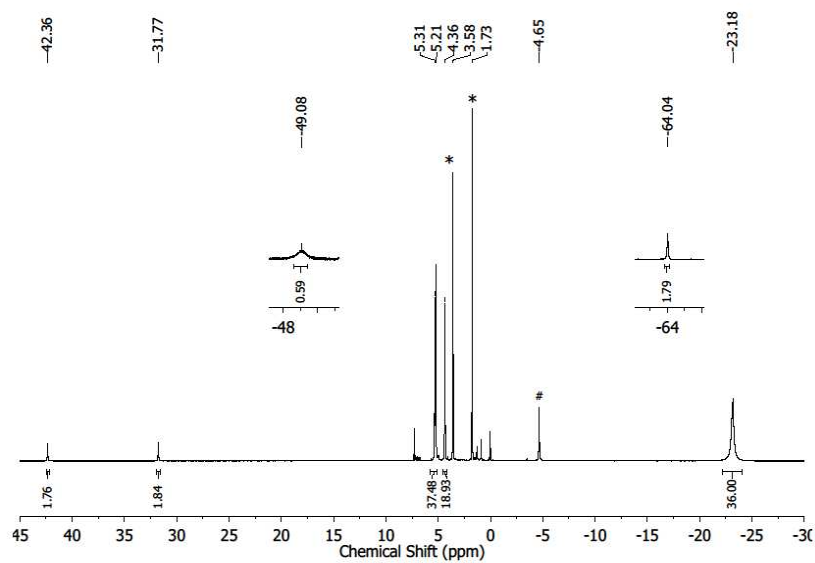


**Figure S8.**  $^1\text{H-NMR}$  spectrum of  $\text{K}\{\text{crypt.222}\}[\text{Co}(\text{hmds})_2(\text{XAN})]$  ( $\text{K}\{\text{crypt.222}\}[\mathbf{7}]$ ) ( $[\text{D}_8]\text{THF}$ , 298 K, 300 MHz). Signals of  $\text{K}\{\text{crypt.222}\}[\text{Co}(\text{hmds})_2]$  ( $\text{K}\{\text{crypt.222}\}[\mathbf{1}]$ ), due to decomposition, are marked with #.

## 7. NMR-scale reactions

In a typical hydrogen transfer experiment 15 mg of the respective cobalt complex were dissolved in 0.7 ml [D8]THF and added to the substrate. For diphenylmethane ( $\text{Ph}_2\text{CH}_2$ ) and ethylbenzene (EtPh) the reaction were done under neat conditions. [D8]THF was added prior to the measurement.

In a typical electron transfer experiment the substrate was deprotonated *in situ* using potassium hydride in presence of crypt.222. The reaction mixture was filtered and added to  $[\text{Co}\{\text{N}(\text{SiMe}_3)_2\}_2]$ . Because of the low solubility in THF the reaction with  $\text{Ph}_3\text{CH}$  was done in 1,2-difluorobenzene. The solvent was removed *in vacuo* and the residue dissolved in [D8]THF.

The chemical shift of the protons of the HMDS and  $^t\text{Bu}$  units of the cobalt complexes and of the substrate are given. The signals of the solvent are marked with \*.

Transfer reactions including phosphines such as  $\text{PCy}_3$  were tracked *via*  $^{31}\text{P}$ -NMR spectroscopy.

### Reaction of $\text{K}\{\text{crypt.222}\}[\text{Co}(\text{hmds})_2(\text{N}^t\text{Bu})]$ ( $\text{K}\{\text{crypt.222}\}[\mathbf{2}]$ ) with different solvents

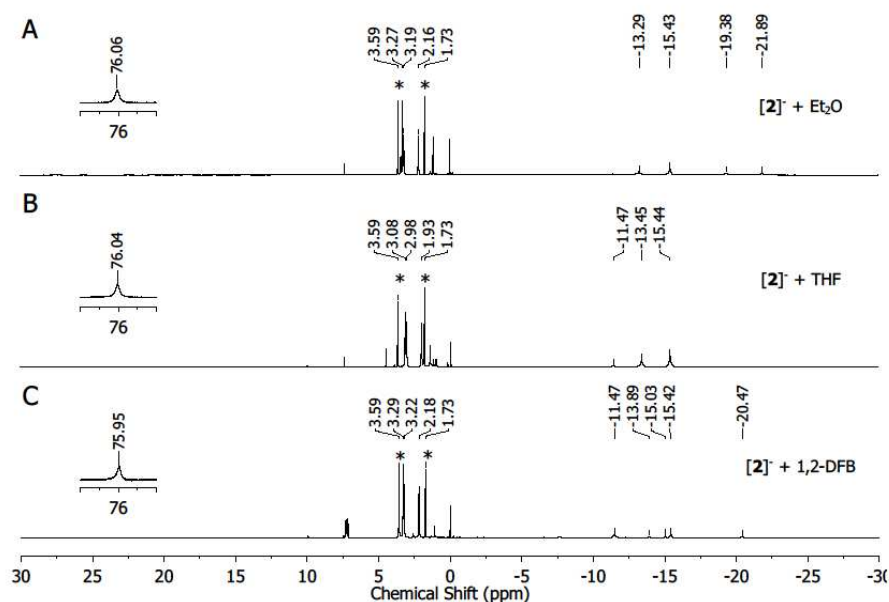


**Figure S9.** **A:** Reaction with diethylether ([D8]THF, 298 K, 300 MHz); **B:** Reaction with THF ([D8]THF, 298 K, 300 MHz); **C:** Reaction with 1,2-difluorobenzene ([D8]THF, 298 K, 300 MHz).

Reaction of  $K\{\text{crypt.222}\}[\text{Co}(\text{hmds})_2(\text{N}^t\text{Bu})]$  ( $K\{\text{crypt.222}\}[\mathbf{2}]$ ) with ethanol (EtOH)

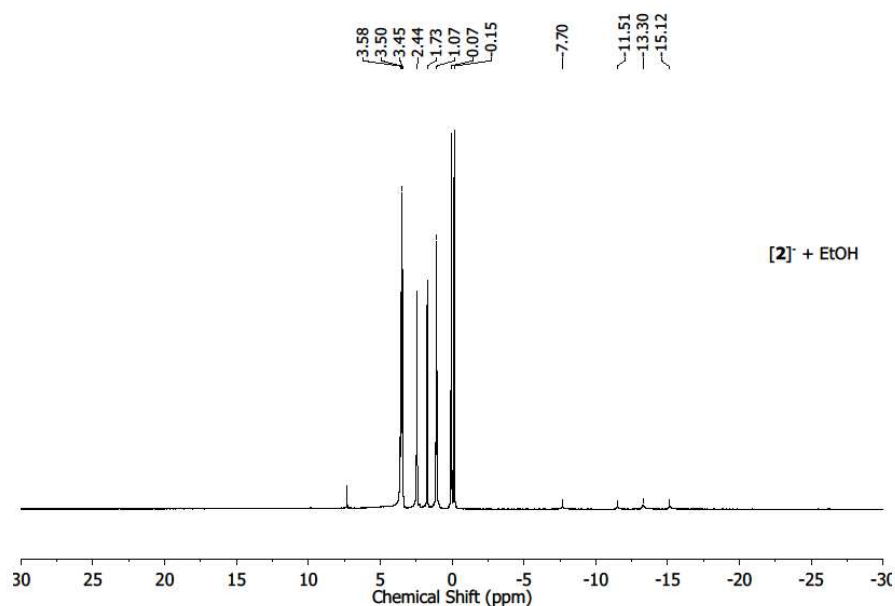


**Figure S10.** Reaction of  $K\{\text{crypt.222}\}[\text{Co}(\text{hmds})_2(\text{N}^t\text{Bu})]$  ( $K\{\text{crypt.222}\}[\mathbf{2}]$ ) with 1 equiv. ethanol ( $[\text{D}_8]\text{THF}$ , 298 K, 300 MHz).

Reaction of  $K\{\text{crypt.222}\}[\text{Co}(\text{hmds})_2(\text{N}^t\text{Bu})]$  ( $K\{\text{crypt.222}\}[\mathbf{2}]$ ) and  $K\{\text{crypt.222}\}[\text{Co}(\text{hmds})_2(\text{HN}^t\text{Bu})]$  ( $K\{\text{crypt.222}\}[\mathbf{3}]$ ) with 1,4-cyclohexadiene (1,4-CHD)

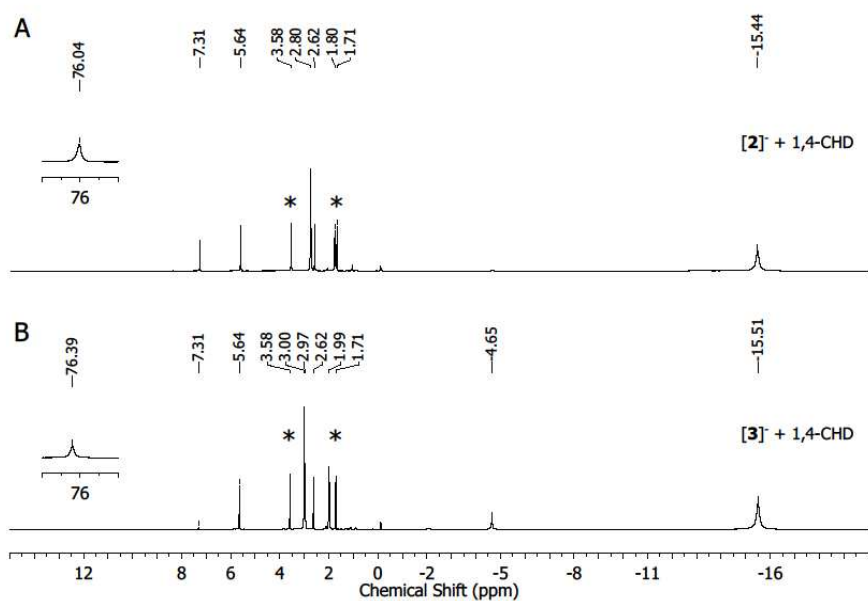


**Figure S11. A:** *in-situ*  $^1\text{H-NMR}$  spectrum of  $K\{\text{crypt.222}\}[\text{Co}(\text{hmds})_2(\text{N}^t\text{Bu})]$  ( $K\{\text{crypt.222}\}[\mathbf{2}]$ ) with 1 equiv. 1,4-CHD ( $[\text{D}_8]\text{THF}$ , 298 K, 300 MHz); **B:** *in-situ*  $^1\text{H-NMR}$  spectrum of  $K\{\text{crypt.222}\}[\text{Co}(\text{hmds})_2(\text{HN}^t\text{Bu})]$  ( $K\{\text{crypt.222}\}[\mathbf{3}]$ ) with 1 equiv. 1,4-CHD ( $[\text{D}_8]\text{THF}$ , 298 K, 300 MHz).

**Reaction of  $K\{\text{crypt.222}\}[\text{Co}(\text{hmds})_2(\text{N}^t\text{Bu})]$  ( $K\{\text{crypt.222}\}[2]$ ) and  $K\{\text{crypt.222}\}[\text{Co}(\text{hmds})_2(\text{HN}^t\text{Bu})]$  ( $K\{\text{crypt.222}\}[3]$ ) with 9,10-dihydroanthracene**

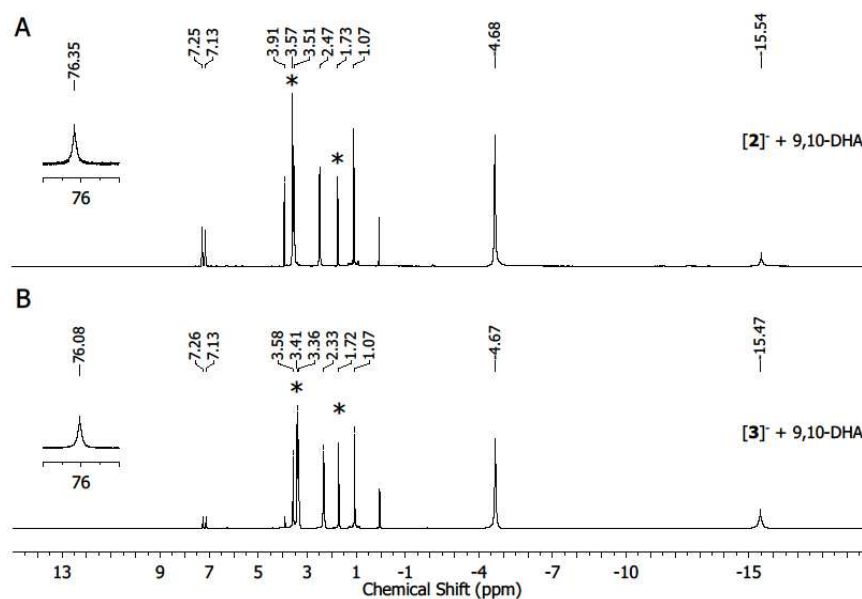


**Figure S12.** **A:** *in-situ*  $^1\text{H-NMR}$  spectrum of  $K\{\text{crypt.222}\}[\text{Co}(\text{hmds})_2(\text{N}^t\text{Bu})]$  ( $K\{\text{crypt.222}\}[2]$ ) with 1 equiv. 9,10-dihydroanthracene ( $[\text{D8}]\text{THF}$ , 298 K, 300 MHz); **B:** *in-situ*  $^1\text{H-NMR}$  spectrum of  $K\{\text{crypt.222}\}[\text{Co}(\text{hmds})_2(\text{HN}^t\text{Bu})]$  ( $K\{\text{crypt.222}\}[3]$ ) with 1 equiv. 9,10-dihydroanthracene ( $[\text{D8}]\text{THF}$ , 298 K, 300 MHz).

**Reaction of  $[K\{2.2.2\}[\text{Co}(\text{hmds})_2(\text{N}^t\text{Bu})]$  ( $K\{\text{crypt.222}\}[2]$ ) and  $K\{\text{crypt.222}\}[\text{Co}(\text{hmds})_2(\text{HN}^t\text{Bu})]$  ( $K\{\text{crypt.222}\}[3]$ ) with xanthene**

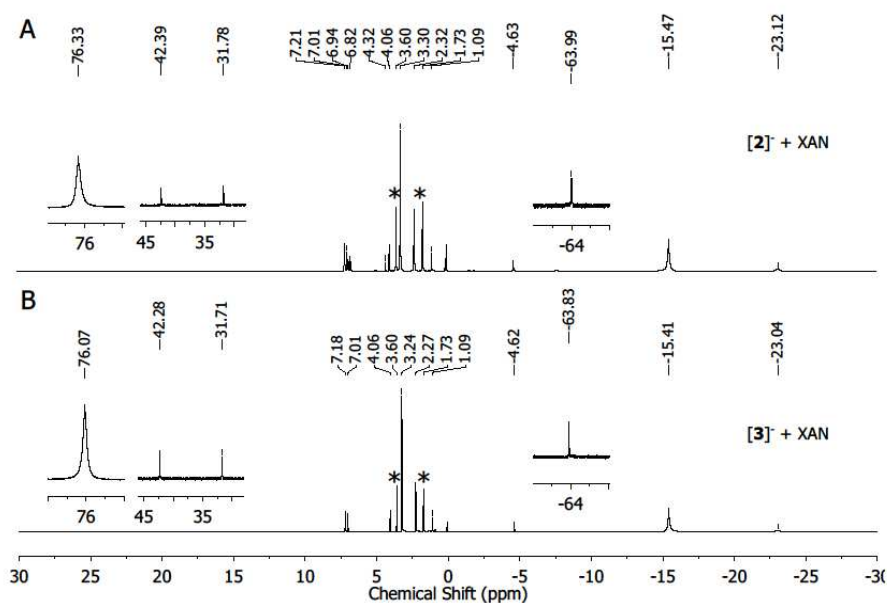


**Figure S13.** **A:** *in-situ*  $^1\text{H-NMR}$  spectrum of  $K\{\text{crypt.222}\}[\text{Co}(\text{hmds})_2(\text{N}^t\text{Bu})]$  ( $K\{\text{crypt.222}\}[2]$ ) with 2 equiv. xanthene ( $[\text{D8}]\text{THF}$ , 298 K, 300 MHz); **B:** *in-situ*  $^1\text{H-NMR}$  spectrum of  $K\{\text{crypt.222}\}[\text{Co}(\text{hmds})_2(\text{HN}^t\text{Bu})]$  ( $K\{\text{crypt.222}\}[3]$ ) with 1 equiv. xanthene ( $[\text{D8}]\text{THF}$ , 298 K, 300 MHz).

Reaction of  $[K\{2.2.2\}[Co(hmds)_2(N^tBu)]$  ( $K\{crypt.222\}[2]$ ) and  $K\{crypt.222\}[Co(hmds)_2(HN^tBu)]$  ( $K\{crypt.222\}[3]$ ) with  $Ph_3CH$

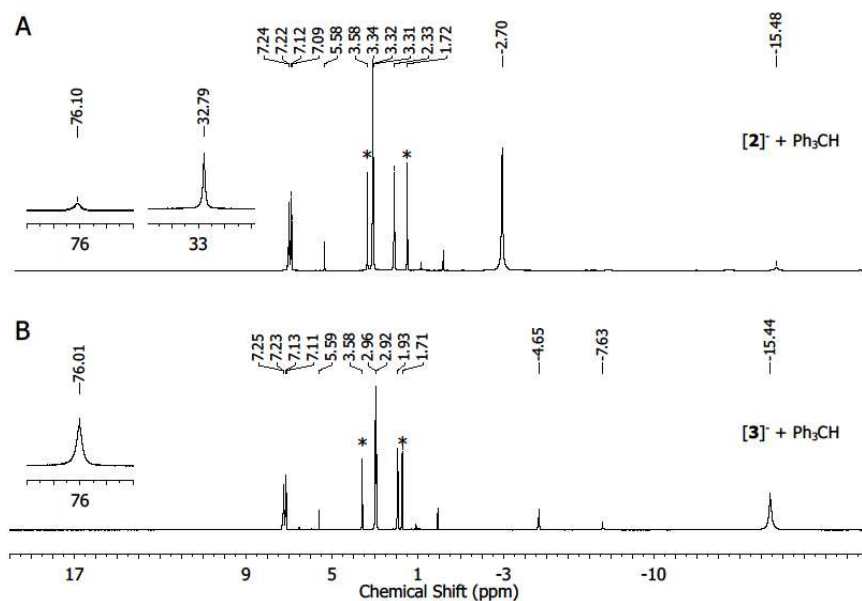


**Figure S14.** **A:** *in-situ*  $^1H$ -NMR spectrum of  $K\{crypt.222\}[Co(hmds)_2(N^tBu)]$  ( $K\{crypt.222\}[2]$ ) with 2 equiv.  $Ph_3CH$  ( $[D_8]THF$ , 298 K, 300 MHz); **B:** *in-situ*  $^1H$ -NMR spectrum of  $K\{crypt.222\}[Co(hmds)_2(HN^tBu)]$  ( $K\{crypt.222\}[3]$ ) with 1 equiv.  $Ph_3CH$  ( $[D_8]THF$ , 298 K, 300 MHz).

Reaction of  $[K\{2.2.2\}[Co(hmds)_2(N^tBu)]$  ( $K\{crypt.222\}[2]$ ) and  $K\{crypt.222\}[Co(hmds)_2(HN^tBu)]$  ( $K\{crypt.222\}[3]$ ) with  $Ph_2CH_2$

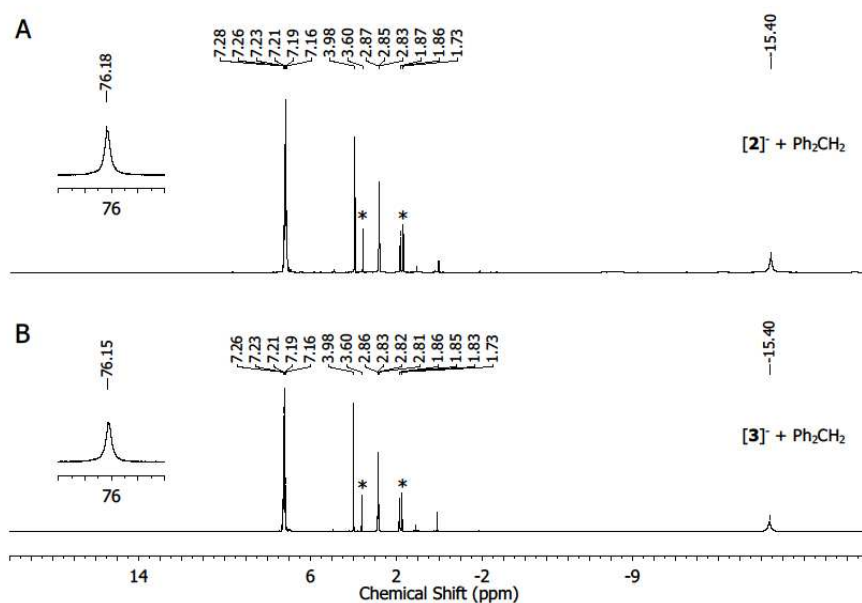


**Figure S15.** **A:**  $^1H$ -NMR spectrum of  $K\{crypt.222\}[Co(hmds)_2(N^tBu)]$  ( $K\{crypt.222\}[2]$ ) with 10 equiv.  $Ph_2CH_2$  ( $[D_8]THF$ , 298 K, 300 MHz) after 12h; **B:**  $^1H$ -NMR spectrum of  $K\{crypt.222\}[Co(hmds)_2(HN^tBu)]$  ( $K\{crypt.222\}[3]$ ) with 10 equiv.  $Ph_2CH_2$  ( $[D_8]THF$ , 298 K, 300 MHz) after 12h.

Reaction of  $[K\{2.2.2\}[Co(hmds)_2(N^tBu)]$  ( $K\{crypt.222\}[2]$ ) and  $K\{crypt.222\}[Co(hmds)_2(HN^tBu)]$  ( $K\{crypt.222\}[3]$ ) with ethylbenzene

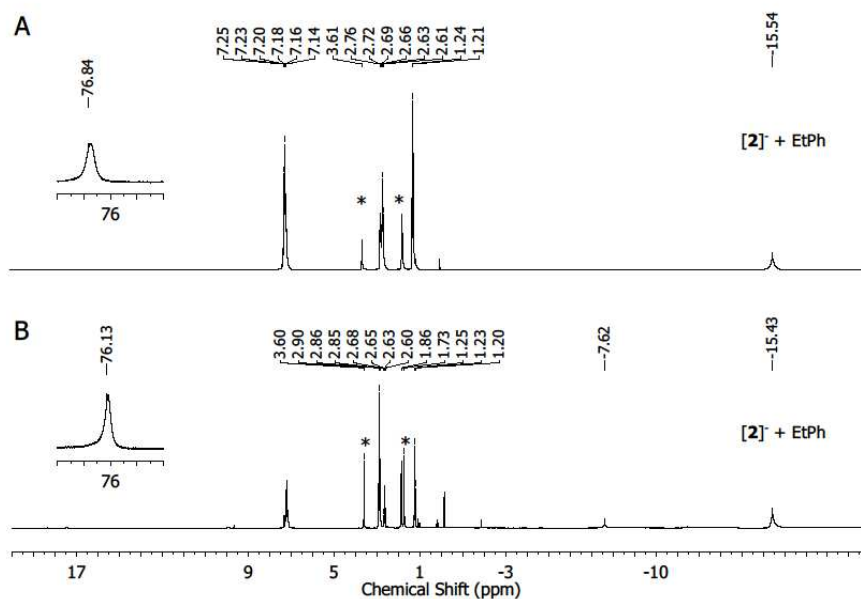


**Figure S16. A:**  $^1H$ -NMR spectrum of  $K\{crypt.222\}[Co(hmds)_2(N^tBu)]$  ( $K\{crypt.222\}[2]$ ) with 10 equiv. ethylbenzene ( $[D_8]THF$ , 298 K, 300 MHz) after 12 h; **B:**  $^1H$ -NMR spectrum of  $K\{crypt.222\}[Co(hmds)_2(N^tBu)]$  ( $K\{crypt.222\}[2]$ ) with 10 equiv. ethylbenzene ( $[D_8]THF$ , 298 K, 300 MHz) after 36 h.

Reaction of  $[K\{2.2.2\}[Co(hmds)_2(N^tBu)]$  ( $K\{crypt.222\}[2]$ ) and  $K\{crypt.222\}[Co(hmds)_2(HN^tBu)]$  ( $K\{crypt.222\}[3]$ ) with 9-fluorene

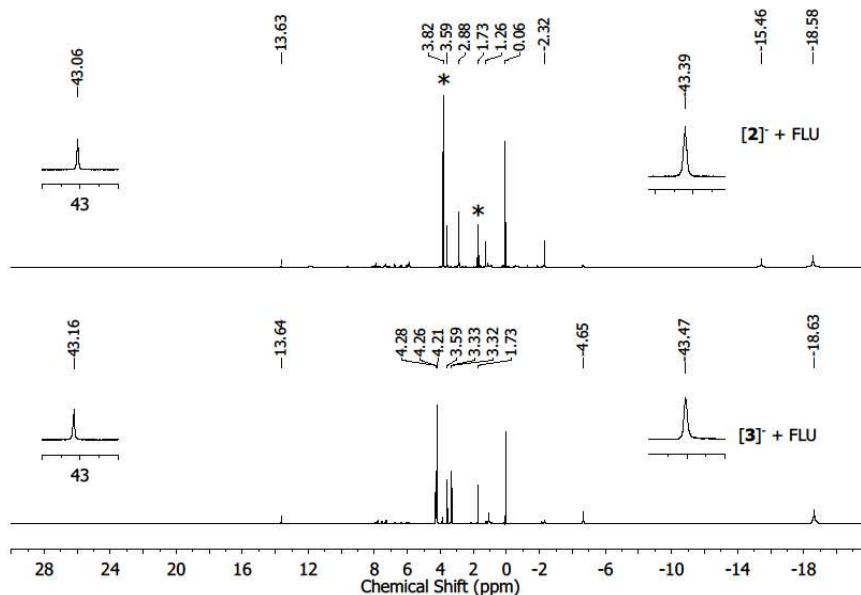


**Figure S17. A:** *in-situ*  $^1H$ -NMR spectrum of  $K\{crypt.222\}[Co(hmds)_2(N^tBu)]$  ( $K\{crypt.222\}[2]$ ) with 2 equiv. 9-fluorene ( $[D_8]THF$ , 298 K, 300 MHz); **B:** *in-situ*  $^1H$ -NMR spectrum of  $K\{crypt.222\}[Co(hmds)_2(HN^tBu)]$  ( $K\{crypt.222\}[3]$ ) with 1 equiv. 9-fluorene ( $[D_8]THF$ , 298 K, 300 MHz).



**Reaction of  $K\{\text{crypt.222}\}[\text{Co}(\text{hmds})_2(\text{N}^t\text{Bu})]$  ( $K\{\text{crypt.222}\}[\mathbf{2}]$ ) and  $K\{\text{crypt.222}\}[\text{Co}(\text{hmds})_2(\text{HN}^t\text{Bu})]$  ( $K\{\text{crypt.222}\}[\mathbf{3}]$ ) with indene**

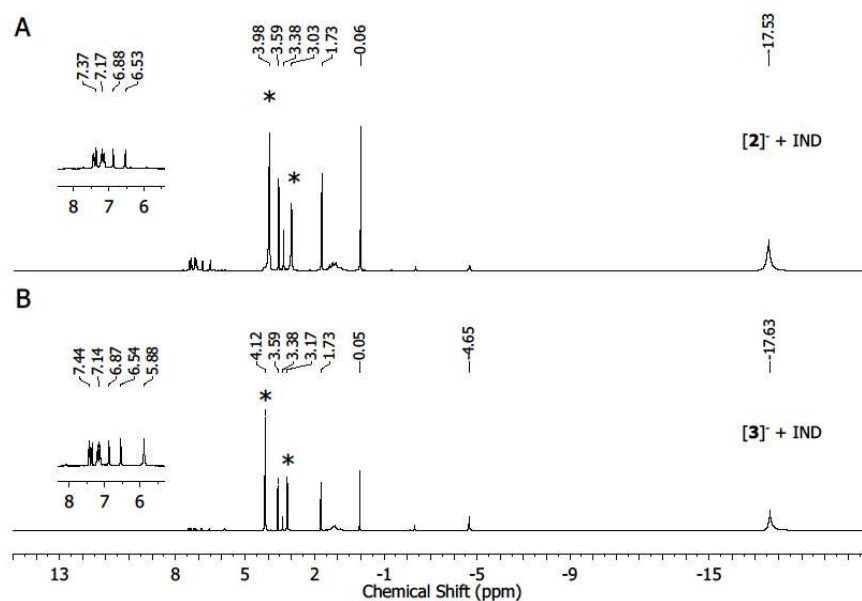


**Figure S18.** **A:** *in-situ*  $^1\text{H-NMR}$  spectrum of  $K\{\text{crypt.222}\}[\text{Co}(\text{hmds})_2(\text{N}^t\text{Bu})]$  ( $\mathbf{2}$ ) with 2 equiv. indene ( $[\text{D8}]\text{THF}$ , 298 K, 300 MHz); **B:** *in-situ*  $^1\text{H-NMR}$  spectrum of  $K\{\text{crypt.222}\}[\text{Co}(\text{hmds})_2(\text{HN}^t\text{Bu})]$  ( $\mathbf{3}$ ) with 1 equiv. indene ( $[\text{D8}]\text{THF}$ , 298 K, 300 MHz).

**Reaction of  $K\{\text{crypt.222}\}[\mathbf{9,10}\text{-Dihydroanthracenide}]$  with  $[\text{Co}\{\text{N}(\text{SiMe}_3)_2\}_2]$**

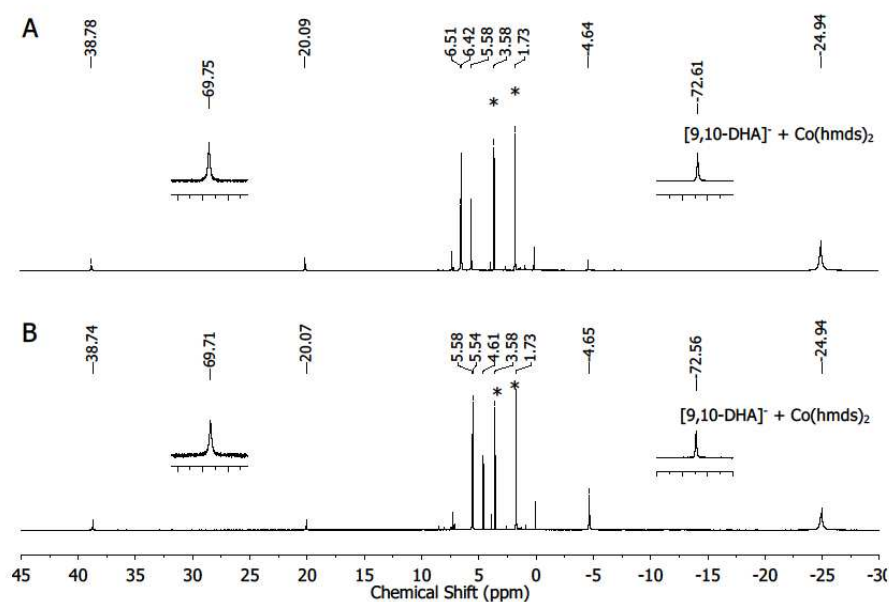


**Figure S19.**  $^1\text{H-NMR}$  spectrum of the reaction of *in situ* generated  $K\{\text{crypt.222}\}[\text{HA}]$  with 1 equiv.  $[\text{Co}\{\text{N}(\text{SiMe}_3)_2\}_2]$  **A:**  $t = 10$  min; **B:**  $t = 24$  h ( $[\text{D8}]\text{THF}$ , 298 K, 300 MHz).

Reaction of K{crypt.222}[Co(hmnds)<sub>2</sub>(9,10-DHA)] (K{crypt.222}[6]) with H<sub>2</sub>N<sup>t</sup>Bu

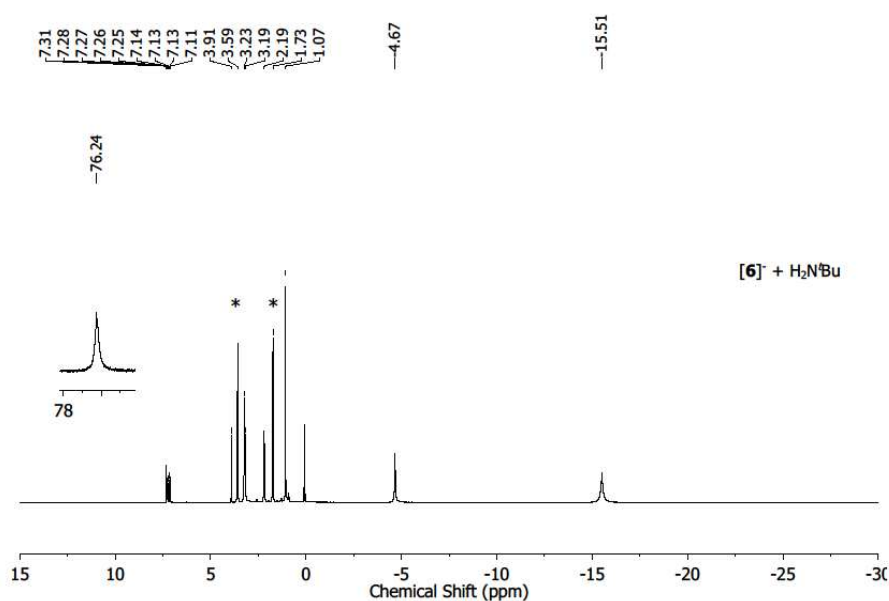


**Figure S20.** *in-situ* <sup>1</sup>H-NMR spectrum of the reaction of K{crypt.222}[6] with 1 equiv. H<sub>2</sub>N<sup>t</sup>Bu ([D<sub>8</sub>]THF, 298 K, 300 MHz).

Reaction of K{crypt.222}[XAN] with [Co{N(SiMe<sub>3</sub>)<sub>2</sub>}]<sub>2</sub>

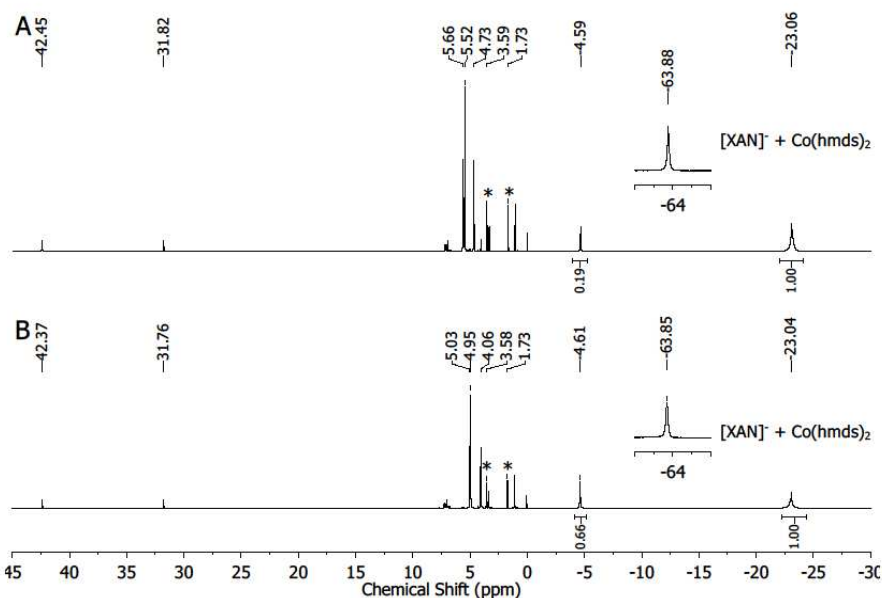


**Figure S21.** <sup>1</sup>H-NMR spectrum of the reaction of *in situ* generated K{crypt.222}[XAN] with 1 equiv. [Co{N(SiMe<sub>3</sub>)<sub>2</sub>}]<sub>2</sub> **A:** t = 10 min; **B:** t = 24 h ([D<sub>8</sub>]THF, 298 K, 300 MHz).



## 8. Kinetic studies

In a typical experiment, a precooled 3 mM solution of the respective cobalt complex was treated with solution of the substrate. When THF was used an immediate color change from red to green was observed, indicating a decomposition of K{crypt.222}[2]. Diethylether was used as solvent for substrates with a BDE below 86 kcal mol<sup>-1</sup>, while 1,2-difluorobenzene was used for the substrates with a higher BDE. Measurements with 1,2-DFB could not be done at -30 °C, due to the melting point of the solvent. To ensure pseudo first order kinetics an excess of 20 equiv. (BDE < 86 kcal mol<sup>-1</sup>) or 500 equiv. (BDE > 86 kcal mol<sup>-1</sup>) was used. The reaction mixture was stirred for 30 s before starting the measurement, to ensure a homogeneous temperature. The absorbance at a wavelength of 850 nm was used for the kinetic studies.

The reaction rates  $k_{obs}$  were determined by the following equation assuming a pseudo-first-order reaction:

$$\ln[A] = -k_{obs}t + \ln[A]_0$$

The half-live times at different temperatures were determined by the following equation assuming a pseudo-first-order reaction:

$$t_{\frac{1}{2}} = \frac{\ln 2}{k_{obs}}$$

**Table S1.** half-live of K{crypt.222} [Co(hmds)2(NtBu)] (K{crypt.222}[2]) in different solvents.

Solvent	$k_{obs} / s^{-1}$	half-live / min
Et <sub>2</sub> O (RT)	$7.69(12) \times 10^{-4}$	16
Et <sub>2</sub> O (-30°C)	$9.96 \times 10^{-5}$	150
DFB (RT)	$1.83 \times 10^{-4}$	63
THF (RT)	estimated	~ 0.2

**Decomposition of K{crypt.222} [Co(hmds)<sub>2</sub>(N<sup>t</sup>Bu)] (K{crypt.222}[2]) in different solvents at room temperature**

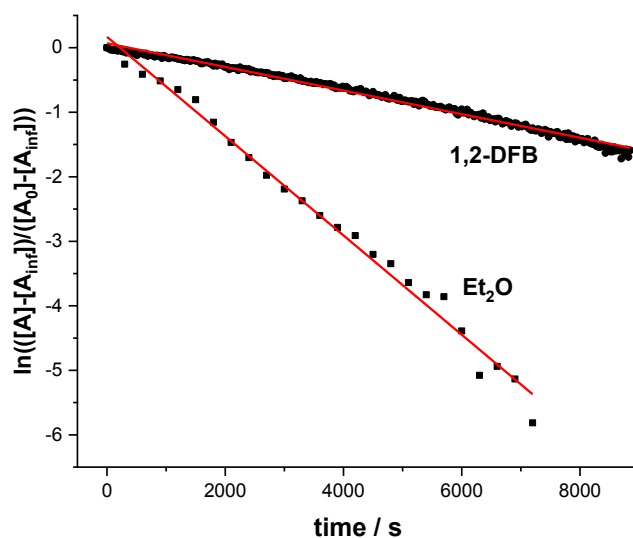


**Figure S24.** Time trace of the absorbance at 850 nm during the decay of K{crypt.222}[2] in different solvents.  $k_{\text{obs}}(\text{Et}_2\text{O}) = 7.69(12) \times 10^{-4} \text{ s}^{-1}$  ( $R^2 = 0.99$ ),  $t_{1/2} = 16 \text{ min}$ ;  $k_{\text{obs}}(1,2\text{-DFB}) = 1.83 \times 10^{-4} \text{ s}^{-1}$  ( $R^2 = 0.99$ ),  $t_{1/2} = 63 \text{ min}$ .

**Decomposition of K{crypt.222} [Co(hmds)<sub>2</sub>(N<sup>t</sup>Bu)] (K{crypt.222}[2]) in diethylether at different temperatures**

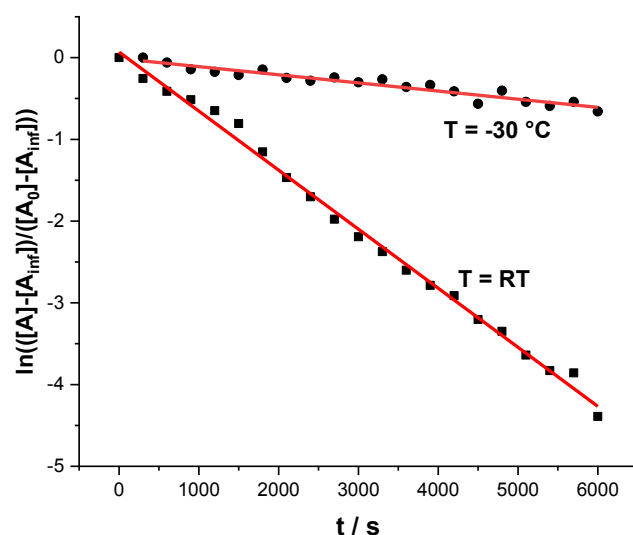


**Figure S25.** Time trace of the absorbance at 850 nm during the decay of K{crypt.222}[2] in different solvents.  $k_{\text{obs}}(\text{Et}_2\text{O}\{\text{RT}\}) = 7.69(12) \times 10^{-4} \text{ s}^{-1}$  ( $R^2 = 0.99$ ),  $t_{1/2} = 16 \text{ min}$ ;  $k_{\text{obs}}(\text{Et}_2\text{O}\{-30\}) = 9.96 \times 10^{-5} \text{ s}^{-1}$  ( $R^2 = 0.93$ ),  $t_{1/2} = 150 \text{ min}$ .

Reaction of K{crypt.222} [Co(HMDS)<sub>2</sub>(N<sup>t</sup>Bu)] (K{crypt.222}[2]) with 20 equiv. substrate in diethylether at -30 °C

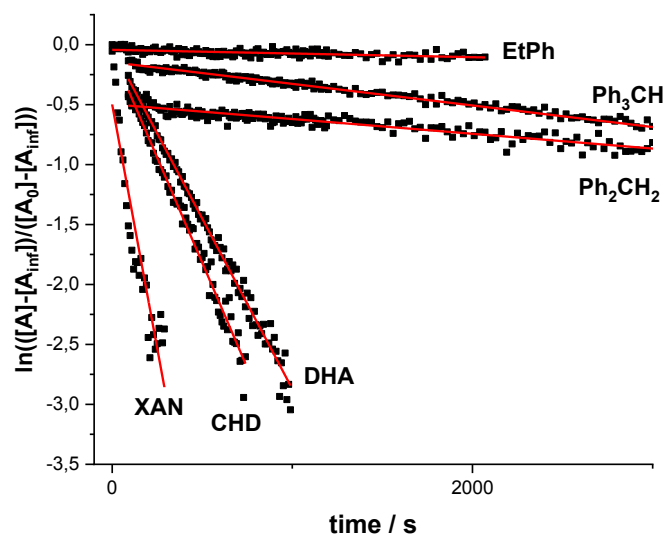


**Figure S26.** Time traces of the absorbance at 850 nm during the reaction of K{crypt.222}[2] with 20 equiv. substrate at -30 °C in Et<sub>2</sub>O.  $k_{\text{obs}}(\text{XAN}) = 8.13(6) \times 10^{-3} \text{ s}^{-1}$  ( $R^2 = 0.87$ );  $k_{\text{obs}}(1,4\text{-CHD}) = 3.51(6) \times 10^{-3} \text{ s}^{-1}$  ( $R^2 = 0.99$ );  $k_{\text{obs}}(9,10\text{-DHA}) = 2.84(3) \times 10^{-3} \text{ s}^{-1}$  ( $R^2 = 0.99$ );  $k_{\text{obs}}(\text{Ph}_3\text{CH}) = 1.80(2) \times 10^{-4} \text{ s}^{-1}$  ( $R^2 = 0.99$ );  $k_{\text{obs}}(\text{Ph}_2\text{CH}_2) = 1.23(3) \times 10^{-4} \text{ s}^{-1}$  ( $R^2 = 0.91$ );  $k_{\text{obs}}(\text{EtPh}) = 3.1(3) \times 10^{-5} \text{ s}^{-1}$  ( $R^2 = 0.34$ ).

**Table S2.** Observed reaction rates  $k_{\text{obs}}$  at -30 °C for the reaction of complex [2]<sup>-</sup> with different substrates in Et<sub>2</sub>O.

Substrate	$k_{\text{obs}} / \text{s}^{-1}$	BDE / kcal mol <sup>-1</sup>	pK <sub>A</sub> (DMSO)
1,4-Cyclohexadiene	$3.35(4) \times 10^{-3}$	$76 \pm 2^{\text{v}}$	$\sim 34^{\text{vi}}$
9,10-Dihydroanthracen	$2.83(2) \times 10^{-3}$	$78 \pm 1.5^{\text{v}}$	$30.1^{\text{vi}}$
Xanthene	$1.08(7) \times 10^{-2}$	$75.5 \pm 2^{\text{vii}}$	$30.0^{\text{vii}}$
Ph <sub>3</sub> CH	$1.80(2) \times 10^{-4}$	$81 \pm 2^{\text{ix}}$	$30.6^{\text{viii}}$
Ph <sub>2</sub> CH <sub>2</sub>	$1.23(3) \times 10^{-4}$	$82^{\text{viii}}$	$32.2^{\text{viii}}$
Ethylbenzene	$3.1(3) \times 10^{-5}$	$85.4 \pm 1.5^{\text{ix}}$	$\sim 40^*$

\* estimated from the pK<sub>a</sub> of toluene

Correlation of the reaction rates ( $k_{\text{obs}}$ ) with the bond dissociation energy (BDE) or  $pK_a$  (DMSO) of the used substrates

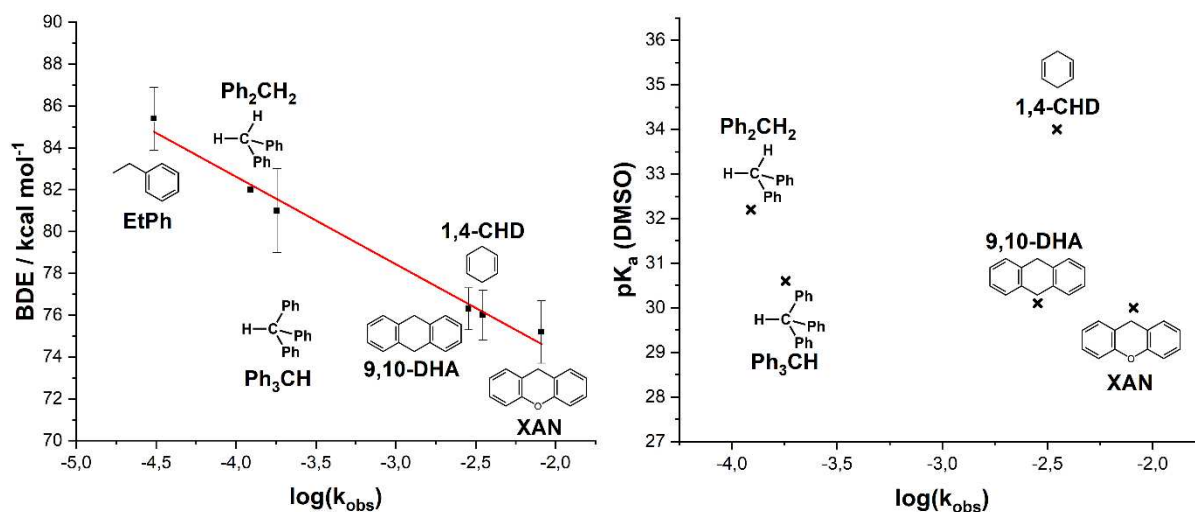


**Figure S27.** left: correlation between the bond dissociation energies (BDE) of the shown substrates and the obtained reaction rate ( $k_{\text{obs}}$ ) ( $R^2 = 0.99$ ). right:  $pK_a$  vs. the obtained reaction rate ( $k_{\text{obs}}$ ) showing no correlation;  $pK_a$  value for ethylbenzene is not known in literature.

Reaction of K{crypt.222} [Co(HMDS)<sub>2</sub>(N<sup>t</sup>Bu)] (K{crypt.222}[2]) with 500 equiv. substrate in 1,2-difluorobenzene at 0 °C

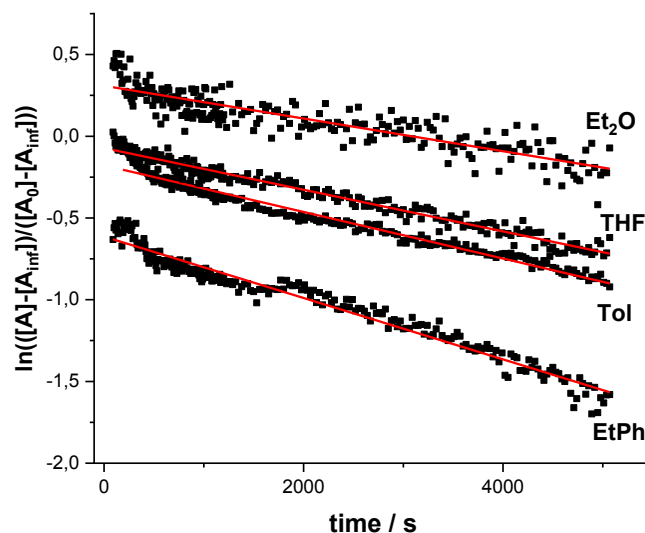


**Figure S28.** Time traces of the absorbance at 850 nm during the reaction of K{crypt.222}[2] with 500 equiv. substrate at 0 °C in 1,2-DFB.  $k_{\text{obs}}(\text{EtPh}) = 1.88(2) \times 10^{-4} \text{ s}^{-1}$  ( $R^2 = 0.96$ );  $k_{\text{obs}}(\text{Tol}) = 1.43(2) \times 10^{-4} \text{ s}^{-1}$  ( $R^2 = 0.97$ );  $k_{\text{obs}}(\text{THF}) = 1.27(1) \times 10^{-4} \text{ s}^{-1}$  ( $R^2 = 0.97$ );  $k_{\text{obs}}(\text{Et}_2\text{O}) = 1.00(3) \times 10^{-4} \text{ s}^{-1}$  ( $R^2 = 0.78$ ).

**Table S3.** Observed reaction rates  $k_{\text{obs}}$  at 0 °C for the reaction of complex  $[2]^-$  with different substrates in 1,2-DFB.

Substrate	$k_{\text{obs}} / \text{s}^{-1}$	BDE / kcal mol <sup>-1</sup>	pK <sub>A</sub> (DMSO)
Ethylbenzene	$1.88(2) \times 10^{-4}$	$85.4 \pm 1.5^{\text{ix}}$	$\sim 40^*$
Toluene	$1.43(2) \times 10^{-4}$	$89.7 \pm 1.2^{\text{ix}}$	$\sim 43^{\text{viii}}$
Tetrahydrofuran	$1.27(1) \times 10^{-4}$	$92.1 \pm 1.6^{\text{ix}}$	$49 \pm 3^{\text{x}}$
Diethylether	$1.00(3) \times 10^{-4}$	$91.7 \pm 3.8^{\text{xi}}$	$49 \pm 3^{\text{x}}$

\* estimated from the pK<sub>a</sub> of toluene

**Correlation of the reaction rates ( $k_{\text{obs}}$ ) with the bond dissociation energy (BDE) or pK<sub>a</sub> (DMSO) of the used substrates**

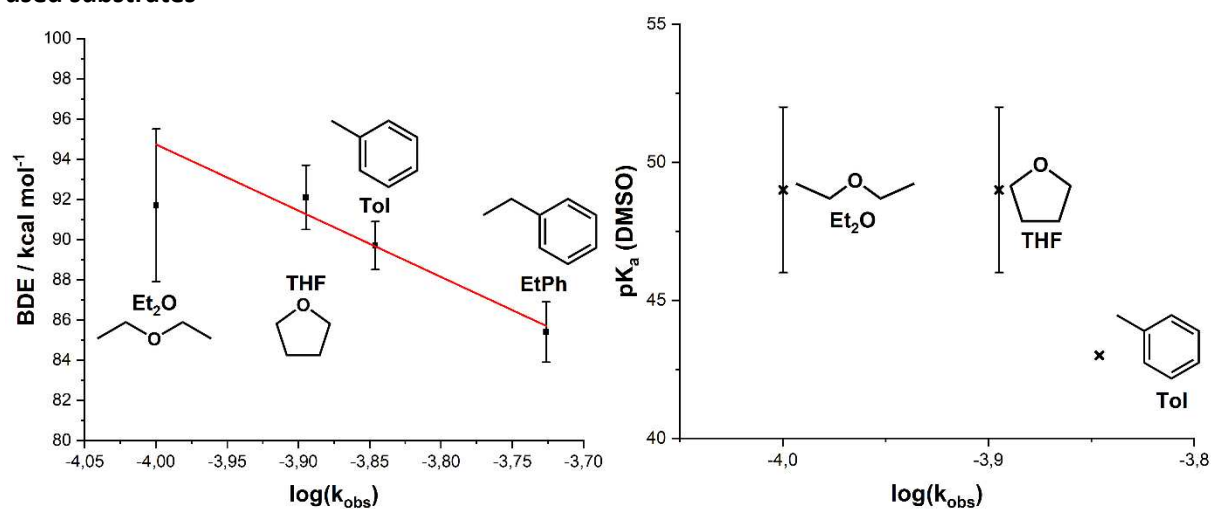


**Figure S29.** left: Correlation between the bond dissociation energies of the shown substrates and the obtained reaction rate ( $k_{\text{obs}}$ ) ( $R^2 = 0.91$ ). right: pK<sub>a</sub> vs. the obtained reaction rate ( $k_{\text{obs}}$ ) showing no correlation; pK<sub>a</sub> value for ethylbenzene is not known in literature.



Reaction of  $K\{\text{crypt.222}\}[\text{Co}(\text{HMDS})_2(\text{N}^t\text{Bu})]$  ( $K\{\text{crypt.222}\}[\mathbf{2}]$ ) with 20 equiv. DHA-( $d_4$ ) in diethylether at  $-30\text{ }^\circ\text{C}$

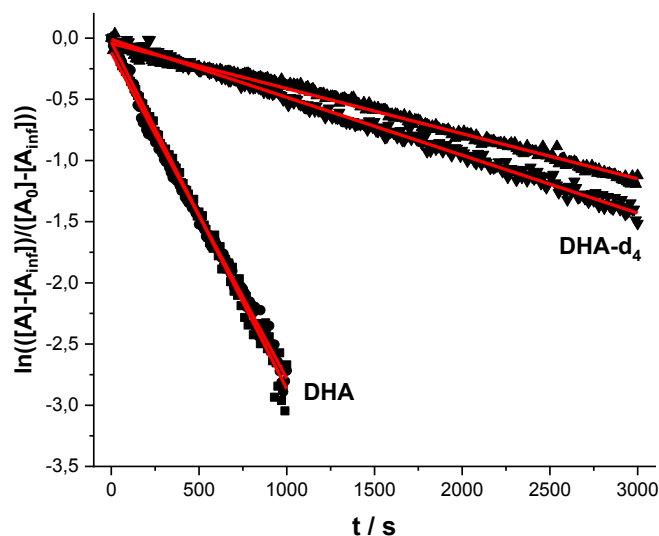


**Figure S30.** Time traces of the absorbance at 850 nm during the reaction of  $K\{\text{crypt.222}\}[\mathbf{2}]$  with 20 equiv. substrate at  $-30\text{ }^\circ\text{C}$  in  $\text{Et}_2\text{O}$ .  $k_{\text{obs}}(9,10\text{-DHA}) = 2.83(2) \times 10^{-3}\text{ s}^{-1}$  ( $R^2 = 0.99$ );  $k_{\text{obs}}(9,10\text{-DHA-}d_4) = 4.21(2) \times 10^{-4}\text{ s}^{-1}$  ( $R^2 = 0.99$ ).

Reaction of  $K\{\text{crypt.222}\}[\text{Co}(\text{HMDS})_2(\text{N}^t\text{Bu})]$  ( $K\{\text{crypt.222}\}[\mathbf{2}]$ ) with 20 equiv. 1,4-CHD in diethylether at different temperatures

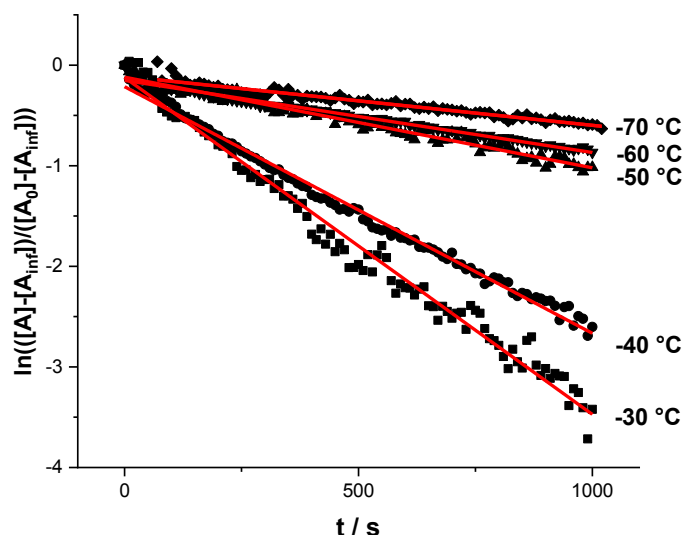


**Figure S31.** Time trace of the absorbance at 850 nm during the reaction of  $K\{\text{crypt.222}\}[\mathbf{2}]$  with 20 equiv. 1,4-CHD at different temperatures.  $k_{\text{obs}}(-30\text{ }^\circ\text{C}) = 3.35(4) \times 10^{-3}\text{ s}^{-1}$  ( $R^2 = 0.98$ );  $k_{\text{obs}}(-40\text{ }^\circ\text{C}) = 2.45(2) \times 10^{-3}\text{ s}^{-1}$  ( $R^2 = 0.99$ );  $k_{\text{obs}}(-50\text{ }^\circ\text{C}) = 9.01(15) \times 10^{-4}\text{ s}^{-1}$  ( $R^2 = 0.97$ );  $k_{\text{obs}}(-60\text{ }^\circ\text{C}) = 7.17(9) \times 10^{-4}\text{ s}^{-1}$  ( $R^2 = 0.98$ );  $k_{\text{obs}}(-70\text{ }^\circ\text{C}) = 4.87(12) \times 10^{-4}\text{ s}^{-1}$  ( $R^2 = 0.95$ ).

### Temperature dependence of the reaction rate $k_{obs}$ of K{crypt.222}[2] with 20 equiv. 1,4-CHD in Et<sub>2</sub>O

The enthalpy of activation ( $\Delta H^\ddagger$ ) and entropy of activation ( $\Delta S^\ddagger$ ) was determined by using the linear form of the Eyring Equation:

$$\ln \frac{k_{obs}}{T} = \frac{-\Delta H^\ddagger}{R} \frac{1}{T} + \ln \frac{k_B}{h} + \frac{\Delta S^\ddagger}{R}$$

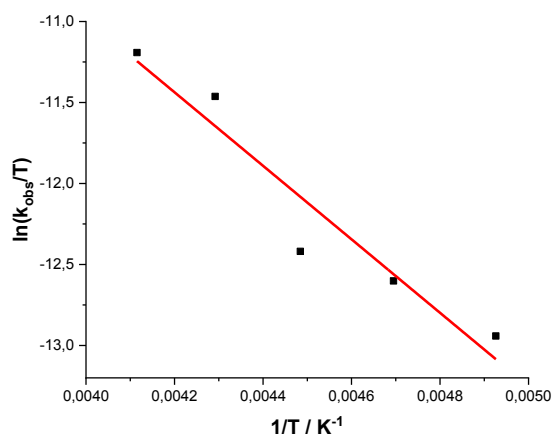


**Figure S32.** Temperature dependence of the reaction rate  $k_{obs}$  of K{crypt.222}[2] with 20 equiv. 1,4-CHD in Et<sub>2</sub>O giving  $\Delta H^\ddagger = 19(3) \text{ kJ mol}^{-1}$  and  $\Delta S^\ddagger = -209(183) \text{ JK}^{-1}\text{mol}^{-1}$ .

## 9. Catalytic reactions

For catalytic reactions involving 1,4-CHD and indene no additional solvent was used and [D<sub>8</sub>]THF was added after a certain amount of time to determine the conversion via <sup>1</sup>H-NMR-spectroscopy. In case of Ph<sub>3</sub>CH the reaction was performed in 1,2-DFB and samples were analyzed in [D<sub>8</sub>]THF. The conversion and yields are calculated from the integrals of the proton signals of *tert*-butylazide (1.26 ppm) and *tert*-butylamine (1.07 ppm). For XAN C<sub>6</sub>Me<sub>6</sub> was used as an internal standard, because of the formation of several side products.

### Catalytic reaction of 1,4-CHD and *tert*-Butylazide with 5 mol% K{crypt.222}[2]

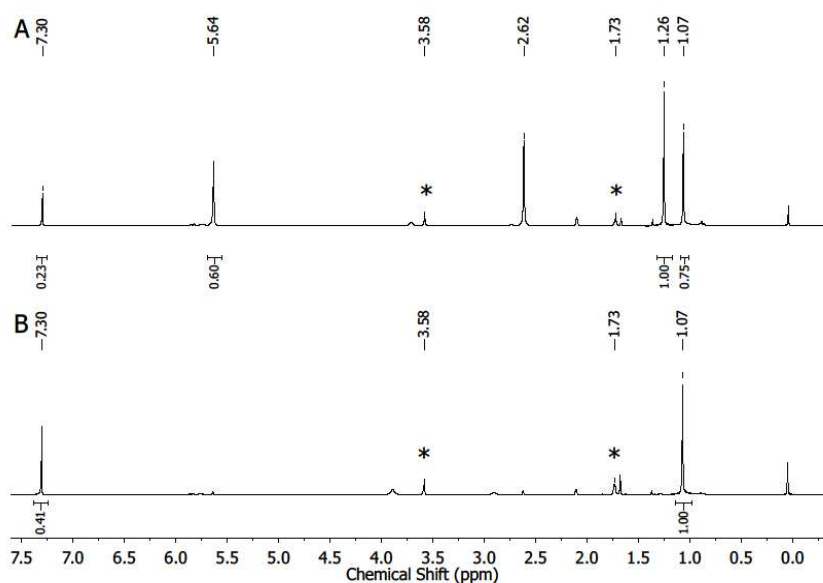


**Figure S33.** *In-situ* <sup>1</sup>H-NMR spectra ([D<sub>8</sub>]THF, 298 K, 300 MHz) after **A:** 12 h (43% yield/conversion); **B:** 36 h (99% yield/conversion).

Catalytic reaction of 9,10-DHA and *tert*-Butylazide with 5 mol% K{crypt.222}[2] in [D8]THF

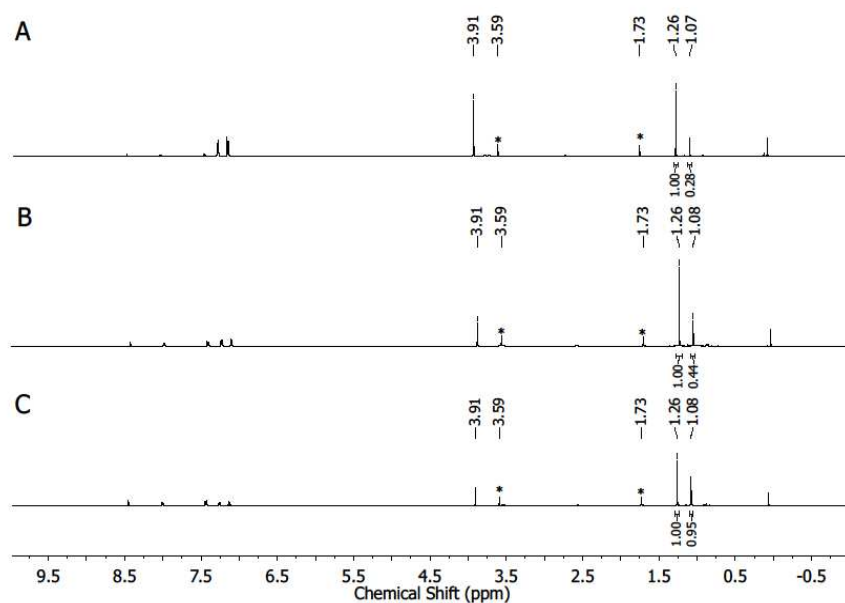


**Figure S34.** *In-situ*  $^1\text{H}$ -NMR spectra ([D8]THF, 298 K, 300 MHz) after **A**: 30min (22% yield/conversion); **B**: 3 h (30% yield/conversion); **C**: 24 h (49% yield/conversion).

Catalytic reaction of xanthene and *tert*-Butylazide with 5 mol% K{crypt.222}[2]

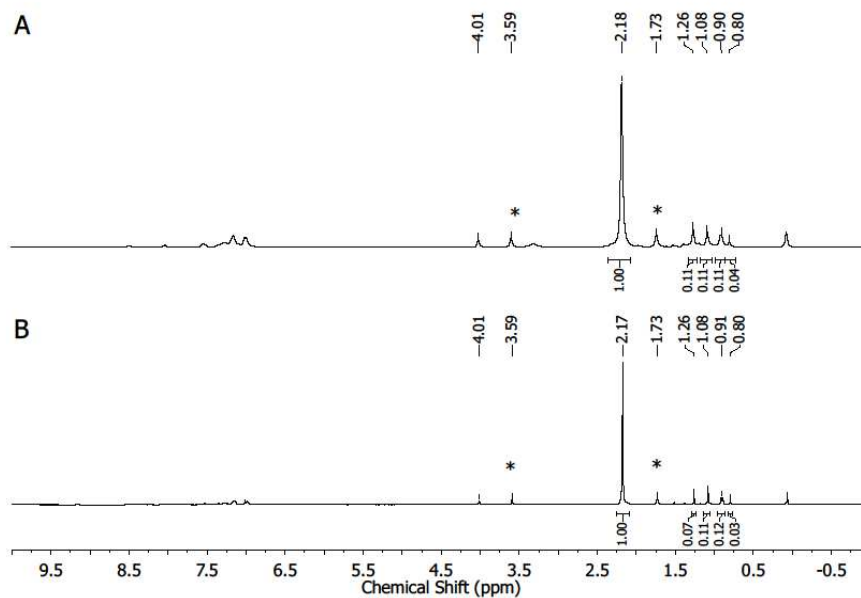


**Figure S35.** *In-situ*  $^1\text{H}$ -NMR spectra ([D8]THF, 298 K, 300 MHz) with internal standard ( $\text{C}_6\text{Me}_6$ ) after **A**: 12 h (50% conversion, 29% yield); **B**: 36 h (61% conversion, 33% yield).

### Catalytic reaction of indene and *tert*-Butylazide with 5 mol% K{crypt.222}[2]

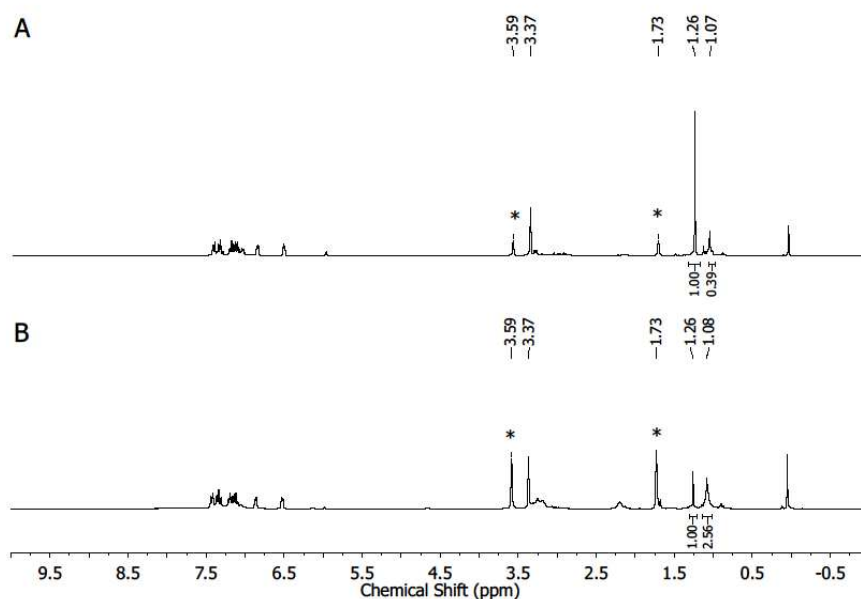


**Figure S36.** *In-situ* <sup>1</sup>H-NMR spectra ([D<sub>8</sub>]THF, 298 K, 300 MHz) after **A**: 12 h (28% yield/conversion); **B**: 36 h (72% yield/conversion).

## 10. Magnetic measurements

Magnetic data of complex K{crypt.222}[2] was recorded using a dried crystalline sample and were corrected for diamagnetic contributions from the sample holder and the diamagnetic susceptibility of the compound using Pascal constants. Obtained paramagnetic susceptibility  $\chi_{\text{para}}$  was fitted using the Curie-Weiss-law  $\chi_{\text{CW}} = \left(\frac{N_A \mu_B^2 n_{\text{eff}}}{3k_B}\right)^2 \frac{1}{T-\theta}$  ( $n_{\text{eff}}$  = effective magnetic moment in Bohr's magnetons per formula unit,  $\theta$  = Weiss temperature) with contributions from a temperature independent paramagnetism  $\chi_{\text{TIP}}$  using the overall equation  $\chi_{\text{para}} T = (\chi_{\text{TIP}} + \chi_{\text{CW}}) T$ .

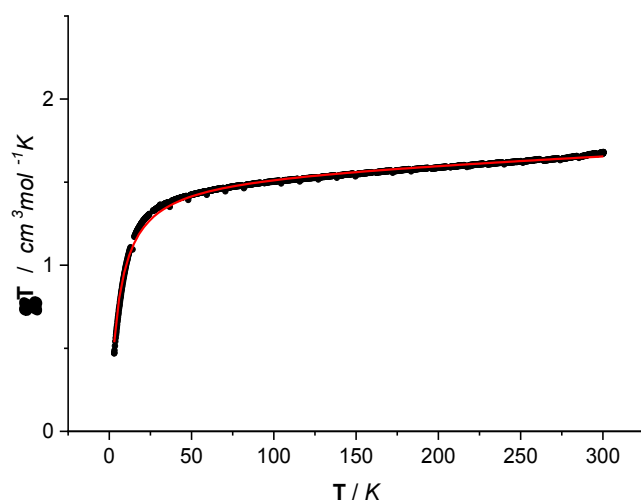


**Figure S37.** Temperature dependence of the molar magnetic susceptibility times temperature product ( $\chi T$  vs.  $T$ ) for compound  $K\{\text{crypt.222}\}[2]$ . Data were collected under an applied dc field of 1 T in a temperature range of 3 to 300 K. Molar diamagnetic correction =  $-2.88 \times 10^{-4} \text{ emu mol}^{-1}$ ,  $\chi_{\text{TIP}} = 4.45(7) \times 10^{-4} \text{ emu mol}^{-1}$ ,  $n_{\text{eff}} = 3.520(2) \mu_{\text{B}} \text{ f.u.}^{-1}$  (f.u. = formula unit),  $\chi_{\text{M}} T = 1.68 \text{ cm}^3 \text{ mol}^{-1} \text{ K}$  (300K),  $\Theta = -5.69(4) \text{ K}$ .

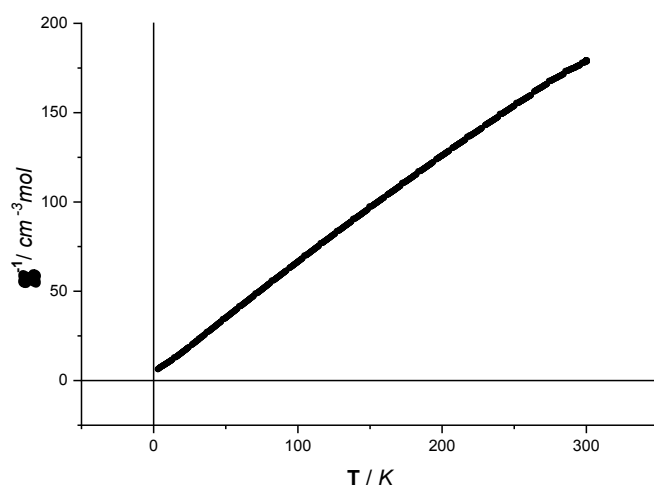


**Figure S38.** Reciprocal molar magnetic susceptibilities ( $\chi^{-1}$ ) for compound  $K\{\text{crypt.222}\}[2]$ . Data were collected under an applied dc field of 1 T in a temperature range of 3 to 300 K.

## 11. EPR measurements

EPR spectra were performed on a Bruker EMXplus (X-band) EPR spectrometer equipped with the Bruker ER4118X-MD5 probehead. The freshly prepared samples were transferred to J. Young quartz EPR tubes and sealed. The solution in the tube was frozen in liquid nitrogen and kept frozen until measured.

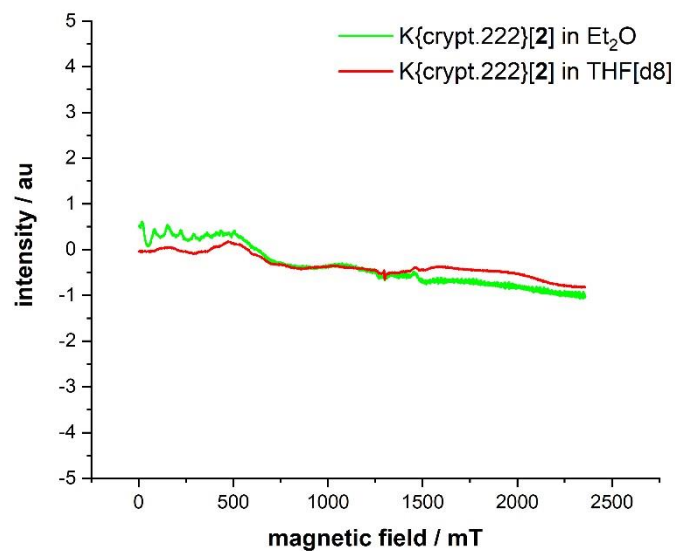


**Figure S39.** X-band EPR spectra of 1 mM K{crypt.222}[2] in diethylether (frequency 9.355294 GHz, 2.0 mW power, 5 G modulation amplitude) and THF[d8] (frequency 9.357518 GHz, 2.0 mW power, 5 G modulation amplitude) and 1 mM Cu(II) standard in H<sub>2</sub>O (frequency 9.35545 GHz, 2.0 mW power, 5 G modulation amplitude) at 12.3 K.

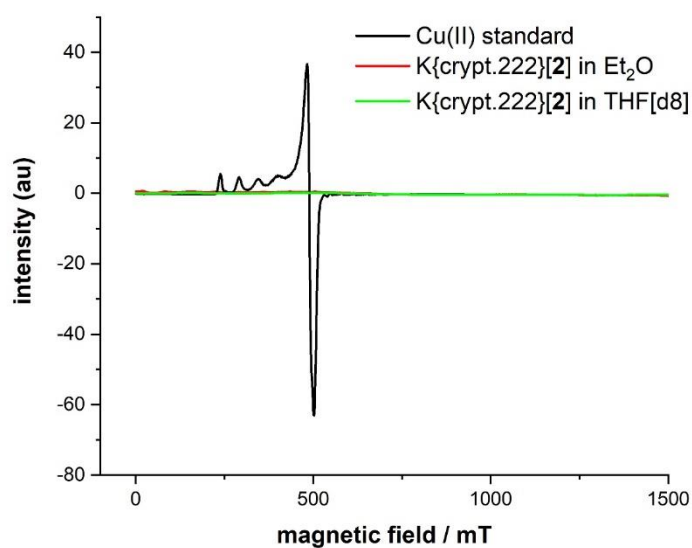


**Figure S40.** X-band EPR spectra of 1 mM Cu(II) standard in H<sub>2</sub>O (frequency 9.35545 GHz, 2.0 mW power, 5 G modulation amplitude) at 12.3 K compared to the measured samples.

## 12. X-Ray diffraction analysis and molecular structures

Data for **1** (CCDC 1936642), **2** (CCDC 1936643), **3** (CCDC 1936645), **4** (CCDC 1936652) were collected at 100 K on a Bruker Quest D8 diffractometer using a graphite-monochromated Mo-K $\alpha$  radiation and equipped with an *Oxford Instrument Cooler Device*. The structures have been solved using OLEX SHELXT V2014/1<sup>[xii]</sup> and refined by means of least-squares procedures on a  $F^2$  with the aid of the program SHELXL-2016/6<sup>[xiii]</sup> included in the softwares package WinGX version 1.63<sup>[xiv]</sup> or using CRYSTALS.<sup>[xv]</sup>

The Atomic Scattering Factors were taken from *International Tables for X-Ray Crystallography*.<sup>[xvi]</sup> All non-hydrogen atoms were refined anisotropically. All hydrogens atoms were refined by using a riding model. Absorption corrections were introduced by using MULTISCAN.<sup>[xvii]</sup> Drawings of molecules are performed with the program DIAMOND with 50% probability displacement ellipsoids for non-H atoms. Depiction of H atoms is usually omitted for clarity.

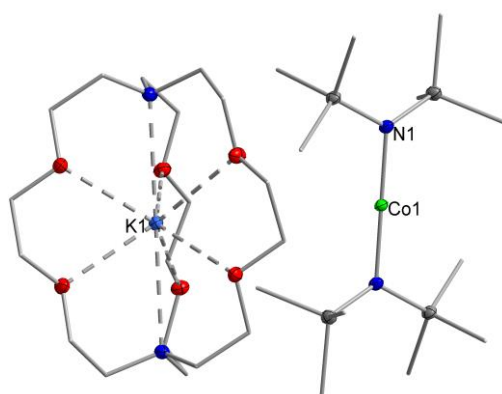
**Table S4.** Selected bond lengths and angles ( $^\circ$ ) of K{crypt.222}[**2**] and K{crypt.222}[**3**]. The Co=NR and the Co-NHR bond lengths are highlighted.

compound		bond lengths/ bond angles
K{crypt.222}[ <b>2</b> ]	Co1-N1 <sub>tBu</sub>	1.7067(12) Å
	Co1-N2 <sub>(hmds)</sub>	1.9382(10) Å
	Co1-N3 <sub>(hmds)</sub>	1.93921(10) Å
	Co1-N1-C1	160.78(12) $^\circ$
K{crypt.222}[ <b>3</b> ]	Co1-N1 <sub>tBu</sub>	1.8832(12) Å
	Co1-N2 <sub>(hmds)</sub>	1.9820(11) Å
	Co1-N3 <sub>(hmds)</sub>	1.9670(11) Å
	Co1-N1-C1	134.79(10) $^\circ$



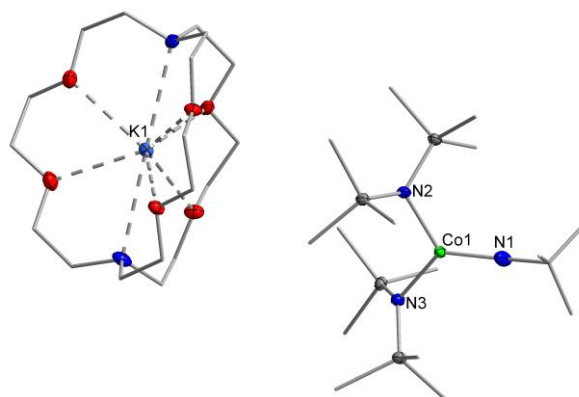
**Table S5. Crystal data and structure refinement for K{crypt.222}[1].**

Identification code	GWX033A_0m
Empirical formula	C <sub>30</sub> H <sub>72</sub> CoKN <sub>4</sub> O <sub>6</sub> Si <sub>4</sub>
Formula weight / g mol <sup>-1</sup>	795.30
Temperature / K	100.0
Crystal system	monoclinic
Space group	<i>P</i> 2/ <i>n</i>
<i>a</i> / Å	13.1431(6)
<i>b</i> / Å	8.7828(4)
<i>c</i> / Å	19.4108(9)
$\alpha$ / °	90
$\beta$ / °	96.567(2)
$\gamma$ / °	90
<i>V</i> / Å <sup>3</sup>	2225.95(18)
<i>Z</i>	2
$\rho_{\text{calc}}$ / g cm <sup>-3</sup>	1.187
$\mu$ / mm <sup>-1</sup>	0.626
F(000)	860.0
Crystal size / mm <sup>3</sup>	0.317 × 0.16 × 0.138
Radiation	MoK $\alpha$ ( $\lambda$ = 0.71073)
2 $\theta$ range for data collection / °	4.638 to 56.864
Index ranges	-17 ≤ <i>h</i> ≤ 17, -11 ≤ <i>k</i> ≤ 11, -26 ≤ <i>l</i> ≤ 25
Reflections collected	69162
Independent reflections	5601 [ <i>R</i> <sub>int</sub> = 0.0505, <i>R</i> <sub>sigma</sub> = 0.0232]
Data/restraints/parameters	5601/0/216
Goodness-of-fit on F <sup>2</sup>	1.064
Final <i>R</i> indexes [ <i>I</i> ≥ 2 $\sigma$ ( <i>I</i> )]	<i>R</i> <sub>1</sub> = 0.0282, <i>wR</i> <sub>2</sub> = 0.0615
Final <i>R</i> indexes [all data]	<i>R</i> <sub>1</sub> = 0.0387, <i>wR</i> <sub>2</sub> = 0.0651
Largest diff. peak/hole / e Å <sup>-3</sup>	0.28/-0.28

**Figure S41.** Section of the crystal structure of K{crypt.222}[1].

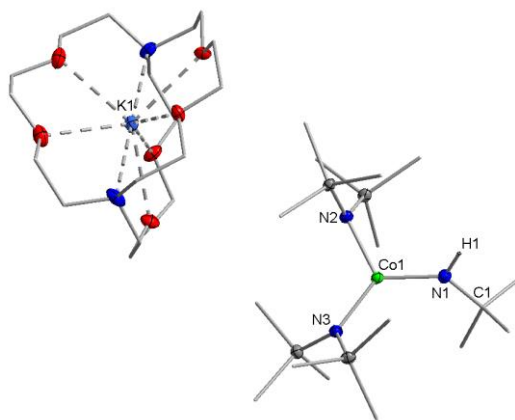
**Table S6. Crystal data and structure refinement for K{crypt.222}[2].**

Identification code	GWX027d_0m
Empirical formula	C <sub>34</sub> H <sub>81</sub> CoKN <sub>5</sub> O <sub>6</sub> Si <sub>4</sub>
Formula weight / g mol <sup>-1</sup>	866.42
Temperature/K	100.01
Crystal system	triclinic
Space group	$P\bar{1}$
<i>a</i> / Å	10.5518(4)
<i>b</i> / Å	14.6119(6)
<i>c</i> / Å	16.9148(7)
$\alpha$ / °	88.045(2)
$\beta$ / °	76.1040(10)
$\gamma$ / °	77.0870(17)
<i>V</i> / Å <sup>3</sup>	2467.08(17)
<i>Z</i>	2
$\rho_{\text{calc}}$ / g cm <sup>-3</sup>	1.166
$\mu$ / mm <sup>-1</sup>	0.570
F(000)	940.0
Crystal size / mm <sup>3</sup>	0.276 × 0.232 × 0.168
Radiation	MoK $\alpha$ ( $\lambda$ = 0.71073)
2 $\theta$ range for data collection / °	4.432 to 56.232
Index ranges	-13 ≤ <i>h</i> ≤ 13, -19 ≤ <i>k</i> ≤ 19, -22 ≤ <i>l</i> ≤ 22
Reflections collected	81474
Independent reflections	12018 [ <i>R</i> <sub>int</sub> = 0.0328, <i>R</i> <sub>sigma</sub> = 0.0218]
Data/restraints/parameters	12018/0/475
Goodness-of-fit on F <sup>2</sup>	1.032
Final <i>R</i> indexes [ <i>I</i> ≥ 2 $\sigma$ ( <i>I</i> )]	<i>R</i> <sub>1</sub> = 0.0273, <i>wR</i> <sub>2</sub> = 0.0616
Final <i>R</i> indexes [all data]	<i>R</i> <sub>1</sub> = 0.0349, <i>wR</i> <sub>2</sub> = 0.0644
Largest diff. peak/hole / e Å <sup>-3</sup>	0.61/-0.35

**Figure S42.** Sections of the crystal structure of K{crypt.222}[2].

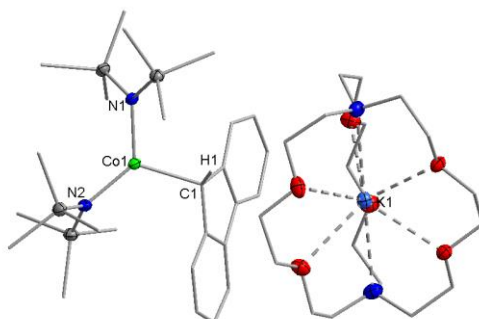
**Table S7. Crystal data and structure refinement for K{crypt.222}[3].**

Identification code	GWX046_0m
Empirical formula	C <sub>34</sub> H <sub>82</sub> CoKN <sub>5</sub> O <sub>6</sub> Si <sub>4</sub>
Formula weight / g mol <sup>-1</sup>	867.43
Temperature/K	100.0
Crystal system	monoclinic
Space group	<i>P</i> 2 <sub>1</sub> / <i>c</i>
<i>a</i> / Å	10.6100(5)
<i>b</i> / Å	28.3422(13)
<i>c</i> / Å	17.0142(8)
$\alpha$ / °	90
$\beta$ / °	104.100(2)
$\gamma$ / °	90
<i>V</i> / Å <sup>3</sup>	4962.2(4)
<i>Z</i>	4
$\rho_{\text{calc}}$ / g cm <sup>-3</sup>	1.161
$\mu$ / mm <sup>-1</sup>	0.567
<i>F</i> (000)	1844.0
Crystal size / mm <sup>3</sup>	0.41 × 0.367 × 0.19
Radiation	MoK $\alpha$ ( $\lambda$ = 0.71073)
2 $\theta$ range for data collection / °	4.21 to 61.052
Index ranges	-15 ≤ <i>h</i> ≤ 13, -39 ≤ <i>k</i> ≤ 40, -24 ≤ <i>l</i> ≤ 23
Reflections collected	205261
Independent reflections	14932 [ <i>R</i> <sub>int</sub> = 0.0496, <i>R</i> <sub>sigma</sub> = 0.0308]
Data/restraints/parameters	14932/0/491
Goodness-of-fit on <i>F</i> <sup>2</sup>	1.095
Final <i>R</i> indexes [ <i>I</i> ≥ 2 $\sigma$ ( <i>I</i> )]	<i>R</i> <sub>1</sub> = 0.0387, <i>wR</i> <sub>2</sub> = 0.0751
Final <i>R</i> indexes [all data]	<i>R</i> <sub>1</sub> = 0.0572, <i>wR</i> <sub>2</sub> = 0.0796
Largest diff. peak/hole / e Å <sup>-3</sup>	0.41/-0.31

**Figure S43.** Sections of the crystal structure of K{crypt.222}[3].

**Table S8. Crystal data and structure refinement for K{crypt.222}[4].**

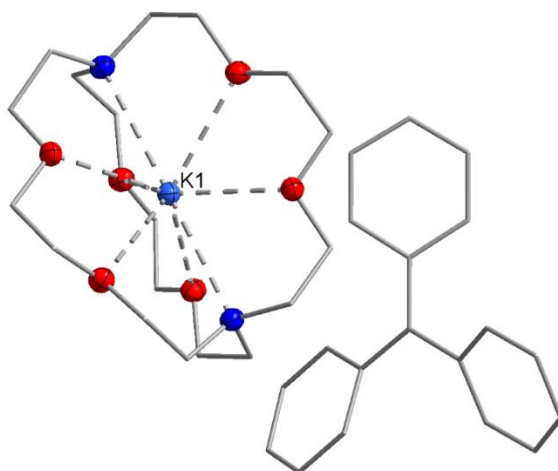
Identification code	XP25_0m
Empirical formula	C <sub>43</sub> H <sub>81</sub> CoKN <sub>4</sub> O <sub>6</sub> Si <sub>4</sub>
Formula weight / g mol <sup>-1</sup>	960.50
Temperature/K	100.0
Crystal system	monoclinic
Space group	<i>P</i> 2 <sub>1</sub> / <i>c</i>
<i>a</i> / Å	12.0165(6)
<i>b</i> / Å	22.5903(11)
<i>c</i> / Å	19.9109(10)
$\alpha$ / °	90
$\beta$ / °	93.379(2)
$\gamma$ / °	90
<i>V</i> / Å <sup>3</sup>	5395.5(5)
<i>Z</i>	4
$\rho_{\text{calc}}$ / g cm <sup>-3</sup>	1.182
$\mu$ / mm <sup>-1</sup>	0.528
<i>F</i> (000)	2068.0
Crystal size / mm <sup>3</sup>	0.57 × 0.201 × 0.186
Radiation	MoK $\alpha$ ( $\lambda$ = 0.71073)
2 $\theta$ range for data collection / °	4.262 to 49.994
Index ranges	-14 ≤ <i>h</i> ≤ 14, -26 ≤ <i>k</i> ≤ 26, -23 ≤ <i>l</i> ≤ 23
Reflections collected	76304
Independent reflections	9492 [ <i>R</i> <sub>int</sub> = 0.0518, <i>R</i> <sub>sigma</sub> = 0.0302]
Data/restraints/parameters	9492/0/556
Goodness-of-fit on <i>F</i> <sup>2</sup>	1.040
Final <i>R</i> indexes [ <i>I</i> ≥ 2 $\sigma$ ( <i>I</i> )]	<i>R</i> <sub>1</sub> = 0.0385, <i>wR</i> <sub>2</sub> = 0.0898
Final <i>R</i> indexes [all data]	<i>R</i> <sub>1</sub> = 0.0543, <i>wR</i> <sub>2</sub> = 0.0956
Largest diff. peak/hole / e Å <sup>-3</sup>	1.23/-0.60



**Figure S44.** Sections of the crystal structure of K{crypt.222}[4].

**Table S9. Crystal data and structure refinement for K{crypt.222}[5].**

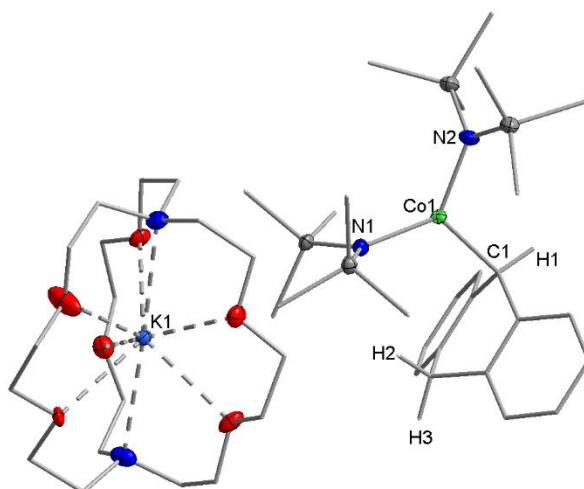
Identification code	XP36
Empirical formula	$C_{37}H_{51}KN_2O_6$
Formula weight / $g\ mol^{-1}$	658.89
Temperature/K	100
Crystal system	monoclinic
Space group	$P2_1/c$
$a / \text{\AA}$	11.3602(7)
$b / \text{\AA}$	16.0189(7)
$c / \text{\AA}$	19.5026(12)
$\alpha / ^\circ$	90
$\beta / ^\circ$	99.060(5)
$\gamma / ^\circ$	90
$V / \text{\AA}^3$	3504.8(3)
Z	4
$\rho_{\text{calc}} / g\ cm^{-3}$	1.249
$\mu / mm^{-1}$	1.704
F(000)	1416.0
Crystal size / $mm^3$	$0.399 \times 0.215 \times 0.177$
Radiation	$CuK\alpha$ ( $\lambda = 1.54186$ )
$2\theta$ range for data collection / $^\circ$	7.178 to 133.982
Index ranges	$-11 \leq h \leq 13, -16 \leq k \leq 19, -23 \leq l \leq 23$
Reflections collected	35516
Independent reflections	6239 [ $R_{\text{int}} = 0.0368, R_{\text{sigma}} = 0.0356$ ]
Data/restraints/parameters	6239/0/415
Goodness-of-fit on $F^2$	0.935
Final $R$ indexes [ $I \geq 2\sigma(I)$ ]	$R_1 = 0.0401, wR_2 = 0.0958$
Final $R$ indexes [all data]	$R_1 = 0.0493, wR_2 = 0.0981$
Largest diff. peak/hole / $e\ \text{\AA}^{-3}$	0.18/-0.27



**Figure S45. Sections of the crystal structure of K{crypt.222}[5].**

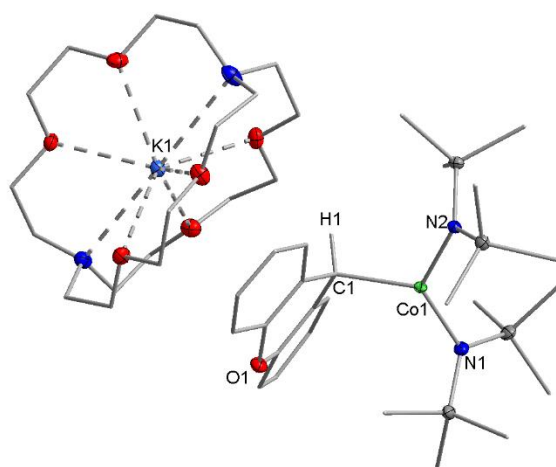
**Table S10. Crystal data and structure refinement for K{crypt.222}[6].**

Identification code	XP38_0m
Empirical formula	C <sub>46</sub> H <sub>87</sub> CoKN <sub>4</sub> O <sub>6.5</sub> Si <sub>4</sub>
Formula weight / g mol <sup>-1</sup>	1010.5
Temperature/K	99.99
Crystal system	monoclinic
Space group	<i>P</i> 2 <sub>1</sub> / <i>n</i>
<i>a</i> / Å	17.5125(12)
<i>b</i> / Å	14.0780(9)
<i>c</i> / Å	23.4465(14)
$\alpha$ / °	90
$\beta$ / °	104.178(2)
$\gamma$ / °	90
<i>V</i> / Å <sup>3</sup>	5604.4(6)
<i>Z</i>	4
$\rho_{\text{calc}}$ / g cm <sup>-3</sup>	1.198
$\mu$ / mm <sup>-1</sup>	0.512
F(000)	2180.0
Crystal size / mm <sup>3</sup>	0.34 × 0.257 × 0.139
Radiation	MoK $\alpha$ ( $\lambda$ = 0.71073)
2 $\theta$ range for data collection / °	4.41 to 52.172
Index ranges	-21 ≤ <i>h</i> ≤ 21, -17 ≤ <i>k</i> ≤ 17, -28 ≤ <i>l</i> ≤ 28
Reflections collected	123515
Independent reflections	11096 [ <i>R</i> <sub>int</sub> = 0.0677, <i>R</i> <sub>sigma</sub> = 0.0300]
Data/restraints/parameters	11096/0/598
Goodness-of-fit on F <sup>2</sup>	1.029
Final <i>R</i> indexes [ <i>I</i> ≥ 2 $\sigma$ ( <i>I</i> )]	<i>R</i> <sub>1</sub> = 0.0342, <i>wR</i> <sub>2</sub> = 0.0718
Final <i>R</i> indexes [all data]	<i>R</i> <sub>1</sub> = 0.0482, <i>wR</i> <sub>2</sub> = 0.0769
Largest diff. peak/hole / e Å <sup>-3</sup>	0.33/-0.33

**Figure S46.** Sections of the crystal structure of K{crypt.222}[6].

**Table S11. Crystal data and structure refinement for K{crypt.222}[7].**

Identification code	XP41_0m
Empirical formula	C <sub>43</sub> H <sub>81</sub> CoKN <sub>4</sub> O <sub>7</sub> Si <sub>4</sub>
Formula weight / g mol <sup>-1</sup>	976.50
Temperature/K	100.02
Crystal system	monoclinic
Space group	<i>P</i> 2 <sub>1</sub> / <i>c</i>
<i>a</i> / Å	11.6101(6)
<i>b</i> / Å	22.2812(12)
<i>c</i> / Å	21.3186(11)
$\alpha$ / °	90
$\beta$ / °	95.079(2)
$\gamma$ / °	90
<i>V</i> / Å <sup>3</sup>	5493.2(5)
<i>Z</i>	4
$\rho_{\text{calc}}$ / g cm <sup>-3</sup>	1.181
$\mu$ / mm <sup>-1</sup>	0.512
<i>F</i> (000)	2100.0
Crystal size / mm <sup>3</sup>	0.292 × 0.115 × 0.089
Radiation	MoK $\alpha$ ( $\lambda$ = 0.71073)
2 $\theta$ range for data collection / °	4.27 to 52.324
Index ranges	-14 ≤ <i>h</i> ≤ 14, -27 ≤ <i>k</i> ≤ 27, -26 ≤ <i>l</i> ≤ 26
Reflections collected	110937
Independent reflections	10874 [ <i>R</i> <sub>int</sub> = 0.0916, <i>R</i> <sub>sigma</sub> = 0.0494]
Data/restraints/parameters	10874/0/553
Goodness-of-fit on <i>F</i> <sup>2</sup>	1.074
Final <i>R</i> indexes [ <i>I</i> ≥ 2 $\sigma$ ( <i>I</i> )]	<i>R</i> <sub>1</sub> = 0.0422 , <i>wR</i> <sub>2</sub> = 0.0742
Final <i>R</i> indexes [all data]	<i>R</i> <sub>1</sub> = 0.0677 , <i>wR</i> <sub>2</sub> = 0.0804
Largest diff. peak/hole / e Å <sup>-3</sup>	0.37/-0.31

**Figure S47. Sections of the crystal structure of K{crypt.222}[7].**

---

## References

- [i] a) D. F. Evans *J. Chem. Soc.* **1959**, 2003; b) E. M. Schubert *J. Chem. Educ.* **1992**, *69*, 62.
- [ii] A. M. Bryan, G. J. Long, F. Grandjean, P. P. Power; *Inorg. Chem.* **2013**, *52*, 12152.
- [iii] C. V. Sastri, J. Lee, K. Oh, Y. J. Lee, J. Lee, T. A. Jackson, K. Ray, H. Hirao, W. Shin, J. A. Halfen, J. Kim, L. Que, S. Shaik, W. Nam, *PNAS*, **2007**, *49*, 19181.
- [iv] J. C. Bottaro, Penwell, E. Paul, R. J. Schmitt, *Synthetic Commun.*, **1997**, *8*, 1465.
- [v] L. J. J. Laarhoven, P. Mulder, D. D. M. Wayner, *Acc. Chem. Res.*, **1999**, *4*, 342.
- [vi] C. J. Reed, T. Agapie, *J. Am. Chem. Soc.*, **2019**, *24*, 9479.
- [vii] F. G. Bordwell, J. Cheng, G. Z. Ji, A. v. Satish, X. Zhang, *J. Am. Chem. Soc.*, **1991**, *26*, 9790.
- [viii] X.-S. Xue, P. Ji, B. Zhou, J.-P. Cheng, *Chem. Rev.*, **2017**, *13*, 8622.
- [ix] Y.-R. Luo, *Comprehensive Handbook of Chemical Bond Energies*; CRC Press: Boca Raton, FL, 2007.
- [x] V. S. Bryantsev, *Chem. Phys. Lett.*, **2013**, 42.
- [xi] O. Kondo, S. W. Sidney, *Int. J. Chem. Kinet.*, **1984**, *8*, 949.
- [xii] O. V. Dolomanov, L. J. Bourhis, R. J. Gildea, J. A. K. Howard, H. Puschmann, *J. Appl. Crystallogr.* **2009**, *42*, 339.
- [xiii] G. M. Sheldrick, *Acta Cryst.* **2015**, *71*, 3.
- [xiv] L. Farrugia, *J. Appl. Crystallogr.*, **1999**, *32*, 837.
- [xv] P. W. Betteridge, J. R. Carruthers, R. I. Cooper, K. Prout, D. J. Watkin *J. Appl. Cryst.* **2003**, *36*, 1487.
- [xvi] *International Tables for X-ray crystallography* (Kynoch Press, Birmingham, England, **1974**) Vol. IV.
- [xvii] *SADABS-2016/2* (Bruker, **2016**).



### **6.9.2 High-Spin Imido Cobalt Complexes with Imidyl Radical Character**

## Supporting Information

### **High-Spin Imido Cobalt Complexes with Imidyl Radical Character\*\***

*Alexander Reckziegel, Manjinder Kour, Beatrice Battistella, Stefan Mebs, Katrin Beuthert, Robert Berger, and C. Gunnar Werncke\**

anie\_202103841\_sm\_miscellaneous\_information.pdf

## Table of Contents

General considerations .....	3
1. Synthesis of $K\{\text{crypt.222}\}[\text{Co}(\text{NDippSiMe}_3)]$ ( $K\{\text{crypt.222}\}[1]$ ) .....	4
2. Synthesis of $^{15}\text{N}_3\text{Dipp}$ .....	5
3. Synthesis of $\text{N}_3\text{Tripp}$ .....	5
4. Synthesis of $K\{18\text{c}6\}[\text{Co}(\text{NDippSiMe}_3)_2\text{NDipp}]$ ( $K\{18\text{c}6\}[2]$ ) .....	6
5. Synthesis of $K\{18\text{c}6\}[\text{Co}(\text{NDippSiMe}_3)_2^{15}\text{NDipp}]$ ( $K\{18\text{c}6\}[^{15}\text{N}-2]$ ) .....	8
6. Synthesis of $K\{2.2.2\}[\text{Co}(\text{NDippSiMe}_3)_2\text{NDipp}]$ ( $K\{\text{crypt.222}\}[2]$ ) .....	9
7. Synthesis of $K[\text{Co}(\text{NDippSiMe}_3)_2\text{NDipp}]$ ( $K[2]$ ).....	10
8. Synthesis of $K\{18\text{c}6\}[\text{Co}(\text{NDippSiMe}_3)_2\text{NTripp}]$ ( $K\{18\text{c}6\}[3]$ ) .....	11
9. Synthesis of $K[\text{Co}(\text{NDippSiMe}_3)_2\text{NTripp}] \times 0.5$ toluene ( $K[3]$ ).....	12
10. Synthesis of $K\{18\text{c}6\}[\text{Co}(\text{NDippSiMe}_3)_2\text{NHDipp}]$ ( $K\{18\text{c}6\}[4]$ ).....	13
11. Synthesis of $K\{2.2.2\}[\text{Co}(\text{NDippSiMe}_3)_2\text{NHDipp}]$ ( $K\{\text{crypt.222}\}[4]$ ).....	15
12. Synthesis of $K[\text{Co}(\text{NDippSiMe}_3)_2\text{NHDipp}]$ ( $K[4]$ ) .....	17
13. Synthesis of $K\{18\text{c}6\}[\text{Co}(\text{NHDipp})_2\text{NDippSiMe}_3]$ ( $K\{18\text{c}6\}[5]$ ).....	18
14. Reaction of $K\{18\text{c}6\}[\text{Co}(\text{NDippSiMe}_3)_2]$ ( $K\{18\text{c}6\}[1]$ ) with mesitylazide .....	19
15. Hydrogen atom transfer (HAT) reactivity.....	20
16. Magnetic measurements.....	22
17. Electron-paramagnetic-resonance spectroscopy (EPR) .....	23
18. X-ray absorption measurements.....	24
19. Quantum chemical calculations .....	27
20. X-Ray diffraction analysis and molecular structures .....	31

## General considerations

All manipulations were carried out in a glovebox or using Schlenk-type techniques under a dry argon atmosphere. Used solvents were dried by continuous distillation over sodium metal for several days, degassed via three freeze-pump cycles and stored over molecular sieves 4 Å. The  $^1\text{H}$  NMR spectra were recorded on a *Bruker AV III 500* or *Bruker AV II 300* NMR spectrometers. Chemical shifts are reported in ppm relative to the residual proton signals of the solvent (for  $^1\text{H}$ ) or relative to the signal of the solvent itself ( $^{13}\text{C}$ ).  $w_{1/2}$  is the line width of a signal at half its maximum intensity. Integrals of the broad signals of the silylamide units were obtained directly or by peak fitting (in case of overlapping signals) using the Mestrenova software package. IR measurements were conducted on a *Bruker Alpha ATR-IR* spectrometer. Elemental analysis was performed by the "in-house" service of the Chemistry Department of the Philipps University Marburg, Germany using a CHN(S) analyzer *vario MICRO Cube (Elementar)*. The UV/VIS measurement were recorded on an *Analytik Jena Specord S600* using *WinASPECT* software and an *UNISOKU CoolSpeK Cryostat*. The DC susceptibility measurements were made in the range of 3 K to 300 K by 1 T on a 9 Tesla instrument from LOT / QD. The diamagnetic correction was performed using the Pascal constants and the experimentally determined value of the polyurethane sample holder. Solution magnetic susceptibilities were determined by the Evans method.<sup>i</sup> Anhydrous  $\text{CoCl}_2$ , *n*-butyl lithium (2.5 M in hexane), 18-crown-6, 2.2.2-cryptand, 1,4-cyclohexadien, 9,10-dihydroanthracen, and tetramethylsilane (TMS) were obtained commercially (Sigma-Aldrich, Acros, Strem, Alfa Aesar) and - if not noted otherwise - used as received. 1,4-cyclohexadiene was degassed, transferred into the glovebox and stored over molecular sieves at  $-35^\circ\text{C}$ . 18-crown-6 was sublimed prior use to remove traces of water.  $\text{K}\{18\text{c}6\}[\text{Co}(\text{NDippSiMe}_3)_2]$  ( $\text{K}\{18\text{c}6\}[\mathbf{1}]$ )<sup>ii</sup>, 1-azido-2,6-di-*iso*-propylbenzene<sup>iii</sup> ( $\text{N}_3\text{Dipp}$ ), 1-azido-2,4,6-trimethylbenzene<sup>iii</sup> ( $\text{N}_3\text{Mes}$ ) and  $\text{KNH}-(2,6\text{-di-iso-propylbenzene})$ <sup>iv</sup> ( $\text{KNHDipp}$ ) were prepared according to literature procedures.

## 1. Synthesis of K{crypt.222}[Co(NDippSiMe<sub>3</sub>)] (K{crypt.222}[1])

100 mg (0.18 mmol, 1 equiv.) Co(NDippSiMe<sub>3</sub>)<sub>2</sub> were dissolved in 2 mL Et<sub>2</sub>O. Addition of 27 mg (0.2 mmol, 1.1 equiv.) KC<sub>8</sub> at -30 °C resulted in colour change from red to a greenish yellow over the course of 2 h. The mixture was filtered and the filtrate was layered with a solution of 67.7 mg crypt.222 (0.18 mmol, 1 equiv.) in 2 mL Et<sub>2</sub>O followed by a layer of 1 mL *n*-pentane. Storage at -35 °C lead to the formation of a microcrystalline greenish yellow solid. After one day, the solution was removed via pipette and the remaining dark yellow plate crystals were rinsed with 2x3mL pentane. Drying *in vacuo* yielded 80 mg (0.09 mmol, 45%) K{crypt.222}[1].

<sup>1</sup>H-NMR (THF-d<sub>8</sub>, 298 K, ppm, 500 MHz): 29.4 (s, *w*<sub>1/2</sub> = 523.1 Hz), 17.3 (s, *w*<sub>1/2</sub> = 48.0 Hz), 16.2 (s, *w*<sub>1/2</sub> = 36.2 Hz), 13.59 (s, *w*<sub>1/2</sub> = 202.4 Hz), 3.18 (s, *w*<sub>1/2</sub> = 13.5 Hz, crypt.222), 3.15 (s, *w*<sub>1/2</sub> = 7.5 Hz, crypt.222), 2.24 (s, *w*<sub>1/2</sub> = 12.5 Hz, crypt.222), -86.7 (s, *w*<sub>1/2</sub> = 147.7 Hz) ppm.

IR (ATR, cm<sup>-1</sup>) *v*: 2954 (m), 2882 (m), 2819 (m), 1582 (w), 1421 (m), 1353 (m), 1315 (m), 1296 (m), 1234 (m), 1198 (s), 1131 (m), 1100 (s), 1078 (m), 1039 (w), 948 (m), 931 (s), 831 (s), 780 (s), 738 (m), 658 (m), 621 (w), 523 (w), 424 (w).

Elemental analysis: calcd. (%) for C<sub>48</sub>H<sub>88</sub>CoKN<sub>4</sub>O<sub>6</sub>Si<sub>2</sub> (971.46 g mol<sup>-1</sup>): C 59.35 H 9.13 N 5.77; found: C 58.92 H 8.757 N 5.93.

EVANS-Method:  $\mu_{\text{eff}} = 3.86 \mu_{\text{B}}$  ([D8]THF+ 1% Si(CH<sub>3</sub>)<sub>4</sub>, 500 MHz, 298 K,  $\mu_{\text{s.o.}} = 3.87 \mu_{\text{B}}$ ).

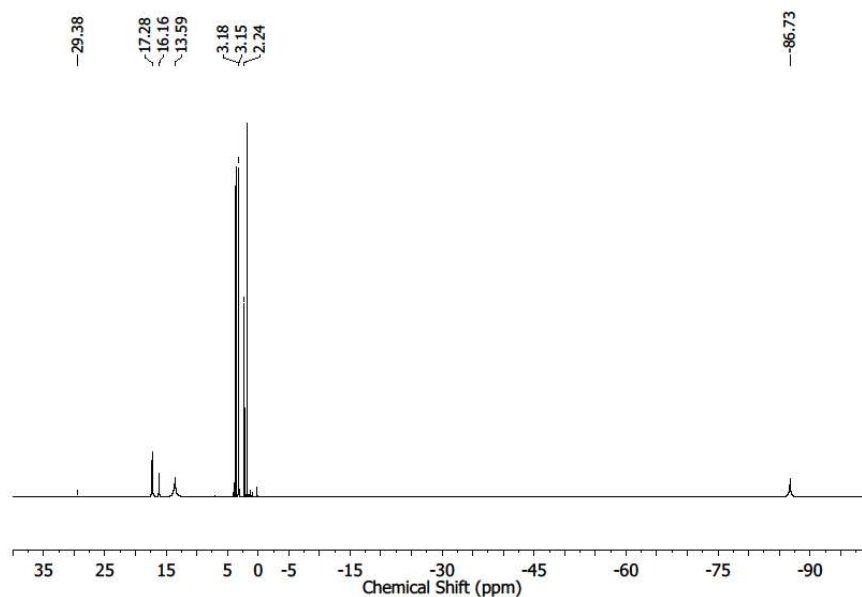


**Figure S1.** <sup>1</sup>H-NMR spectrum of K{crypt.222}[Co(NDippSiMe<sub>3</sub>)<sub>2</sub>] (K{crypt.222}[1]) (THF-d<sub>8</sub>, 298 K, 500 MHz).

## 2. Synthesis of $^{15}\text{N}_3\text{Dipp}$

The synthesis was done similar to the synthesis of 1-azido-2,6-di-iso-propylbenzene described by Spencer et. al.<sup>iii</sup> Attention, organic azides are potentially explosive in larger quantities.

0.1 mL 2,6-di-iso-propylaniline (0.1 g, 0.5 mmol, 1 equiv.) were added to 0.45 mL conc. HCl at -25 °C resulting in a colourless slurry. A solution of 0.1 g  $\text{NaBF}_4$  (0.9 mmol, 1.9 equiv.) in 0.5 mL  $\text{H}_2\text{O}$  was added dropwise, followed by a solution of 40 mg  $\text{NaNO}_2$  (0.6 mmol, 1.1 equiv.) in 0.5 mL  $\text{H}_2\text{O}$ . After stirring for 30 min at -30°C the solvent was filtered of and the residue was washed three times ice cooled  $\text{H}_2\text{O}$ . The obtained yellow solid was added to a solution of 100 mg  $\text{Na}^{15}\text{N}_3$  (1.5 mmol, 3 equiv.) in 3 mL ice cooled  $\text{H}_2\text{O}$  resulting in a concomitant gas evolution. After stirring for 1 h at RT the formation of a yellow oily phase was observed. 5 mL *n*-pentane were added. The organic phase was separated and the aqueous phase was extracted with 2 x 10 mL pentane. The combined organic layers were concentrated under reduced pressure at 0 °C yielding a yellow oil. Purification via column chromatography (*n*-pentane) yielding 56 mg (0.3 mmol, 48%) of the product as pale yellow oil.

$^1\text{H-NMR}$  ( $\text{CDCl}_3\text{-d}_1$ , 298 K, ppm, 250 MHz): 7.22-7.12 (m, 3H,  $\text{CH}_{\text{arom.}}$ ), 3.36 (sep,  $J = 6.8$  Hz, 2H,  $\text{CH}(\text{CH}_3)_2$ ), 1.27 (d,  $J = 6.8$  Hz, 12 H,  $\text{CH}(\text{CH}_3)_2$ ) ppm.

**IR** (ATR,  $\text{cm}^{-1}$ ) v: 3068 (w), 2961 (s), 2870 (m), 2086 (s), 1619 (m), 1588 (w), 1459 (s), 1437 (s), 1384 (w), 1363 (w), 1333 (w), 1289 (w), 1263 (m), 1234 (w), 1200 (w), 1170 (w), 1146 (w), 1106 (w), 1058 (w), 1044 (w), 933 (w), 884 (w), 823 (w), 790 (m), 744 (s), 695 (w), 621 (w), 578 (m).

## 3. Synthesis of $\text{N}_3\text{Tripp}$

The synthesis was done similar to the synthesis of mesitylazide described by Smith et. al.<sup>v</sup> Attention, organic azides are potentially explosive in larger quantities.

2.7 mL 1-bromo-2,4,6-tri-iso-propylbenzene (3 g, 10 mmol, 2 equiv.) were dissolved in 20 ml THF and added dropwise to 257 mg magnesium flakes (10 mmol, 2 equiv.). The reaction mixture was heated to reflux for 5 h. The resulting GRIGNARD-reagent was added to a solution of 1.04 g tosylazide (5 mmol, 1 equiv.) in 10 ml  $\text{Et}_2\text{O}$  at 0 °C. The precipitated solid was filtered of, washed with 2 x 10 mL  $\text{Et}_2\text{O}$  and 10 mL pentane. After addition of 10 mL  $\text{Et}_2\text{O}$  a solution of 1.40 g  $\text{Na}_4\text{P}_2\text{O}_7$  (5 mmol, 1 equiv.) in 15 mL water was added dropwise at 0 °C. The reaction mixture warmed to r.t. and stirred for 18 h. The organic phase was separated and the aqueous phase was extracted with 2 x 10 mL pentane. The combined organic layers were concentrated under reduced pressure yielding an orange oil. Purification via column chromatography (*n*-pentane) yielding 1.34 g (5.5 mmol, 55%) of the product as pale yellow oil.

$^1\text{H-NMR}$  ( $\text{CDCl}_3\text{-d}_1$ , 298 K, ppm, 250 MHz): 7.00 (s, 2H), 3.36 (sep, 2H), 2.89 (sep, 1H), 1.30-1.24 (m, 18 H) ppm.

**IR** (ATR,  $\text{cm}^{-1}$ ) v: 2961 (s), 2930 (m), 2870 (m), 2115 (vs), 1601 (w), 1461 (s), 1383 (w), 1362 (w), 1320 (w), 1304 (m), 1259 (w), 1244 (w), 1189 (w), 1164 (w), 1104 (w), 1072 (w), 1016 (w), 942 (w), 922 (w), 867 (m), 792 (w), 739 (w), 714 (w), 652 (w), 584 (w), 544 (w), 460 (w), 419 (w).

#### 4. Synthesis of K{18c6}[Co(NDippSiMe<sub>3</sub>)<sub>2</sub>NDipp] (K{18c6}{2})

84.6 mg (0.1 mmol, 1 equiv.) K{18c6}[Co(NDippSiMe<sub>3</sub>)<sub>2</sub>] K{18c6}{1} were dissolved in 2 mL Et<sub>2</sub>O and 1 mL THF. Addition of 20 mg (0.1 mmol, 1 equiv.) N<sub>3</sub>Dipp at -30 °C resulted in an immediate colour change from green to brown under concomitant gas evolution. After stirring the mixture for 5 min, the mixture was layered with 3 mL n-pentane and stored at -35 °C. After one day, the solution was removed via pipette and the remaining dark yellow plate crystals were rinsed with 2x3 mL pentane. Drying *in vacuo* yielded 91 mg (0.09 mmol, 89%) K{18c6}{2}.

<sup>1</sup>H-NMR (THF-d<sub>8</sub>, 298 K, ppm, 300 MHz): 98.3 (s, *w*<sub>1/2</sub> = 8772 Hz), 68.3 (s, *w*<sub>1/2</sub> = 1341 Hz), 47.1 (s, *w*<sub>1/2</sub> = 763.1 Hz), 33.4 (s, *w*<sub>1/2</sub> = 613.3 Hz), 29.5 (s, *w*<sub>1/2</sub> = 323.2 Hz), 9.96 (s, *w*<sub>1/2</sub> = 381.5 Hz), 3.68 (s, *w*<sub>1/2</sub> = 21.6 Hz, 18c6), -12.6 (s, *w*<sub>1/2</sub> = 337.6 Hz), -17.3 (s, *w*<sub>1/2</sub> = 465.4 Hz), -33.6 (s, *w*<sub>1/2</sub> = 65.9 Hz), -70.0 (s, *w*<sub>1/2</sub> = 4355 Hz) ppm.

IR (ATR, cm<sup>-1</sup>) ν: 3056 (m), 2951 (m), 2898 (m), 2861 (m), 1585 (w), 1419 (s), 1235 (m), 1101 (vs), 961 (m), 932 (m), 833 (s), 781 (m), 742 (m), 668 (w), 540 (w), 436 (w).

Elemental analysis: calcd. (%) for C<sub>54</sub>H<sub>93</sub>CoKN<sub>3</sub>O<sub>6</sub>Si<sub>2</sub> (1034.55 g mol<sup>-1</sup>): C 62.69 H 9.06 N 4.06; found: C 62.22 H 9.069 N 4.06.

EVANS-Method: μ<sub>eff</sub> = 4.90 μ<sub>B</sub> ([D8]THF+ 1% Si(CH<sub>3</sub>)<sub>4</sub>, 500 MHz, 298 K, μ<sub>s.o.</sub> = 4.89 μ<sub>B</sub>).

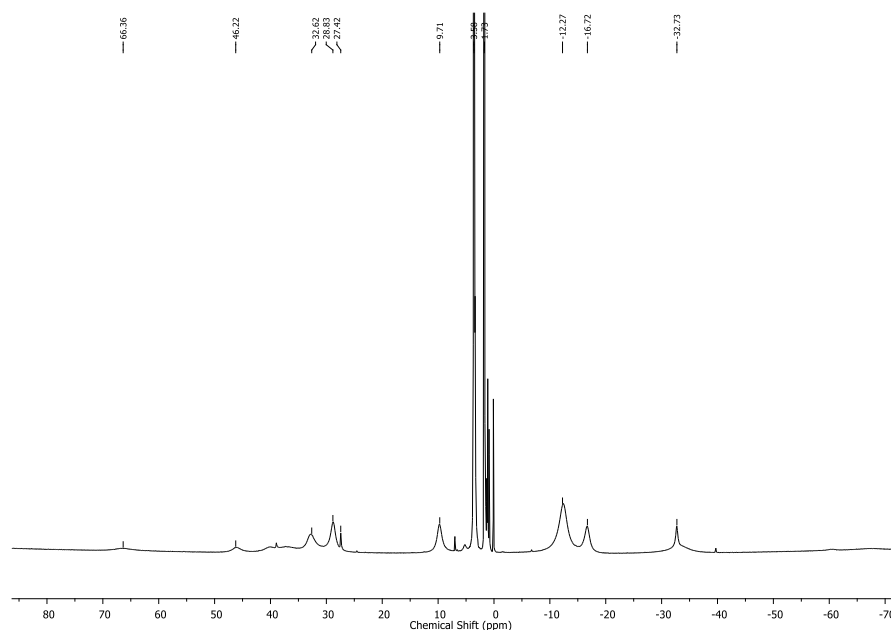
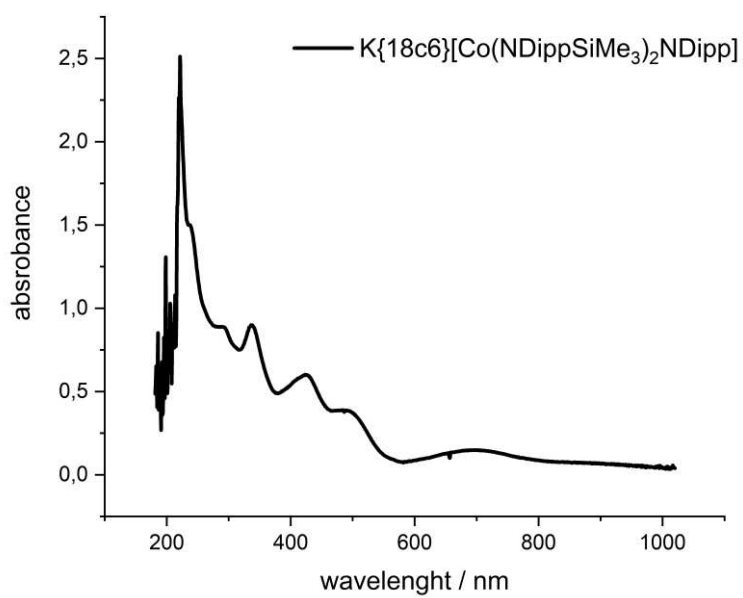


Figure S2. <sup>1</sup>H NMR spectrum of K{18c6}[Co(NDippSiMe<sub>3</sub>)<sub>2</sub>NDipp] (K{18c6}{2}) in (THF-d<sub>8</sub>, 298 K, 300 MHz).



**Figure S3.** UV-VIS spectrum of  $\text{K}\{18\text{c}6\}[\text{Co}(\text{NDippSiMe}_3)_2\text{NDipp}]$  ( $\text{K}\{18\text{c}6\}[\mathbf{2}]$ ) in THF.



## 5. Synthesis of $\text{K}\{18\text{c}6\}[\text{Co}(\text{NDippSiMe}_3)_2^{15}\text{NDipp}]$ ( $\text{K}\{18\text{c}6\}[\text{}^{15}\text{N-2}]$ )

41.6 mg (0.1 mmol, 1 equiv.)  $\text{K}\{18\text{c}6\}[\text{Co}(\text{NDippSiMe}_3)_2]$  ( $\text{K}\{18\text{c}6\}[\text{1}]$ ) were dissolved in 2 mL  $\text{Et}_2\text{O}$  and 1 mL THF. Addition of 10 mg (0.1 mmol, 1 equiv.)  $^{15}\text{N}_3\text{Dipp}$  at  $-30\text{ }^\circ\text{C}$  resulted in an immediate colour change from green to dark brown under concomitant gas evolution. After stirring the mixture for 5 min, the mixture was layered with 3 mL n-pentane and stored at  $-35\text{ }^\circ\text{C}$ . After one day, the solution was removed via pipette and the remaining dark red plate crystals were rinsed with 2x3 mL pentane. Drying *in vacuo* yielded 36 mg (0.04 mmol, 72%)  $\text{K}\{18\text{c}6\}[\text{}^{15}\text{N-2}]$ .

IR (ATR,  $\text{cm}^{-1}$ )  $\nu$ : 2952 (m), 2891 (m), 2858 (m), 1584 (w), 1455 (m), 1421 (m), 1392 (vs), 1376 (m), 1351 (m), 1313 (m), 1284 (m), 1235 (m), 1190 (s), 1103 (vs), 1054 (m), 960 (m), 903 (m), 880 (s), 831, 780 (m), 744 (m), 666 (w), 619 (w), 572 (w), 540 (w), 495 (w), 436 (w).

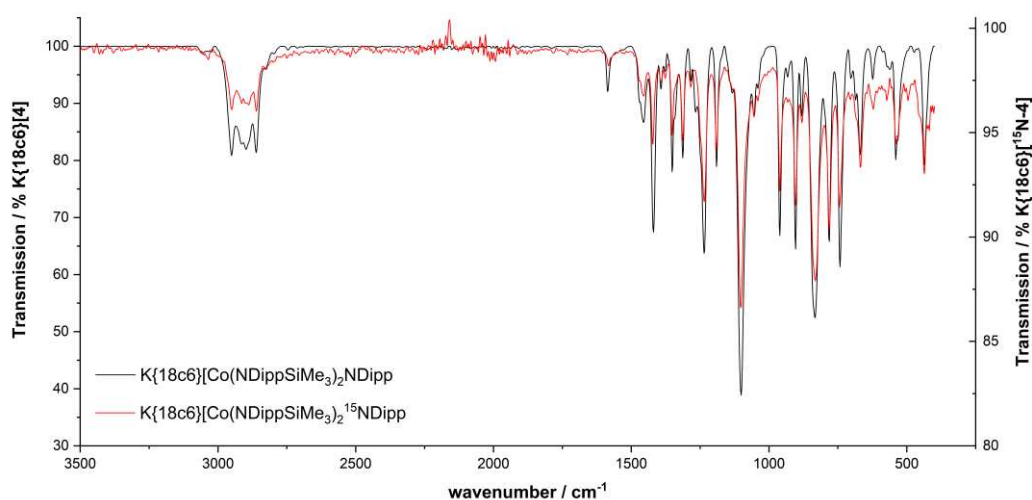


**Figure S4.** IR-spectra of  $\text{K}\{18\text{c}6\}[\text{Co}(\text{NDippSiMe}_3)_2\text{NDipp}]$  ( $\text{K}\{18\text{c}6\}[\text{2}]$ ) (black) and  $\text{K}\{18\text{c}6\}[\text{Co}(\text{NDippSiMe}_3)_2^{15}\text{NDipp}]$  ( $\text{K}\{18\text{c}6\}[\text{}^{15}\text{N-2}]$ ) (red) in solid state at 293 K.

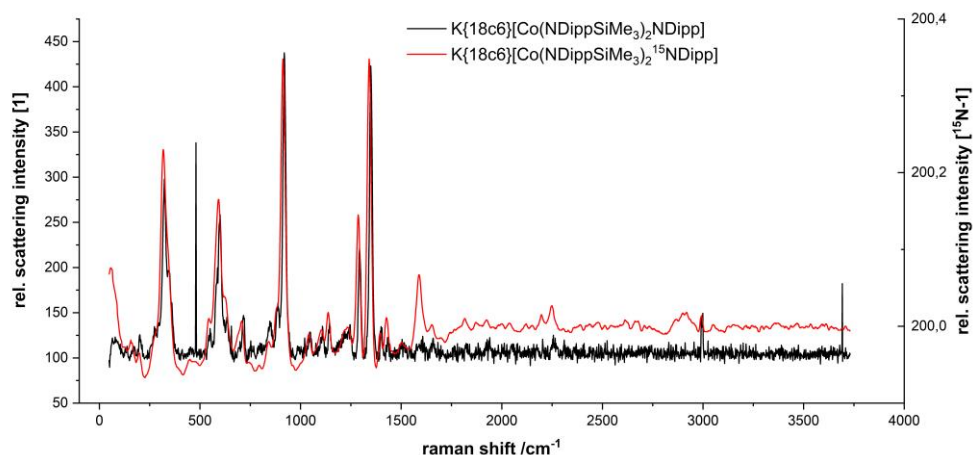


**Figure S5.** RAMAN-spectra of  $\text{K}\{18\text{c}6\}[\text{Co}(\text{NDippSiMe}_3)_2\text{NDipp}]$  ( $\text{K}\{18\text{c}6\}[\text{2}]$ ) (black) and  $\text{K}\{18\text{c}6\}[\text{Co}(\text{NDippSiMe}_3)_2^{15}\text{NDipp}]$  ( $\text{K}\{18\text{c}6\}[\text{}^{15}\text{N-2}]$ ) (red) in solid state at 293 K (532 nm excitation).

## 6. Synthesis of $K\{2.2.2\}[Co(NDippSiMe_3)_2NDipp]$ ( $K\{crypt.222\}[2]$ )

The synthesis of  $K\{crypt.222\}[2]$  was done equivalent to  $K\{18c6\}[2]$  starting from  $[K\{2.2.2\}][Co(NDippSiMe_3)_2]$  ( $K\{crypt.222\}[1]$ ): Yield: 60 mg (0.05 mmol, 74%)  $K\{crypt.222\}[2]$ .

$^1H$ -NMR (THF- $d_8$ , 298 K, ppm, 500 MHz): 98.3 (s,  $w_{1/2}$  = 8772 Hz), 67.0 (s,  $w_{1/2}$  = 1262 Hz), 46.1 (s,  $w_{1/2}$  = 756.1 Hz), 39.9 (s,  $w_{1/2}$  = 1047.6 Hz), 37.3 (s,  $w_{1/2}$  = 1863.1 Hz), 32.9 (s,  $w_{1/2}$  = 803.8 Hz), 28.9 (s,  $w_{1/2}$  = 467.9 Hz), 9.84 (s,  $w_{1/2}$  = 418.2 Hz), 3.68 (s,  $w_{1/2}$  = 21.6 Hz, 18c6), 3.62k (s,  $w_{1/2}$  = 21.6 Hz, 18c6), 2.62 (s,  $w_{1/2}$  = 21.6 Hz, 18c6) -12.4 (s,  $w_{1/2}$  = 803.5 Hz), -16.6 (s,  $w_{1/2}$  = 526.2 Hz), -32.7 (s,  $w_{1/2}$  = 215.5 Hz), -67.6 (s,  $w_{1/2}$  = 2048.4 Hz) ppm.

IR (ATR,  $cm^{-1}$ )  $\nu$ : 2950 (w), 2882 (w), 2860 (w), 1584 (w), 1458 (w), 1421 (m), 1354 (m), 1312 (m), 1296 (w), 1234 (s), 1189 (m), 1131 (w), 1099 (s), 948 (m), 930 (m), 904 (s), 881 (w), 837 (s), 777 (s), 740 (s), 669 (w), 622 (w), 571 (w), 539 (w), 435 (m).

Elemental analysis: calcd. (%) for  $C_{60}H_{105}CoKN_5O_6Si_2$  (1146.73 g mol $^{-1}$ ): C 62.84 H 9.23 N 6.11; found: C 62.69 H 9.154 N 5.96.

EVANS-Method:  $\mu_{eff}$  = 4.51  $\mu_B$  ([D8]THF+1 % TMS, 250 MHz, 298 K,  $\mu_{s.o.}$  = 3.78  $\mu_B$ ).

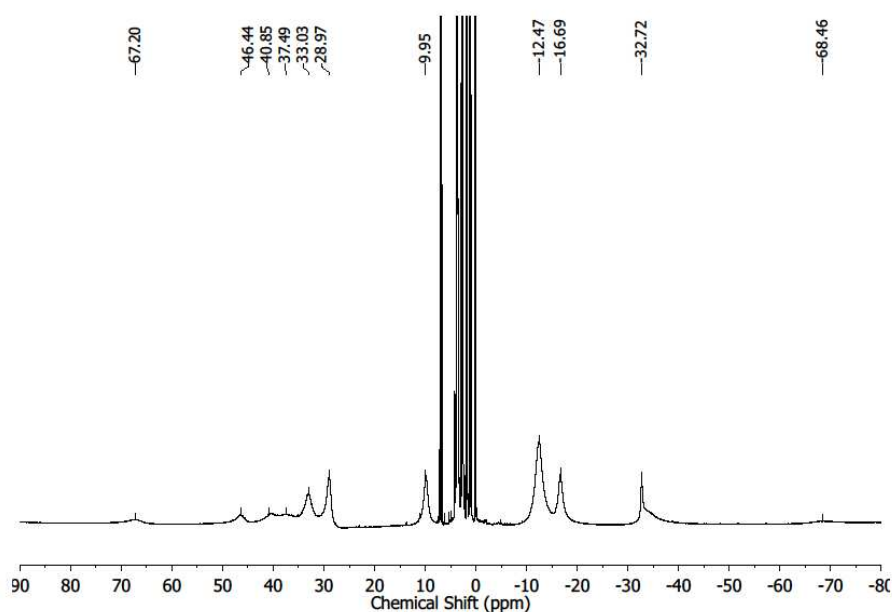


**Figure S6.**  $^1H$  NMR spectrum of  $K\{2.2.2\}[Co(NDippSiMe_3)_2NDipp]$  ( $K\{crypt.222\}[4]$ ) (THF- $d_8$ , 298 K, 300 MHz).

## 7. Synthesis of K[Co(NDippSiMe<sub>3</sub>)<sub>2</sub>NDipp] (K[2])

67.5 mg (0.1 mmol, 1 equiv.) K[Co(NDippSiMe<sub>3</sub>)<sub>2</sub>] K[1] were dissolved in 2 mL Et<sub>2</sub>O. Addition of 20 mg (0.1 mmol, 1 equiv.) N<sub>3</sub>Dipp at -30 °C resulted in an immediate colour change from yellowish green to dark red under concomitant gas evolution. After stirring the mixture for 5 min, the mixture was layered with 3 mL n-pentane and stored at -35 °C. After one day, the solution was removed via pipette and the remaining dark red plate crystals were rinsed with 2x3mL pentane. Drying *in vacuo* yielded 27.3 mg (0.04 mmol, 40 %) K[2].

<sup>1</sup>H-NMR (THF-d<sub>8</sub>, 298 K, ppm, 250 MHz): 95.1 (s), 67.1 (s,  $w_{1/2}$  = 404.7 Hz), 46.7 (s,  $w_{1/2}$  = 610.1 Hz), 33.2 (s,  $w_{1/2}$  = 699.4 Hz), 29.3 (s,  $w_{1/2}$  = 412.1 Hz), 9.54 (s,  $w_{1/2}$  = 524.9 Hz), -12.3 (s,  $w_{1/2}$  = 458.2 Hz), -16.8 (s,  $w_{1/2}$  = 415.6 Hz), -33.2 (s,  $w_{1/2}$  = 88.4 Hz), -67.8 (s) ppm.

IR (ATR, cm<sup>-1</sup>) v: 2951 (m), 2862 (m), 1577 (w), 1566 (w), 1459 (w), 1420 (m), 1393 (m), 1353 (m), 1311 (m), 1234 (s), 1187 (s), 1135 (w), 1101 (m), 1053 (w), 899 (m), 878 (m), 828 (vs), 783 (s), 748 (s), 669 (m), 624 (w), 542 (m), 434 (m).

**Elemental analysis:** calcd. (%) for C<sub>42</sub>H<sub>69</sub>CoKN<sub>3</sub>Si<sub>2</sub> (770.24 g mol<sup>-1</sup>): C 65.49 H 9.03 N 5.46; found: C 65.20 H 8.861 N 5.93.

**EVANS-Method:**  $\mu_{\text{eff}}$  = 4.26  $\mu_{\text{B}}$  ([D8]THF+ 1% Si(CH<sub>3</sub>)<sub>4</sub>, 500 MHz, 298 K,  $\mu_{\text{s.o.}}$  = 3.87  $\mu_{\text{B}}$ ).

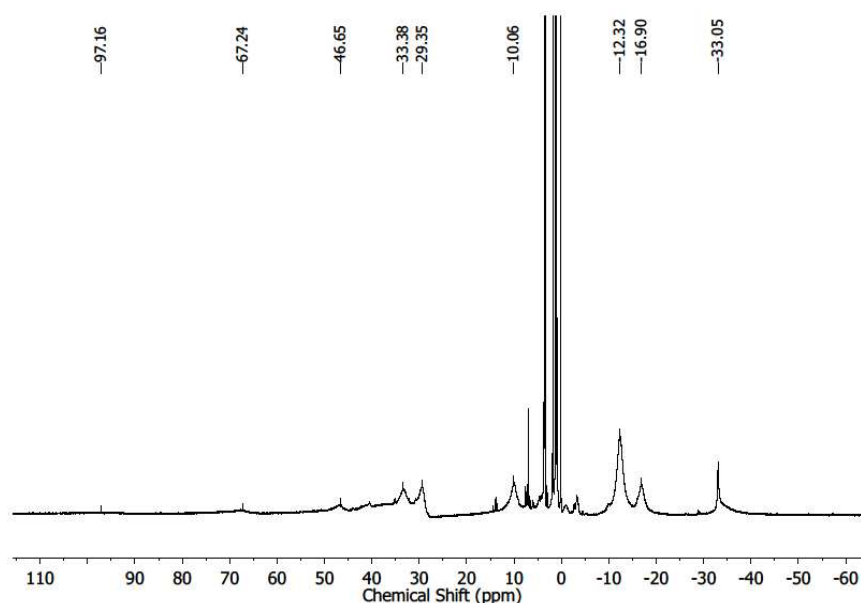


**Figure S7.** <sup>1</sup>H-NMR spectrum of K[Co(NDippSiMe<sub>3</sub>)<sub>2</sub>NDipp] (K[2]) (THF-d<sub>8</sub>, 298 K, 300 MHz).

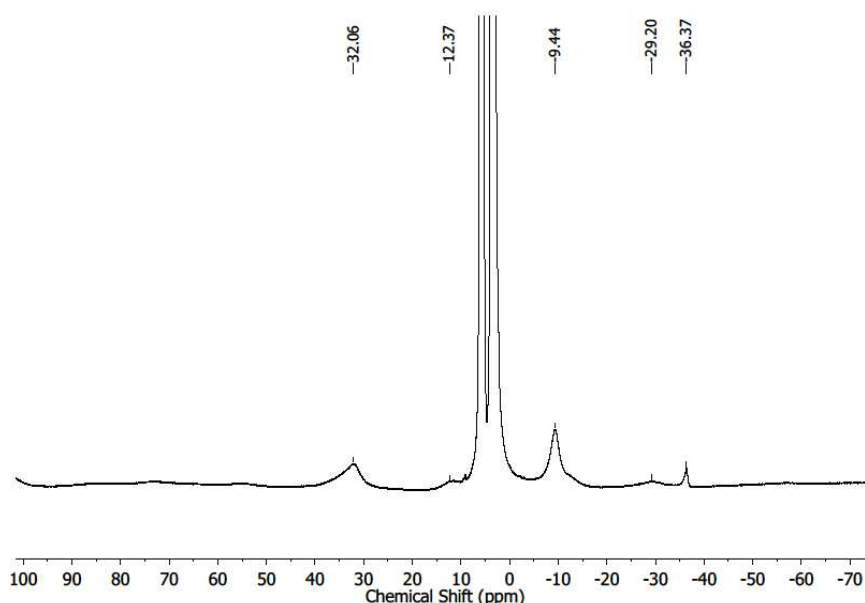


**Figure S8.**  $^1\text{H}$ -NMR spectrum of  $\text{K}[\text{Co}(\text{NDippSiMe}_3)_2\text{NDipp}]$  (**K[2]**) ( $\text{Et}_2\text{O}$ , 298 K, 500 MHz).

## 8. Synthesis of $\text{K}\{18\text{c}6\}[\text{Co}(\text{NDippSiMe}_3)_2\text{NTripp}]$ (**K{18c6}{3}**)

140 mg (0.2 mmol, 1 equiv.)  $\text{K}\{18\text{c}6\}[\text{Co}(\text{NDippSiMe}_3)_2]$  **K{18c6}{1}** were dissolved in 2 mL  $\text{Et}_2\text{O}$  and 1 mL THF. Addition of 40 mg (0.2 mmol, 1 equiv.)  $\text{N}_3\text{Tripp}$  at  $-30\text{ }^\circ\text{C}$  resulted in an immediate colour change from green to brown under concomitant gas evolution. After stirring the mixture for 5 min, the mixture was layered with 3 mL n-pentane and stored at  $-35\text{ }^\circ\text{C}$ . After one day, the solution was removed via pipette and the remaining dark brown needle crystals were rinsed with 2x3mL pentane. Drying *in vacuo* yielded 122 mg (0.1 mmol, 70%) **K{18c6}{3}**.

$^1\text{H}$ -NMR (THF- $d_8$ , 298 K, ppm, 250 MHz): 67.3 (s,  $w_{1/2} = 13409$  Hz), 47.0 (s,  $w_{1/2} = 4375$  Hz), 37.3 (s,  $w_{1/2} = 3545$  Hz), 33.1 (s,  $w_{1/2} = 408$  Hz), 28.8 (s,  $w_{1/2} = 281$  Hz), 25.1 (s,  $w_{1/2} = 37$  Hz), 9.80 (s,  $w_{1/2} = 300$  Hz), 3.38 (s,  $w_{1/2} = 6.7$  Hz, 18c6),  $-12.6$  (s,  $w_{1/2} = 809$  Hz),  $-33.1$  (s,  $w_{1/2} = 131$  Hz),  $-33.7$  (s,  $w_{1/2} = 3582$  Hz),  $-67.0$  (s,  $w_{1/2} = 8381$  Hz) ppm.

IR (ATR,  $\text{cm}^{-1}$ ) v: 2950 (m), 2895 (m), 2860 (m), 1582 (w), 1455 (w), 1421 (m), 1351 (m), 1310 (m), 1235 (s), 1190 (m), 1100 (vs), 1052 (m), 960 (m), 903 (s), 831 (s), 776 (s), 742 (m), 666 (m), 542 (w), 528 (w), 436 (m).

**Elemental analysis:** calcd. (%) for  $\text{C}_{57}\text{H}_{99}\text{CoKN}_3\text{O}_6\text{Si}_2$  ( $1076.64\text{ g mol}^{-1}$ ): C 63.59 H 9.27 N 3.90; found: C 63.58 H 8.8045 N 3.95.

**EVANS-Method:**  $\mu_{\text{eff}} = 4.24\ \mu_{\text{B}}$  ([D8]THF+ 1%  $\text{Si}(\text{CH}_3)_4$ , 500 MHz, 298 K,  $\mu_{\text{s.o.}} = 4.89\ \mu_{\text{B}}$ ).

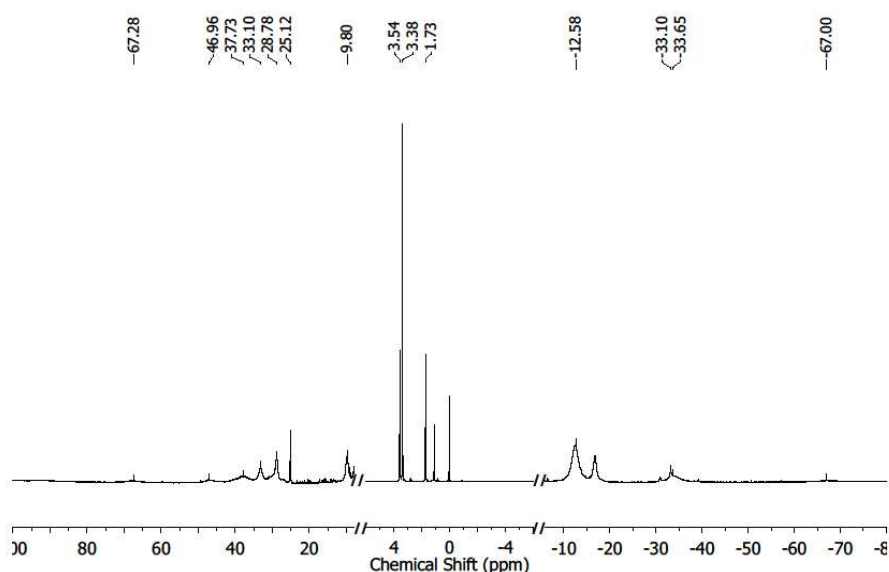


**Figure S9.**  $^1\text{H}$ -NMR spectrum of  $\text{K}\{18\text{c}6\}[\text{Co}(\text{NDippSiMe}_3)_2\text{NTripp}]$  ( $\text{K}\{18\text{c}6\}[\mathbf{3}]$ ) ( $\text{THF-d}_8$ , 298 K, 300 MHz).

## 9. Synthesis of $\text{K}[\text{Co}(\text{NDippSiMe}_3)_2\text{NTripp}] \times 0.5$ toluene ( $\mathbf{K}[\mathbf{3}]$ )

80 mg (0.12 mmol, 1 equiv.)  $\text{K}[\text{Co}(\text{NDippSiMe}_3)_2]$   $\mathbf{K}[\mathbf{1}]$  were dissolved in 2 mL toluene. Addition of 33 mg (0.13 mmol, 1.1 equiv.)  $\text{N}_3\text{Tripp}$  at  $-30^\circ\text{C}$  resulted in an immediate colour change from green to dark red under concomitant gas evolution. The mixture was filtered and stored at  $-35^\circ\text{C}$ . After one day, the solution was removed via pipette and the remaining dark red crystals were rinsed with 2x3mL pentane. Drying *in vacuo* yielded 95 mg (0.11 mmol, 95 %)  $\mathbf{K}[\mathbf{3}]$ .

$^1\text{H}$ -NMR ( $\text{THF-d}_8$ , 298 K, ppm, 250 MHz): 65.1 (s,  $w_{1/2} = 3883$  Hz), 44.4 (s,  $w_{1/2} = 4144$  Hz), 33.3 (s,  $w_{1/2} = 483$  Hz), 29.0 (s,  $w_{1/2} = 591$  Hz), 27.6 (s,  $w_{1/2} = 475$  Hz), 25.4 (s,  $w_{1/2} = 33.4$  Hz), 9.87 (s,  $w_{1/2} = 345$  Hz),  $-12.1$  (s,  $w_{1/2} = 433$  Hz),  $-16.9$  (s,  $w_{1/2} = 394$  Hz),  $-31.1$  (s,  $w_{1/2} = 79.0$  Hz),  $-33.4$  (s,  $w_{1/2} = 499$  Hz) ppm.

IR (ATR,  $\text{cm}^{-1}$ )  $\nu$ : 3051 (m), 2952 (m), 2924 (m), 2863 (m), 1585 (w), 1574 (w), 1459 (m), 1416 (m), 1379 (w), 1357 (w), 1308 (m), 1235 (m), 1189 (m), 1101 (m), 904 (s), 881 (m), 829 (vs), 780 (vs), 739 (m), 725 (m), 673 (m), 663 (m), 540 (m), 529 (m), 462 (w), 433 (m).

**Elemental analysis:** calcd. (%) for  $\text{C}_{97}\text{H}_{158}\text{Co}_2\text{K}_2\text{N}_6\text{Si}_4$  (1716.78  $\text{g mol}^{-1}$ ): C 67.86 H 9.28 N 4.90; found: C 67.73 H 8.778 N 4.87.

**EVANS-Method:**  $\mu_{\text{eff}} = 4.36 \mu_{\text{B}}$  ( $[\text{D}8]\text{THF} + 1\% \text{Si}(\text{CH}_3)_4$ , 500 MHz, 298 K,  $\mu_{\text{s.o.}} = 4.89 \mu_{\text{B}}$ ).

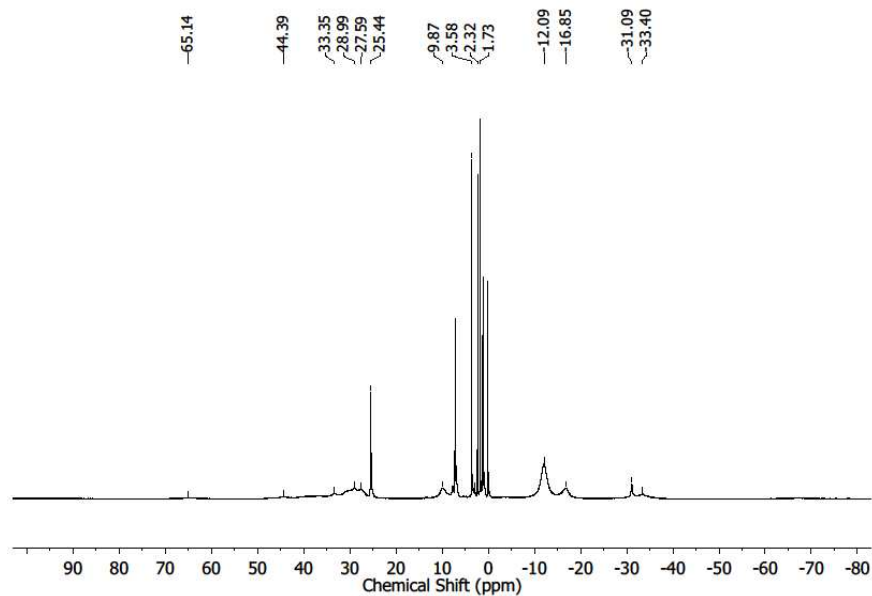


**Figure S10.**  $^1\text{H}$ -NMR spectrum of  $\text{K}[\text{Co}(\text{NDippSiMe}_3)_2\text{NTripp}]$  (**K[3]**) ( $\text{THF-d}_8$ , 298 K, 300 MHz).

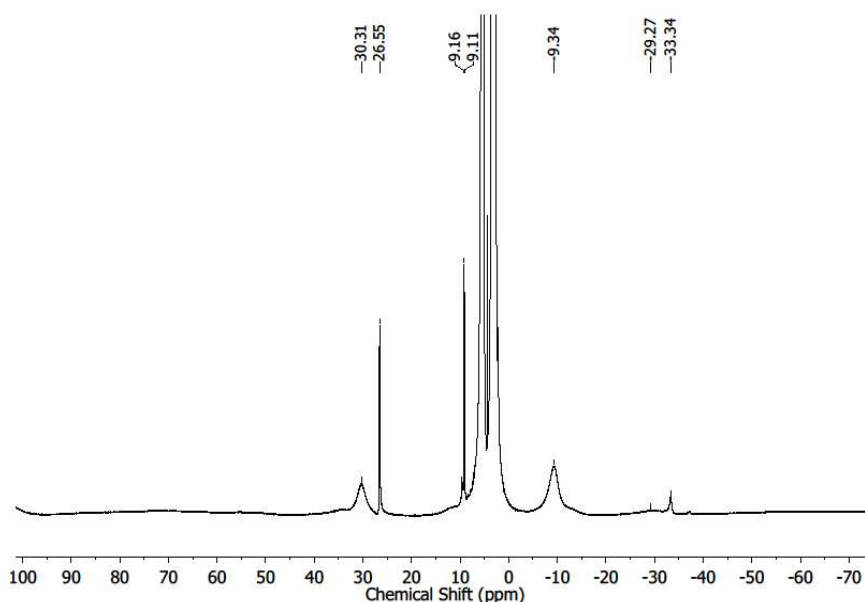


**Figure S11.**  $^1\text{H}$ -NMR spectrum of  $\text{K}[\text{Co}(\text{NDippSiMe}_3)_2\text{NTripp}]$  (**K[3]**) ( $\text{Et}_2\text{O}$ , 298 K, 500 MHz).

### 10. Synthesis of $\text{K}\{\mathbf{18c6}\}[\text{Co}(\text{NDippSiMe}_3)_2\text{NHDipp}]$ ( $\text{K}\{\mathbf{18c6}\}\{\mathbf{4}\}$ )

50 mg (0.09 mmol, 1 equiv.)  $\text{Co}(\text{NDippSiMe}_3)_2$  and 19.3 mg (0.09 mmol, 1equiv.) **18c6** were dissolved in 2 mL  $\text{Et}_2\text{O}$ . 23.7 mg (0.09 mmol, 1 equiv.) **KNHDipp** were added at  $-30^\circ\text{C}$  and the reaction mixture

warmed to RT. After 30 min, the solvent was removed *in vacuo* and the resulting orange powder were rinsed with 2x3mL pentane. Drying *in vacuo* yielded 61 mg (0.06 mmol, 65%) K{18c6}[4].

**<sup>1</sup>H-NMR** (THF-d<sub>8</sub>, 298 K, 500 MHz): 83.6 (s,  $w_{1/2}$  = 210.5 Hz), 28.2 (s,  $w_{1/2}$  = 359.5 Hz), 4.13 (s, 18c6,  $w_{1/2}$  = 11.5 Hz), 2.72 (s,  $w_{1/2}$  = 793.8 Hz), -2.55 (s,  $w_{1/2}$  = 2247 Hz), -8.71 (s,  $w_{1/2}$  = 1067 Hz), -26.0 (s,  $w_{1/2}$  = 151.4 Hz), -27.6 (s,  $w_{1/2}$  = 1274 Hz) -51.8 (s,  $w_{1/2}$  = 19.5 Hz) ppm.

**IR** (ATR, cm<sup>-1</sup>) v: 2956 (w), 2922 (w), 2863 (w), 1598(w), 1583 (w), 1463 (w), 1418 (m), 1340 (m), 1308 (m), 1273 (m), 1238 (w), 113 (w), 1098(s), 1037 (w), 910 (s), 878 (m), 840 (m), 783 (s), 738 (m), 678 (w), 626 (w), 561 (w), 535 (m), 436 (m).

*Attempts to crystallize K{18c6}[4] led to the formation of a mixture of orange (K{18c6}[4]) and green (K{18c6}[5]) crystals. Separation was not possible.*

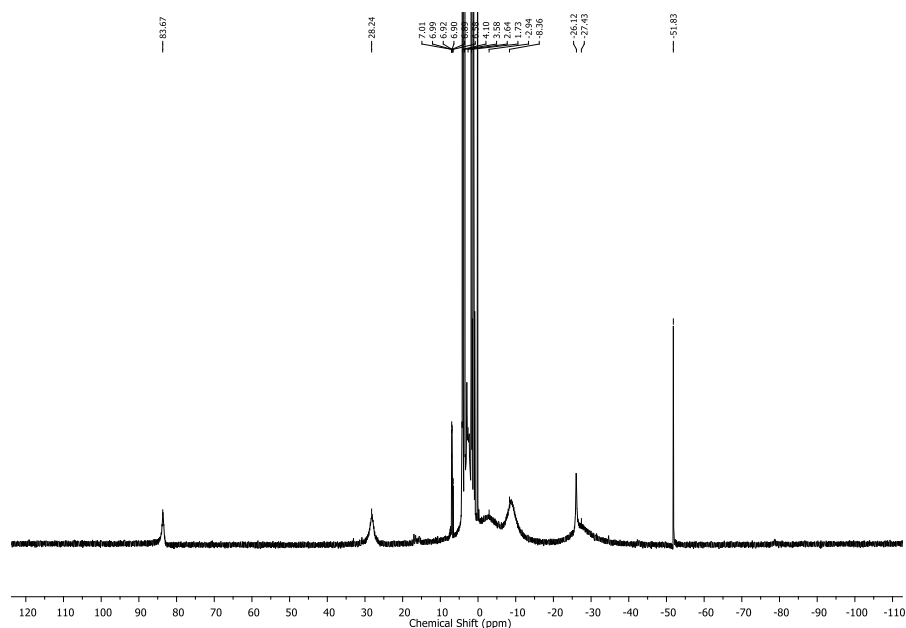


**Figure S12.** <sup>1</sup>H NMR spectrum of K{18c6}[Co(NDippSiMe<sub>3</sub>)<sub>2</sub>NHDipp] (K{18c6}[4]) (THF-d<sub>8</sub>, 298 K, 300 MHz).

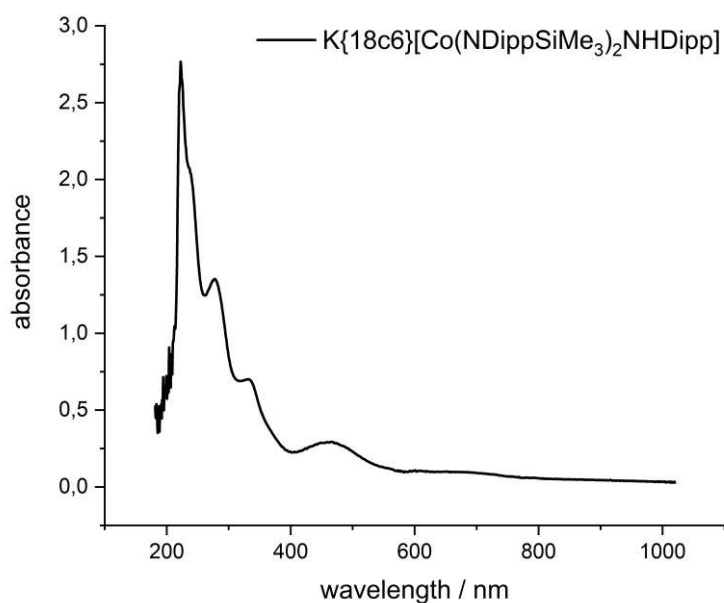


**Figure S13.** UV-VIS spectrum of  $\text{K}\{18\text{c}6\}[\text{Co}(\text{NDippSiMe}_3)_2\text{NHDipp}]$  ( $\text{K}\{18\text{c}6\}\{4\}$ ) in  $\text{Et}_2\text{O}$ .

### 11. Synthesis of $\text{K}\{2.2.2\}[\text{Co}(\text{NDippSiMe}_3)_2\text{NHDipp}]$ ( $\text{K}\{\text{crypt.222}\}\{4\}$ )

30 mg (0.05 mmol, 1 equiv.)  $\text{Co}(\text{NDippSiMe}_3)_2$  and 20.3 mg (0.05 mmol, 1equiv.) 2.2.2-cryptand were dissolved in 2 mL  $\text{Et}_2\text{O}$ . 11.6 mg (0.05 mmol, 1 equiv.)  $\text{KNHDipp}$  were added at  $-30^\circ\text{C}$  and the reaction mixture warmed to RT. After stirring the mixture for 30 min, the mixture was filtered and the filtrate was layered with 3 mL n-pentane and stored at  $-35^\circ\text{C}$ . After one day, the solution was removed via pipette and the remaining orange needle crystals were rinsed with 2x3mL pentane. Drying *in vacuo* yielded 36 mg (0.03 mmol, 58%)  $\text{K}\{\text{crypt.222}\}\{4\}$ .

$^1\text{H}$ -NMR (THF- $d_8$ , 298 K, 500 MHz): 83.6 (s,  $w_{1/2} = 281.3$  Hz), 28.2 (s,  $w_{1/2} = 555.9$  Hz), 27.6 (s,  $w_{1/2} = 64.6$  Hz), 4.32 (s, 2.2.2,  $w_{1/2} = 31.9$  Hz), 4.23 (s, 2.2.2,  $w_{1/2} = 33.8$  Hz), 3.20 (s, 2.2.2,  $w_{1/2} = 29.9$  Hz),  $-2.81$  (s,  $w_{1/2} = 905.0$  Hz),  $-8.71$  (s,  $w_{1/2} = 1498$  Hz),  $-26.0$  (s,  $w_{1/2} = 195.4$  Hz),  $-51.8$  (s,  $w_{1/2} = 23.5$  Hz) ppm.

IR (ATR,  $\text{cm}^{-1}$ )  $\nu$ : 2952 (w), 2884 (w), 2813 (w), 1584 (w), 1459 (w), 1445 (w), 1419 (m), 1354 (m), 1304 (m), 1232 (m), 1182 (w), 1133 (m), 1101 (s), 1037 (w), 947 (m), 907 (s), 832 (s), 778 (s), 731 (m), 662 (w), 557 (w), 525 (m), 436 (m).

**Elemental analysis:** calcd. (%) for  $\text{C}_{60}\text{H}_{106}\text{CoKN}_5\text{O}_6\text{Si}_2$  ( $1147.74$  g  $\text{mol}^{-1}$ ): C 62.79 H 9.31 N 6.10; found: C 62.32 H 9.162 N 6.01.

**EVANS-Method:**  $\mu_{\text{eff}} = 4.59$   $\mu_{\text{B}}$  ([D8]THF+1 % TMS, 250 MHz, 298 K,  $\mu_{\text{s.o.}} = 3.78$   $\mu_{\text{B}}$ ).



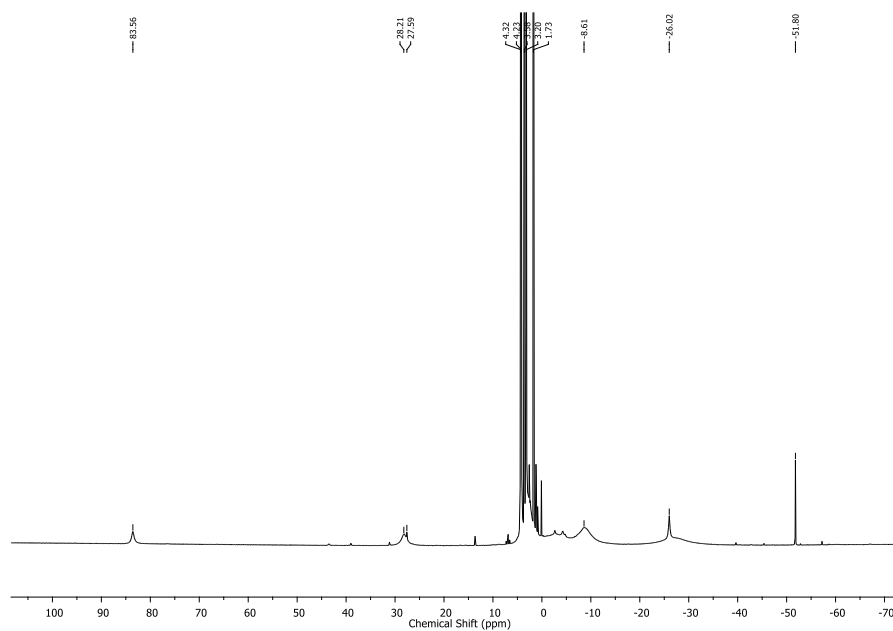


**Figure S14.**  $^1\text{H}$  NMR spectrum of  $\text{K}\{2.2.2\}[\text{Co}(\text{NDippSiMe}_3)_2\text{NHDipp}]$  ( $\text{K}\{\text{crypt.222}\}\{4\}$ ) ( $\text{THF-d}_8$ , 298 K, 300 MHz).

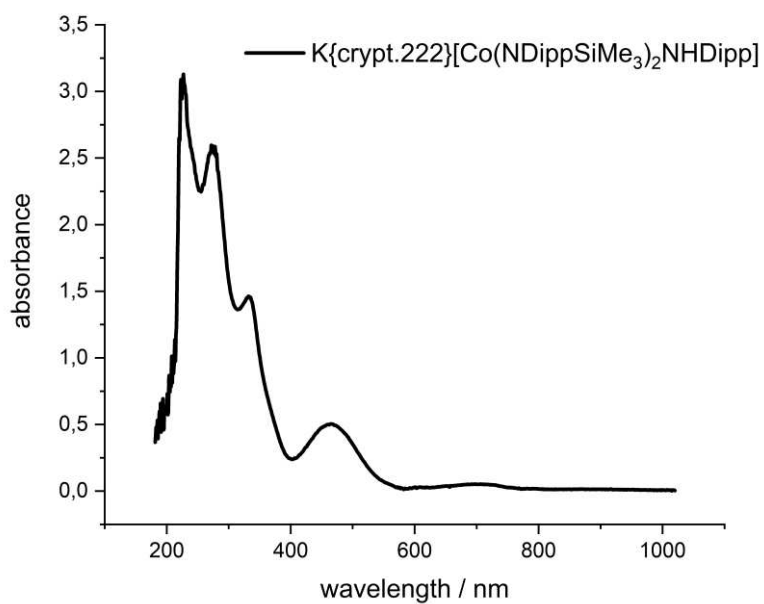


**Figure S15.** UV-VIS spectrum of  $[\text{K}\{2.2.2\}][\text{Co}(\text{NDippSiMe}_3)_2\text{NHDipp}]$  ( $\text{K}\{\text{crypt.222}\}\{4\}$ ) in  $\text{Et}_2\text{O}$ .

## 12. Synthesis of K[Co(NDippSiMe<sub>3</sub>)<sub>2</sub>NHDipp] (K[4])

55 mg Co(NDippSiMe<sub>3</sub>)<sub>2</sub> (0.1 mmol, 1 equiv.) were dissolved in 2 mL toluene and added to a suspension of 11.6 mg KNHDipp (0.09 mmol, 0.9 equiv.) in toluene. After stirring the mixture for 2 h a yellow solid precipitated. The solution was removed via pipette and the residue was washed with 3 x 2 mL *n*-pentane. Drying *in vacuo* yielded 35 mg (0.05 mmol, 50%) K[4] as pale yellow solid. Crystal suitable for X-ray analysis could be obtained by layering a saturated Et<sub>2</sub>O solution with *n*-pentane at -30 °C.

<sup>1</sup>H-NMR (THF-d<sub>8</sub>, 298 K, 500 MHz): 84.6 (s, *w*<sub>1/2</sub> = 121.3 Hz), 28.3 (s, *w*<sub>1/2</sub> = 219.5 Hz), -3.42 (s, *w*<sub>1/2</sub> = 704.5 Hz), -8.91 (s, *w*<sub>1/2</sub> = 616.6 Hz), -26.4 (s, *w*<sub>1/2</sub> = 98.3 Hz), -27.1 (s, *w*<sub>1/2</sub> = 1088 Hz), -52.3 (s, *w*<sub>1/2</sub> = 18.0 Hz) ppm.

IR (ATR, cm<sup>-1</sup>) *v*: 2972 (w), 2952 (w), 2920 (w), 2896 (w), 2865 (w), 2839 (w), 1579 (w), 1460 (w), 1380 (s), 1358 (w), 1343 (w), 1309 (m), 1275 (w), 1234 (s), 1220 (w), 1194 (w), 1183 (m), 1140 (w), 1103 (w), 1052 (w), 1038 (w), 9225 (w), 905 (s), 880 (m), 828 (vs), 780 (s), 750 (s), 724 (m), 691 (w), 660 (m), 623 (w), 569 (w), 556 (w), 531 (m), 478 (w), 461 (w), 432 (m).

**Elemental analysis:** calcd. (%) for C<sub>42</sub>H<sub>70</sub>CoKN<sub>3</sub>Si<sub>2</sub> (771.24 g mol<sup>-1</sup>): C 65.41 H 9.15 N 5.45; found: C 65.17 H 8.816 N 5.13.

**EVANS-Method:**  $\mu_{\text{eff}} = 4.26 \mu_{\text{B}}$  ([D8]THF+1 % TMS, 500 MHz, 298 K,  $\mu_{\text{s.o.}} = 3.78 \mu_{\text{B}}$ ).

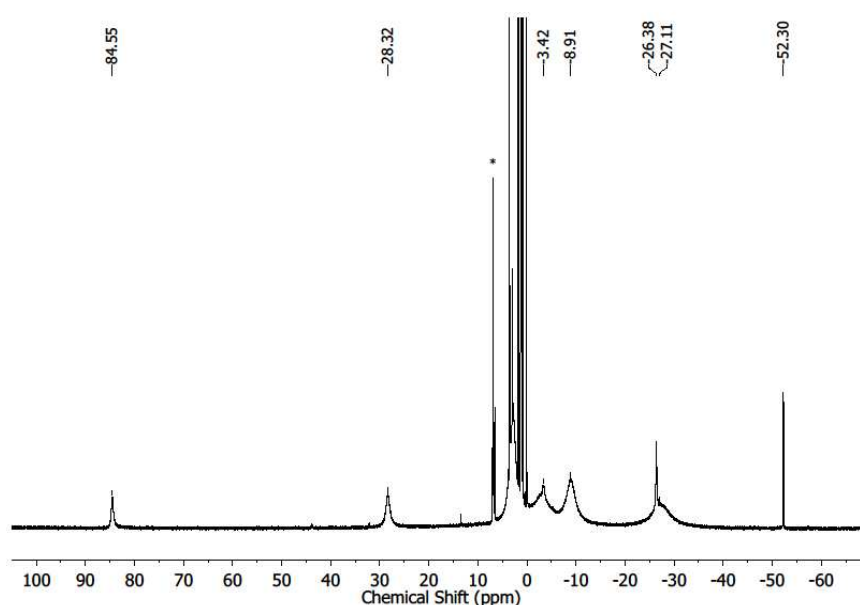


**Figure S16.** <sup>1</sup>H-NMR spectrum of K[Co(NDippSiMe<sub>3</sub>)<sub>2</sub>NHDipp] (K[4]) (THF-d<sub>8</sub>, 298 K, 300 MHz). Signals of decomposition products are marked with \*.

### 13. Synthesis of K{18c6}[Co(NHDipp)<sub>2</sub>NDippSiMe<sub>3</sub>] (K{18c6}[5])

52 mg Co(NDippSiMe<sub>3</sub>)<sub>2</sub> (0.09 mmol, 1 equiv.) and 49 mg 18c6 (0.19 mmol, 2 equiv.) were dissolved in 2 mL Et<sub>2</sub>O. The solution was added to a suspension of 40 mg KNHDipp (0.19 mmol, 2 equiv.) in 1 mL Et<sub>2</sub>O. Over the course of 3 h the precipitation of a green solid was observed, which was filtered off and washed with 3 x 3 mL precooled Et<sub>2</sub>O. For recrystallization the solid was dissolved in 2 mL THF and layered with 2 mL *n*-pentane. After one day at -30 °C, the solution was removed via pipette and the remaining green crystals were rinsed with 2x3mL pentane. Drying *in vacuo* yielded 13.7 mg (0.02mmol, 20%) K{18c6}[5].

<sup>1</sup>H-NMR (THF-d<sub>8</sub>, 298 K, 500 MHz): 66.6 (s, *w*<sub>1/2</sub> = 652 Hz), 43.5 (s, *w*<sub>1/2</sub> = 100 Hz), 40.4 (s, *w*<sub>1/2</sub> = 27.3 Hz), 31.3 (s, *w*<sub>1/2</sub> = 27.0 Hz), 13.7 (s, *w*<sub>1/2</sub> = 27.9 Hz), 5.46 (s, 18c6, *w*<sub>1/2</sub> = 25.5 Hz), -1.33 (s, *w*<sub>1/2</sub> = 69.9 Hz), -2.95 (s, *w*<sub>1/2</sub> = 107 Hz), -3.89 (s, *w*<sub>1/2</sub> = 191.3 Hz), -4.72 (s, *w*<sub>1/2</sub> = 125 Hz), -45.3 (s, *w*<sub>1/2</sub> = 24.8 Hz) -54.3 (s, *w*<sub>1/2</sub> = 22.5 Hz), -57.22 (s, *w*<sub>1/2</sub> = 24.6 Hz) ppm.

IR (ATR, cm<sup>-1</sup>) *v*: 2954 (m), 2863 (m), 1586 (w), 1453 (w), 1418 (s), 1379 (m), 1233 (m), 1187 (w), 1102 (vs), 1040 (w), 960 (m), 933 (m), 882 (s), 835 (m), 801 (m), 776 (w), 737 (m), 668 (w), 620 (w), 565 (w), 530 (m), 429 (m).

**Elemental analysis:** calcd. (%) for C<sub>51</sub>H<sub>86</sub>CoKN<sub>3</sub>O<sub>6</sub>Si (963.38 g mol<sup>-1</sup>): C 63.58 H 9.00 N 4.36; found: C 64.01 H 8.91 N 4.53.

**EVANS-Method:**  $\mu_{\text{eff}} = 4.28 \mu_{\text{B}}$  ([D8]THF+1 % TMS, 250 MHz, 298 K,  $\mu_{\text{s.o.}} = 3.78 \mu_{\text{B}}$ ).

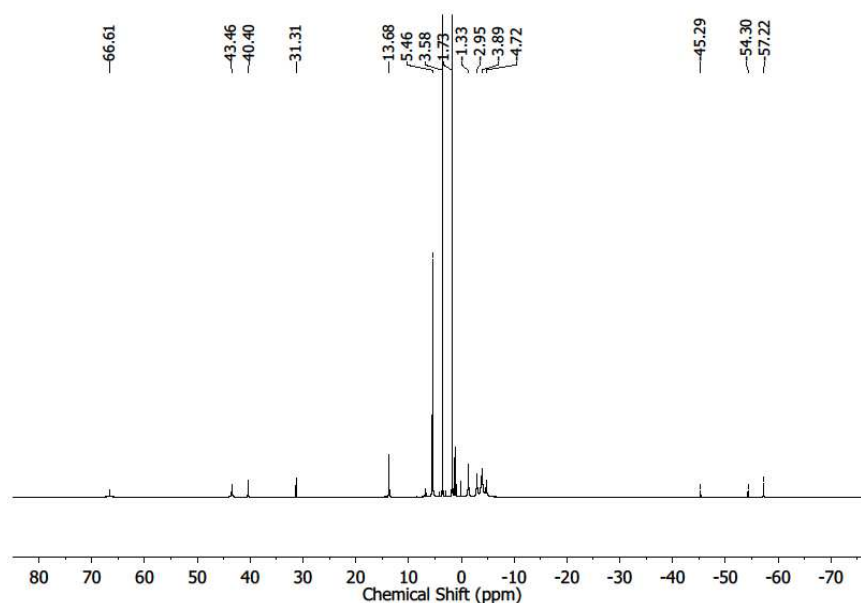


**Figure S17.** <sup>1</sup>H-NMR spectrum of K{crypt.222}[Co(NHDipp)<sub>2</sub>NDippSiMe<sub>3</sub>] (K{crypt.222}[5]) (THF-d<sub>8</sub>, 298 K, 500 MHz).

#### 14. Reaction of K{18c6}[Co(NDippSiMe<sub>3</sub>)<sub>2</sub>] (K{18c6}[1]) with mesitylazide

110 mg K{18c6}[Co(NDippSiMe<sub>3</sub>)<sub>2</sub>] K{18c6}[1] (0.13 mmol, 1 equiv.) were dissolved in 2 mL THF and 1 mL Et<sub>2</sub>O. Addition of 18.7 mg N<sub>3</sub>Mes (0.13 mmol, 1 equiv.) at -35 °C resulted in an immediate colour change from yellowish green to dark green under concomitant gas evolution. After stirring for 15 minutes, the solution was layered with 3 mL pentane and stored at -35 °C. A mixture of yellowish brown (K{18c6}[Co(NDippSiMe<sub>3</sub>)<sub>2</sub>NMes] K{18c6}[6]) and light blue crystals (K{18c6}[CoNHDipp(NDippSiMe<sub>3</sub>)-(μ-NMesSiMe<sub>3</sub>)] K{18c6}[7]) suitable for x-ray diffraction could be obtained.

<sup>1</sup>H-NMR (THF-d<sub>8</sub>, 298 K, ppm, 300 MHz): δ = 42.2 (s), 37.2 (s), 29.5 (s), 19.4 (s), 3.95 (s, 18c6), -2.19 (s), -3.26 (s), -10.6 (s), -15.8 (s), 35.0 (s) ppm.

**Elemental analysis:** calcd. (%) for C<sub>51</sub>H<sub>87</sub>CoKN<sub>3</sub>O<sub>6</sub>Si<sub>2</sub> (992.47 g mol<sup>-1</sup>): C 61.72 H 8.84 N 4.23; found: C 61.38 H 8.604 N 4.11.

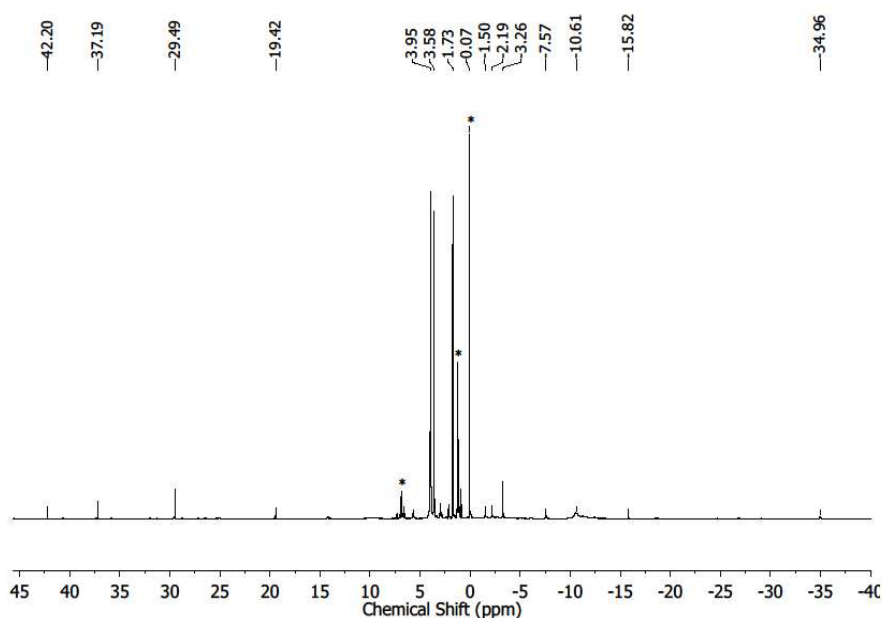


**Figure S18.** *in situ* <sup>1</sup>H-NMR spectrum of the reaction of K{18c6}[Co(NDippSiMe<sub>3</sub>)<sub>2</sub>] (K{18c6}[1]) with N<sub>3</sub>Mes (THF-d<sub>8</sub>, 298 K, 300 MHz). Signals of decomposition products are marked with \*.

## 15. Hydrogen atom transfer (HAT) reactivity

In a typical experiment 30 mg of the respective complex were dissolved in 0.5 mL THF- $d_8$  and added to 5 equiv. of the respective substrate in 0.1 mL THF- $d_8$ . Due to the observed exchange of amido ligands for the expected product ( $[7]^-$ ) the complexes with crypt.222 coordinated cation were used.

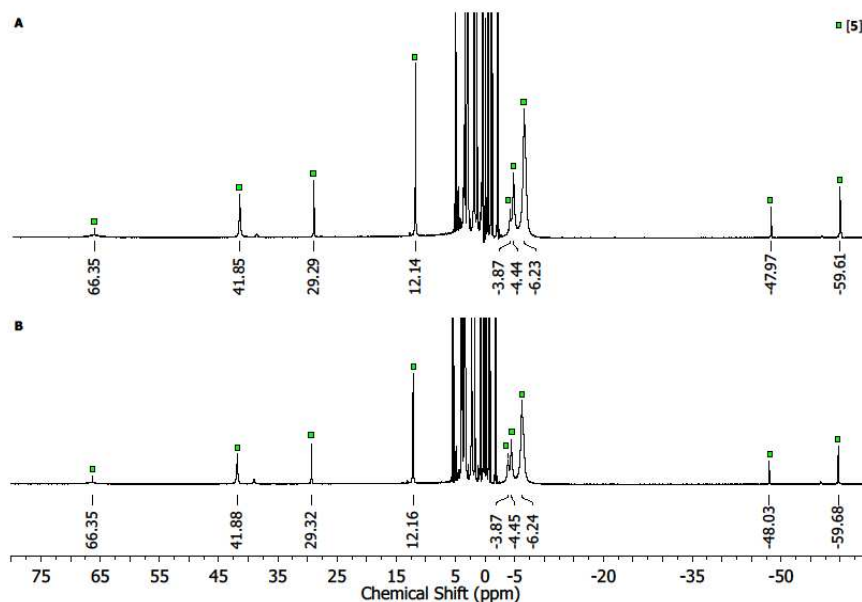


**Figure S19.** Reaction of  $\text{K}\{\text{crypt.222}\}[\text{Co}(\text{NDippSiMe}_3)_2\text{NDipp}]$  ( $\text{K}\{\text{crypt.222}\}[2]$ ) with 5 equiv. of 1,4-cyclohexadiene **A:**  $t = 1$  h; **B:**  $t = 24$  h (THF- $d_8$ , 298 K, 300 MHz).

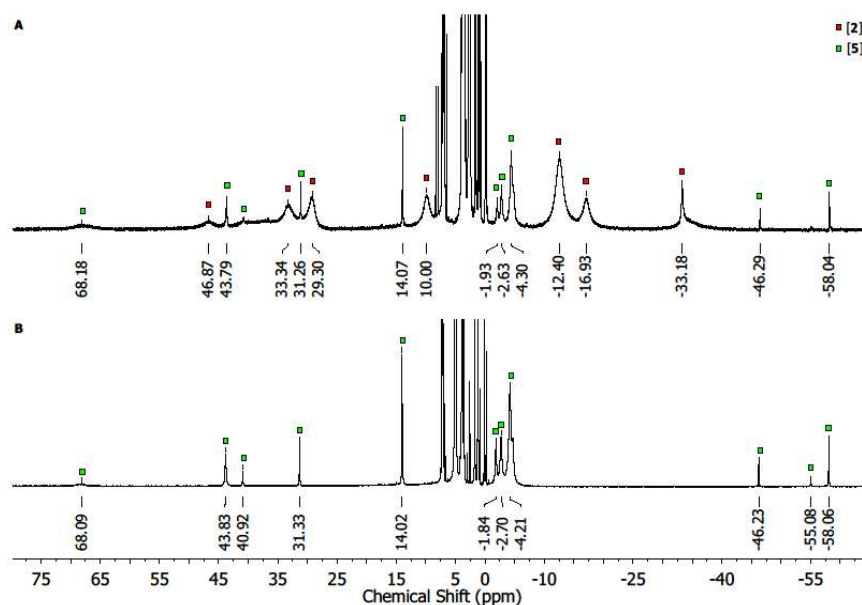


**Figure S20.** Reaction of  $\text{K}\{\text{crypt.222}\}[\text{Co}(\text{NDippSiMe}_3)_2\text{NDipp}]$  ( $\text{K}\{\text{crypt.222}\}[2]$ ) with 5 equiv. of 9,10-dihydroanthracene. **A:**  $t = 1$  h; **B:**  $t = 24$  h (THF- $d_8$ , 298 K, 300 MHz).

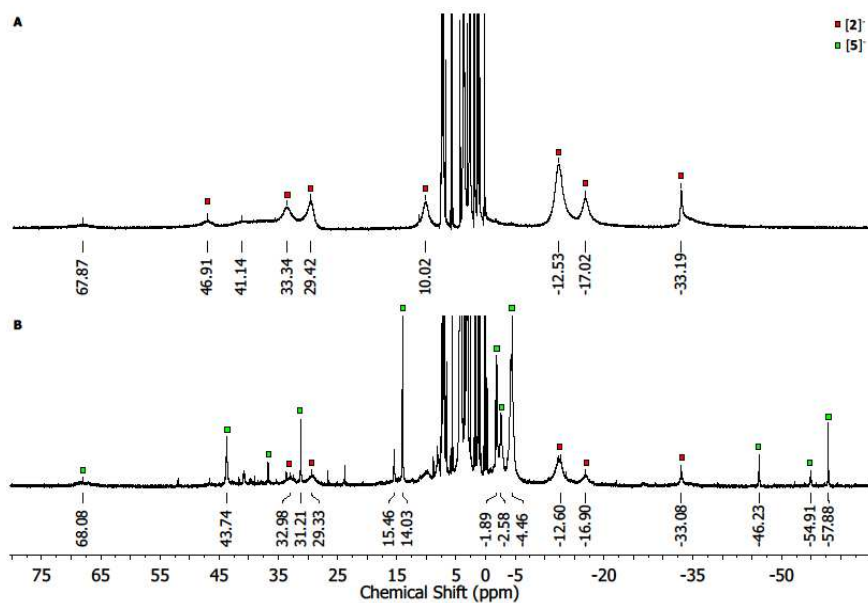


**Figure S21.** Reaction of  $K\{\text{crypt.222}\}[\text{Co}(\text{NDippSiMe}_3)_2\text{NDipp}]$  ( $K\{\text{crypt.222}\}[2]$ ) with 5 equiv. of triphenylmethane. **A:**  $t = 1$  h; **B:**  $t = 48$  h (THF- $d_8$ , 298 K, 300 MHz).

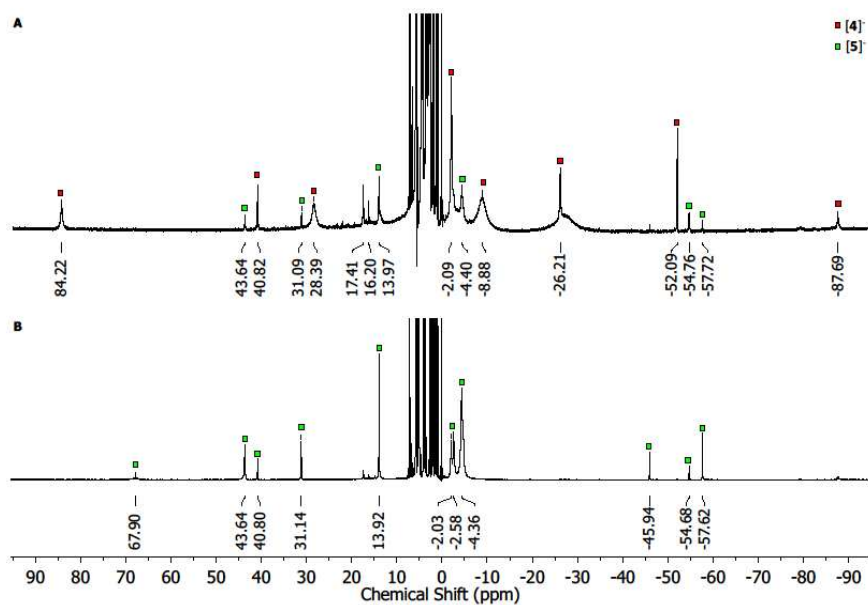


**Figure S22.** Reaction of  $K\{\text{crypt.222}\}[\text{Co}(\text{NDippSiMe}_3)_2\text{NHDipp}]$  ( $K\{\text{crypt.222}\}[4]$ ) with 5 equiv. of 1,4-cyclohexadiene **A:**  $t = 30$  min; **B:**  $t = 24$  h (THF- $d_8$ , 298 K, 300 MHz).

## 16. Magnetic measurements

Magnetic data of complex K{18c6}[2] was recorded using a dried crystalline sample and were corrected for diamagnetic contributions from the sample holder and the diamagnetic susceptibility of the compound using Pascal constants. Obtained paramagnetic susceptibility  $\chi_{\text{para}}$  was fitted using the Curie-Weiss-law  $\chi_{\text{CW}} = \left(\frac{N_A \mu_B^2 n_{\text{eff}}}{3k_B}\right)^2 \frac{1}{T-\theta}$  ( $n_{\text{eff}}$  = effective magnetic moment in Bohr's magnetons per formula unit,  $\theta$  = Weiss temperature) with contributions from a temperature independent paramagnetism  $\chi_{\text{TIP}}$  using the overall equation  $\chi_{\text{para}}T = (\chi_{\text{TIP}} + \chi_{\text{CW}})T$ .

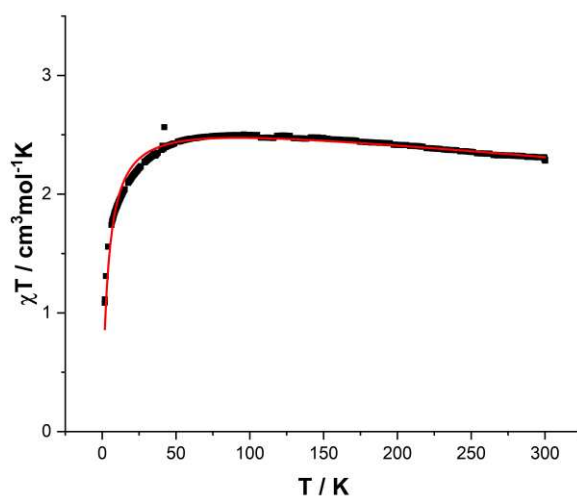


**Figure S23.** Temperature dependence of the molar magnetic susceptibility times temperature product ( $\chi T$  vs.  $T$ ) for compound K{18c6}[2]. Data were collected under an applied dc field of 1 T in a temperature range of 3 to 300 K. Molar diamagnetic correction =  $-6.77 \times 10^{-4}$  emu mol $^{-1}$ ,  $\chi_{\text{TIP}} = 1.14 (2) \times 10^{-3}$  emu mol $^{-1}$ ,  $n_{\text{eff}} = 4.635(4) \mu_B$  f.u. $^{-1}$  (f.u. = formula unit),  $\chi_{\text{M}}T = 2.33$  cm $^3$  mol $^{-1}$  K (300K),  $\theta = -3.87(6)$  K.

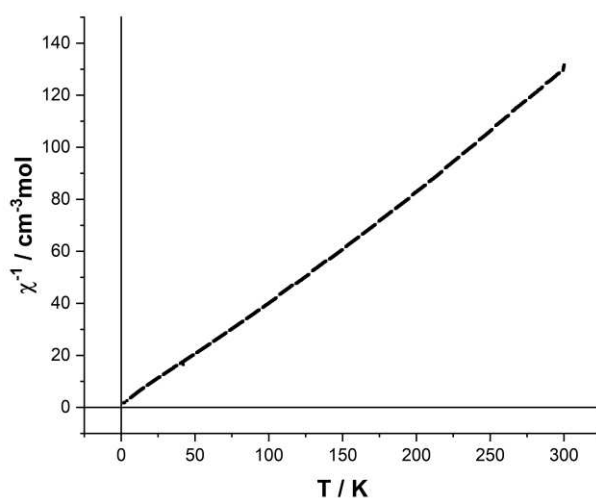


**Figure S24.** Reciprocal molar magnetic susceptibilities ( $\chi^{-1}$ ) for compound K{18c6}[2]. Data were collected under an applied dc field of 1 T in a temperature range of 3 to 300 K.

## 17. Electron-paramagnetic-resonance spectroscopy (EPR)

EPR spectra were performed on a Bruker EMXplus (X-band) EPR spectrometer equipped with the Bruker ER4118X-MD5 probehead. The freshly prepared samples were transferred to J. Young quartz EPR tubes and sealed. The solution in the tube was frozen in liquid nitrogen and kept frozen until measured.

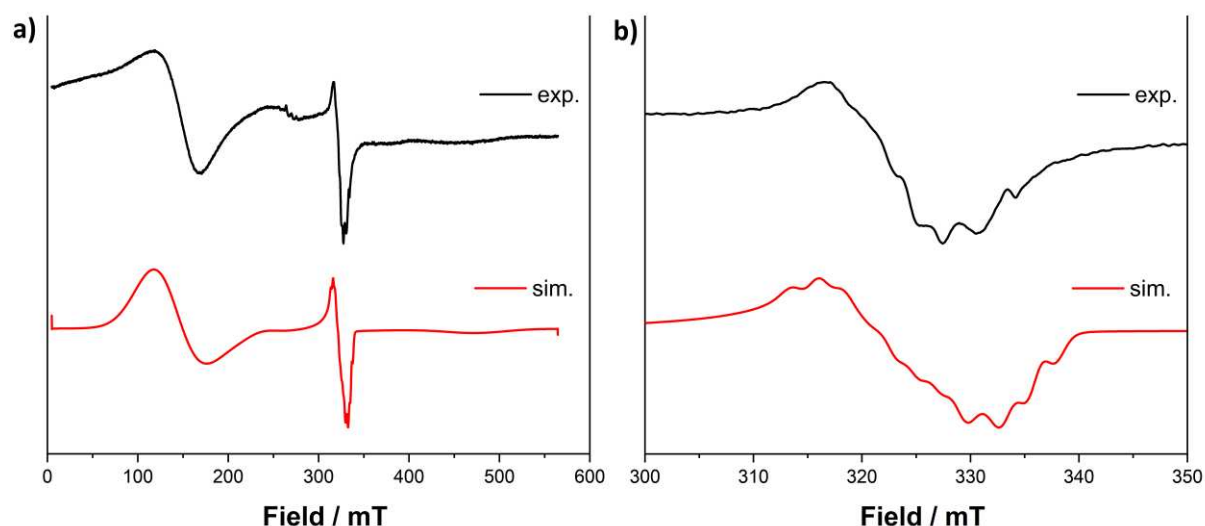


**Figure S25. a):** X-Band EPR spectrum of K{18c6}[2] in frozen THF (frequency 9.351632 GHz, 1.0 mW power, 5 G modulation amplitude) collected at 12.9 K (black). Simulation of data using the program EasySpin (red).<sup>[vi]</sup> Fitting parameters:  $S_1 = 3/2$ ,  $g_{11} = 5.0$ ,  $g_{12} = 1.4$ ;  $S_2 = 1/2$ ,  $g_{21} = 2.9$ ,  $g_{22} = 2.05$ ,  $A_{22}({}^1\text{H}) = 6.8$  G,  $A_{22}({}^{14}\text{N}) = 5.0$  G,  $A_{22}({}^{59}\text{Co}) = 4.3$  G. **b):** Enlargement of  $S_2$  showing the hyperfine splitting.

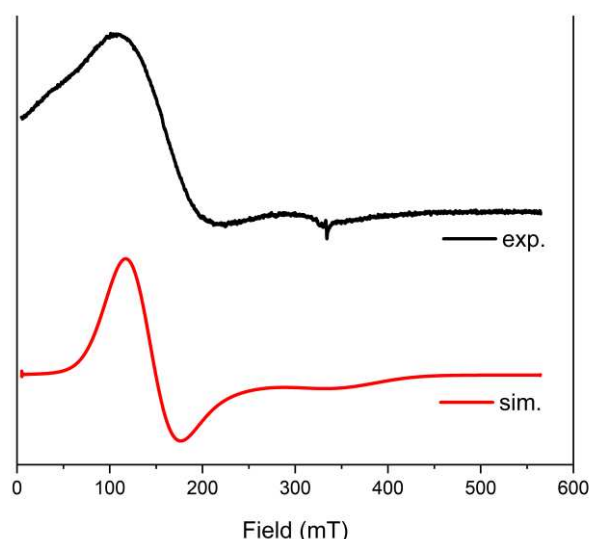


**Figure S26.** X-Band EPR spectrum of K{crypt.222}[4] in frozen THF (frequency 9.353045 GHz, 1.0 mW power, 5 G modulation amplitude) collected at 13 K (black). Simulation of data using the program EasySpin (red).<sup>[vi]</sup> Fitting parameters:  $S_1 = 3/2$ ,  $g_{11} = 5.0$ ,  $g_{12} = 1.9$ .



## 18. X-ray absorption measurements

XAS measurements were conducted for powder and solution samples at the KMC3 beamline of the BESSY synchrotron at the Helmholtz-Zentrum Berlin (HZB). Data collection was performed at 20 K in a liquid-helium cryostat in fluorescence detection mode using a 13 element ultra-low energy resolving Silicon drift detector (SDD) from Canberra. Over 25 spectra were averaged for each compound in order to improve the signal-to-noise ratio. Averaged spectra were background-corrected and normalized using in-house software. Subsequently, unfiltered  $k^3$ -weighted spectra and phase functions from FEFF8.5<sup>[55]</sup> were used for least-squares curve-fitting of the EXAFS with in-house software and for calculation of Fourier-transforms representing  $k$ -values between 2 and 14 Å<sup>-1</sup>. Data were multiplied by a fractional cosine window (10% at low and high  $k$ -side); the amplitude reduction factor  $S_0^2$  was 1.0. For the frozen solution Me-THF was used as solvent for K{18c6}[2], K{crypt.222}[4] and K{crypt.222}[1], while a mixture of toluene and Et<sub>2</sub>O (1:1) was used for K[2].

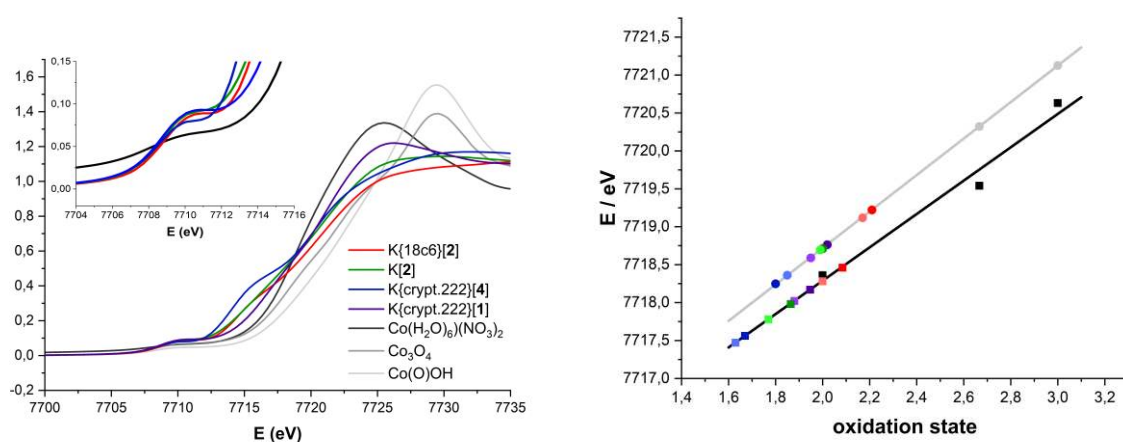


**Figure S27.** left: Solid state XANES of for the shown complexes including Co(II)(NO<sub>3</sub>)<sub>2</sub>aq, Co<sub>3</sub>O<sub>4</sub> and Co(III)(O)OH as standards. right: Fitting of the oxidation state of K{18c6}[2] (red), K[2] (green), K{crypt.222}[4] (blue) and K{crypt.222}[1] (purple).

**Table S1.** Determined oxidation state of the complexes and standards (method: hs = half step, int = integral).

Complex	Oxidation State			
	powder		solution	
	hs	int	hs	int
K{18c6}[2]	2.1	2.2	2.0	2.2
K[2]	1.9	2.0	1.8	2.0
K{crypt.222}[4]	1.7	1.8	1.6	1.9
K{crypt.222}[1]	1.9	2.0	1.9	2.0
Co(II)(NO <sub>3</sub> ) <sub>2</sub> aq		2.0		
Co <sub>3</sub> O <sub>4</sub>		2.7		
Co(III)O(OH)		3.0		

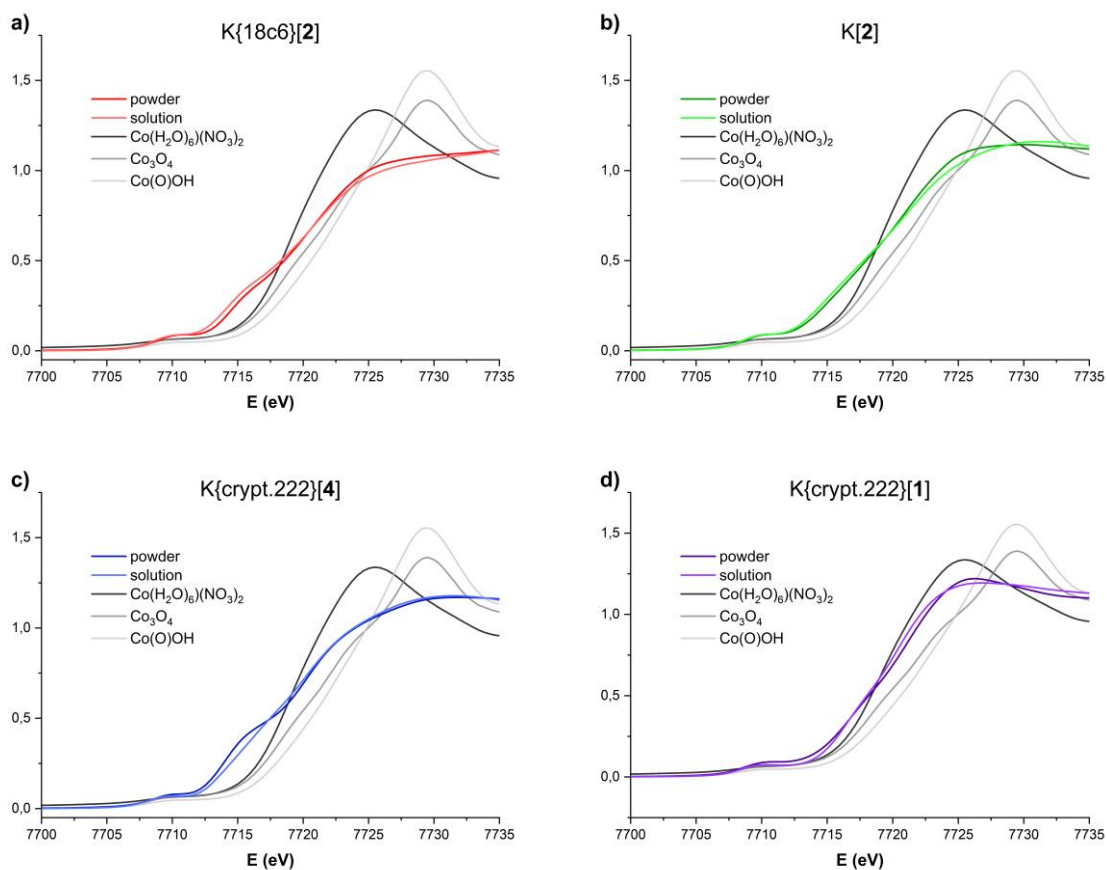


**Figure S28.** XANES of K{18c6}[2] (a), K[2] (b), K{crypt.222}[4] (c) and K{crypt.222}[1] (d) measured as powder and frozen solution including Co(II)(NO<sub>3</sub>)<sub>2</sub>aq, Co<sub>3</sub>O<sub>4</sub> and Co(III)(O)OH as standards.

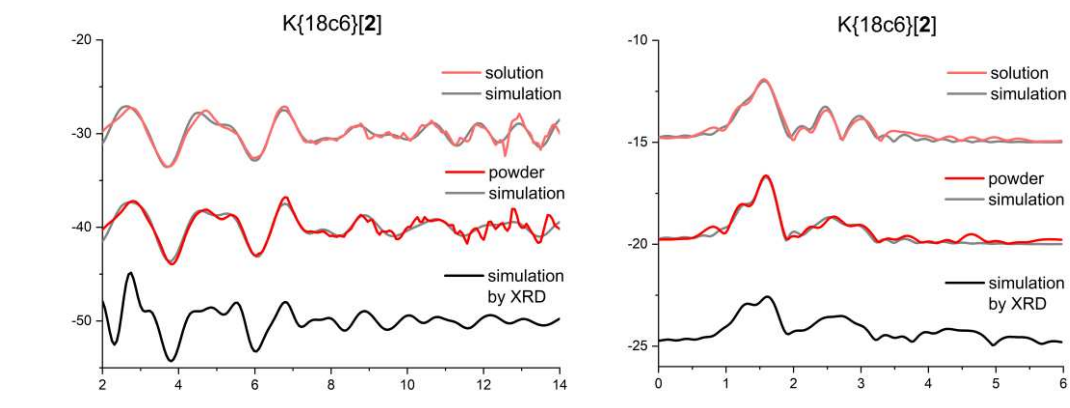


**Figure S29.**  $k^3$  weighted EXAFS (left) and FT of EXAFS (right) of K{18c6}[2].

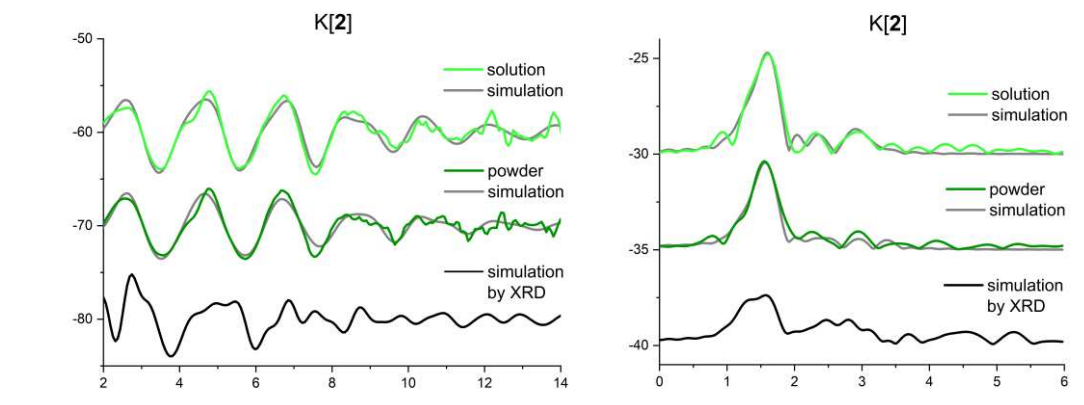


**Figure S30.**  $k^3$  weighted EXAFS (left) and FT of EXAFS (right) of K[2].

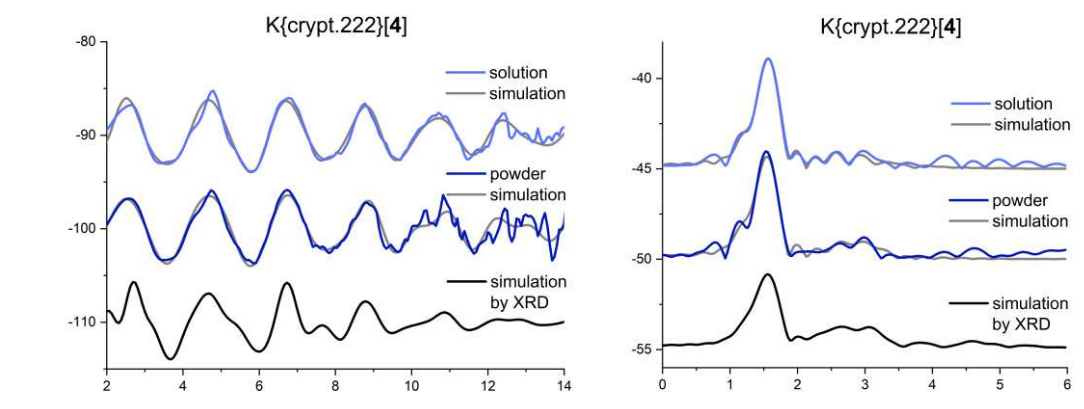


**Figure S31.**  $k^3$  weighted EXAFS (left) and FT of EXAFS (right) of K{crypt.222}[4].

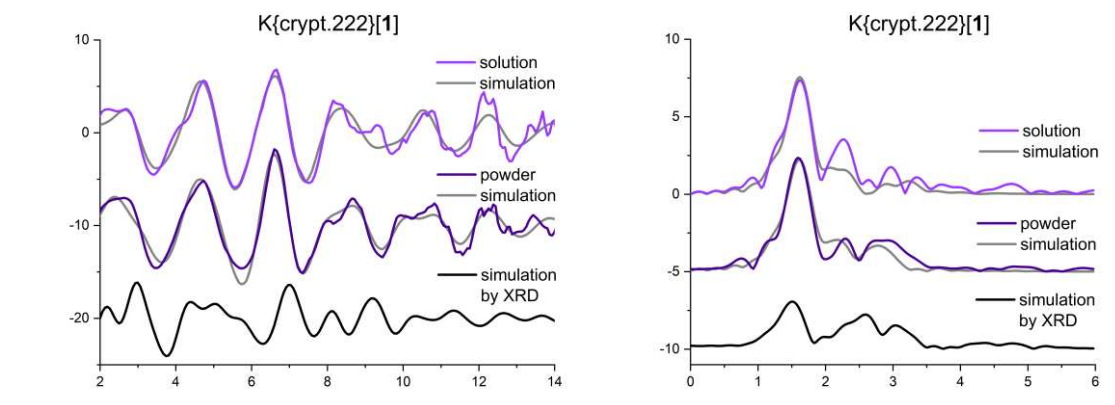


**Figure S32.**  $k^3$  weighted EXAFS (left) and FT of EXAFS (right) of K{crypt.222}[1].

## 19. Quantum chemical calculations

Experimental X-ray single crystal data were used to construct input structures of complex  $K\{18c6\}[Co(NDippSiMe_3)_2NDipp]$  ( $K\{18c6\}[2]$ ) for subsequent quantum chemical studies. In all calculations, anionic complexes  $[Co(NDippSiMe_3)_2NDipp]^-$  ( $[2]^-$ ),  $[Co(NDippSiMe_3)_2NHDipp]^-$  ( $[4]^-$ ) and cationic crown ether complexes  $(K\{18c6\})^+$  were treated independently to reduce CPU time and computational costs. Energy-minimized equilibrium structures, harmonic vibrational frequencies, infrared (IR) absorption strengths of all systems were computed with the TURBOMOLE (V7.4.0) program package<sup>[vii]</sup> assuming gas phase conditions.

All electronic structures in their various spin states (h.s., i.s. and l.s.) were studied through dispersion-corrected density functional theory (DFT-D3(0)) to account for dispersive intramolecular interactions.<sup>[viii]</sup> The 6-31G(d,p) basis set was used for C, H, O, N and Si atoms and the def2-SVP basis set for Co. In all calculations, the multipole-accelerated-resolution-of-identity-J (MARI-J) approximation for the Coulomb energy contribution was applied using corresponding default auxiliary basis sets. For numerical integrations the m5 integration grid was used to determine exchange–correlation contributions. The default criterion for the self-consistent field (SCF) energy convergence ( $10^{-7} E_h$ ) was used throughout the calculations. For structure energy minimization, the root mean square (RMS) of energy gradient and displacements were converged up to values below  $5 \cdot 10^{-4} E_h a_0^{-1}$  and  $5 \cdot 10^{-4} a_0$ , respectively, the norm of analytic gradients of the energy with respect to displacements of the nuclei remained below  $10^{-3} E_h a_0^{-1}$  and the estimated energy change between two optimization steps was below  $10^{-6} E_h$ . Various density functionals including the generalized gradient approximation (GGA) functionals BLYP and BP; hybrid functional B3-LYP; meta-hybrid functional M06; and the meta-GGA functional M06-L were used for determining the electronic energy differences between different spin states. Stationary points on the Born-Oppenheimer potential energy hypersurface as determined in the energy minimization procedure were subsequently confirmed as local minima by computation of the harmonic force field. The character of vibrational normal modes was assigned by visual inspection. The Gabedit plotting program was used to convolute and to plot both experimental and theoretical IR spectra, where Gaussian line shape functions with a full width at half maximum (FWHM) value of  $13 \text{ cm}^{-1}$  were chosen for the theoretical spectra. Computed harmonic vibrational wavenumbers were scaled by 0.962 for the selected method. Isosurface plots of spin-density distributions and molecular orbitals were made with the aid of the GaussView 5 program.<sup>[ix]</sup>

For NBO calculations, full energy minimizations of the complex structures in the selected spin states were carried out at the same level (but without MARI-J) with the GAUSSIAN16 program package.<sup>[x]</sup> The integral evaluation made use of the grid denoted as “SuperFineGrid”. Criteria for the SCF energy convergence were chosen to be  $10^{-8} E_h$  and the maximal change of a density matrix element was required to remain on the order of  $10^{-6}$  or below. Threshold values for maximum gradient components and displacements during the energy minimization of the structures were chosen to be  $4.5 \cdot 10^{-4} E_h a_0^{-1}$  and  $1.8 \cdot 10^{-3} a_0$  respectively. The RMS gradient components and displacements were converged to  $3 \cdot 10^{-4} E_h a_0^{-1}$  and  $1.2 \cdot 10^{-3} a_0$ . Harmonic vibrational frequency calculations at the equilibrium structures confirmed them as minima on the potential energy hypersurface.

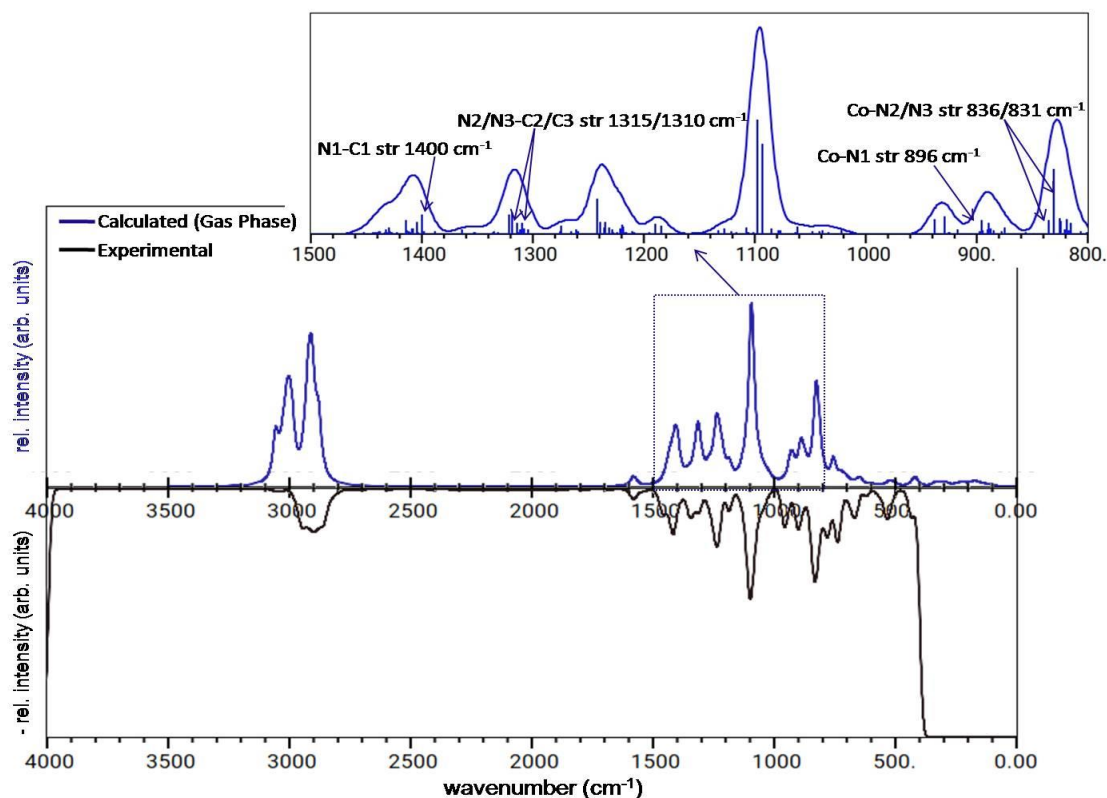


**Figure S33.** Combined theoretical (blue, high-spin; computed on DFT-D3/M06-L level within the double-harmonic approximation and experimental IR spectra (black) of  $K\{18c6\}[2]$ .

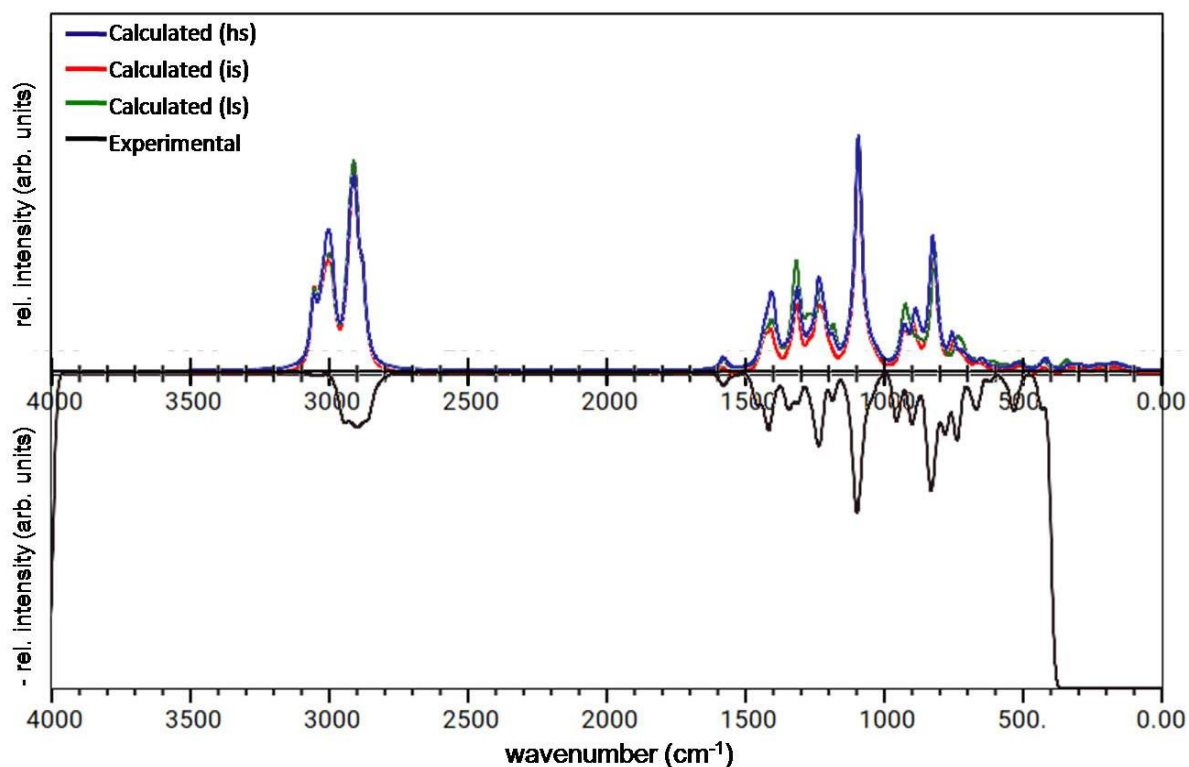


**Figure S34.** Combined experimental (black) and calculated (computed on the DFT-D3/M06-L level within the double-harmonic approximation in different spin states: h.s. (black), i.s. (red), l.s. (green)) IR spectra of  $K\{18c6\}[2]$ .



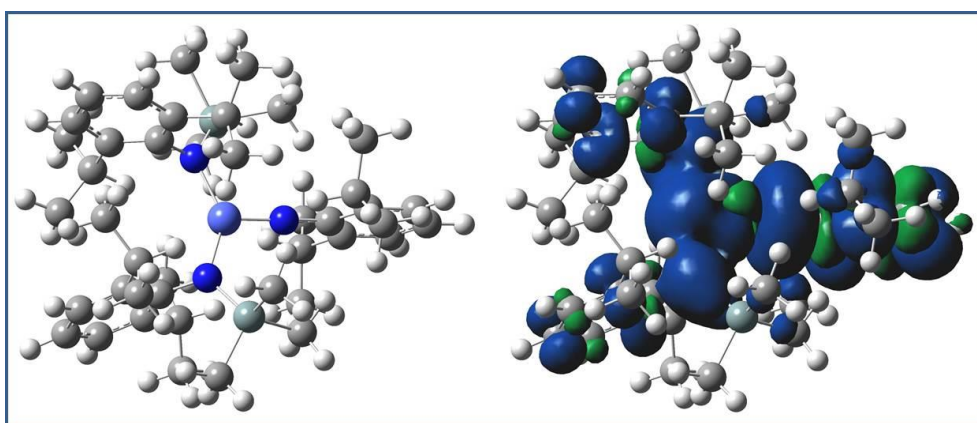


**Figure S35.** : Total spin density distribution of the complex  $[2]^-$  in high-spin state. An isosurface value of 0.003 a.u. is chosen.

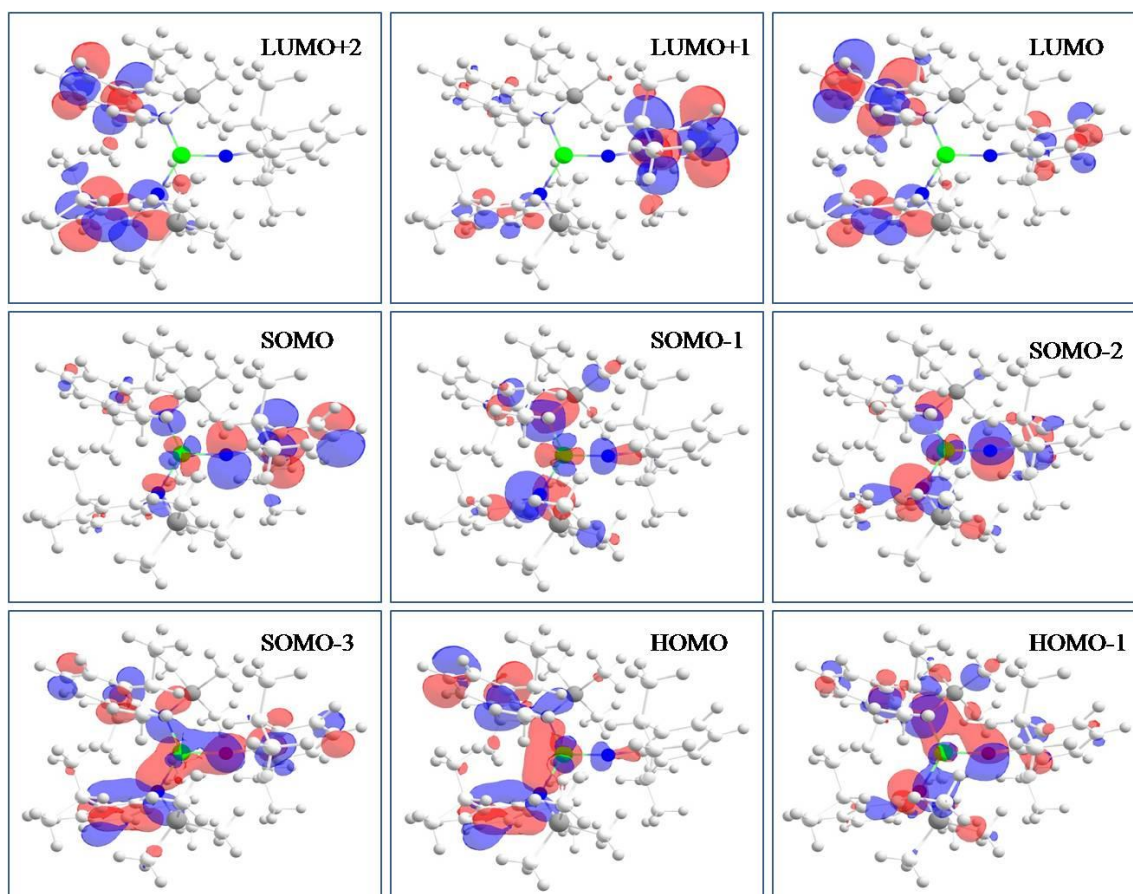


**Figure S36.** Molecular orbitals of complex  $[2]^-$ , calculated at DFT-D3/M06-L level.

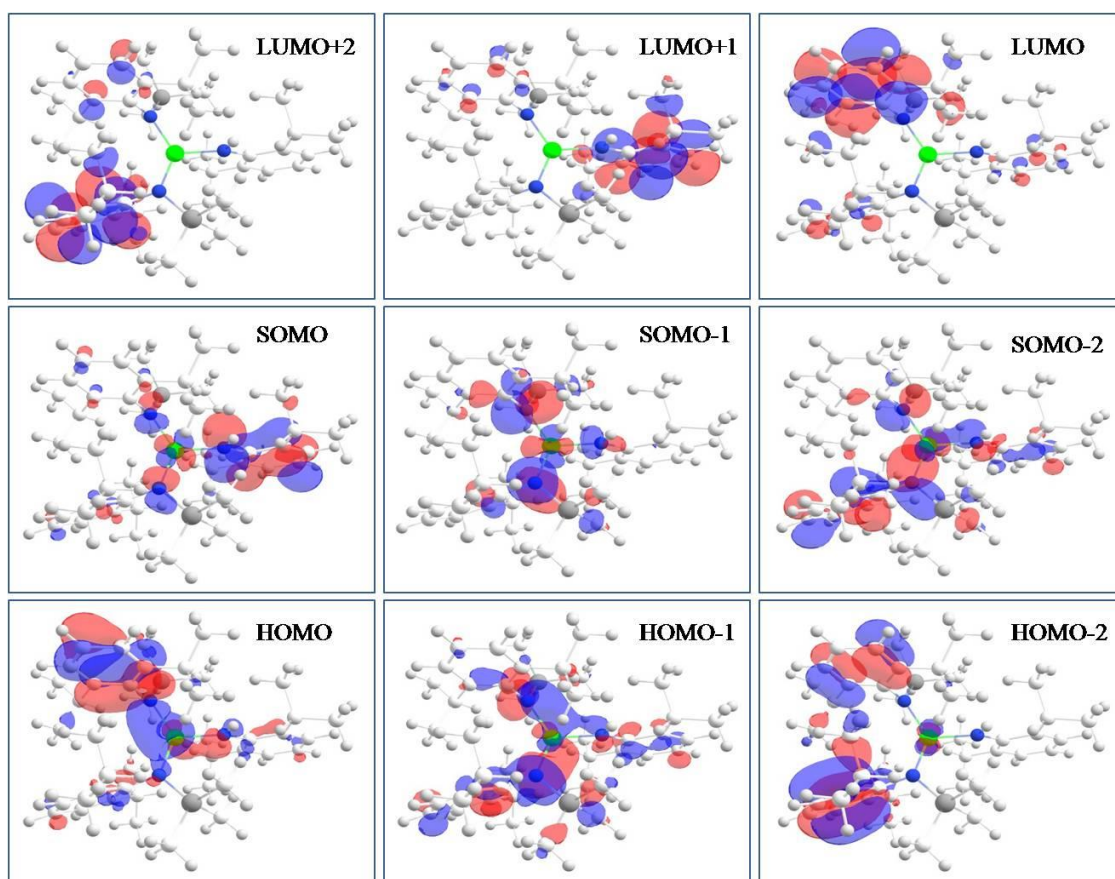


**Figure S37.** Molecular orbitals of complex [4]<sup>-</sup>, calculated at DFT-D3/M06-L level.

## 20. X-Ray diffraction analysis and molecular structures

Data for K{crypt.222}[1] (CCDC 2056475), K{18c6}[2] (CCDC 2056468), K{crypt.222}[2] (CCDC 2056470), K[2] (CCDC 2056477), K{18c6}[3] (CCDC 2056474), K[3] (CCDC 2056465), K{18c6}[4] (CCDC 2056469), K{crypt.222}[4] (CCDC 2056472), K[4] (CCDC 2056477), K{18c6}[5] (CCDC 2056471), K{18c6}[6] (CCDC 2056476), K{18c6}[7] (CCDC 2056467), were collected at 100 K on a Bruker Quest D8 diffractometer using a graphite-monochromated Mo-K $\alpha$  radiation and equipped with an *Oxford Instrument Cooler Device*. Data for K{crypt.222}[5] (CCDC 2056473) was collected at 100 K a STOE IPDS2 diffractometer using a graphite-monochromated Mo-K $\alpha$  radiation ( $\lambda = 0.71073\text{\AA}$ ) and equipped with an *Oxford Cryosystems Cryostream Cooler Device*. The structures have been solved using either OLEX SHELXT V2014/1<sup>[xi]</sup> and refined by means of least-squares procedures on a  $F^2$  with the aid of the program SHELXL-2016/6<sup>[ii]</sup> include in the software package WinGX version 1.63<sup>[xii]</sup> or using CRYSTALS.<sup>[xiii]</sup> The Atomic Scattering Factors were taken from *International Tables for X-Ray Crystallography*.<sup>[xiv]</sup> All non-hydrogen atoms were refined anisotropically. All hydrogens atoms were refined by using a riding model. Absorption corrections were introduced by using the MULTISCAN and X-Red program.<sup>[xv, ix]</sup> Drawings of molecules are performed with the programs DIAMOND and POV-Ray with 50% probability displacement ellipsoids for non-H atoms. Depiction of H atoms is generally omitted for clarity with the exception of N–H functionalities.

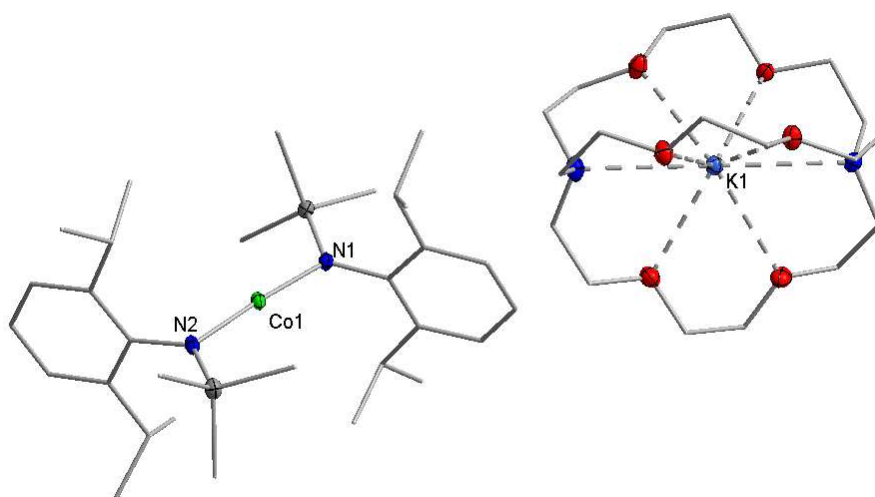
**Table S2.** Selected bond lengths (Å) and angles (°) of the described imidyl and amido complexes.

	Complex	Co1-N1/Å	Co1-N2/Å	N1-C1/Å	Co1-N1-C1/°
Imidyl	K{18c6}[2]	1.751(1)	-	1.347(2)	178.8(2)
	K{crypt.222}[2]	1.750(3)	-	1.342(4)	174.7(2)
	K[2]	1.750(3)	-	1.338(4)	174.9(3)
	K{18c6}[3]	1.757(2)	-	1.344(2)	171.9(1)
	K[3]	1.754(2)	-	1.351(2)	173.5(2)
	K{18c6}[6]	1.752(2)	-	1.344(2)	168.9(1)
Amido	K{18c6}[4]	1.923(3)	-	1.379(5)	146.2(3)
	K{crypt.222}[4]	1.921(2)	-	1.375(3)	141.2(2)
	K[4]	1.942(2)	-	1.355(3)	148.4(2)
	K{18c6}[5]	1.919(3)	1.926(3)	-	-
	K{crypt.222}[5]	1.920(3)	1.934(3)	-	-



**Table S1.** Crystal data and structure refinement for K{crypt.222}[1].

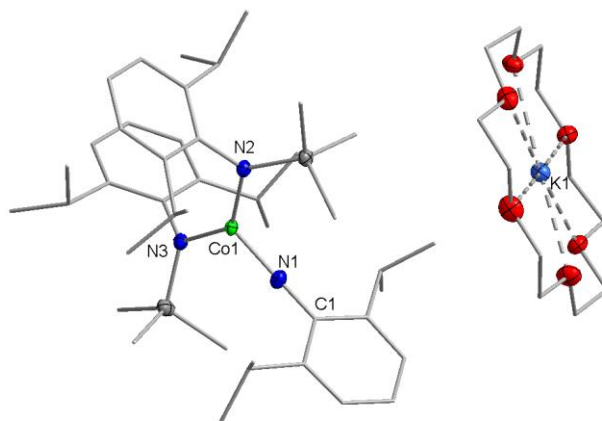
Identification code	K_crypt222_1
Empirical formula	C <sub>48</sub> H <sub>88</sub> CoKN <sub>4</sub> O <sub>6</sub> Si <sub>2</sub>
Formula weight / g mol <sup>-1</sup>	971.43
Temperature / K	100.0
Crystal system	monoclinic
Space group	<i>P</i> 2 <sub>1</sub> / <i>c</i>
<i>a</i> / Å	9.7656(5)
<i>b</i> / Å	21.0088(11)
<i>c</i> / Å	26.9283(15)
$\alpha$ / °	90
$\beta$ / °	94.638(2)
$\gamma$ / °	90
<i>V</i> / Å <sup>3</sup>	5506.6(5)
<i>Z</i>	4
$\rho_{\text{calc}}$ / g cm <sup>-3</sup>	1.172
$\mu$ / mm <sup>-1</sup>	0.477
F(000)	2104.0
Crystal size / mm <sup>3</sup>	0.613 × 0.306 × 0.296
Radiation	MoK $\alpha$ ( $\lambda$ = 0.71073)
2 $\theta$ range for data collection / °	4.164 to 53.594
Index ranges	-12 ≤ <i>h</i> ≤ 12, -26 ≤ <i>k</i> ≤ 26, -34 ≤ <i>l</i> ≤ 34
Reflections collected	101247
Independent reflections	11785 [ <i>R</i> <sub>int</sub> = 0.0601, <i>R</i> <sub>sigma</sub> = 0.0367]
Data/restraints/parameters	11785/0/573
Goodness-of-fit on F <sup>2</sup>	1.028
Final <i>R</i> indexes [ <i>I</i> ≥ 2 $\sigma$ ( <i>I</i> )]	<i>R</i> <sub>1</sub> = 0.0355, <i>wR</i> <sub>2</sub> = 0.0720
Final <i>R</i> indexes [all data]	<i>R</i> <sub>1</sub> = 0.0534, <i>wR</i> <sub>2</sub> = 0.0779
Largest diff. peak/hole / e Å <sup>-3</sup>	0.28/-0.26



**Figure S38.** Molecular structure of K{crypt.222}[1] within the crystal.

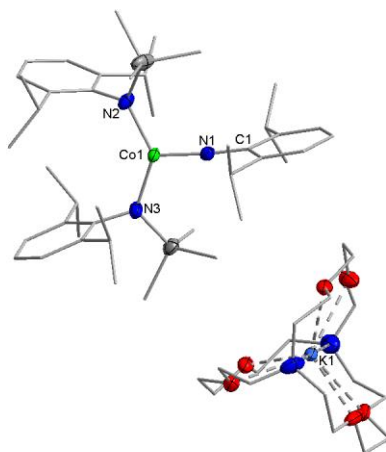
**Table S2.** Crystal data and structure refinement for K{18c6}[2] x thf.

Identification code	K_18c6_2
Empirical formula	C <sub>58</sub> H <sub>101</sub> CoKN <sub>3</sub> O <sub>6</sub> Si <sub>2</sub>
Formula weight / g mol <sup>-1</sup>	1106.62
Temperature / K	99.99
Crystal system	triclinic
Space group	$\bar{P}$
<i>a</i> / Å	12.4460(8)
<i>b</i> / Å	16.1066(10)
<i>c</i> / Å	16.6585(11)
$\alpha$ / °	89.678(2)
$\beta$ / °	89.307(2)
$\gamma$ / °	81.807(2)
<i>V</i> / Å <sup>3</sup>	3305.1(4)
<i>Z</i>	2
$\rho_{\text{calc}}$ / g cm <sup>-3</sup>	1.112
$\mu$ / mm <sup>-1</sup>	0.405
F(000)	1200.0
Crystal size / mm <sup>3</sup>	0.281 × 0.252 × 0.152
Radiation	MoK $\alpha$ ( $\lambda$ = 0.71073)
2 $\theta$ range for data collection / °	4.458 to 52.132
Index ranges	-15 ≤ <i>h</i> ≤ 15, -19 ≤ <i>k</i> ≤ 19, -20 ≤ <i>l</i> ≤ 20
Reflections collected	60987
Independent reflections	13073 [ <i>R</i> <sub>int</sub> = 0.0482, <i>R</i> <sub>sigma</sub> = 0.0415]
Data/restraints/parameters	13073/18/677
Goodness-of-fit on F <sup>2</sup>	1.019
Final <i>R</i> indexes [ <i>I</i> ≥ 2 $\sigma$ ( <i>I</i> )]	<i>R</i> <sub>1</sub> = 0.0399, <i>wR</i> <sub>2</sub> = 0.0857
Final <i>R</i> indexes [all data]	<i>R</i> <sub>1</sub> = 0.0626, <i>wR</i> <sub>2</sub> = 0.0942
Largest diff. peak/hole / e Å <sup>-3</sup>	0.62/-0.36

**Figure S39.** Molecular structure of K{18c6}[2] x thf within the crystal.

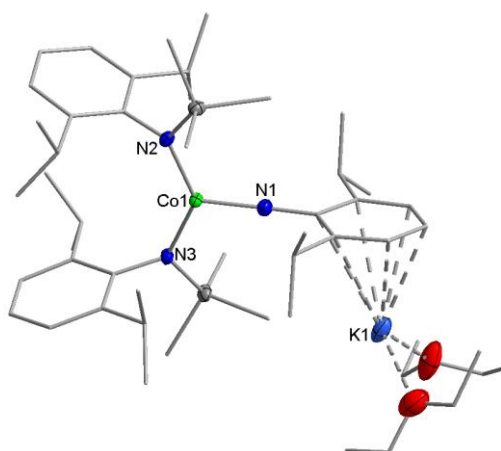
**Table S3.** Crystal data and structure refinement for K{crypt.222}[2].

Identification code	K_crypt222_2
Empirical formula	C <sub>60</sub> H <sub>104</sub> CoKN <sub>5</sub> O <sub>6</sub> Si <sub>2</sub>
Formula weight / g mol <sup>-1</sup>	1145.69
Temperature / K	100.0
Crystal system	monoclinic
Space group	<i>P</i> 2 <sub>1</sub> / <i>c</i>
<i>a</i> / Å	14.7203(9)
<i>b</i> / Å	19.9098(13)
<i>c</i> / Å	24.1567(17)
$\alpha$ / °	90
$\beta$ / °	92.047(3)
$\gamma$ / °	90
<i>V</i> / Å <sup>3</sup>	7075.3(8)
<i>Z</i>	4
$\rho_{\text{calc}}$ / g cm <sup>-3</sup>	1.076
$\mu$ / mm <sup>-1</sup>	0.380
F(000)	2484.0
Crystal size / mm <sup>3</sup>	0.816 × 0.196 × 0.131
Radiation	MoK $\alpha$ ( $\lambda$ = 0.71073)
2 $\theta$ range for data collection / °	4.288 to 51.998
Index ranges	-18 ≤ <i>h</i> ≤ 18, -24 ≤ <i>k</i> ≤ 24, -29 ≤ <i>l</i> ≤ 29
Reflections collected	154179
Independent reflections	13901 [ <i>R</i> <sub>int</sub> = 0.1382, <i>R</i> <sub>sigma</sub> = 0.0627]
Data/restraints/parameters	13901/369/834
Goodness-of-fit on F <sup>2</sup>	1.048
Final <i>R</i> indexes [ <i>I</i> ≥ 2 $\sigma$ ( <i>I</i> )]	<i>R</i> <sub>1</sub> = 0.0738, <i>wR</i> <sub>2</sub> = 0.1525
Final <i>R</i> indexes [all data]	<i>R</i> <sub>1</sub> = 0.1089, <i>wR</i> <sub>2</sub> = 0.1640
Largest diff. peak/hole / e Å <sup>-3</sup>	0.49/-0.50

**Figure S40.** Molecular structure of K{crypt.222}[2] within the crystal.

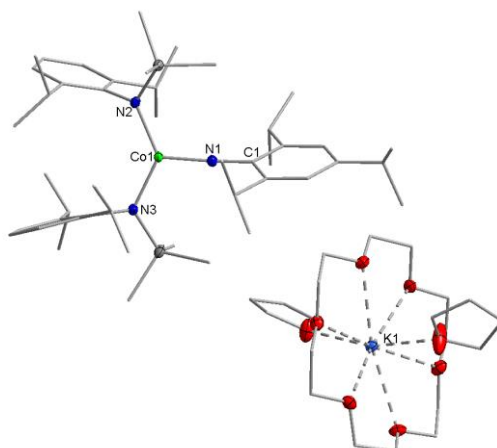
**Table S4.** Crystal data and structure refinement for K[2] x 2 Et<sub>2</sub>O.

Identification code	K_2
Empirical formula	C <sub>50</sub> H <sub>89</sub> CoKN <sub>3</sub> O <sub>2</sub> Si <sub>2</sub>
Formula weight / g mol <sup>-1</sup>	918.45
Temperature / K	100.04
Crystal system	monoclinic
Space group	<i>P</i> 2 <sub>1</sub> / <i>c</i>
<i>a</i> / Å	12.31087(8)
<i>b</i> / Å	20.9662(15)
<i>c</i> / Å	23.4201(16)
$\alpha$ / °	90
$\beta$ / °	101.876(2)
$\gamma$ / °	90
<i>V</i> / Å <sup>3</sup>	5915.5(7)
<i>Z</i>	4
$\rho_{\text{calc}}$ / g cm <sup>-3</sup>	1.031
$\mu$ / mm <sup>-1</sup>	0.435
F(000)	2000.0
Crystal size / mm <sup>3</sup>	0.281 × 0.211 × 0.179
Radiation	MoK $\alpha$ ( $\lambda$ = 0.71073)
2 $\theta$ range for data collection / °	4.05 to 52.196
Index ranges	-15 ≤ <i>h</i> ≤ 15, -25 ≤ <i>k</i> ≤ 25, -28 ≤ <i>l</i> ≤ 28
Reflections collected	133894
Independent reflections	11701 [ <i>R</i> <sub>int</sub> = 0.0630, <i>R</i> <sub>sigma</sub> = 0.0282]
Data/restraints/parameters	11701/1/566
Goodness-of-fit on F <sup>2</sup>	1.028
Final <i>R</i> indexes [ <i>I</i> ≥ 2 $\sigma$ ( <i>I</i> )]	<i>R</i> <sub>1</sub> = 0.0515, <i>wR</i> <sub>2</sub> = 0.1243
Final <i>R</i> indexes [all data]	<i>R</i> <sub>1</sub> = 0.0667, <i>wR</i> <sub>2</sub> = 0.1330
Largest diff. peak/hole / e Å <sup>-3</sup>	1.00/-0.63

**Figure S41.** Molecular structure of K[2] x 2 Et<sub>2</sub>O within the crystal.

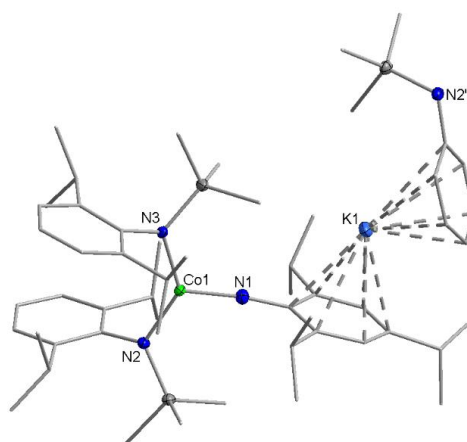
**Table S5.** Crystal data and structure refinement for K{18c6}[3] x 2 thf.

Identification code	K_18c6_3
Empirical formula	C <sub>65</sub> H <sub>115</sub> CoKN <sub>3</sub> O <sub>8</sub> Si <sub>2</sub>
Formula weight / g mol <sup>-1</sup>	1220.30
Temperature / K	100.01
Crystal system	monoclinic
Space group	<i>P</i> 2 <sub>1</sub> / <i>c</i>
<i>a</i> / Å	12.9888(7)
<i>b</i> / Å	15.3413(8)
<i>c</i> / Å	35.4637(19)
$\alpha$ / °	90
$\beta$ / °	99.157(2)
$\gamma$ / °	90
<i>V</i> / Å <sup>3</sup>	6976.6(6)
<i>Z</i>	4
$\rho_{\text{calc}}$ / g cm <sup>-3</sup>	1.162
$\mu$ / mm <sup>-1</sup>	0.391
F(000)	2654.0
Crystal size / mm <sup>3</sup>	0.624 × 0.225 × 0.18
Radiation	MoK $\alpha$ ( $\lambda$ = 0.71073)
2 $\theta$ range for data collection / °	4.386 to 52.202
Index ranges	-16 ≤ <i>h</i> ≤ 16, -18 ≤ <i>k</i> ≤ 18, -43 ≤ <i>l</i> ≤ 43
Reflections collected	194650
Independent reflections	13817 [ <i>R</i> <sub>int</sub> = 0.0566, <i>R</i> <sub>sigma</sub> = 0.0251]
Data/restraints/parameters	13817/0/759
Goodness-of-fit on F <sup>2</sup>	1.044
Final <i>R</i> indexes [ <i>I</i> ≥ 2 $\sigma$ ( <i>I</i> )]	<i>R</i> <sub>1</sub> = 0.0384, <i>wR</i> <sub>2</sub> = 0.0830
Final <i>R</i> indexes [all data]	<i>R</i> <sub>1</sub> = 0.0517, <i>wR</i> <sub>2</sub> = 0.0883
Largest diff. peak/hole / e Å <sup>-3</sup>	0.52/-0.37

**Figure S42.** Molecular structure of K{18c6}[3] x 2 thf within the crystal.

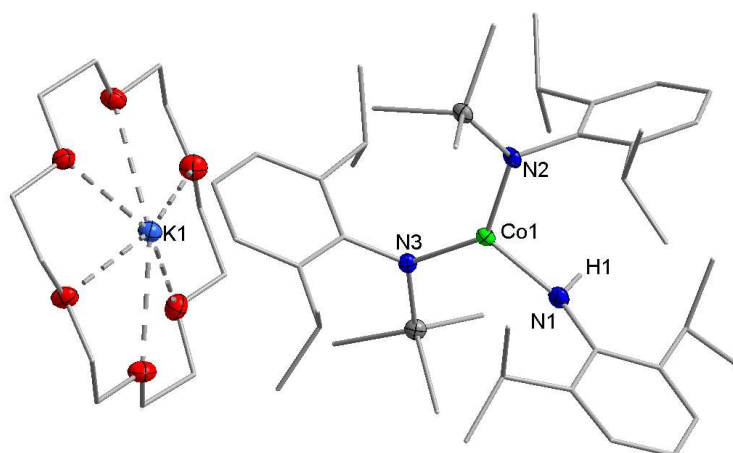
**Table S6.** Crystal data and structure refinement for K[3] x 0.5 toluene.

Identification code	K_3
Empirical formula	C <sub>45</sub> H <sub>75</sub> CoKN <sub>3</sub> Si <sub>2</sub> (x 0.5 C <sub>7</sub> H <sub>8</sub> )
Formula weight / g mol <sup>-1</sup>	858.35
Temperature / K	99.99
Crystal system	monoclinic
Space group	<i>P</i> 2 <sub>1</sub> / <i>c</i>
<i>a</i> / Å	12.6348(5)
<i>b</i> / Å	21.0266(10)
<i>c</i> / Å	19.5733(9)
$\alpha$ / °	90
$\beta$ / °	100.629(2)
$\gamma$ / °	90
<i>V</i> / Å <sup>3</sup>	5110.8(4)
<i>Z</i>	4
$\rho_{\text{calc}}$ / g cm <sup>-3</sup>	1.116
$\mu$ / mm <sup>-1</sup>	0.497
F(000)	1860.0
Crystal size / mm <sup>3</sup>	0.151 × 0.108 × 0.101
Radiation	MoK $\alpha$ ( $\lambda$ = 0.71073)
2 $\theta$ range for data collection / °	4.416 to 51.436
Index ranges	-15 ≤ <i>h</i> ≤ 15, -25 ≤ <i>k</i> ≤ 25, -20 ≤ <i>l</i> ≤ 23
Reflections collected	43265
Independent reflections	9718 [ <i>R</i> <sub>int</sub> = 0.0582, <i>R</i> <sub>sigma</sub> = 0.0498]
Data/restraints/parameters	9718/122/553
Goodness-of-fit on F <sup>2</sup>	1.034
Final <i>R</i> indexes [ <i>I</i> ≥ 2 $\sigma$ ( <i>I</i> )]	<i>R</i> <sub>1</sub> = 0.0398, <i>wR</i> <sub>2</sub> = 0.0764
Final <i>R</i> indexes [all data]	<i>R</i> <sub>1</sub> = 0.0637, <i>wR</i> <sub>2</sub> = 0.0832
Largest diff. peak/hole / e Å <sup>-3</sup>	0.31/-0.29

**Figure S43.** Molecular structure of K[3] x 0.5 toluene within the crystal with depiction of the interaction of the potassium ion with the aryl ring of the silylamide ligand of a neighboring molecule of K[5].

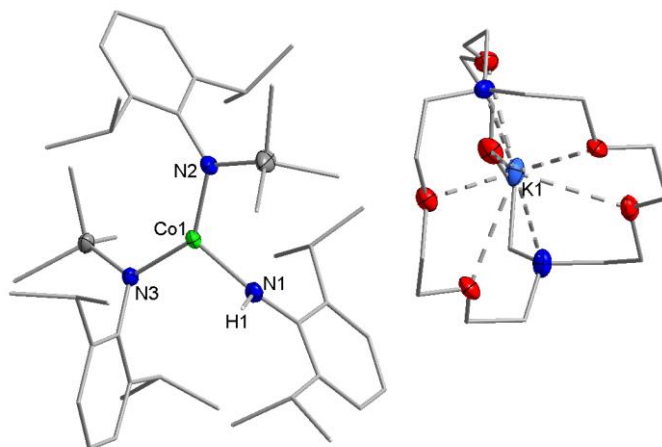
**Table S7.** Crystal data and structure refinement for K{18c6}[4].

Identification code	K_18c6_4
Empirical formula	C <sub>54</sub> H <sub>95</sub> CoKN <sub>3</sub> O <sub>6</sub> Si <sub>2</sub>
Formula weight / g mol <sup>-1</sup>	1036.53
Temperature / K	100.0
Crystal system	monoclinic
Space group	<i>P</i> 2 <sub>1</sub> / <i>c</i>
<i>a</i> / Å	13.4458(9)
<i>b</i> / Å	23.8166(15)
<i>c</i> / Å	18.2859(12)
$\alpha$ / °	90
$\beta$ / °	92.721(2)
$\gamma$ / °	90
<i>V</i> / Å <sup>3</sup>	5849.2(7)
<i>Z</i>	4
$\rho_{\text{calc}}$ / g cm <sup>-3</sup>	1.177
$\mu$ / mm <sup>-1</sup>	0.452
F(000)	2248.0
Crystal size / mm <sup>3</sup>	0.25 × 0.207 × 0.196
Radiation	MoK $\alpha$ ( $\lambda$ = 0.71073)
2 $\theta$ range for data collection / °	4.084 to 49.998
Index ranges	-15 ≤ <i>h</i> ≤ 15, 0 ≤ <i>k</i> ≤ 28, 0 ≤ <i>l</i> ≤ 21
Reflections collected	10405
Independent reflections	10405 [ <i>R</i> <sub>int</sub> = 0.0833, <i>R</i> <sub>sigma</sub> = 0.0546]
Data/restraints/parameters	10405/0/627
Goodness-of-fit on F <sup>2</sup>	1.123
Final <i>R</i> indexes [ <i>I</i> ≥ 2 $\sigma$ ( <i>I</i> )]	<i>R</i> <sub>1</sub> = 0.0477, <i>wR</i> <sub>2</sub> = 0.1084
Final <i>R</i> indexes [all data]	<i>R</i> <sub>1</sub> = 0.0626, <i>wR</i> <sub>2</sub> = 0.1148
Largest diff. peak/hole / e Å <sup>-3</sup>	0.35/-0.42

**Figure S44.** Molecular structure of K{18c6}[4] within the crystal.

**Table S8.** Crystal data and structure refinement for K{crypt.222}[4].

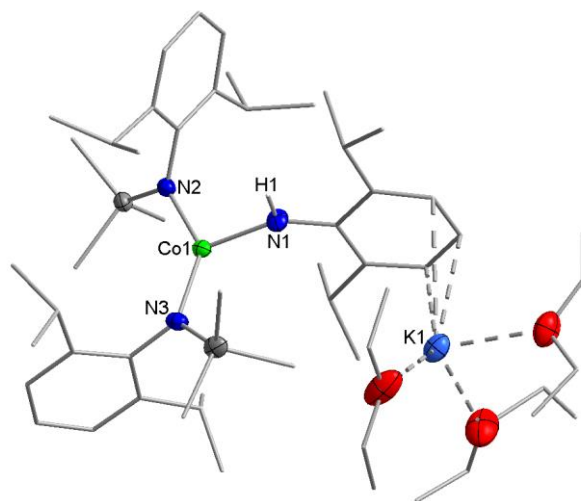
Identification code	K_crypt222_4
Empirical formula	C <sub>60</sub> H <sub>106</sub> CoKN <sub>5</sub> O <sub>6</sub> Si <sub>2</sub>
Formula weight / g mol <sup>-1</sup>	1147.70
Temperature / K	100.01
Crystal system	triclinic
Space group	$\bar{P}$
<i>a</i> / Å	13.1561(12)
<i>b</i> / Å	13.8460(13)
<i>c</i> / Å	19.2494(18)
$\alpha$ / °	104.256(3)
$\beta$ / °	99.591(3)
$\gamma$ / °	95.234(3)
<i>V</i> / Å <sup>3</sup>	3318.7(5)
<i>Z</i>	2
$\rho_{\text{calc}}$ / g cm <sup>-3</sup>	1.149
$\mu$ / mm <sup>-1</sup>	0.406
F(000)	1246.0
Crystal size / mm <sup>3</sup>	0.267 × 0.256 × 0.182
Radiation	MoK $\alpha$ ( $\lambda$ = 0.71073)
2 $\theta$ range for data collection / °	4.452 to 52.216
Index ranges	-16 ≤ <i>h</i> ≤ 16, -17 ≤ <i>k</i> ≤ 16, -23 ≤ <i>l</i> ≤ 23
Reflections collected	60393
Independent reflections	13129 [ <i>R</i> <sub>int</sub> = 0.0782, <i>R</i> <sub>sigma</sub> = 0.0664]
Data/restraints/parameters	13129/0/897
Goodness-of-fit on F <sup>2</sup>	1.033
Final <i>R</i> indexes [ <i>I</i> ≥ 2 $\sigma$ ( <i>I</i> )]	<i>R</i> <sub>1</sub> = 0.0510, <i>wR</i> <sub>2</sub> = 0.0960
Final <i>R</i> indexes [all data]	<i>R</i> <sub>1</sub> = 0.0900, <i>wR</i> <sub>2</sub> = 0.1093
Largest diff. peak/hole / e Å <sup>-3</sup>	0.49/-0.42

**Figure S45.** Molecular structure of K{crypt.222}[4] within the crystal.



**Table S9.** Crystal data and structure refinement for K[4] x 3 Et<sub>2</sub>O

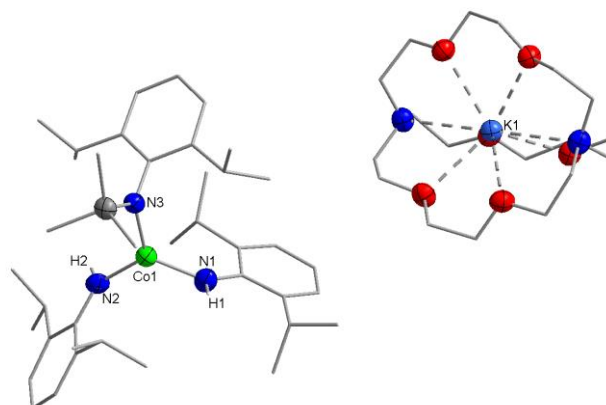
Identification code	K_4
Empirical formula	C <sub>54</sub> H <sub>98</sub> CoKN <sub>3</sub> O <sub>3</sub> Si <sub>2</sub>
Formula weight / g mol <sup>-1</sup>	991.56
Temperature / K	295.0
Crystal system	triclinic
Space group	$\bar{P}$
<i>a</i> / Å	13.0945(6)
<i>b</i> / Å	13.1053(6)
<i>c</i> / Å	19.5413(9)
$\alpha$ / °	104.877(2)
$\beta$ / °	103.330(2)
$\gamma$ / °	105.2640(10)
<i>V</i> / Å <sup>3</sup>	2962.5(2)
<i>Z</i>	2
$\rho_{\text{calc}}$ / g cm <sup>-3</sup>	1.112
$\mu$ / mm <sup>-1</sup>	0.440
F(000)	1082.0
Crystal size / mm <sup>3</sup>	0.245 × 0.236 × 0.228
Radiation	MoK $\alpha$ ( $\lambda$ = 0.71073)
2 $\theta$ range for data collection / °	3.912 to 52.108
Index ranges	-16 ≤ <i>h</i> ≤ 16, -16 ≤ <i>k</i> ≤ 16, -24 ≤ <i>l</i> ≤ 24
Reflections collected	70152
Independent reflections	11663 [ <i>R</i> <sub>int</sub> = 0.0452, <i>R</i> <sub>sigma</sub> = 0.0373]
Data/restraints/parameters	11663/0/604
Goodness-of-fit on F <sup>2</sup>	1.026
Final <i>R</i> indexes [ <i>I</i> ≥ 2 $\sigma$ ( <i>I</i> )]	<i>R</i> <sub>1</sub> = 0.0607, <i>wR</i> <sub>2</sub> = 0.1509
Final <i>R</i> indexes [all data]	<i>R</i> <sub>1</sub> = 0.0809, <i>wR</i> <sub>2</sub> = 0.1632
Largest diff. peak/hole / e Å <sup>-3</sup>	01.42/-0.78

**Figure S46.** Molecular structure of K[4] x 3 Et<sub>2</sub>O within the crystal.



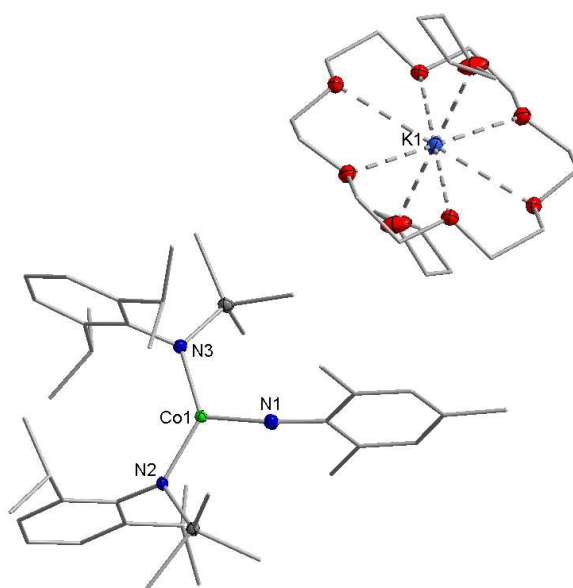
**Table S11.** Crystal data and structure refinement for K{crypt.222}[5].

Identification code	K_crypt222_5
Empirical formula	C <sub>57</sub> H <sub>98</sub> CoKN <sub>5</sub> O <sub>6</sub> Si <sub>2</sub>
Formula weight / g mol <sup>-1</sup>	1075.52
Temperature / K	100.0
Crystal system	orthorhombic
Space group	<i>P</i> 2 <sub>1</sub> 2 <sub>1</sub> 2 <sub>1</sub>
<i>a</i> / Å	13.4767(11)
<i>b</i> / Å	17.1448(14)
<i>c</i> / Å	26.657(2)
$\alpha$ / °	90
$\beta$ / °	90
$\gamma$ / °	90
<i>V</i> / Å <sup>3</sup>	6159.2(9)
<i>Z</i>	4
$\rho_{\text{calc}}$ / g cm <sup>-3</sup>	1.160
$\mu$ / mm <sup>-1</sup>	0.414
F(000)	2332.0
Crystal size / mm <sup>3</sup>	0.2 × 0.2 × 0.1
Radiation	MoK $\alpha$ ( $\lambda$ = 0.71073)
2 $\theta$ range for data collection / °	4.752 to 53.694
Index ranges	-17 ≤ <i>h</i> ≤ 17, -21 ≤ <i>k</i> ≤ 20, -33 ≤ <i>l</i> ≤ 33
Reflections collected	60389
Independent reflections	13033 [ <i>R</i> <sub>int</sub> = 0.0858, <i>R</i> <sub>sigma</sub> = 0.0601]
Data/restraints/parameters	13033/0/663
Goodness-of-fit on F <sup>2</sup>	0.892
Final <i>R</i> indexes [ <i>I</i> ≥ 2 $\sigma$ ( <i>I</i> )]	<i>R</i> <sub>1</sub> = 0.0362, <i>wR</i> <sub>2</sub> = 0.0774
Final <i>R</i> indexes [all data]	<i>R</i> <sub>1</sub> = 0.0576, <i>wR</i> <sub>2</sub> = 0.0822
Largest diff. peak/hole / e Å <sup>-3</sup>	0.32/-0.46
Flack parameter	-0.008(8)

**Figure S48.** Molecular structure of K{crypt.222}[5] within the crystal.

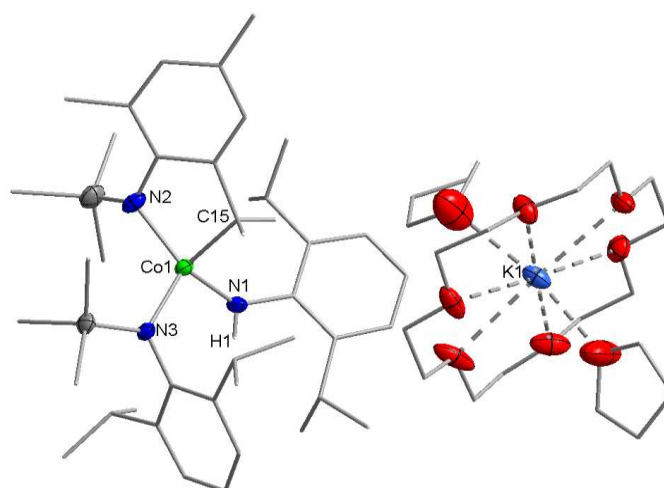
**Table S12.** Crystal data and structure refinement for K{18c6}[6] x 2 thf.

Identification code	K_18c6_6
Empirical formula	C <sub>55</sub> H <sub>95</sub> CoKN <sub>3</sub> O <sub>7</sub> Si <sub>2</sub>
Formula weight / g mol <sup>-1</sup>	1064.54
Temperature / K	100.0
Crystal system	monoclinic
Space group	<i>P</i> 2 <sub>1</sub> / <i>n</i>
<i>a</i> / Å	14.4598(9)
<i>b</i> / Å	23.3862(14)
<i>c</i> / Å	17.7039(10)
$\alpha$ / °	90
$\beta$ / °	96.592(2)
$\gamma$ / °	90
<i>V</i> / Å <sup>3</sup>	5947.2(6)
<i>Z</i>	4
$\rho_{\text{calc}}$ / g cm <sup>-3</sup>	1.189
$\mu$ / mm <sup>-1</sup>	0.448
<i>F</i> (000)	2000.0
Crystal size / mm <sup>3</sup>	0.325 × 0.198 × 0.168
Radiation	MoK $\alpha$ ( $\lambda$ = 0.71073)
2 $\theta$ range for data collection / °	3.862 to 52.266
Index ranges	-17 ≤ <i>h</i> ≤ 17, -28 ≤ <i>k</i> ≤ 28, -21 ≤ <i>l</i> ≤ 21
Reflections collected	127325
Independent reflections	11820 [ <i>R</i> <sub>int</sub> = 0.0497, <i>R</i> <sub>sigma</sub> = 0.0268]
Data/restraints/parameters	11820/0/642
Goodness-of-fit on <i>F</i> <sup>2</sup>	1.046
Final <i>R</i> indexes [ <i>I</i> ≥ 2 $\sigma$ ( <i>I</i> )]	<i>R</i> <sub>1</sub> = 0.0344, <i>wR</i> <sub>2</sub> = 0.0723
Final <i>R</i> indexes [all data]	<i>R</i> <sub>1</sub> = 0.0483, <i>wR</i> <sub>2</sub> = 0.0771
Largest diff. peak/hole / e Å <sup>-3</sup>	0.41/-0.32

**Figure S49.** Molecular structure of K{18c6}[6] x 2 thf within the crystal.

**Table S13.** Crystal data and structure refinement for K{18c6}[7] x 2 thf.

Identification code	K_18c6_7
Empirical formula	C <sub>63</sub> H <sub>111</sub> CoKN <sub>3</sub> O <sub>9</sub> Si <sub>2</sub>
Formula weight / g mol <sup>-1</sup>	1208.75
Temperature / K	100.0
Crystal system	monoclinic
Space group	<i>P</i> 2 <sub>1</sub> / <i>n</i>
<i>a</i> / Å	12.6793(7)
<i>b</i> / Å	24.0847(14)
<i>c</i> / Å	24.5208(14)
$\alpha$ / °	90
$\beta$ / °	94.138(2)
$\gamma$ / °	90
<i>V</i> / Å <sup>3</sup>	7468.6(7)
<i>Z</i>	4
$\rho_{\text{calc}}$ / g cm <sup>-3</sup>	1.075
$\mu$ / mm <sup>-1</sup>	0.366
<i>F</i> (000)	2624.0
Crystal size / mm <sup>3</sup>	0.405 × 0.287 × 0.104
Radiation	MoK $\alpha$ ( $\lambda$ = 0.71073)
2 $\theta$ range for data collection / °	3.77 to 52.134
Index ranges	-15 ≤ <i>h</i> ≤ 15, -29 ≤ <i>k</i> ≤ 29, -30 ≤ <i>l</i> ≤ 30
Reflections collected	91044
Independent reflections	14742 [ <i>R</i> <sub>int</sub> = 0.1088, <i>R</i> <sub>sigma</sub> = 0.0715]
Data/restraints/parameters	14742/0/708
Goodness-of-fit on <i>F</i> <sup>2</sup>	1.018
Final <i>R</i> indexes [ <i>I</i> ≥ 2 $\sigma$ ( <i>I</i> )]	<i>R</i> <sub>1</sub> = 0.0675, <i>wR</i> <sub>2</sub> = 0.1528
Final <i>R</i> indexes [all data]	<i>R</i> <sub>1</sub> = 0.1137, <i>wR</i> <sub>2</sub> = 0.1739
Largest diff. peak/hole / e Å <sup>-3</sup>	0.95/-0.63

**Figure S50.** Molecular structure of K{18c6}[7] x 2 thf within the crystal.

---

## References

- [i] a) D. F. Evans *J. Chem. Soc.* **1959**, 2003; b) E. M. Schubert, *J. Chem. Educ.* **1992**, *69*, 62.
- [ii] C. Lin, J. C. Fettinger, F. Grandjean, G. J. Long, P. P. Power, *Inorg. Chem.* **2014**, *53*, 9400.
- [iii] L. P. Spencer, R. Altwer, P. Wei, L. Gelmini, J. Gauld, D. W. Stephan, *Organometallics* **2003**, *19*, 3841.
- [iv] W. J. Evans, M. A. Ansari, J. W. Ziller, S. I. Khan, *Inorg. Chem.* **1996**, *35*, 5435.
- [v] P. A. Smith, C. D. Rowe, L. B. Bruner, *J. Org. Chem.* **1969**, *11*, 3430.
- [vi] S. Stoll, A. Schweiger, *J. Magn. Reson.* **2006**, *1*, 42.
- [vii] TURBOMOLE V7.4 2019, a development of University of Karlsruhe and Forschungszentrum Karlsruhe GmbH, 1989-2007, TURBOMOLE GmbH, since 2007, available from <http://www.turbomole.com>
- [viii] S. Grimme, J. Antony, S. Ehrlich and H. Krieg, *J. Chem. Phys.* **2010**, *132*, 154104.
- [ix] R. Dennington, T. Keith, J. Millam: Semichem Inc., Shawnee Mission KS, *Gauss View*, Version 5, **2009**.
- [x] Gaussian 16, Revision A.03, M. J. Frisch, G. W. Trucks, H. B. Schlegel, G. E. Scuseria, M. A. Robb, J. R. Cheeseman, G. Scalmani, V. Barone, G. A. Petersson, H. Nakatsuji, X. Li, M. Caricato, A. V. Marenich, J. Bloino, B. G. Janesko, R. Gomperts, B. Mennucci, H. P. Hratchian, J. V. Ortiz, A. F. Izmaylov, J. L. Sonnenberg, D. Williams-Young, F. Ding, F. Lipparini, F. Egidi, J. Goings, B. Peng, A. Petrone, T. Henderson, D. Ranasinghe, V. G. Zakrzewski, J. Gao, N. Rega, G. Zheng, W. Liang, M. Hada, M. Ehara, Toyota, R. Fukuda, J. Hasegawa, M. Ishida, T. Nakajima, Y. Honda, O. Kitao, H. Nakai, T. Vreven, K. Throssell, J. A. Montgomery, Jr., J. E. Peralta, F. Ogliaro, M. J. Bearpark, J. J. Heyd, E. N. Brothers, K. N. V. N. Staroverov, T. A. Keith, R. Kobayashi, J. Normand, K. Raghavachari, A. P. Rendell, J. C. Burant, S. S. Iyengar, J. Tomasi, M. Cossi, J. M. Millam, M. Klene, C. Adamo, R. Cammi, J. W. Ochterski, R. L. Martin, K. Morokuma, O. Farkas, J. B. Foresman, and D. J. Fox, Gaussian, Inc., Wallingford CT, **2016**.
- [xi] G. M. Sheldrick, *Acta Cryst.* **2015**, *71*, 3.
- [xii] L. Farrugia, *J. Appl. Crystallogr.* **1999**, *32*, 837.
- [xiii] P. W. Betteridge, J. R. Carruthers, R. I. Cooper, K. Prout, D. J. Watkin, *J. Appl. Cryst.* **2003**, *36*, 1487.
- [xiv] *International Tables for X-ray crystallography* (Kynoch Press, Birmingham, England, 1974) Vol. IV.
- [xv] *SADABS-2016/2* (Bruker, **2016**).
- [ix] X-Area, X-Red 1.63.1.0 (STOE, **2016**).

**6.9.3 On the Synthesis of a T-shaped Imido Nickel Complex and Trigonal Amido Nickel Complexes**

# European Journal of Inorganic Chemistry

Supporting Information

## **On the Synthesis of a T-Shaped Imido Nickel Complex and Trigonal Amido Nickel Complexes**

Alexander Reckziegel, Beatrice Battistella, and C. Gunnar Werncke\*



## Table of Contents

1.	NMR spectroscopy .....	2
1.1.	NMR spectra of the used starting materials and isolated complexes.....	2
1.2.	H Atom Abstraction Reactivity of $K\{18c6\}[Ni(N\{Dipp\}SiMe_3)(N\{Ph\}SiMe_3)(NDipp)]$ (1) .....	3
1.3.	Reaction of $[Ni(N\{Dipp\}SiMe_3)_2]$ with organic alkali metal salts.....	4
2.	Electron-paramagnetic-resonance spectroscopy (EPR) .....	10
3.	X-ray diffraction analysis and molecular structures .....	11

## 1. NMR spectroscopy

### 1.1. NMR spectra of the used starting materials and isolated complexes

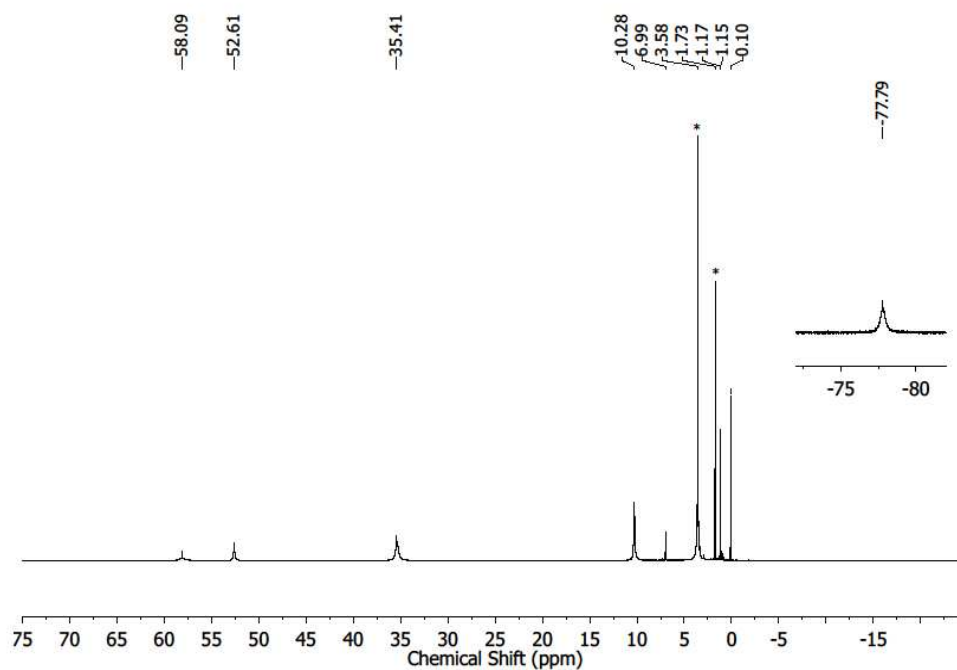


Figure S1.  $^1\text{H}$  NMR spectrum (300 MHz, 300 K,  $\text{THF-d}_8$ )  $[\text{Ni}(\text{N}\{\text{Dipp}\}\text{SiMe}_3)_2]$ . Signals of the solvent are marked with \*.

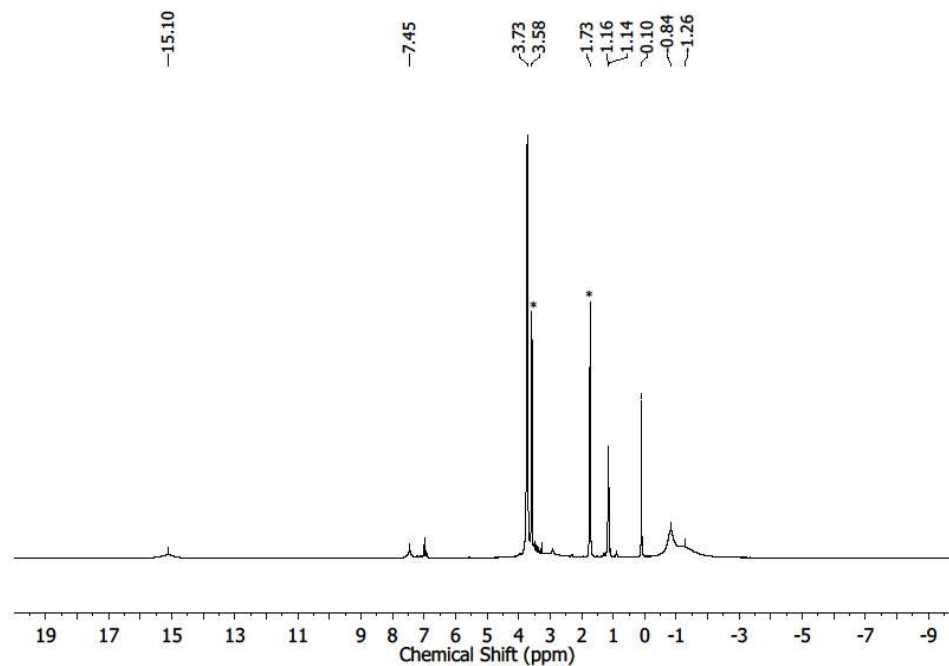


Figure S2.  $^1\text{H}$  NMR spectrum (300 MHz, 300 K,  $\text{THF-d}$ )  $\text{K}\{18\text{c}6\}[\text{Ni}(\text{N}\{\text{Dipp}\}\text{SiMe}_3)_2]$ . Signals of the solvent are marked with \*.

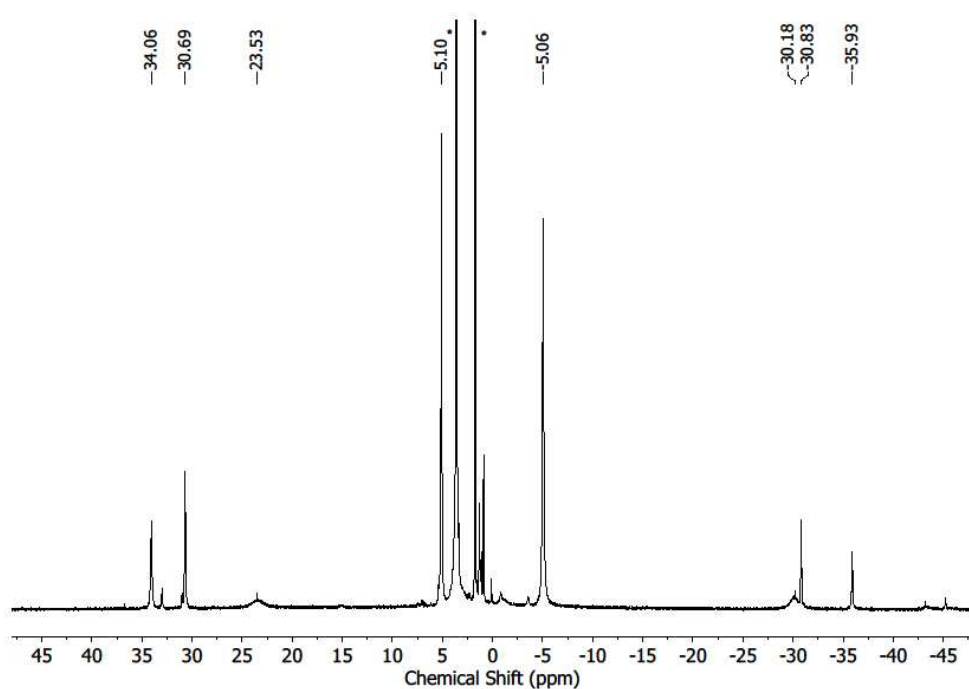


Figure S3.  $^1\text{H}$  NMR spectrum (300 MHz, 300 K,  $\text{THF-d}_8$ )  $\text{K}\{18\text{c}6\}[\text{Ni}(\text{N}\{\text{Dipp}\}\text{SiMe}_3)_2(\text{NPh}_2)]$ . Signals of the solvent and 18c6 are marked with \*.

## 1.2. H Atom Abstraction Reactivity of $\text{K}\{18\text{c}6\}[\text{Ni}(\text{N}\{\text{Dipp}\}\text{SiMe}_3)(\text{N}\{\text{Ph}\}\text{SiMe}_3)(\text{NDipp})]$ (**1**)

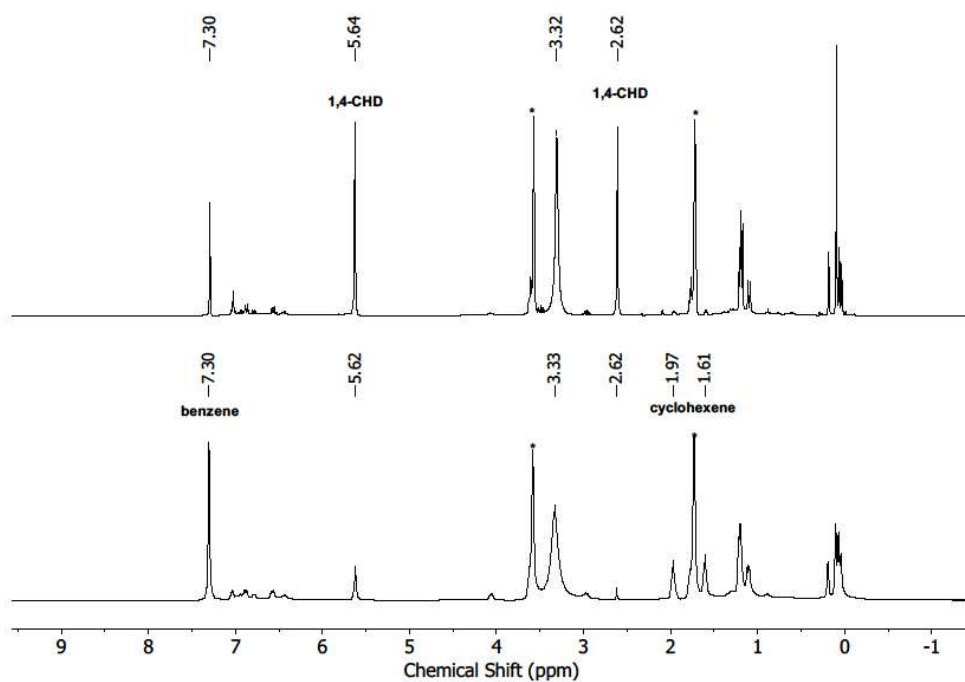


Figure S4.  $^1\text{H}$  NMR spectrum (300 MHz, 300 K,  $\text{THF-d}_8$ ) of a reaction of  $\text{K}\{18\text{c}6\}[\text{Ni}(\text{N}\{\text{Dipp}\}\text{SiMe}_3)(\text{N}\{\text{Ph}\}\text{SiMe}_3)(\text{NDipp})]$  (**1**) with 1,4-CHD (A:  $t = 5\text{ min}$ , B:  $t = 24\text{ h}$ ).

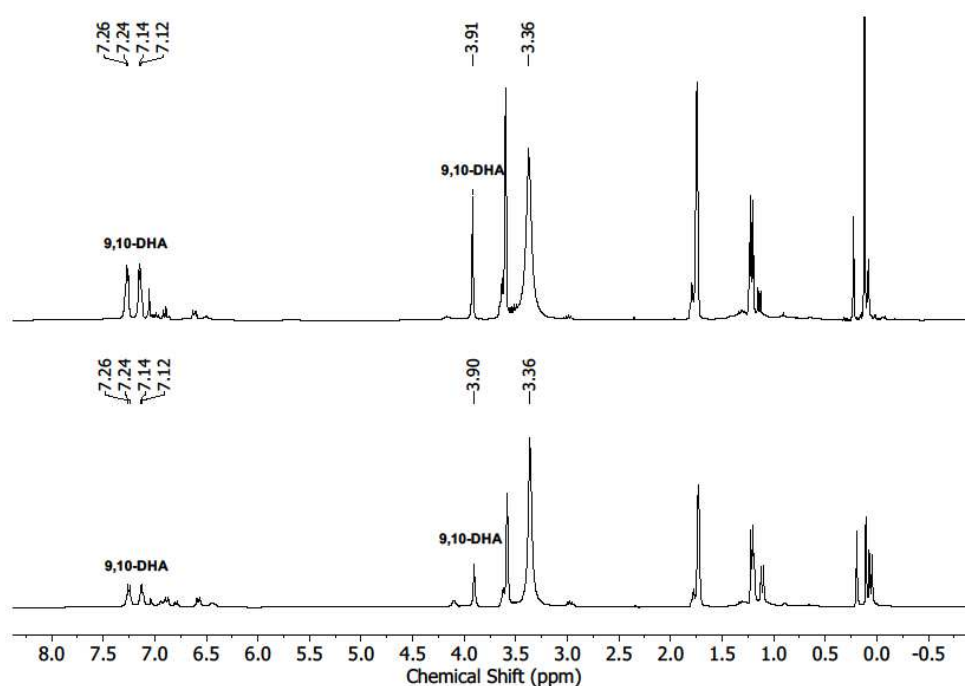


Figure S5.  $^1\text{H}$  NMR spectrum (300 MHz, 300 K,  $\text{THF-d}_8$ ) of a reaction of  $\text{K}\{18\text{c}6\}[\text{Ni}(\text{N}\{\text{Dipp}\}\text{SiMe}_3)(\text{N}\{\text{Ph}\}\text{SiMe}_3)(\text{NDipp})]$  (1) with 9,10-DHA (A:  $t = 5$  min, B:  $t = 24$  h).

### 1.3. Reaction of $[\text{Ni}(\text{N}\{\text{Dipp}\}\text{SiMe}_3)_2]$ with organic alkali metal salts

In a typical NMR experiment 1 equiv.  $[\text{Ni}(\text{N}\{\text{Dipp}\}\text{SiMe}_3)_2]$  were dissolved in 0.3 ml  $\text{THF-d}_8$  and added to a mixture of the respective alkali metal salt and 18c6 in 0.3 mL  $\text{THF-d}_8$ .

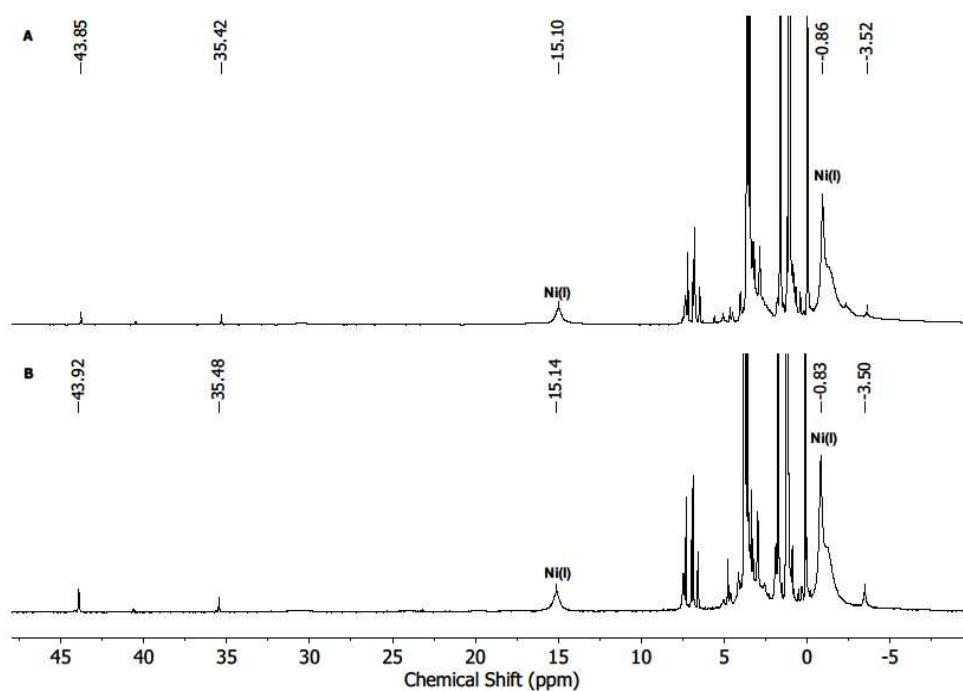
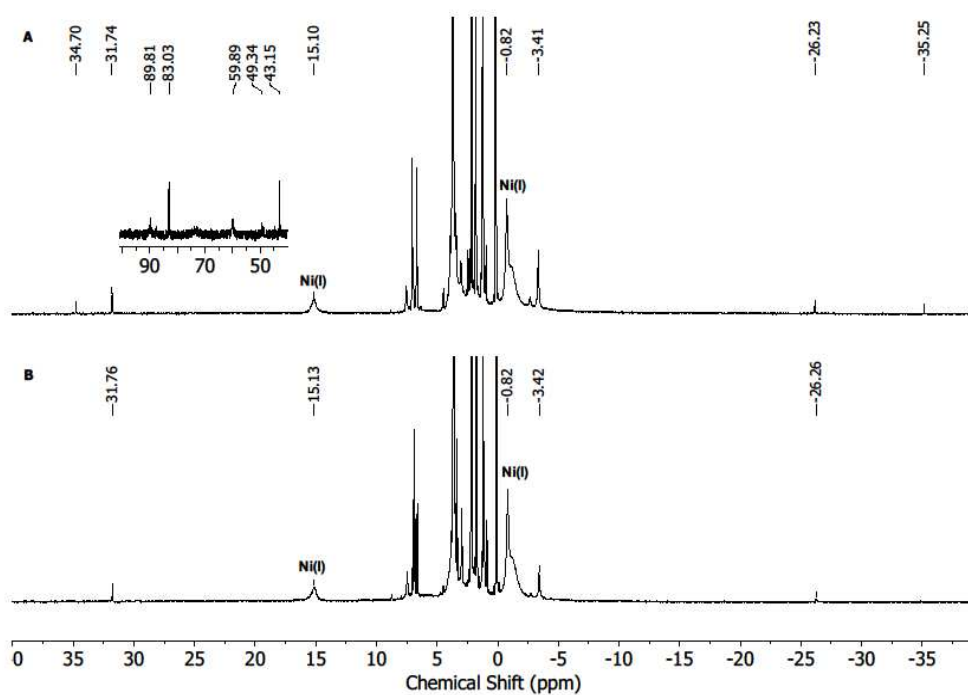
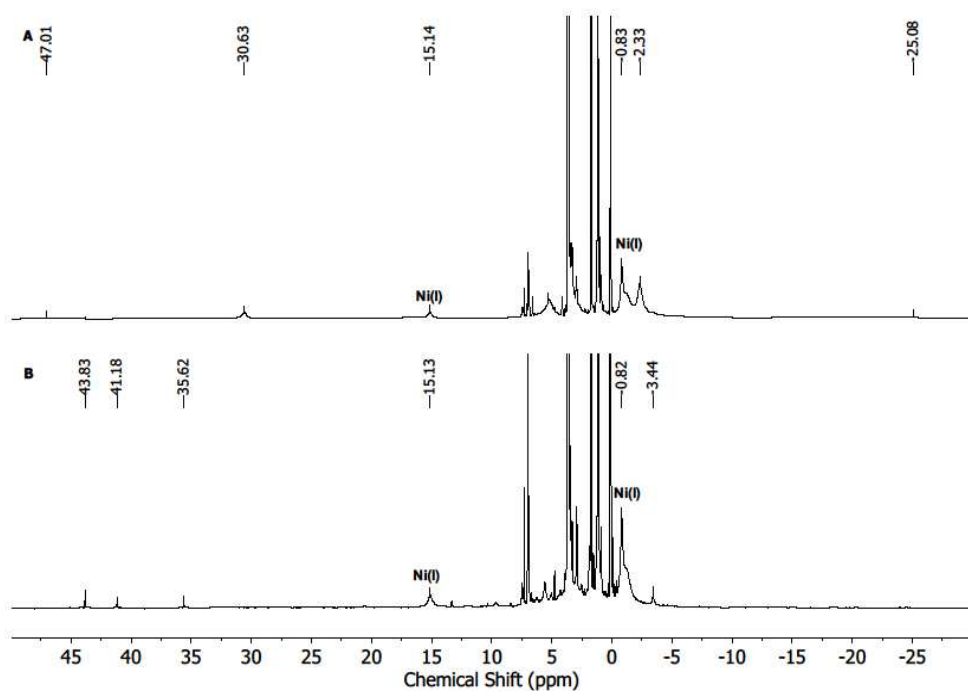


Figure S6.  $^1\text{H}$  NMR spectrum (300 MHz, 300 K,  $\text{THF-d}_8$ ) of a reaction of  $[\text{Ni}(\text{N}\{\text{Dipp}\}\text{SiMe}_3)_2]$  with  $\text{KNHDipp}$  in the presence of 18c6 (A:  $t = 5$  min, B:  $t = 24$  h).



**Figure S7.**  $^1\text{H}$  NMR spectrum (300 MHz, 300 K,  $\text{THF-d}_8$ ) of a reaction of  $[\text{Ni}(\text{N}\{\text{Dipp}\}\text{SiMe}_3)_2]$  with KNHMe in the presence of 18c6. (A: t = 5 min, B: t = 24 h).



**Figure S8.**  $^1\text{H}$  NMR spectrum (300 MHz, 300 K,  $\text{THF-d}_8$ ) of a reaction of  $[\text{Ni}(\text{N}\{\text{Dipp}\}\text{SiMe}_3)_2]$  with LiNHdipp in the presence of 18c6. (A: t = 5 min, B: t = 24 h).

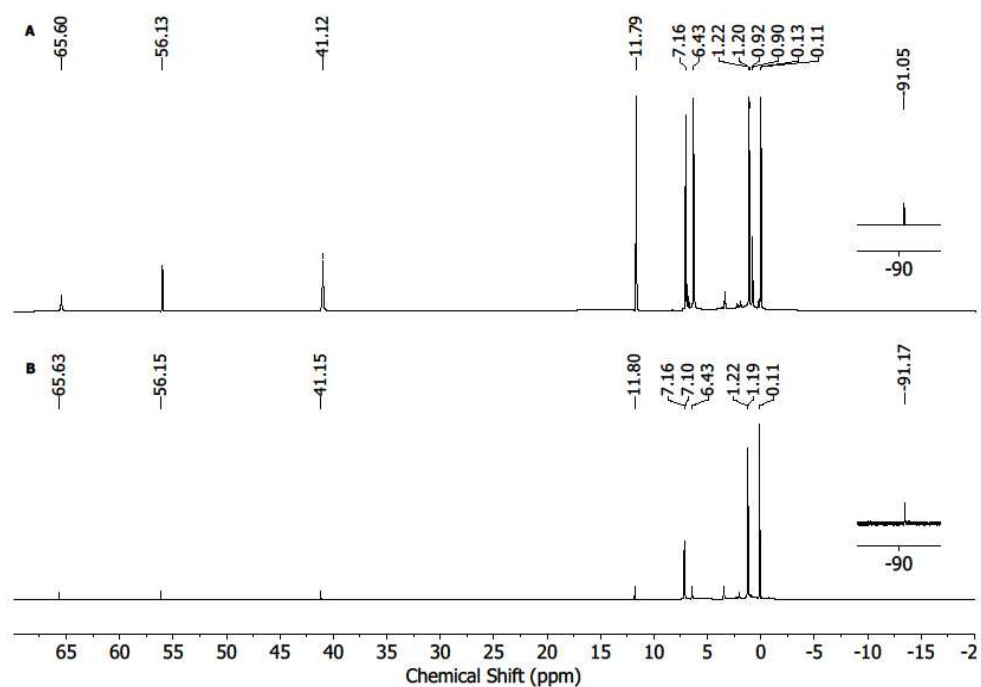


**Figure S9.**  $^1\text{H}$  NMR spectrum (300 MHz, 300 K,  $\text{C}_6\text{D}_6$ ) of a reaction of  $[\text{Ni}(\text{N}\{\text{Dipp}\}\text{SiMe}_3)_2]$  with  $\text{LiNHdipp}$  (A: t = 5 min, B: t = 24 h).

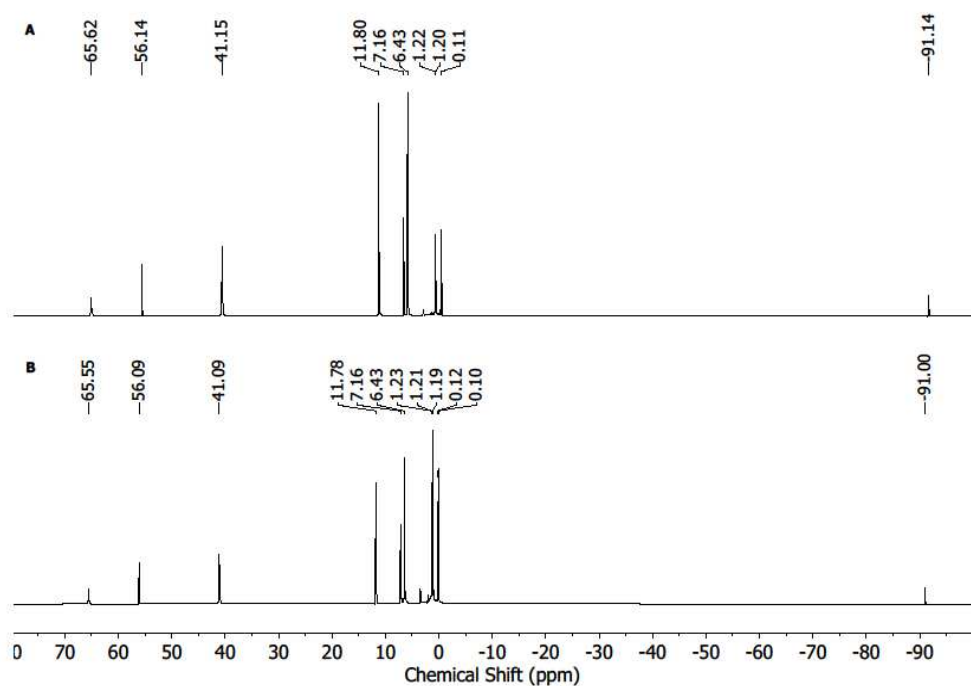


**Figure S10.**  $^1\text{H}$  NMR spectrum (300 MHz, 300 K,  $\text{C}_6\text{D}_6$ ) of a reaction of  $[\text{Ni}(\text{N}\{\text{Dipp}\}\text{SiMe}_3)_2]$  with  $\text{LiNH}^t\text{Bu}$  (A: t = 5 min, B: t = 24 h).

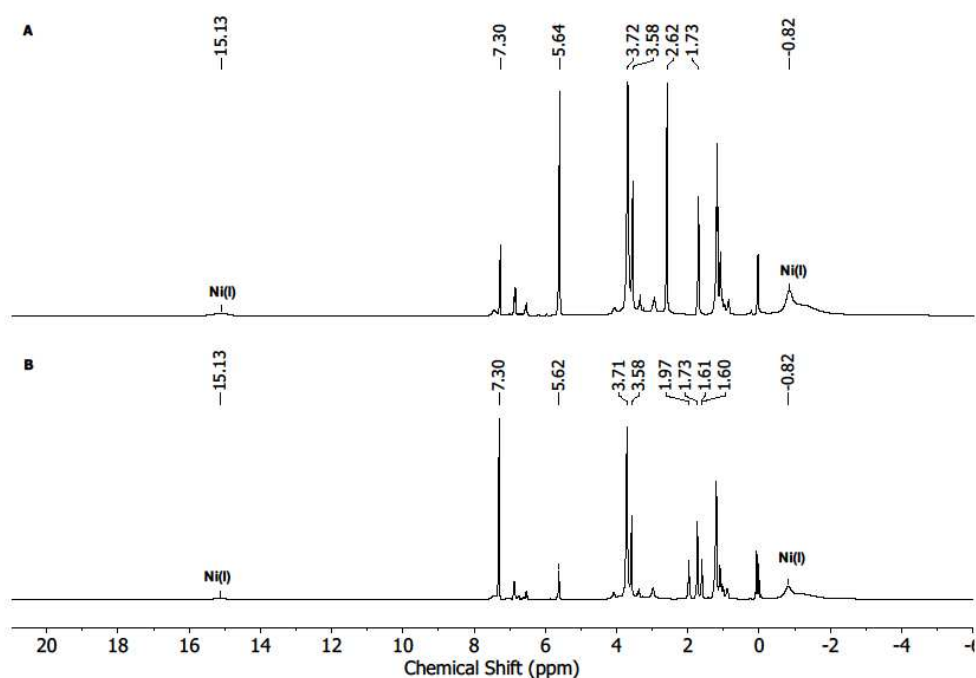


Figure S11.  $^1\text{H}$  NMR spectrum (300 MHz, 300 K,  $\text{THF-d}_8$ ) of a reaction of  $[\text{Ni}(\text{N}\{\text{Dipp}\}\text{SiMe}_3)_2]$  with KNHDipp in the presence of 18c6 and 1,4-CHD (A:  $t = 5$  min, B:  $t = 24$  h).

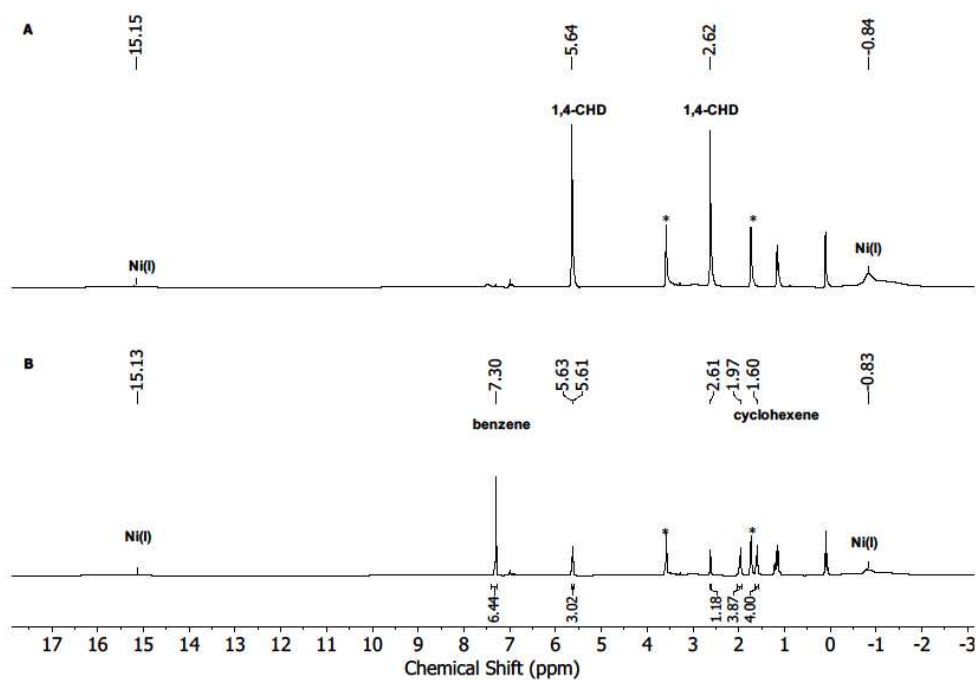
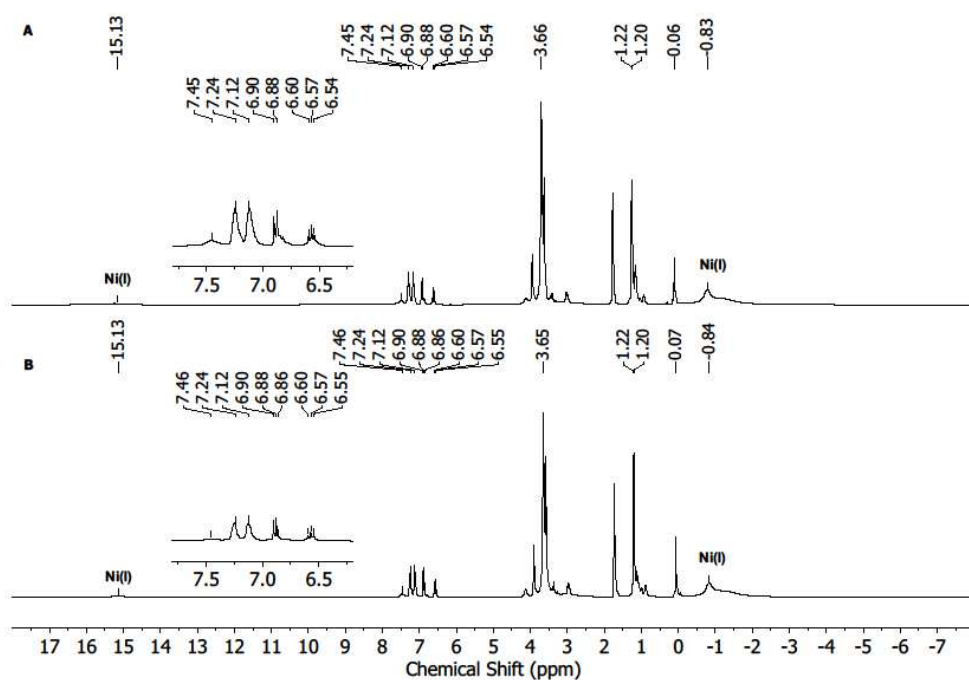
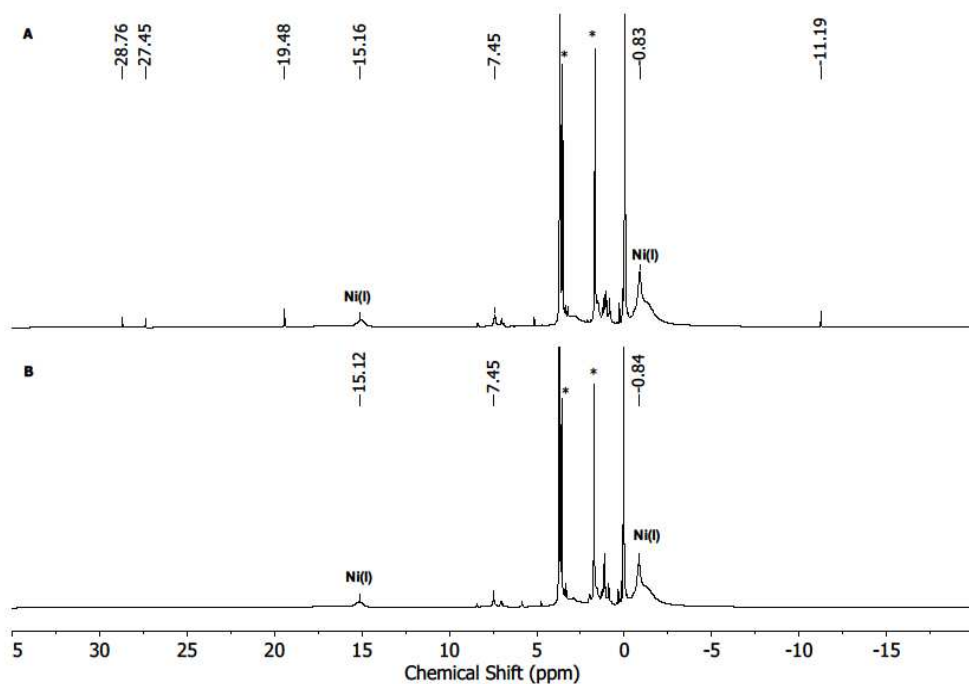


Figure S12.  $^1\text{H}$  NMR spectrum (300 MHz, 300 K,  $\text{THF-d}_8$ ) of a reaction of  $\text{K}[\text{Ni}(\text{N}\{\text{Dipp}\}\text{SiMe}_3)_2]$  with 1,4-CHD (A:  $t = 5$  min, B:  $t = 24$  h), showing a selective conversion to benzene (7.30 ppm (6H)) and cyclohexene (5.61 ppm (2 H), 1.97 ppm (4H), 1.60 ppm (4H)).



**Figure S13.**  $^1\text{H}$  NMR spectrum (300 MHz, 300 K,  $\text{THF-d}_8$ ) of a reaction of  $[\text{Ni}(\text{N}\{\text{Dipp}\}\text{SiMe}_3)_2]$  with KNHDipp in the presence of 18c6 and 9,10-DHA (A: t = 5min, B: t = 24h).



**Figure S14.**  $^1\text{H}$  NMR spectrum (300 MHz, 300 K,  $\text{THF-d}_8$ ) of a reaction of  $[\text{Ni}(\text{N}\{\text{Dipp}\}\text{SiMe}_3)_2]$  with KHMDS in the presence of 18c6 (A: t = 5min, B: t = 24h).



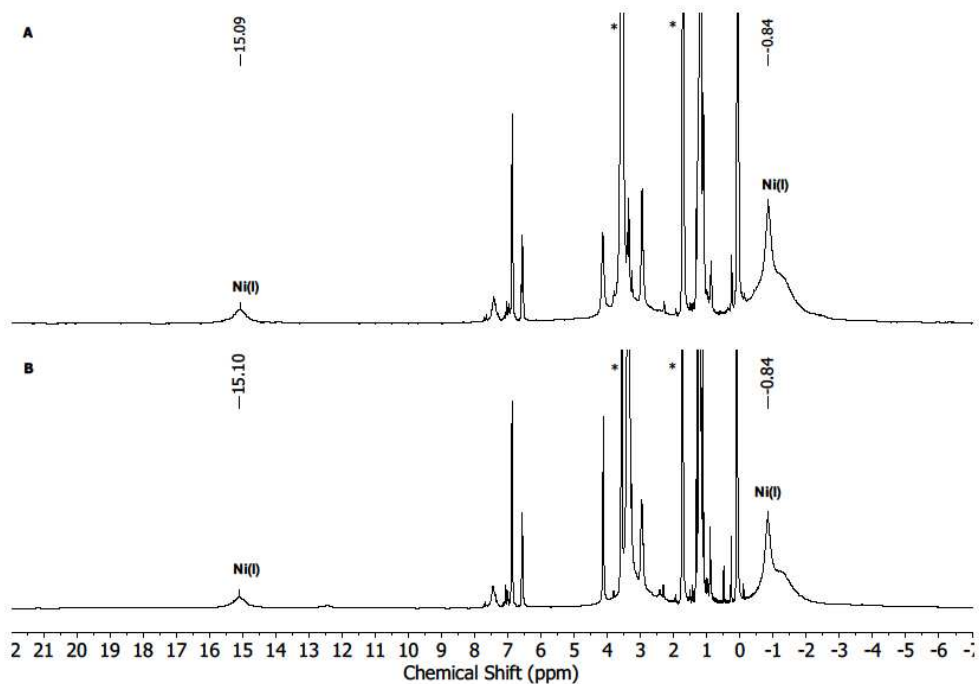


**Figure S15.**  $^1\text{H}$  NMR spectrum (300 MHz, 300 K,  $\text{THF-d}_8$ ) of a reaction of  $[\text{Ni}(\text{N}\{\text{Dipp}\}\text{SiMe}_3)_2]$  with  $\text{KOtBu}$  in the presence of 18c6 (A: t = 5 min, B: t = 24 h).

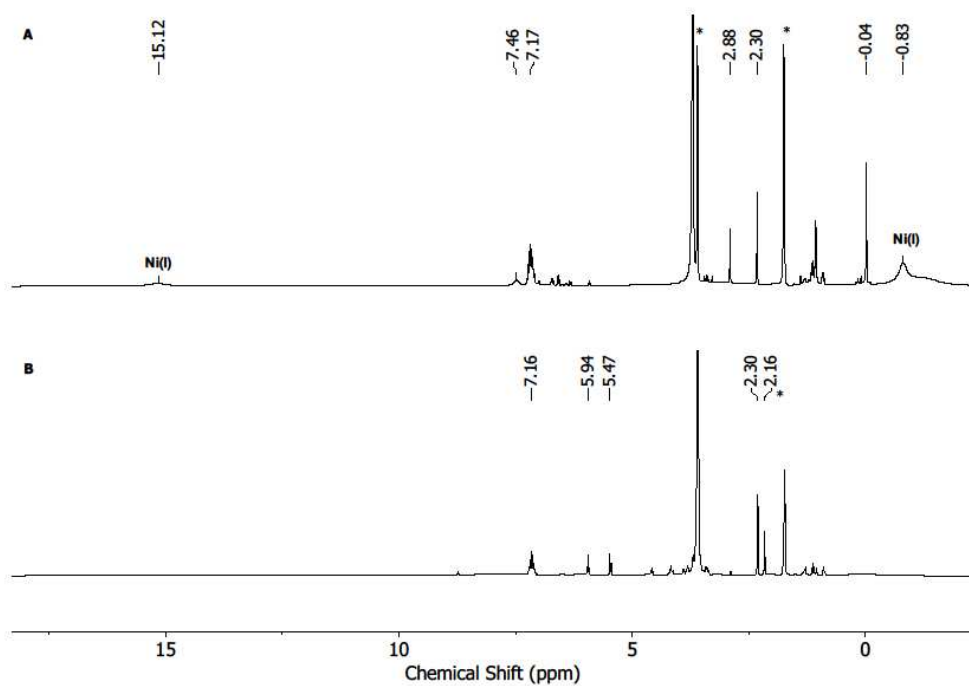


**Figure S16.**  $^1\text{H}$  NMR spectrum (300 MHz, 300 K,  $\text{THF-d}_8$ ) of a reaction of  $[\text{Ni}(\text{N}\{\text{Dipp}\}\text{SiMe}_3)_2]$  with benzyl potassium in the presence of 18c6 (A) and reference of benzyl potassium in the presence of 18c6 (B).

## 2. Electron-paramagnetic-resonance spectroscopy (EPR)

EPR spectra were performed on a Bruker EMXplus (X-band) EPR spectrometer equipped with the Bruker ER4118X-MD5 probehead. The freshly prepared samples were transferred to J. Young quartz EPR tubes and sealed. The solution in the tube was frozen in liquid nitrogen and kept frozen until measured.

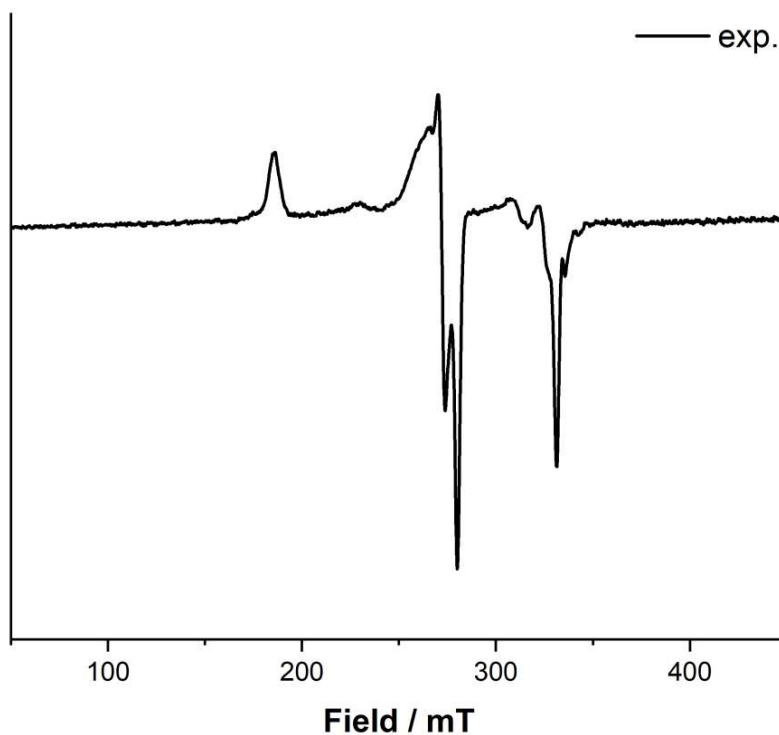
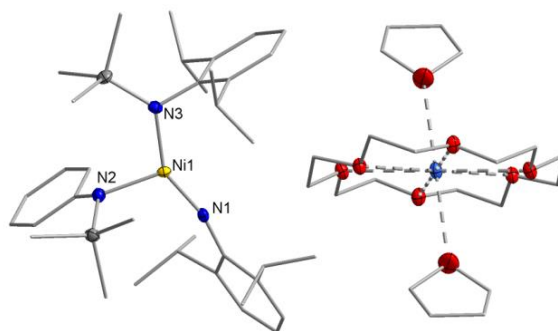


**Figure S1. a):** X-Band EPR spectrum of  $K\{18c6\}[1]$  in frozen Me-THF (frequency 9.352717 GHz, 1.0 mW power, 5 G modulation amplitude) collected at 13.4 K shows a rhombic signal consistent with a low spin nickel (III):  $S_1 = 1/2$ ,  $g_{11} = 2.6$ ,  $g_{12} = 2.2$ ,  $g_{13} = 2.0$ . A second signal set of an unidentified species could be observed. Isolation or further characterisation of the second species, presumable the imido complex prior to the  $SiMe_3$ -group shift ( $K\{18c6\}[Ni(N\{Dipp\}SiMe_3)_2(NPh)]$ ), was not possible.

### 3. X-ray diffraction analysis and molecular structures

**Table S1.** Crystal data and structure refinement for K{18c6}[1].

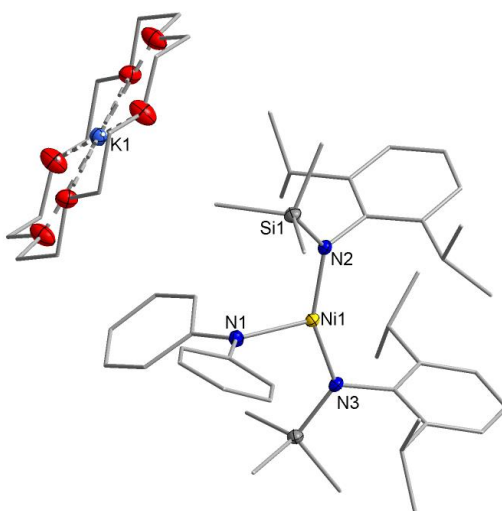
Identification code	K18c6_1
Empirical formula	C <sub>56</sub> H <sub>97</sub> KN <sub>2</sub> NiO <sub>8</sub> Si <sub>2</sub>
Formula weight	1094.35
Temperature/K	99.97
Crystal system	triclinic
Space group	P-1
a/Å	10.1672(5)
b/Å	12.7839(6)
c/Å	25.2499(12)
α/°	83.402(2)
β/°	89.991(2)
γ/°	69.910(2)
Volume/Å <sup>3</sup>	3059.1(3)
Z	2
ρ <sub>calc</sub> /cm <sup>3</sup>	1.188
μ/mm <sup>-1</sup>	0.475
F(000)	1186.0
Crystal size/mm <sup>3</sup>	0.217 × 0.118 × 0.116
Radiation	MoKα (λ = 0.71073)
2θ range for data collection/°	4.27 to 52.16
Index ranges	-12 ≤ h ≤ 12, -15 ≤ k ≤ 15, -31 ≤ l ≤ 31
Reflections collected	51710
Independent reflections	12101 [R <sub>int</sub> = 0.0861, R <sub>sigma</sub> = 0.0782]
Data/restraints/parameters	12101/0/666
Goodness-of-fit on F <sup>2</sup>	1.041
Final R indexes [I >= 2σ (I)]	R <sub>1</sub> = 0.0573, wR <sub>2</sub> = 0.1028
Final R indexes [all data]	R <sub>1</sub> = 0.0967, wR <sub>2</sub> = 0.1143
Largest diff. peak/hole / e Å <sup>-3</sup>	1.15/-0.65



**Figure S17.** Molecular structure of K{18c6}[1] within the crystal.

**Table S2.** Crystal data and structure refinement for K{18c6}[2].

Identification code	K18c6_2
Empirical formula	C <sub>54</sub> H <sub>86</sub> KN <sub>3</sub> NiO <sub>6</sub> Si <sub>2</sub>
Formula weight	1027.24
Temperature/K	100.0
Crystal system	triclinic
Space group	P-1
a/Å	12.3163(4)
b/Å	12.4119(5)
c/Å	19.2449(7)
α/°	90.6120(10)
β/°	96.4580(10)
γ/°	101.0660(10)
Volume/Å <sup>3</sup>	2867.35(18)
Z	2
ρ <sub>calc</sub> /cm <sup>3</sup>	1.190
μ/mm <sup>-1</sup>	0.500
F(000)	1108.0
Crystal size/mm <sup>3</sup>	0.145 × 0.135 × 0.069
Radiation	MoKα (λ = 0.71073)
2θ range for data collection/°	3.906 to 51.385
Index ranges	-14 ≤ h ≤ 15, -15 ≤ k ≤ 15, -23 ≤ l ≤ 23
Reflections collected	45154
Independent reflections	10834 [R <sub>int</sub> = 0.0580, R <sub>sigma</sub> = 0.0593]
Data/restraints/parameters	10834/0/621
Goodness-of-fit on F <sup>2</sup>	1.076
Final R indexes [I >= 2σ (I)]	R <sub>1</sub> = 0.0356, wR <sub>2</sub> = 0.0821
Final R indexes [all data]	R <sub>1</sub> = 0.0531, wR <sub>2</sub> = 0.0857
Largest diff. peak/hole / e Å <sup>-3</sup>	0.26/-0.25

**Figure S18.** Molecular structure of K{18c6}[2]. within the crystal.

**Table S3.** Crystal data and structure refinement for <sup>n</sup>Bu<sub>4</sub>N[3].

Identification code	nBu4N_3
Empirical formula	C <sub>46</sub> H <sub>89</sub> BrN <sub>3</sub> NiSi <sub>2</sub>
Formula weight	879.00
Temperature/K	100.0
Crystal system	orthorhombic
Space group	Pbca
a/Å	18.0823(9)
b/Å	25.176(1)
c/Å	25.469(1)
α/°	90
β/°	90
γ/°	90
Volume/Å <sup>3</sup>	11594.6(10)
Z	8
ρ <sub>calc</sub> /g/cm <sup>3</sup>	1.007
μ/mm <sup>-1</sup>	1.092
F(000)	3816.0
Crystal size/mm <sup>3</sup>	0.104 × 0.102 × 0.085
Radiation	MoKα (λ = 0.71073)
2θ range for data collection/°	3.912 to 50
Index ranges	-21 ≤ h ≤ 21, -29 ≤ k ≤ 29, -30 ≤ l ≤ 30
Reflections collected	129138
Independent reflections	10202 [R <sub>int</sub> = 0.1635, R <sub>sigma</sub> = 0.0859]
Data/restraints/parameters	10202/0/558
Goodness-of-fit on F <sup>2</sup>	1.044
Final R indexes [I ≥ 2σ (I)]	R <sub>1</sub> = 0.0632, wR <sub>2</sub> = 0.1369
Final R indexes [all data]	R <sub>1</sub> = 0.1034, wR <sub>2</sub> = 0.1472
Largest diff. peak/hole / e Å <sup>-3</sup>	0.47/-0.83

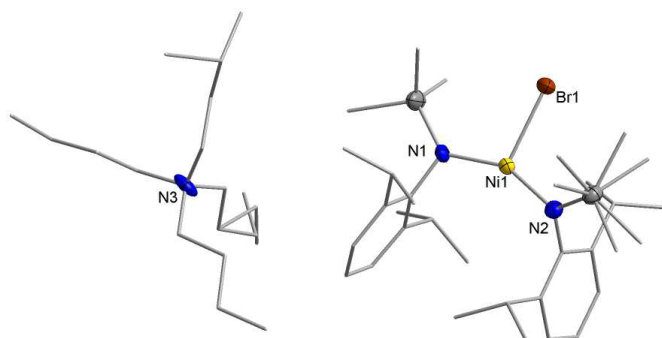


**Figure S19.** Molecular structure of <sup>n</sup>Bu<sub>4</sub>N[3] within the crystal. Disorders on two terminal ethyl groups of the <sup>n</sup>Bu<sub>4</sub>N cation are found.

**6.9.4 Intricate Road to Linear Anionic Nickel(I) Hexamethyldisilazani-  
de  $[\text{Ni}(\text{N}(\text{SiMe}_3)_2)_2]^-$**

## Supporting information

# The Intricate Road to Linear Anionic Nickel(I) Hexamethyldisilazanide $[\text{Ni}(\text{N}(\text{SiMe}_3)_2)_2]^-$

A. Reckziegel,<sup>a</sup> B. Battistella,<sup>b</sup> A. Schmidt,<sup>a</sup> C. G. Werncke,<sup>a,\*</sup>

a) Philipps-University Marburg, Hans-Meerwein-Straße 4, D-35032 Marburg, Germany

b) Institute of Chemistry, Humboldt-Universität zu Berlin, Brook-Taylor-Strasse 2, D-12489, Berlin, Germany

\*E-Mail: [gunnar.werncke@chemie.uni-marburg.de](mailto:gunnar.werncke@chemie.uni-marburg.de)

## Table of Contents

1. NMR spectra of isolated compounds .....	3
2. Reactivity studies.....	6
3. UV-VIS spectra .....	8
4. Temperature dependent measurements.....	10
5. Electron-paramagnetic-resonance spectroscopy (EPR) .....	14
6. X-Ray diffraction analysis and molecular structures .....	16



## 1. NMR spectra of isolated compounds

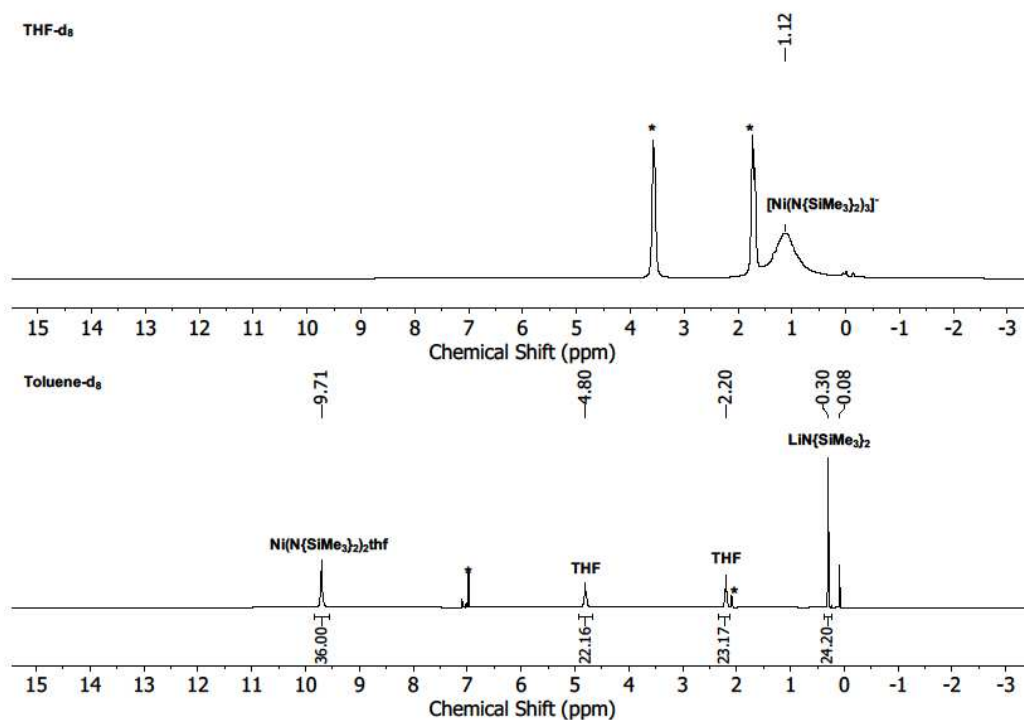


Figure **Figure S1**. <sup>1</sup>H-NMR spectrum (300 MHz, 298 K) of Li(thf)<sub>x</sub>[Ni(N{SiMe<sub>3</sub>})<sub>2</sub>]<sub>3</sub> (Li(thf)<sub>x</sub>[**1**]; R = SiMe<sub>3</sub>) in THF-d<sub>8</sub> (top) and toluene-d<sub>8</sub> (bottom). Signals of the solvent are marked with \*.

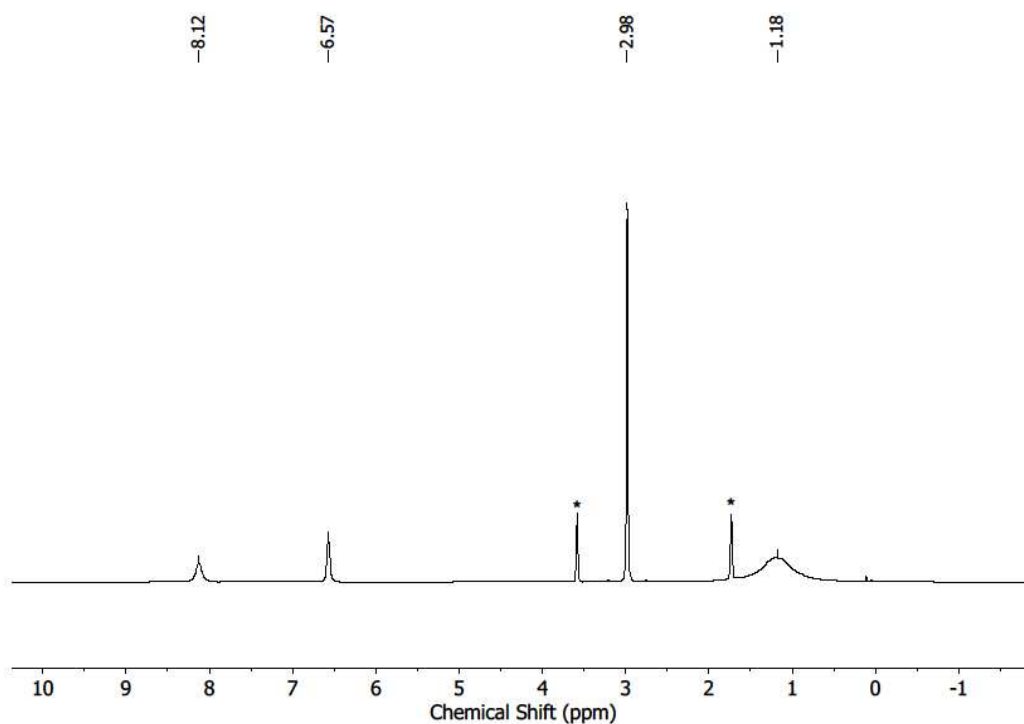
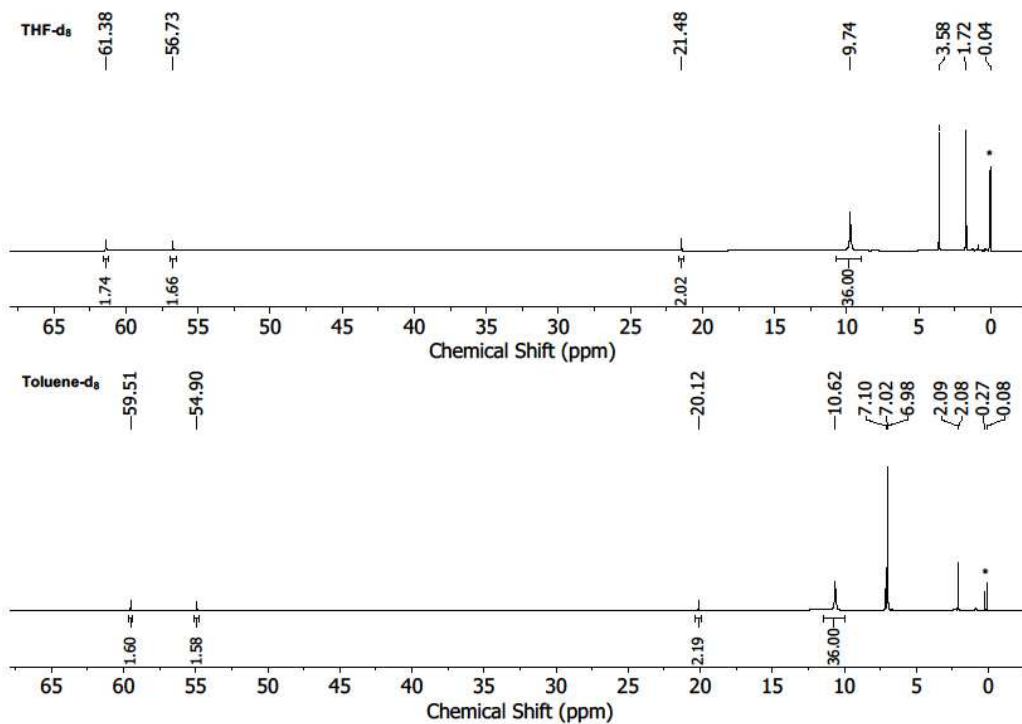
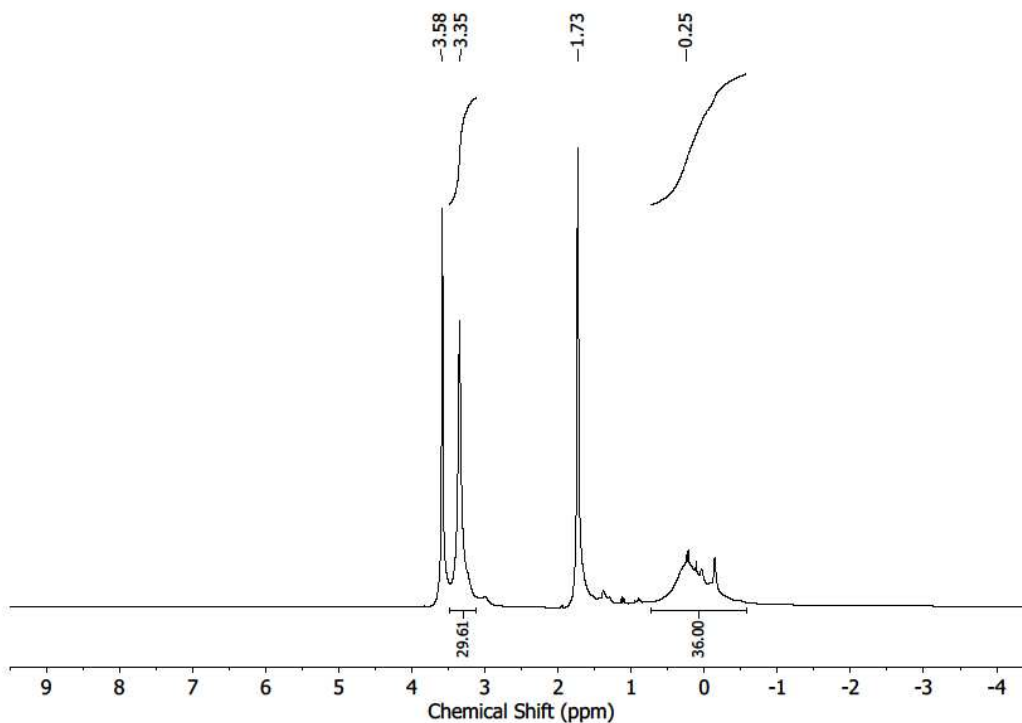


Figure **S2**. <sup>1</sup>H-NMR spectrum (300 MHz, 298 K, THF-d<sub>8</sub>) of Li(dmap)<sub>4</sub>[Ni(N{SiMe<sub>3</sub>})<sub>2</sub>]<sub>3</sub> (Li(dmap)<sub>4</sub>[**1**]). Signals of the solvent are marked with \*.



**Figure S3.**  $^1\text{H-NMR}$  spectrum of  $[\text{Ni}(\text{N}(\text{SiMe}_3)_2)_2(2,2'\text{-bipy})]$  (**[4]**) in  $\text{THF-d}_8$  (top) and  $\text{toluene-d}_8$  (bottom). Signals of decomposition product are marked with \*.



**Figure S4.**  $^1\text{H-NMR}$  spectrum (298 K, 300 MHz) of  $\text{K}\{18\text{c}6\}[\text{Ni}(\text{N}(\text{SiMe}_3)_2)_2]$  ( $\text{K}\{18\text{c}6\}$  (**[6]**)) in  $\text{THF-d}_8$ .

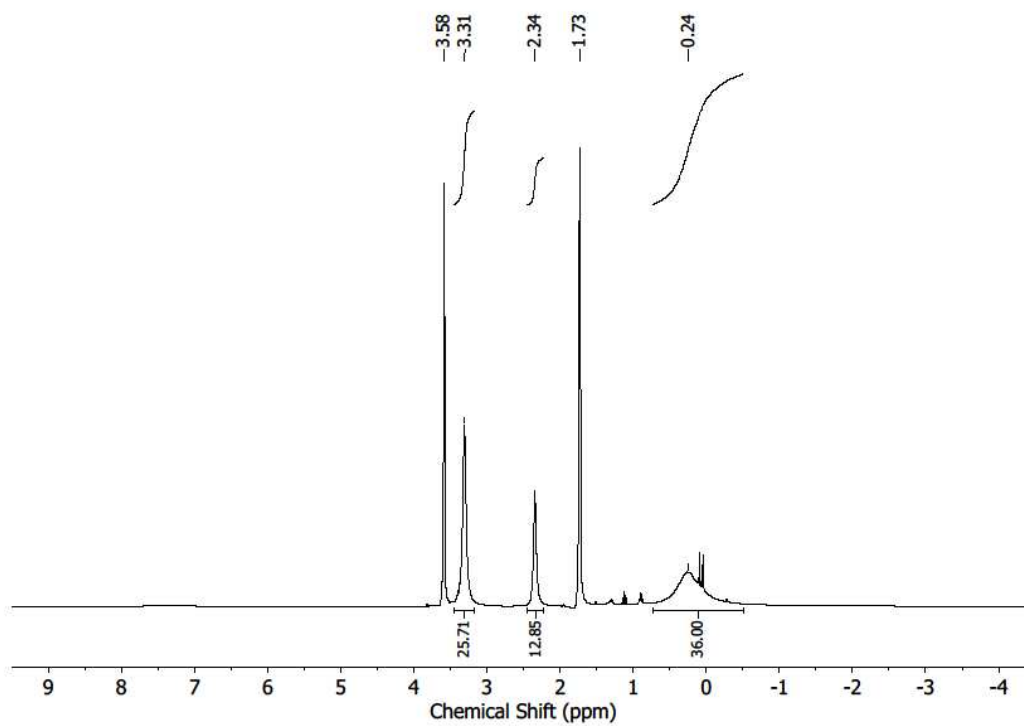


**Figure S5.**  $^1\text{H}$  NMR spectrum (298 K, 300 MHz) of  $\text{K}\{\text{crypt.222}\}[\text{Ni}(\text{N}\{\text{SiMe}_3\}_2)_2]$  ( $\text{K}\{\text{crypt}\}\{\mathbf{6}\}$ ) in  $\text{THF-d}_8$ .

## 2. Reactivity studies

In a typical experiment 15 mg of the respective nickel complex were dissolved in 0.3 ml deuterated solvent (THF- $d_8$ , toluene- $d_8$ ) and added to the substrate dissolved in 0.3 mL of the same solvent.

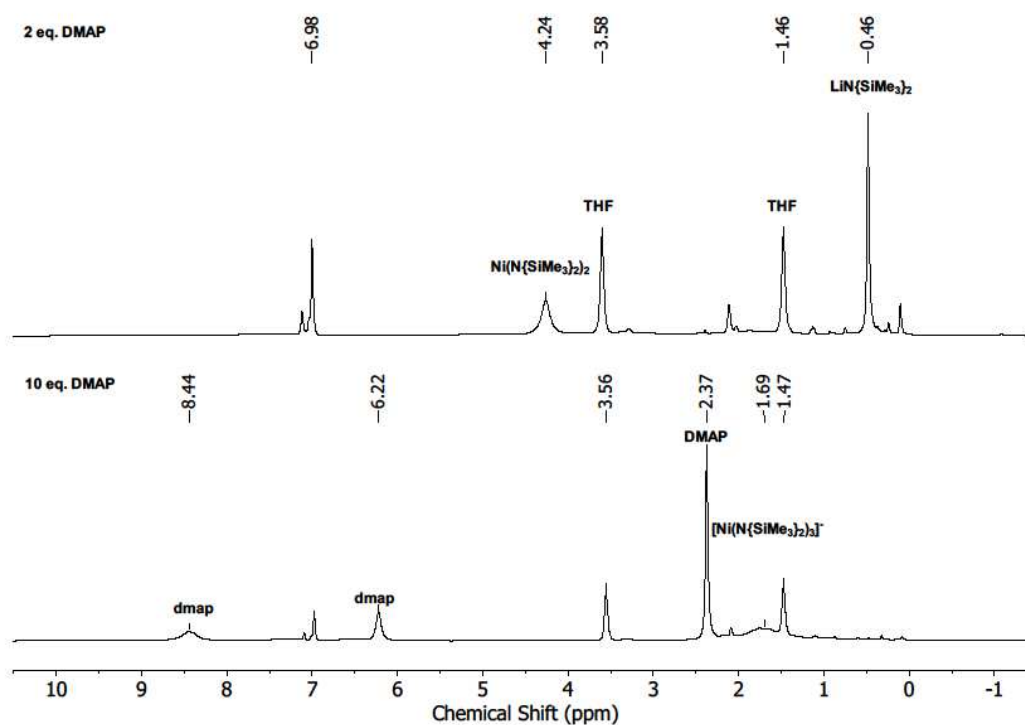


**Figure S6.** *In situ*  $^1\text{H}$  NMR spectrum (298 K, 300 MHz, toluene- $d_8$ ) of  $\text{Li}(\text{thf})_x[\text{Ni}(\text{N}(\text{SiMe}_3)_2)_3]$  ( $\text{Li}(\text{thf})_x[\mathbf{1}]$ ) with 2 (top) and 10 (bottom) equivalents 4-dimethylaminopyridine (dmap).

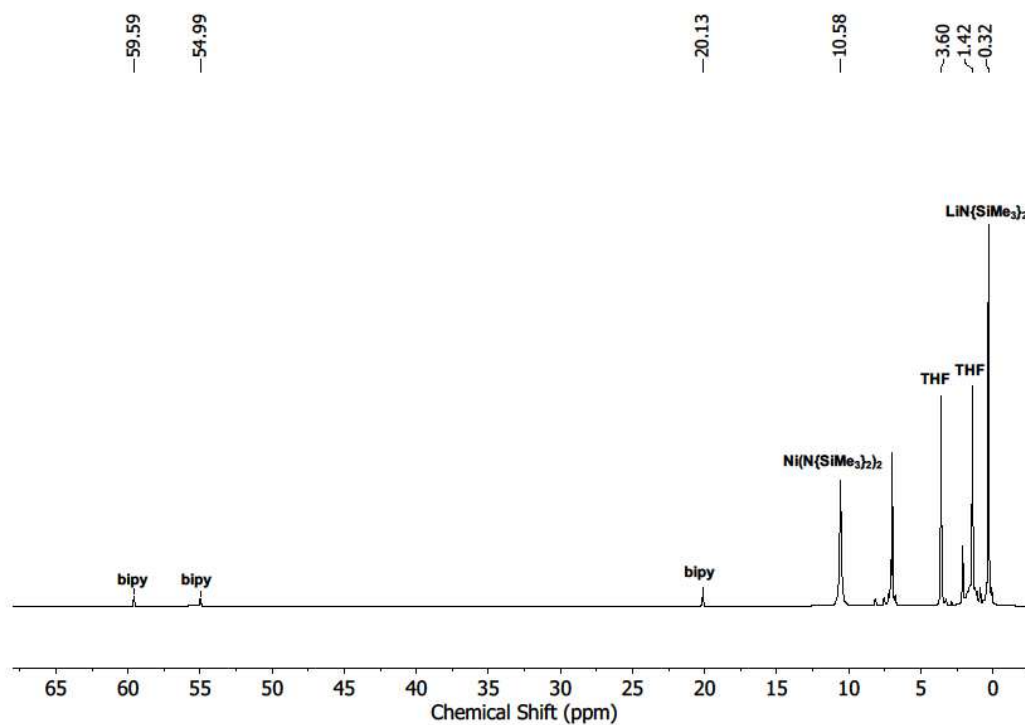


**Figure S7.** *In situ*  $^1\text{H}$  NMR spectrum (298 K, 300 MHz) of  $\text{Li}(\text{thf})_x[\text{Ni}(\text{N}(\text{SiMe}_3)_2)_3]$  ( $\text{Li}(\text{thf})_x[\mathbf{1}]$ ) with 2,2'-bipyridine in toluene- $d_8$ , showing the formation of  $\text{Ni}(\text{N}(\text{SiMe}_3)_2)_2$ bipy ( $\mathbf{4}$ ).

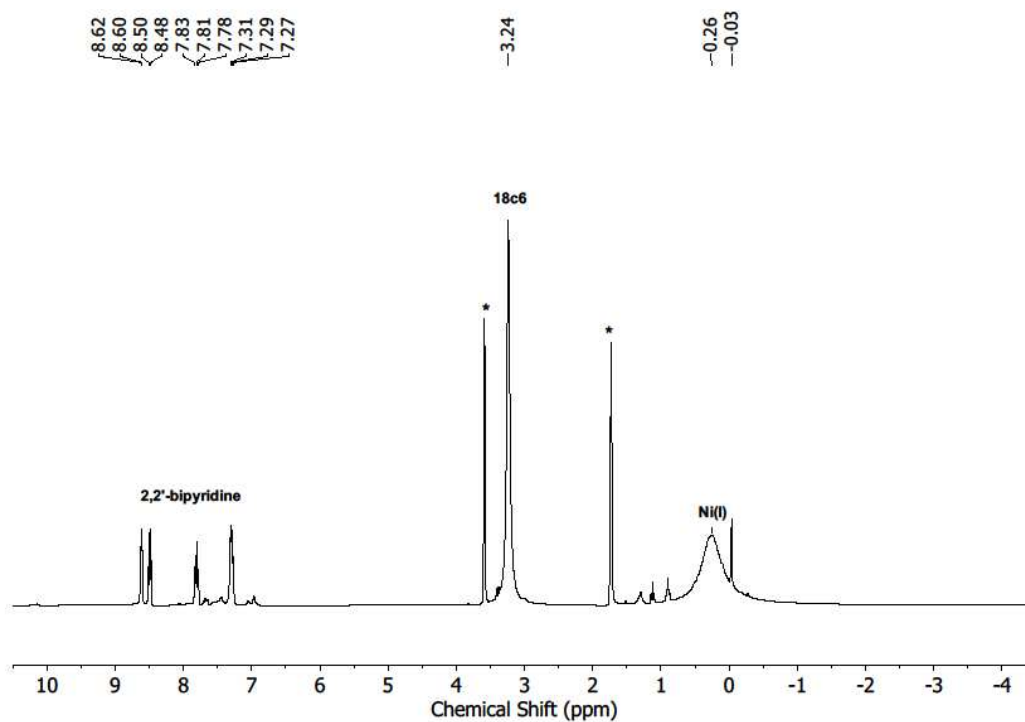


**Figure S8.** *In situ* <sup>1</sup>H NMR spectrum (298 K, 300 MHz) of K{18c6}[Ni(N{SiMe<sub>3</sub>})<sub>2</sub>]<sub>2</sub> (K{18c6}[6]) with 2,2'-bipyridine in THF-d<sub>8</sub>, showing no reaction.

**Table S1.** <sup>1</sup>H NMR shift of the N(SiMe<sub>3</sub>)<sub>2</sub> ligand of mentioned nickel complexes.

compound	coordination geometry	chemical shift /ppm	solvent/temperature
[Ni <sup>II</sup> (N(SiMe <sub>3</sub> ) <sub>3</sub> ) <sup>-</sup> ]	trigonal	1.12	THF-d <sub>8</sub> / 300K
Ni <sup>II</sup> (N(SiMe <sub>3</sub> ) <sub>2</sub> )	linear	10.70 <sup>1</sup>	toluene-d <sub>8</sub> / 300K
[Ni <sup>II</sup> (N(SiMe <sub>3</sub> ) <sub>2</sub> (thf))]	trigonal	9.11	toluene-d <sub>8</sub> / 183K
[Ni <sup>II</sup> (N(SiMe <sub>3</sub> ) <sub>2</sub> (dmap) <sub>2</sub> )]	square planar	4.24	toluene-d <sub>8</sub> / 300K
[Ni <sup>II</sup> (N(SiMe <sub>3</sub> ) <sub>2</sub> bipy)]	tetrahedral	9.74	toluene-d <sub>8</sub> / 300K
[Ni <sup>I</sup> (N(SiMe <sub>3</sub> ) <sub>2</sub> ) <sub>2</sub> ] <sup>-</sup>	linear	0.25	THF-d <sub>8</sub> / 300K

### 3. UV-VIS spectra

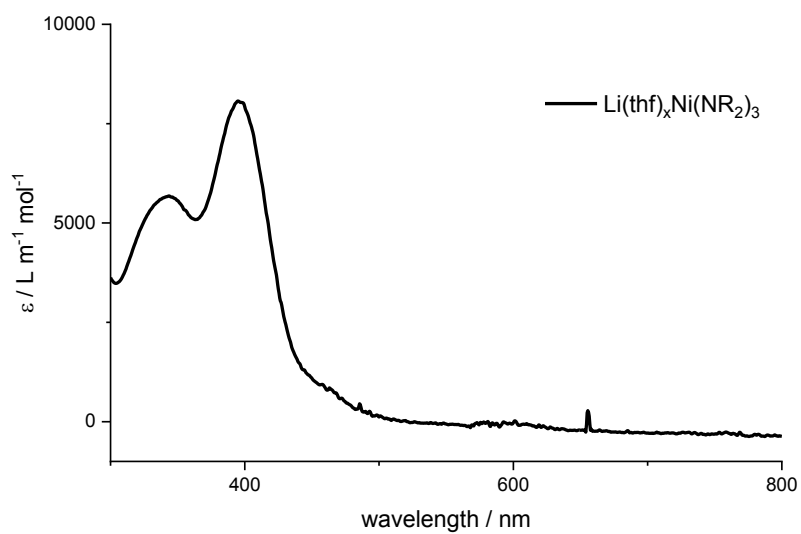


**Figure S9.** UV-VIS spectra of  $\text{Li}(\text{thf})_x\text{Ni}(\text{N}\{\text{SiMe}_3\}_2)_3$  ( $\text{Li}(\text{thf})_x\text{[1]}$ ) in THF at 300 K.

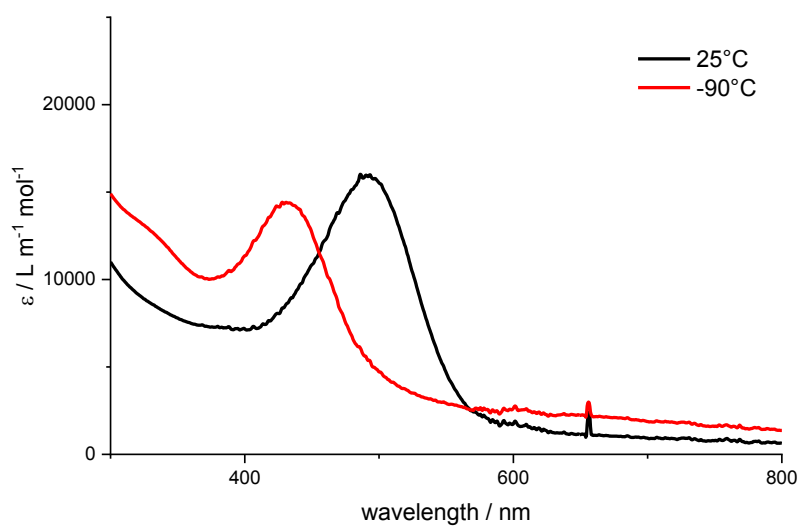


**Figure S10.** UV-VIS spectra of  $\text{Li}(\text{thf})_x\text{Ni}(\text{N}\{\text{SiMe}_3\}_2)_3$  ( $\text{Li}(\text{thf})_x\text{[1]}$ ) in toluene at 300 K (black) and 183 K (red).

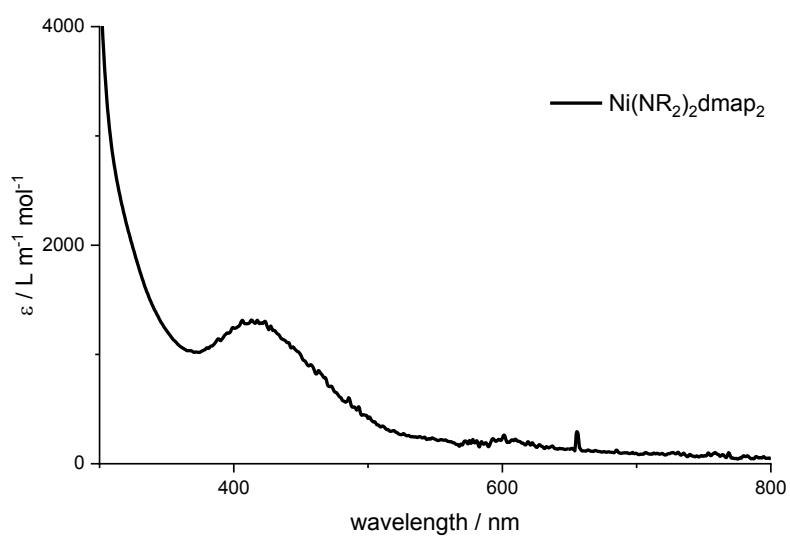


**Figure S11.** UV-VIS spectra of  $[\text{Ni}(\text{N}(\text{SiMe}_3)_2)_2(\text{dmap})_2]$  (**2**) in toluene.

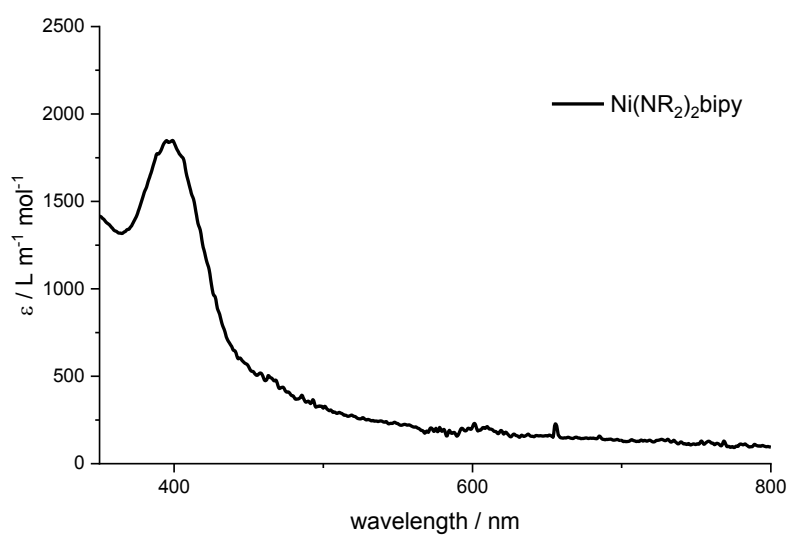


**Figure S12.** UV-VIS spectra of  $[\text{Ni}(\text{N}(\text{SiMe}_3)_2)_2\text{bipy}]$  (**4**) in toluene.

#### 4. Temperature dependent measurements

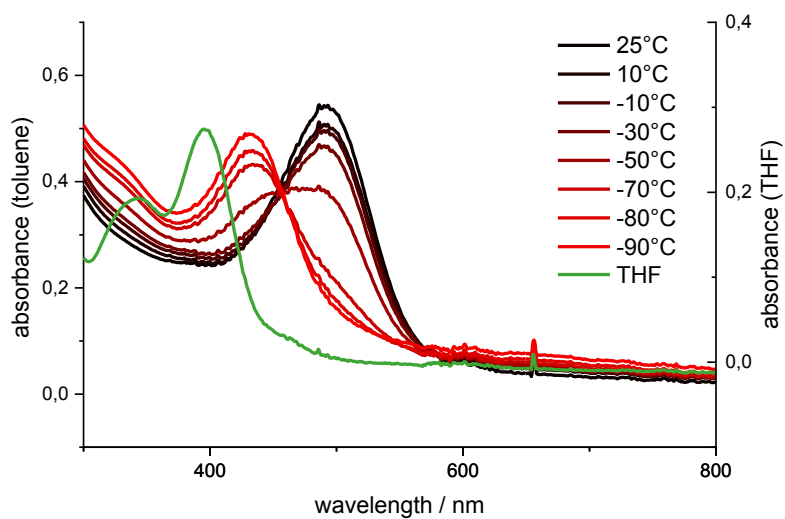


**Figure S13.** UV-VIS spectra of  $\text{Li}(\text{thf})_x\text{Ni}(\text{N}\{\text{SiMe}_3\}_2)_3$  ( $\text{Li}(\text{thf})_x[1]$ ) in THF (green) and in toluene at 300 K to 183 K (black to red).

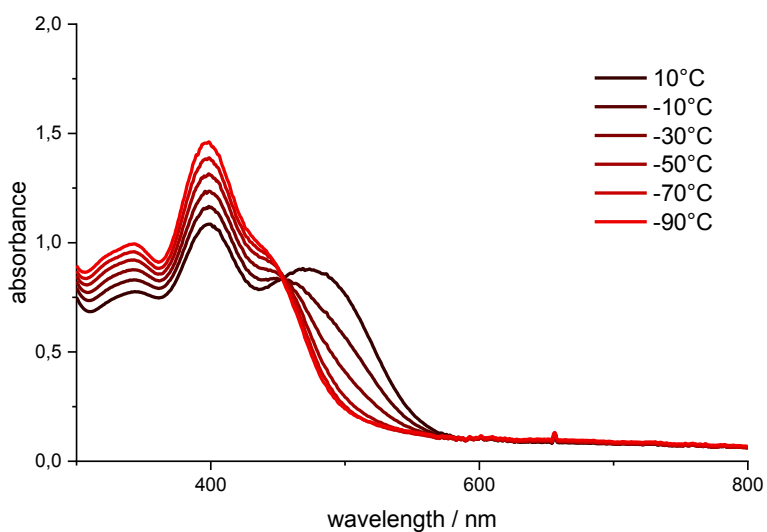


**Figure S14.** UV-VIS spectra of  $\text{Li}(\text{thf})_x\text{Ni}(\text{N}\{\text{SiMe}_3\}_2)_3$  ( $\text{Li}(\text{thf})_x[1]$ ) in  $\text{Et}_2\text{O}$  290 K to 183 K.



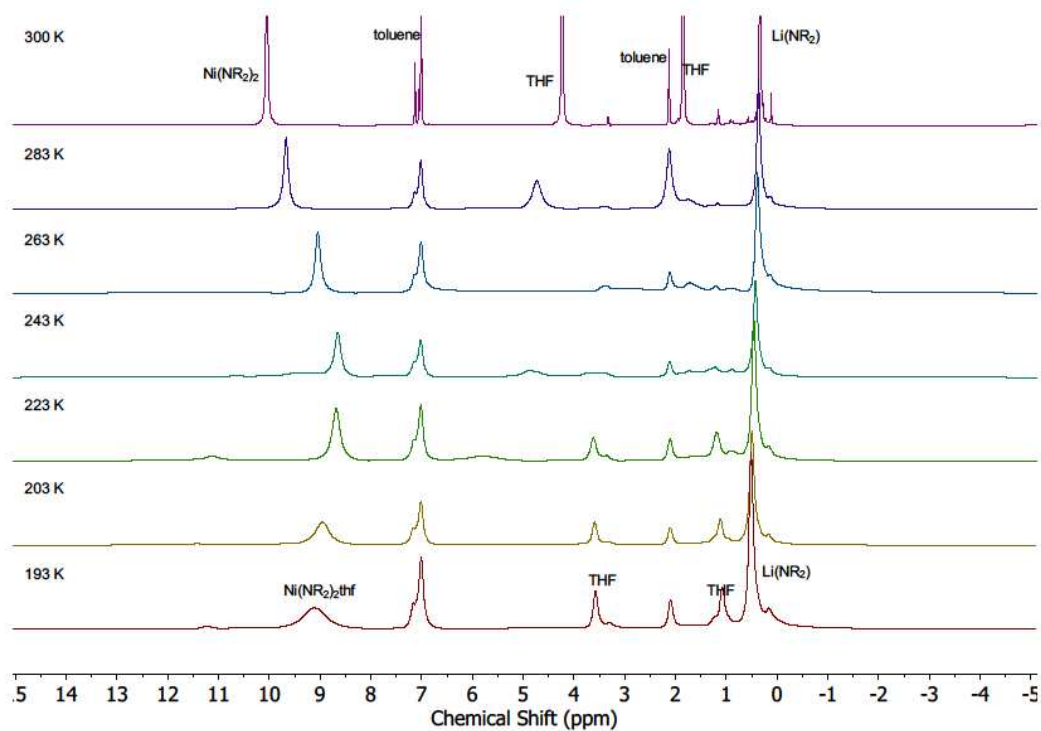


**Figure S15.** Temperature dependent  $^1\text{H}$  NMR spectrum (500 MHz) of  $\text{Li}(\text{thf})_x[\text{Ni}(\text{N}(\text{SiMe}_3)_2)_3]$  ( $\text{Li}(\text{thf})_x[\mathbf{1}]$ ) in  $\text{toluene-d}_8$  from 300 K to 193 K.

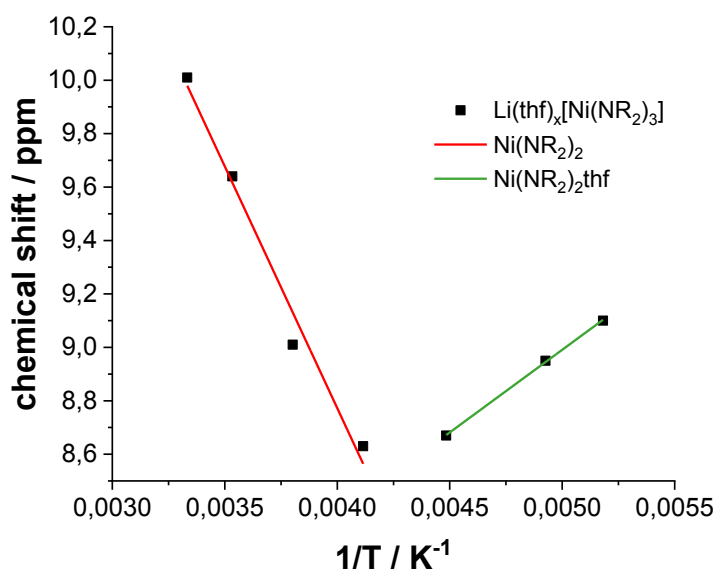


**Figure S16.** Curie-Weiss plot of the temperature dependent  $^1\text{H}$  NMR spectra (500 MHz) of  $\text{Li}(\text{thf})_x[\text{Ni}(\text{N}(\text{SiMe}_3)_2)_3]$  ( $\text{Li}(\text{thf})_x[\mathbf{1}]$ ) in  $\text{THF-d}_8$  from 300 K to 193 K.

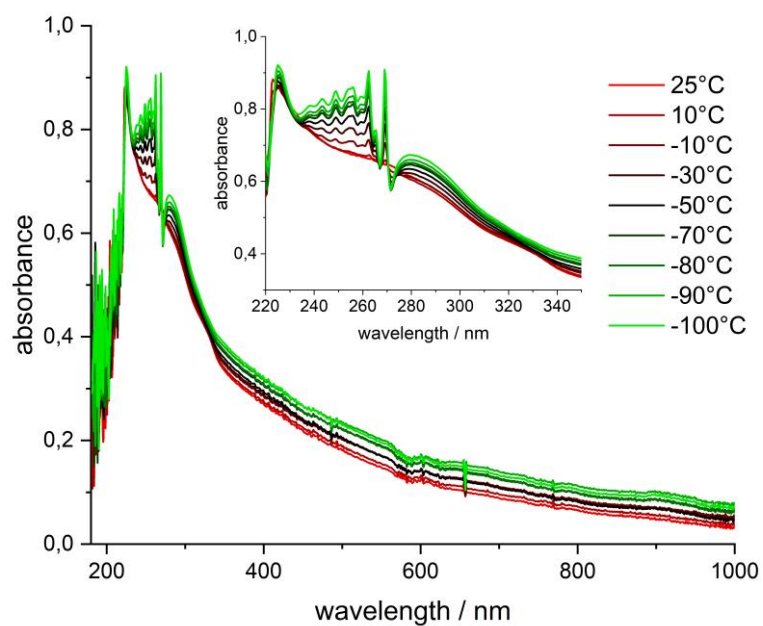


**Figure S17.** Temperature dependent UV-VIS spectra of  $\text{K}\{18\text{c}6\}\text{Ni}(\text{N}\{\text{SiMe}_3\}_2)_2$  ( $\text{K}\{18\text{c}6\}[\mathbf{6}]$ ) in  $\text{Et}_2\text{O}$ .

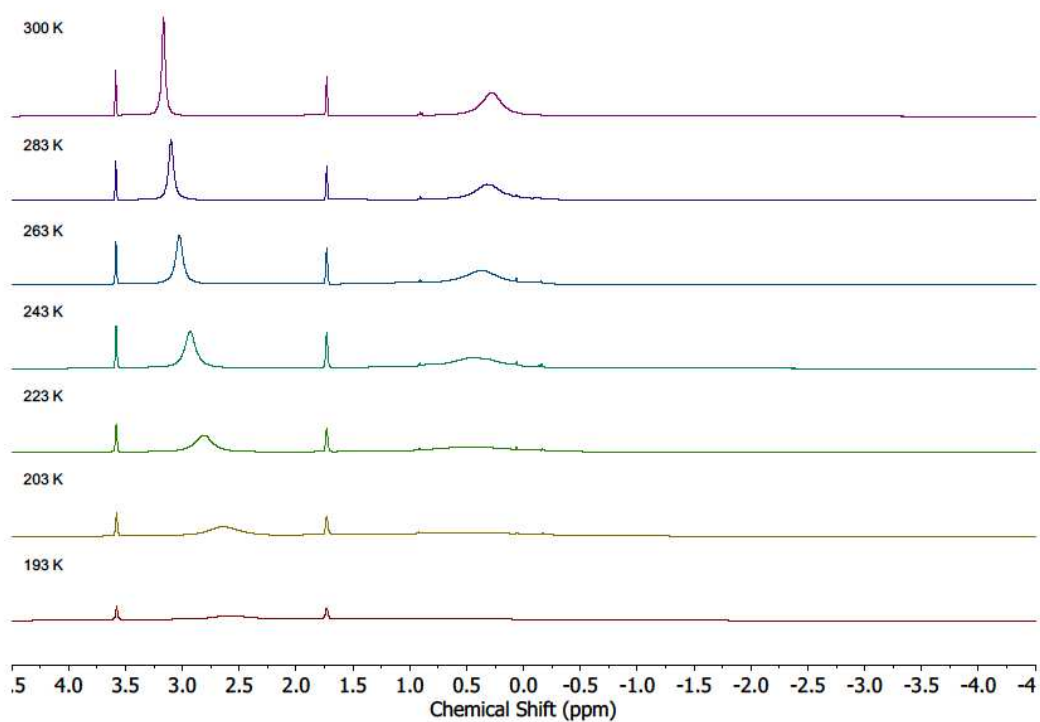


**Figure S18.** Stacked temperature dependent  $^1\text{H}$  NMR spectra (500 MHz) of  $\text{K}\{18\text{c}6\}[\text{Ni}(\text{N}\{\text{SiMe}_3\}_2)_2]$  ( $\text{K}\{18\text{c}6\}[\mathbf{6}]$ ) in  $\text{THF-d}_8$  from 300 K to 193 K.

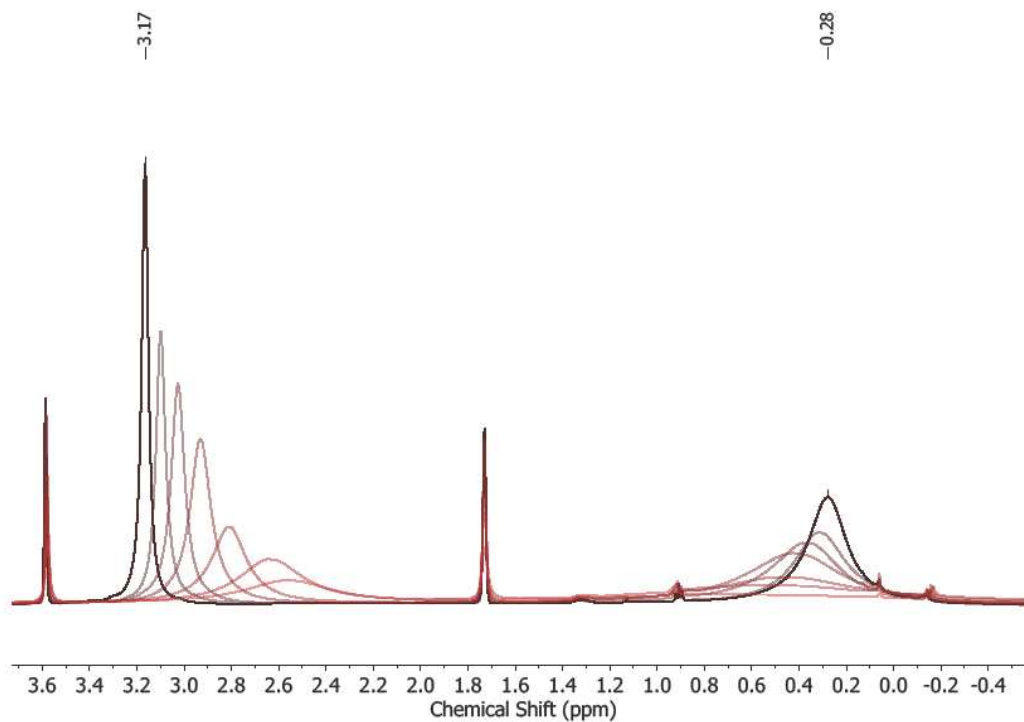


**Figure S19.** Overlay of temperature dependent  $^1\text{H}$  NMR spectra (500 MHz) of  $\text{K}\{18\text{c}6\}[\text{Ni}(\text{N}\{\text{SiMe}_3\}_2)_2]$  ( $\text{K}\{18\text{c}6\}[6]$ ) in  $\text{THF-d}_8$  from 300 K to 193 K.

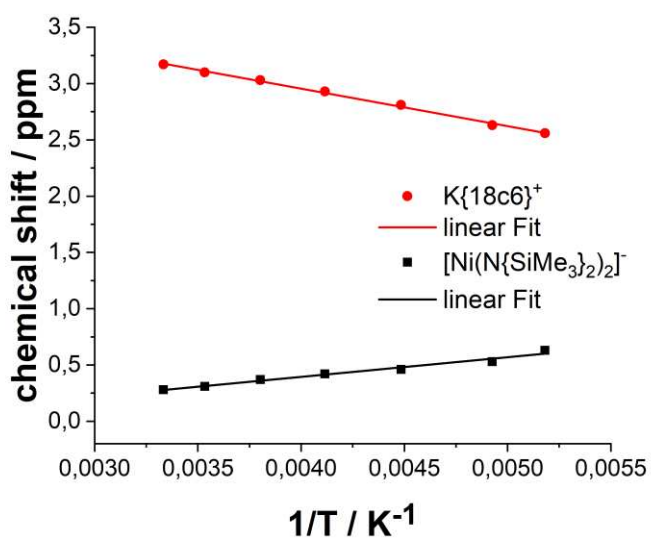


**Figure S20.** Curie-Weiss plot of the temperature dependent  $^1\text{H}$  NMR spectra (500 MHz) of  $\text{K}\{18\text{c}6\}[\text{Ni}(\text{N}\{\text{SiMe}_3\}_2)_2]$  ( $\text{K}\{18\text{c}6\}[6]$ ) in  $\text{THF-d}_8$  from 300 K to 193 K.  $y_0(\text{K}\{18\text{c}6\}^+) = 4.28$  ppm,  $y_0([\text{Ni}(\text{N}\{\text{SiMe}_3\}_2)_2]^-) = -0.30$  ppm.

## 5. Electron-paramagnetic-resonance spectroscopy (EPR)

X-Band EPR spectra were performed on a Bruker EMXplus (X-band) EPR spectrometer equipped with the Bruker ER4118X-MD5 probehead. The freshly prepared samples were transferred to J. Young quartz EPR tubes and sealed. The solution in the tube was frozen in liquid nitrogen and kept frozen until measured.

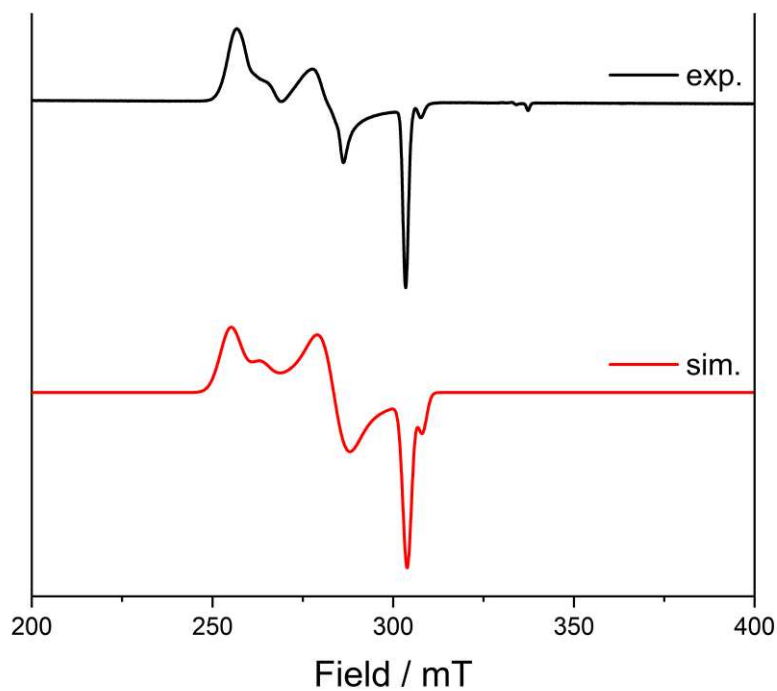


**Figure S21. a):** X-Band EPR spectrum of  $K\{18c6\}[6]$  in frozen Me-THF (frequency 9.352656 GHz, 1.0 mW power, 5 G modulation amplitude) collected at 13.3 K (black). Simulation of data using the program EasySpin (red).<sup>2</sup> Fitting parameters:  $S_1 = 1/2$ ,  $g_{11} = 2.62$ ,  $g_{12} = 2.36$ ,  $g_{13} = 2.2$ , weight = 0.8;  $S_2 = 1/2$ ,  $g_{21} = 2.54$ ,  $g_{22} = 2.35$ ,  $g_{23} = 2.17$ , weight = 0.2.

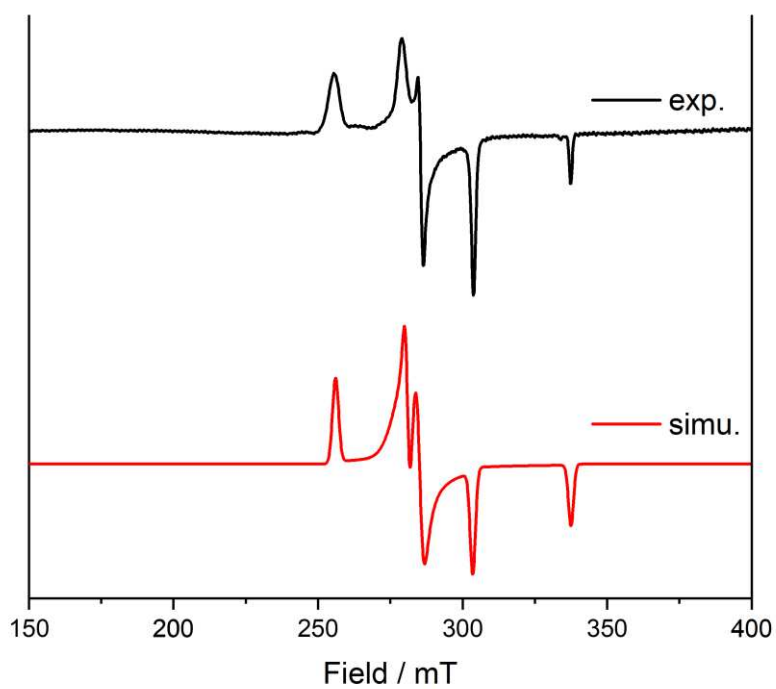


**Figure S22. a):** X-Band EPR spectrum of K{crypt}[6] in frozen Me-THF (frequency 9.354146 GHz, 1.0 mW power, 5 G modulation amplitude) collected at 12.74 K (black). Simulation of data using the program EasySpin (red).<sup>2</sup>Fitting parameters:  $S_1 = 1/2$ ,  $g_{11} = 2.40$ ,  $g_{12} = 2.35$ ,  $g_{13} = 2.20$ , weight = 0.35;  $S_2 = 1/2$ ,  $g_{21} = 2.61$ ,  $g_{22} = 2.38$ ,  $g_{23} = 1.98$ , weight = 0.65.

## 6. X-Ray diffraction analysis and molecular structures

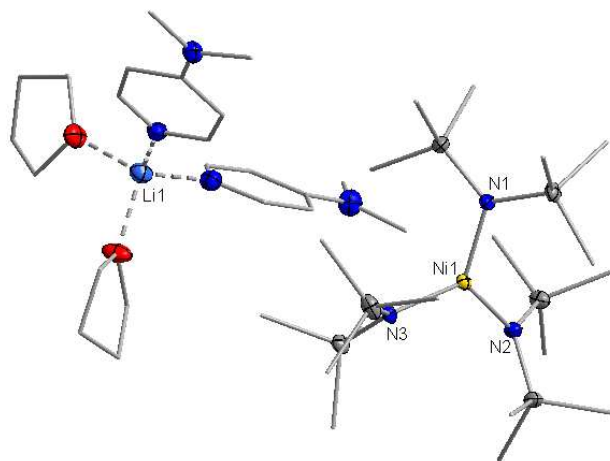
Data for Li(thf)<sub>2</sub>(dmap)<sub>2</sub>[**1**] (CCDC 2141857), Li(dmap)<sub>4</sub>[**1**] (CCDC 2141859), **2** (CCDC 2141856), **3** (CCDC 2141853), **4** (CCDC 2141854), K[**5**] (CCDC 2141860), K{18c6}[**6**] (CCDC 2141858), K{18c6}(thf)<sub>2</sub>[**6**] (CCDC 2141861);K{crypt}[**6**] (CCDC 2141855) were collected at 100 K on a Bruker Quest D8 diffractometer using a graphite-monochromated Mo-K $\alpha$  radiation and equipped with an *Oxford Instrument* The structures have been solved using either OLEX SHELXT V2014/1<sup>3</sup> and refined by means of least-squares procedures on a F<sup>2</sup> with the aid of the program SHELXL-2016/6<sup>2</sup> include in the software package WinGX version 1.63<sup>4</sup> or using CRYSTALS.<sup>5</sup> The scattering factors for all the atoms were used as listed in the *International Tables for X-Ray Crystallography*.<sup>6</sup> All non-hydrogen atoms were refined anisotropically. All hydrogens atoms were refined by using a riding model. Absorption corrections were introduced by using the MULTISCAN program.<sup>7</sup> Drawings of molecules are performed with the programs DIAMOND and POV-Ray with 50% probability displacement ellipsoids for non-H atoms. Depiction of H atoms is omitted for clarity.

**Table S2.** Selected bond lengths and angles (°) of K{18c6}[**6**] and K{18c6}thf<sub>2</sub>[**6**].

compound		bond lengths/ bond angles
K{18c6}[ <b>6</b> ]	Ni1–N1	1.8656(10) Å
	N1–Ni1–N1'	180°
	Si1–N1–N1'–Si2	14.66(8)
K{18c6}thf <sub>2</sub> [ <b>6</b> ]	Ni1–N1	1.854(2) Å
	Ni1–N2	1.863(2) Å
	N1–Ni1–N2	179.59(12)°
	Si1–N1–N2–Si3	26.9(2)

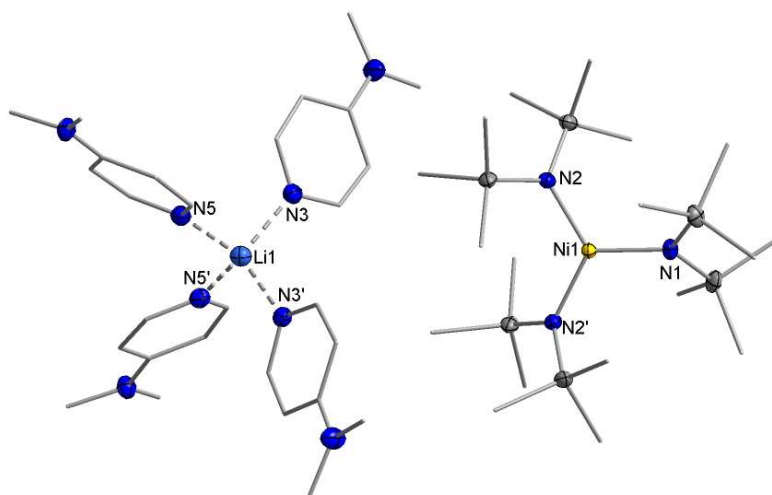
**Table S3. Crystal data and structure refinement for Li(thf)<sub>2</sub>(dmap)<sub>2</sub>[1].**

Identification code	Li_thf2_dmap2_1
Empirical formula	C <sub>40</sub> H <sub>90</sub> LiN <sub>7</sub> NiO <sub>2</sub> Si <sub>6</sub>
Formula weight	935.37
Temperature/K	100.0
Crystal system	monoclinic
Space group	<i>P</i> 2 <sub>1</sub> / <i>c</i>
<i>a</i> /Å	12.1205(5)
<i>b</i> /Å	21.2905(9)
<i>c</i> /Å	21.2981(9)
$\alpha$ /°	90
$\beta$ /°	92.822(2)
$\gamma$ /°	90
Volume/Å <sup>3</sup>	5489.3(4)
<i>Z</i>	4
$\rho_{\text{calc}}$ /g/cm <sup>3</sup>	1.132
$\mu$ /mm <sup>-1</sup>	0.512
<i>F</i> (000)	2040.0
Crystal size/mm <sup>3</sup>	0.305 × 0.204 × 0.198
Radiation	MoK $\alpha$ ( $\lambda$ = 0.71073)
2 $\theta$ range for data collection/°	3.87 to 64.094
Index ranges	-14 ≤ <i>h</i> ≤ 17, -29 ≤ <i>k</i> ≤ 31, -30 ≤ <i>l</i> ≤ 31
Reflections collected	113762
Independent reflections	17235 [ <i>R</i> <sub>int</sub> = 0.0342, <i>R</i> <sub>sigma</sub> = 0.0313]
Data/restraints/parameters	17235/0/536
Goodness-of-fit on <i>F</i> <sup>2</sup>	1.040
Final <i>R</i> indexes [ <i>I</i> ≥ 2 $\sigma$ ( <i>I</i> )]	<i>R</i> <sub>1</sub> = 0.0399, <i>wR</i> <sub>2</sub> = 0.0834
Final <i>R</i> indexes [all data]	<i>R</i> <sub>1</sub> = 0.0589, <i>wR</i> <sub>2</sub> = 0.0901
Largest diff. peak/hole / e Å <sup>-3</sup>	0.55/-0.46

**Figure S23. Molecular structure of Li(thf)<sub>2</sub>(dmap)<sub>2</sub>[1] within the crystal.**

**Table S4. Crystal data and structure refinement for Li(dmap)<sub>4</sub>[1].**

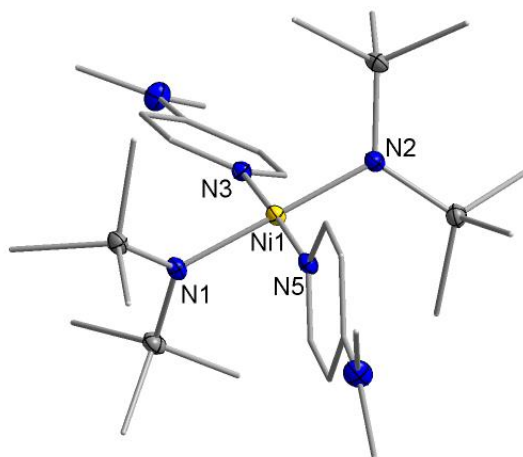
Identification code	Li_dmap4_1
Empirical formula	C <sub>46</sub> H <sub>94</sub> LiN <sub>11</sub> NiSi <sub>6</sub>
Formula weight	1035.51.51
Temperature/K	100.0
Crystal system	monoclinic
Space group	<i>C</i> 2/ <i>c</i>
<i>a</i> /Å	24.1102(8)
<i>b</i> /Å	18.8728(8)
<i>c</i> /Å	17.2234(8)
$\alpha$ /°	90
$\beta$ /°	129.466(2)
$\gamma$ /°	90
Volume/Å <sup>3</sup>	6050.3(5)
<i>Z</i>	4
$\rho_{\text{calc}}$ /g/cm <sup>3</sup>	1.137
$\mu$ /mm <sup>-1</sup>	0.478
<i>F</i> (000)	2248.0
Crystal size/mm <sup>3</sup>	0.352 × 0.213 × 0.150
Radiation	MoK $\alpha$ ( $\lambda$ = 0.71073)
2 $\theta$ range for data collection/°	4.316 to 53.62
Index ranges	-30 ≤ <i>h</i> ≤ 30, -23 ≤ <i>k</i> ≤ 23, -21 ≤ <i>l</i> ≤ 21
Reflections collected	71202
Independent reflections	6480 [ <i>R</i> <sub>int</sub> = 0.0747, <i>R</i> <sub>sigma</sub> = 0.0371]
Data/restraints/parameters	6480/0/308
Goodness-of-fit on <i>F</i> <sup>2</sup>	0.926
Final <i>R</i> indexes [ <i>I</i> ≥ 2 $\sigma$ ( <i>I</i> )]	<i>R</i> <sub>1</sub> = 0.0345, <i>wR</i> <sub>2</sub> = 0.1095
Final <i>R</i> indexes [all data]	<i>R</i> <sub>1</sub> = 0.0422, <i>wR</i> <sub>2</sub> = 0.1157
Largest diff. peak/hole / e Å <sup>-3</sup>	0.64/-0.37

**Figure S24. Molecular structure of Li(dmap)<sub>4</sub>[1] within the crystal.**



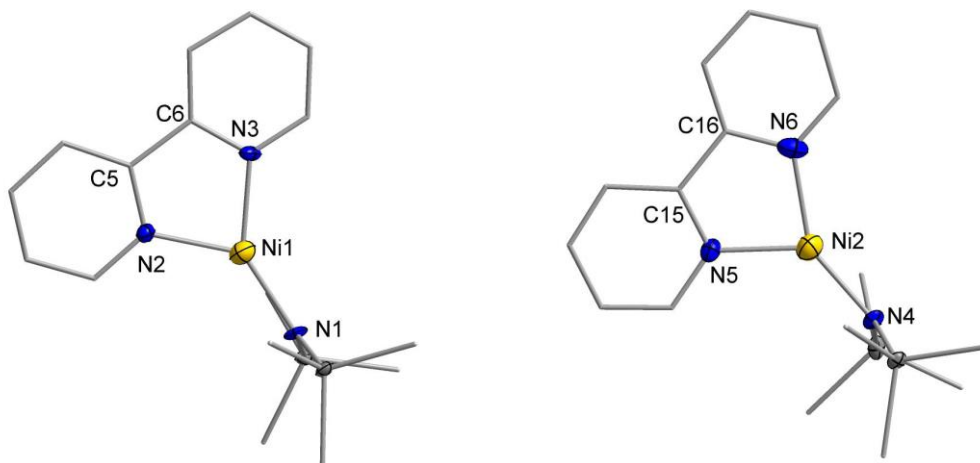
**Table S5. Crystal data and structure refinement for [2].**

Identification code	2
Empirical formula	C <sub>26</sub> H <sub>56</sub> N <sub>6</sub> NiSi <sub>4</sub>
Formula weight	623.83
Temperature/K	100.0
Crystal system	triclinic
Space group	$P\bar{1}$
a/Å	10.1763(3)
b/Å	11.7706(4)
c/Å	16.4839(6)
$\alpha/^\circ$	83.0950(10)
$\beta/^\circ$	82.5220(10)
$\gamma/^\circ$	65.4640(10)
Volume/Å <sup>3</sup>	1776.09(10)
Z	2
$\rho_{\text{calc}}/\text{g}/\text{cm}^3$	1.166
$\mu/\text{mm}^{-1}$	0.705
F(000)	676.0
Crystal size/mm <sup>3</sup>	0.152 × 0.111 × 0.087
Radiation	MoK $\alpha$ ( $\lambda = 0.71073$ )
2 $\theta$ range for data collection/ $^\circ$	4.404 to 51.552
Index ranges	-12 ≤ h ≤ 12, -14 ≤ k ≤ 14, -20 ≤ l ≤ 20
Reflections collected	56072
Independent reflections	6793 [R <sub>int</sub> = 0.1569, R <sub>sigma</sub> = 0.1084]
Data/restraints/parameters	6793/0/344
Goodness-of-fit on F <sup>2</sup>	0.990
Final R indexes [I ≥ 2 $\sigma$ (I)]	R <sub>1</sub> = 0.0329, wR <sub>2</sub> = 0.0626
Final R indexes [all data]	R <sub>1</sub> = 0.0818, wR <sub>2</sub> = 0.0661
Largest diff. peak/hole / e Å <sup>-3</sup>	0.35/-0.64

**Figure S25. Molecular structure of [2] within the crystal.**

**Table S6. Crystal data and structure refinement for [3].**

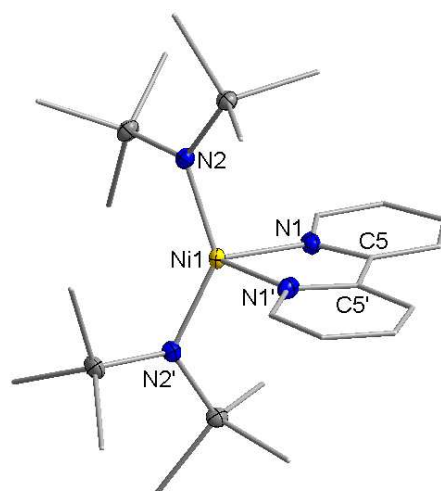
Identification code	3
Empirical formula	C <sub>32</sub> H <sub>52</sub> N <sub>6</sub> Ni <sub>2</sub> Si <sub>4</sub>
Formula weight	750.57
Temperature/K	100.0
Crystal system	triclinic
Space group	$P\bar{1}$
a/Å	8.2455(6)
b/Å	11.4486(8)
c/Å	22.1000(15)
$\alpha/^\circ$	102.88(2)
$\beta/^\circ$	93.031(2)
$\gamma/^\circ$	101.199
Volume/Å <sup>3</sup>	1984.9(2)
Z	2
$\rho_{\text{calc}}/\text{g/cm}^3$	1.256
$\mu/\text{mm}^{-1}$	1.098
F(000)	796.0
Crystal size/mm <sup>3</sup>	0.555 × 0.266 × 0.143
Radiation	MoK $\alpha$ ( $\lambda = 0.71073$ )
2 $\theta$ range for data collection/ $^\circ$	3.734 to 52.222
Index ranges	-10 ≤ h ≤ 10, -14 ≤ k ≤ 14, -27 ≤ l ≤ 27
Reflections collected	24593
Independent reflections	7797 [R <sub>int</sub> = 0.0375, R <sub>sigma</sub> = 0.0472]
Data/restraints/parameters	7797/0/409
Goodness-of-fit on F <sup>2</sup>	1.059
Final R indexes [I ≥ 2 $\sigma$ (I)]	R <sub>1</sub> = 0.0725, wR <sub>2</sub> = 0.2216
Final R indexes [all data]	R <sub>1</sub> = 0.0928, wR <sub>2</sub> = 0.2397
Largest diff. peak/hole / e Å <sup>-3</sup>	1.29/-1.28



**Figure S26. Molecular structure of [3] within the crystal.**

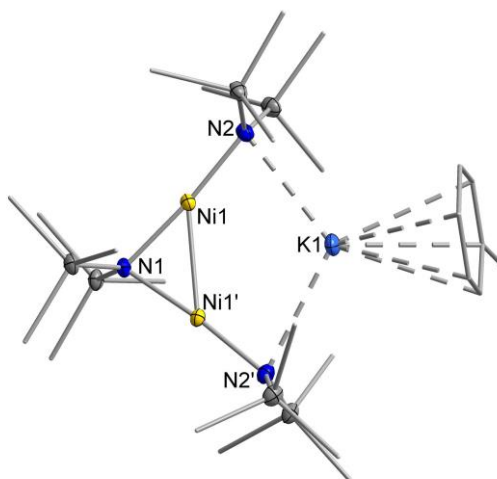
**Table S7. Crystal data and structure refinement for 4.**

Identification code	4
Empirical formula	C <sub>22</sub> H <sub>44</sub> N <sub>4</sub> NiSi <sub>4</sub>
Formula weight	535.68
Temperature/K	100.0
Crystal system	monoclinic
Space group	C2/c
a/Å	13.1730(8)
b/Å	16.1653(10)
c/Å	14.9430(9)
α/°	90
β/°	107.837(2)
γ/°	90
Volume/Å <sup>3</sup>	3029.1(3)
Z	4
ρ <sub>calc</sub> /g/cm <sup>3</sup>	1.175
μ/mm <sup>-1</sup>	0.815
F(000)	1152.0
Crystal size/mm <sup>3</sup>	0.592 × 0.116 × 0.114
Radiation	MoKα (λ = 0.71073)
2θ range for data collection/°	4.11 to 60.882
Index ranges	-18 ≤ h ≤ 18, -22 ≤ k ≤ 22, -20 ≤ l ≤ 21
Reflections collected	43979
Independent reflections	4592 [R <sub>int</sub> = 0.0393, R <sub>sigma</sub> = 0.0274]
Data/restraints/parameters	4592/0/147
Goodness-of-fit on F <sup>2</sup>	1.052
Final R indexes [I >= 2σ (I)]	R <sub>1</sub> = 0.0311, wR <sub>2</sub> = 0.0655
Final R indexes [all data]	R <sub>1</sub> = 0.0437, wR <sub>2</sub> = 0.0694
Largest diff. peak/hole / e Å <sup>-3</sup>	0.36/-0.31

**Figure S27. Molecular structure of 4 within the crystal.**

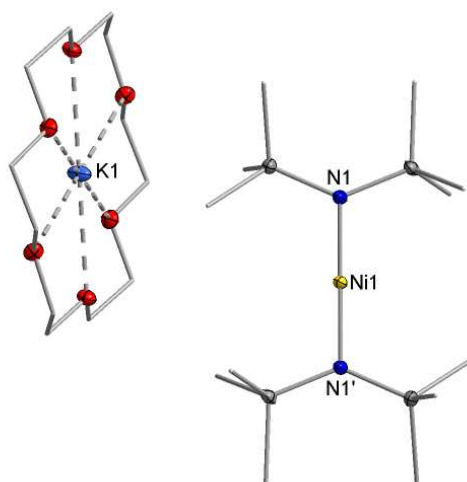
**Table S8. Crystal data and structure refinement for K(toluene)[5].**

Identification code	K_5
Empirical formula	C <sub>25</sub> H <sub>61</sub> KN <sub>3</sub> Ni <sub>2</sub> Si <sub>6</sub>
Formula weight	728.82
Temperature/K	100.0
Crystal system	monoclinic
Space group	C2/c
a/Å	19.7018(9)
b/Å	12.9492(6)
c/Å	18.3439(13)
α/°	90
β/°	120.9380(10)
γ/°	90
Volume/Å <sup>3</sup>	4014.1(4)
Z	4
ρ <sub>calc</sub> /g/cm <sup>3</sup>	1.206
μ/mm <sup>-1</sup>	1.239
F(000)	1564.0
Crystal size/mm <sup>3</sup>	0.149 × 0.139 × 0.139
Radiation	MoKα (λ = 0.71073)
2θ range for data collection/°	3.998 to 52.4
Index ranges	-24 ≤ h ≤ 24, -16 ≤ k ≤ 16, -22 ≤ l ≤ 22
Reflections collected	46252
Independent reflections	4026 [R <sub>int</sub> = 0.0248, R <sub>sigma</sub> = 0.0170]
Data/restraints/parameters	4026/0/191
Goodness-of-fit on F <sup>2</sup>	1.060
Final R indexes [I ≥ 2σ (I)]	R <sub>1</sub> = 0.0223, wR <sub>2</sub> = 0.0501
Final R indexes [all data]	R <sub>1</sub> = 0.0290, wR <sub>2</sub> = 0.0523
Largest diff. peak/hole / e Å <sup>-3</sup>	0.28/-0.23

**Figure S28. Molecular structure of K(toluene)[5] within the crystal.**

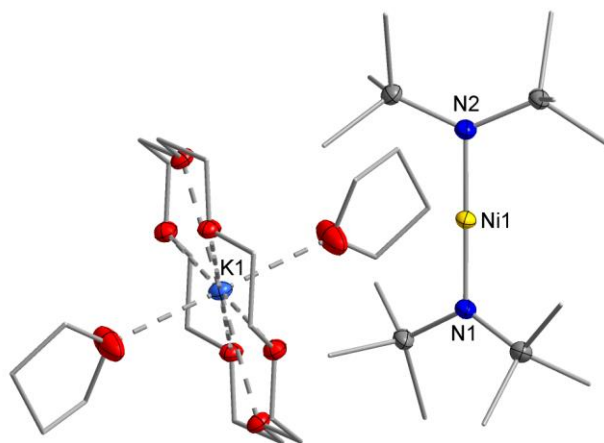
**Table S9. Crystal data and structure refinement for K{18c6}[6].**

Identification code	K_18c6_6
Empirical formula	C <sub>24</sub> H <sub>60</sub> KN <sub>2</sub> NiO <sub>6</sub> Si <sub>4</sub>
Formula weight	682.91
Temperature/K	100.04
Crystal system	triclinic
Space group	P-1
a/Å	9.6327(5)
b/Å	9.9520(6)
c/Å	10.8959(6)
α/°	116.311(2)
β/°	94.914(2)
γ/°	97.387(2)
Volume/Å <sup>3</sup>	916.51(9)
Z	1
ρ <sub>calc</sub> /g/cm <sup>3</sup>	1.237
μ/mm <sup>-1</sup>	0.808
F(000)	369.0
Crystal size/mm <sup>3</sup>	0.601 × 0.125 × 0.112
Radiation	MoKα (λ = 0.71073)
2θ range for data collection/°	4.224 to 58.93
Index ranges	-13 ≤ h ≤ 13, -13 ≤ k ≤ 13, -15 ≤ l ≤ 15
Reflections collected	30607
Independent reflections	5072 [R <sub>int</sub> = 0.0378, R <sub>sigma</sub> = 0.0302]
Data/restraints/parameters	5072/0/181
Goodness-of-fit on F <sup>2</sup>	1.029
Final R indexes [I ≥ 2σ (I)]	R <sub>1</sub> = 0.0288, wR <sub>2</sub> = 0.0566
Final R indexes [all data]	R <sub>1</sub> = 0.0426, wR <sub>2</sub> = 0.0604
Largest diff. peak/hole / e Å <sup>-3</sup>	0.35/-0.31

**Figure S29. Molecular structure of K{18c6}[6] within the crystal.**

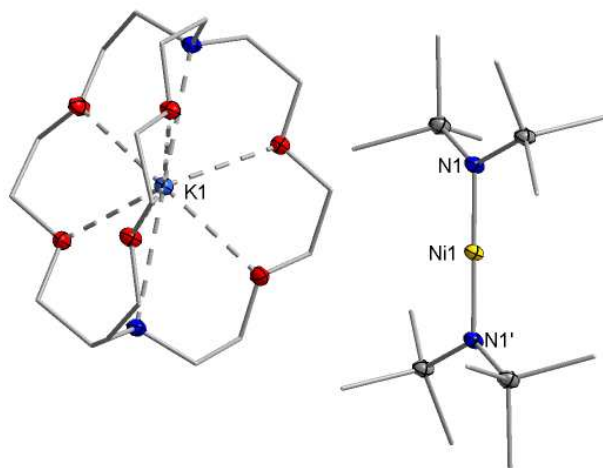
**Table S10. Crystal data and structure refinement for K{18c6}(thf)<sub>2</sub>[6].**

Identification code	K_18c6_thf2_6
Empirical formula	C <sub>32</sub> H <sub>76</sub> KN <sub>2</sub> NiO <sub>8</sub> Si <sub>4</sub>
Formula weight	827.11
Temperature/K	100.0
Crystal system	triclinic
Space group	P-1
a/Å	10.9885(6)
b/Å	11.3613(6)
c/Å	20.4616(11)
α/°	98.121(2)
β/°	92.146(2)
γ/°	111.520(2)
Volume/Å <sup>3</sup>	2341.5(2)
Z	2
ρ <sub>calc</sub> /g/cm <sup>3</sup>	1.173
μ/mm <sup>-1</sup>	0.647
F(000)	898.0
Crystal size/mm <sup>3</sup>	0.24 × 0.107 × 0.088
Radiation	MoKα (λ = 0.71073)
2θ range for data collection/°	3.908 to 50.816
Index ranges	-13 ≤ h ≤ 13, -13 ≤ k ≤ 13, -24 ≤ l ≤ 24
Reflections collected	45319
Independent reflections	8574 [R <sub>int</sub> = 0.0657, R <sub>sigma</sub> = 0.0640]
Data/restraints/parameters	8574/0/448
Goodness-of-fit on F <sup>2</sup>	1.027
Final R indexes [I ≥ 2σ (I)]	R <sub>1</sub> = 0.0484, wR <sub>2</sub> = 0.1014
Final R indexes [all data]	R <sub>1</sub> = 0.0740, wR <sub>2</sub> = 0.1093
Largest diff. peak/hole / e Å <sup>-3</sup>	0.92/-0.65

**Figure S30. Molecular structure of K{18c6}(thf)<sub>2</sub>[6] within the crystal.**

**Table S11. Crystal data and structure refinement for K{crypt}[6].**

Identification code	K_crypt_6
Empirical formula	C <sub>30</sub> H <sub>72</sub> KN <sub>4</sub> NiO <sub>6</sub> Si <sub>4</sub>
Formula weight	795.08
Temperature/K	100.0
Crystal system	monoclinic
Space group	<i>P</i> 2 <sub>1</sub> / <i>n</i>
<i>a</i> /Å	13.1239(5)
<i>b</i> /Å	8.7825(4)
<i>c</i> /Å	19.3861(7)
$\alpha$ /°	90
$\beta$ /°	96.849(2)
$\gamma$ /°	90
Volume/Å <sup>3</sup>	2218.51(15)
<i>Z</i>	2
$\rho_{\text{calc}}$ /g/cm <sup>3</sup>	1.190
$\mu$ /mm <sup>-1</sup>	0.678
<i>F</i> (000)	862.0
Crystal size/mm <sup>3</sup>	0.204 × 0.169 × 0.121
Radiation	MoK $\alpha$ ( $\lambda$ = 0.71073)
2 $\theta$ range for data collection/°	4.232 to 52.08
Index ranges	-16 ≤ <i>h</i> ≤ 16, -10 ≤ <i>k</i> ≤ 10, -23 ≤ <i>l</i> ≤ 23
Reflections collected	72221
Independent reflections	4382 [ <i>R</i> <sub>int</sub> = 0.1097, <i>R</i> <sub>sigma</sub> = 0.0449]
Data/restraints/parameters	4382/0/216
Goodness-of-fit on <i>F</i> <sup>2</sup>	1.050
Final <i>R</i> indexes [ <i>I</i> ≥ 2 $\sigma$ ( <i>I</i> )]	<i>R</i> <sub>1</sub> = 0.0246, <i>wR</i> <sub>2</sub> = 0.0577
Final <i>R</i> indexes [all data]	<i>R</i> <sub>1</sub> = 0.0420, <i>wR</i> <sub>2</sub> = 0.0591
Largest diff. peak/hole / e Å <sup>-3</sup>	0.29/-0.20

**Figure S31. Molecular structure of K{crypt}[6] within the crystal.**

## References

- (1) Faust, M.; Bryan, A. M.; Mansikkamäki, A.; Vasko, P.; Olmstead, M. M.; Tuononen, H. M.; Grandjean, F.; Long, G. J.; Power, P. P. The Instability of Ni{N(SiMe<sub>3</sub>)<sub>2</sub>}<sub>2</sub>: A Fifty Year Old Transition Metal Silylamide Mystery. *Angew. Chem. Int. Ed.* **2015**, *54* (44), 12914–12917. DOI: 10.1002/anie.201505518.
- (2) Stoll, S.; Schweiger, A. EasySpin, a comprehensive software package for spectral simulation and analysis in EPR. *J. Magn. Reson.* **2006**, *178* (1), 42–55. DOI: 10.1016/j.jmr.2005.08.013.
- (3) Sheldrick, G. M. Crystal structure refinement with SHELXL. *Acta Cryst. C* **2015**, *71* (Pt 1), 3–8. DOI: 10.1107/S2053229614024218.
- (4) Farrugia, L. J. WinGX suite for small-molecule single-crystal crystallography. *J. Appl. Crystallogr.* **1999**, *32* (4), 837–838. DOI: 10.1107/S0021889899006020.
- (5) Betteridge, P. W.; Carruthers, J. R.; Cooper, R. I.; Prout, K.; Watkin, D. J. CRYSTALS version 12: software for guided crystal structure analysis. *J. Appl. Crystallogr.* **2003**, *36* (6), 1487. DOI: 10.1107/S0021889803021800.
- (6) Schmitz, W. International Tables for X-ray Crystallography, vol. IV (Ergänzungsband). Herausgegeben von der International Union of Crystallography. The Kynoch Press, Birmingham, England, 1974, 366 Seiten einschließlich Tabellen und Sachwortverzeichnis. *Krist. Techn.* **1975**, *10* (11), K120-K120. DOI: 10.1002/crat.19750101116.
- (7) Bruker. *SADABS-2016/2*; Bruker, 2016.



**6.9.5 Hydrogen Atom Abstraction by Trigonal Imido Cobalt Complexes**  
– Impact of structure onto reactivity

# **Hydrogen Atom Abstraction by Trigonal Imido Cobalt Complexes – Impact of structure onto reactivity**

A. Reckziegel,<sup>a</sup> B. Battistella,<sup>b</sup> C. Millidoni,<sup>a</sup> K. Ray,<sup>b</sup> C. G. Werncke,<sup>a</sup>

a) Philipps-University Marburg, Hans-Meerwein-Straße 4, D-35032 Marburg, Germany

b) Humboldt-Universität zu Berlin, Brook-Taylor-Strasse 2, 12489 Berlin, Germany

## Table of Contents

General considerations .....	3
1. Synthesis of $K\{\text{crypt.222}\}[\text{Co}(\text{hmds})_2(\text{NCMe}_2\text{Et})]$ (1) .....	4
2. Synthesis of $K\{\text{crypt.222}\}[\text{Co}(\text{hmds})_2(\text{N}(\text{H})\text{CMe}_2\text{Et})]$ (1H).....	5
3. Synthesis of $K\{\text{crypt.222}\}[\text{Co}(\text{hmds})_2(\text{NAda})]$ (2).....	6
4. Synthesis of $K\{\text{crypt.222}\}[\text{Co}(\text{hmds})_2(\text{N}(\text{H})\text{Ada})]$ (2H) .....	7
5. Synthesis of $K\{\text{crypt.222}\}[\text{Co}(\text{hmds})_2(\text{NCMe}_2\text{Ph})]$ ( $K\{\text{crypt.222}\}[3]$ ).....	8
6. Synthesis of $K\{\text{crypt.222}\}[\text{Co}(\text{hmds})_2(\text{N}(\text{H})\text{CMe}_2\text{Ph})]$ (3H).....	9
7. Synthesis of $K\{18\text{c}6\}[\text{Co}(\text{hmds})_2(\text{N}_4\text{Ph}_2)]$ (5).....	10
8. Synthesis of $K\{\text{crypt.222}\}[\text{Co}(\text{hmds})_2(\text{NMes})]$ (6) .....	11
9. Synthesis of $K\{\text{crypt.222}\}[\text{Co}(\text{hmds})_2(\text{N}(\text{H})\text{Mes})]$ (6H).....	12
10. Synthesis of $K\{\text{crypt.222}\}[\text{Co}(\text{hmds})_2(\text{N-2,6-dimethylphenyl})]$ (7) .....	13
11. Synthesis of $K\{\text{crypt.222}\}[\text{Co}(\text{hmds})_2(\text{N}(\text{H})\text{-2,6-dimethylphenyl})]$ (7H).....	14
12. Synthesis of $K\{\text{crypt.222}\}[\text{Co}(\text{hmds})_2(\text{N-4-methoxy-2,6-dimethylphenyl})]$ (8).....	15
13. Synthesis of $K\{\text{crypt.222}\}[\text{Co}(\text{hmds})_2(\text{N}(\text{H})\text{-4-methoxy-2,6-dimethylphenyl})]$ (8H) .....	16
14. Synthesis of $K\{\text{crypt.222}\}[\text{Co}(\text{hmds})_2(\text{N-4-chloro-2,6-dimethylphenyl})]$ (9) .....	17
15. Synthesis of $K\{\text{crypt.222}\}[\text{Co}(\text{hmds})_2(\text{N}(\text{H})\text{-4-chloro-2,6-dimethylphenyl})]$ (9H) .....	18
16. Synthesis of $K\{\text{crypt.222}\}[\text{Co}(\text{hmds})_2(\text{N-4-flouro-2,6-dimethylphenyl})]$ (10) .....	19
17. Synthesis of $K\{\text{crypt.222}\}[\text{Co}(\text{hmds})_2(\text{N}(\text{H})\text{-4-fluoro-2,6-dimethylphenyl})]$ (10H).....	20
18. Synthesis of $K\{\text{crypt.222}\}[\text{Co}(\text{hmds})_2(\text{TEMPO})]$ (11).....	21
19. Synthesis of $K\{\text{crypt.222}\}[\text{Co}(\text{hmds})_2(\text{NPh}_2)]$ (12).....	22
20. Mechanism of decomposition.....	23
21. Electron-paramagnetic-resonance spectra (EPR).....	24
22. Temperature dependent NMR spectra .....	31
23. NMR scale reactions.....	32
24. UV-Vis spectra .....	47
25. Kinetic studies .....	50
26. X-Ray diffraction analysis and molecular structures.....	53

## General considerations

All manipulations were carried out in a glovebox or using Schlenk-type techniques under a dry argon atmosphere. Used solvents were dried by continuous distillation over sodium metal for several days, degassed via three freeze-pump cycles and stored over molecular sieves 4 Å. The  $^1\text{H}$  NMR spectra were recorded on a *Bruker AV III 500* or *Bruker AV II 300* NMR spectrometers. Chemical shifts are reported in ppm relative to the residual proton signals of the solvent (for  $^1\text{H}$ ) or relative to the signal of the solvent itself ( $^{13}\text{C}$ ).  $w_{1/2}$  is the line width of a signal at half its maximum intensity. Integrals of the broad signals of the silylamide units were obtained directly or by peak fitting (in case of overlapping signals) using the Mestrenova software package. IR measurements were conducted on a *Bruker Alpha ATR-IR* spectrometer. Elemental analysis was performed by the “in-house” service of the Chemistry Department of the Philipps University Marburg, Germany using a CHN(S) analyzer *vario MICRO Cube (Elementar)*. The UV/VIS measurement were recorded on an *Analytik Jena Specord S600* using *WinASPECT* software and an *UNISOKU CoolSpek Cryostat*. Solution magnetic susceptibilities were determined by the Evans method.<sup>[1]</sup> Anhydrous  $\text{CoCl}_2$ , n-butyl lithium (2.5 M in hexane), 18-crown-6, 2.2.2-cryptand, Adamantylazide, 1,4-cyclohexadien, 9,10-dihydroanthracen, xanthene, triphenylmethane, diphenylmethane and tetramethylsilane (TMS) were obtained commercially (Sigma-Aldrich, Acros, Strem, Alfa Aesar) and - if not noted otherwise - used as received. 1,4-cyclohexadiene was degassed, transferred into the glovebox and stored over molecular sieves at  $-35\text{ }^\circ\text{C}$ . 18-crown-6 was sublimed prior use to remove traces of water.  $\text{K}\{\text{crypt.222}\}[\text{Co}(\text{hmds})_2]$ <sup>[2]</sup>,  $\text{K}\{\text{crypt.222}\}[\text{Co}(\text{hmds})_2\text{Cl}]$ <sup>[3]</sup>, tertiary alkyl azides<sup>[4]</sup> and aryl azides<sup>[5]</sup> were prepared according to literature procedures.

## 1. Synthesis of K{crypt.222}[Co(hmds)<sub>2</sub>(NCMe<sub>2</sub>Et)] (1)

70 mg K{crypt.222}[Co(hmds)<sub>2</sub>] (0.1 mmol, 1 equiv.) was dissolved in 2 mL Et<sub>2</sub>O. Addition of 10 mg N<sub>3</sub>CMe<sub>2</sub>Et (0.1 mmol, 1 equiv.) at -35 °C resulted in an immediate colour change from green to red under concomitant gas evolution. After stirring for 5 minutes, the solution was layered with 3 mL pentane and stored at -35 °C. After one day, the supernatant solution was removed via pipette and the residue was rinsed with 2x3 mL pentane. Drying in *vacuo* afford **1** as dark red crystals (66 mg, 0.1 mmol, 85%).

**<sup>1</sup>H-NMR** ([D<sub>8</sub>]THF, 298 K, ppm, 300 MHz): δ = 37.5 (s, NCMe<sub>2</sub>Et, 2 H), 26.4 (s, NCMe<sub>2</sub>Et, 6 H), 8.33 (s, NCMe<sub>2</sub>Et, 3 H), 3.37 (s, crypt.222, 12 H), 3.33 (s, crypt.222, 12 H), 2.35 (s, crypt.222, 12 H), -2.68 (s, SiMe<sub>3</sub>, 36 H) ppm.

**IR** (ATR, cm<sup>-1</sup>) v: 2942 (m), 2882 (m), 2825 (m), 1354 (m), 1260 (w), 1227 (m), 1132 (m), 1101 (s), 1076 (m), 1058 (w), 1011 (s), 951 (s), 930 (m), 885 (m), 862 (m), 819 (vs), 772 (m), 751 (s), 702 (w), 656 (s), 607 (m).

**Elemental analysis:** calcd. (%) for C<sub>35</sub>H<sub>83</sub>CoKN<sub>5</sub>O<sub>6</sub>Si<sub>4</sub> (880.45 g mol<sup>-1</sup>): C 47.75 H 9.50 N 7.95; found: C 47.45 H 9.113 N 8.02.

**EVANS-Method:** μ<sub>eff</sub> = 3.21 μ<sub>B</sub> (Evans, [D<sub>8</sub>]THF + 1% Si(CH<sub>3</sub>)<sub>4</sub>, 500 MHz, 298 K, μ<sub>s.o.</sub> = 2.83 μ<sub>B</sub>).

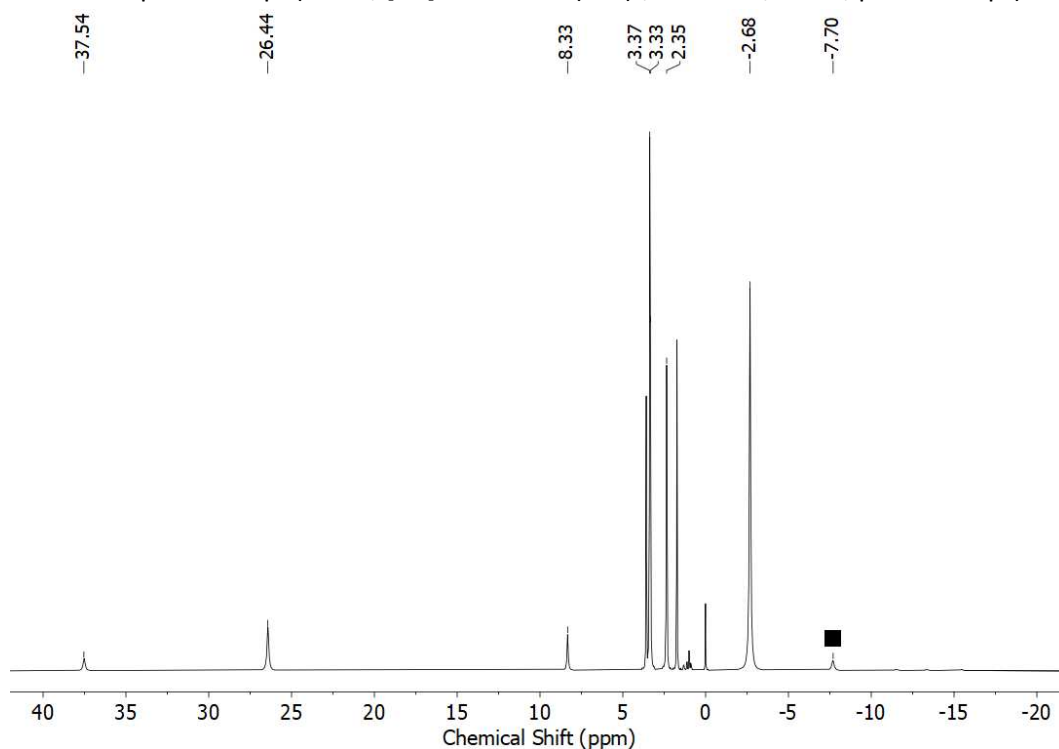


**Figure S1.** <sup>1</sup>H-NMR spectrum of K{crypt.222}[Co(hmds)<sub>2</sub>(NCMe<sub>2</sub>Et)] (**1**) ([D<sub>8</sub>]THF, 298 K, 300 MHz). The signal of the side-product K{crypt.222}[Co(hmds)<sub>3</sub>] is marked with ■.

## 2. Synthesis of K{crypt.222}[Co(hmds)<sub>2</sub>(N(H)CMe<sub>2</sub>Et)] (1H)

75 mg K{crypt.222}[Co(hmds)<sub>2</sub>(NCMe<sub>2</sub>Et)] (0.09 mmol, 1 equiv.) was dissolved in 2 mL Et<sub>2</sub>O. Addition of 5  $\mu$ L 1,4-cyclohexadiene (0.09 mmol, 1 equiv.) at RT resulted in a colour change from red to green. After stirring the mixture for 15 min, all volatiles were removed under reduced pressure. The residue was dissolved in 2 mL Et<sub>2</sub>O, filtered and layered with 3 mL pentane. Storage at -35 °C lead to the formation of a green crystalline solid. After one day, the supernatant solution was removed via pipette and the residue was rinsed with 2x3 mL pentane. Drying in *vacuo* afford **1H** as green crystals (65 mg, 0.07 mmol, 87%).

**<sup>1</sup>H-NMR** ([D<sub>8</sub>]THF, 298 K, ppm, 300 MHz):  $\delta$  = 77.4 (s, N(H)CMe<sub>2</sub>Et, 2 H), 60.9 (s, N(H)CMe<sub>2</sub>Et, 6 H), 43.4 (s, N(H)CMe<sub>2</sub>Et, 3 H), 2.82 (s, crypt.222, 12 H), 2.78 (s, crypt.222, 12 H), 1.81 (s, crypt.222, 12 H), -15.4 (s, SiMe<sub>3</sub>, 36 H) ppm.

**IR** (ATR, cm<sup>-1</sup>)  $\nu$ : 2942 (w), 2885 (m), 2817 (w), 1352 (m), 1258, (w), 1229 (m), 1132 (m), 1103 (s), 1076 (m), 1021 (m), 949 (m), 932 (m), 889 (w), 864 (m), 819 (s), 768 (m), 749 (m), 698 (w), 656 (m), 605 (m), 523 (w).

**Elemental analysis:** calcd. (%) for C<sub>35</sub>H<sub>84</sub>CoKN<sub>5</sub>O<sub>6</sub>Si<sub>4</sub> (881.46 g mol<sup>-1</sup>): C 47.69 H 9.61 N 7.95; found: C 47.67 H 9.38 N 8.06.

**EVANS-Method:**  $\mu_{\text{eff}} = 4.27 \mu_{\text{B}}$  (Evans, [D<sub>8</sub>]THF + 1% Si(CH<sub>3</sub>)<sub>4</sub>, 500 MHz, 298 K,  $\mu_{\text{s.o.}} = 3.87 \mu_{\text{B}}$ ).

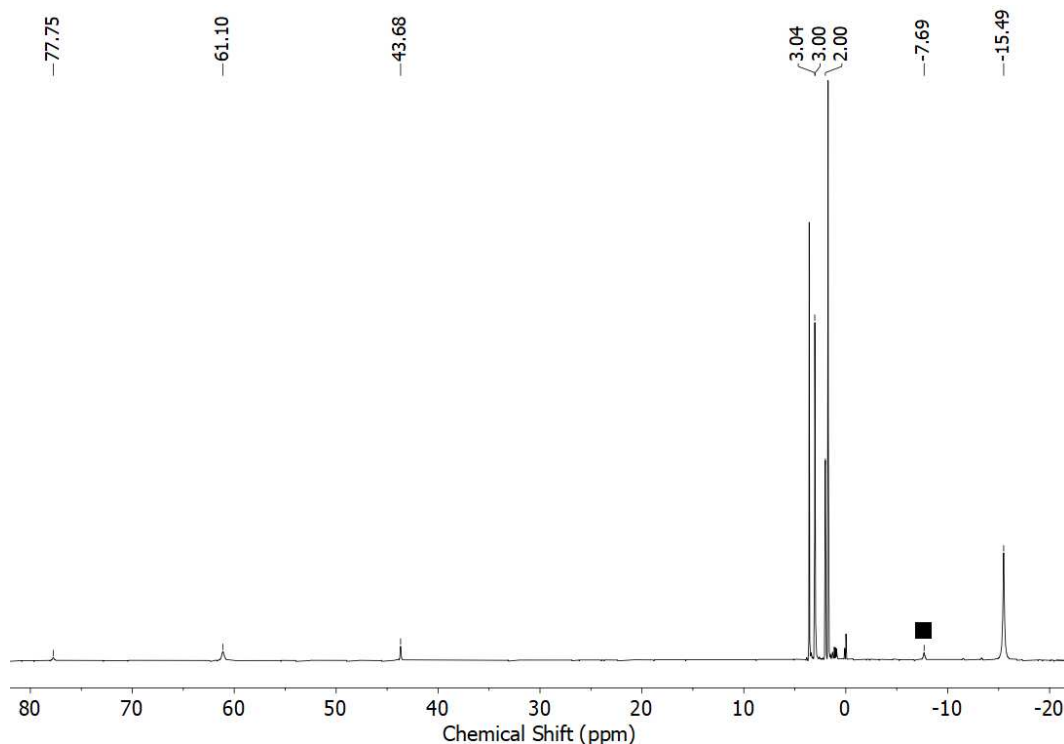


**Figure S2.** <sup>1</sup>H-NMR spectrum of K{crypt.222}[Co(hmds)<sub>2</sub>(N(H)CMe<sub>2</sub>Et)] (**1H**) ([D<sub>8</sub>]THF, 298 K, 300 MHz). The signal of the side-product K{crypt.222}[Co(hmds)<sub>3</sub>] is marked with ■.



## 4. Synthesis of K{crypt.222}[Co(hmds)<sub>2</sub>(N(H)Ada)] (2H)

70 mg K{crypt.222}[Co(hmds)<sub>2</sub>] (0.09 mmol, 1 equiv.) was dissolved in 2 mL Et<sub>2</sub>O and cooled to -30 °C. A precooled solution of 15.6 mg N<sub>3</sub>Ada (0.09 mmol, 1 equiv.) and 4.2 μL 1,4-cyclohexadiene (0.05 mmol, 0.5 equiv.) was added resulted in an immediate colour change from yellowish green to dark red under concomitant gas evolution. After stirring the mixture for 15 min a colour change to bright green was observed. All volatiles were removed under reduced pressure. The residue was dissolved in 2 mL Et<sub>2</sub>O, filtered and layered with 3 mL pentane. Storage at -35 °C led to the formation of a green crystalline solid. After one day, the supernatant solution was removed via pipette and the residue was rinsed with 2x3 mL pentane. Drying in *vacuo* afford **2H** as green crystals (60 mg, 0.06 mmol, 71%).

<sup>1</sup>H-NMR ([D<sub>8</sub>]THF, 298 K, ppm, 300 MHz): δ = 39.8 (s, N(H)Ada), 34.7 (s, N(H)Ada), 20.7 (s, N(H)Ada), 16.0 (s, N(H)Ada), 2.77 (s, crypt.222), 1.78 (s, crypt.222), -15.2 (s, SiMe<sub>3</sub>) ppm.

IR (ATR, cm<sup>-1</sup>) v: 2938 (m), 2922 (m), 2883 (s), 2848 (m), 2828 (m), 2811 (m), 1476 (m), 1443 (m), 1355 (s), 1298 (m), 1260 (m), 1231 (s), 1131 (s), 1103 (vs), 1078 (s), 1058 (m), 1011 (vs), 948 (s), 931 (s), 891 (m), 866 (s), 827 (vs), 817 (vs), 772 (s), 750 (s), 697 (m), 660 (s), 609 (m), 522 (m).

**Elemental analysis:** calcd. (%) for C<sub>40</sub>H<sub>88</sub>CoKN<sub>5</sub>O<sub>6</sub>Si<sub>4</sub> (945.54 g mol<sup>-1</sup>): C 50.81 H 9.38 N 7.41; found: C 50.56 H 8.952 N 7.61.

**EVANS-Method:** μ<sub>eff</sub> = 4.49 μ<sub>B</sub> (Evans, THF-d<sub>8</sub>+ 1% Si(CH<sub>3</sub>)<sub>4</sub>, 500 MHz, 298 K, μ<sub>s.o.</sub> = 3.87 μ<sub>B</sub>).

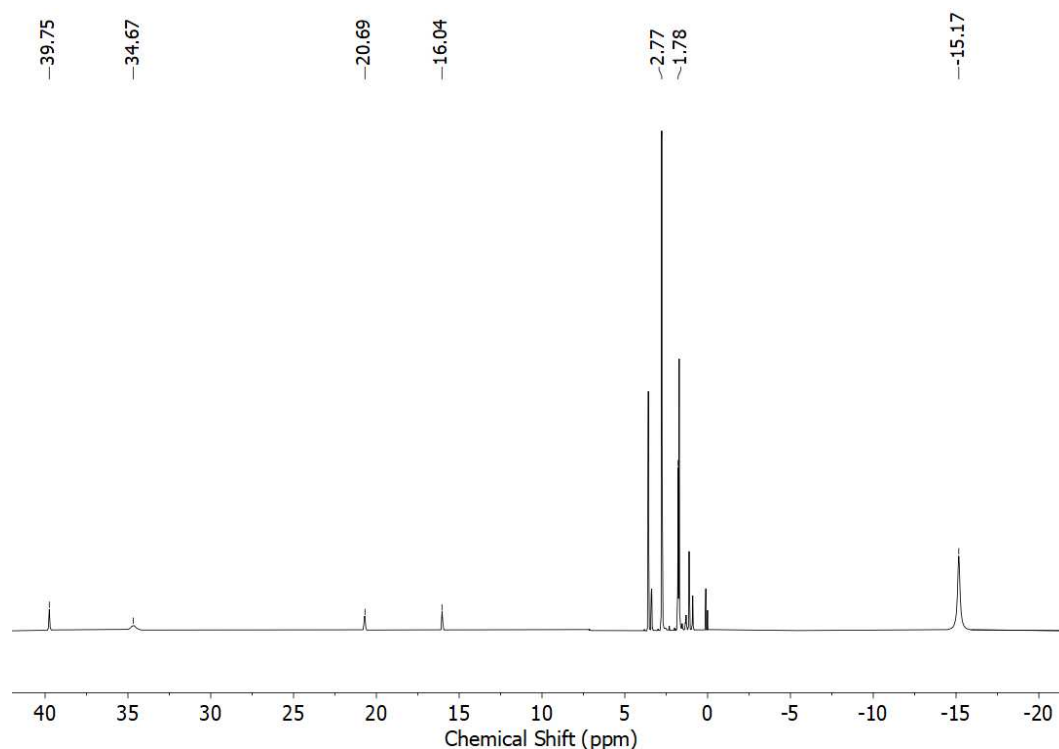


**Figure S4.** <sup>1</sup>H-NMR spectrum of K{crypt.222}[Co(hmds)<sub>2</sub>(NHAda)] (**2H**) ([D<sub>8</sub>]THF, 298 K, 300 MHz).



## 5. Synthesis of $\text{K}\{\text{crypt.222}\}[\text{Co}(\text{hmds})_2(\text{NCMe}_2\text{Ph})]$ ( $\text{K}\{\text{crypt.222}\}[\mathbf{3}]$ )

50 mg  $\text{K}\{\text{crypt.222}\}[\text{Co}(\text{hmds})_2]$  (0.07 mmol, 1 equiv.) was dissolved in 2 mL  $\text{Et}_2\text{O}$ . Addition of 10 mg  $\text{N}_3\text{CMe}_2\text{Ph}$  (0.07 mmol, 1 equiv.) at  $-35\text{ }^\circ\text{C}$  resulted in an immediate colour change from yellowish green to dark red under concomitant gas evolution. 2 mL precooled *n*-pentane were added and the reaction mixture concentrated to 2 mL, which leads to the formation of dark red crystalline plates. The supernatant solution is removed via pipette and the residue is washed with 3x1 mL of a precooled mixture of  $\text{Et}_2\text{O}$  and *n*-pentane (1:1). Drying in *vacuo* afford  $\mathbf{3}$  as dark red microcrystalline solid (20 mg, 0.02mmol, 34%).

$^1\text{H-NMR}$  ( $\text{THF-d}_8$ , 298 K, ppm, 500 MHz):  $\delta = 25.5$  (s, 6H,  $\text{NCMe}_2\text{Ph}$ ), 15.5 (s, 2H,  $\text{NCMe}_2\text{Ph}$ ), 14.30 (s, 1H,  $\text{NCMe}_2\text{Ph}$ ), 14.28 (s, 1H,  $\text{NCMe}_2\text{Ph}$ ), 6.70 (s, 1H,  $\text{NCMe}_2\text{Ph}$ ), 3.43 (s, 12H, crypt.222), 3.39 (s, 12H, crypt.222), 2.40 (s, 12H, crypt.222),  $-2.68$  (s, 36 H,  $\text{SiMe}_3$ ) ppm.

**IR** (ATR,  $\text{cm}^{-1}$ ) v: 2942 (m), 2885 (s), 2817 (m), 1354 (m), 1443, (s), 1235 (m), 1295 (m), 1258 (vs), 1231 (s), 1132 (vs), 1101 (vs), 1076 (s), 1002 (vs), 949 (m), 930 (m), 883 (m), 862 (vs), 817 (vs), 776 (m), 766 (s), 749 (s), 702 (s), 661 (s), 607 (s), 549 (m), 523(m).

**Elemental analysis:** calcd. (%) for  $\text{C}_{39}\text{H}_{83}\text{CoKN}_5\text{O}_6\text{Si}_4$  (928.49  $\text{g mol}^{-1}$ ): C 50.45 H 9.01 N 7.54; found: C 50.01 H 8.694 N 7.62.

**EVANS-Method:**  $\mu_{\text{eff}} = 3.66\ \mu_{\text{B}}$  (Evans,  $\text{THF-d}_8 + 1\% \text{Si}(\text{CH}_3)_4$ , 500 MHz, 298 K,  $\mu_{\text{s.o.}} = 2.83\ \mu_{\text{B}}$ ).

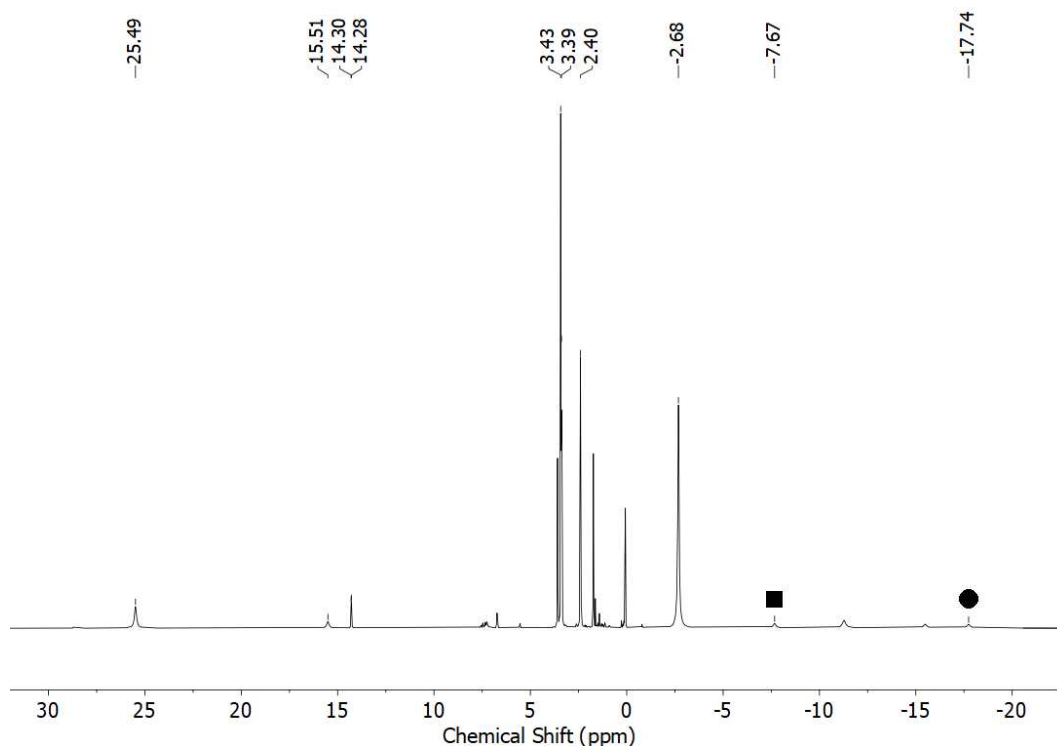


**Figure S5.**  $^1\text{H-NMR}$  spectrum of  $\text{K}\{\text{crypt.222}\}[\text{Co}(\text{hmds})_2\text{N}(\text{CMe}_2\text{Ph})]$  ( $\mathbf{3}$ ) ( $[\text{D}_8]\text{THF}$ , 298 K, 500 MHz). The signal ( $\text{K}\{\text{crypt.222}\}[\text{Co}(\text{hmds})_3]$ ) (■, side-product) and  $\text{K}\{\text{crypt.222}\}[\text{Co}(\text{hmds})_2\text{N}(\text{H})(\text{CMe}_2\text{Ph})]$  (●, subsequent H atom abstraction) are marked.

## 6. Synthesis of K{crypt.222}[Co(hmds)<sub>2</sub>(N(H)CMe<sub>2</sub>Ph)] (3H)

60 mg K{crypt.222}[Co(hmds)<sub>2</sub>(NCMe<sub>2</sub>Ph)] (0.06 mmol, 1 equiv.) was dissolved in 2 mL Et<sub>2</sub>O. Addition of 6  $\mu$ L 1,4-cyclohexadiene (0.06 mmol, 1 equiv.) at RT resulted in a colour change from red to green. After stirring the mixture for 15 min, all volatiles were removed under reduced pressure. The residue was dissolved in 2 mL Et<sub>2</sub>O, filtered, concentrated under reduced pressure. Storage at -35 °C lead to the formation of a green crystalline solid. After one day, the supernatant solution was removed via pipette and the residue was rinsed with 2x3 mL pentane. Drying in *vacuo* afford **3H** as green crystals (35 mg, 0.04 mmol, 58%).

<sup>1</sup>H-NMR ([D8]THF, 298 K, ppm, 300 MHz):  $\delta$  = 71.3 (s, N(H)CMe<sub>2</sub>Ph), 57.4 (s, N(H)CMe<sub>2</sub>Ph), 27.3 (s, N(H)CMe<sub>2</sub>Ph), 17.9 (s, N(H)CMe<sub>2</sub>Ph), 3.19 (s, crypt.222), 3.16 (s, crypt.222), 2.17 (s, crypt.222), -17.7 (s, SiMe<sub>3</sub>) ppm.

IR (ATR, cm<sup>-1</sup>)  $\nu$ : 2942 (w), 2882 (w), 2817 (w), 1476 (w), 1352 (w), 1295 (w), 1258 (w), 1233 (w), 1132 (w), 1103 (m), 1076 (w), 1058 (w), 1027 (w), 1004 (w), 951 (w), 932 (w), 889 (w), 864 (w), 827 (m), 819 (m), 766 (w), 749 (w), 704 (w), 661 (w), 609 (w), 564 (w), 523 (w).

**Elemental analysis:** calcd. (%) for C<sub>39</sub>H<sub>84</sub>CoKN<sub>5</sub>O<sub>6</sub>Si<sub>4</sub> (929.50 g mol<sup>-1</sup>): C 50.40 H 9.11 N 7.53; found: C 50.79 H 8.58 N 7.36.

**EVANS-Method:**  $\mu_{\text{eff}} = 3.91 \mu_{\text{B}}$  (Evans, [D8]THF + 1% Si(CH<sub>3</sub>)<sub>4</sub>, 500 MHz, 298 K,  $\mu_{\text{s.o.}} = 3.87 \mu_{\text{B}}$ ).

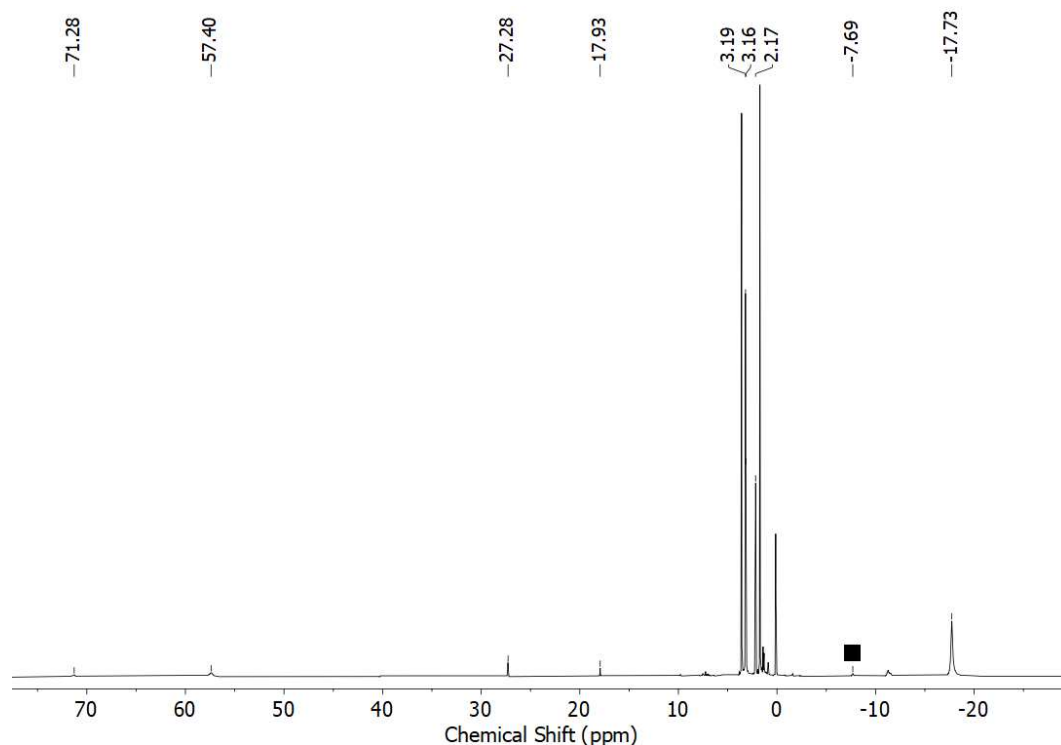


**Figure S6.** <sup>1</sup>H-NMR spectrum of K{crypt.222}[Co(hmds)<sub>2</sub>(NHCMe<sub>2</sub>Ph)] (**3H**) ([D8]THF, 298 K, 300 MHz). The signal of the side-product K{crypt.222}[Co(hmds)<sub>3</sub>] is marked with ■.

## 7. Synthesis of K{18c6}[Co(hmds)<sub>2</sub>(N<sub>4</sub>Ph<sub>2</sub>)] (5)

80 mg K{18c6}[Co(hmds)<sub>2</sub>] (0.12 mmol, 1 equiv.) was dissolved in 2 mL Et<sub>2</sub>O. Addition of 30 mg N<sub>3</sub>Mes (0.12 mmol, 1 equiv.) at -35 °C resulted in an immediate colour change from yellowish green to dark green under concomitant gas evolution. After stirring for 5 minutes, the solution was layered with 3 mL pentane and stored at -35 °C. After one day, the supernatant solution was removed via pipette and the residue was rinsed with 2x3 mL pentane. Drying in *vacuo* afford **5** as dark green microcrystalline solid (72 mg, mmol, %).

<sup>1</sup>H-NMR (THF-d<sub>8</sub>, 298 K, ppm, 300 MHz): δ = 60.3 (s, NPh), 47.5 (s, NPh), 3.93 (s, 18c6), 0.11 (s, SiMe<sub>3</sub>), -9.48 (s, NPh) ppm.

IR (ATR, cm<sup>-1</sup>) v: 2942 (w), 2889 (m), 1585 (w), 1480 (m), 1453 (w), 1350 (m), 1272 (w), 1233 (m), 1103 (vs), 1025 (w), 982 (m), 959 (s), 885 (w), 862 (m), 821 (vs), 778 (m), 757 (m), 745 (m), 691 (m), 661 (m), 609 (w).

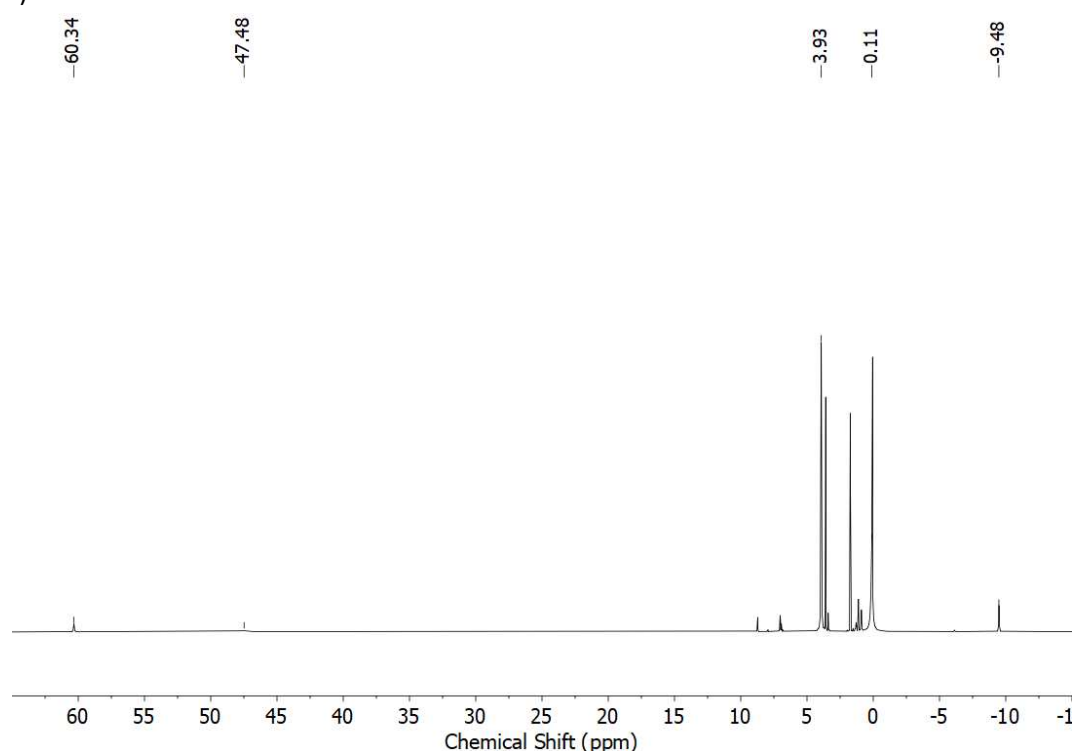


**Figure S7.** <sup>1</sup>H-NMR spectrum of K18c6[Co(hmds)<sub>2</sub>(N<sub>4</sub>Ph<sub>2</sub>)] (**5**) ([D<sub>8</sub>]THF, 298 K, 500 MHz).

## 8. Synthesis of K{crypt.222}[Co(hmds)<sub>2</sub>(NMe<sub>3</sub>)] (6)

99 mg K{crypt.222}[Co(hmds)<sub>2</sub>] (0.12 mmol, 1 equiv.) was dissolved in 2 mL Et<sub>2</sub>O. Addition of 20 mg N<sub>3</sub>Mes (0.12 mmol, 1 equiv.) at -35 °C resulted in an immediate colour change from yellowish green to dark green under concomitant gas evolution. After stirring for 5 minutes, the solution was layered with 3 mL pentane and stored at -35 °C. After one day, the supernatant solution was removed via pipette and the residue was rinsed with 2x3 mL pentane. Drying in *vacuo* afford **6** as dark green microcrystalline solid (99 mg, 0.11 mmol, 86%). Crystals suitable for X-ray diffraction could be obtained by layering a saturated 1,2-DFB solution with n-pentane and storage at -35 °C.

**<sup>1</sup>H-NMR** (THF-d<sub>8</sub>, 298 K, ppm, 500 MHz): δ = 494.4 (s, NMe<sub>3</sub>), 375.2 (s, NMe<sub>3</sub>), 351.1 (s, NMe<sub>3</sub>), 3.33 (s, crypt.222), 3.29 (s, crypt.222), 2.30 (s, crypt.222), -9.05 (s, SiMe<sub>3</sub>, 36 H) ppm.

**IR** (ATR, cm<sup>-1</sup>) ν: 2940 (w), 2885 (w), 2812 (w), 1354 (w), 1297, (w), 1258 (w), 1231 (m), 1132 (w), 1103 (s), 1079 (m), 996 (m), 949 (m), 932 (w), 879 (m), 862 (m), 821 (vs), 776 (s), 749 (s), 702 (w), 661 (m), 609 (w), 523 (w).

**Elemental analysis:** calcd. (%) for C<sub>39</sub>H<sub>83</sub>CoKN<sub>5</sub>O<sub>6</sub>Si<sub>4</sub> (928.49 g mol<sup>-1</sup>): C 50.45 H 9.01 N 7.54; found: C 50.46 H 8.897 N 7.72.

**EVANS-Method:** μ<sub>eff</sub> = 4.51 μ<sub>B</sub> (Evans, THF-d<sub>8</sub>+ 1% Si(CH<sub>3</sub>)<sub>4</sub>, 500 MHz, 298 K, μ<sub>s.o.</sub> = 4.90 μ<sub>B</sub>).

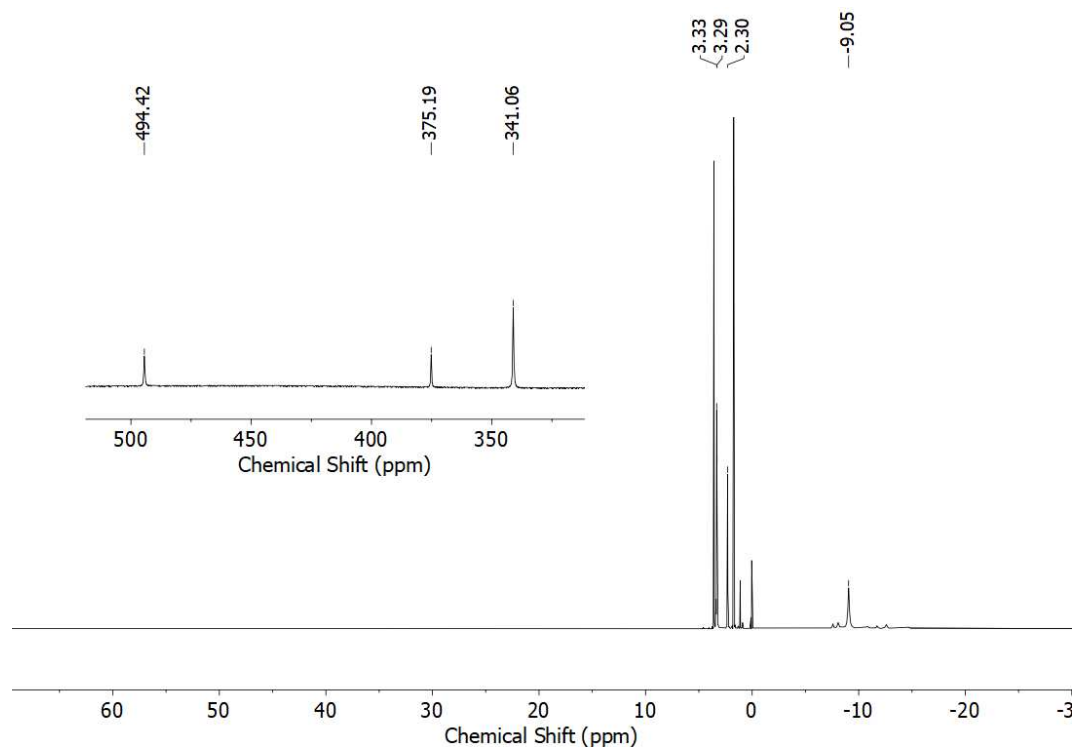


**Figure S8.** <sup>1</sup>H-NMR spectrum of K{crypt.222}[Co(hmds)<sub>2</sub>(NMe<sub>3</sub>)] (6) ([D<sub>8</sub>]THF, 298 K, 500 MHz).

## 9. Synthesis of $K\{\text{crypt.222}\}[\text{Co}(\text{hmds})_2(\text{N}(\text{H})\text{Mes})]$ (**6H**)

50 mg  $\text{Co}(\text{hmds})_2$  (0.14 mmol, 1 equiv.) and 49.6 mg crypt.222 (0.14 mmol, 1 equiv.) were dissolved in 2 mL  $\text{Et}_2\text{O}$ . The solution was added to a solution of 22.8 mg  $\text{KNHMe}$  (0.14 mmol, 1 equiv.) in 1 mL  $\text{Et}_2\text{O}$ . After stirring for 4 hours, the solution was filtered and layered with 3 mL pentane. Storage at  $-35\text{ }^\circ\text{C}$  lead to the precipitance of a yellowish green crystalline solid. Washing with 3 mL n-pentane and drying in *vacuo* afford **6H** as yellowish green crystals (90 mg, 0.11 mmol, 74 %) suitable for X-ray diffraction.  $^1\text{H-NMR}$  ( $\text{THF-d}_8$ , 298 K, ppm, 300 MHz):  $\delta = 90.7$  (s, N(H)Mes) 78.0 (s, N(H)Mes), 74.8 (s, N(H)Mes), 49.5 (s, N(H)Mes), 38.1 (s, N(H)Mes), -3.75 (s, crypt.222), 2.77 (s; crypt.222),  $-12.8$  (s,  $\text{SiMe}_3$ ) ppm.

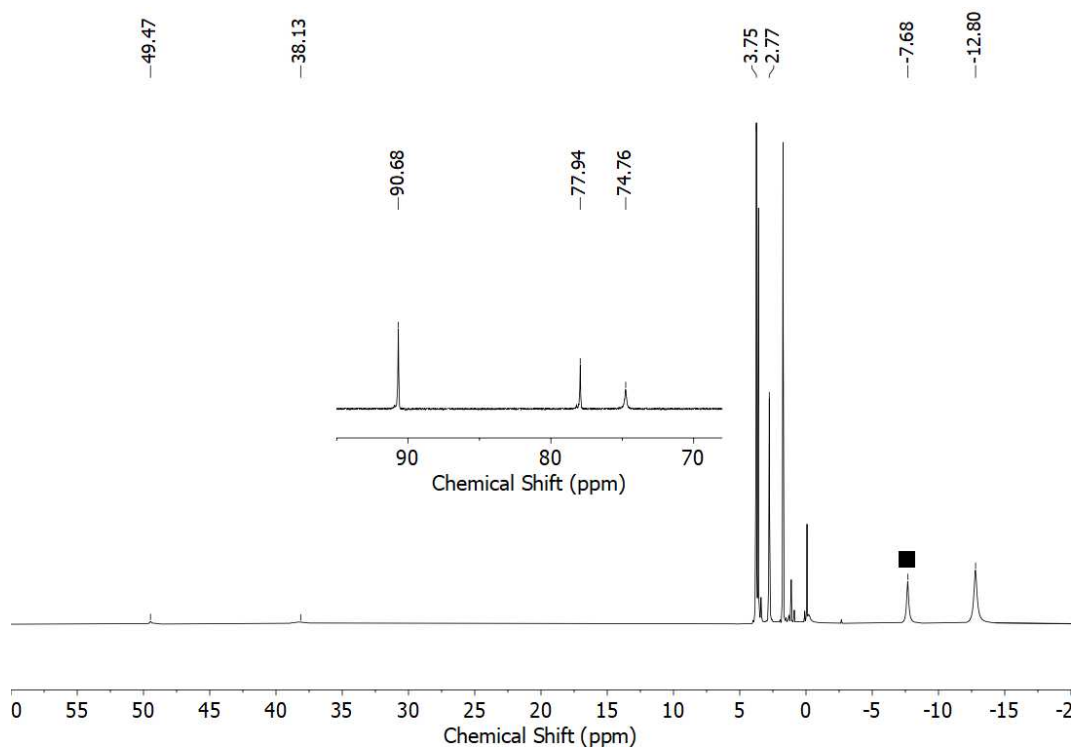


**Figure S9.**  $^1\text{H-NMR}$  spectrum of  $K\{\text{crypt.222}\}[\text{Co}(\text{hmds})_2(\text{NHMe})]$  (**6H**) ( $[\text{D}_8]\text{THF}$ , 298 K, 500 MHz). The signal of the side-product  $K\{\text{crypt.222}\}[\text{Co}(\text{hmds})_3]$  is marked with ■.

## 10. Synthesis of $K\{\text{crypt.222}\}[\text{Co}(\text{hmds})_2(\text{N-2,6-dimethylphenyl})]$ (7)

108 mg  $K\{\text{crypt.222}\}[\text{Co}(\text{hmds})_2]$  (0.14 mmol, 1 equiv.) was dissolved in 2 mL  $\text{Et}_2\text{O}$ . Addition of 20 mg 1-Azido-2,6-dimethylbenzene (0.14 mmol, 1 equiv.) at  $-35^\circ\text{C}$  resulted in an immediate colour change from yellowish green to dark green under concomitant gas evolution. After stirring for 5 minutes, the solution was layered with 3 mL pentane and stored at  $-35^\circ\text{C}$ . After one day, the supernatant solution was removed via pipette and the residue was rinsed with 2x3 mL pentane. Drying in *vacuo* afford **7** as dark yellow crystals (104 mg, 0.11 mmol, 84%)

$^1\text{H-NMR}$  ( $\text{THF-d}_8$ , 298 K, ppm, 300 MHz): 397.49 (s, N-2,6-DiMePh), 360.13 (s, N-2,6-DiMePh), 3.58 (s, crypt.222), 3.52 (s, crypt.222), 2.52 (s, crypt.222), -10.22 (s,  $\text{N}(\text{SiMe}_3)_2$ ) ppm.

**IR** (ATR,  $\text{cm}^{-1}$ )  $\nu$ : 2942 (w), 2885 (m), 2815 (m), 1476 (w), 1460 (w), 1445 (w), 1420 (w), 1354 (m), 1295 (m), 1260 (w), 1231 (s), 1132 (m), 1103 (s), 1076 (m), 996 (m), 949 (m), 932 (m), 881 (m), 862 (m), 819 (vs), 776 (m), 747 (m), 704 (w), 661 (m), 609 (w), 523 (w).

**Elemental analysis:** calcd. (%) for  $\text{C}_{38}\text{H}_{81}\text{CoKN}_5\text{O}_6\text{Si}_4$  ( $914.47\text{ g mol}^{-1}$ ): C 49.91 H 8.93 N 7.66; found: C 50.16 H 8.61 N 7.47.

**EVANS-Method:**  $\mu_{\text{eff}} = 4.72\ \mu_{\text{B}}$  (Evans,  $\text{THF-d}_8 + 1\% \text{Si}(\text{CH}_3)_4$ , 500 MHz, 298 K,  $\mu_{\text{s.o.}} = 4.90\ \mu_{\text{B}}$ ).

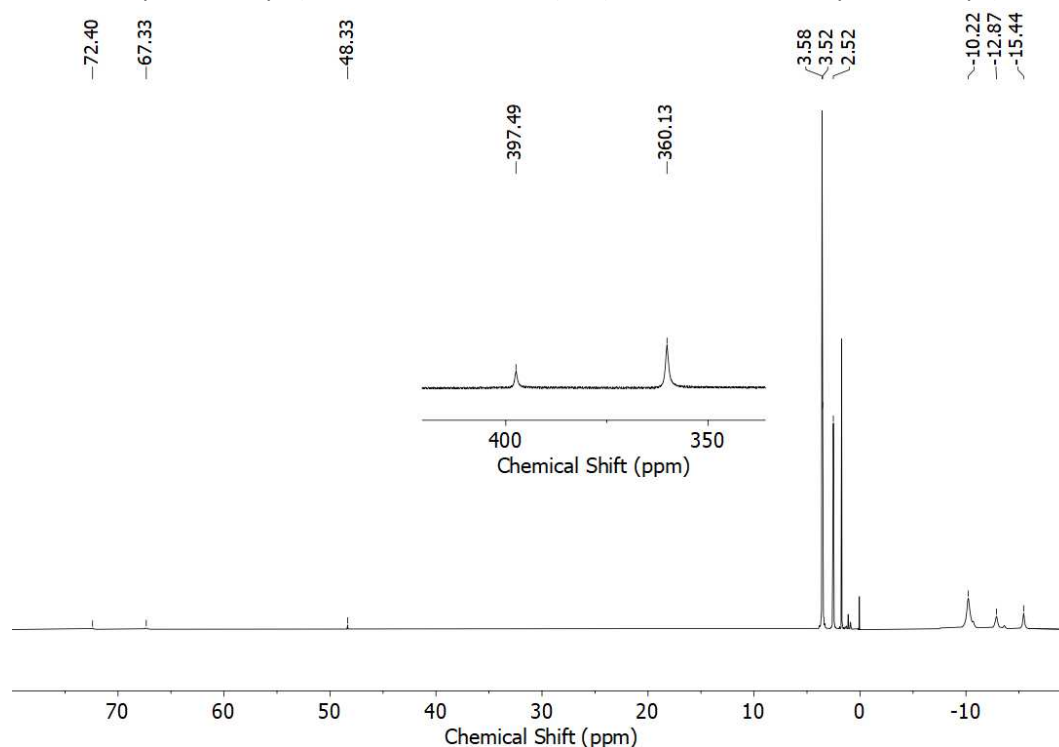


**Figure S10.**  $^1\text{H-NMR}$  spectrum of  $K\{\text{crypt.222}\}[\text{Co}(\text{hmds})_2(\text{N-2,6-DiMePh})]$  (**7**) ( $[\text{D}_8]\text{THF}$ , 298 K, 300 MHz).

## 11. Synthesis of $\text{K}\{\text{crypt.222}\}[\text{Co}(\text{hmds})_2(\text{N}(\text{H})\text{-2,6-dimethylphenyl})]$ (**7H**)

108 mg  $\text{K}\{\text{crypt.222}\}[\text{Co}(\text{hmds})_2]$  (0.1 mmol, 1 equiv.) was dissolved in 2 mL  $\text{Et}_2\text{O}$ . Addition of 20 mg 1-Azido-2,6-dimethylbenzene (0.1 mmol, 1 equiv.) in 0,1 mL 1,4-cyclohexdiene resulted in an immediate colour change from yellowish green to dark green under concomitant gas evolution. After stirring for 18 hours all volatiles were removed under reduced pressure. The residue was washed with 3x3mL *n*-pentane and dried *in vacuo*. **7H** was obtained as dark green solid (56 mg, 0.06mmol, 51%). Crystals suitable for X-ray diffraction could be obtained by layering a saturated solution of  $\text{Et}_2\text{O}$  with *n*-pentane at  $-30^\circ\text{C}$ .

*The  $^1\text{H-NMR}$  spectra shows the formation of two different products which could not be separated.*

## 12. Synthesis of $\text{K}\{\text{crypt.222}\}[\text{Co}(\text{hmds})_2(\text{N-4-methoxy-2,6-dimethylphenyl})]$ (**8**)

90 mg  $\text{K}\{\text{crypt.222}\}[\text{Co}(\text{hmds})_2]$  (0.1 mmol, 1 equiv.) was dissolved in 2 mL  $\text{Et}_2\text{O}$ . Addition of 20 mg 1-Azido-4-methoxy-2,6-dimethylbenzene (0.1 mmol, 1 equiv.) at  $-35\text{ }^\circ\text{C}$  resulted in an immediate colour change from yellowish green to dark green under concomitant gas evolution. After stirring for 5 minutes, the solution was layered with 3 mL pentane and stored at  $-35\text{ }^\circ\text{C}$ . After one day, the supernatant solution was removed via pipette and the residue was rinsed with 2x3 mL pentane. Drying in *vacuo* afford **8** as dark yellow crystals (86 mg, 0.08 mmol, 80%)

$^1\text{H-NMR}$  ( $\text{THF-d}_8$ , 298 K, ppm, 300 MHz):  $\delta$  = 281.35 (s, N-4-OMe-2,6-DiMePh), 247.91 (s, N-4-OMe-2,6-DiMePh), 45.50 (s, N-4-OMe-2,6-DiMePh), 3.67 (s, crypt.222), 2.66 (s, crypt.222), -6.83 (s,  $\text{N}(\text{SiMe}_3)_2$ ) ppm.

**IR** (ATR,  $\text{cm}^{-1}$ )  $\nu$ : 2940 (w), 2885 (m), 1476 (w), 1352 (m), 1293 (w), 1260 (w), 1231 (s), 1149 (w), 1132 (w), 1103 (s), 1076 (m), 996 (s), 949 (m), 930 (w), 883 (w), 862 (m), 817 (vs), 774 (m), 747 (m), 704 (w), 661 (m), 609 (w), 523 (w).

**Elemental analysis:** calcd. (%) for  $\text{C}_{39}\text{H}_{83}\text{CoKN}_5\text{O}_7\text{Si}_4$  ( $944.49\text{ g mol}^{-1}$ ): C 49.60 H 8.86 N 7.42; found: C 49.28 H 8.70 N 7.72.

**EVANS-Method:**  $\mu_{\text{eff}} = 4.46\ \mu_{\text{B}}$  (Evans,  $\text{THF-d}_8$ + 1%  $\text{Si}(\text{CH}_3)_4$ , 500 MHz, 298 K,  $\mu_{\text{s.o.}} = 4.90\ \mu_{\text{B}}$ ).

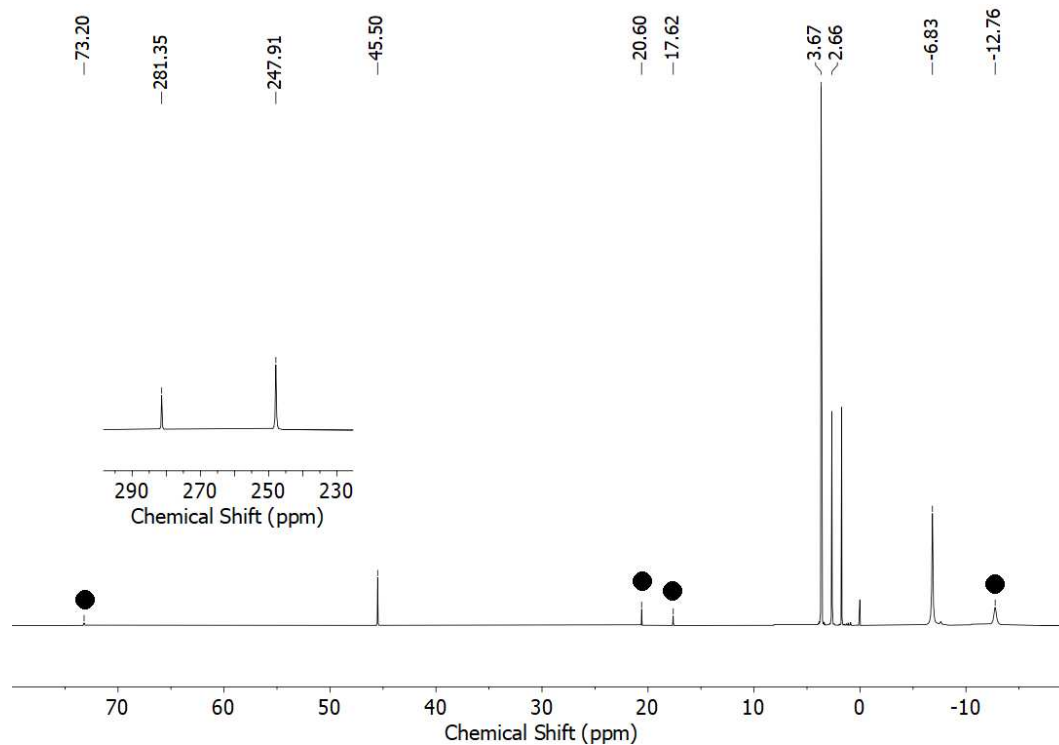


**Figure S11.**  $^1\text{H-NMR}$  spectrum of  $\text{K}\{\text{crypt.222}\}[\text{Co}(\text{hmds})_2(\text{N-4-OMe-2,6-DiMePh})]$  (**8**) ( $[\text{D}_8]\text{THF}$ , 298 K, 300 MHz).  $\text{K}\{\text{crypt.222}\}[\text{Co}(\text{hmds})_2\text{N}(\text{H})\text{-4-OMe-2,6-DiMePh}]$  (H atom abstraction product) is marked with •.



### 13. Synthesis of $\text{K}\{\text{crypt.222}\}[\text{Co}(\text{hmds})_2(\text{N}(\text{H})\text{-4-methoxy-2,6-dimethylphenyl})]$ (**8H**)

89.8 mg  $\text{K}\{\text{crypt.222}\}[\text{Co}(\text{hmds})_2]$  (0.1 mmol, 1 equiv.) was dissolved in 2 mL  $\text{Et}_2\text{O}$ . Addition of 20 mg 1-Azido-4-methoxy-2,6-dimethylbenzene (0.1 mmol, 1 equiv.) in 0,1 mL 1,4 cyclohexdiene resulted in an immediate colour change from yellowish green to dark yellow under concomitant gas evolution. After stirring for 18 hours all volatiles were removed under reduced pressure. The residue was washed with 3x3mL *n*-pentane and dried *in vacuo*. **8H** was obtained as dark yellow solid (72 mg, 0.08mmol, 80%). Crystals suitable for X-ray diffraction could be obtained by layering a saturated solution of  $\text{Et}_2\text{O}$  with *n*-pentane at  $-30^\circ\text{C}$ .

$^1\text{H-NMR}$  ( $\text{THF-d}_8$ , 298 K, ppm, 500 MHz):  $\delta$  = 73.6 (s, N(H)-4-OMe-2,6-DiMePh), 40.4 (s, N(H)-4-OMe-2,6-DiMePh), 20.8 (s, N(H)-4-OMe-2,6-DiMePh), 4.24 (s, crypt.222), 3.22 (s, crypt.222),  $-12.8$  (s,  $\text{SiMe}_3$ ) ppm.

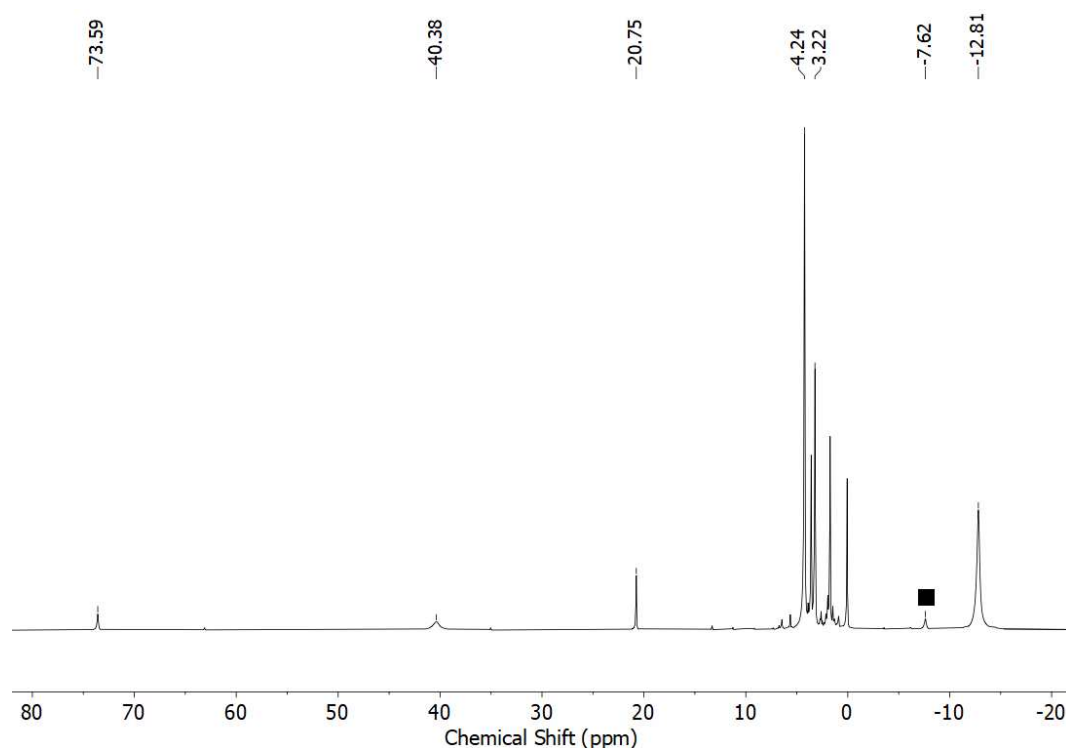


**Figure S12.**  $^1\text{H-NMR}$  spectrum of  $\text{K}\{\text{crypt.222}\}[\text{Co}(\text{hmds})_2(\text{N-4-OMe-2,6-DiMePh})]$  (**8H**) ( $[\text{D}_8]\text{THF}$ , 298 K, 300 MHz). The signal of the side-product  $\text{K}\{\text{crypt.222}\}[\text{Co}(\text{hmds})_3]$  is marked with ■.

## 14. Synthesis of $\text{K}\{\text{crypt.222}\}[\text{Co}(\text{hmds})_2(\text{N-4-chloro-2,6-dimethylphenyl})]$ (**9**)

44 mg  $\text{K}\{\text{crypt.222}\}[\text{Co}(\text{hmds})_2]$  (0.05 mmol, 1 equiv.) was dissolved in 2 mL  $\text{Et}_2\text{O}$ . Addition of 10 mg 1-Azido-4-chloro-2,6-dimethylbenzene (0.05 mmol, 1 equiv.) at  $-35\text{ }^\circ\text{C}$  resulted in an immediate colour change from yellowish green to dark green under concomitant gas evolution. After stirring for 5 minutes, the solution was layered with 3 mL pentane and stored at  $-35\text{ }^\circ\text{C}$ . After one day, the supernatant solution was removed via pipette and the residue was rinsed with 2x3 mL pentane. Drying in *vacuo* afford **9** as dark yellow crystals (42 mg, 0.04 mmol, 80%)

$^1\text{H-NMR}$  ( $\text{THF-d}_8$ , 298 K, ppm, 300 MHz): 416.48 (s, N-4Cl-2,6-DiMePh), 382.52 (s, N-4Cl-2,6-DiMePh), 3.44 (s, crypt.222), 2.48 (s, crypt.222), -10.15 (s,  $\text{N}(\text{SiMe}_3)_2$ ) ppm.

**IR** (ATR,  $\text{cm}^{-1}$ )  $\nu$ : 2942 (m), 2882 (m), 2815 (w), 1460 (w), 1445 (w), 1414 (w), 1354 (m), 1297 (m), 1260 (w), 1233 (s), 1132 (m), 1103 (s), 1079 (s), 990 (s), 949 (s), 932 (m), 879 (m), 862 (s), 819 (s), 776 (s), 749 (s), 704 (m), 661 (s), 609 (m), 523 (m).

**Elemental analysis:** calcd. (%) for  $\text{C}_{38}\text{H}_{80}\text{ClCoKN}_5\text{O}_6\text{Si}_4$  (948.91  $\text{g mol}^{-1}$ ): C 48.10 H 8.50 N 7.38; found: C 48.13 H 8.07 N 7.31.

**EVANS-Method:**  $\mu_{\text{eff}} = 4.61\ \mu_{\text{B}}$  (Evans,  $\text{THF-d}_8 + 1\% \text{Si}(\text{CH}_3)_4$ , 500 MHz, 298 K,  $\mu_{\text{s.o.}} = 4.90\ \mu_{\text{B}}$ ).

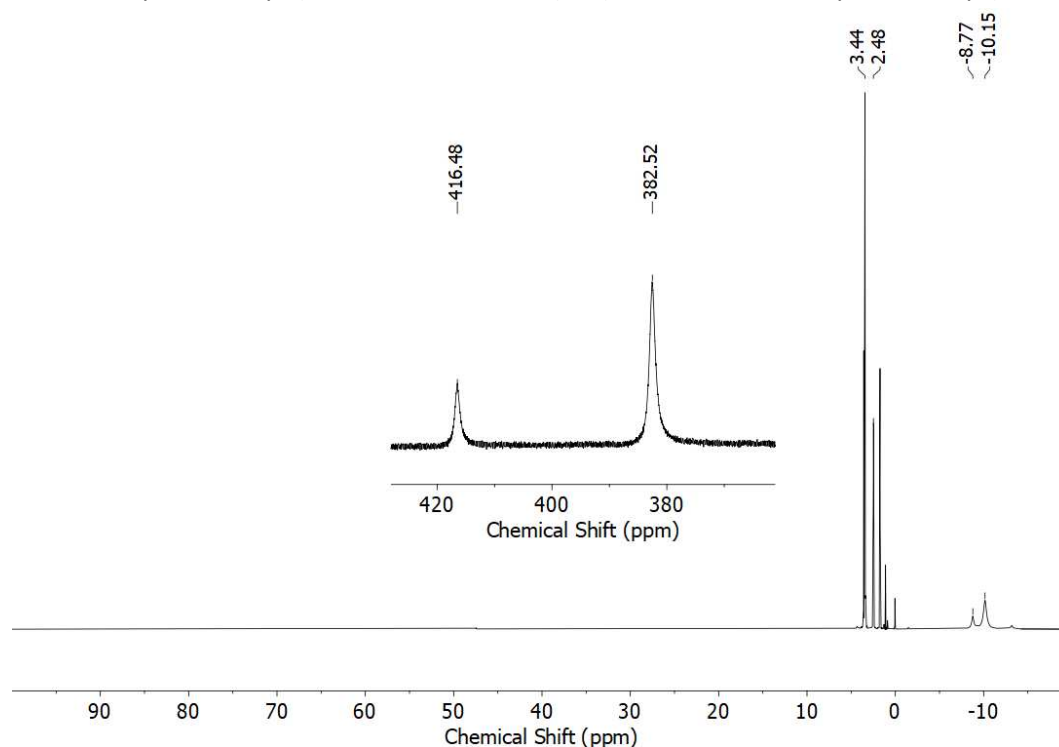


**Figure S13.**  $^1\text{H-NMR}$  spectrum of  $\text{K}\{\text{crypt.222}\}[\text{Co}(\text{hmds})_2(\text{N-4-Cl-2,6-DiMePh})]$  (**9**) ( $[\text{D}_8]\text{THF}$ , 298 K, 300 MHz).

## 15. Synthesis of $\text{K}\{\text{crypt.222}\}[\text{Co}(\text{hmds})_2(\text{N}(\text{H})\text{-4-chloro-2,6-dimethylphenyl})]$ (**9H**)

87.6 mg  $\text{K}\{\text{crypt.222}\}[\text{Co}(\text{hmds})_2]$  (0.1 mmol, 1 equiv.) was dissolved in 2 mL  $\text{Et}_2\text{O}$ . Addition of 20 mg 1-Azido-2,6-dimethylbenzene (0.1 mmol, 1 equiv.) in 0.1 mL 1,4-cyclohexadiene resulted in an immediate colour change from yellowish green to dark green under concomitant gas evolution. After stirring for 18 hours all volatiles were removed under reduced pressure. The residue was washed with 3x3mL *n*-pentane and dried *in vacuo*. **9H** was obtained as dark green solid (76 mg, 0.08 mmol, 87%). Crystals suitable for X-ray diffraction could be obtained by layering a saturated solution of  $\text{Et}_2\text{O}$  with *n*-pentane at  $-30^\circ\text{C}$ .

$^1\text{H-NMR}$  ( $\text{THF-d}_8$ , 298 K, ppm, 500 MHz):  $\delta$  = 73.2 (s, N(H)-4-chloro-2,6-dimethylphenyl), 38.7 (s, N(H)-4-chloro-2,6-dimethylphenyl), 3.85 (s, crypt.222), 2.84 (s, crypt.222),  $-13.2$  (s,  $\text{SiMe}_3$ , 36 H) ppm.

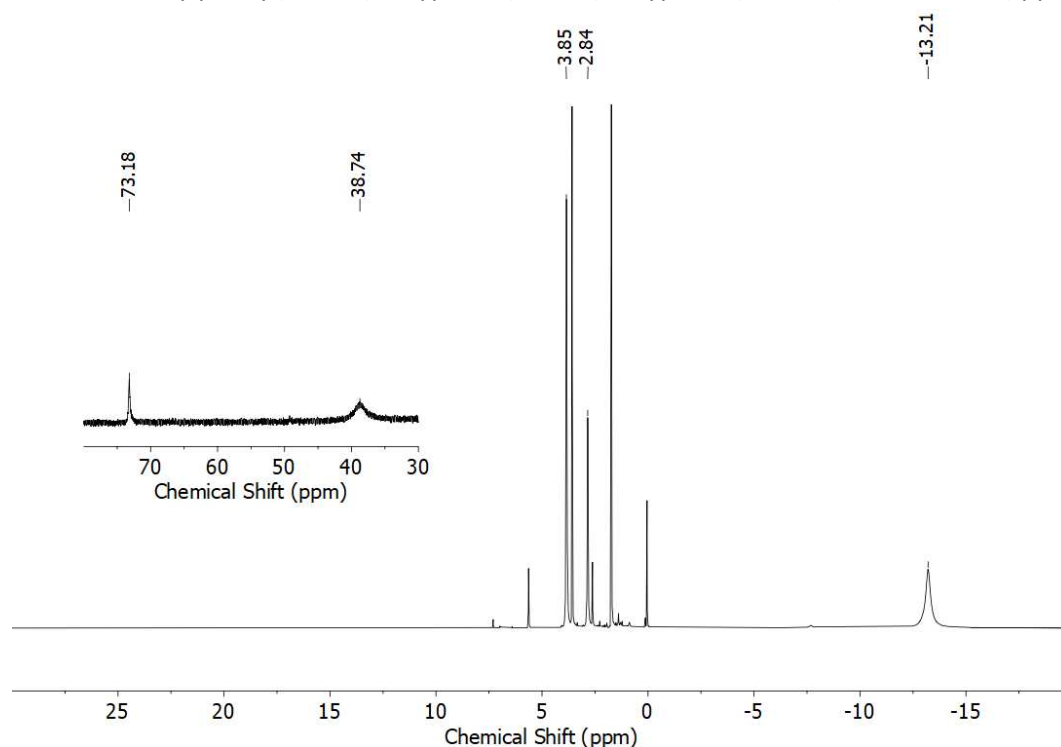


**Figure S14.**  $^1\text{H-NMR}$  spectrum of  $\text{K}\{\text{crypt.222}\}[\text{Co}(\text{hmds})_2(\text{N}(\text{H})\text{-4-chloro-2,6-dimethylphenyl})]$  (**9H**) ( $[\text{D}_8]\text{THF}$ , 298 K, 300 MHz).

## 16. Synthesis of $K\{\text{crypt.222}\}[\text{Co}(\text{hmds})_2(\text{N-4-flouro-2,6-dimethylphenyl})]$ (**10**)

95 mg  $K\{\text{crypt.222}\}[\text{Co}(\text{hmds})_2]$  (0.12 mmol, 1 equiv.) was dissolved in 2 mL  $\text{Et}_2\text{O}$ . Addition of 20 mg 1-Azido-4-flouro-2,6-dimethylbenzene (0.12 mmol, 1 equiv.) at  $-35^\circ\text{C}$  resulted in an immediate colour change from yellowish green to dark yellow under concomitant gas evolution. After stirring for 5 minutes, the solution was layered with 3 mL pentane and stored at  $-35^\circ\text{C}$ . After one day, the supernatant solution was removed via pipette and the residue was rinsed with 2x3 mL pentane. Drying in *vacuo* afford **10** as dark yellow crystals (94 mg, 0.11 mmol, 84%)

$^1\text{H-NMR}$  ( $\text{THF-d}_8$ , 298 K, ppm, 300 MHz): 371.97 (s, N-4-F-2,6-DiMePh), 363.87 (s, N-4-F-2,6-DiMePh), 3.67 (s, crypt.222), 3.62 (s, crypt.222), 2.60 (s, crypt.222), -9.09 (s,  $\text{N}(\text{SiMe}_3)_2$ ) ppm.

**IR** (ATR,  $\text{cm}^{-1}$ )  $\nu$ : 2940 (w), 2885 (w), 1474 (w), 1354 (m), 1260 (w), 1231 (m), 1132, (m) 1103 (s), 1076 (m), 996 (s), 951 (m), 932 (m), 883 (m), 862 (m), 819 (s), 776 (m), 749 (m), 704 (w), 661 (m), 609 (m).

**Elemental analysis:** calcd. (%) for  $\text{C}_{38}\text{H}_{80}\text{CoFKN}_5\text{O}_6\text{Si}_4$  ( $932.46 \text{ g mol}^{-1}$ ): C 48.95 H 8.65 N 7.51; found: C 49.05 H 8.43 N 7.03.

**EVANS-Method:**  $\mu_{\text{eff}} = 4.94 \mu_{\text{B}}$  (Evans,  $\text{THF-d}_8 + 1\% \text{Si}(\text{CH}_3)_4$ , 500 MHz, 298 K,  $\mu_{\text{s.o.}} = 4.90 \mu_{\text{B}}$ ).

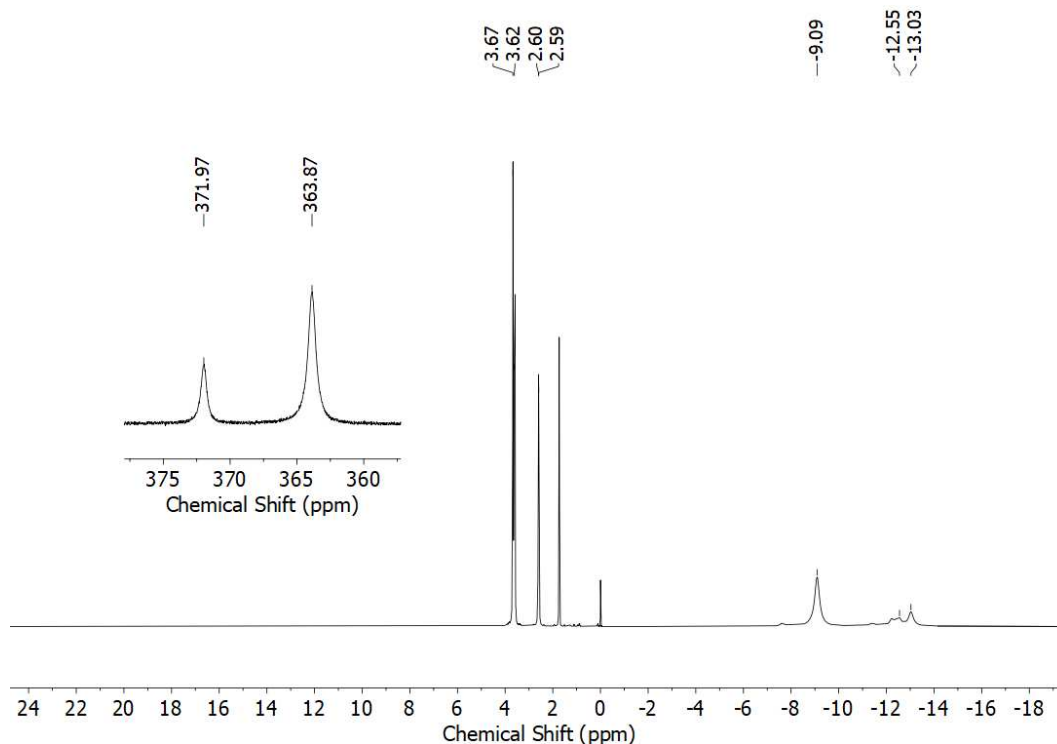


**Figure S15.**  $^1\text{H-NMR}$  spectrum of  $K\{\text{crypt.222}\}[\text{Co}(\text{hmds})_2(\text{N-4-F-2,6-DiMePh})]$  (**10**) ( $[\text{D}_8]\text{THF}$ , 298 K, 300 MHz).

## 17. Synthesis of $K\{\text{crypt.222}\}[\text{Co}(\text{hmds})_2(\text{N}(\text{H})\text{-4-fluoro-2,6-dimethylphenyl})]$ (**10H**)

96.3 mg  $K\{\text{crypt.222}\}[\text{Co}(\text{hmds})_2]$  (0.1 mmol, 1 equiv.) was dissolved in 2 mL  $\text{Et}_2\text{O}$ . Addition of 20 mg 1-Azido-2,6-dimethylbenzene (0.1 mmol, 1 equiv.) in 0.1 mL 1,4-cyclohexadiene resulted in an immediate colour change from yellowish green to dark green under concomitant gas evolution. After stirring for 18 hours all volatiles were removed under reduced pressure. The residue was washed with 3x3 mL *n*-pentane and dried *in vacuo*. **10H** was obtained as dark green solid (56 mg, 0.06 mmol, 58%). Crystals suitable for X-ray diffraction could be obtained by layering a saturated solution of  $\text{Et}_2\text{O}$  with *n*-pentane at  $-30^\circ\text{C}$ .

$^1\text{H-NMR}$  ( $\text{THF-d}_8$ , 298 K, ppm, 500 MHz):  $\delta = 72.3$  (s, N(H)-4-fluoro-2,6-dimethylphenyl), 40.6 (s, N(H)-4-fluoro-2,6-dimethylphenyl), 4.00 (s, crypt.222), 2.95 (s, crypt.222),  $-13.1$  (s,  $\text{SiMe}_3$ , 36 H) ppm.

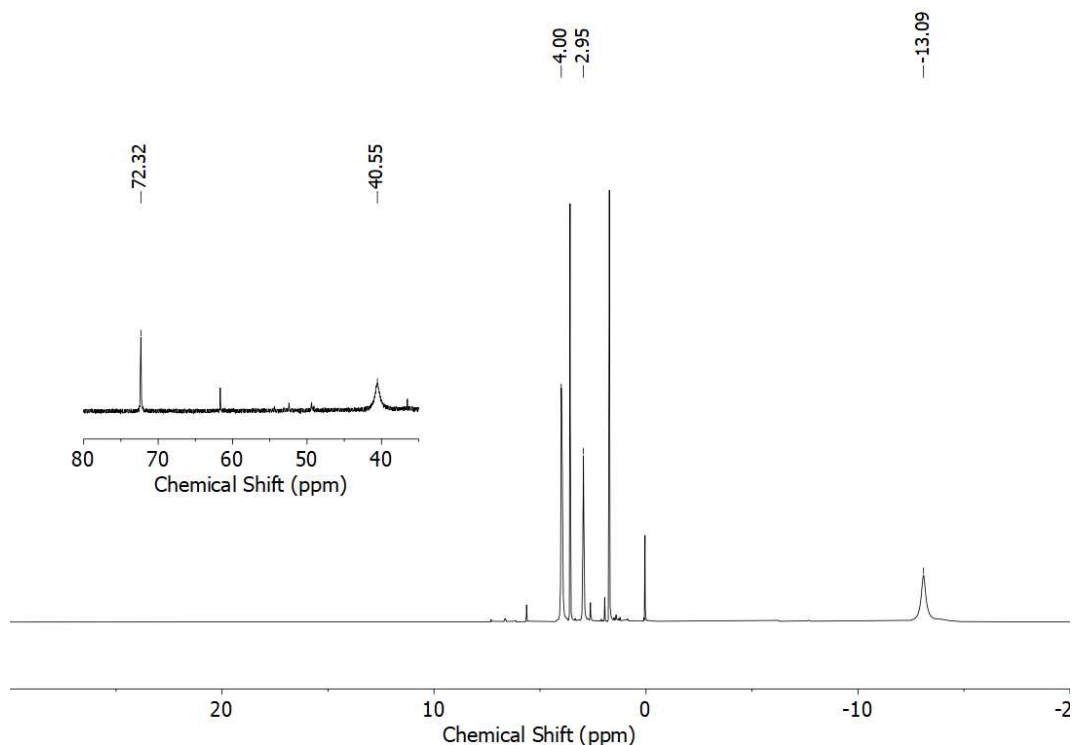


**Figure S16.**  $^1\text{H-NMR}$  spectrum of  $K\{\text{crypt.222}\}[\text{Co}(\text{hmds})_2(\text{N-4-F-2,6-DiMePh})]$  (**10H**) ( $[\text{D}_8]\text{THF}$ , 298 K, 500 MHz).

## 18. Synthesis of K{crypt.222}[Co(hmds)<sub>2</sub>(TEMPO)] (11)

60 mg K{crypt.222}Co(hmds)<sub>2</sub> (0.08 mmol, 1 equiv.) were dissolved in 2 mL Et<sub>2</sub>O and the solution cooled to -35°C. Addition to 12 mg TEMPO (0.08 mmol, 1 equiv.) at -35 °C resulted in an immediate colour change from yellow to green. The solution was filtered, layered with 3 mL pentane and stored at -35 °C. After one day, the supernatant solution was removed via pipette and the residue was rinsed with 2x3 mL pentane. Drying in *vacuo* afford **11** as green crystals (64 mg, 0.07 mmol, 89%).

<sup>1</sup>H-NMR (THF-d<sub>8</sub>, 298 K, ppm, 300 MHz): δ=90.1 (s, TEMPO), 43.0 (s, TEMPO), 33.9 (s, TEMPO), 20.4 (s, TEMPO), 15.3 (s, TEMPO), 2.84 (s, crypt.222), 1.83 (s, crypt.222), 0.18 (s, TEMPO), -18.5 (s, N(SiMe<sub>3</sub>)<sub>2</sub>) ppm.

IR (ATR, cm<sup>-1</sup>) v: 2940 (w), 2926 (w), 2882, 2815 (w), 1443 (w), 1354 (w), 1299 (w), 1258 (w), 1231 (w), 1132 (m), 1103 (m), 1079 (m), 1058 (w), 1017 (m), 949 (m), 932 (w), 893 (w), 866 (m), 827 (s), 766 (m), 749 (m), 700 (w), 661 (m), 609 (w), 523 (w).

Elemental analysis: calcd. (%) for C<sub>39</sub>H<sub>90</sub>CoKN<sub>5</sub>O<sub>7</sub>Si<sub>4</sub> (951.55 g mol<sup>-1</sup>): C 49.23 H 9.53 N 7.36; found: C 49.67 H 9.03 N 7.23.

EVANS-Method: μ<sub>eff</sub> = 4.41 μ<sub>B</sub> (Evans, [D8]THF + 1% Si(CH<sub>3</sub>)<sub>4</sub>, 500 MHz, 298 K, μ<sub>s.o.</sub> = 3.87 μ<sub>B</sub>).

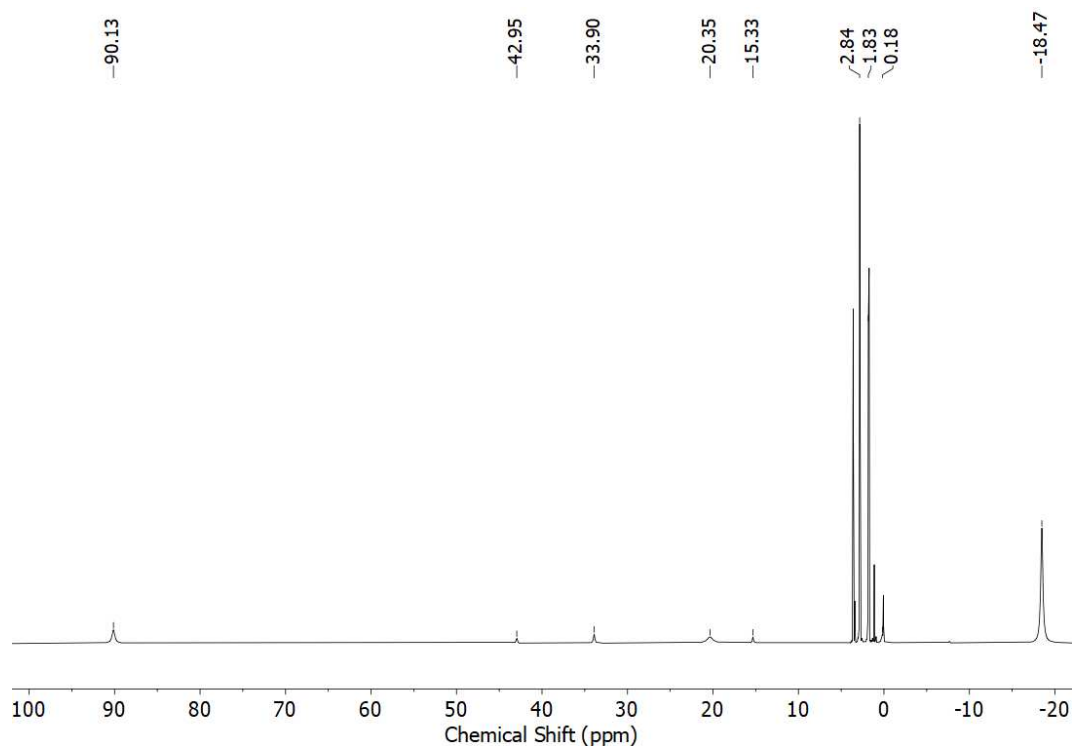


Figure S17. <sup>1</sup>H-NMR spectrum of K{crypt.222}[Co(hmds)<sub>2</sub>(TEMPO)] (**11**) ([D8]THF, 298 K, 300 MHz).

## 19. Synthesis of K{crypt.222}[Co(hmds)<sub>2</sub>(NPh<sub>2</sub>)] (12)

60 mg Co(hmds)<sub>2</sub> (0.13 mmol, 1 equiv.) and 44.8 mg crypt.222 (0.13 mmol, 1 equiv.) were dissolved in 2 mL Et<sub>2</sub>O. The solution was added to a solution of 27.6 mg KNPh<sub>2</sub> (0.13 mmol, 1 equiv.) in 1 mL Et<sub>2</sub>O. After stirring for 4 hours, the solution was filtered and layered with 3 mL pentane. Storage at -35 °C lead to the precipitance of green crystalline solid. Washing with 3 mL n-pentane and drying in *vacuo* afford **12** as green crystals (80 mg, 0.08 mmol, 63 %) suitable for X-ray diffraction.

<sup>1</sup>H-NMR (THF-d<sub>8</sub>, 298 K, ppm, 300 MHz): δ = 31.8 (s, NPh<sub>2</sub>), 3.85 (s, crypt.222), 3.81 (s, crypt.222), 2.83 (s, crypt.222), -13.7 (s, N(SiMe<sub>3</sub>)<sub>2</sub>), -36.6 (s, NPh<sub>2</sub>), -39.0 (s, NPh<sub>2</sub>) ppm.

IR (ATR, cm<sup>-1</sup>) v: 2939 (w), 2882 (m), 2813 (w), 1577 (m), 1478 (w), 1355 (m), 1322 (m), 1293 (w), 1233 (w), 1171 (w), 1132 (w), 1103 (s), 1004 (m), 989 (s), 947 (m), 886 (w), 862 (m), 816 (vs), 777 (m), 746 (m), 693 (w), 660 (m), 608 (w), 523 (w), 504(w).

Elemental analysis: calcd. (%) for C<sub>42</sub>H<sub>82</sub>CoKN<sub>5</sub>O<sub>6</sub>Si<sub>4</sub> (963.52 g mol<sup>-1</sup>): C 52.36 H 8.58 N 7.27; found: C 52.72 H 8.29 N 7.23.

EVANS-Method: μ<sub>eff</sub> = 4.65 μ<sub>B</sub> (Evans, THF-d<sub>8</sub>+ 1% Si(CH<sub>3</sub>)<sub>4</sub>, 500 MHz, 298 K, μ<sub>s.o.</sub> = 3.87 μ<sub>B</sub>).

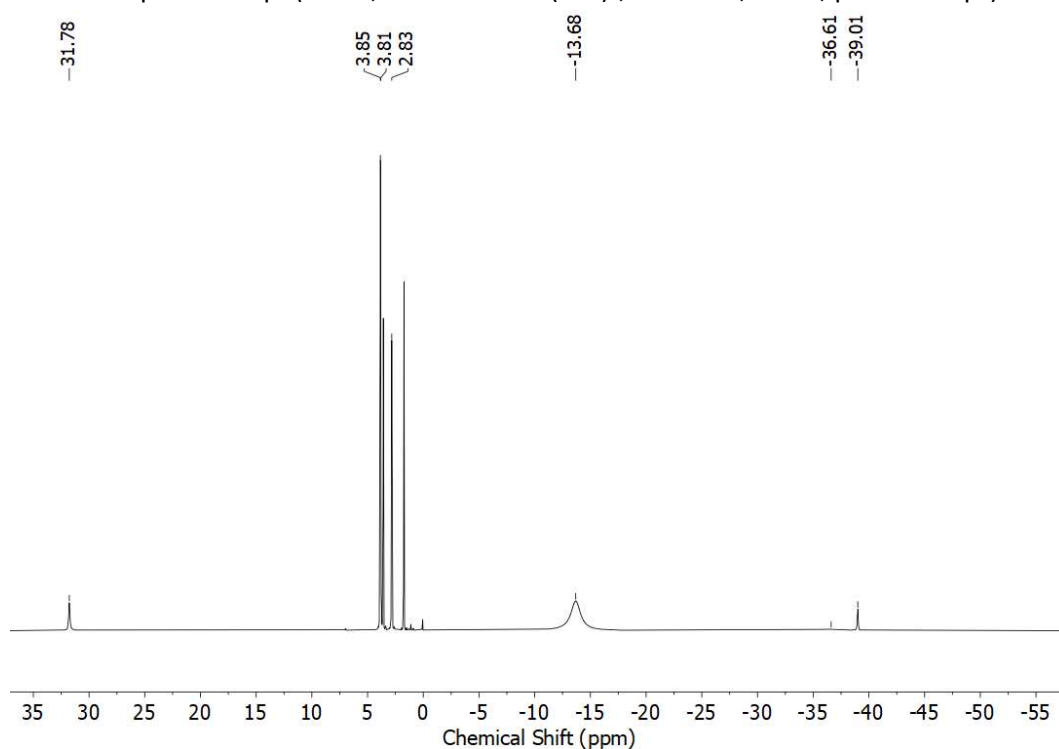
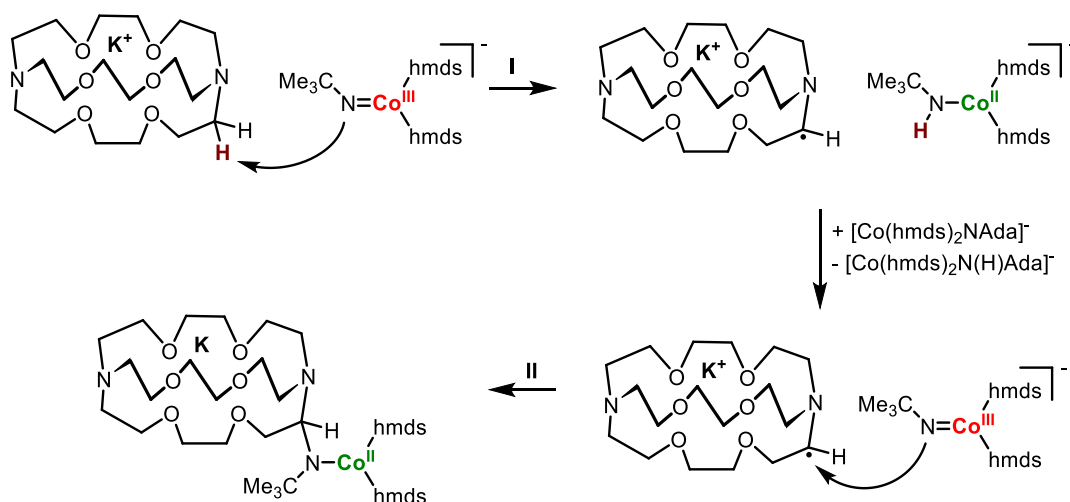
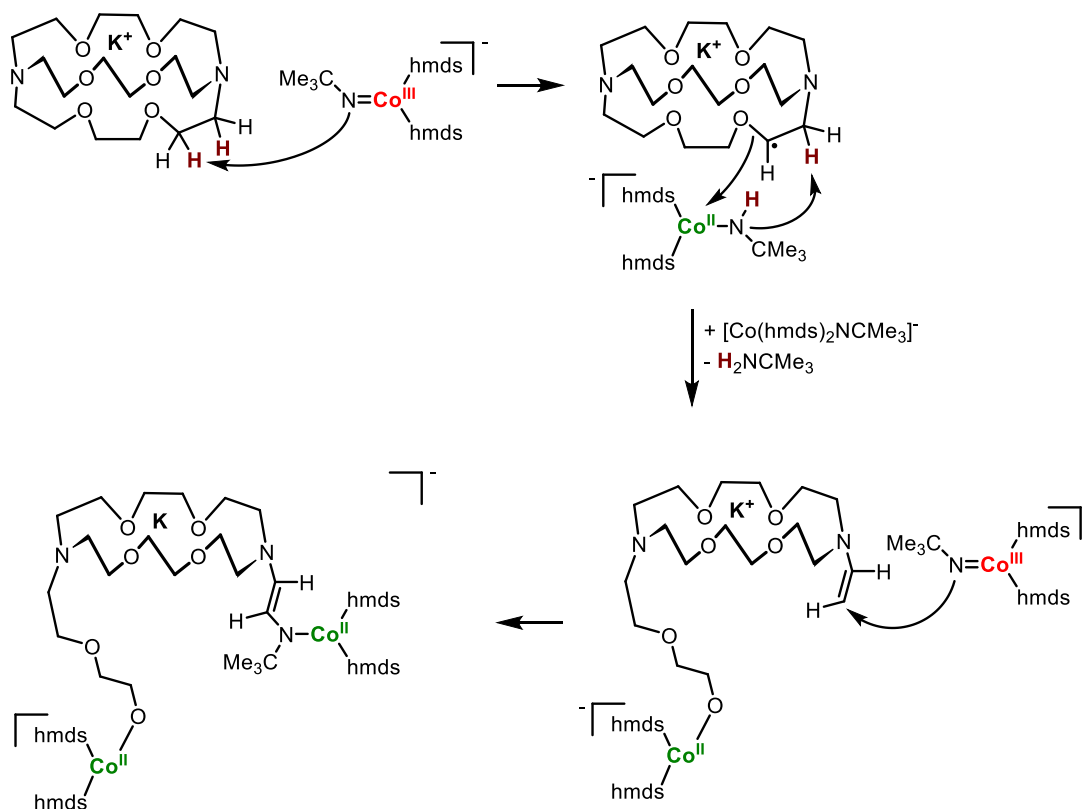


Figure S18. <sup>1</sup>H-NMR spectrum of K{crypt.222}[Co(hmds)<sub>2</sub>(NPh<sub>2</sub>)] (**12**) ([D<sub>8</sub>]THF, 298 K, 300 MHz).

## 20. Mechanism of decomposition



**Figure S19.** Formation of IX by hydrogen atom abstraction from crypt.222 by  $[\text{Co}(\text{hmds})_2\text{NAda}]^-$  (I) followed by C-N-bond formation between a second equivalent  $[\text{Co}(\text{hmds})_2\text{NAda}]^-$  and the dehydrogenated crypt.222 (II). The formation of the adamantly complexes 2X follows the same mechanism.



**Figure S20.** Formation of IX2 by hydrogen atom abstraction from crypt.222 by  $[\text{Co}(\text{hmds})_2\text{NCMe}_3]^-$ . The next steps are presumable concerted. A C-O bond cleavage and Co-O bond formation is observed followed by an hydrogen atom abstraction by the N(H)CMe<sub>3</sub> ligand. Finally the formation of an C-C double bond and a Co-C bond formation between the opened crypt.222 and an second equivalent  $[\text{Co}(\text{hmds})_2\text{NCMe}_3]^-$  takes place.



## 21. Cyclic voltammetry

The redox behavior of the complexes (**I**, **1**, **2**, **3**, **6**, **1H**, **1H**, **2H**, **3H**, **12**, **II**) was examined by cyclic voltammetry. A microcell HC “closed” stand (rhd instruments) was used in combination with a temperature controller (rhd instruments) and an AUTOLAB PGSTAT 204 (Metrohm GmbH) potentiostat/galvanostat. The measurements were performed at  $25 \pm 0.1$  °C, using a TSC 70 Closed (rhd instruments) Pt cell in a three-electrode configuration with Pt wires acting as pseudo reference and as working electrode. To secure reproducible conditions the electrodes were freshly polished, rinsed with acetone and dried in vacuo for 2 hours. 2 mM of analyte and 0.1 M nBu<sub>4</sub>N[PF<sub>6</sub>], which acted as electrolyte, were used in the default measurement setup. The [FcCp<sub>2</sub>] / [FcCp<sub>2</sub>]<sup>+</sup> (Fc/Fc<sup>+</sup>) redox couple was utilized as internal standard. However, due to the fast decomposition the complexes under the measurement conditions it was not possible to get reliable voltammograms at scan rates < 200 mV/s. Peak potentials and currents of the first full cycle of each measurement were determined.

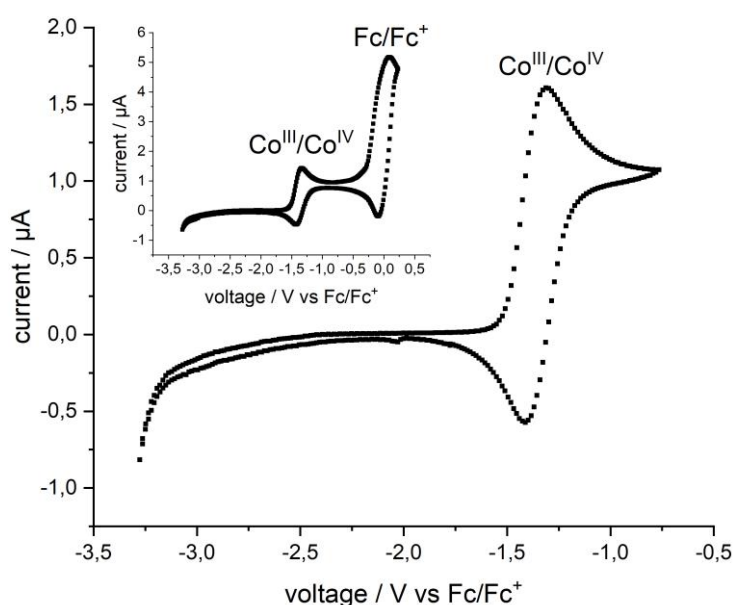


**Figure S21.** Cyclic voltammogram of K{crypt.222}[Co(hmds)<sub>2</sub>N<sup>t</sup>Bu] (**I**) in 1,2-difluorobenzene at a scan rate of 200 mV/s (4 mM, 0.1 M nBu<sub>4</sub>NPF<sub>6</sub>, vs. Fc/Fc<sup>+</sup>) in the presence of ferrocene.  $E_{1/2}$  (Fc/Fc<sup>+</sup>) = -1.36 V.

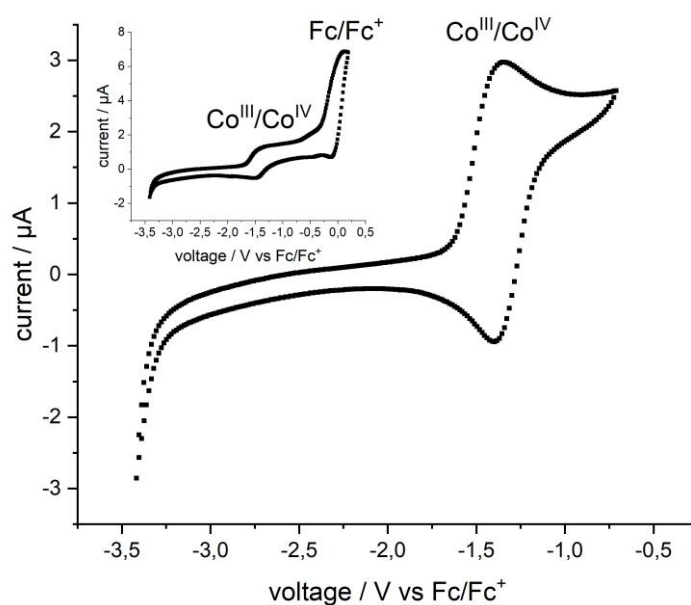


**Figure S22.** Cyclic voltammogram of K{crypt.222}[Co(hmds)<sub>2</sub>NCMe<sub>2</sub>Et] (**1**) in 1,2-difluorobenzene at a scan rate of 200mV/s (4 mM, 0.1 M <sup>n</sup>Bu<sub>4</sub>NPF<sub>6</sub>, vs. Fc/Fc<sup>+</sup>) in the presence of ferrocene. E<sub>1/2</sub> (Fc/Fc<sup>+</sup>) = -1.43 V.

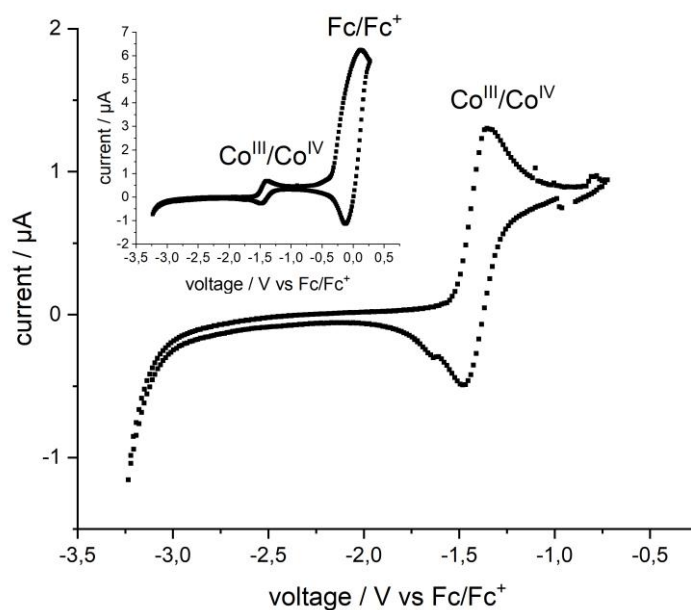


**Figure S23.** Cyclic voltammogram of K{crypt.222}[Co(hmds)<sub>2</sub>NAda] (**2**) in 1,2-difluorobenzene at a scan rate of 200mV/s (4 mM, 0.1 M <sup>n</sup>Bu<sub>4</sub>NPF<sub>6</sub>, vs. Fc/Fc<sup>+</sup>) in the presence of ferrocene. E<sub>1/2</sub> (Fc/Fc<sup>+</sup>) = -1.41 V.

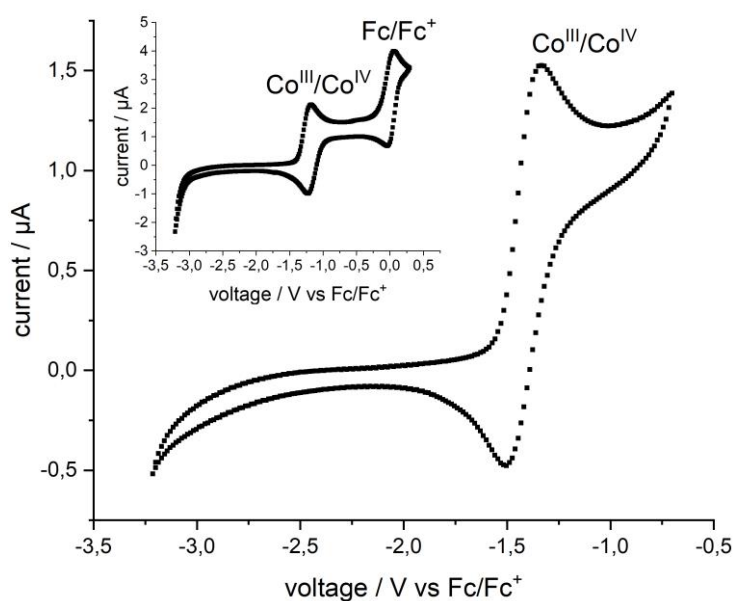


**Figure S24.** Cyclic voltammogram of  $\text{K}\{\text{crypt.222}\}[\text{Co}(\text{hmds})_2\text{NCMe}_2\text{Ph}]$  (**3**) in 1,2-difluorobenzene at a scan rate of 200mV/s (4 mM, 0.1 M  $n\text{Bu}_4\text{NPF}_6$ , vs.  $\text{Fc}/\text{Fc}^+$ ) in the presence of ferrocene.  $E_{1/2}(\text{Fc}/\text{Fc}^+) = -1.21$  V.

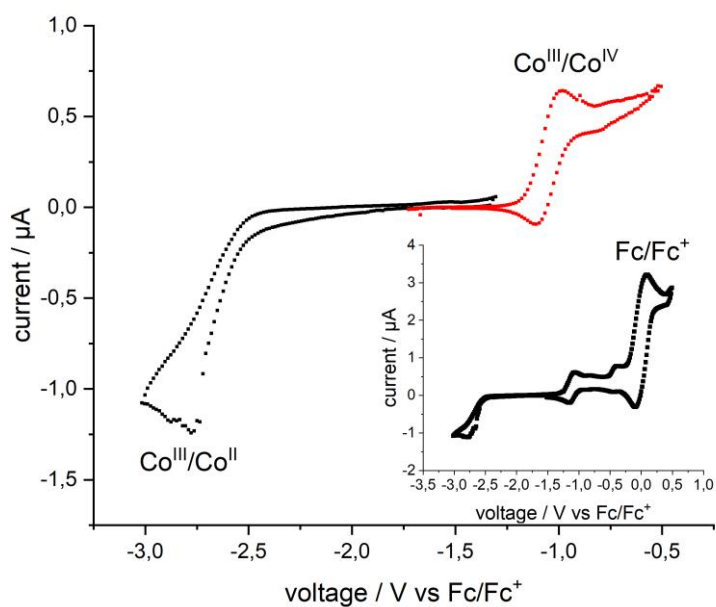


**Figure S25.** Cyclic voltammogram of  $\text{K}\{\text{crypt.222}\}[\text{Co}(\text{hmds})_2\text{NMes}]$  (**6**) in 1,2-difluorobenzene at a scan rate of 100mV/s (4 mM, 0.1 M  $n\text{Bu}_4\text{NPF}_6$ , vs.  $\text{Fc}/\text{Fc}^+$ ) in the presence of ferrocene.  $E_{1/2}(\text{Fc}/\text{Fc}^+) = -1.04$  V.

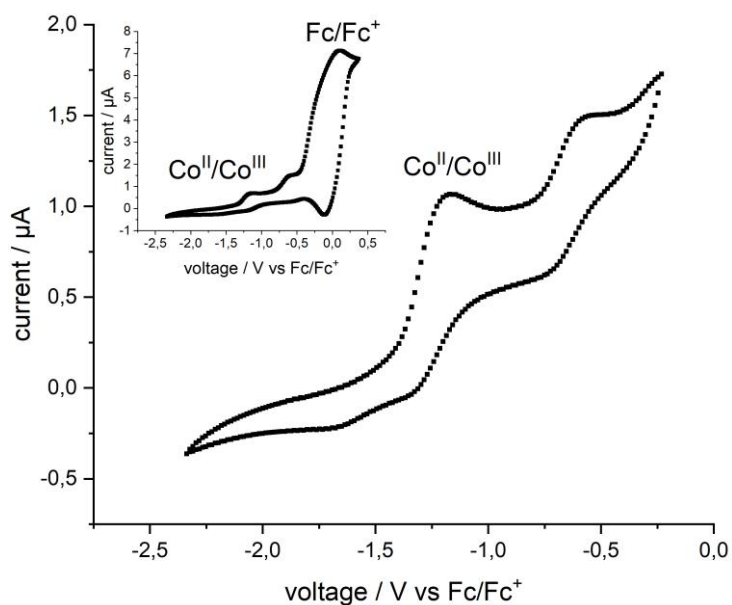


**Figure S26.** Cyclic voltammogram of K{crypt.222}[Co(hmds)<sub>2</sub>NH'Bu] (**1H**) in 1,2-difluorobenzene at a scan rate of 200mV/s (2 mM, 0.1 M <sup>n</sup>Bu<sub>4</sub>NPF<sub>6</sub>, vs. Fc/Fc<sup>+</sup>) in the presence of ferrocene.

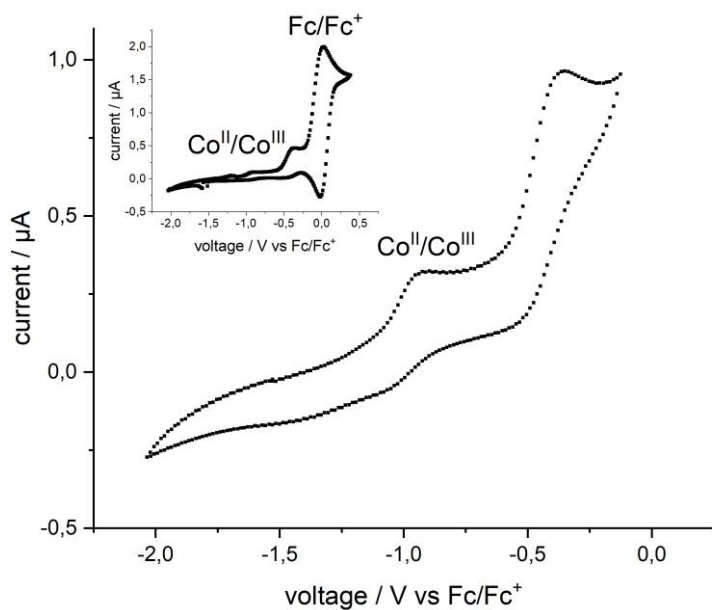


**Figure S27.** Cyclic voltammogram of K{crypt.222}[Co(hmds)<sub>2</sub>N(H)CMe<sub>2</sub>Et] (**1H**) in 1,2-difluorobenzene at a scan rate of 200mV/s (2 mM, 0.1 M <sup>n</sup>Bu<sub>4</sub>NPF<sub>6</sub>, vs. Fc/Fc<sup>+</sup>) in the presence of ferrocene.

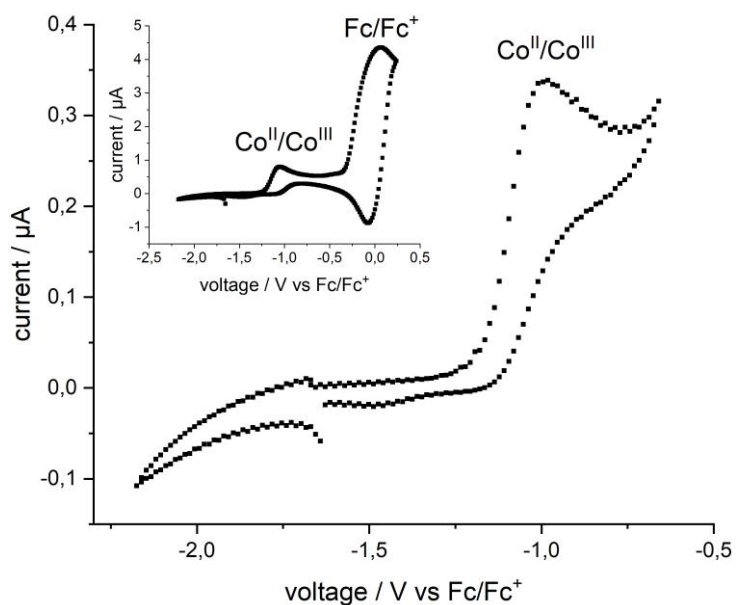


**Figure S28.** Cyclic voltammogram of K{crypt.222}[Co(hmds)<sub>2</sub>NHAda] (**2H**) in 1,2-difluorobenzene at a scan rate of 200mV/s (2 mM, 0.1 M <sup>n</sup>Bu<sub>4</sub>NPF<sub>6</sub>, vs. Fc/Fc<sup>+</sup>) in the presence of ferrocene.

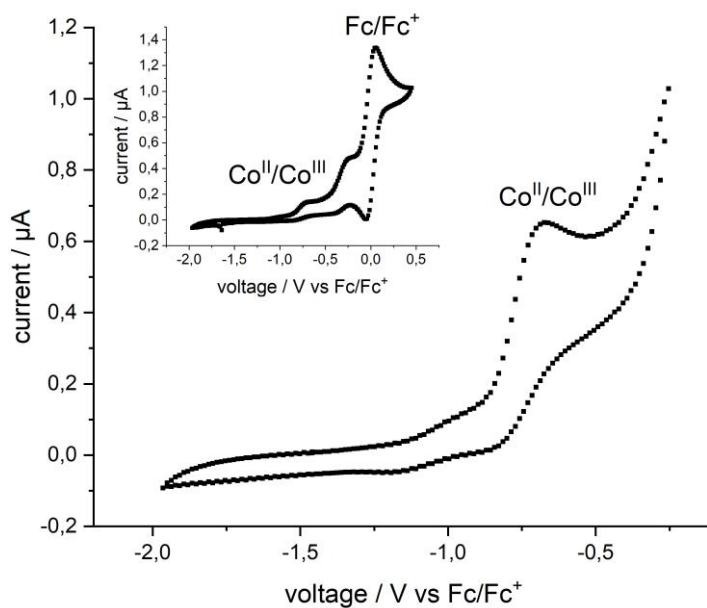


**Figure S29.** Cyclic voltammogram of K{crypt.222}[Co(hmds)<sub>2</sub>NHCMe<sub>2</sub>Ph] (**3H**) in 1,2-difluorobenzene at a scan rate of 200mV/s (2 mM, 0.1 M <sup>n</sup>Bu<sub>4</sub>NPF<sub>6</sub>, vs. Fc/Fc<sup>+</sup>) in the presence of ferrocene.

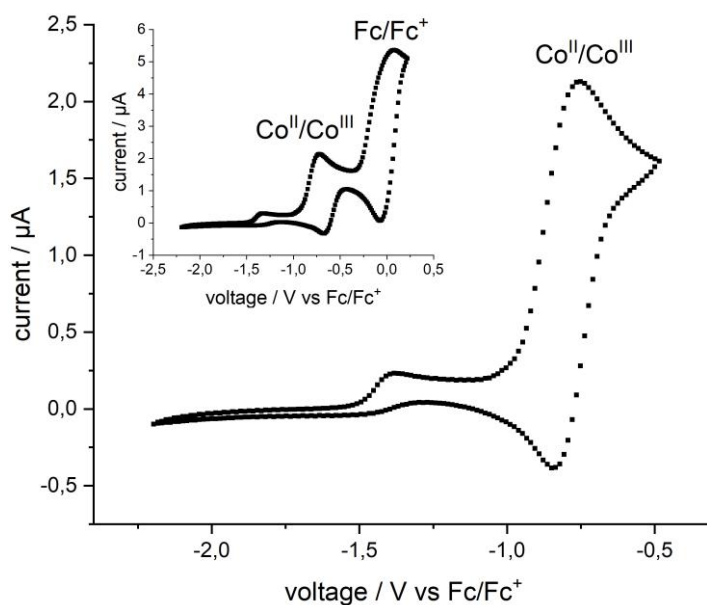


**Figure S30.** Cyclic voltammogram of K{crypt.222}[Co(hmnds)<sub>2</sub>NPh<sub>2</sub>] (**12**) in 1,2-difluorobenzene at a scan rate of 200mV/s (2 mM, 0.1 M <sup>n</sup>Bu<sub>4</sub>NPF<sub>6</sub>, vs. Fc/Fc<sup>+</sup>) in the presence of ferrocene. E<sub>1/2</sub> (Fc/Fc<sup>+</sup>) = -0.70 V.

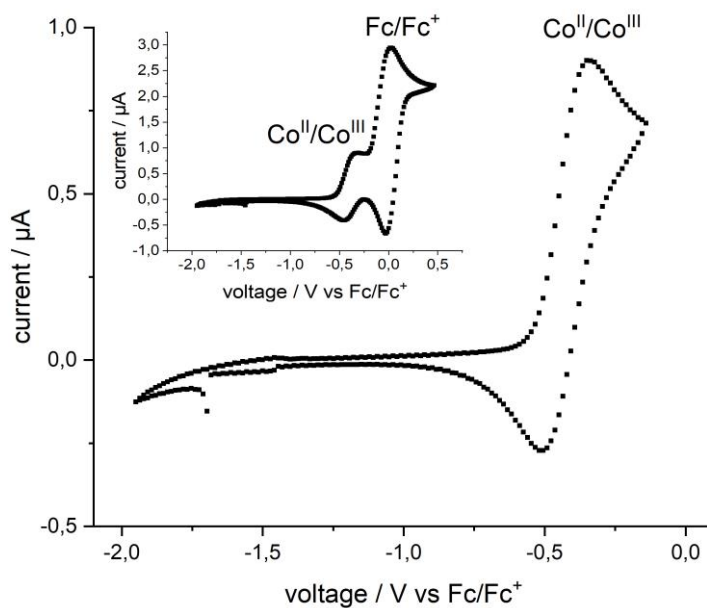


**Figure S31.** Cyclic voltammogram of K{crypt.222}[Co(hmnds)<sub>3</sub>] (**II**) in 1,2-difluorobenzene at a scan rate of 200mV/s (2 mM, 0.1 M <sup>n</sup>Bu<sub>4</sub>NPF<sub>6</sub>, vs. Fc/Fc<sup>+</sup>) in the presence of ferrocene. E<sub>1/2</sub> (Fc/Fc<sup>+</sup>) = -0.40 V.

## 22. Electron-paramagnetic-resonance spectra (EPR)

EPR spectra were performed on a Bruker EMXplus (X-band) EPR spectrometer equipped with the Bruker ER4118X-MD5 probehead. The freshly prepared samples were transferred to J. Young quartz EPR tubes and sealed. The solution in the tube was frozen in liquid nitrogen and kept frozen until measured.

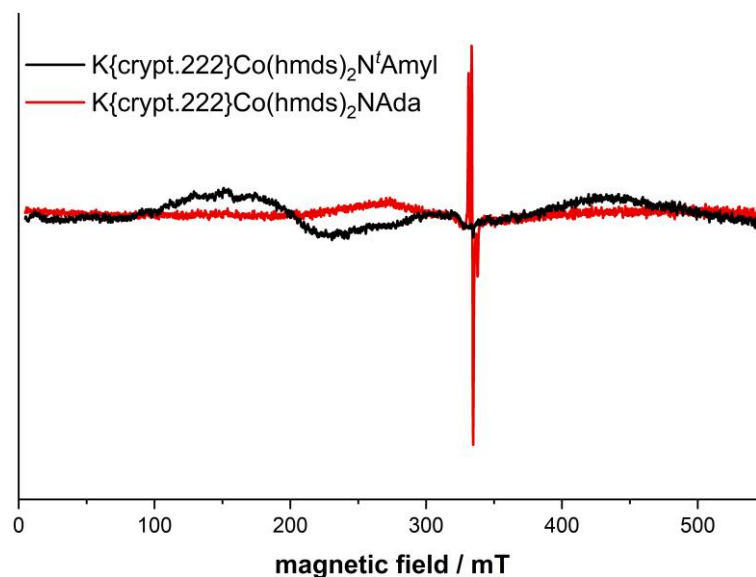


**Figure S32.** X-Band EPR spectra of  $\text{K}\{\text{crypt.222}\}[\text{Co}(\text{hmnds})_2\text{NCMe}_2\text{Et}]$  (**1**) (71 K, frequency 9.354145 GHz, 1.0 mW power, 5 G modulation amplitude) (black), and  $\text{K}\{\text{crypt.222}\}[\text{Co}(\text{hmnds})_2\text{NAda}]$  (**2**) (18 K, frequency 9.355372 GHz, 1.0 mW power, 5 G modulation amplitude) (red) in frozen Me-THF.

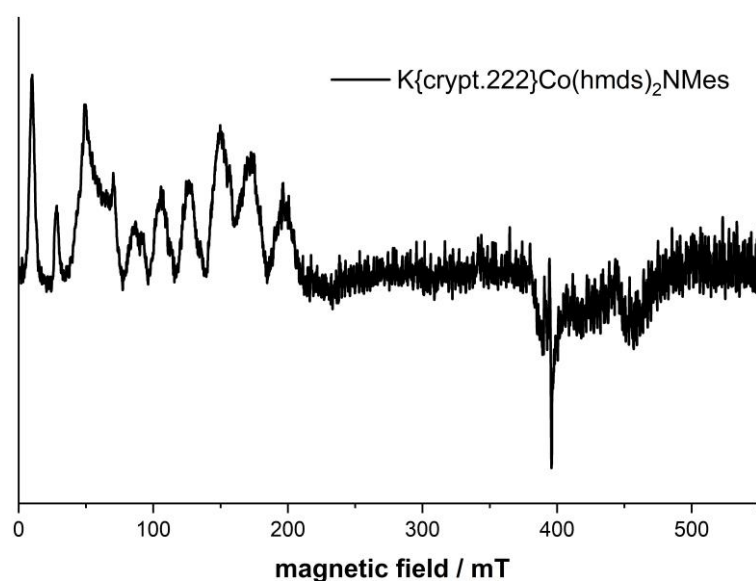


**Figure S33.** X-Band EPR spectra of  $\text{K}\{\text{crypt.222}\}[\text{Co}(\text{hmnds})_2\text{NMes}]$  (**6**) (13 K, frequency 9.353658 GHz, 1.0 mW power, 5 G modulation amplitude) in frozen Me-THF.

## 23. Temperature dependent NMR spectra

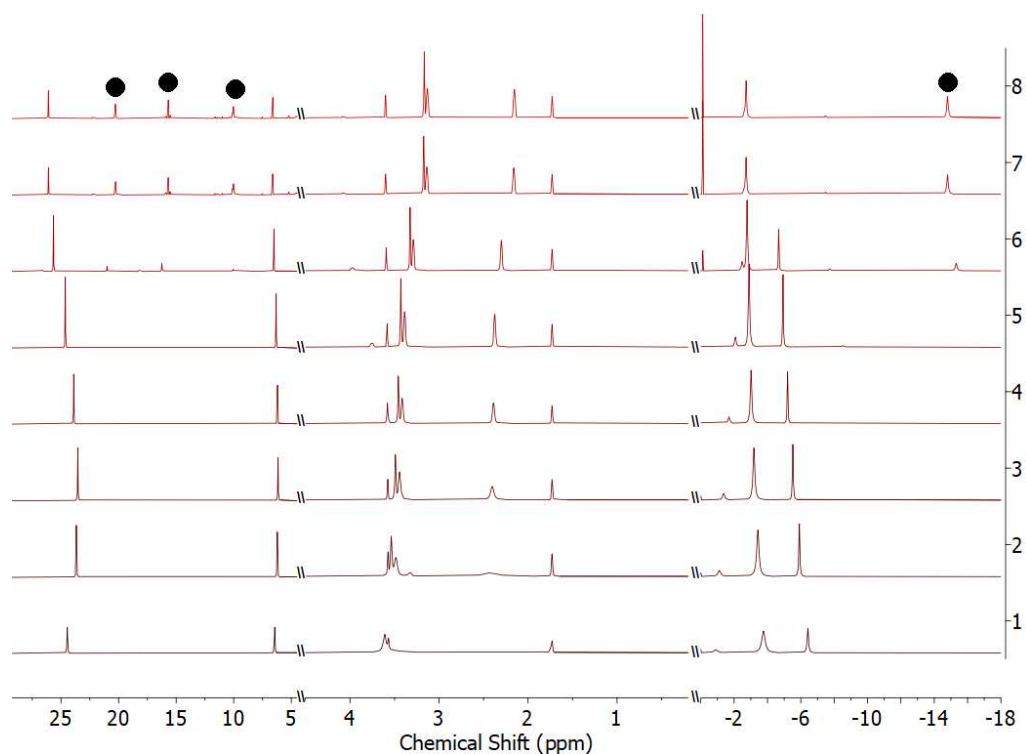


**Figure S34.** Temperature dependent  $^1\text{H}$ -NMR spectra of  $\text{K}\{\text{crypt.222}\}[\text{Co}(\text{hmnds})_2\text{NAda}]$  (**2**) from 193 K to 300 K ( $[\text{D}_8]\text{THF}$ , 500 MHz). Signals of decomposition product  $\text{K}\{\text{crypt.222}\}[\text{Co}(\text{hmnds})_2\text{NHAda}]$  (**2H**) marked with ●.

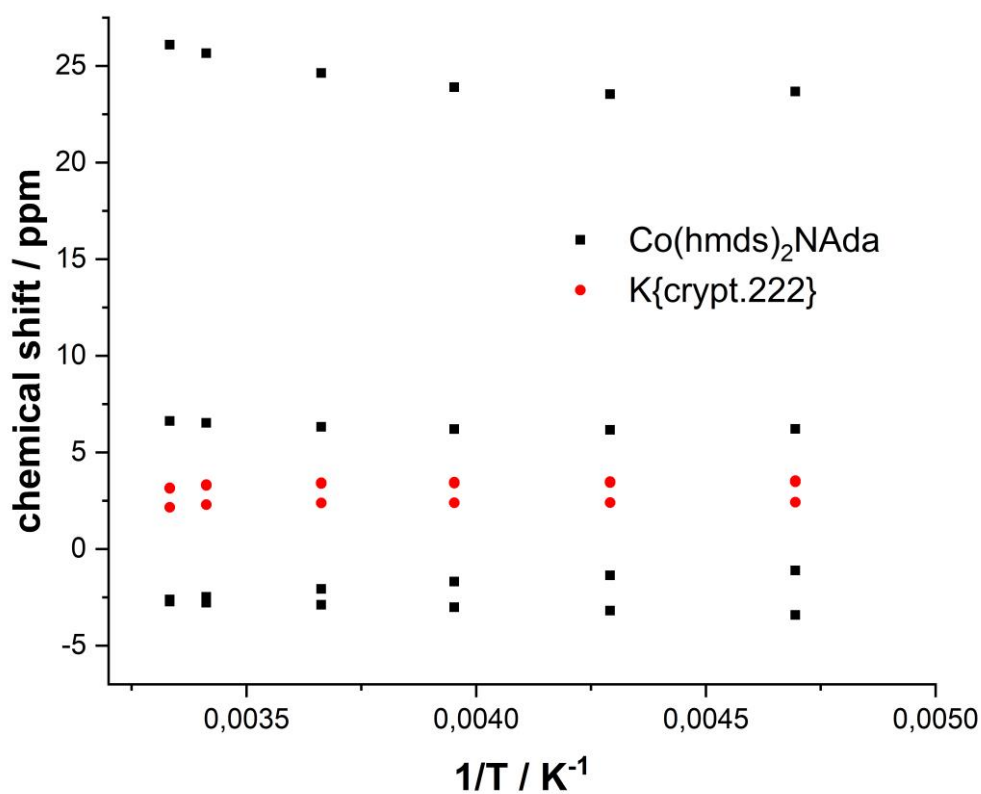


**Figure S1.** Curie-Weiss plot of the temperature dependent  $^1\text{H}$  NMR spectra (500 MHz) of  $\text{K}\{\text{crypt.222}\}[\text{Co}(\text{N}(\text{SiMe}_3)_2)_2\text{NAda}]$  (**2**) in  $\text{THF-d}_8$  from 193 K to 300 K.



## 24. NMR scale reactions

In a typical hydrogen transfer experiment 15 mg of the respective cobalt complex were dissolved in 0.7 ml [D8]THF and added to the substrate. The chemical shift of the protons of the HMDS and Imido/Amido substituent of the cobalt complexes as well as of the substrate are given.

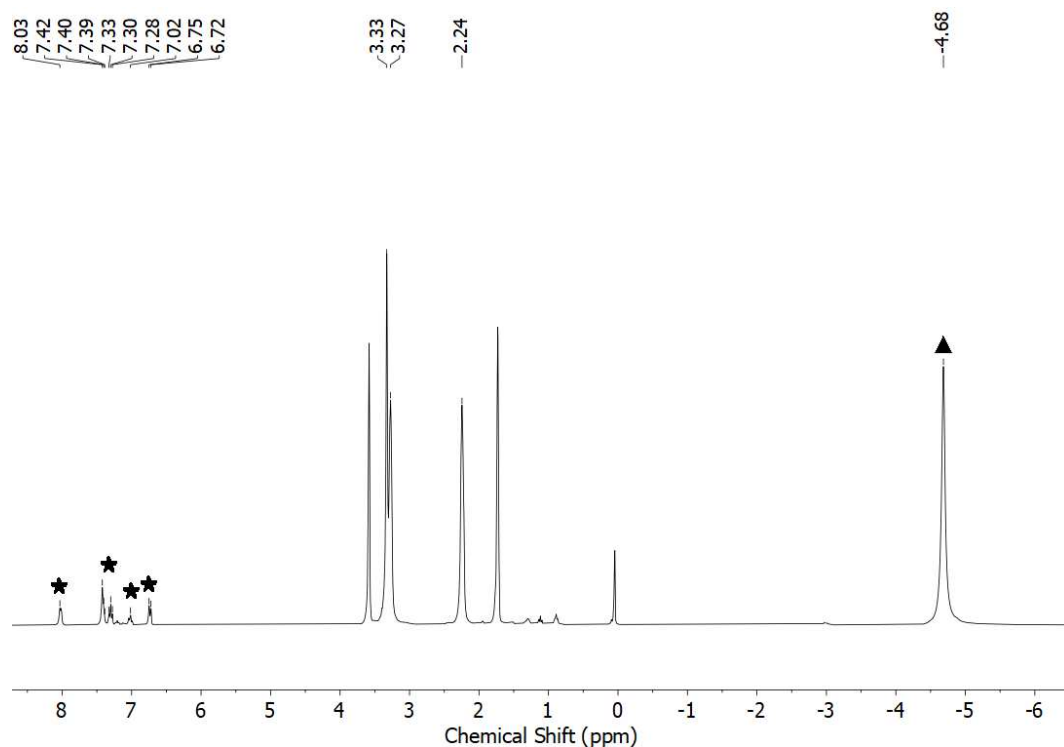


**Figure S35.**  $^1\text{H-NMR}$  spectrum of the reaction of  $\text{K}\{\text{crypt.222}\}[\text{Co}(\text{hmDS})_2]$  with  $\text{N}_3\text{CMePh}_2$  ([D8]THF, 298 K, 300 MHz). The hmDS signal of  $\text{K}\{\text{crypt.222}\}[\text{Co}(\text{hmd})_2]$  is marked with  $\blacktriangle$  and the signals of the formed *N*-(1-Phenylethylidene)benzenamine with  $\star$ .<sup>[6]</sup>

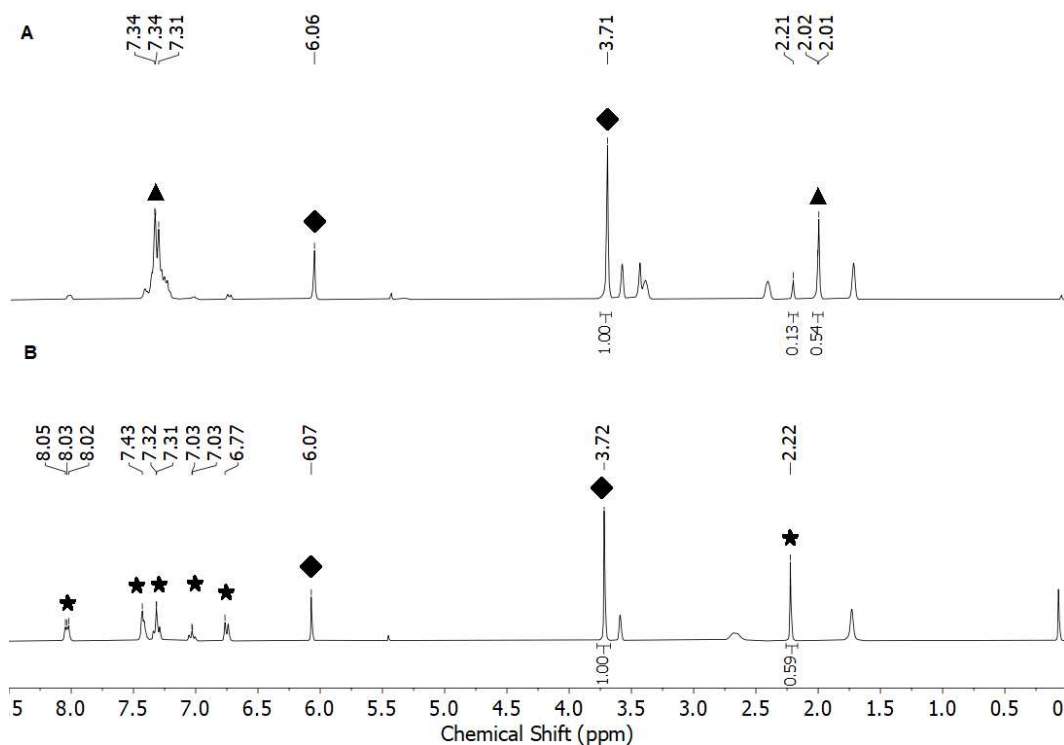


**Figure S36.**  $^1\text{H-NMR}$  spectra of the reaction of 10 mol%  $\text{K}\{\text{crypt.222}\}[\text{Co}(\text{hmds})_2]$  with  $\text{N}_3\text{CMePh}_2$  ( $[\text{D}_8]\text{THF}$ , 298 K, 300 MHz); **A:**  $t = 5$  min; **B:**  $t = 4$  h. The signals of  $\text{N}_3\text{CMePh}_2$  is marked with  $\blacktriangle$ , the signals of the formed  $N$ -(1-Phenylethylidene)benzenamine with  $\star$  and the signal of 1,3,5-trimethoxybenzene is marked with  $\blacklozenge$ .

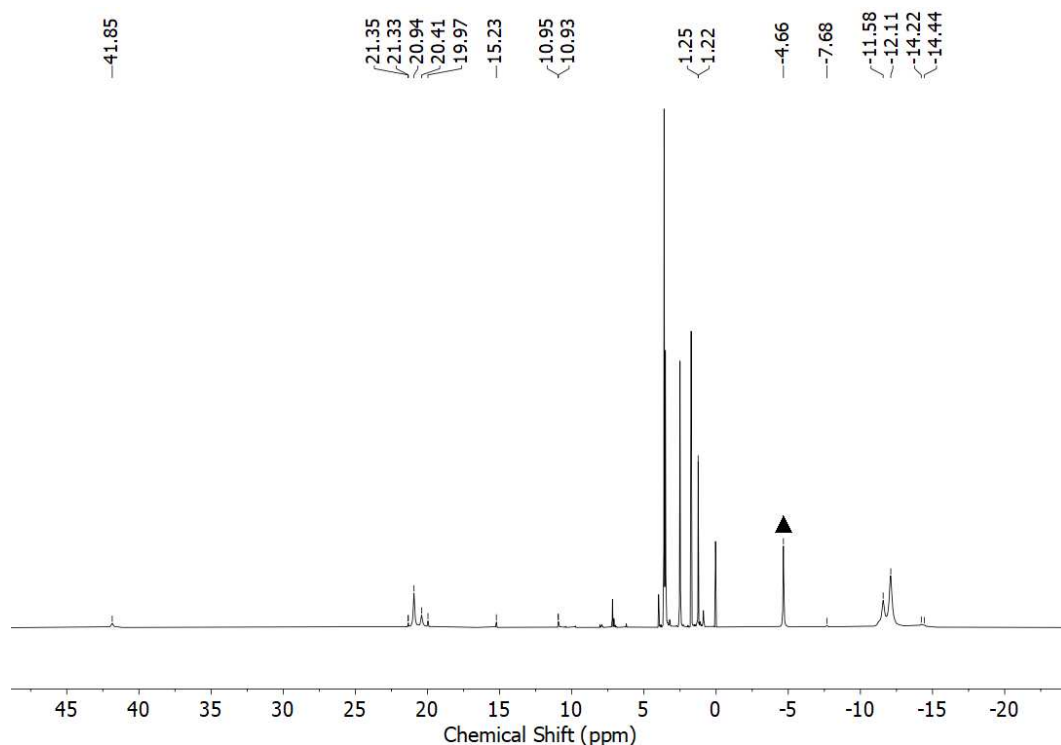


**Figure S37.**  $^1\text{H-NMR}$  spectrum of the reaction of  $\text{K}\{\text{crypt.222}\}[\text{Co}(\text{hmds})_2]$  with  $\text{N}_3\text{Dipp}$  ( $[\text{D}_8]\text{THF}$ , 298 K, 300 MHz). The hmds signal of  $\text{K}\{\text{crypt.222}\}[\text{Co}(\text{hmd})_2]$  is marked with  $\blacktriangle$ .

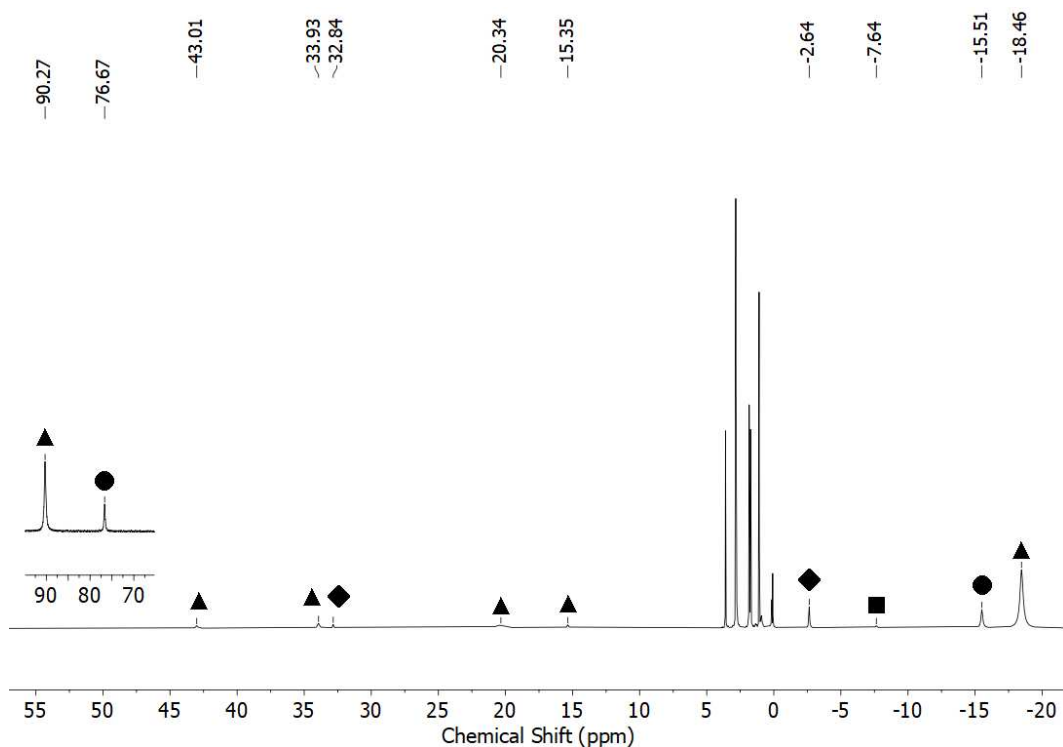


**Figure S38.**  $^1\text{H-NMR}$  spectrum of the reaction of  $\text{K}\{\text{crypt.222}\}[\text{Co}(\text{hmds})_2\text{NCMe}_3]$  (**I**) with 1 equiv. TEMPOH ( $\text{D}_8$ )THF, 298 K, 300 MHz). The signals of  $\text{K}\{\text{crypt.222}\}[\text{Co}(\text{hmds})_2\text{NCMe}_3]$  (**I**) is marked with  $\blacklozenge$ ,  $\text{K}\{\text{crypt.222}\}[\text{Co}(\text{hmds})_2\text{N}(\text{H})\text{CMe}_3]$  (**IH**) is marked with  $\bullet$ , of  $\text{K}\{\text{crypt.222}\}[\text{Co}(\text{hmd})_3]$  with  $\blacksquare$ , and of  $\text{K}\{\text{crypt.222}\}[\text{Co}(\text{hmd})_2\text{TEMPO}]$  (**11**) with  $\blacktriangle$ .

### $\text{K}\{\text{crypt.222}\}[\text{Co}(\text{hmds})_2\text{NCMe}_2\text{Et}]$

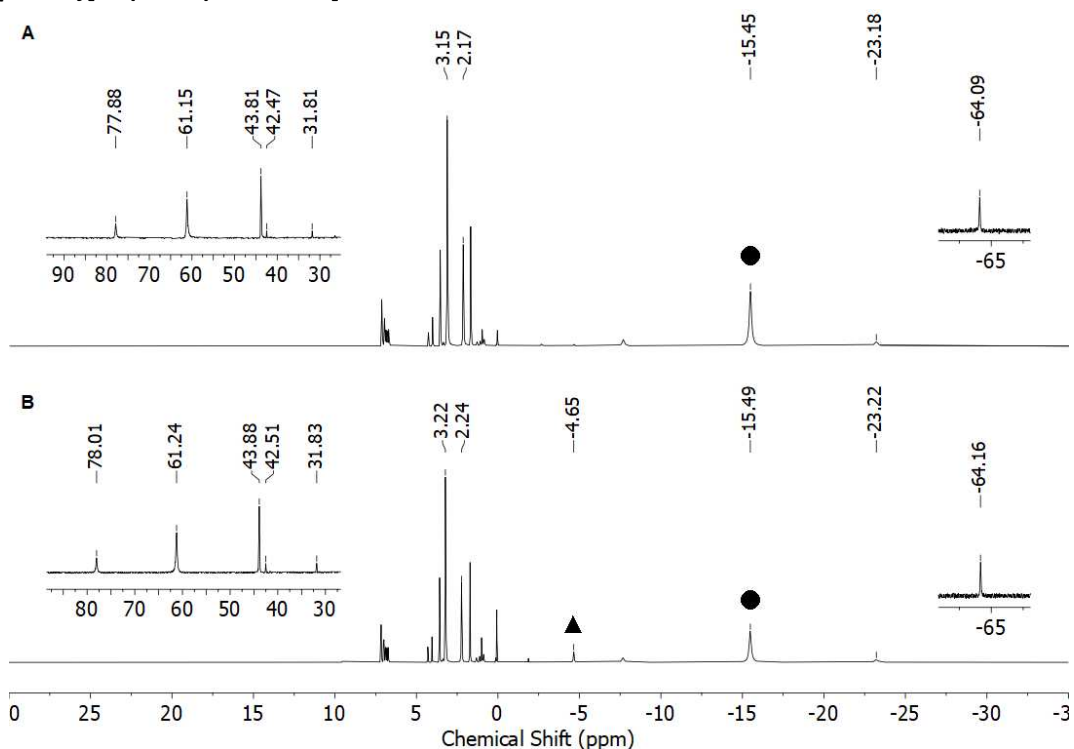


**Figure S39.**  $^1\text{H-NMR}$  spectrum of the reaction of  $\text{K}\{\text{crypt.222}\}[\text{Co}(\text{hmds})_2\text{NCMe}_2\text{Et}]$  (**1**) with 2 equiv. xanthene; **A**:  $t = 10$  min; **B**:  $t = 24$  h ( $\text{D}_8$ )THF, 298 K, 300 MHz). The hmds signal of  $\text{K}\{\text{crypt.222}\}[\text{Co}(\text{hmds})_2\text{N}(\text{H})\text{CMe}_2\text{Et}]$  (**1H**) is marked with  $\bullet$ , and of  $\text{K}\{\text{crypt.222}\}[\text{Co}(\text{hmd})_2]$  with  $\blacktriangle$ .

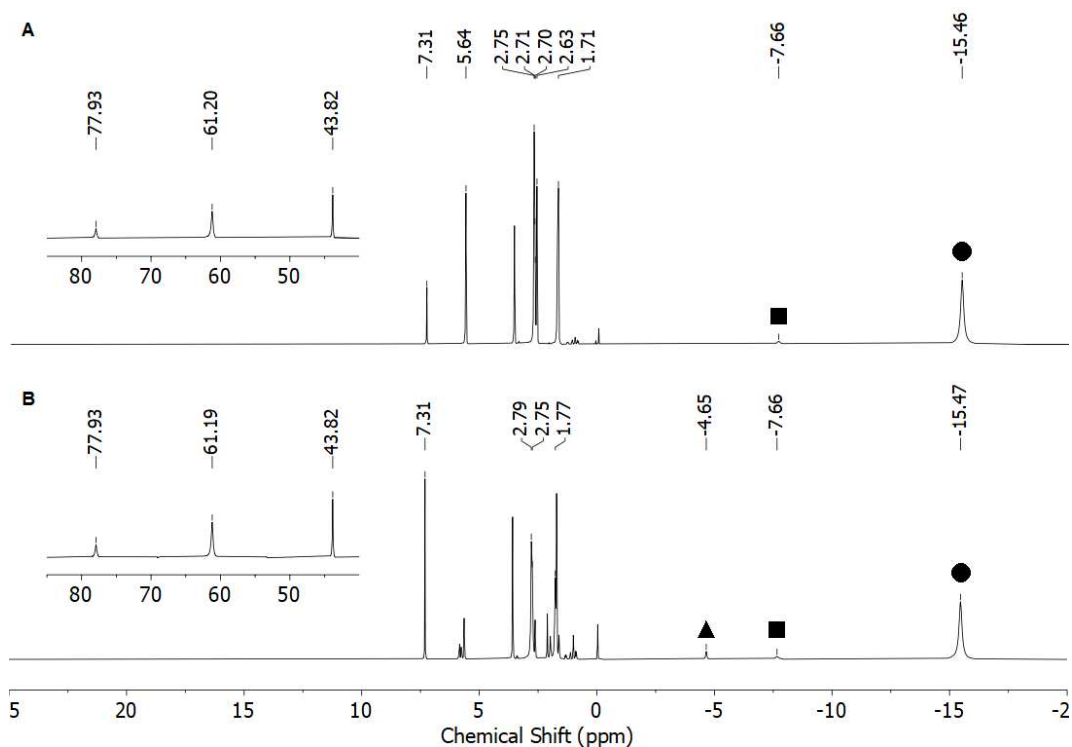


**Figure S40.**  $^1\text{H-NMR}$  spectrum of the reaction of  $\text{K}\{\text{crypt.222}\}[\text{Co}(\text{hmnds})_2\text{NCMe}_2\text{Et}]$  (**1**) with 2 equiv. 1,4-cyclohexadiene; **A**:  $t = 10$  min; **B**:  $t = 24$  h ( $[\text{D8}]\text{THF}$ , 298 K, 300 MHz). The hmnds signal of  $\text{K}\{\text{crypt.222}\}[\text{Co}(\text{hmnds})_2\text{N}(\text{H})\text{CMe}_2\text{Et}]$  (**1H**) is marked with ●, of  $\text{K}\{\text{crypt.222}\}[\text{Co}(\text{hmd})_3]$  with ■, and of  $\text{K}\{\text{crypt.222}\}[\text{Co}(\text{hmd})_2]$  with ▲.

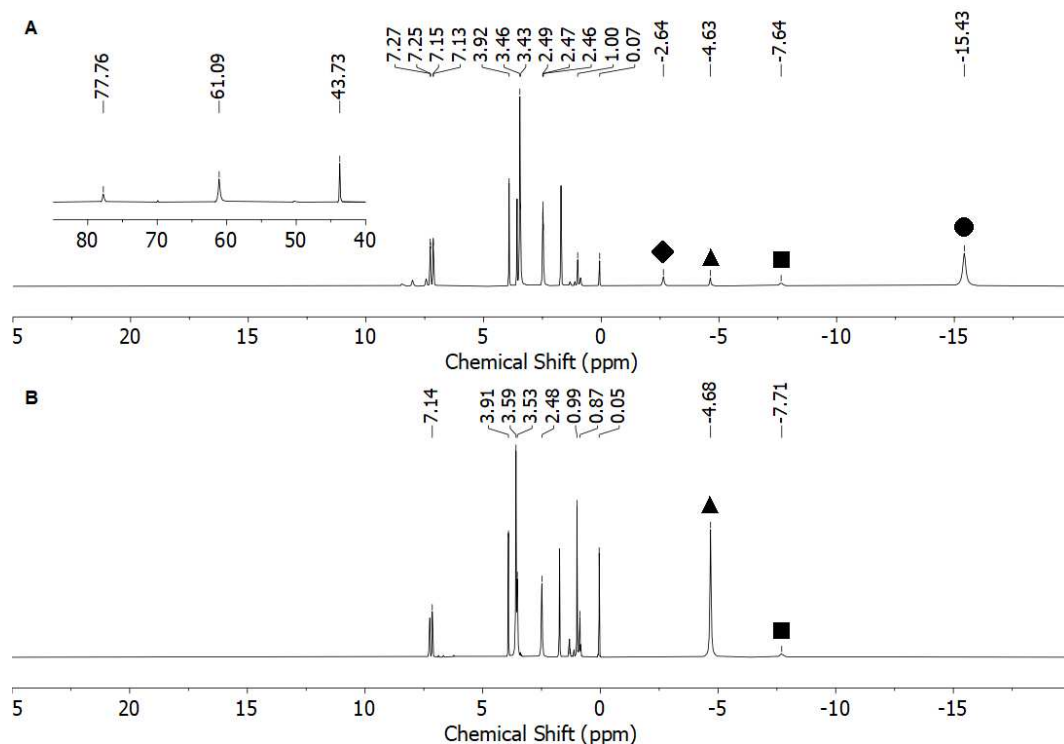


**Figure S41.**  $^1\text{H-NMR}$  spectrum of the reaction of  $\text{K}\{\text{crypt.222}\}[\text{Co}(\text{hmnds})_2\text{NCMe}_2\text{Et}]$  (**1**) with 2 equiv. 9,10-dihydroanthracene; **A**:  $t = 10$  min; **B**:  $t = 24$  h ( $[\text{D8}]\text{THF}$ , 298 K, 300 MHz). The hmnds signal of  $\text{K}\{\text{crypt.222}\}[\text{Co}(\text{hmnds})_2\text{N}(\text{H})\text{CMe}_2\text{Et}]$  (**1H**) is marked with ●, of  $\text{K}\{\text{crypt.222}\}[\text{Co}(\text{hmd})_3]$  (**II**) with ■, and of  $\text{K}\{\text{crypt.222}\}[\text{Co}(\text{hmd})_2]$  with ▲.

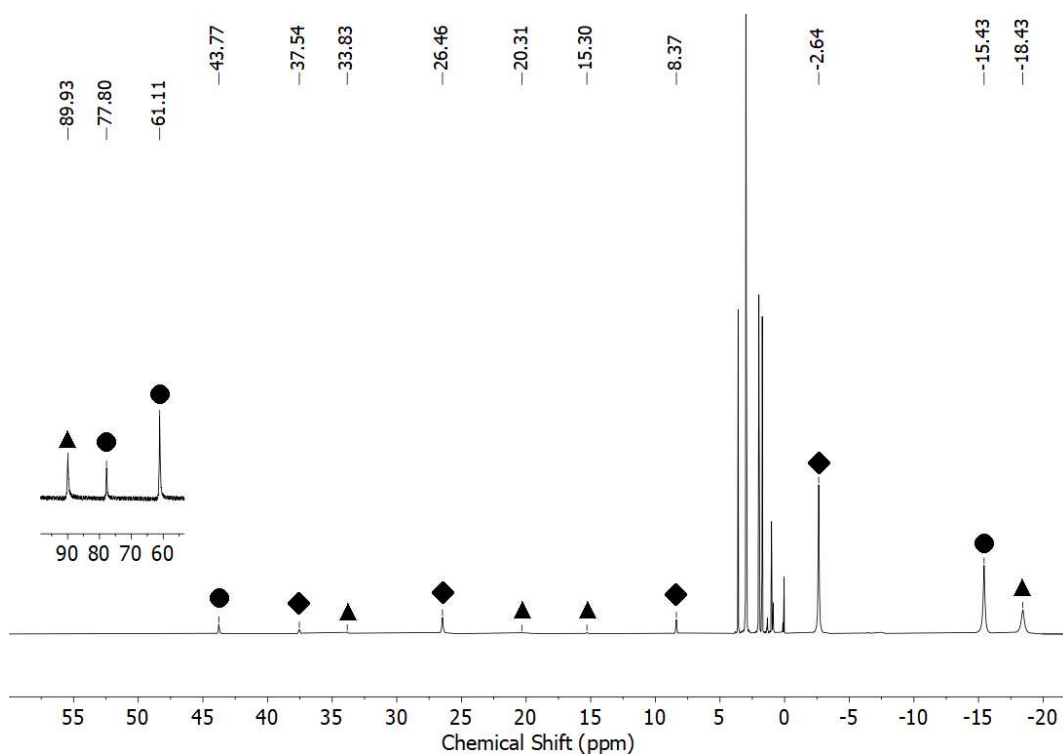


**Figure S42.**  $^1\text{H-NMR}$  spectrum of the reaction of  $\text{K}\{\text{crypt.222}\}[\text{Co}(\text{hmnds})_2\text{NCMe}_2\text{Et}]$  (**1**) with 1 equiv. TEMPOH ( $\text{D8}$ )THF, 298 K, 300 MHz). The signals of  $\text{K}\{\text{crypt.222}\}[\text{Co}(\text{hmnds})_2\text{NCMe}_2\text{Et}]$  (**1**) is marked with ◆,  $\text{K}\{\text{crypt.222}\}[\text{Co}(\text{hmnds})_2\text{N}(\text{H})\text{CMe}_2\text{Et}]$  (**1H**) is marked with ●, and of  $\text{K}\{\text{crypt.222}\}[\text{Co}(\text{hmd})_2\text{TEMPO}]$  (**11**) with ▲.

### $\text{K}\{\text{crypt.222}\}[\text{Co}(\text{hmnds})_2\text{NAda}]$

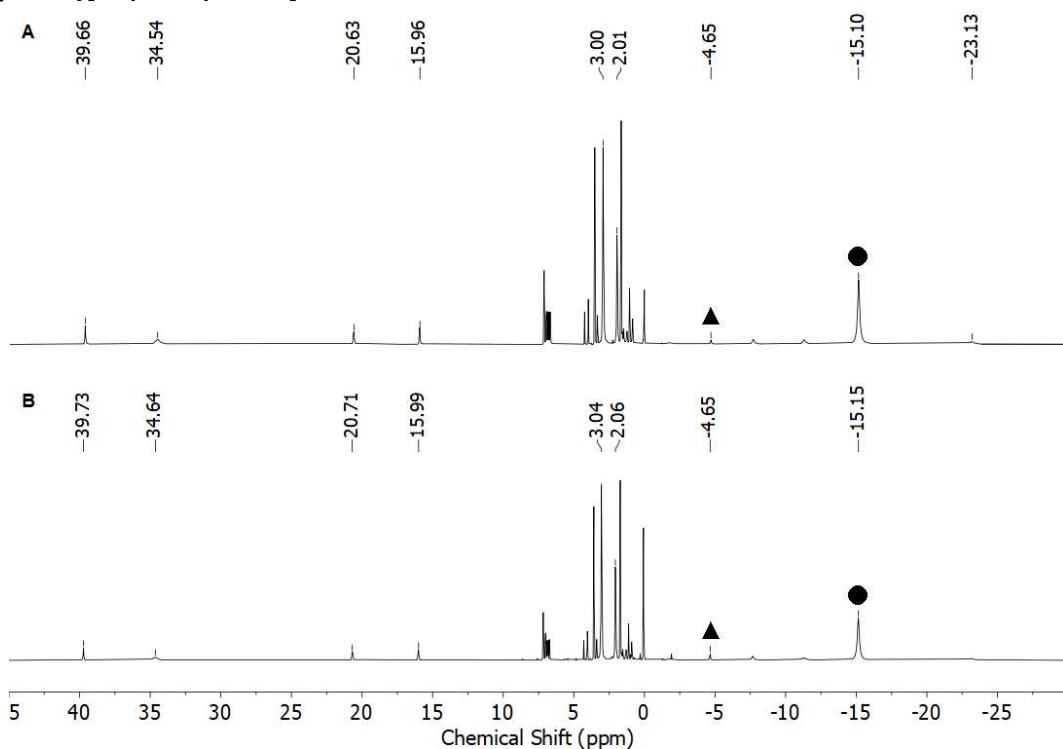


**Figure S43.**  $^1\text{H-NMR}$  spectrum of the reaction of *in situ* generated  $\text{K}\{\text{crypt.222}\}[\text{Co}(\text{hmnds})_2\text{NAda}]$  (**2**) with 2 equiv. xanthene; **A**:  $t = 10$  min; **B**:  $t = 24$  h ( $\text{D8}$ )THF, 298 K, 300 MHz). The hmnds signal of  $\text{K}\{\text{crypt.222}\}[\text{Co}(\text{hmnds})_2\text{N}(\text{H})\text{Ada}]$  (**2H**) is marked with ● and of  $\text{K}\{\text{crypt.222}\}[\text{Co}(\text{hmd})_2]$  with ▲.

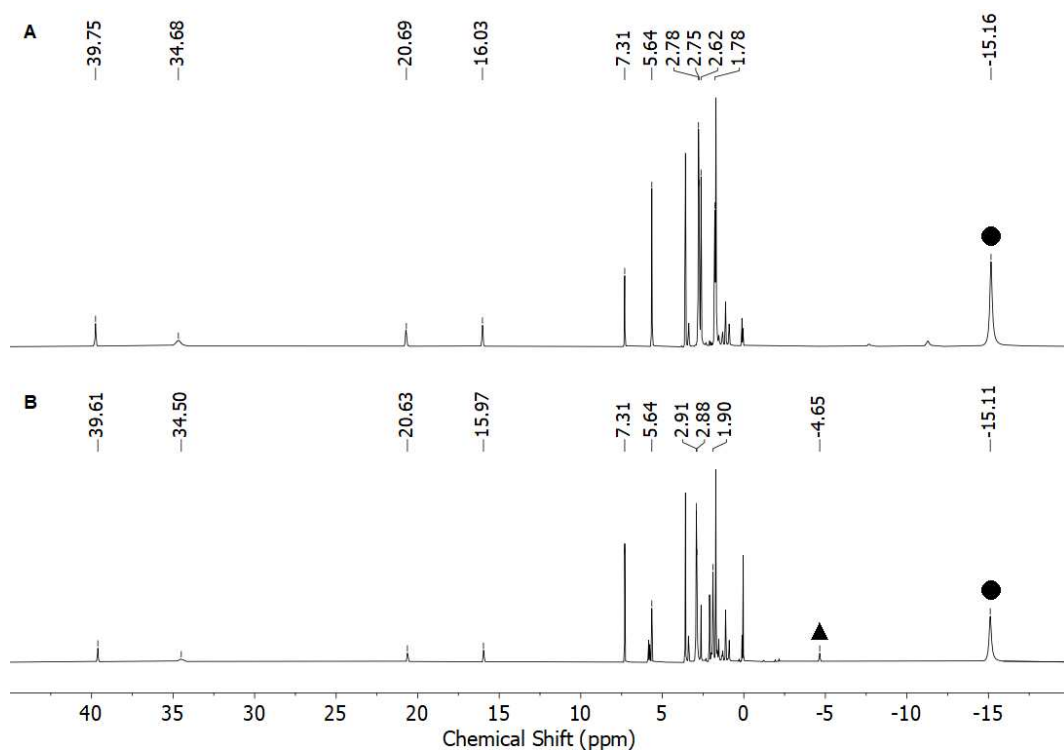


**Figure S44.**  $^1\text{H-NMR}$  spectrum of the reaction of *in situ* generated  $\text{K}\{\text{crypt.222}\}[\text{Co}(\text{hmde})_2\text{NAda}]$  (**2**) with 2 equiv. 1,4-cyclohexadiene; **A**:  $t = 10$  min; **B**:  $t = 24$  h ([D8]THF, 298 K, 300 MHz). The hmde signal of  $\text{K}\{\text{crypt.222}\}[\text{Co}(\text{hmde})_2\text{N}(\text{H})\text{Ada}]$  (**2H**) is marked with ● and of  $\text{K}\{\text{crypt.222}\}[\text{Co}(\text{hmd})_2]$  with ▲.

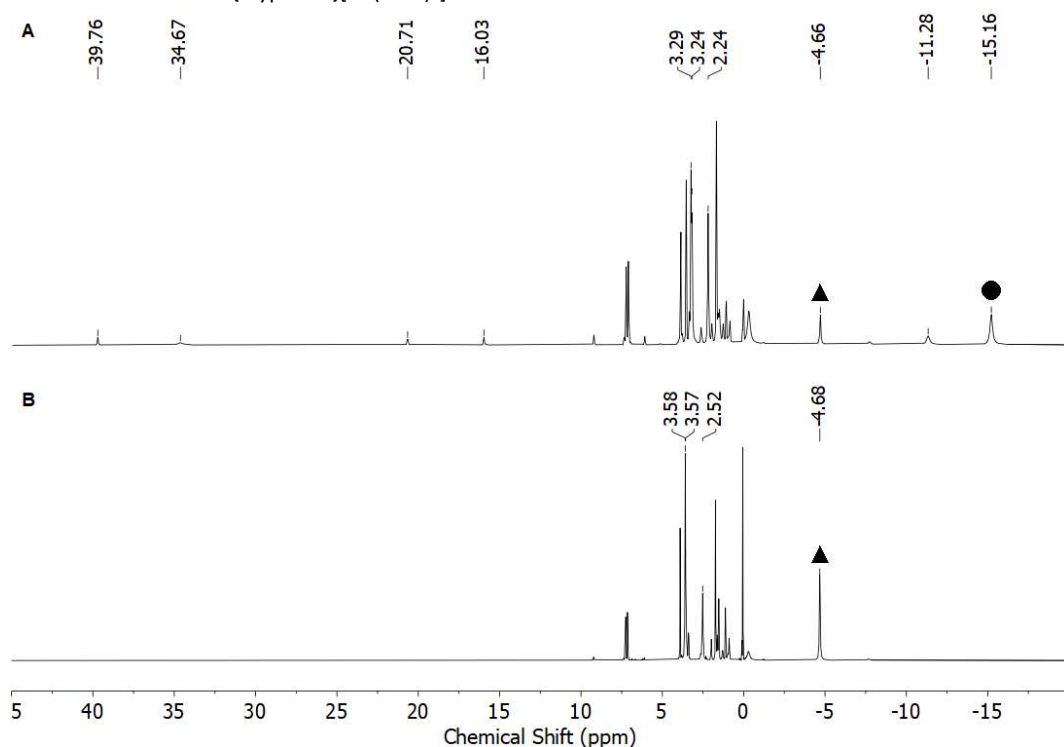


**Figure S45.**  $^1\text{H-NMR}$  spectrum of the reaction of *in situ* generated  $\text{K}\{\text{crypt.222}\}[\text{Co}(\text{hmde})_2\text{NAda}]$  (**2**) with 2 equiv. 9,10-dihydroanthracene; **A**:  $t = 10$  min; **B**:  $t = 24$  h ([D8]THF, 298 K, 300 MHz). The hmde signal of  $\text{K}\{\text{crypt.222}\}[\text{Co}(\text{hmde})_2\text{N}(\text{H})\text{Ada}]$  (**2H**) is marked with ● and of  $\text{K}\{\text{crypt.222}\}[\text{Co}(\text{hmd})_2]$  with ▲.

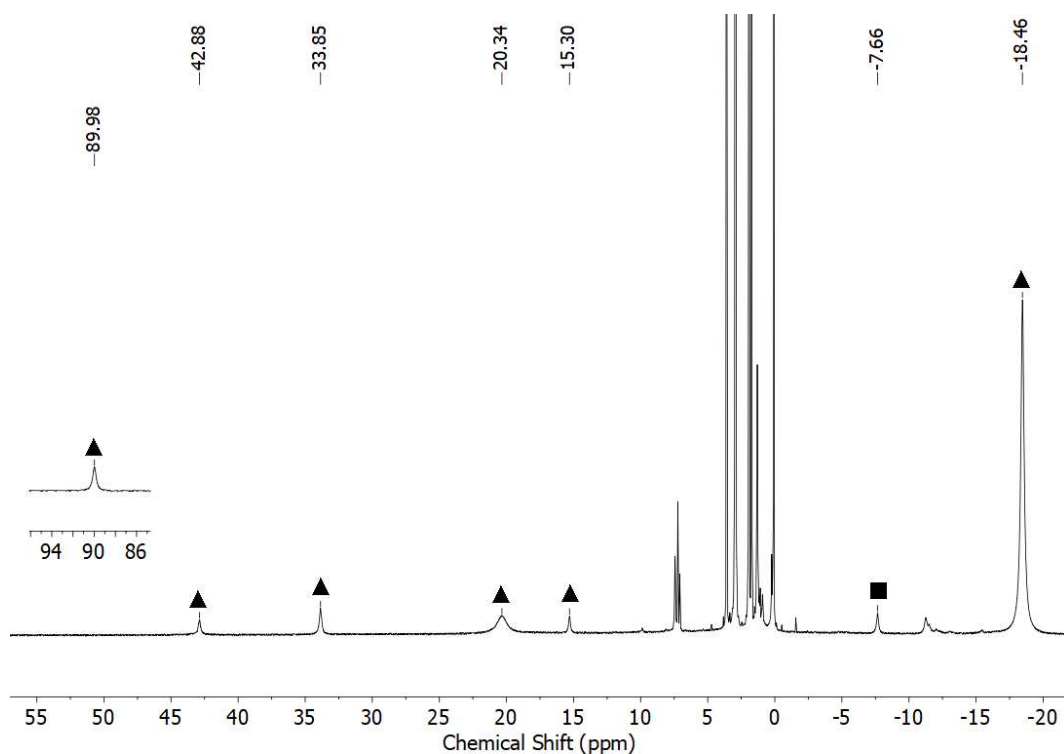


**Figure S46.**  $^1\text{H-NMR}$  spectrum of the reaction of  $\text{K}\{\text{crypt.222}\}[\text{Co}(\text{hmds})_2\text{NAda}]$  (**2**) with 1 equiv. TEMPOH ( $\text{D8}$ )THF, 298 K, 300 MHz). The signals of  $\text{K}\{\text{crypt.222}\}[\text{Co}(\text{hmd})_3]$  (**II**) with  $\blacksquare$ , and of  $\text{K}\{\text{crypt.222}\}[\text{Co}(\text{hmd})_2\text{TEMPO}]$  (**11**) with  $\blacktriangle$ .

### $\text{K}\{\text{crypt.222}\}[\text{Co}(\text{hmds})_2\text{NCMe}_2\text{Ph}]$

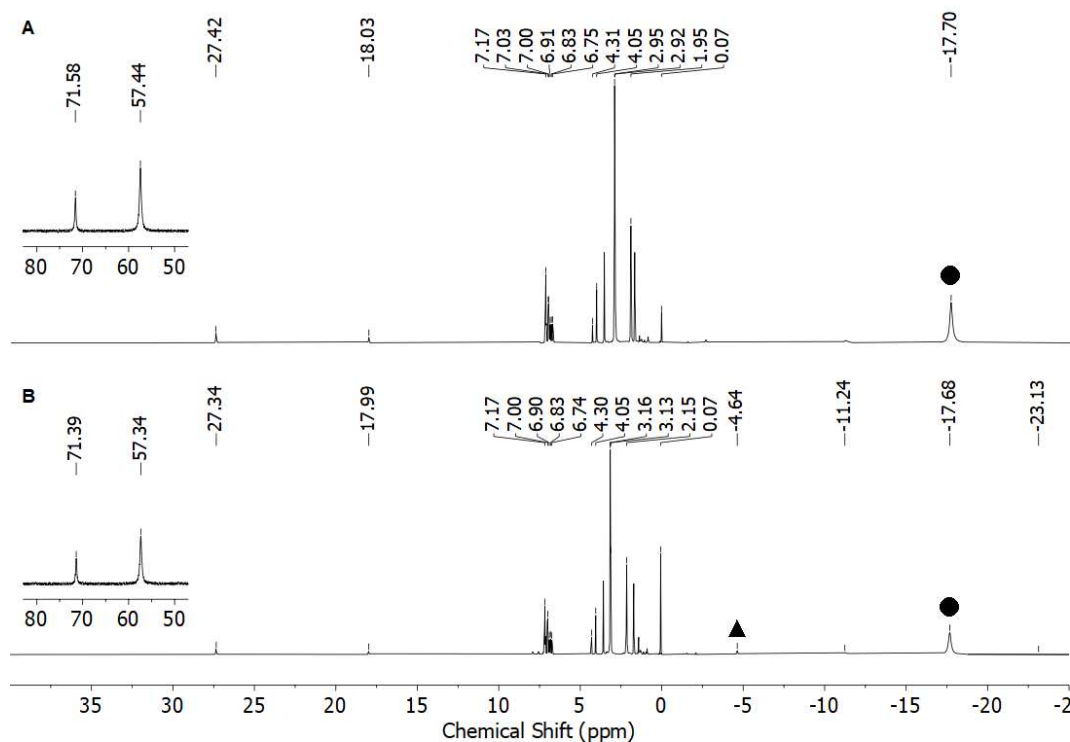


**Figure S47.**  $^1\text{H-NMR}$  spectrum of the reaction of  $\text{K}\{\text{crypt.222}\}[\text{Co}(\text{hmds})_2\text{NCMe}_2\text{Ph}]$  (**3**) with 2 equiv. xanthene; **A**:  $t = 10$  min; **B**:  $t = 24$  h ( $\text{D8}$ )THF, 298 K, 300 MHz). The hmds signal of  $\text{K}\{\text{crypt.222}\}[\text{Co}(\text{hmds})_2\text{N}(\text{H})\text{CMe}_2\text{Ph}]$  (**3H**) is marked with  $\bullet$ , and of  $\text{K}\{\text{crypt.222}\}[\text{Co}(\text{hmd})_2]$  with  $\blacktriangle$ .

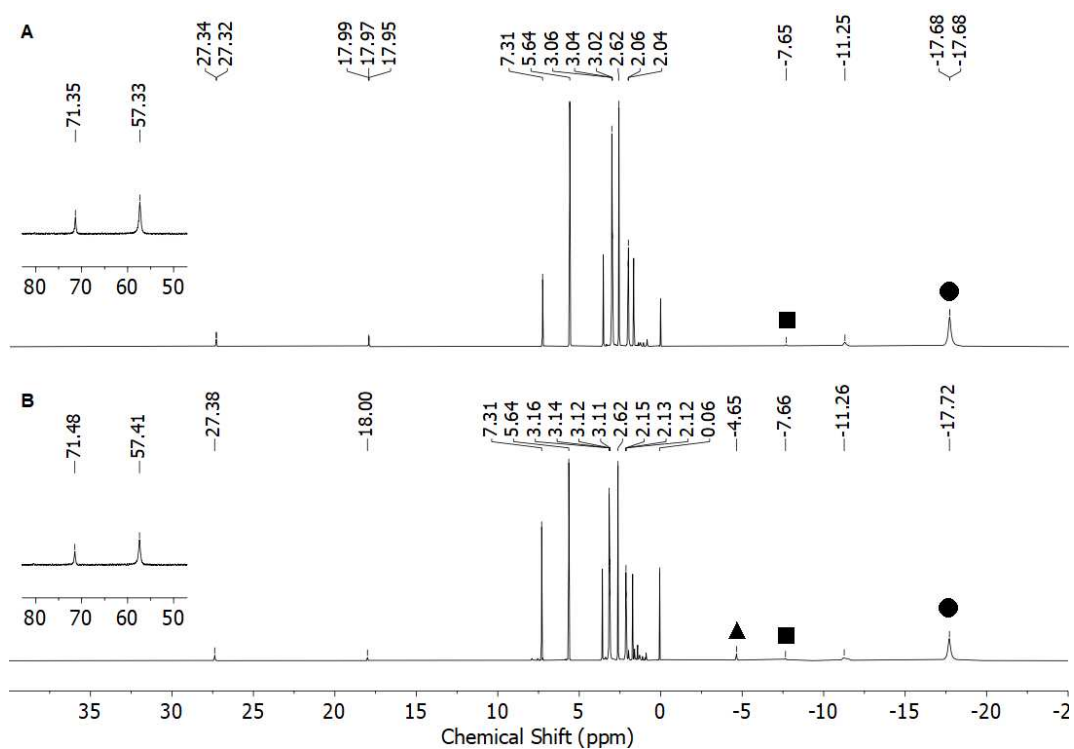


**Figure S48.**  $^1\text{H}$ -NMR spectrum of the reaction of  $\text{K}\{\text{crypt.222}\}[\text{Co}(\text{hmds})_2\text{NCMe}_2\text{Ph}]$  (**3**) with 2 equiv. 1,4-cyclohexadiene; **A**:  $t = 10$  min; **B**:  $t = 24$  h ( $[\text{D}8]\text{THF}$ , 298 K, 300 MHz). The hmds signal of  $\text{K}\{\text{crypt.222}\}[\text{Co}(\text{hmds})_2\text{N}(\text{H})\text{CMe}_2\text{Ph}]$  (**3H**) is marked with ●, of  $\text{K}\{\text{crypt.222}\}[\text{Co}(\text{hmd})_3]$  (**II**) with ■, and of  $\text{K}\{\text{crypt.222}\}[\text{Co}(\text{hmd})_2]$  with ▲.

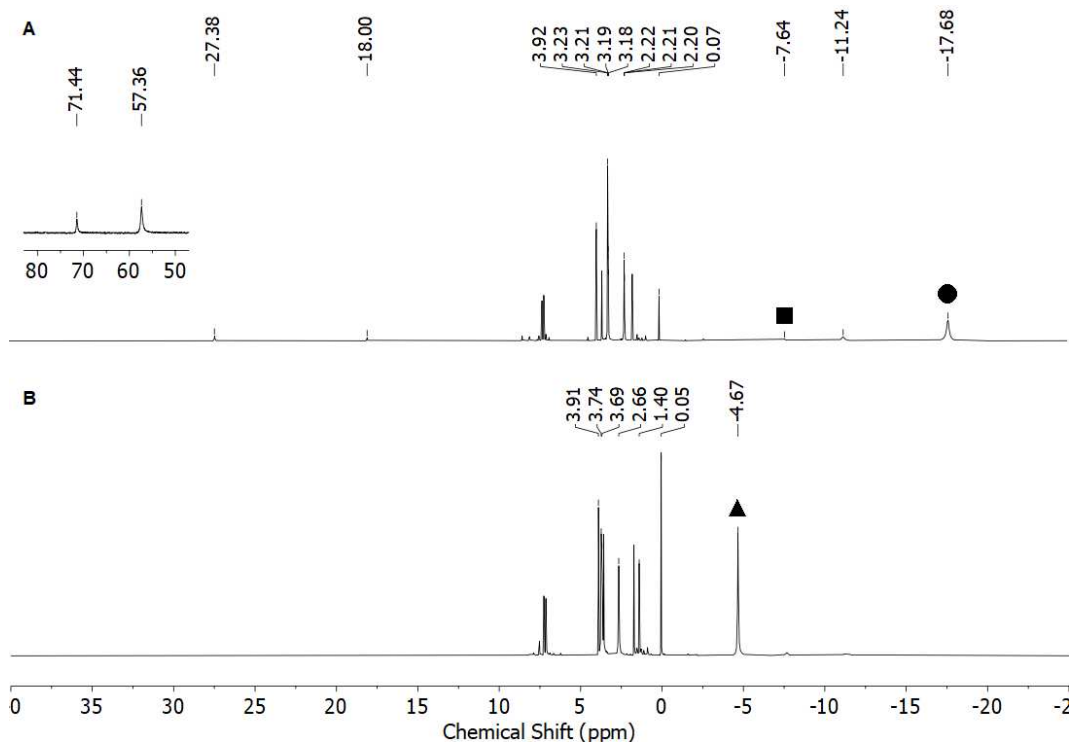


**Figure S49.**  $^1\text{H}$ -NMR spectrum of the reaction of  $\text{K}\{\text{crypt.222}\}[\text{Co}(\text{hmds})_2\text{NCMe}_2\text{Ph}]$  (**3**) with 2 equiv. 9,10-dihydroanthracene; **A**:  $t = 10$  min; **B**:  $t = 24$  h ( $[\text{D}8]\text{THF}$ , 298 K, 300 MHz). The hmds signal of  $\text{K}\{\text{crypt.222}\}[\text{Co}(\text{hmds})_2\text{N}(\text{H})\text{CMe}_2\text{Ph}]$  (**3H**) is marked with ●, of  $\text{K}\{\text{crypt.222}\}[\text{Co}(\text{hmd})_3]$  (**II**) with ■, and of  $\text{K}\{\text{crypt.222}\}[\text{Co}(\text{hmd})_2]$  with ▲.



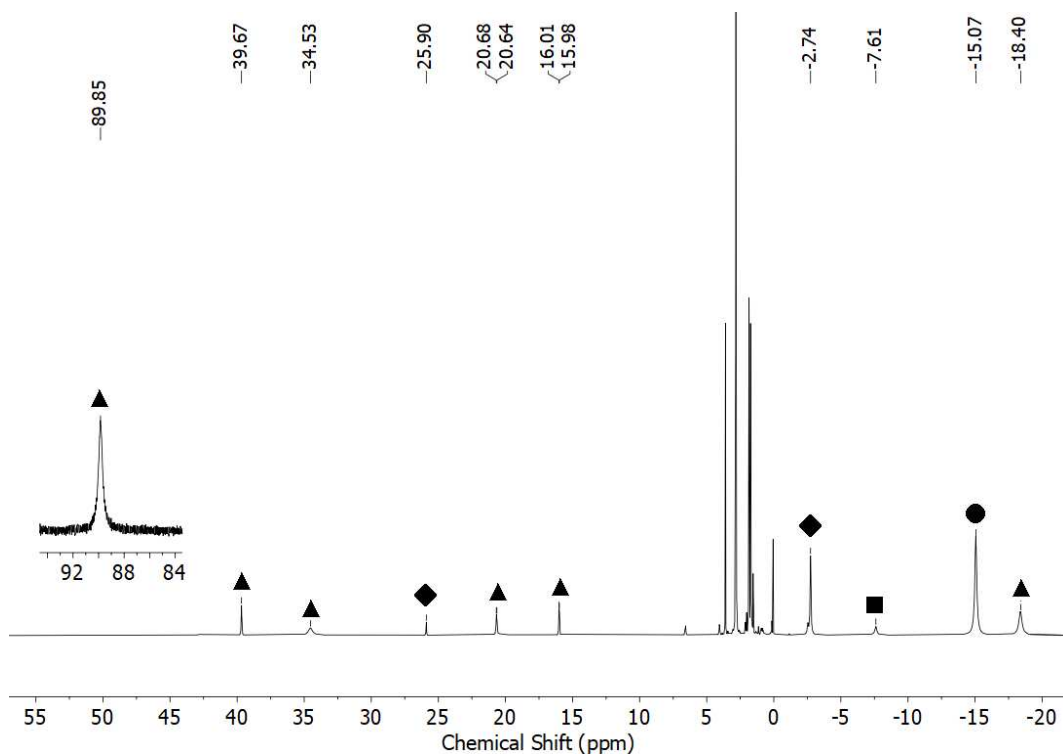


**Figure S50.**  $^1\text{H-NMR}$  spectrum of the reaction of  $\text{K}\{\text{crypt.222}\}[\text{Co}(\text{hmds})_2\text{NCMe}_2\text{Ph}]$  (**3**) with 1 equiv. TEMPOH ( $[\text{D8}]\text{THF}$ , 298 K, 300 MHz). The signals of  $\text{K}\{\text{crypt.222}\}[\text{Co}(\text{hmds})_2\text{NCMe}_2\text{Ph}]$  (**3**) is marked with ◆,  $\text{K}\{\text{crypt.222}\}[\text{Co}(\text{hmds})_2\text{N}(\text{H})\text{CMe}_2\text{Ph}]$  (**3H**) is marked with ●, of  $\text{K}\{\text{crypt.222}\}[\text{Co}(\text{hmd})_3]$  (**II**) with ■, and of  $\text{K}\{\text{crypt.222}\}[\text{Co}(\text{hmd})_2\text{TEMPO}]$  (**11**) with ▲.

### $\text{K}\{\text{crypt.222}\}[\text{Co}(\text{hmds})_2\text{NMes}]$

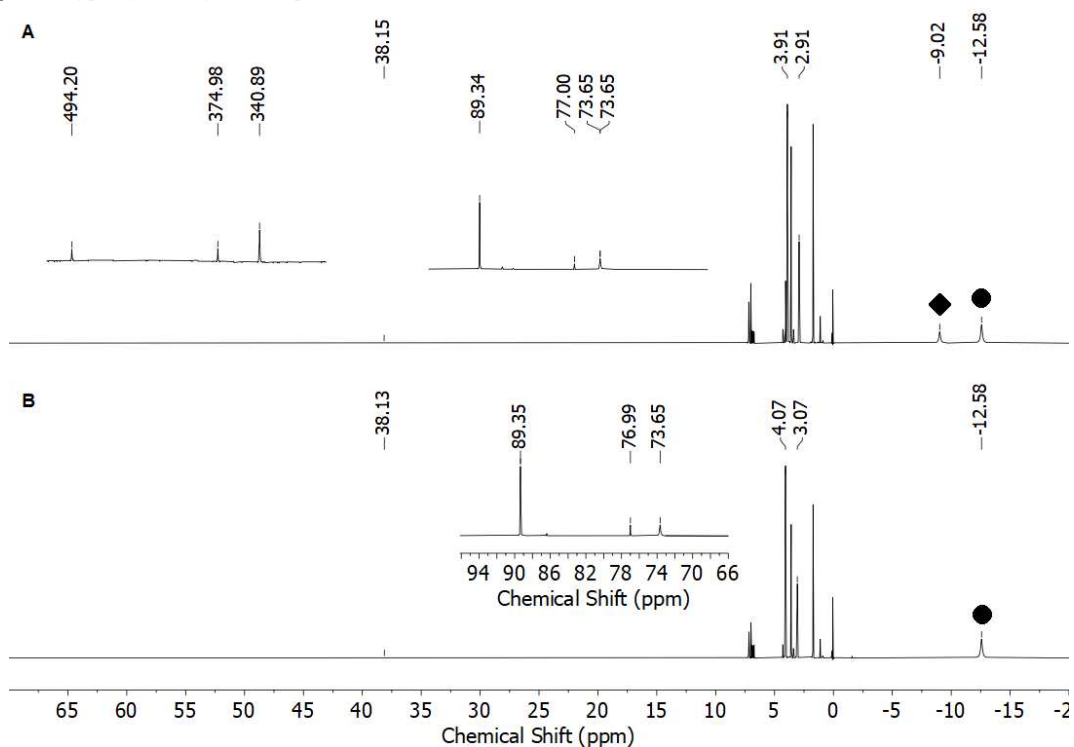


**Figure S51.**  $^1\text{H-NMR}$  spectrum of the reaction of  $\text{K}\{\text{crypt.222}\}[\text{Co}(\text{hmds})_2\text{NMes}]$  (**6**) with 2 equiv. xanthene; **A**:  $t = 10$  min; **B**:  $t = 24$  h ( $[\text{D8}]\text{THF}$ , 298 K, 300 MHz). The hmds signal of  $\text{K}\{\text{crypt.222}\}[\text{Co}(\text{hmds})_2\text{NMes}]$  (**6**) is marked with ◆ and  $\text{K}\{\text{crypt.222}\}[\text{Co}(\text{hmds})_2\text{N}(\text{H})\text{Mes}]$  (**6H**) is marked with ●.

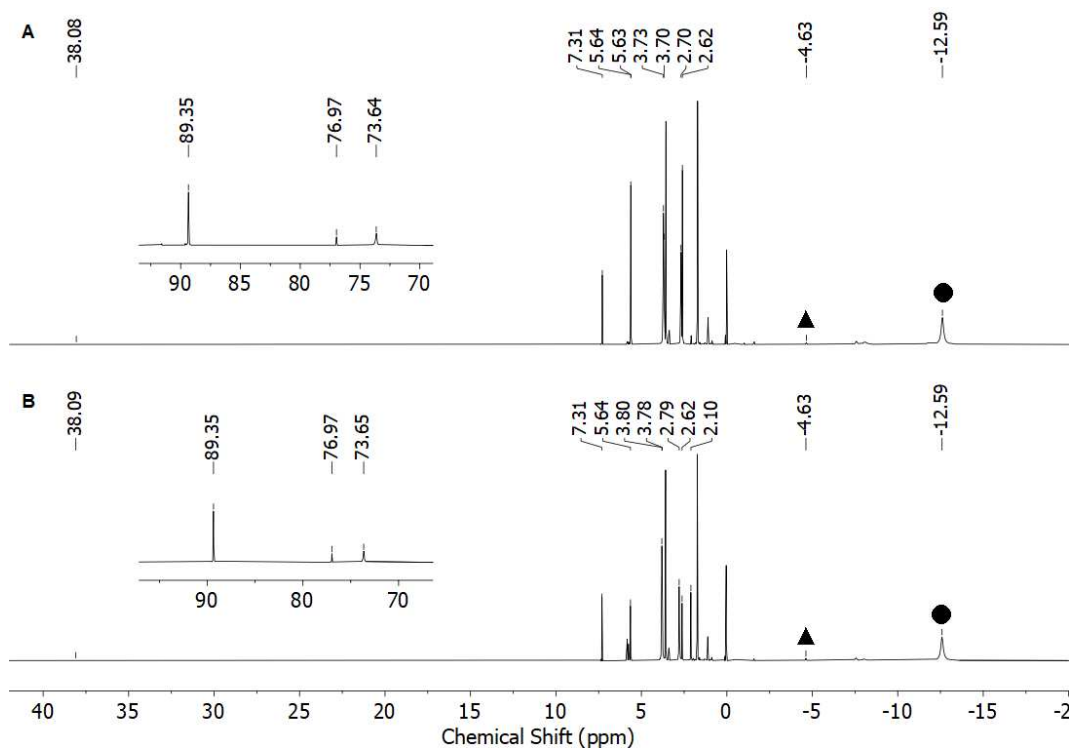


**Figure S52.**  $^1\text{H-NMR}$  spectrum of the reaction of  $\text{K}\{\text{crypt.222}\}[\text{Co}(\text{hmde})_2\text{NMes}]$  (**6**) with 2 equiv. 1,4-cyclohexadiene; **A**:  $t = 10$  min; **B**:  $t = 24$  h ( $[\text{D8}]\text{THF}$ , 298 K, 300 MHz). The hmde signal of  $\text{K}\{\text{crypt.222}\}[\text{Co}(\text{hmde})_2\text{NMes}]$  (**6**) is marked with  $\blacklozenge$  and  $\text{K}\{\text{crypt.222}\}[\text{Co}(\text{hmde})_2\text{N}(\text{H})\text{Mes}]$  (**6H**) is marked with  $\bullet$ .

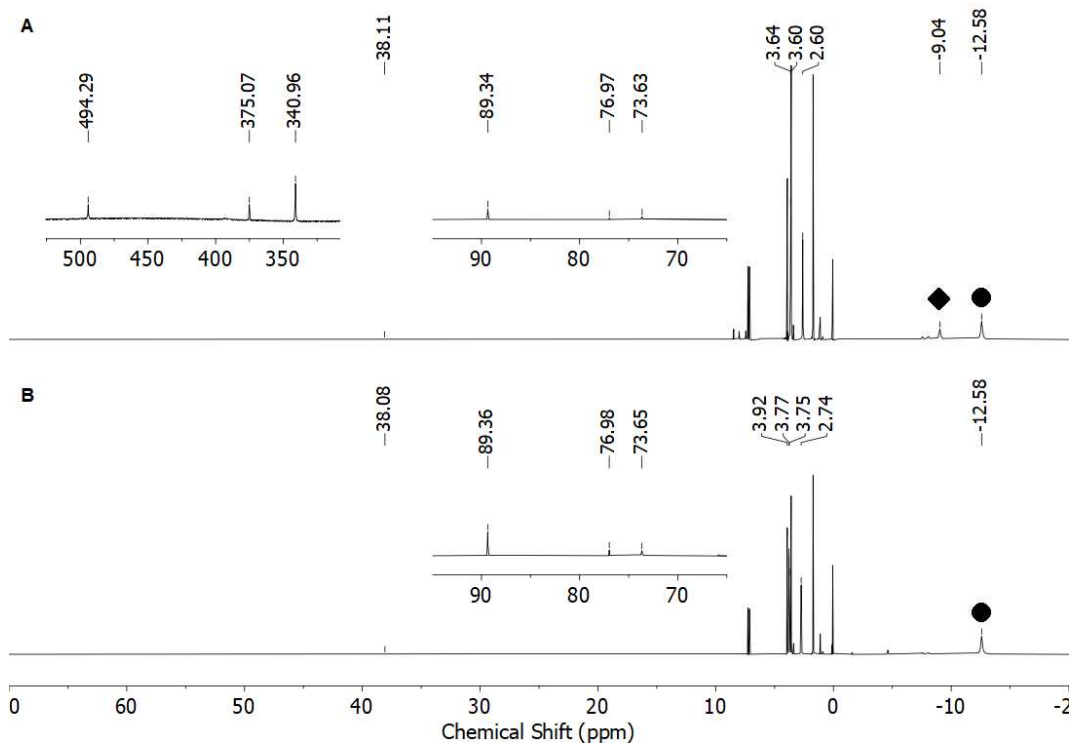


**Figure S53.**  $^1\text{H-NMR}$  spectrum of the reaction of  $\text{K}\{\text{crypt.222}\}[\text{Co}(\text{hmde})_2\text{NMes}]$  (**6**) with 2 equiv. 9,10-dihydroanthracene; **A**:  $t = 10$  min; **B**:  $t = 24$  h ( $[\text{D8}]\text{THF}$ , 298 K, 300 MHz). The hmde signal of  $\text{K}\{\text{crypt.222}\}[\text{Co}(\text{hmde})_2\text{NMes}]$  (**6**) is marked with  $\blacklozenge$  and  $\text{K}\{\text{crypt.222}\}[\text{Co}(\text{hmde})_2\text{N}(\text{H})\text{Mes}]$  (**6H**) is marked with  $\bullet$ .

### K{crypt.222}[Co(hmds)<sub>2</sub>N-Aryle]

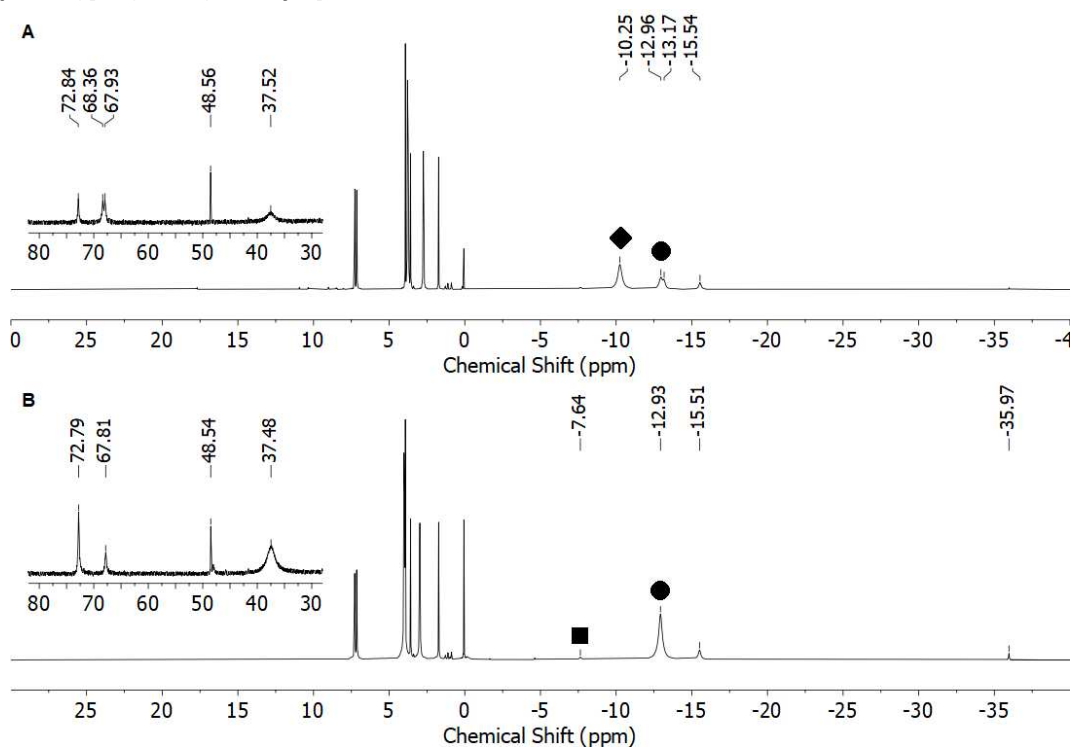


**Figure S54.** <sup>1</sup>H-NMR spectrum of the reaction of K{crypt.222}[Co(hmds)<sub>2</sub>N-2,6-DiMePh] (7) with 2 equiv. 9,10-dihydroanthracene; A: t = 10 min; B: t = 24 h ([D<sub>8</sub>]THF, 298 K, 300 MHz). The hmds signal of K{crypt.222}[Co(hmds)<sub>2</sub>N-2,6-DiMePh] (7) is marked with ◆, K{crypt.222}[Co(hmds)<sub>2</sub>N(H)-2,6-DiMePh] (7H) is marked with ● and of K{crypt.222}[Co(hmd)<sub>3</sub>] (II) with ■.

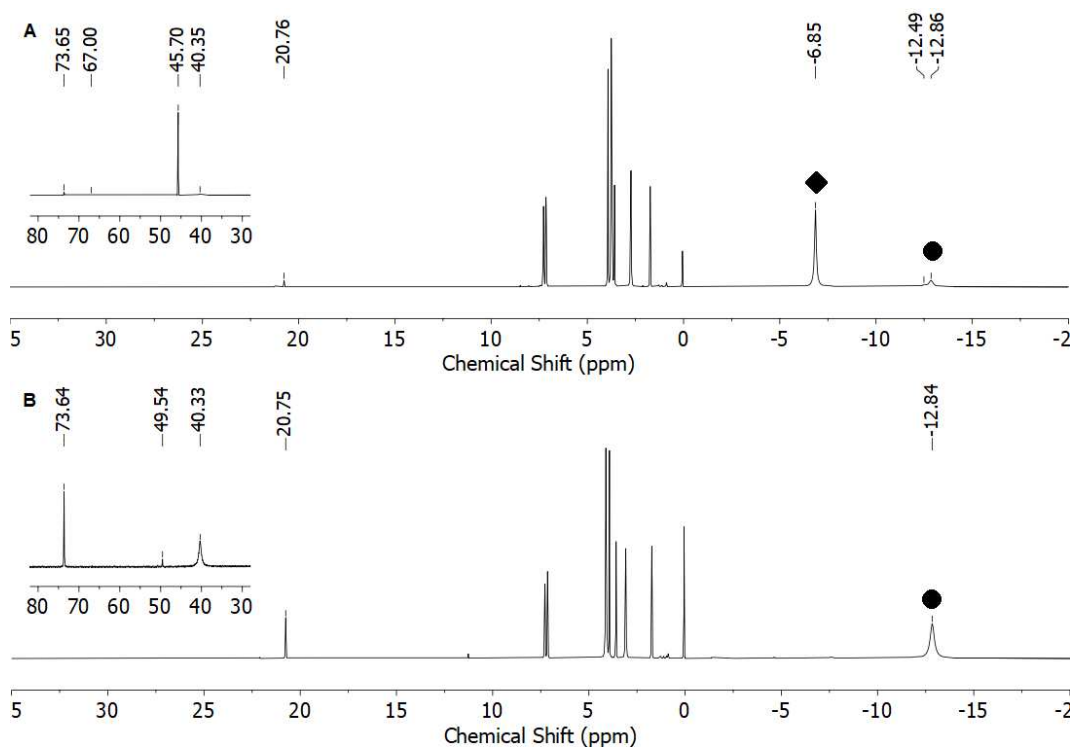


**Figure S55.** <sup>1</sup>H-NMR spectrum of the reaction of K{crypt.222}[Co(hmds)<sub>2</sub>N-4-OMe-2,6-DiMePh] (8) with 2 equiv. 9,10-dihydroanthracene; A: t = 10 min; B: t = 24 h ([D<sub>8</sub>]THF, 298 K, 300 MHz). The hmds signal of K{crypt.222}[Co(hmds)<sub>2</sub>N-4-OMe-2,6-DiMePh] (8) is marked with ◆ and K{crypt.222}[Co(hmds)<sub>2</sub>N(H)-4-OMe-2,6-DiMePh] (8H) is marked with ●.

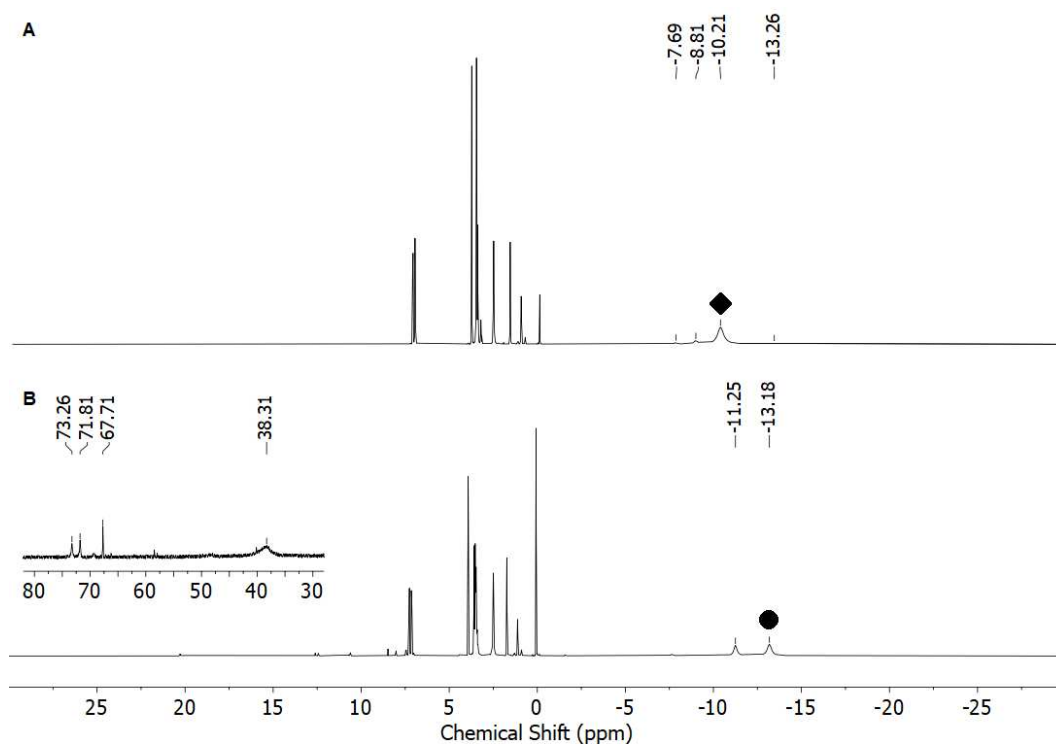


**Figure S56.**  $^1\text{H}$ -NMR spectrum of the reaction of  $\text{K}\{\text{crypt.222}\}[\text{Co}(\text{hmde})_2\text{N-4-Cl-2,6-DiMePh}]$  (**9**) with 2 equiv. 9,10-dihydroanthracene; **A**:  $t = 10$  min; **B**:  $t = 24$  h ( $[\text{D}_8]\text{THF}$ , 298 K, 300 MHz). The hmde signal of  $\text{K}\{\text{crypt.222}\}[\text{Co}(\text{hmde})_2\text{N-4-Cl-2,6-DiMePh}]$  (**9**) is marked with  $\blacklozenge$  and  $\text{K}\{\text{crypt.222}\}[\text{Co}(\text{hmde})_2\text{N(H)-4-Cl-2,6-DiMePh}]$  (**9H**) is marked with  $\bullet$ .

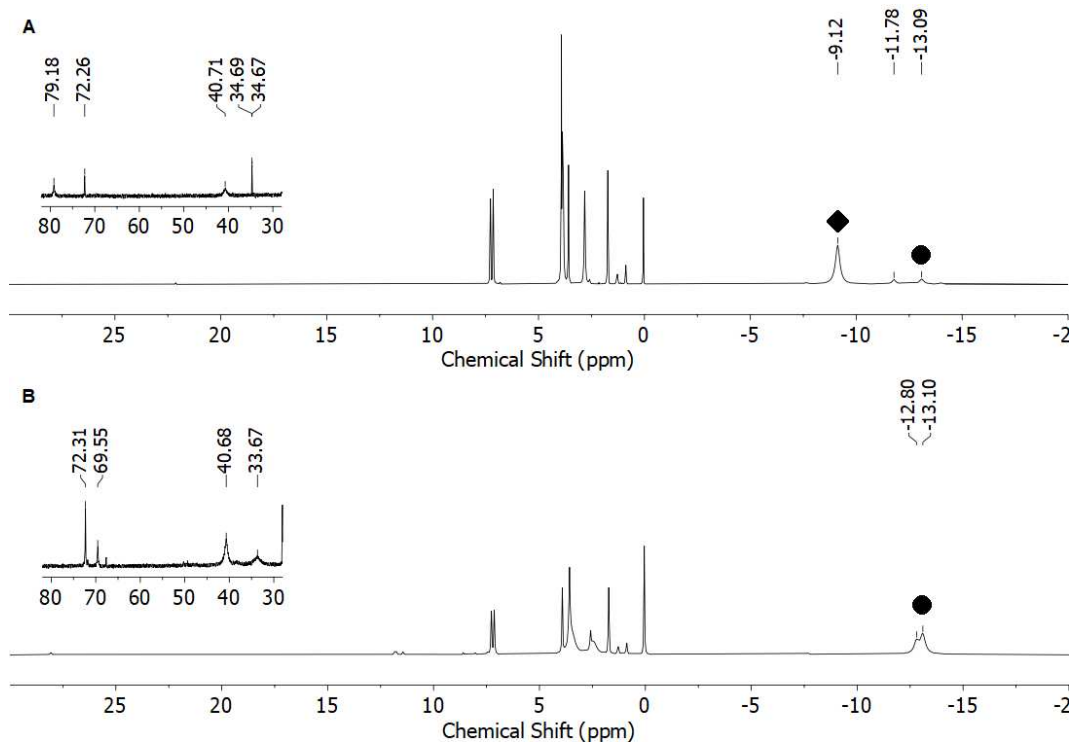


**Figure S57.**  $^1\text{H}$ -NMR spectrum of the reaction of  $\text{K}\{\text{crypt.222}\}[\text{Co}(\text{hmde})_2\text{N-4-F-2,6-DiMePh}]$  (**10**) with 2 equiv. 9,10-dihydroanthracene; **A**:  $t = 10$  min; **B**:  $t = 24$  h ( $[\text{D}_8]\text{THF}$ , 298 K, 300 MHz). The hmde signal of  $\text{K}\{\text{crypt.222}\}[\text{Co}(\text{hmde})_2\text{N-4-F-2,6-DiMePh}]$  (**10**) is marked with  $\blacklozenge$  and  $\text{K}\{\text{crypt.222}\}[\text{Co}(\text{hmde})_2\text{N(H)-4-F-2,6-DiMePh}]$  (**10H**) is marked with  $\bullet$ .

## Acid-Base Reactions

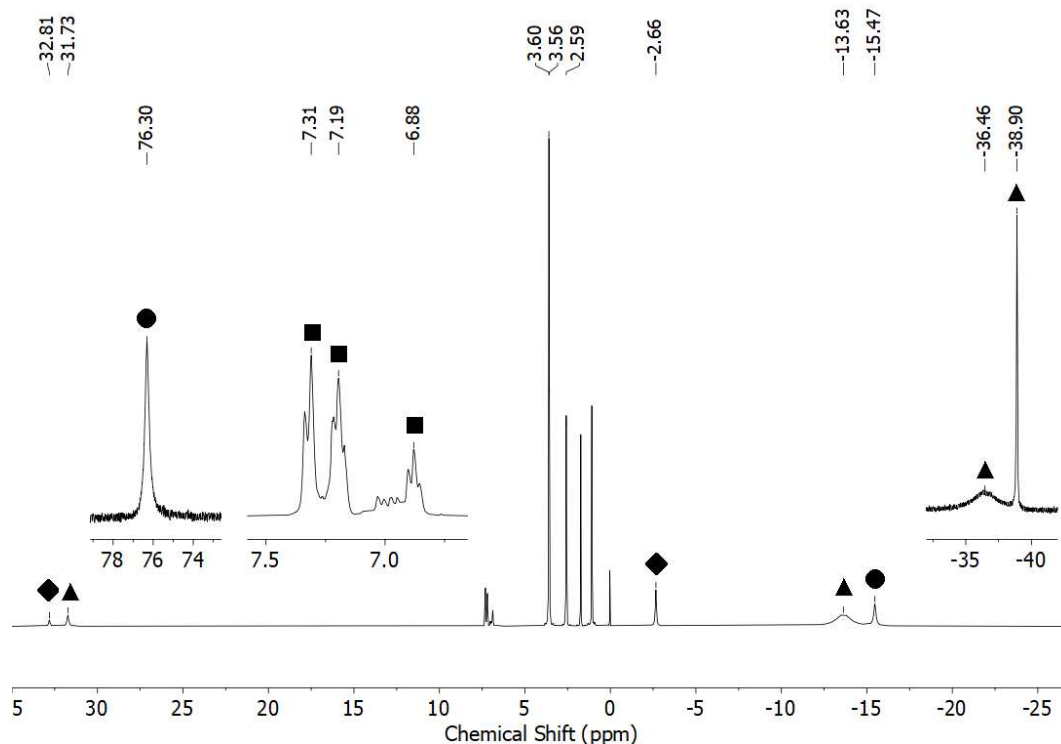


**Figure S58.**  $^1\text{H-NMR}$  spectrum of the reaction of  $\text{K}\{\text{crypt.222}\}[\text{Co}(\text{hmnds})_2\text{N}^t\text{Bu}]$  (**I**) with Diphenylamine ( $[\text{D8}]\text{THF}$ , 298 K, 300 MHz). The signals of  $\text{K}\{\text{crypt.222}\}[\text{Co}(\text{hmnds})_2\text{N}^t\text{Bu}]$  (**I**) are marked with  $\blacklozenge$ , of  $\text{K}\{\text{crypt.222}\}[\text{Co}(\text{hmnds})_2\text{N}(\text{H})^t\text{Bu}]$  (**II**) are marked with  $\bullet$ , of  $\text{K}\{\text{crypt.222}\}[\text{Co}(\text{hmnds})_2\text{NPh}_2]$  (**12**) with  $\blacktriangle$ , and of Tetraphenylhydrazine with  $\blacksquare$ .<sup>[7]</sup>

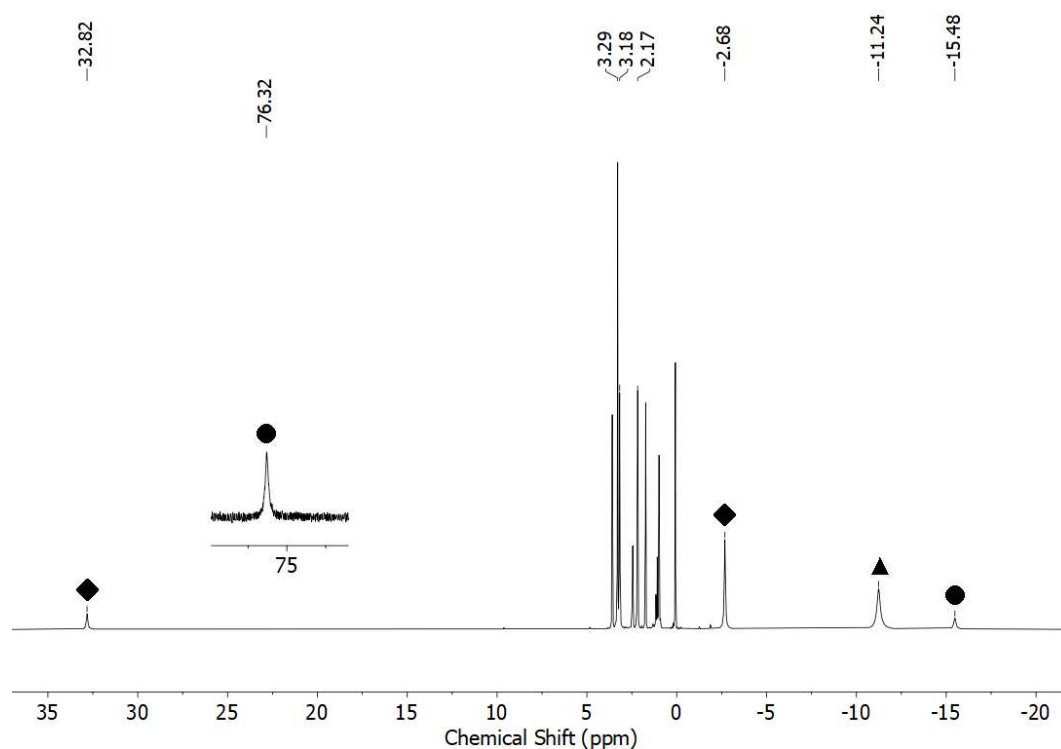


**Figure S59.**  $^1\text{H-NMR}$  spectrum of the reaction of  $\text{K}\{\text{crypt.222}\}[\text{Co}(\text{hmnds})_2\text{N}^t\text{Bu}]$  (**I**) with  $\text{Et}_3\text{NHCl}$  ( $[\text{D8}]\text{THF}$ , 298 K, 300 MHz). The signals of  $\text{K}\{\text{crypt.222}\}[\text{Co}(\text{hmnds})_2\text{N}^t\text{Bu}]$  (**I**) are marked with  $\blacklozenge$ , of  $\text{K}\{\text{crypt.222}\}[\text{Co}(\text{hmnds})_2\text{N}(\text{H})^t\text{Bu}]$  (**II**) are marked with  $\bullet$  and of  $\text{K}\{\text{crypt.222}\}[\text{Co}(\text{hmnds})_2\text{Cl}]$  with  $\blacktriangle$ .<sup>[3]</sup>

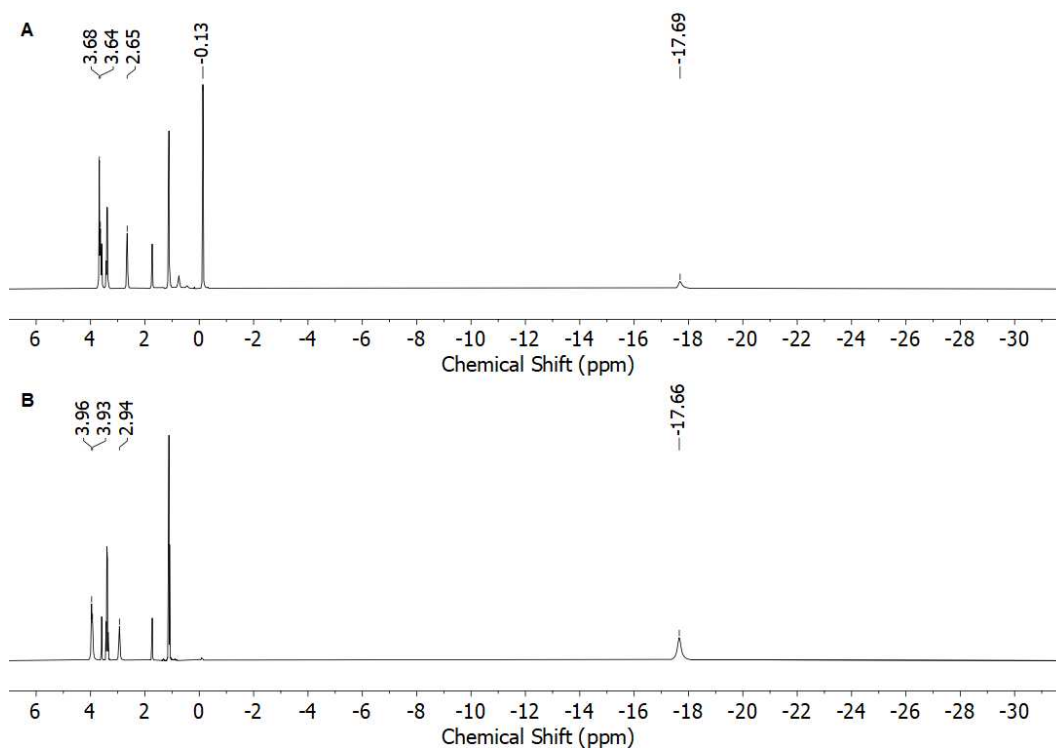


**Figure S60.** A:  $^1\text{H-NMR}$  spectrum of the reaction of  $\text{K}\{\text{crypt.222}\}[\text{Co}(\text{hmds})_2\text{N}(\text{H})^t\text{Bu}]$  (**IH**) with MeLi (1.6 M in  $\text{Et}_2\text{O}$ ); B:  $^1\text{H-NMR}$  spectrum of the reaction of  $\text{K}\{\text{crypt.222}\}[\text{Co}(\text{hmds})_2\text{Cl}]^{[3]}$  with MeLi (1.6 M in  $\text{Et}_2\text{O}$ ) ( $[\text{D8}]\text{THF}$ , 298 K, 300 MHz).

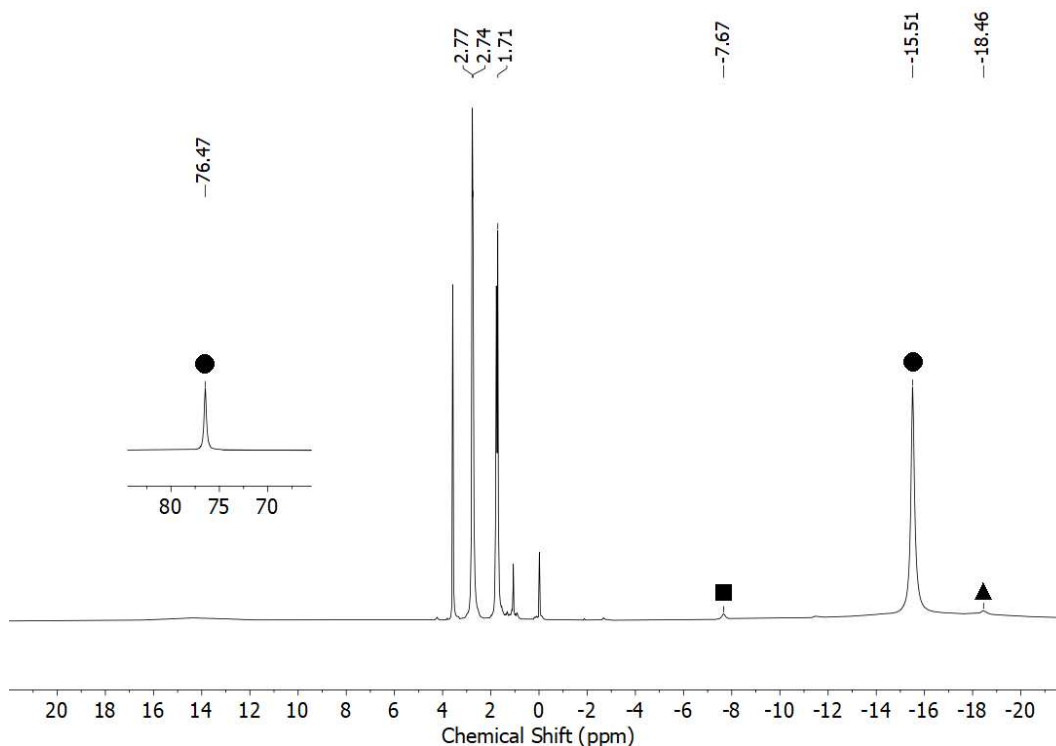


**Figure S61.**  $^1\text{H-NMR}$  spectrum of the reaction of  $\text{K}\{\text{crypt.222}\}[\text{Co}(\text{hmds})_2\text{N}(\text{H})^t\text{Bu}]$  (**IH**) with TEMPO ( $[\text{D8}]\text{THF}$ , 298 K, 300 MHz). The signals of  $\text{K}\{\text{crypt.222}\}[\text{Co}(\text{hmds})_2\text{N}(\text{H})^t\text{Bu}]$  (**IH**) are marked with ●, of  $\text{K}\{\text{crypt.222}\}[\text{Co}(\text{hmds})_2\text{TEMPO}]$  (**11**) with ▲, and of  $\text{K}\{\text{crypt.222}\}[\text{Co}(\text{hmds})_3]$  (**II**) with ■.

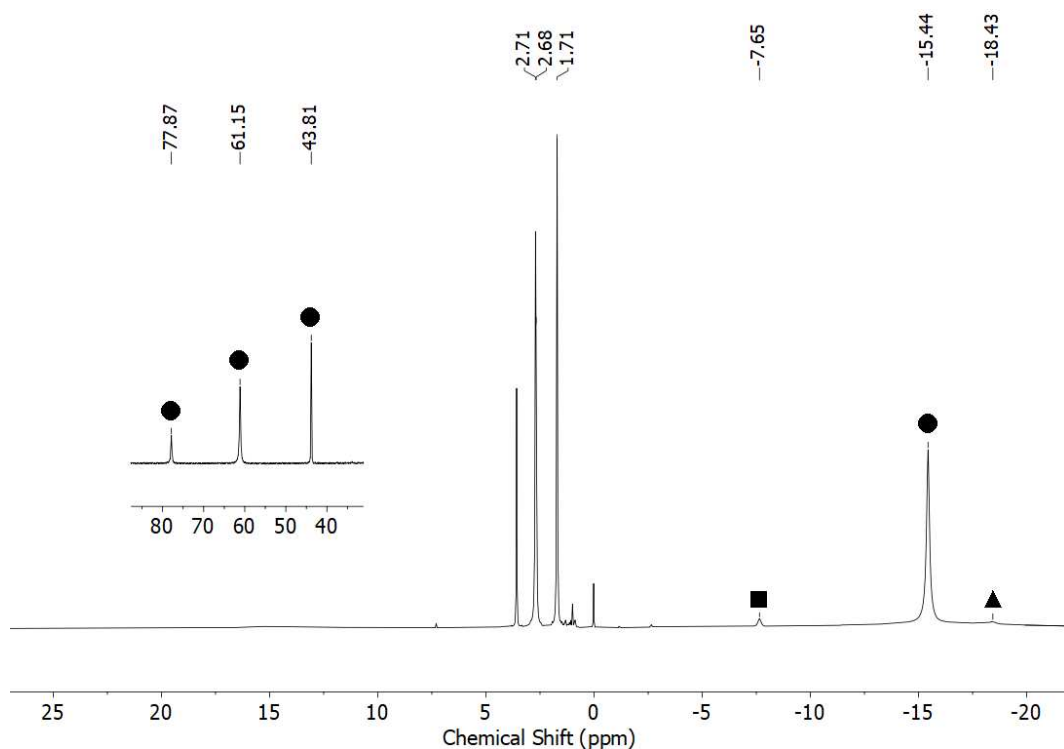


**Figure S62.**  $^1\text{H-NMR}$  spectrum of the reaction of  $\text{K}\{\text{crypt.222}\}[\text{Co}(\text{hmnds})_2\text{N}(\text{H})\text{CMe}_2\text{Et}]$  (**1H**) with TEMPO ([D8]THF, 298 K, 300 MHz). The signals of  $\text{K}\{\text{crypt.222}\}[\text{Co}(\text{hmnds})_2\text{N}(\text{H})\text{CMe}_2\text{Et}]$  (**1H**) are marked with ●, of  $\text{K}\{\text{crypt.222}\}[\text{Co}(\text{hmnds})_2\text{TEMPO}]$  (**11**) with ▲, and of  $\text{K}\{\text{crypt.222}\}[\text{Co}(\text{hmnds})_3]$  (**II**) with ■.

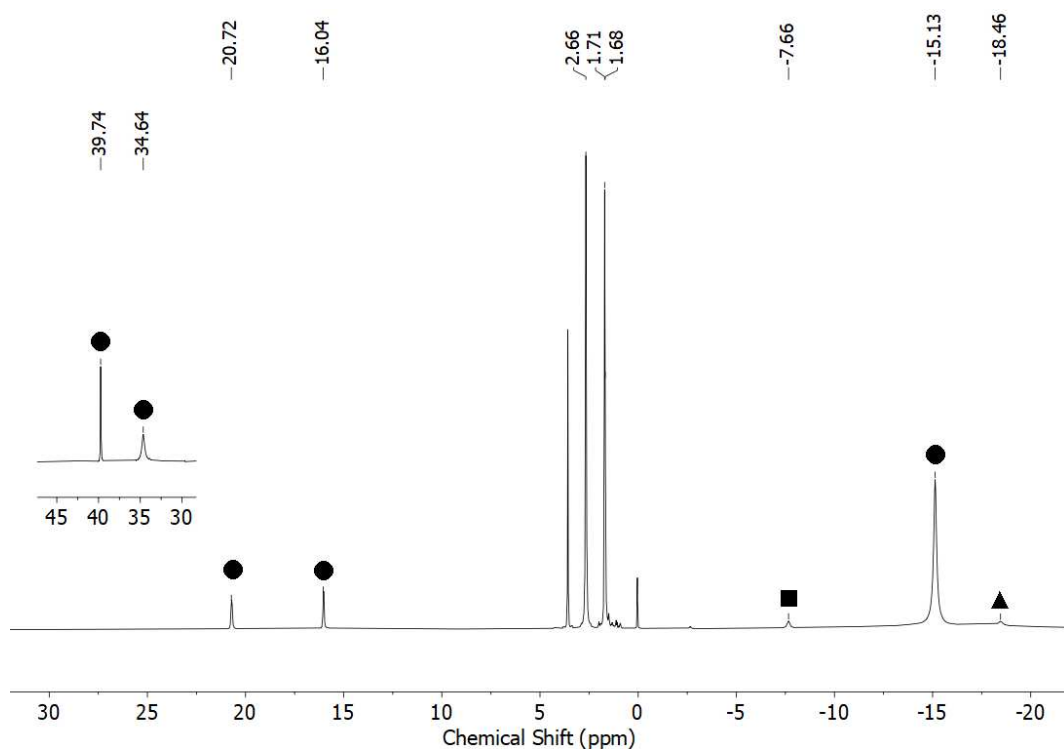


**Figure S63.**  $^1\text{H-NMR}$  spectrum of the reaction of  $\text{K}\{\text{crypt.222}\}[\text{Co}(\text{hmnds})_2\text{N}(\text{H})\text{Ada}]$  (**2H**) with TEMPO ([D8]THF, 298 K, 300 MHz). The signals of  $\text{K}\{\text{crypt.222}\}[\text{Co}(\text{hmnds})_2\text{N}(\text{H})\text{Ada}]$  (**2H**) are marked with ●, of  $\text{K}\{\text{crypt.222}\}[\text{Co}(\text{hmnds})_2\text{TEMPO}]$  (**11**) with ▲, and of  $\text{K}\{\text{crypt.222}\}[\text{Co}(\text{hmnds})_3]$  (**II**) with ■.

## 25. UV-Vis spectra

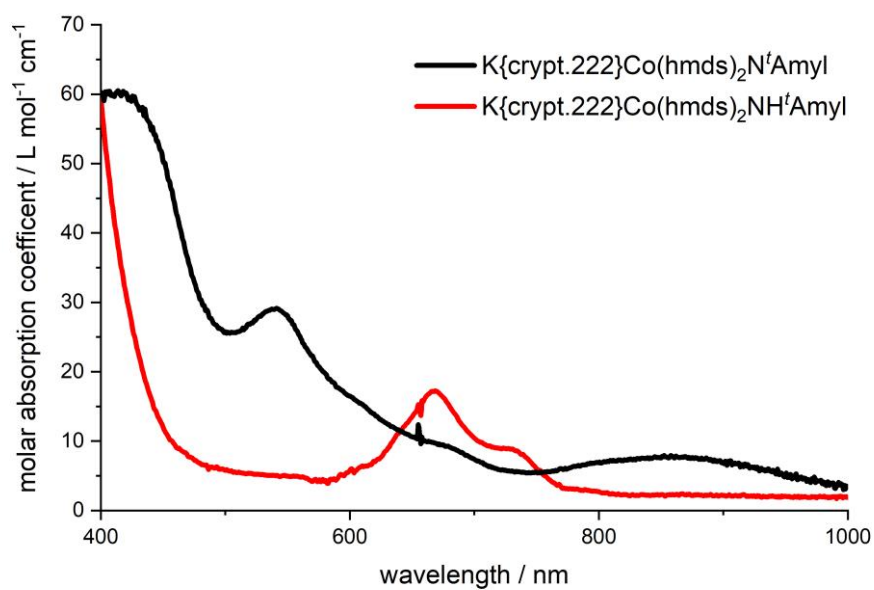


**Figure S64.** UV-Vis spectra of K{crypt.222}[Co(hmds)<sub>2</sub>NCMe<sub>2</sub>Et] (**1**, black) and K{crypt.222}[Co(hmds)<sub>2</sub>N(H)CMe<sub>2</sub>Et] (**1H**, red) in diethylether at -30°C.

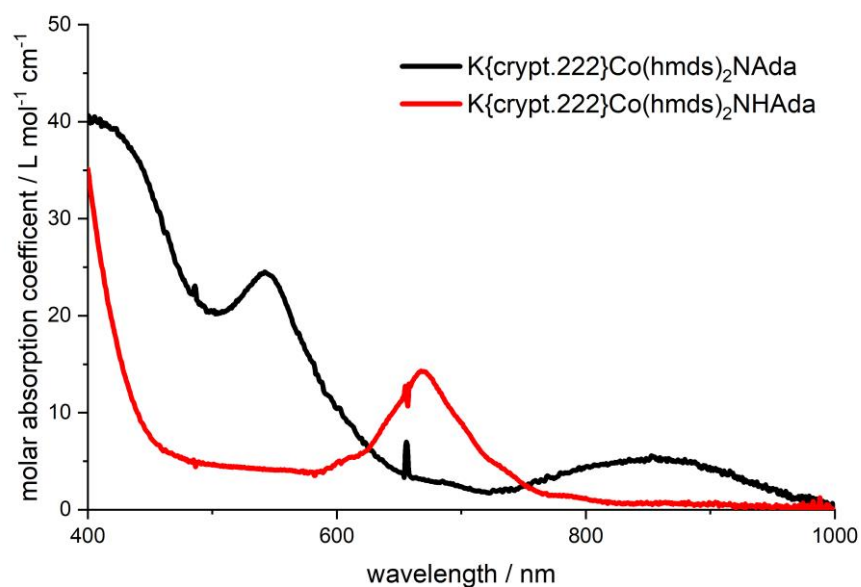


**Figure S65.** UV-Vis spectra of K{crypt.222}[Co(hmds)<sub>2</sub>NAda] (**2**, black) and K{crypt.222}[Co(hmds)<sub>2</sub>N(H)Ada] (**2H**, red) in diethylether at -30°C.



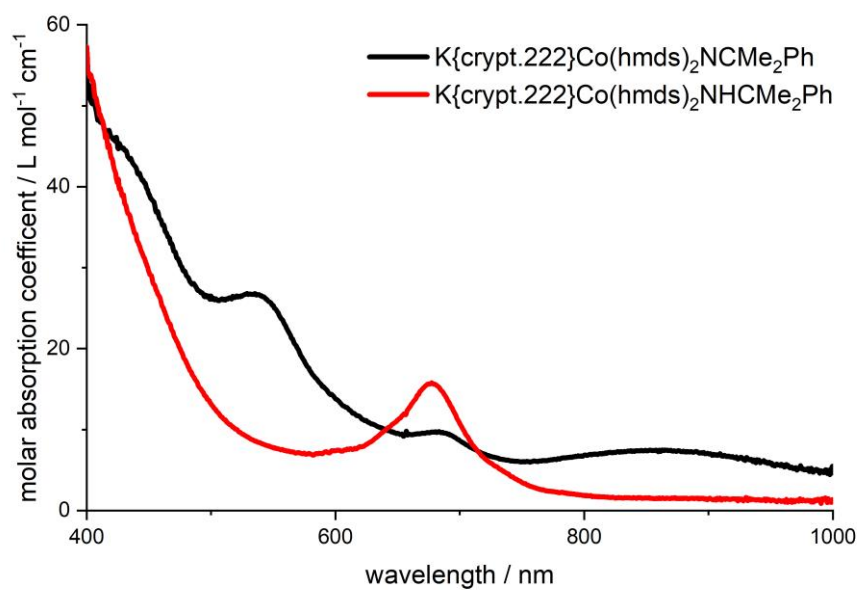


**Figure S66.** UV-Vis spectra of K{crypt.222}[Co(hmnds)<sub>2</sub>NCMe<sub>2</sub>Ph] (**3**, black) and K{crypt.222}[Co(hmnds)<sub>2</sub>N(H)CMe<sub>2</sub>Ph] (**3H**, red) in diethylether at -30°C.

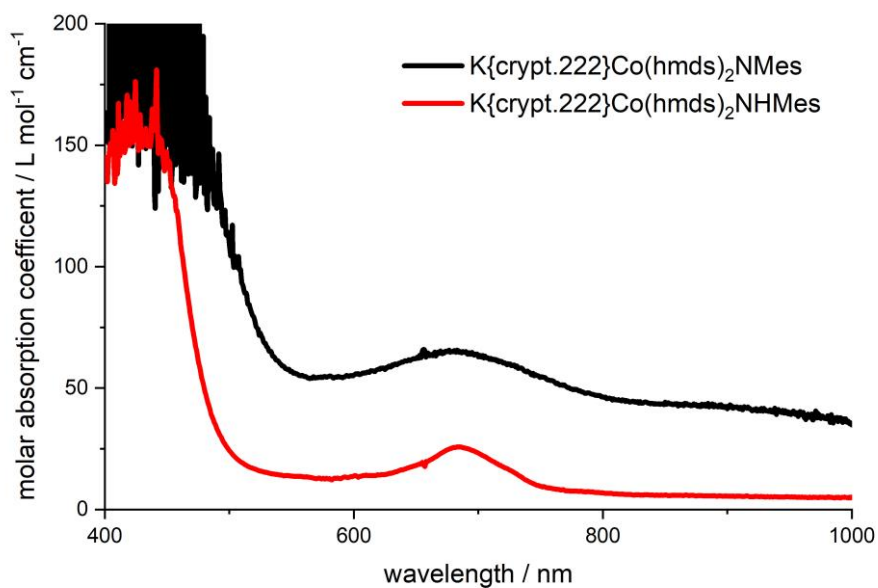


**Figure S67.** UV-Vis spectra of K{crypt.222}[Co(hmnds)<sub>2</sub>NMes] (**6**, black) and K{crypt.222}[Co(hmnds)<sub>2</sub>N(H)Mes] (**6H**, red) in diethylether at 25°C.

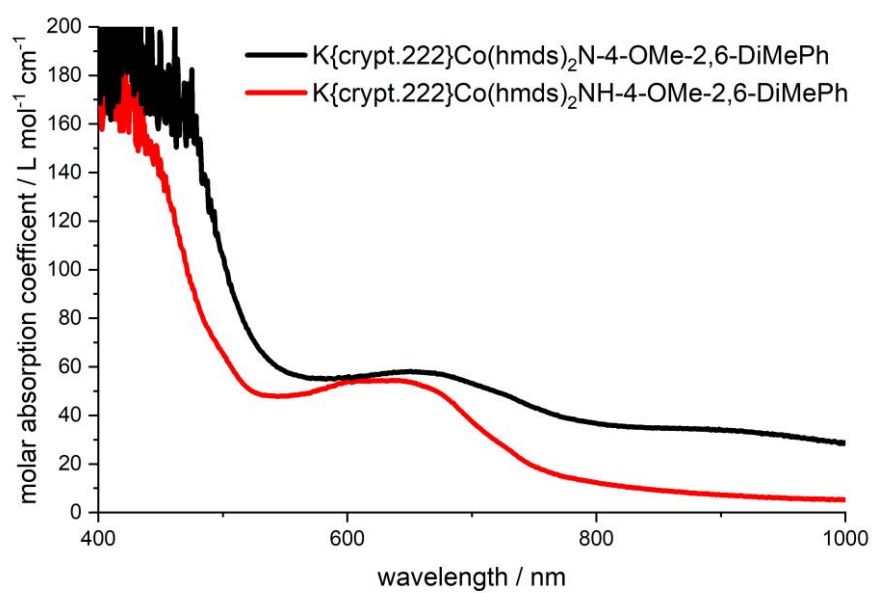


**Figure S68.** UV-Vis spectra of K{crypt.222}[Co(hm<sub>2</sub>s)<sub>2</sub>N-4-OMe-2,6-DiMePh] (**8**, black) and K{crypt.222}[Co(hm<sub>2</sub>s)<sub>2</sub>N(H)-4-OMe-2,6-DiMePh] (**8H**, red) in diethylether at 25°C.

## 26. Kinetic studies

In a typical experiment, a precooled 2mM solution of the respective cobalt complex was treated with solution of the substrate (20 eq.). For **2**, a solution of  $K\{\text{crypt.222}\}[\text{Co}(\text{hmd})_2]$  was precooled and a mixture of the substrate and  $\text{N}_3\text{Ada}$  was added. The absorbance at a wavelength of 850 nm was used for the kinetic studies.

Reaction of  $K\{\text{crypt.222}\}[\text{Co}(\text{hmds})_2\text{CMe}_3]$  (**1**) (2mM) with 20 equiv. substrate in diethylether at  $-30^\circ\text{C}$

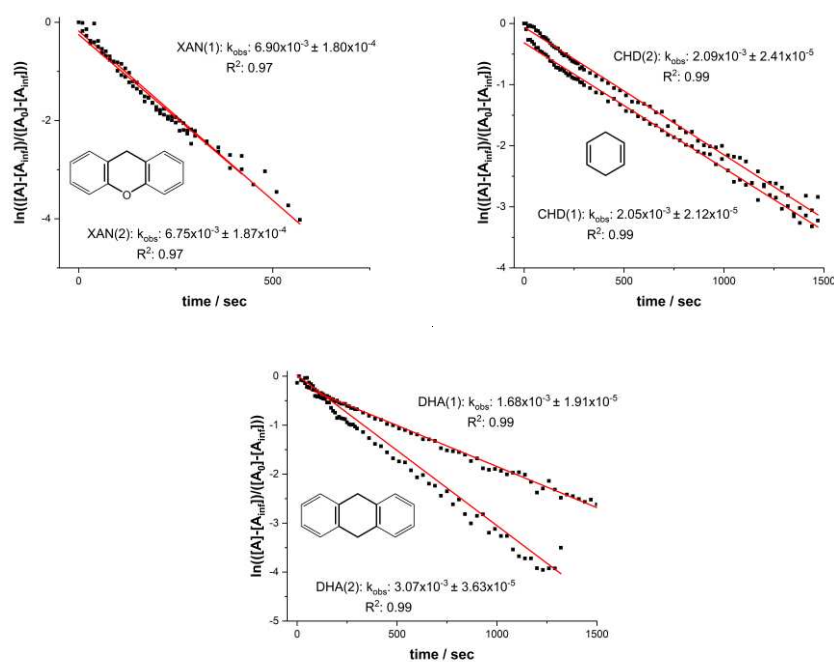


**Figure S69.** Time traces of the absorbance at 850 nm during the Reaction of  $K\{\text{crypt.222}\}[\text{Co}(\text{hmds})_2\text{tBu}]$  (**1**) with 20 equiv. of the respective substrate (XAN, CHD, DHA) in diethylether at  $-30^\circ\text{C}$ .

**Reaction of K{crypt.222}[Co(hmnds)<sub>2</sub>CMe<sub>2</sub>Et] (1) (2mM) with 20 equiv. substrate in diethylether at –30°C**

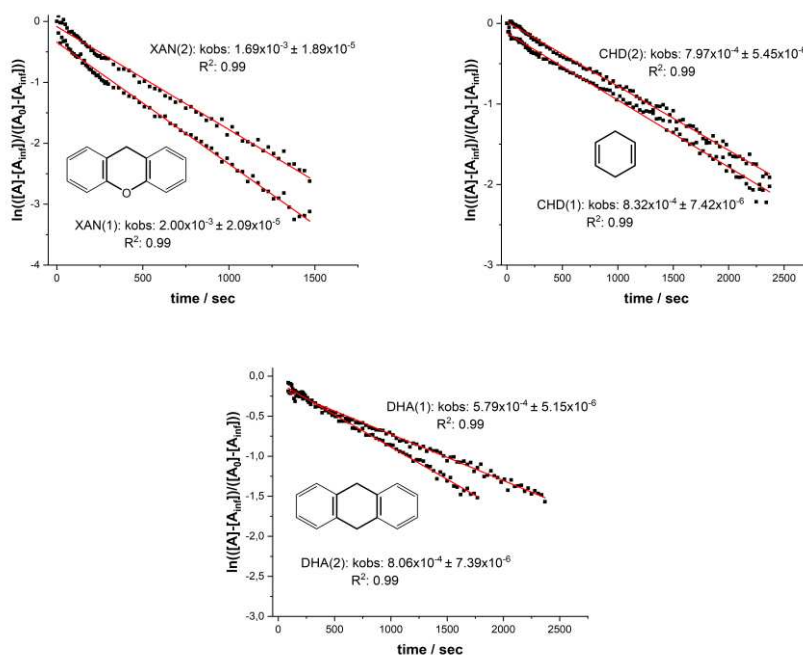


**Figure S70.** Time traces of the absorbance at 850 nm during the Reaction of K{crypt.222}[Co(hmnds)<sub>2</sub>NCMe<sub>2</sub>Et] (1) with 20 equiv. of the respective substrate (XAN, CHD, DHA) in diethylether at –30°C.

**Reaction of K{crypt.222}[Co(hmnds)<sub>2</sub>NAda] (2) (2 mM) with 20 equiv. substrate in diethylether at –30°C**

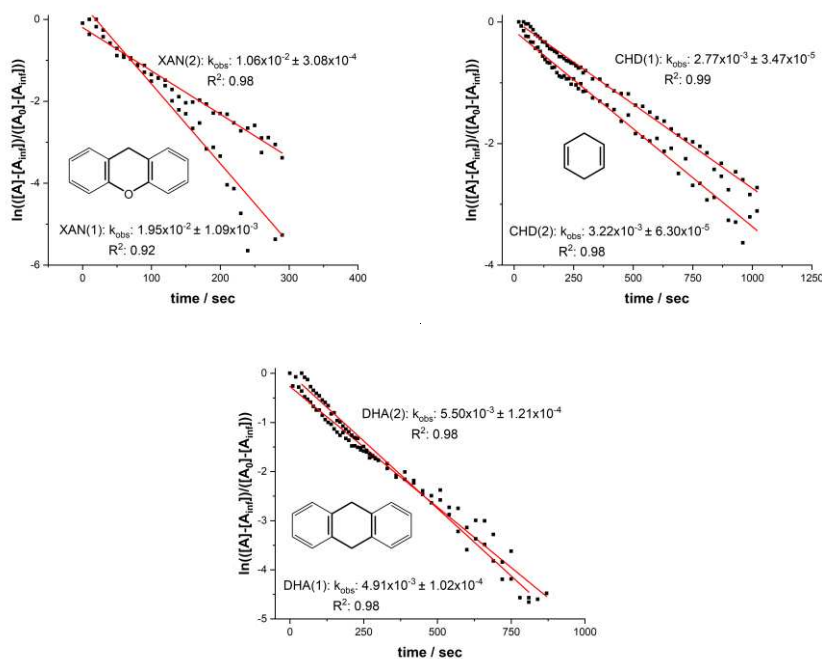


**Figure S71.** Time traces of the absorbance at 850 nm during the Reaction of K{crypt.222}[Co(hmnds)<sub>2</sub>NAda] (2) with 20 equiv. of the respective substrate (XAN, CHD, DHA) in diethylether at –30°C.

**Reaction of K{crypt.222}[Co(hm<sub>ds</sub>)<sub>2</sub>CMe<sub>2</sub>Ph] (3) (2 mM) with 20 equiv. substrate in diethylether at –30°C**

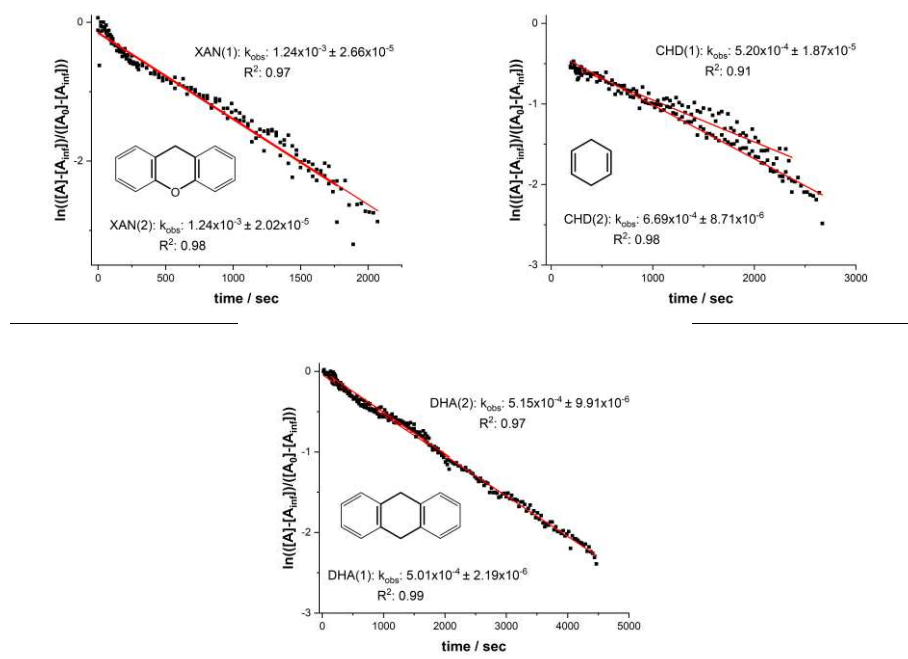


**Figure S72.** Time traces of the absorbance at 850 nm during the Reaction of K{crypt.222}[Co(hm<sub>ds</sub>)<sub>2</sub>NCMe<sub>2</sub>Ph] (3) with 20 equiv. of the respective substrate (XAN, CHD, DHA) in diethylether at –30°C.

**Reaction of K{crypt.222}[Co(hm<sub>ds</sub>)<sub>2</sub>Mes] (6) (2 mM) with 20 equiv. substrate in diethylether at –30°C**

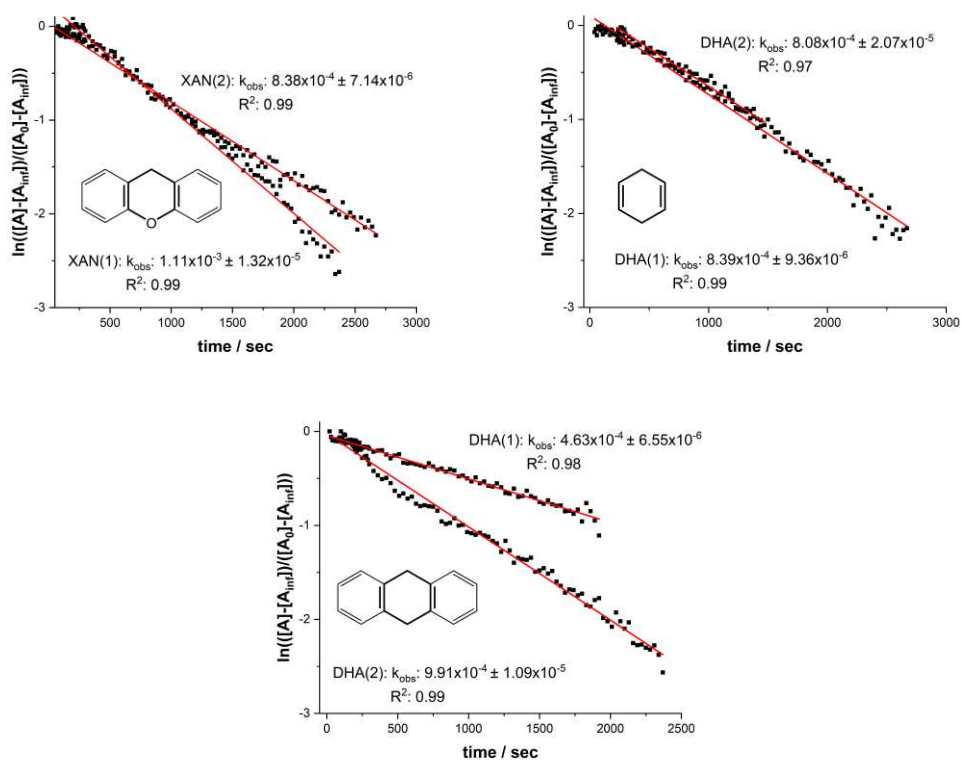


**Figure S73.** Time traces of the absorbance at 850 nm during the Reaction of K{crypt.222}[Co(hm<sub>ds</sub>)<sub>2</sub>NMe<sub>3</sub>] (6) with 20 equiv. of the respective substrate (XAN, CHD, DHA) in diethylether at –30°C.

## 27. X-Ray diffraction analysis and molecular structures

Data for **1** (CCDC 2234764), **1H** (CCDC 2234759), **2** (CCDC 2234774), **2H** (CCDC 2234757), **2X** (CCDC 2234763), **3** (CCDC 2234767), **3H** (CCDC 2234770), **4** (CCDC 2234769), **5** (CCDC 2234761), **6** (CCDC 2234766), **6H** (CCDC 2234773), **7** (CCDC 2234758), **7H** (CCDC 2238309), **8** (CCDC 2238310), **8H** (CCDC 2234768), **9** (CCDC 2234762), **9H** (CCDC 2234765), **10** (CCDC 2238311), **10H** (CCDC 2234760), **11** (CCDC 2234772), **IX** (CCDC 2234771), were collected at 100 K on a Bruker Quest D8 diffractometer using a graphite-monochromated Mo-K $\alpha$  radiation and equipped with an *Oxford Instrument Cooler Device*. The structures have been solved using either OLEX SHELXT V2014/1<sup>[8]</sup> and refined by means of least-squares procedures on a F<sup>2</sup> with the aid of the program SHELXL-2016/6<sup>[ii]</sup> include in the softwares package WinGX version 1.63<sup>[9]</sup> or using CRYSTALS.<sup>[10]</sup>

The Atomic Scattering Factors were taken from *International Tables for X-Ray Crystallography*.<sup>[11]</sup> All non-hydrogen atoms were refined anisotropically. All hydrogens atoms were refined by using a riding model. Absorption corrections were introduced by using the MULTISCAN and X-Red program.<sup>[12]</sup> Drawings of molecules are performed with the programs DIAMOND and POV-Ray with 50% probability displacement ellipsoids for non-H atoms. Depiction of H atoms is omitted for clarity.

Complex	Co1-N <sub>Imido/Amido</sub> / Å	Co1-N <sub>Imido/Amido</sub> -C1 / °	N1-C1/ Å
<b>1</b>	1.673(2)	166.3	1.438(7) 1.452(7)
<b>2</b>	1.758(8)	145.5(8)	1.41(1)
<b>3</b>	1.691(1)	167.6(1)	1.423(2)
<b>6</b>	1.751(2)	169.1(2)	1.349(2)
<b>7</b>	1.776(2)	163.2(2)	1.335(3)
<b>8</b>	1.724(3)	176.3(2)	1.348(4)
	1.710(3)	167.2(3)	1.351(4)
<b>9</b>	1.753(4)	164.2(3)	1.330(6)
<b>10</b>	1.751(8)	172.6(9)	1.33(1)
<b>1H</b>	1.880(3)	136.3(3)	1.454(3)
<b>2H</b>	1.899(2)	131.9(2)	1.446(3)
<b>3H</b>	1.898(2)	135.1(2)	1.449(2)
<b>6H</b>	1.935(2)	139.3(2)	1.375(3)
<b>7H</b>	1.920(2)	139.7(2)	1.367(3)
<b>8H</b>	1.921(1)	139.7(1)	1.374(2)
<b>9H</b>	1.944(3)	142.0(3)	1.368(4)
<b>10H</b>	1.940(2)	139.9(2)	1.373(3)

Table S1. Crystal data and structure refinement for IX.

Identification code	IX
Empirical formula	C <sub>39</sub> H <sub>92</sub> CoKN <sub>5</sub> O <sub>6</sub> Si <sub>4</sub>
Formula weight / g mol <sup>-1</sup>	937.56
Temperature / K	100.01
Crystal system	monoclinic
Space group	<i>P</i> 2 <sub>1</sub> / <i>n</i>
<i>a</i> / Å	20.2034(11)
<i>b</i> / Å	13.4966(7)
<i>c</i> / Å	22.6483(12)
$\alpha$ / °	90
$\beta$ / °	109.509(2)
$\gamma$ / °	90
<i>V</i> / Å <sup>3</sup>	5821.1(5)
<i>Z</i>	4
$\rho_{\text{calc}}$ / g cm <sup>-3</sup>	1.070
$\mu$ / mm <sup>-1</sup>	0.488
F(000)	2044.0
Crystal size / mm <sup>3</sup>	0.44 × 0.206 × 0.13
Radiation	MoK $\alpha$ ( $\lambda$ = 0.71073)
2 $\theta$ range for data collection / °	4.478 to 52.14
Index ranges	-24 ≤ <i>h</i> ≤ 24, -16 ≤ <i>k</i> ≤ 16, -27 ≤ <i>l</i> ≤ 27
Reflections collected	91600
Independent reflections	11499 [ <i>R</i> <sub>int</sub> = 0.0991, <i>R</i> <sub>sigma</sub> = 0.0552]
Data/restraints/parameters	11499/0/522
Goodness-of-fit on <i>F</i> <sup>2</sup>	1.023
Final <i>R</i> indexes [ <i>I</i> ≥ 2 $\sigma$ ( <i>I</i> )]	<i>R</i> <sub>1</sub> = 0.0512, <i>wR</i> <sub>2</sub> = 0.1007
Final <i>R</i> indexes [all data]	<i>R</i> <sub>1</sub> = 0.0793, <i>wR</i> <sub>2</sub> = 0.1101
Largest diff. peak/hole / e Å <sup>-3</sup>	0.86/-0.58

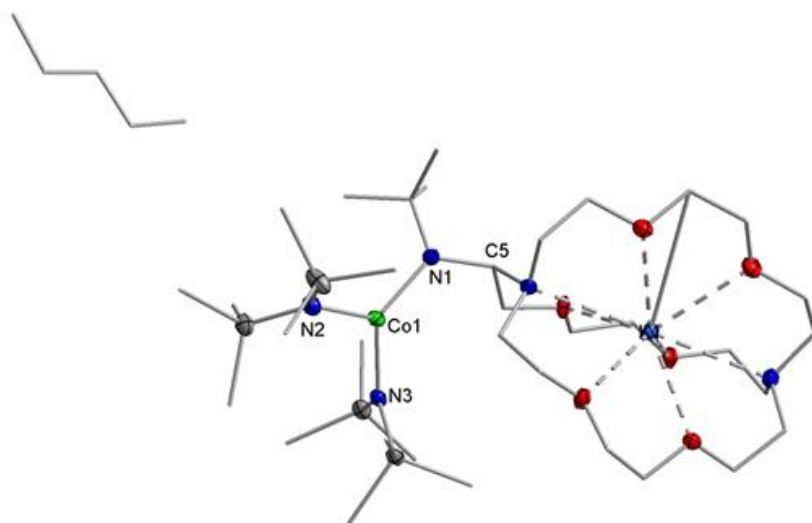
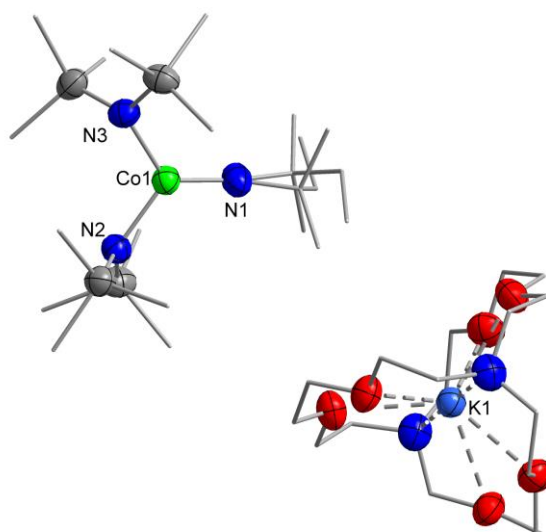


Figure S74. Molecular structure of IX within the crystal.

**Table S2. Crystal data and structure refinement for 1.**

Identification code	1
Empirical formula	C <sub>35</sub> H <sub>83</sub> CoKN <sub>5</sub> O <sub>6</sub> Si <sub>4</sub>
Formula weight / g mol <sup>-1</sup>	880.45
Temperature / K	270
Crystal system	triclinic
Space group	
<i>a</i> / Å	11.1305(7)
<i>b</i> / Å	14.5935(7)
<i>c</i> / Å	16.7817(10)
<i>α</i> / °	76.870(2)
<i>β</i> / °	84.742(2)
<i>γ</i> / °	77.550(2)
<i>V</i> / Å <sup>3</sup>	2589.3(3)
<i>Z</i>	2
$\rho_{\text{calc}}$ / g cm <sup>-3</sup>	1.129
$\mu$ / mm <sup>-1</sup>	0.544
F(000)	9568.0
Crystal size / mm <sup>3</sup>	0.347 × 0.213 × 0.152
Radiation	MoK $\alpha$ ( $\lambda$ = 0.71073)
2 $\theta$ range for data collection / °	3.752 to 52.018
Index ranges	-13 ≤ <i>h</i> ≤ 13, -18 ≤ <i>k</i> ≤ 17, -20 ≤ <i>l</i> ≤ 20
Reflections collected	86331
Independent reflections	10186 [ <i>R</i> <sub>int</sub> = 0.0386, <i>R</i> <sub>sigma</sub> = 0.0223]
Data/restraints/parameters	10186/0/533
Goodness-of-fit on <i>F</i> <sup>2</sup>	1.112
Final <i>R</i> indexes [ <i>I</i> ≥ 2 $\sigma$ ( <i>I</i> )]	<i>R</i> <sub>1</sub> = 0.0390, <i>wR</i> <sub>2</sub> = 0.1052
Final <i>R</i> indexes [all data]	<i>R</i> <sub>1</sub> = 0.0464, <i>wR</i> <sub>2</sub> = 0.1087
Largest diff. peak/hole / e Å <sup>-3</sup>	0.60/-0.36



**Figure S75. Molecular structure of 1 within the crystal.**



**Table S3. Crystal data and structure refinement for 1H.**

Identification code	1H
Empirical formula	C <sub>35</sub> H <sub>84</sub> CoKN <sub>5</sub> O <sub>6</sub> Si <sub>4</sub>
Formula weight / g mol <sup>-1</sup>	881.46
Temperature / K	100
Crystal system	triclinic
Space group	
<i>a</i> / Å	10.6200(9)
<i>b</i> / Å	14.6725(14)
<i>c</i> / Å	16.9790(14)
$\alpha$ / °	87.982(7)
$\beta$ / °	75.533(7)
$\gamma$ / °	76.839(7)
<i>V</i> / Å <sup>3</sup>	2493.9(4)
<i>Z</i>	2
$\rho_{\text{calc}}$ / g cm <sup>-3</sup>	1.174
$\mu$ / mm <sup>-1</sup>	4.697
F(000)	958.0
Crystal size / mm <sup>3</sup>	0.5 × 0.3 × 0.1
Radiation	CuK $\alpha$ ( $\lambda$ = 1.54186)
2 $\theta$ range for data collection / °	6.188 to 152.486
Index ranges	-12 ≤ <i>h</i> ≤ 12, -18 ≤ <i>k</i> ≤ 15, -19 ≤ <i>l</i> ≤ 21
Reflections collected	47162
Independent reflections	10175 [ <i>R</i> <sub>int</sub> = 0.0485, <i>R</i> <sub>sigma</sub> = 0.0376]
Data/restraints/parameters	10175/0/488
Goodness-of-fit on <i>F</i> <sup>2</sup>	1.043
Final <i>R</i> indexes [ <i>I</i> ≥ 2 $\sigma$ ( <i>I</i> )]	<i>R</i> <sub>1</sub> = 0.0508, <i>wR</i> <sub>2</sub> = 0.1280
Final <i>R</i> indexes [all data]	<i>R</i> <sub>1</sub> = 0.0664, <i>wR</i> <sub>2</sub> = 0.1388
Largest diff. peak/hole / e Å <sup>-3</sup>	0.30/-0.53

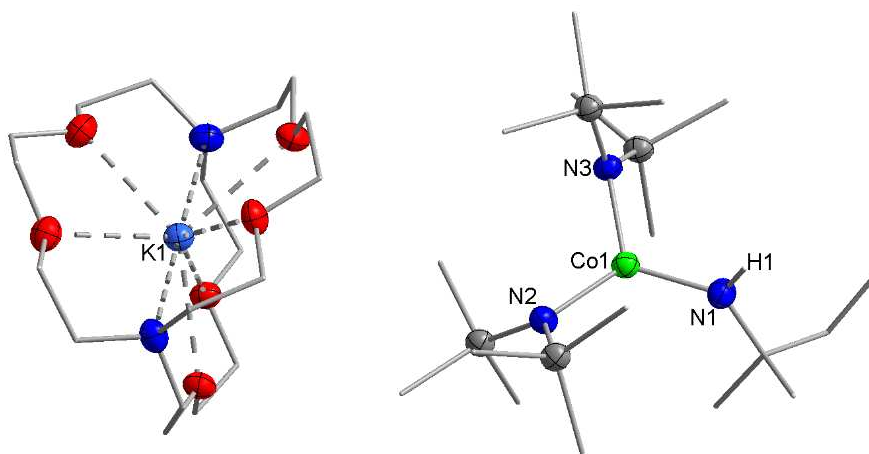


**Figure S76. Molecular structure of 1H within the crystal.**

**Table S4. Crystal data and structure refinement for 2.**

Identification code	2
Empirical formula	C <sub>40</sub> H <sub>87</sub> CoKN <sub>5</sub> O <sub>6</sub> Si <sub>4</sub>
Formula weight / g mol <sup>-1</sup>	944.53
Temperature / K	100.00
Crystal system	monoclinic
Space group	<i>P</i> 2 <sub>1</sub> / <i>c</i>
<i>a</i> / Å	15.7407(8)
<i>b</i> / Å	11.2145(6)
<i>c</i> / Å	30.1943(16)
$\alpha$ / °	90
$\beta$ / °	97.600(2)
$\gamma$ / °	90
<i>V</i> / Å <sup>3</sup>	5283.2(5)
<i>Z</i>	4
$\rho_{\text{calc}}$ / g cm <sup>-3</sup>	1.187
$\mu$ / mm <sup>-1</sup>	0.538
F(000)	2048.0
Crystal size / mm <sup>3</sup>	0.287 × 0.261 × 0.114
Radiation	MoK $\alpha$ ( $\lambda$ = 0.71073)
2 $\theta$ range for data collection / °	4.472 to 52.818
Index ranges	-19 ≤ <i>h</i> ≤ 19, -14 ≤ <i>k</i> ≤ 13, -37 ≤ <i>l</i> ≤ 37
Reflections collected	108613
Independent reflections	10750 [ <i>R</i> <sub>int</sub> = 0.1150, <i>R</i> <sub>sigma</sub> = 0.0789]
Data/restraints/parameters	10750/0/492
Goodness-of-fit on F <sup>2</sup>	1.035
Final <i>R</i> indexes [ <i>I</i> ≥ 2 $\sigma$ ( <i>I</i> )]	<i>R</i> <sub>1</sub> = 0.1094, <i>wR</i> <sub>2</sub> = 0.2488
Final <i>R</i> indexes [all data]	<i>R</i> <sub>1</sub> = 0.1802, <i>wR</i> <sub>2</sub> = 0.2875
Largest diff. peak/hole / e Å <sup>-3</sup>	1.31/-1.00

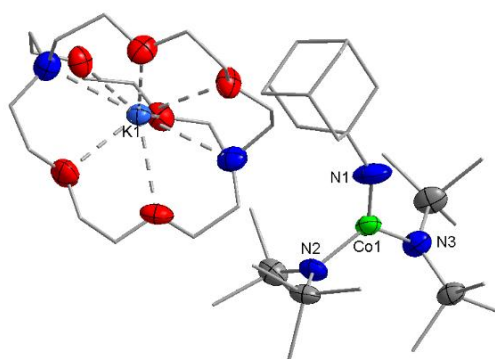


**Figure S77. Molecular structure of 2 within the crystal.**

Table S5. Crystal data and structure refinement for 2X.

Identification code	2X
Empirical formula	C <sub>40</sub> H <sub>86</sub> CoKN <sub>5</sub> O <sub>6</sub> Si <sub>4</sub>
Formula weight / g mol <sup>-1</sup>	943.52
Temperature / K	100.00
Crystal system	monoclinic
Space group	<i>P</i> 2 <sub>1</sub> / <i>c</i>
<i>a</i> / Å	13.9871(6)
<i>b</i> / Å	14.9574(7)
<i>c</i> / Å	25.6926(12)
$\alpha$ / °	90
$\beta$ / °	102.2390(10)
$\gamma$ / °	90
<i>V</i> / Å <sup>3</sup>	5253.0(4)
<i>Z</i>	4
$\rho_{\text{calc}}$ / g cm <sup>-3</sup>	1.193
$\mu$ / mm <sup>-1</sup>	0.541
F(000)	2044.0
Crystal size / mm <sup>3</sup>	0.319 × 0.315 × 0.303
Radiation	MoK $\alpha$ ( $\lambda$ = 0.71073)
2 $\theta$ range for data collection / °	4.58 to 53.656
Index ranges	-17 ≤ <i>h</i> ≤ 17, -18 ≤ <i>k</i> ≤ 18, -32 ≤ <i>l</i> ≤ 32
Reflections collected	124982
Independent reflections	11232 [ <i>R</i> <sub>int</sub> = 0.0328, <i>R</i> <sub>sigma</sub> = 0.0166]
Data/restraints/parameters	11232/0/526
Goodness-of-fit on F <sup>2</sup>	1.017
Final <i>R</i> indexes [ <i>I</i> ≥ 2 $\sigma$ ( <i>I</i> )]	<i>R</i> <sub>1</sub> = 0.0284, <i>wR</i> <sub>2</sub> = 0.0686
Final <i>R</i> indexes [all data]	<i>R</i> <sub>1</sub> = 0.0357, <i>wR</i> <sub>2</sub> = 0.0723
Largest diff. peak/hole / e Å <sup>-3</sup>	0.59/-0.41

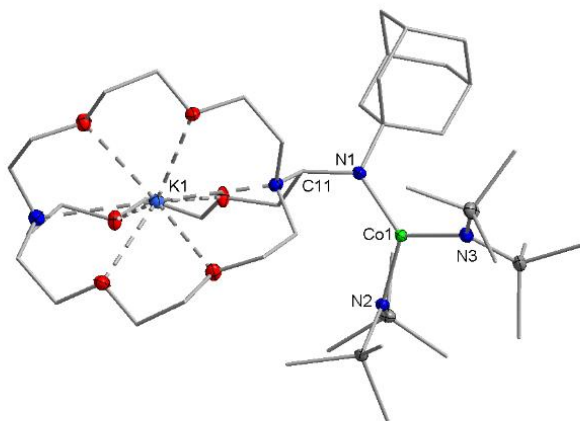


Figure S78. Molecular structure of 2X within the crystal.

Table S6. Crystal data and structure refinement for 2H.

Identification code	2H
Empirical formula	C <sub>40</sub> H <sub>88</sub> CoKN <sub>5</sub> O <sub>6</sub> Si <sub>4</sub>
Formula weight / g mol <sup>-1</sup>	945.54
Temperature / K	100.00
Crystal system	monoclinic
Space group	<i>P</i> 2 <sub>1</sub> / <i>c</i>
<i>a</i> / Å	15.5063(6)
<i>b</i> / Å	11.2887(6)
<i>c</i> / Å	30.4054(14)
$\alpha$ / °	90
$\beta$ / °	97.128(2)
$\gamma$ / °	90
<i>V</i> / Å <sup>3</sup>	5281.2(4)
<i>Z</i>	4
$\rho_{\text{calc}}$ / g cm <sup>-3</sup>	1.189
$\mu$ / mm <sup>-1</sup>	0.538
F(000)	2052.0
Crystal size / mm <sup>3</sup>	0.344 × 0.189 × 0.106
Radiation	MoK $\alpha$ ( $\lambda$ = 0.71073)
2 $\theta$ range for data collection / °	3.852 to 52.448
Index ranges	-19 ≤ <i>h</i> ≤ 19, -14 ≤ <i>k</i> ≤ 14, -37 ≤ <i>l</i> ≤ 37
Reflections collected	94138
Independent reflections	10609 [ <i>R</i> <sub>int</sub> = 0.0589, <i>R</i> <sub>sigma</sub> = 0.0388]
Data/restraints/parameters	10609/0/530
Goodness-of-fit on <i>F</i> <sup>2</sup>	1.067
Final <i>R</i> indexes [ <i>I</i> ≥ 2 $\sigma$ ( <i>I</i> )]	<i>R</i> <sub>1</sub> = 0.0387, <i>wR</i> <sub>2</sub> = 0.0933
Final <i>R</i> indexes [all data]	<i>R</i> <sub>1</sub> = 0.0520, <i>wR</i> <sub>2</sub> = 0.0987
Largest diff. peak/hole / e Å <sup>-3</sup>	0.80/-0.30

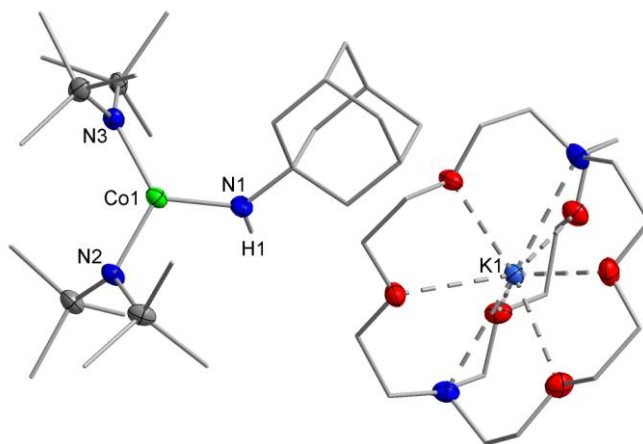
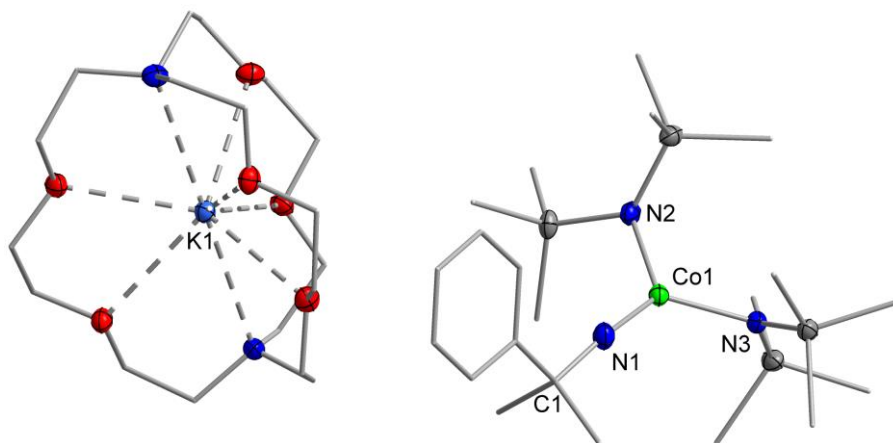


Figure S79. Molecular structure of 2H within the crystal.

**Table S7. Crystal data and structure refinement for 3.**

Identification code	3
Empirical formula	C <sub>39</sub> H <sub>83</sub> CoKN <sub>5</sub> O <sub>6</sub> Si <sub>4</sub>
Formula weight / g mol <sup>-1</sup>	928.49
Temperature / K	100.00
Crystal system	triclinic
Space group	
<i>a</i> / Å	12.3214(7)
<i>b</i> / Å	13.4551(7)
<i>c</i> / Å	16.5083(9)
<i>α</i> / °	75.187(2)
<i>β</i> / °	83.370(2)
<i>γ</i> / °	80.304(2)
<i>V</i> / Å <sup>3</sup>	2600.5(2)
<i>Z</i>	2
$\rho_{\text{calc}}$ / g cm <sup>-3</sup>	1.186
$\mu$ / mm <sup>-1</sup>	0.546
F(000)	1004.0
Crystal size / mm <sup>3</sup>	0.472 × 0.158 × 0.142
Radiation	MoK $\alpha$ ( $\lambda$ = 0.71073)
2 $\theta$ range for data collection / °	4.068 to 66.178
Index ranges	-18 ≤ <i>h</i> ≤ 18, -20 ≤ <i>k</i> ≤ 20, -24 ≤ <i>l</i> ≤ 23
Reflections collected	111470
Independent reflections	17745 [ <i>R</i> <sub>int</sub> = 0.0408, <i>R</i> <sub>sigma</sub> = 0.0341]
Data/restraints/parameters	17745/0/519
Goodness-of-fit on F <sup>2</sup>	1.022
Final <i>R</i> indexes [ <i>I</i> ≥ 2 $\sigma$ ( <i>I</i> )]	<i>R</i> <sub>1</sub> = 0.0352, <i>wR</i> <sub>2</sub> = 0.0776
Final <i>R</i> indexes [all data]	<i>R</i> <sub>1</sub> = 0.0514, <i>wR</i> <sub>2</sub> = 0.0832
Largest diff. peak/hole / e Å <sup>-3</sup>	0.44/-0.41



**Figure S80. Molecular structure of 3 within the crystal.**

Table S8. Crystal data and structure refinement for 3H.

Identification code	3H
Empirical formula	C <sub>39</sub> H <sub>84</sub> CoKN <sub>5</sub> O <sub>6</sub> Si <sub>4</sub>
Formula weight / g mol <sup>-1</sup>	929.50
Temperature / K	100.00
Crystal system	monoclinic
Space group	<i>P</i> 2 <sub>1</sub> / <i>c</i>
<i>a</i> / Å	11.2589(5)
<i>b</i> / Å	27.9172(11)
<i>c</i> / Å	16.6677(7)
$\alpha$ / °	90
$\beta$ / °	91.085(2)
$\gamma$ / °	90
<i>V</i> / Å <sup>3</sup>	5238.0(4)
<i>Z</i>	4
$\rho_{\text{calc}}$ / g cm <sup>-3</sup>	1.176
$\mu$ / mm <sup>-1</sup>	0.542
F(000)	2012.0
Crystal size / mm <sup>3</sup>	0.1 × 0.1 × 0.1
Radiation	MoK $\alpha$ ( $\lambda$ = 0.71073)
2 $\theta$ range for data collection / °	3.902 to 60.79
Index ranges	-16 ≤ <i>h</i> ≤ 16, -39 ≤ <i>k</i> ≤ 39, -23 ≤ <i>l</i> ≤ 23
Reflections collected	144610
Independent reflections	15754 [ <i>R</i> <sub>int</sub> = 0.0622, <i>R</i> <sub>sigma</sub> = 0.0371]
Data/restraints/parameters	15754/0/523
Goodness-of-fit on <i>F</i> <sup>2</sup>	1.155
Final <i>R</i> indexes [ <i>I</i> ≥ 2 $\sigma$ ( <i>I</i> )]	<i>R</i> <sub>1</sub> = 0.0505, <i>wR</i> <sub>2</sub> = 0.0910
Final <i>R</i> indexes [all data]	<i>R</i> <sub>1</sub> = 0.0620, <i>wR</i> <sub>2</sub> = 0.0946
Largest diff. peak/hole / e Å <sup>-3</sup>	0.39/-0.43

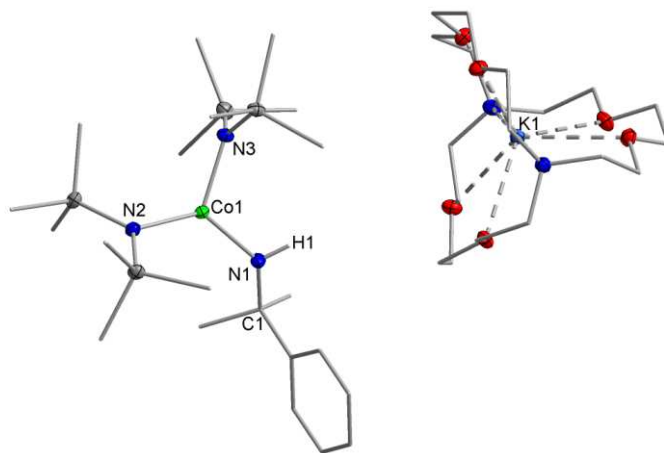


Figure S81. Molecular structure of 3H within the crystal.

Table S9. Crystal data and structure refinement for 4X.

Identification code	4X
Empirical formula	$C_{88}H_{168}Co_2K_2N_{10}O_{12}Si_8$
Formula weight / $g\ mol^{-1}$	1979.09
Temperature / K	100
Crystal system	triclinic
Space group	
$a / \text{\AA}$	17.981(8)
$b / \text{\AA}$	17.8074(8)
$c / \text{\AA}$	18.6957(7)
$\alpha / ^\circ$	79.0650(10)
$\beta / ^\circ$	88.1230(10)
$\gamma / ^\circ$	78.100(2)
$V / \text{\AA}^3$	5500.7(4)
$Z$	2
$\rho_{\text{calc}} / g\ cm^{-3}$	1.195
$\mu / mm^{-1}$	0.520
F(000)	2132.0
Crystal size / $mm^3$	$0.162 \times 0.123 \times 0.102$
Radiation	MoK $\alpha$ ( $\lambda = 0.71073$ )
2 $\theta$ range for data collection / $^\circ$	4 to 53.232
Index ranges	$-21 \leq h \leq 21, -22 \leq k \leq 22, -23 \leq l \leq 23$
Reflections collected	134021
Independent reflections	23088 [ $R_{\text{int}} = 0.0774, R_{\text{sigma}} = 0.0537$ ]
Data/restraints/parameters	23088/0/1123
Goodness-of-fit on $F^2$	1.112
Final $R$ indexes [ $I \geq 2\sigma(I)$ ]	$R_1 = 0.0687, wR_2 = 0.1357$
Final $R$ indexes [all data]	$R_1 = 0.0887, wR_2 = 0.1441$
Largest diff. peak/hole / $e\ \text{\AA}^{-3}$	1.44/-0.75

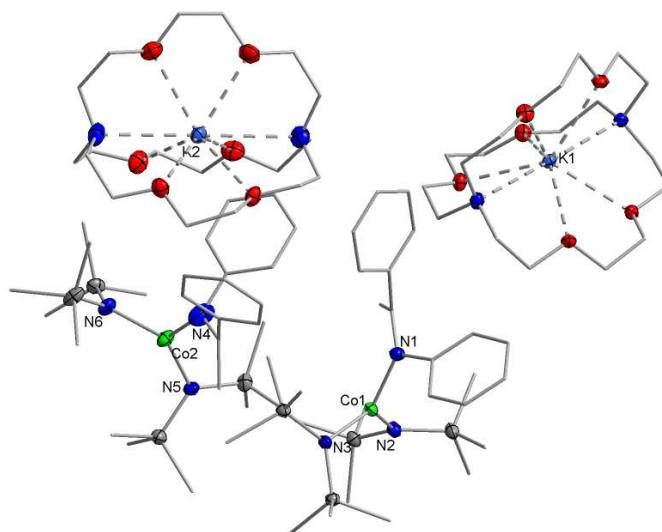


Figure S82. Molecular structure of 4X within the crystal.

Table S10. Crystal data and structure refinement for 5.

Identification code	5
Empirical formula	C <sub>36</sub> H <sub>70</sub> CoKN <sub>6</sub> O <sub>6</sub> Si <sub>4</sub>
Formula weight / g mol <sup>-1</sup>	893.37
Temperature / K	100
Crystal system	triclinic
Space group	
<i>a</i> / Å	13.4222(6)
<i>b</i> / Å	13.6226(6)
<i>c</i> / Å	15.8918(7)
<i>α</i> / °	72.151(2)
<i>β</i> / °	70.447(2)
<i>γ</i> / °	61.936(1)
<i>V</i> / Å <sup>3</sup>	2377.1(2)
<i>Z</i>	2
$\rho_{\text{calc}}$ / g cm <sup>-3</sup>	1.248
$\mu$ / mm <sup>-1</sup>	0.595
F(000)	956.0
Crystal size / mm <sup>3</sup>	0.369 × 0.267 × 0.127
Radiation	MoK $\alpha$ ( $\lambda$ = 0.71073)
2 $\theta$ range for data collection / °	3.762 to 53.182
Index ranges	-18 ≤ <i>h</i> ≤ 18, -18 ≤ <i>k</i> ≤ 18, -21 ≤ <i>l</i> ≤ 21
Reflections collected	61950
Independent reflections	12716 [ <i>R</i> <sub>int</sub> = 0.0328, <i>R</i> <sub>sigma</sub> = 0.0275]
Data/restraints/parameters	12716/0/499
Goodness-of-fit on <i>F</i> <sup>2</sup>	1.028
Final <i>R</i> indexes [ <i>I</i> ≥ 2 $\sigma$ ( <i>I</i> )]	<i>R</i> <sub>1</sub> = 0.0393, <i>wR</i> <sub>2</sub> = 0.1024
Final <i>R</i> indexes [all data]	<i>R</i> <sub>1</sub> = 0.0518, <i>wR</i> <sub>2</sub> = 0.1101
Largest diff. peak/hole / e Å <sup>-3</sup>	1.02/-0.86

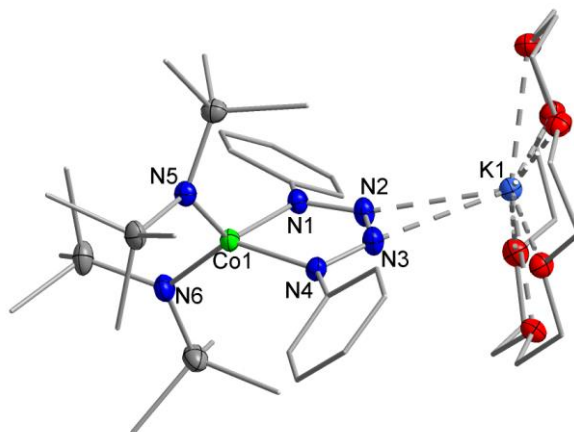


Figure S83. Molecular structure of 5 within the crystal.



Table S11. Crystal data and structure refinement for 6.

Identification code	6
Empirical formula	C <sub>39</sub> H <sub>83</sub> CoKN <sub>5</sub> O <sub>6</sub> Si <sub>4</sub>
Formula weight / g mol <sup>-1</sup>	928.48
Temperature / K	100
Crystal system	triclinic
Space group	
<i>a</i> / Å	12.5504(7)
<i>b</i> / Å	13.2399(8)
<i>c</i> / Å	17.4818(10)
$\alpha$ / °	85.810(2)
$\beta$ / °	86.531(2)
$\gamma$ / °	85.828(2)
<i>V</i> / Å <sup>3</sup>	2885.0(3)
<i>Z</i>	2
$\rho_{\text{calc}}$ / g cm <sup>-3</sup>	1.069
$\mu$ / mm <sup>-1</sup>	0.492
F(000)	1004.0
Crystal size / mm <sup>3</sup>	0.329 × 0.265 × 0.204
Radiation	MoK $\alpha$ ( $\lambda$ = 0.71073)
2 $\theta$ range for data collection / °	4.644 to 54.392
Index ranges	-16 ≤ <i>h</i> ≤ 16, -16 ≤ <i>k</i> ≤ 16, -22 ≤ <i>l</i> ≤ 22
Reflections collected	142529
Independent reflections	12645 [ <i>R</i> <sub>int</sub> = 0.0265, <i>R</i> <sub>sigma</sub> = 0.0139]
Data/restraints/parameters	12645/0/559
Goodness-of-fit on <i>F</i> <sup>2</sup>	1.037
Final <i>R</i> indexes [ <i>I</i> ≥ 2 $\sigma$ ( <i>I</i> )]	<i>R</i> <sub>1</sub> = 0.0355, <i>wR</i> <sub>2</sub> = 0.0928
Final <i>R</i> indexes [all data]	<i>R</i> <sub>1</sub> = 0.0406, <i>wR</i> <sub>2</sub> = 0.0960
Largest diff. peak/hole / e Å <sup>-3</sup>	0.91/-0.45

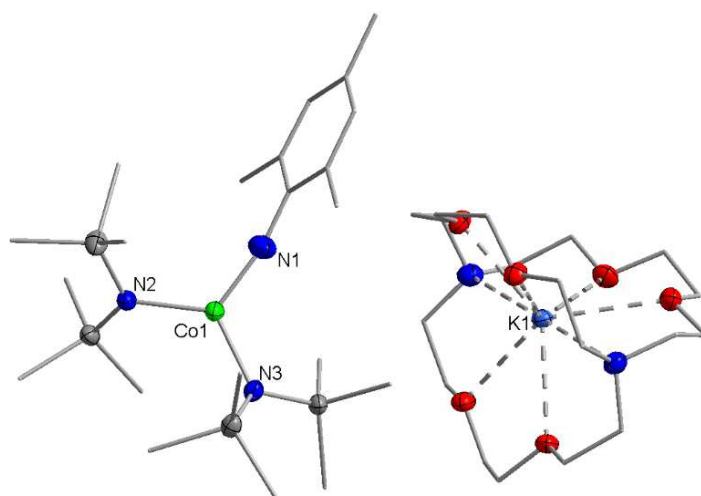
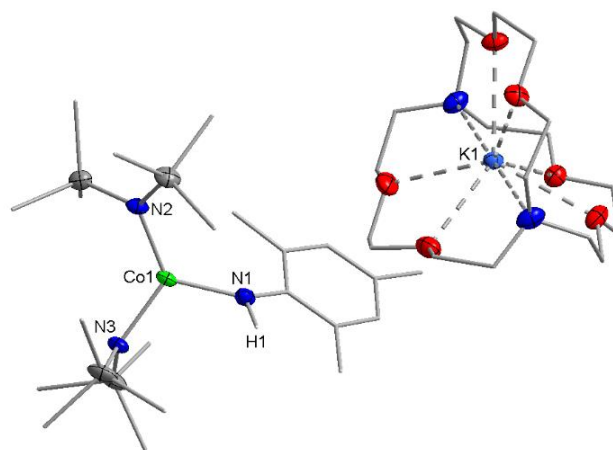


Figure S84. Molecular structure of 6 within the crystal.

**Table S12. Crystal data and structure refinement for 6H.**

Identification code	6H
Empirical formula	C <sub>39</sub> H <sub>85</sub> CoKN <sub>5</sub> O <sub>6</sub> Si <sub>4</sub>
Formula weight / g mol <sup>-1</sup>	930.50
Temperature / K	100
Crystal system	triclinic
Space group	
<i>a</i> / Å	10.7578(7)
<i>b</i> / Å	15.4892(10)
<i>c</i> / Å	16.8988(11)
$\alpha$ / °	90.014(2)
$\beta$ / °	101.365(2)
$\gamma$ / °	95.135(2)
<i>V</i> / Å <sup>3</sup>	2749.1(3)
<i>Z</i>	2
$\rho_{\text{calc}}$ / g cm <sup>-3</sup>	1.124
$\mu$ / mm <sup>-1</sup>	0.516
F(000)	1008.0
Crystal size / mm <sup>3</sup>	0.458 × 0.369 × 0.193
Radiation	MoK $\alpha$ ( $\lambda$ = 0.71073)
2 $\theta$ range for data collection / °	4.488 to 52.208
Index ranges	-13 ≤ <i>h</i> ≤ 13, -19 ≤ <i>k</i> ≤ 19, -20 ≤ <i>l</i> ≤ 20
Reflections collected	35837
Independent reflections	10869 [ <i>R</i> <sub>int</sub> = 0.0476, <i>R</i> <sub>sigma</sub> = 0.0498]
Data/restraints/parameters	10869/0/524
Goodness-of-fit on <i>F</i> <sup>2</sup>	1.027
Final <i>R</i> indexes [ <i>I</i> ≥ 2 $\sigma$ ( <i>I</i> )]	<i>R</i> <sub>1</sub> = 0.0416, <i>wR</i> <sub>2</sub> = 0.0941
Final <i>R</i> indexes [all data]	<i>R</i> <sub>1</sub> = 0.0573, <i>wR</i> <sub>2</sub> = 0.1011
Largest diff. peak/hole / e Å <sup>-3</sup>	0.89/-0.67



**Figure S85. Molecular structure of 6H within the crystal.**

Table S13. Crystal data and structure refinement for 7.

Identification code	7
Empirical formula	C <sub>38</sub> H <sub>81</sub> CoKN <sub>5</sub> O <sub>6</sub> Si <sub>4</sub>
Formula weight / g mol <sup>-1</sup>	914.46
Temperature / K	100
Crystal system	triclinic
Space group	
<i>a</i> / Å	12.2583(4)
<i>b</i> / Å	13.3092(5)
<i>c</i> / Å	16.4049(6)
$\alpha$ / °	74.7480(10)
$\beta$ / °	86.8670(10)
$\gamma$ / °	86.4980(10)
<i>V</i> / Å <sup>3</sup>	2598.02(16)
<i>Z</i>	2
$\rho_{\text{calc}}$ / g cm <sup>-3</sup>	1.169
$\mu$ / mm <sup>-1</sup>	0.545
F(000)	988.0
Crystal size / mm <sup>3</sup>	0.354 × 0.23 × 0.194
Radiation	MoK $\alpha$ ( $\lambda$ = 0.71073)
2 $\theta$ range for data collection / °	4.112 to 51.342
Index ranges	-14 ≤ <i>h</i> ≤ 14, -15 ≤ <i>k</i> ≤ 16, -21 ≤ <i>l</i> ≤ 21
Reflections collected	41846
Independent reflections	9828 [ <i>R</i> <sub>int</sub> = 0.0310, <i>R</i> <sub>sigma</sub> = 0.0264]
Data/restraints/parameters	9828/348/510
Goodness-of-fit on <i>F</i> <sup>2</sup>	1.045
Final <i>R</i> indexes [ <i>I</i> ≥ 2 $\sigma$ ( <i>I</i> )]	<i>R</i> <sub>1</sub> = 0.0374, <i>wR</i> <sub>2</sub> = 0.0895
Final <i>R</i> indexes [all data]	<i>R</i> <sub>1</sub> = 0.0429, <i>wR</i> <sub>2</sub> = 0.0926
Largest diff. peak/hole / e Å <sup>-3</sup>	0.99/-0.47

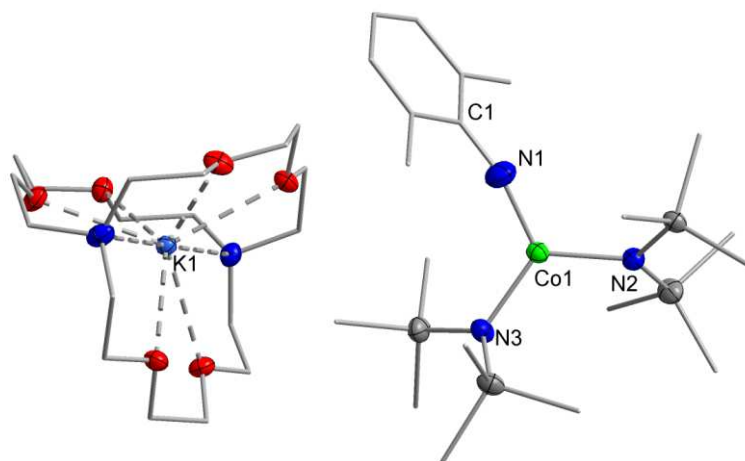
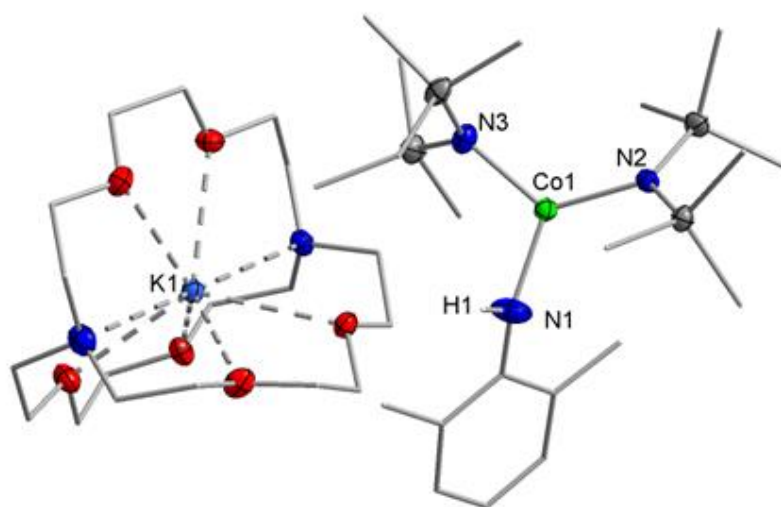


Figure S86. Molecular structure of 7 within the crystal.

**Table S14. Crystal data and structure refinement for 7H.**

Identification code	7H
Empirical formula	C <sub>38</sub> H <sub>82</sub> CoKN <sub>5</sub> O <sub>6</sub> Si <sub>4</sub>
Formula weight / g mol <sup>-1</sup>	915.47
Temperature / K	100
Crystal system	triclinic
Space group	
<i>a</i> / Å	12.3313(6)
<i>b</i> / Å	13.3739(6)
<i>c</i> / Å	16.2715(7)
<i>α</i> / °	77.0320(10)
<i>β</i> / °	86.665(2)
<i>γ</i> / °	86.073(2)
<i>V</i> / Å <sup>3</sup>	2606.3(2)
<i>Z</i>	2
$\rho_{\text{calc}}$ / g cm <sup>-3</sup>	1.167
$\mu$ / mm <sup>-1</sup>	0.543
F(000)	990.0
Crystal size / mm <sup>3</sup>	0.399 × 0.103 × 0.088
Radiation	MoK $\alpha$ ( $\lambda$ = 0.71073)
2 $\theta$ range for data collection / °	4.104 to 56.4
Index ranges	-16 ≤ <i>h</i> ≤ 16, -17 ≤ <i>k</i> ≤ 17, -21 ≤ <i>l</i> ≤ 21
Reflections collected	82580
Independent reflections	12819 [ <i>R</i> <sub>int</sub> = 0.0622, <i>R</i> <sub>sigma</sub> = 0.0421]
Data/restraints/parameters	12819/1/514
Goodness-of-fit on <i>F</i> <sup>2</sup>	1.030
Final <i>R</i> indexes [ <i>I</i> ≥ 2 $\sigma$ ( <i>I</i> )]	<i>R</i> <sub>1</sub> = 0.0386, <i>wR</i> <sub>2</sub> = 0.0826
Final <i>R</i> indexes [all data]	<i>R</i> <sub>1</sub> = 0.0555, <i>wR</i> <sub>2</sub> = 0.0891
Largest diff. peak/hole / e Å <sup>-3</sup>	0.41/-0.31



**Figure S87. Molecular structure of 7H within the crystal.**

Table S15. Crystal data and structure refinement for 8.

Identification code	8
Empirical formula	C <sub>78</sub> H <sub>166</sub> Co <sub>2</sub> K <sub>2</sub> N <sub>10</sub> O <sub>14</sub> Si <sub>8</sub>
Formula weight / g mol <sup>-1</sup>	1888.98
Temperature / K	100
Crystal system	triclinic
Space group	
<i>a</i> / Å	16.1241(9)
<i>b</i> / Å	18.3266(11)
<i>c</i> / Å	19.2706(11)
<i>α</i> / °	105.517(2)
<i>β</i> / °	97.580(2)
<i>γ</i> / °	98.243(2)
<i>V</i> / Å <sup>3</sup>	5344.7(5)
<i>Z</i>	2
$\rho_{\text{calc}}$ / g cm <sup>-3</sup>	1.174
$\mu$ / mm <sup>-1</sup>	0.533
F(000)	2040.0
Crystal size / mm <sup>3</sup>	0.147 × 0.066 × 0.058
Radiation	MoK $\alpha$ ( $\lambda$ = 0.71073)
2 $\theta$ range for data collection / °	3.81 to 51.482
Index ranges	-19 ≤ <i>h</i> ≤ 19, -22 ≤ <i>k</i> ≤ 22, -23 ≤ <i>l</i> ≤ 23
Reflections collected	109982
Independent reflections	20336 [ <i>R</i> <sub>int</sub> = 0.0587, <i>R</i> <sub>sigma</sub> = 0.0461]
Data/restraints/parameters	20336/0/1152
Goodness-of-fit on F <sup>2</sup>	1.014
Final <i>R</i> indexes [ <i>I</i> ≥ 2 $\sigma$ ( <i>I</i> )]	<i>R</i> <sub>1</sub> = 0.0449, <i>wR</i> <sub>2</sub> = 0.0984
Final <i>R</i> indexes [all data]	<i>R</i> <sub>1</sub> = 0.0779, <i>wR</i> <sub>2</sub> = 0.1149
Largest diff. peak/hole / e Å <sup>-3</sup>	0.45/-0.69

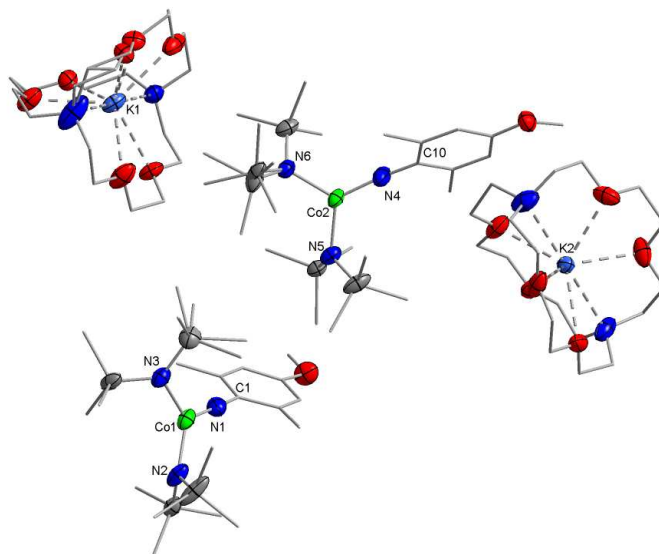
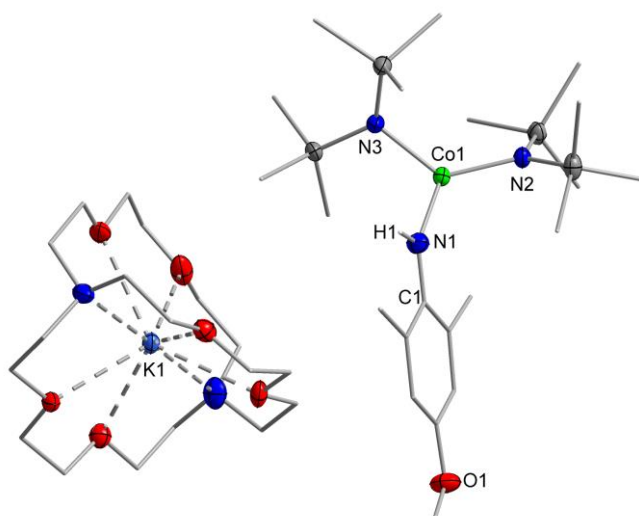


Figure S88. Molecular structure of 8 within the crystal.

**Table S16. Crystal data and structure refinement for 8H.**

Identification code	8H
Empirical formula	C <sub>39</sub> H <sub>80</sub> CoKN <sub>5</sub> O <sub>7</sub> Si <sub>4</sub>
Formula weight / g mol <sup>-1</sup>	941.47
Temperature / K	100.00
Crystal system	triclinic
Space group	
<i>a</i> / Å	12.5840(5)
<i>b</i> / Å	13.3551(6)
<i>c</i> / Å	17.5196(7)
<i>α</i> / °	110.3090(10)
<i>β</i> / °	93.313(2)
<i>γ</i> / °	93.058(2)
<i>V</i> / Å <sup>3</sup>	2748.2(2)
<i>Z</i>	2
$\rho_{\text{calc}}$ / g cm <sup>-3</sup>	1.1138
$\mu$ / mm <sup>-1</sup>	0.518
F(000)	1014.0
Crystal size / mm <sup>3</sup>	0.337 × 0.299 × 0.213
Radiation	MoK $\alpha$ ( $\lambda$ = 0.71073)
2 $\theta$ range for data collection / °	3.93 to 52.05
Index ranges	-15 ≤ <i>h</i> ≤ 15, -16 ≤ <i>k</i> ≤ 16, -21 ≤ <i>l</i> ≤ 21
Reflections collected	114317
Independent reflections	10840 [ <i>R</i> <sub>int</sub> = 0.0324, <i>R</i> <sub>sigma</sub> = 0.0155]
Data/restraints/parameters	10840/0/533
Goodness-of-fit on <i>F</i> <sup>2</sup>	1.038
Final <i>R</i> indexes [ <i>I</i> ≥ 2 $\sigma$ ( <i>I</i> )]	<i>R</i> <sub>1</sub> = 0.0302, <i>wR</i> <sub>2</sub> = 0.0766
Final <i>R</i> indexes [all data]	<i>R</i> <sub>1</sub> = 0.0328, <i>wR</i> <sub>2</sub> = 0.0783
Largest diff. peak/hole / e Å <sup>-3</sup>	0.43/-0.35



**Figure S89. Molecular structure of 8H within the crystal.**

Table S17. Crystal data and structure refinement for 9.

Identification code	9
Empirical formula	C <sub>39</sub> H <sub>80</sub> ClCoKN <sub>5</sub> O <sub>6</sub> Si <sub>4</sub>
Formula weight / g mol <sup>-1</sup>	948.91
Temperature / K	100
Crystal system	triclinic
Space group	
<i>a</i> / Å	12.5383(10)
<i>b</i> / Å	13.2254(11)
<i>c</i> / Å	17.6290(15)
<i>α</i> / °	109.838(2)
<i>β</i> / °	93.766(2)
<i>γ</i> / °	93.855(3)
<i>V</i> / Å <sup>3</sup>	2731.4(4)
<i>Z</i>	2
$\rho_{\text{calc}}$ / g cm <sup>-3</sup>	1.154
$\mu$ / mm <sup>-1</sup>	0.568
F(000)	1020.0
Crystal size / mm <sup>3</sup>	0.301 × 0.11 × 0.051
Radiation	MoK $\alpha$ ( $\lambda$ = 0.71073)
2 $\theta$ range for data collection / °	3.906 to 51.478
Index ranges	-15 ≤ <i>h</i> ≤ 15, -16 ≤ <i>k</i> ≤ 16, -21 ≤ <i>l</i> ≤ 21
Reflections collected	79332
Independent reflections	10391 [ <i>R</i> <sub>int</sub> = 0.0873, <i>R</i> <sub>sigma</sub> = 0.0532]
Data/restraints/parameters	10931/0/519
Goodness-of-fit on <i>F</i> <sup>2</sup>	1.108
Final <i>R</i> indexes [ <i>I</i> ≥ 2 $\sigma$ ( <i>I</i> )]	<i>R</i> <sub>1</sub> = 0.0720, <i>wR</i> <sub>2</sub> = 0.1470
Final <i>R</i> indexes [all data]	<i>R</i> <sub>1</sub> = 0.0910, <i>wR</i> <sub>2</sub> = 0.1549
Largest diff. peak/hole / e Å <sup>-3</sup>	0.77/-0.70

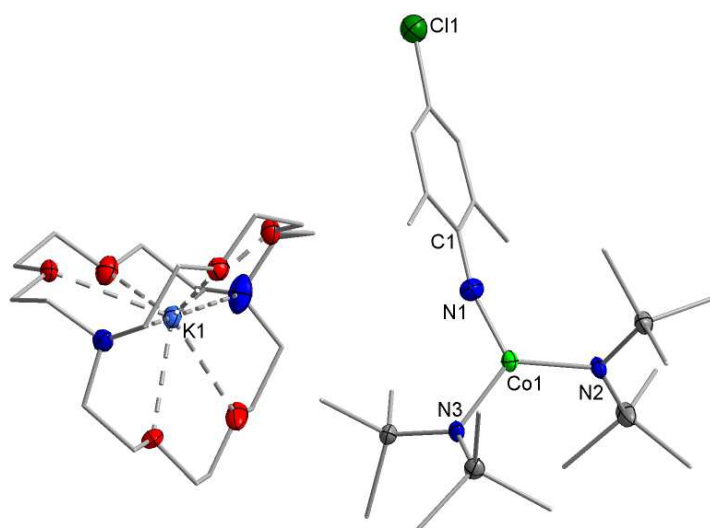
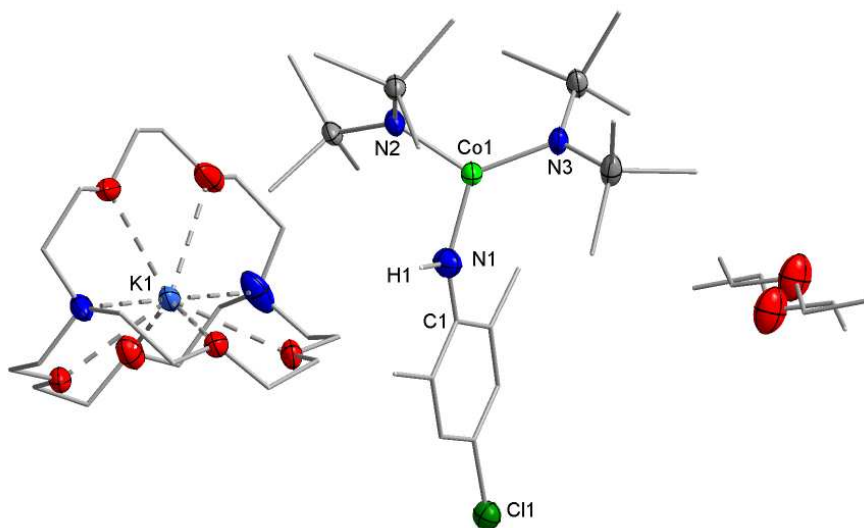


Figure S90. Molecular structure of 9 within the crystal.

**Table S18. Crystal data and structure refinement for 9H.**

Identification code	9H
Empirical formula	C <sub>40</sub> H <sub>84</sub> ClCoKN <sub>5</sub> O <sub>6.5</sub> Si <sub>4</sub>
Formula weight / g mol <sup>-1</sup>	984.96
Temperature / K	100
Crystal system	triclinic
Space group	
<i>a</i> / Å	12.5184(6)
<i>b</i> / Å	13.1475(5)
<i>c</i> / Å	17.6938(8)
<i>α</i> / °	109.5130(10)
<i>β</i> / °	92.858(2)
<i>γ</i> / °	94.477(2)
<i>V</i> / Å <sup>3</sup>	2727.6(2)
<i>Z</i>	2
$\rho_{\text{calc}}$ / g cm <sup>-3</sup>	1.199
$\mu$ / mm <sup>-1</sup>	0.572
F(000)	1060.0
Crystal size / mm <sup>3</sup>	0.239 × 0.128 × 0.08
Radiation	MoK $\alpha$ ( $\lambda$ = 0.71073)
2 $\theta$ range for data collection / °	4.412 to 51.386
Index ranges	-15 ≤ <i>h</i> ≤ 15, -16 ≤ <i>k</i> ≤ 16, -21 ≤ <i>l</i> ≤ 21
Reflections collected	74206
Independent reflections	10354 [ <i>R</i> <sub>int</sub> = 0.0789, <i>R</i> <sub>sigma</sub> = 0.0466]
Data/restraints/parameters	10354/90/566
Goodness-of-fit on <i>F</i> <sup>2</sup>	1.029
Final <i>R</i> indexes [ <i>I</i> ≥ 2 $\sigma$ ( <i>I</i> )]	<i>R</i> <sub>1</sub> = 0.0539, <i>wR</i> <sub>2</sub> = 0.1260
Final <i>R</i> indexes [all data]	<i>R</i> <sub>1</sub> = 0.0753, <i>wR</i> <sub>2</sub> = 0.1373
Largest diff. peak/hole / e Å <sup>-3</sup>	1.36/-0.93



**Figure S91. Molecular structure of 9H within the crystal.**



Table S19. Crystal data and structure refinement for 10H.

Identification code	10
Empirical formula	C <sub>38</sub> H <sub>80</sub> CoFKN <sub>5</sub> O <sub>6</sub> Si <sub>4</sub>
Formula weight / g mol <sup>-1</sup>	932.46
Temperature / K	100.00
Crystal system	Orthorhombic
Space group	Pbcn
<i>a</i> / Å	16.0620(8)
<i>b</i> / Å	22.6638(9)
<i>c</i> / Å	30.2809(14)
$\alpha$ / °	90
$\beta$ / °	90
$\gamma$ / °	90
<i>V</i> / Å <sup>3</sup>	11023.0(9)
<i>Z</i>	8
$\rho_{\text{calc}}$ / g cm <sup>-3</sup>	1.124
$\mu$ / mm <sup>-1</sup>	0.518
F(000)	4016.0
Crystal size / mm <sup>3</sup>	0.08 × 0.282 × 0.478
Radiation	MoK $\alpha$ ( $\lambda$ = 0.71073)
2 $\theta$ range for data collection / °	3.838 to 52
Index ranges	-19 ≤ <i>h</i> ≤ 19, -27 ≤ <i>k</i> ≤ 27, -37 ≤ <i>l</i> ≤ 37
Reflections collected	352471
Independent reflections	10832 [ <i>R</i> <sub>int</sub> = 0.1310, <i>R</i> <sub>sigma</sub> = 0.0407]
Data/restraints/parameters	10832/37/606
Goodness-of-fit on F <sup>2</sup>	1.276
Final <i>R</i> indexes [ <i>I</i> ≥ 2 $\sigma$ ( <i>I</i> )]	<i>R</i> <sub>1</sub> = 0.1418, <i>wR</i> <sub>2</sub> = 0.3238
Final <i>R</i> indexes [all data]	<i>R</i> <sub>1</sub> = 0.1489, <i>wR</i> <sub>2</sub> = 0.3259
Largest diff. peak/hole / e Å <sup>-3</sup>	0.73/-1.06

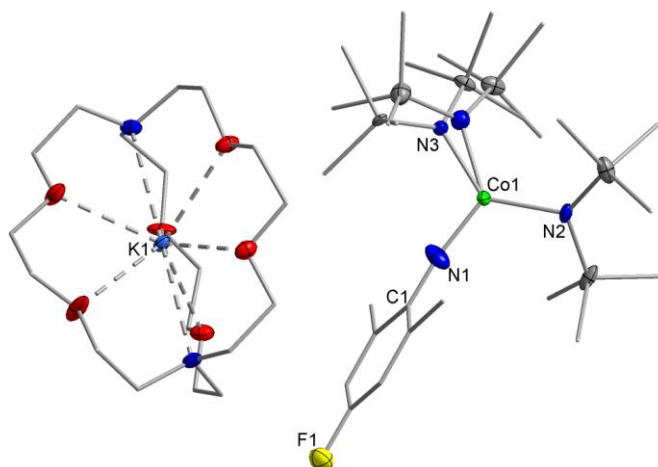


Figure S92. Molecular structure of 10H within the crystal.

Table S20. Crystal data and structure refinement for 10H.

Identification code	10H
Empirical formula	C <sub>38</sub> H <sub>81</sub> CoFKN <sub>5</sub> O <sub>6</sub> Si <sub>4</sub>
Formula weight / g mol <sup>-1</sup>	933.46
Temperature / K	100.00
Crystal system	triclinic
Space group	<i>P</i> $\bar{1}$
<i>a</i> / Å	12.3293(5)
<i>b</i> / Å	13.3682(6)
<i>c</i> / Å	16.3136(7)
$\alpha$ / °	77.0900(10)
$\beta$ / °	86.113(2)
$\gamma$ / °	85.837(2)
<i>V</i> / Å <sup>3</sup>	2610.25(19)
<i>Z</i>	2
$\rho_{\text{calc}}$ / g cm <sup>-3</sup>	1.188
$\mu$ / mm <sup>-1</sup>	0.546
F(000)	1006.0
Crystal size / mm <sup>3</sup>	0.168 × 0.107 × 0.088
Radiation	MoK $\alpha$ ( $\lambda$ = 0.71073)
2 $\theta$ range for data collection / °	4.3 to 52.076
Index ranges	-15 ≤ <i>h</i> ≤ 15, -16 ≤ <i>k</i> ≤ 16, -20 ≤ <i>l</i> ≤ 20
Reflections collected	63996
Independent reflections	10186 [ <i>R</i> <sub>int</sub> = 0.0343, <i>R</i> <sub>sigma</sub> = 0.0244]
Data/restraints/parameters	10186/0/523
Goodness-of-fit on <i>F</i> <sup>2</sup>	1.241
Final <i>R</i> indexes [ <i>I</i> ≥ 2 $\sigma$ ( <i>I</i> )]	<i>R</i> <sub>1</sub> = 0.0435, <i>wR</i> <sub>2</sub> = 0.0829
Final <i>R</i> indexes [all data]	<i>R</i> <sub>1</sub> = 0.0481, <i>wR</i> <sub>2</sub> = 0.0845
Largest diff. peak/hole / e Å <sup>-3</sup>	0.33/-0.31

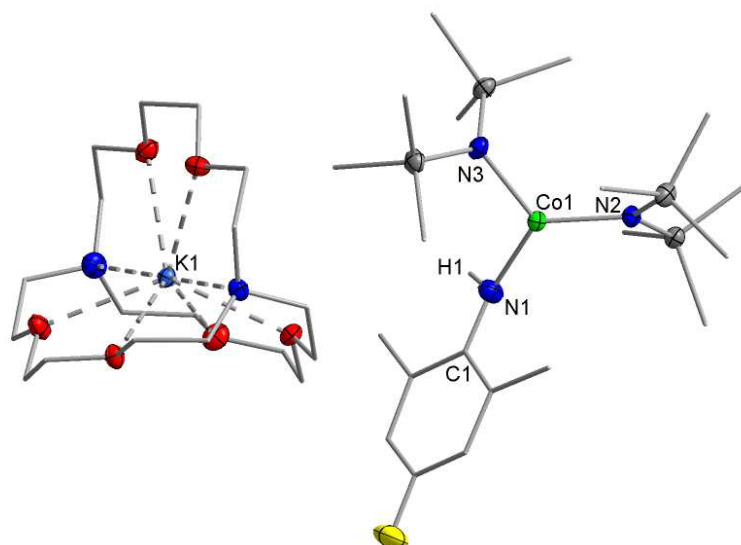


Figure S93. Molecular structure of 10H within the crystal.

Table S21. Crystal data and structure refinement for 11.

Identification code	11
Empirical formula	C <sub>41</sub> H <sub>95</sub> CoKN <sub>5</sub> O <sub>7.5</sub> Si <sub>4</sub>
Formula weight / g mol <sup>-1</sup>	988.60
Temperature / K	100
Crystal system	triclinic
Space group	<i>P</i> $\bar{1}$
<i>a</i> / Å	11.2985(6)
<i>b</i> / Å	15.4322(9)
<i>c</i> / Å	16.3950(9)
$\alpha$ / °	95.331(2)
$\beta$ / °	97.279(2)
$\gamma$ / °	90.257(3)
<i>V</i> / Å <sup>3</sup>	2823.0(3)
<i>Z</i>	2
$\rho_{\text{calc}}$ / g cm <sup>-3</sup>	1.163
$\mu$ / mm <sup>-1</sup>	0.508
F(000)	1076.0
Crystal size / mm <sup>3</sup>	0.17 × 0.152 × 0.103
Radiation	MoK $\alpha$ ( $\lambda$ = 0.71073)
2 $\theta$ range for data collection / °	4.148 to 52.06
Index ranges	-13 ≤ <i>h</i> ≤ 13, -19 ≤ <i>k</i> ≤ 19, -20 ≤ <i>l</i> ≤ 20
Reflections collected	91876
Independent reflections	11110 [ <i>R</i> <sub>int</sub> = 0.0844, <i>R</i> <sub>sigma</sub> = 0.0448]
Data/restraints/parameters	11110/54/577
Goodness-of-fit on F <sup>2</sup>	1.089
Final <i>R</i> indexes [ <i>I</i> ≥ 2 $\sigma$ ( <i>I</i> )]	<i>R</i> <sub>1</sub> = 0.0558, <i>wR</i> <sub>2</sub> = 0.1269
Final <i>R</i> indexes [all data]	<i>R</i> <sub>1</sub> = 0.0712, <i>wR</i> <sub>2</sub> = 0.1344
Largest diff. peak/hole / e Å <sup>-3</sup>	1.52/-0.40

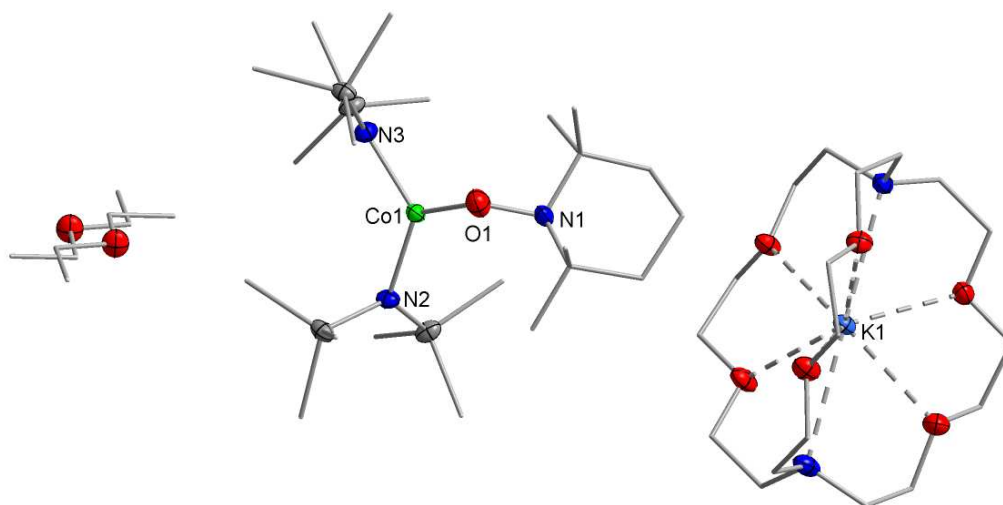


Figure S94. Molecular structure of 11 within the crystal.

- [1] D. F. Evans, *J. Chem. Soc.* **1959**, 2003.
- [2] A. Reckziegel, C. Pietzonka, F. Kraus, C. G. Werncke, *Angew. Chem.* **2020**, 8527.
- [3] R. Weller, L. Völlinger, C. G. Werncke, *Eur. J. Inorg. Chem.* **2021**, 2021, 4383.
- [4] J. C. Bottaro, P. E. Penwell, R. J. Schmitt, *Synthetic Commun* **1997**, 27, 1465.
- [5] D. G. Brown, N. Sanguantrakun, B. Schulze, U. S. Schubert, C. P. Berlinguette, *J. Am. Chem. Soc.* **2012**, 134, 12354.
- [6] A. Peeters, P. Valvekens, R. Ameloot, G. Sankar, C. E. A. Kirschhock, D. E. de Vos, *ACS Catal.* **2013**, 3, 597.
- [7] Y. Zhang, Q. Tang, M. Luo, *Org. Biomol. Chem.* **2011**, 9, 4977.
- [8] G. M. Sheldrick, *Acta Cryst. C* **2015**, 71, 3.
- [9] L. J. Farrugia, *J. Appl. Crystallogr.* **1999**, 32, 837.
- [10] P. W. Betteridge, J. R. Carruthers, R. I. Cooper, K. Prout, D. J. Watkin, *J. Appl. Crystallogr.* **2003**, 36, 1487.
- [11] C. P. Brock, T. Hahn, H. Wondratschek, U. Müller, U. Shmueli, E. Prince, A. Authier, V. Kopský, D. B. Litvin, E. Arnold et al., International Union of Crystallography, Chester, England, **2021**.
- [12] Bruker, *SADABS-2016/2*, Bruker, **2016**.

**6.9.6 Between imide, imidyl and nitrene – an imido iron complex in two oxidation states**

## **Between Imide, Imidyl and Nitrene – An Imido Iron Complex in Two Oxidation States**

Sascha Reith,<sup>a</sup> Serhiy Demeshko,<sup>b</sup> Beatrice Battistella,<sup>c</sup> Alexander Reckziegel,<sup>a</sup>  
Christian Schneider,<sup>a</sup> Andreas Stoy,<sup>a</sup> Crispin Lichtenberg,<sup>a</sup> Franc Meyer,<sup>b</sup> Dominik  
Munz\*,<sup>d,e</sup> C. Gunnar Werncke\*,<sup>a</sup>

a) Philipps-University Marburg, Department of Chemistry, Hans-Meerwein-Straße 4,  
D-35037 Marburg, Germany

b) University of Göttingen, Institute for Inorganic Chemistry, Tammannstraße 4, D-  
37077 Göttingen, Germany

c) Humboldt-University Berlin, Institute for Chemistry, Brook-Taylor-Straße 2, D-  
12489 Berlin, Germany

d) Saarland University, Inorganic Chemistry: Coordination Chemistry, Campus C4.1,  
D-66123 Saarbrücken, Germany

e) Friedrich-Alexander University Erlangen-Nürnberg, Inorganic Chemistry,  
Egerlandstraße 1, D-91058 Erlangen, Germany

# Table of Contents

General considerations.....	2
Synthesis of $K\{\text{crypt.222}\}[\text{Fe}(\text{N}\{\text{Dipp}\}\text{SiMe}_3)]$ .....	3
Synthesis of $K\{\text{crypt.222}\}[\text{Fe}(\text{NMe}_3)(\text{N}\{\text{Dipp}\}\text{SiMe}_3)_2]$ ( $K\{\text{crypt.222}\}[1]$ ).....	4
Synthesis of $[\text{Fe}(\text{NMe}_3)(\text{N}\{\text{Dipp}\}\text{SiMe}_3)_2]$ ( $[1]$ ).....	5
Synthesis of $K\{\text{crypt.222}\}[\text{Fe}(\text{N}\{\text{Dipp}\}\text{SiMe}_3)_2(\eta^2\text{-S}_2\text{CNMe}_3)]$ ( $K\{\text{crypt.222}\}[2]$ ).....	7
Reactivity of Imido Complexes with Phosphines.....	9
Reactivity towards carbon monoxide.....	11
Hydrogen atom transfer (HAT) reactivity .....	12
Cyclic voltammetry .....	16
Mössbauer spectroscopy.....	19
Magnetic measurements.....	20
Electron-paramagnetic-resonance spectroscopy (EPR) .....	24
Quantum chemical calculations .....	25
X-Ray diffraction analysis and molecular structures .....	34

## General considerations

All manipulations were carried out in a glovebox or using Schlenk-type techniques under a dry argon atmosphere. Used solvents were dried by continuous distillation over sodium metal for several days, degassed via three freeze-pump cycles and stored over molecular sieves 4 Å. The  $^1\text{H}$  NMR spectra were recorded on a *Bruker AV III 500* or a *Bruker AV II 300* NMR spectrometers. Chemical shifts are reported in ppm relative to the residual proton signals of the solvent (for  $^1\text{H}$ ) or relative to the signal of the solvent itself ( $^{13}\text{C}$ ). The  $^{31}\text{P}$  NMR spectra were recorded on a *Bruker AV III HD 300* and chemical shifts are reported in ppm relative to  $\text{H}_3\text{PO}_4$ .  $w_{1/2}$  is the line width of a signal at half its maximum intensity. Integrals of the broad signals of the silylamide units were obtained directly or by peak fitting (in case of overlapping signals) using the MestReNova software package. IR measurements were conducted on a *Bruker Alpha ATR-IR* spectrometer. Elemental analyses were performed by the “in-house” service of the Chemistry Department of the Philipps University Marburg, Germany using a CHN(S) analyzer *vario MICRO Cube (Elementar)*. The UV/VIS measurement were recorded on an *Analytik Jena Specord S600* spectrometer using *WinASPECT* software and an *UNISOKU CoolSpeK Cryostat*. The distinct signal at around 680 nm is assigned to a lamp change. Solution magnetic susceptibilities were determined by the Evans method.<sup>1</sup> EPR measurements considering the conversion of TEMPO–H to the TEMPO radical were carried out at room temperature at X-band (9.38 GHz) by using a *Bruker/Magnettech ESR 5000* spectrometer (experimental parameters: microwave frequency = 9.38 GHz, microwave power = 1 mW, modulation amplitude = 0.5 G and 2 G, modulation frequency = 100 kHz). 2.2.2-cryptand (crypt.222), 1,4-cyclohexadiene, 2,2,6,6-tetramethylpiperidinyloxy, carbon disulfide ( $\text{CS}_2$ ), and tetramethylsilane (TMS) were obtained commercially (Sigma-Aldrich, Acros, Strem, Alfa Aesar) and -if not noted otherwise- used as received. 1,4-cyclohexadiene and carbon disulfide were degassed, transferred into a glovebox and stored at  $-35\text{ }^\circ\text{C}$ .  $[\text{Fe}(\text{N}\{\text{Dipp}\}\text{SiMe}_3)_2]$ ,<sup>2</sup> and 1-azido-2,4,6-trimethylbenzene ( $\text{N}_3\text{Mes}$ )<sup>3</sup> and 1-hydroxy-2,2,6,6-tetramethylpiperidin (TEMPO-H)<sup>4</sup> were prepared according to the respective literature procedures.



## Synthesis of K{crypt.222}[Fe(N{Dipp}SiMe<sub>3</sub>)<sub>2</sub>]

580 mg (1.05 mmol, 1 equiv.) [Fe(N{Dipp}SiMe<sub>3</sub>)<sub>2</sub>] were dissolved in 20 mL Et<sub>2</sub>O. Addition of 180 mg (1.31 mmol, 1.25 equiv.) K<sub>2</sub>C<sub>8</sub> at -30 °C resulted in a color change from red to brown. After stirring the mixture for 10 minutes the suspension was filtered and the filtrate was layered with a solution of 414 mg (1.10 mmol, 1.05 equiv.) crypt.222 in 15 mL Et<sub>2</sub>O. Storage at -35 °C led to the precipitation of a dark green crystalline solid. After filtration all remaining volatiles were removed *in vacuo* to afford 909 mg (0.93 mmol, 89%) of K{crypt.222}[Fe(N{Dipp}SiMe<sub>3</sub>)<sub>2</sub>].

**<sup>1</sup>H-NMR** (THF-d<sub>8</sub>, 298 K, ppm, 500 MHz): 28.71 (s,  $w_{1/2}$  = 367 Hz), 27.35 (s,  $w_{1/2}$  = 462.4 Hz), 12.17 (s,  $w_{1/2}$  = 166 Hz), 2.76 (s,  $w_{1/2}$  = 37 Hz, crypt), 2.70 (s,  $w_{1/2}$  = 41 Hz, crypt), 1.84 (s,  $w_{1/2}$  = 35 Hz, crypt), 1.22 (s,  $w_{1/2}$  = 9.5 Hz), -0.6 (s,  $w_{1/2}$  = 950 Hz), -100.5 (s,  $w_{1/2}$  = 1420 Hz).

**IR** (ATR, cm<sup>-1</sup>)  $\nu$ : 2942 (m), 2884 (m), 2838 (m), 1577 (w), 1469 (w), 1453 (w), 1448 (w), 1423 (m), 1356 (m), 1314 (m), 1294 (w), 1234 (s), 1223 (s), 1193 (m), 1135 (m), 1100 (vs), 1072 (s), 1051 (w), 947 (m), 926 (vs), 880 (w), 836 (vs), 780 (s), 747 (m), 660 (m), 617 (w), 538 (w), 521 (w), 429 (m).

**Elemental analysis:** calcd. (%) for C<sub>48</sub>H<sub>88</sub>FeKN<sub>4</sub>O<sub>6</sub>Si<sub>2</sub> (968.37 g mol<sup>-1</sup>): C 59.54 H 9.16 N 5.79; found: C 59.74 H 9.112 N 5.83.

**Solution magnetic susceptibility:**  $\mu_{\text{eff}} = 4.66 \mu_{\text{B}}$  (THF-d<sub>8</sub>+ 1% Si(CH<sub>3</sub>)<sub>4</sub>, 500 MHz, 298 K).

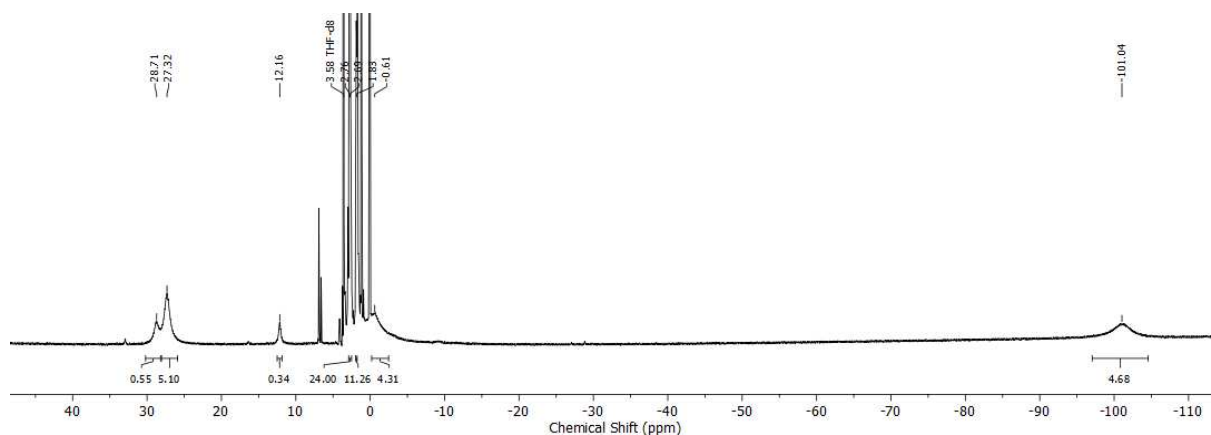


**Figure S1.** <sup>1</sup>H-NMR spectrum of K{crypt.222}[Fe(N{Dipp}SiMe<sub>3</sub>)<sub>2</sub>] in THF-d<sub>8</sub> (298 K, 300 MHz).

## Synthesis of $K\{\text{crypt.222}\}[\text{Fe}(\text{NMe}_3)(\text{N}\{\text{Dipp}\}\text{SiMe}_3)_2]$ ( $K\{\text{crypt.222}\}[1]$ )

### Path A:

80 mg (0.1 mmol, 1 equiv.)  $K\{\text{crypt}\}[\text{Fe}(\text{N}\{\text{Dipp}\}\text{SiMe}_3)_2]$  were dissolved in a mixture of 2 mL  $\text{Et}_2\text{O}$  and 1 mL THF. Addition of 14 mg (0.1 mmol, 1 equiv.)  $\text{N}_3\text{Mes}$  at  $-35\text{ }^\circ\text{C}$  resulted in an immediate color change from green to dark green under concomitant gas evolution. After stirring the mixture for 5 minutes, the mixture was layered with 3 mL *n*-pentane and stored at  $-35\text{ }^\circ\text{C}$ . After one day, the solution was removed via pipette and the remaining dark green crystals were rinsed with 2x3 mL pentane. Drying *in vacuo* yielded 78 mg (0.1 mmol, 86%)  $K\{\text{crypt.222}\}[1]$ .

### Path B:

100 mg (0.15 mmol, 1 equiv.)  $[\text{Fe}(\text{NMe}_3)(\text{N}\{\text{Dipp}\}\text{SiMe}_3)_2]$  (**[1]**) were dissolved in 3 mL  $\text{Et}_2\text{O}$ . After addition of 49.0 mg (0.14 mmol, 0.95 equiv.) crypt.222 and 22.0 mg (0.16 mmol, 1.1 equiv.)  $\text{KC}_8$  the suspension was stirred for 30 min. Meanwhile, a color change from brown to yellowish brown was observed. The suspension was filtered, the filtrate layered with 3 mL *n*-pentane and stored at  $-35\text{ }^\circ\text{C}$ . After one day, the solution was removed via pipette and the remaining dark yellow crystals were rinsed with 2x3 mL pentane. The crystals were characterized through X-ray diffraction analysis and  $^1\text{H}$  NMR spectroscopy.

$^1\text{H-NMR}$  (THF- $d_8$ , 298 K, ppm, 300 MHz): 45.2 (s,  $w_{1/2} = 85$  Hz), 11.0 (s,  $w_{1/2} = 1060$  Hz), 5.83 (s,  $w_{1/2} = 870$  Hz), 3.50 (s,  $w_{1/2} = 21.2$  Hz), 2.50 (s,  $w_{1/2} = 14.7$  Hz),  $-3.20$  (s,  $w_{1/2} = 475$  Hz),  $-39.6$  (s,  $w_{1/2} = 470$  Hz).

**IR** (ATR,  $\text{cm}^{-1}$ )  $\nu$ : 2975 (m), 2880 (m), 2973 (m), 1596 (w), 1465 (w), 1425 (s), 1350 (s), 1298 (s), 1240 (vs), 1194 (s), 1090 (vs), 1073 (vs), 946 (s), 900 (s), 825 (vs), 773 (s), 738 (m), 669 (m), 542 (w), 432 (w).

**Elemental analysis:** calcd. (%) for  $\text{C}_{57}\text{H}_{99}\text{FeKN}_5\text{O}_6\text{Si}_2$  ( $1101.56\text{ g mol}^{-1}$ ): C 62.15 H 9.06 N 6.36; found: C 61.82 H 8.851 N 6.38.

**Solution magnetic susceptibility:**  $\mu_{\text{eff}} = 5.39\ \mu_{\text{B}}$  (THF- $d_8$ + 1%  $\text{Si}(\text{CH}_3)_4$ , 500 MHz, 298 K).

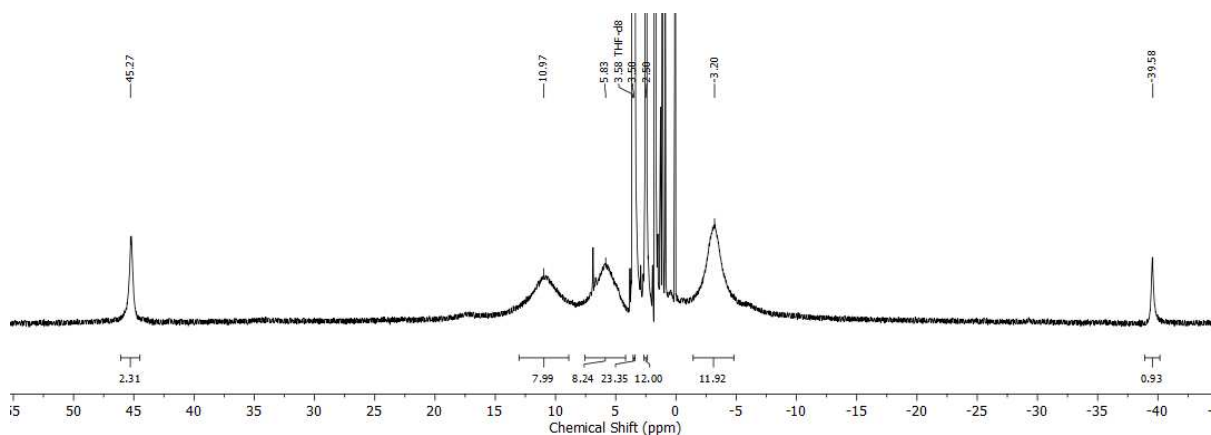


**Figure S2.**  $^1\text{H}$  NMR spectrum of  $K\{\text{crypt.222}\}[\text{Fe}(\text{NMe}_3)(\text{N}\{\text{Dipp}\}\text{SiMe}_3)_2]$  ( $K\{\text{crypt.222}\}[1]$ ) in THF- $d_8$  (298 K, 300 MHz).

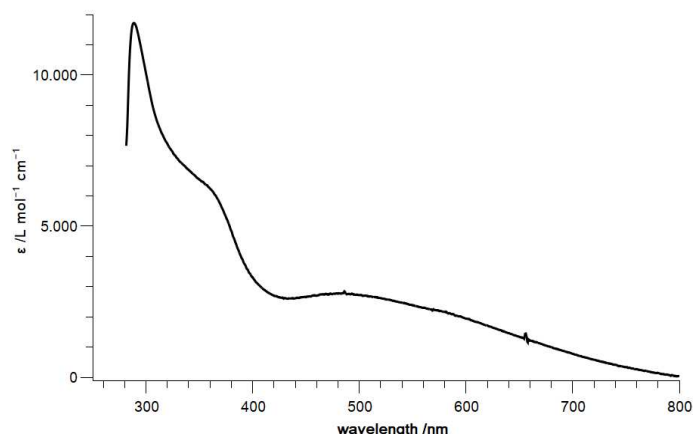


**Figure S3.** UV-VIS spectrum of  $\text{K}\{\text{crypt.222}\}[\text{Fe}(\text{NMes})(\text{N}\{\text{Dipp}\}\text{SiMe}_3)_2]$  ( $\text{K}\{\text{crypt.222}\}[\mathbf{1}]$ ) in 1,2-DFB.

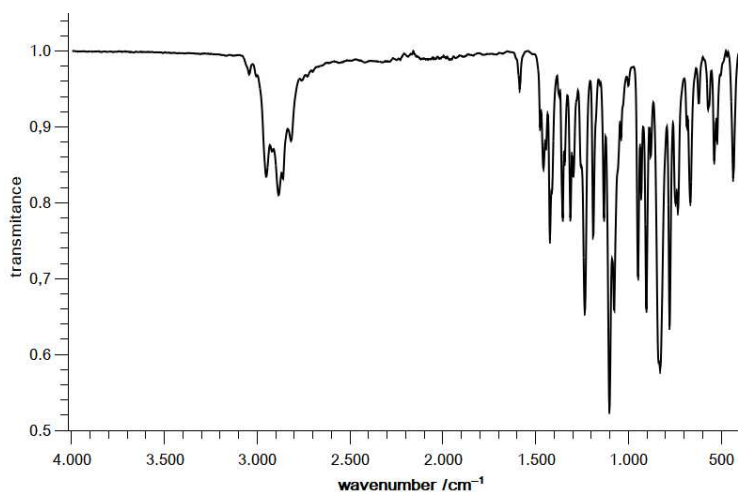


**Figure S4.** ATR IR-spectrum of  $\text{K}\{\text{crypt.222}\}[\text{Fe}(\text{NMes})(\text{N}\{\text{Dipp}\}\text{SiMe}_3)_2]$  ( $\text{K}\{\text{crypt.222}\}[\mathbf{1}]$ ).

### Synthesis of $[\text{Fe}(\text{NMes})(\text{N}\{\text{Dipp}\}\text{SiMe}_3)_2]$ ( $\mathbf{1}$ )

#### Path A:

50.0 mg (0.05 mmol, 1 equiv.)  $\text{K}\{\text{crypt.222}\}[\mathbf{1}]$  were dissolved in 1 mL 1,2-difluorobenzene. After addition of 12.0 mg (0.05 mmol, 1 equiv.)  $\text{AgOTf}$  the solution was stirred for 3 hours. The solvent was removed *in vacuo* and the brown residue was dissolved in  $\text{C}_6\text{D}_6$ . The obtained  $^1\text{H-NMR}$  spectra showed the formation of  $\mathbf{1}$ . No further purification was carried out due to the high purity of  $\mathbf{1}$  by **Path B**.

#### Path B:

300 mg (0.50 mmol, 1 equiv.)  $[\text{Fe}(\text{N}\{\text{Dipp}\}\text{SiMe}_3)_2]$  were dissolved in 3 mL *n*-pentane. Addition of 88 mg (0.50 mmol, 1 equiv.)  $\text{N}_3\text{Mes}$  at  $-35\text{ }^\circ\text{C}$  resulted in an immediate color change from red to brown under concomitant gas evolution. After stirring the mixture for 30 minutes, the solution was stored at  $-35\text{ }^\circ\text{C}$ . After two days, the solution was removed via a Pasteur pipette and the remaining brown crystals were dried *in vacuo* yielding 236 mg (0.34 mmol, 64%)  $\mathbf{1}$ .

**$^1\text{H-NMR}$**  ( $\text{C}_6\text{D}_6$ , 298 K, ppm, 300 MHz): 78.1 (s,  $w_{1/2} = 141$  Hz), 6.82 (s), 6.72 (s), 6.62 (s), 6.55 (s,  $w_{1/2} = 4.7$  Hz), -12.3 (s,  $w_{1/2} = 670$  Hz), -41.7 (s,  $w_{1/2} = 190$  Hz).

**IR** (ATR,  $\text{cm}^{-1}$ )  $\nu$ : 3041 (m), 2951 (m), 2883 (m), 2861 (m), 2816 (m), 1606 (w), 1585 (w), 1476 (m), 1445 (m), 1422 (m), 1313 (m), 1296 (m), 1235 (s), 1132 (m), 1102 (vs), 1077 (s), 1040 (w), 948 (s), 930 (m), 905 (s), 828 (vs), 778 (s), 745 (m), 667 (w), 620 (w), 570 (m), 537 (m), 523 (m), 435 (m).

**Elemental analysis:** calcd. (%) for  $\text{C}_{39}\text{H}_{63}\text{FeN}_2\text{Si}_2$  ( $685.97$  g  $\text{mol}^{-1}$ ): C 68.29 H 9.26 N 6.13; found: C 68.70 H 9.142 N 6.20.

**Solution magnetic susceptibility:**  $\mu_{\text{eff}} = 4.98 \mu_{\text{B}}$  ( $\text{C}_6\text{D}_6 + 1\%$   $\text{Si}(\text{CH}_3)_4$ , 500 MHz, 298 K).

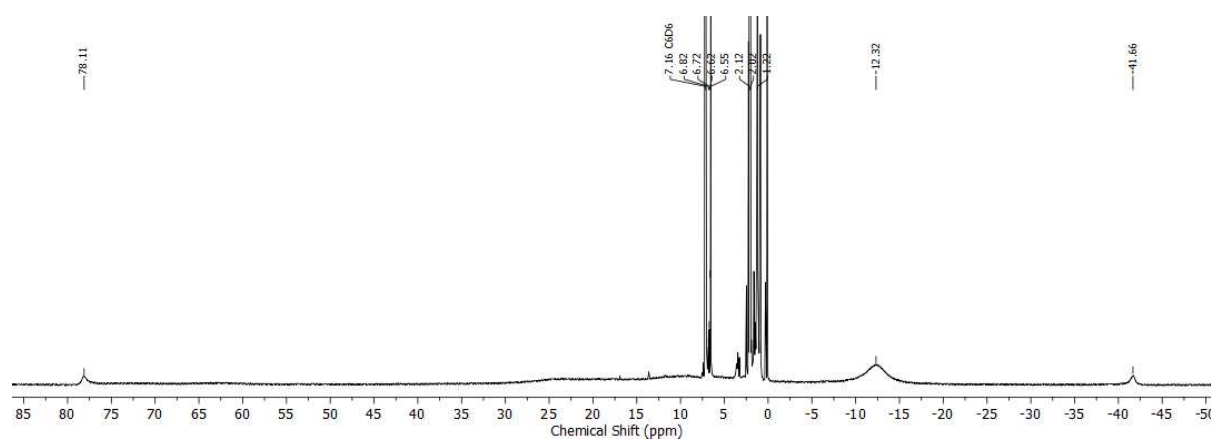


**Figure S5.**  $^1\text{H NMR}$  spectrum of  $[\text{Fe}(\text{NMes})(\text{N}\{\text{Dipp}\}\text{SiMe}_3)_2]$  ([1]) in  $\text{C}_6\text{D}_6$  (298 K, 300 MHz).

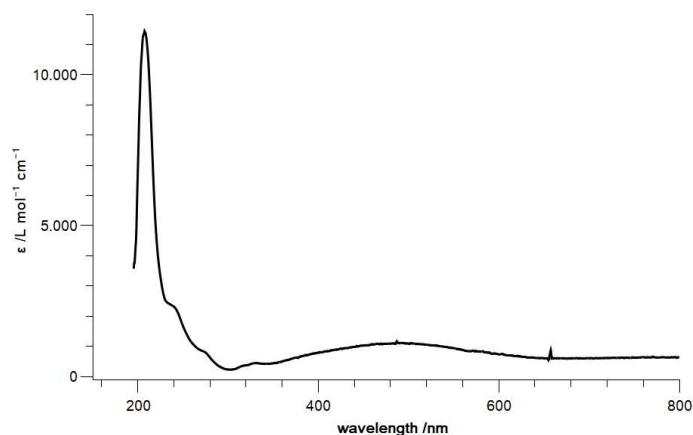


**Figure S6.** UV-VIS spectrum of  $[\text{Fe}(\text{NMes})(\text{N}\{\text{Dipp}\}\text{SiMe}_3)_2]$  ([1]) in *n*-pentane.

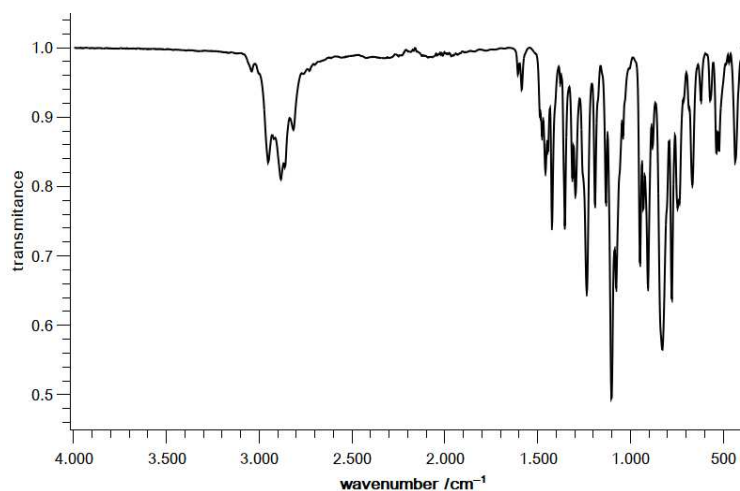


**Figure S7.** ATR IR-spectrum of  $[\text{Fe}(\text{NMes})(\text{N}\{\text{Dipp}\}\text{SiMe}_3)_2]$  ([1]).

### Synthesis of $\text{K}\{\text{crypt.222}\}[\text{Fe}(\text{N}\{\text{Dipp}\}\text{SiMe}_3)_2(\eta^2\text{-S}_2\text{CNMes})]$ ( $\text{K}\{\text{crypt.222}\}[\mathbf{2}]$ )

40 mg (0.040 mmol, 1 equiv.)  $\text{K}\{\text{crypt.222}\}[\text{Fe}(\text{N}(\text{Dipp})\text{SiMe}_3)_2(\text{NMes})]$  ( $\text{K}\{\text{crypt.222}\}[\mathbf{1}]$ ) were dissolved in 3 mL 1,2-difluorobenzene. To the solution 3 mg (0.04 mmol, 1 equiv.)  $\text{CS}_2$  were added. While stirring the mixture for 30 minutes, a color change from dark green to reddish was observed. The solution was layered with 3 mL *n*-pentane and stored at  $-35^\circ\text{C}$ . After one day, the solution was removed via a Pasteur pipette and the remaining dark red crystals were rinsed with 2x3mL pentane. Drying *in vacuo* yielded 37 mg (0.03 mmol, 80%)  $\text{K}\{\text{crypt.222}\}[\mathbf{2}]$ .

**$^1\text{H-NMR}$**  (THF- $d_8$ , 298 K, ppm, 300 MHz): 81.3 (s,  $w_{1/2} = 350$  Hz), 15.8 (s,  $w_{1/2} = 218$  Hz), 9.64 (s,  $w_{1/2} = 720$  Hz), 3.67 (s, cryptand), 2.74 (s, cryptand,  $w_{1/2} = 49.7$  Hz),  $-5.61$  (s,  $w_{1/2} = 2430$  Hz),  $-69.8$  (s,  $w_{1/2} = 340$  Hz).

**IR** (ATR,  $\text{cm}^{-1}$ )  $\nu$ : 2954 (m), 2882 (m), 2864 (m), 2813 (m), 1544 (m), 1475 (w), 1457 (m), 1423 (m), 1378 (m), 1353 (w), 1296 (m), 1234 (s), 1205 (m), 1177 (w), 1131 (m), 1101 (vs), 1076 (s), 949 (s), 889 (m), 866 (m), 832 (vs), 778 (vs), 751 (s), 690 (s), 671 (m), 618 (w), 572 (w), 537 (m), 524 (m), 437 (m).

**Elemental analysis:** calcd. (%) for  $\text{C}_{58}\text{H}_{99}\text{FeKN}_5\text{O}_6\text{S}_2\text{Si}_2$  ( $1177.69$  g  $\text{mol}^{-1}$ ): C 59.15 H 8.47 N 5.95 S 5.44; found: C 59.51 H 8.431 N 5.67 S 5.65.

**Solution magnetic susceptibility:**  $\mu_{\text{eff}} = 5.84 \mu_{\text{B}}$  (THF- $d_8$ + 1%  $\text{Si}(\text{CH}_3)_4$ , 500 MHz, 298 K).

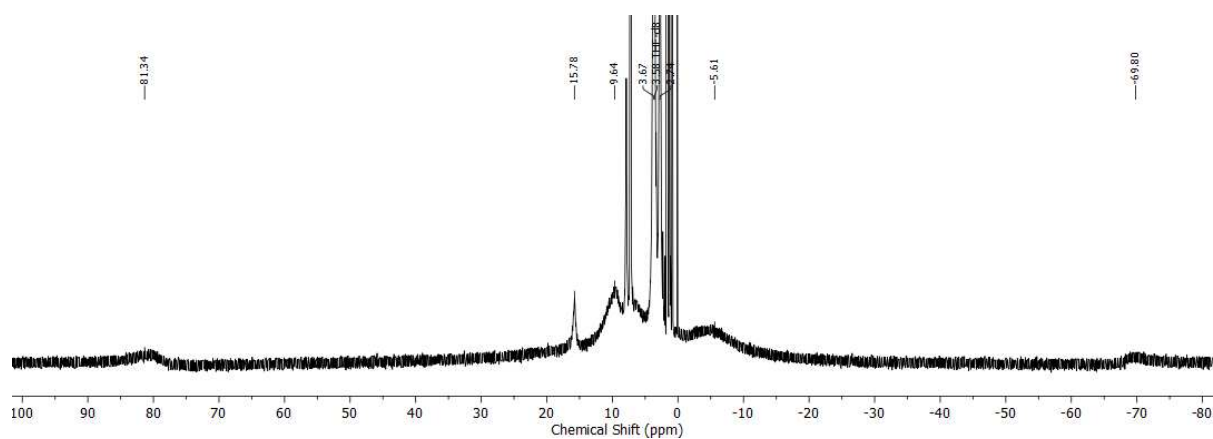


**Figure S8.**  $^1\text{H}$  NMR spectrum of  $\text{K}\{\text{crypt.222}\}[\text{Fe}(\text{N}\{\text{Dipp}\}\text{SiMe}_3)_2(\eta^2\text{-S}_2\text{CNMes})]$  ( $\text{K}\{\text{crypt.222}\}[\mathbf{2}]$ ) in  $\text{THF-d}_8$  (298 K, 300 MHz).

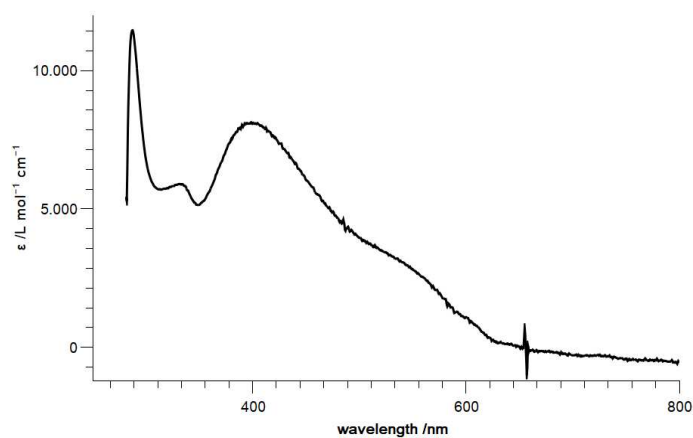


**Figure S9.** UV-VIS spectrum of  $\text{K}\{\text{crypt.222}\}[\text{Fe}(\text{N}\{\text{Dipp}\}\text{SiMe}_3)_2(\eta^2\text{-S}_2\text{CNMes})]$  ( $\text{K}\{\text{crypt.222}\}[\mathbf{2}]$ ) in 1,2-DFB.

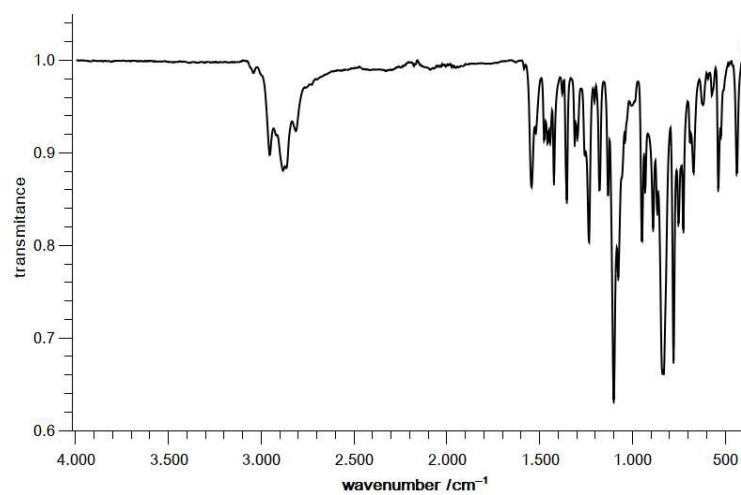


**Figure S10.** ATR IR-spectrum of  $\text{K}\{\text{crypt}\}[\text{Fe}(\text{N}\{\text{Dipp}\}\text{SiMe}_3)_2(\eta^2\text{-S}_2\text{CNMes})]$  ( $\text{K}\{\text{crypt.222}\}[\mathbf{2}]$ ).

## Reactivity of Imido Complexes with Phosphines

### Reaction of K{crypt.222}[1] with PEt<sub>3</sub>

To a solution of 30 mg (0.03 mmol, 1 equiv.) K{crypt.222}[1], dissolved in 0.4 mL THF, a second solution of 6 mg (0.05 mmol, 2 equiv.) PEt<sub>3</sub>, dissolved in 0.2 mL THF, was added. After stirring the solution for 24 h the reaction mixture was analyzed by <sup>31</sup>P NMR. No formation of Et<sub>3</sub>P=NMe<sub>3</sub> ( $\delta = 6.8$  ppm) was observed. An authentic sample of Et<sub>3</sub>P=NMe<sub>3</sub> was prepared via the Staudinger reaction between PEt<sub>3</sub> and N<sub>3</sub>Me<sub>3</sub> to confirm this signal. The signal at  $\delta = -16.8$  ppm belongs to the employed PEt<sub>3</sub>.

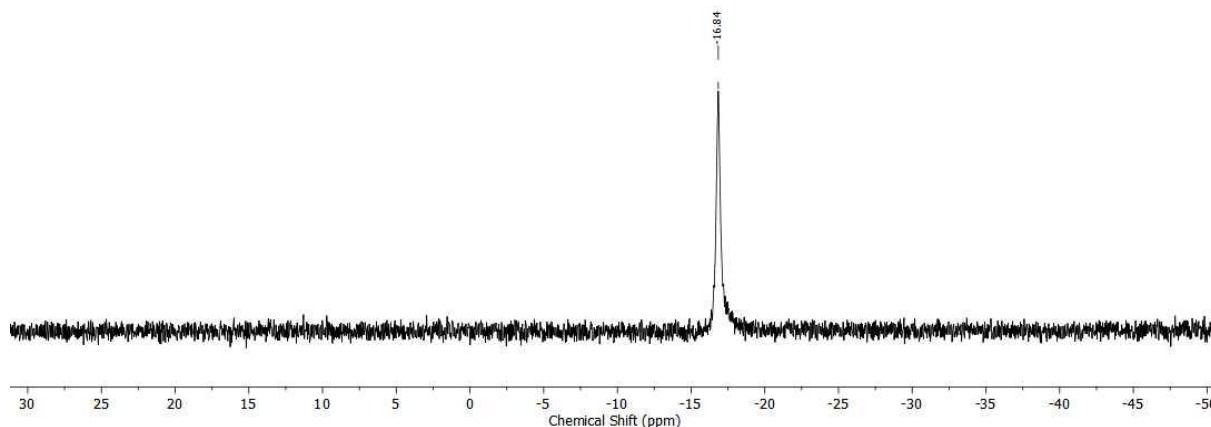


**Figure S11.** <sup>31</sup>P NMR spectrum of K{crypt.222}[Fe(NMe<sub>3</sub>)(N{Dipp}SiMe<sub>3</sub>)<sub>2</sub>] (K{crypt.222}[1]) and 2 equiv. of PEt<sub>3</sub> in THF after 24 h (298 K, 250 MHz).

After addition of the stronger complex agent 2,2'-bipyridin (5 mg, 0.03 mmol, 1.3 equiv.) the solution was stirred for additional 24 h. No other signals besides that of PEt<sub>3</sub> could be observed by <sup>31</sup>P NMR spectroscopy (Figure S12).

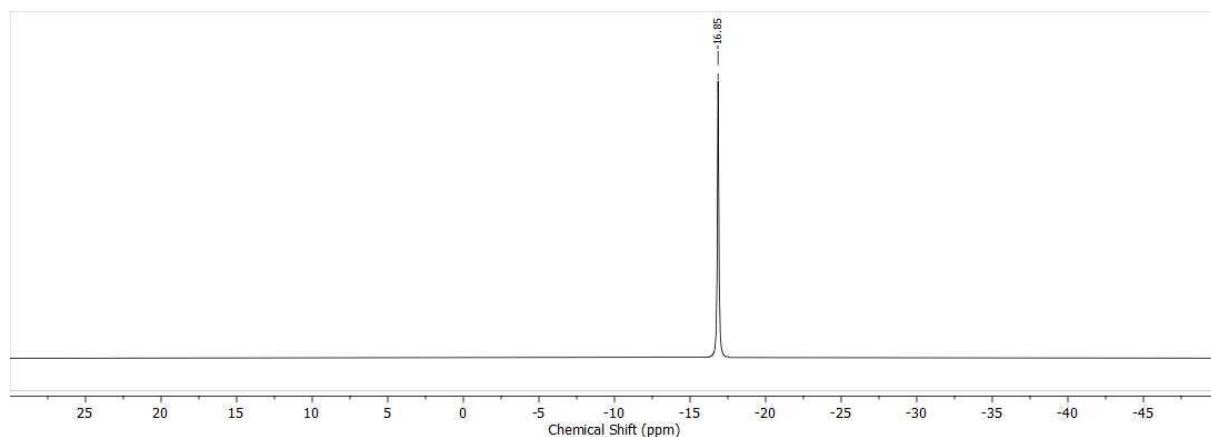


**Figure S112.** <sup>31</sup>P NMR spectrum of the abovementioned reaction mixture (K{crypt.222}[Fe(NMe<sub>3</sub>)(N{Dipp}SiMe<sub>3</sub>)<sub>2</sub>] (K{crypt.222}[1]) and 2 equiv. of PEt<sub>3</sub> in THF-d<sub>8</sub>) which was treated with 2,2'-bipyridin and measured again after 24 h (298 K, 250 MHz).

Independent reaction of Et<sub>3</sub>P=NMe<sub>3</sub> with [1]<sup>-</sup> or with the iron(II) silylamide K{crypt.222}[Fe(N{Dipp}SiMe<sub>3</sub>)<sub>2</sub>], resulting from a successful nitrene transfer of [1]<sup>-</sup> to PEt<sub>3</sub>, gave no interactions by means of <sup>31</sup>P NMR spectroscopy.

### Reaction of [1] with $\text{PEt}_3$

To a solution of 30 mg (0.04 mmol, 1 equiv.) [1], dissolved in 0.4 mL *n*-pentane, a second solution of 10 mg (0.08 mmol, 2 equiv.)  $\text{PEt}_3$ , dissolved in 0.2 mL *n*-pentane, was added. After stirring the solution for 24 h the reaction mixture was analyzed by  $^{31}\text{P}$  NMR with no observable formation of  $\text{Et}_3\text{P}=\text{NMe}_s$  ( $\delta = 6.8$  ppm). Only a very broad and small signal of the employed  $\text{PEt}_3$  was observed (Figure S12), which is attributed to reversible binding of the phosphine to [1].

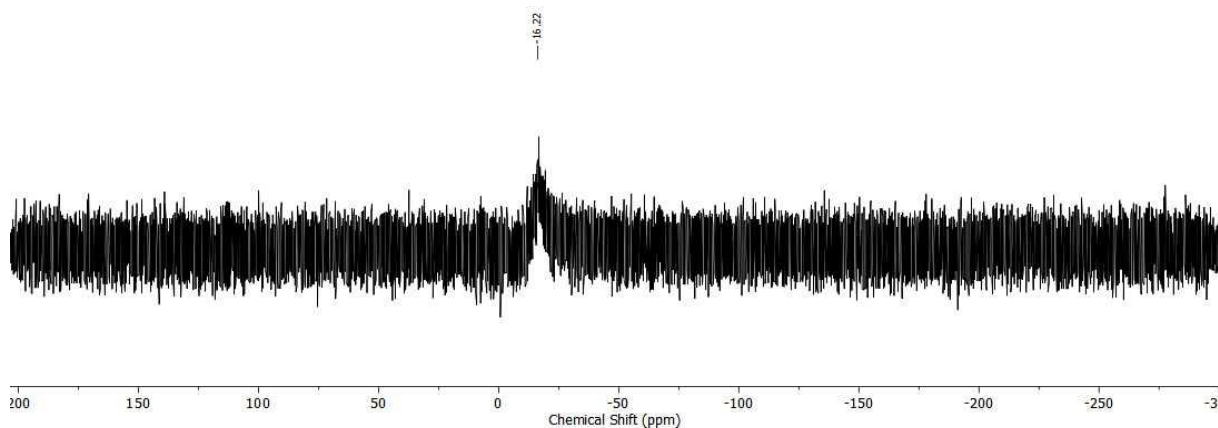


**Figure S13.**  $^{31}\text{P}$  NMR spectrum of  $\text{K}\{\text{crypt.222}\}[\text{Fe}(\text{NMes})(\text{N}\{\text{Dipp}\}\text{SiMe}_3)_2]$  ( $\text{K}\{\text{crypt.222}\}[\mathbf{1}]$ ) with added 2 equiv. of  $\text{PEt}_3$  in  $\text{THF-d}_8$  after 24 h (298 K, 250 MHz).

After addition of the stronger complex agent 2,2'-bipyridin (8 mg, 0.05 mmol, 1.3 equiv.) the reversible phosphine coordination is blocked with reoccurrence of a sharp signal for  $\text{PEt}_3$  as well as observation of a signal at  $\delta = 6.8$  ppm that corresponds to  $\text{Et}_3\text{P}=\text{NMe}_s$  (Figure S14).

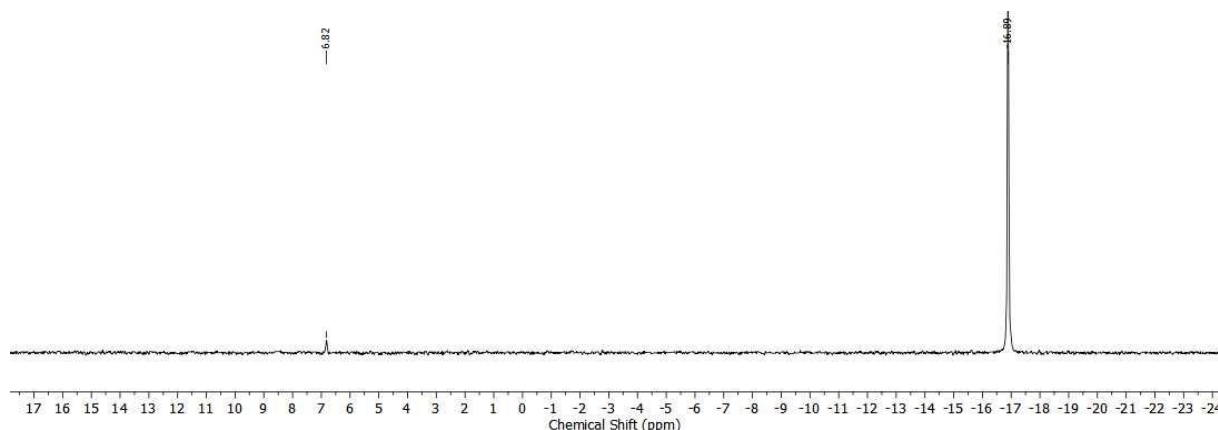


**Figure S14.**  $^{31}\text{P}$  NMR spectrum of  $[\text{Fe}(\text{N}(\text{NMes})\{\text{Dipp}\}\text{SiMe}_3)_2]$  ( $\mathbf{1}$ ) with added 2 equiv. of  $\text{PEt}_3$  in  $\text{THF-d}_8$  after 24 h (298 K, 250 MHz).

Independent reaction of  $\text{Et}_3\text{P}=\text{NMe}_s$  with [1] or with the iron(II) silylamide  $[\text{Fe}(\text{N}\{\text{Dipp}\}\text{SiMe}_3)_2]$ , resulting from a successful nitrene transfer of [1] to  $\text{PEt}_3$ , revealed no interactions by means of  $^{31}\text{P}$  NMR spectroscopy.



## Reactivity towards carbon monoxide

### Reaction of K{crypt.222}[1] with CO

30 mg (0.03 mmol, 1 equiv.) K{crypt.222}[1] were dissolved in 0.5 mL THF-d<sub>8</sub> in a J-Young NMR tube and 1 atm. CO was added. The green solution was analyzed by <sup>1</sup>H NMR spectroscopy after 24 h. Formation of MesNCO (integrated signals) is visible (Figure 15).<sup>5</sup>

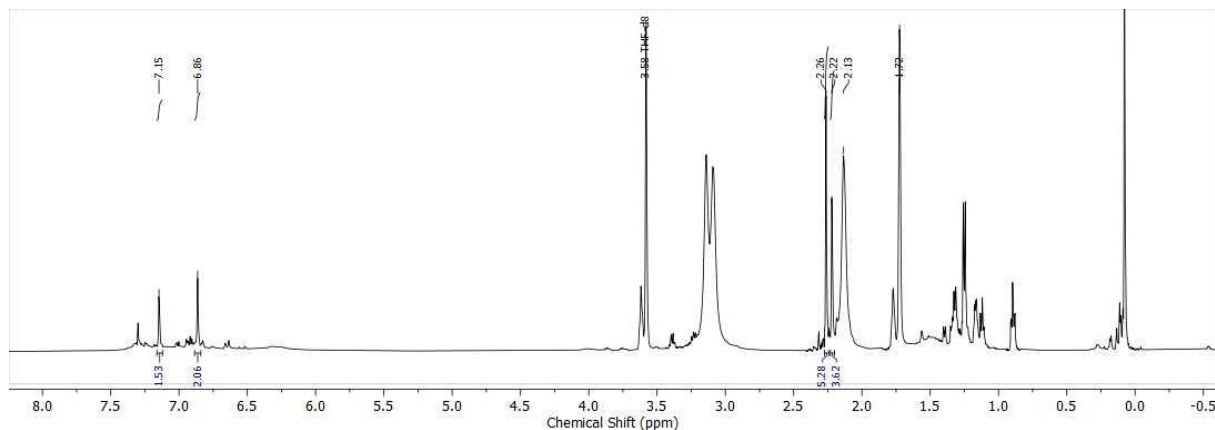


**Figure S15.** <sup>1</sup>H NMR spectrum of K{crypt.222}[Fe(NMes)(N{Dipp}SiMe<sub>3</sub>)<sub>2</sub>] (K{crypt.222}[1]) 24 h after addition of 1 atm. CO in THF-d<sub>8</sub> (298 K, 300 MHz).

### Reaction of [1] with CO

30 mg (0.04 mmol, 1 equiv.) [1] were dissolved in 0.5 mL C<sub>6</sub>D<sub>6</sub> in a J-Young NMR tube and 1 atm. CO was added. The brown solution was analyzed by <sup>1</sup>H NMR spectroscopy after 24 h (Figure S16) yielding only the signature of the employed [1].

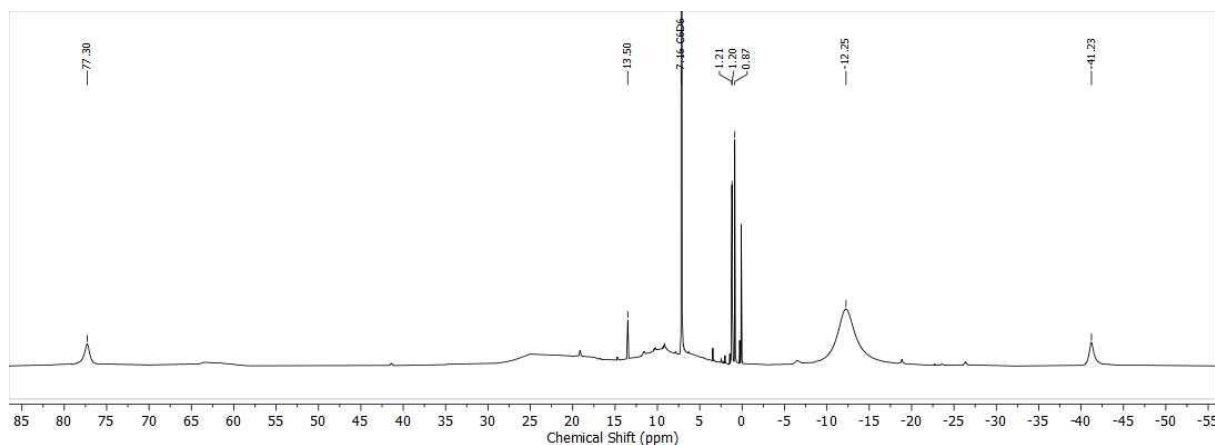


**Figure S16.** <sup>1</sup>H NMR spectrum of [Fe(NMes)(N{Dipp}SiMe<sub>3</sub>)<sub>2</sub>] ([1]) 24 h after addition of 1 atm CO in C<sub>6</sub>D<sub>6</sub> after 24 h (298 K, 300 MHz).

## Hydrogen atom transfer (HAT) reactivity

### Reaction of K{crypt.222}[1] with 1,4-Cyclohexadiene

To a solution of 25 mg (0.02 mmol, 1 equiv.) K{crypt.222}[1], dissolved in 0.5 mL tetrahydrofuran- $d_8$ , 4 mg (0.04 mmol, 2 equiv.) 1,4-CHD were added. After stirring the solution for 24 hours formation of benzene ( $\delta = 7.30$  ppm, 73 % conversion) was observed by  $^1\text{H}$  NMR spectroscopy. Attempts for identification and isolation of the presumably resulting iron amide complex or any other iron containing reaction product via crystallisation was not successful.

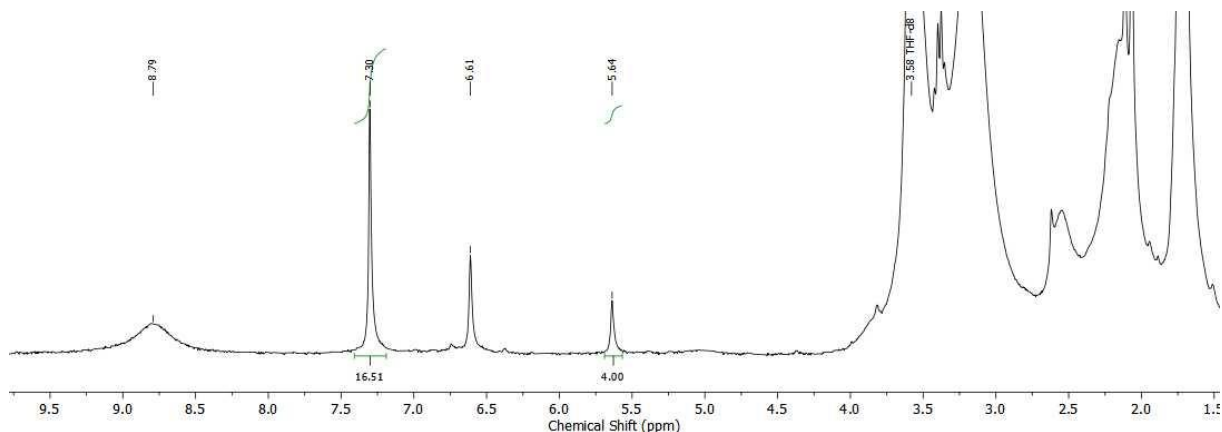


**Figure S17.**  $^1\text{H}$  NMR spectrum of K{crypt.222}[Fe(NMes)(N{Dipp}SiMe $_3$ ) $_2$ ] (K{crypt.222}[1]) 24 h after addition of 2 equiv. 1,4-CHD in THF- $d_8$  (298 K, 300 MHz).

### Reaction of [1] with 1,4-Cyclohexadiene

To a solution of 30 mg (0.04 mmol, 1 equiv.) [1], dissolved in 0.5 mL toluene- $d_8$ , 7 mg (0.09 mmol, 2 equiv.) 1,4-CHD were added. After stirring the solution for 24 h formation of benzene ( $\delta = 7.12$  ppm, 39% conversion) was observed by  $^1\text{H}$  NMR. Attempts for identification and isolation of the presumably resulting iron amide complex or any other iron containing reaction product via crystallisation was not successful.

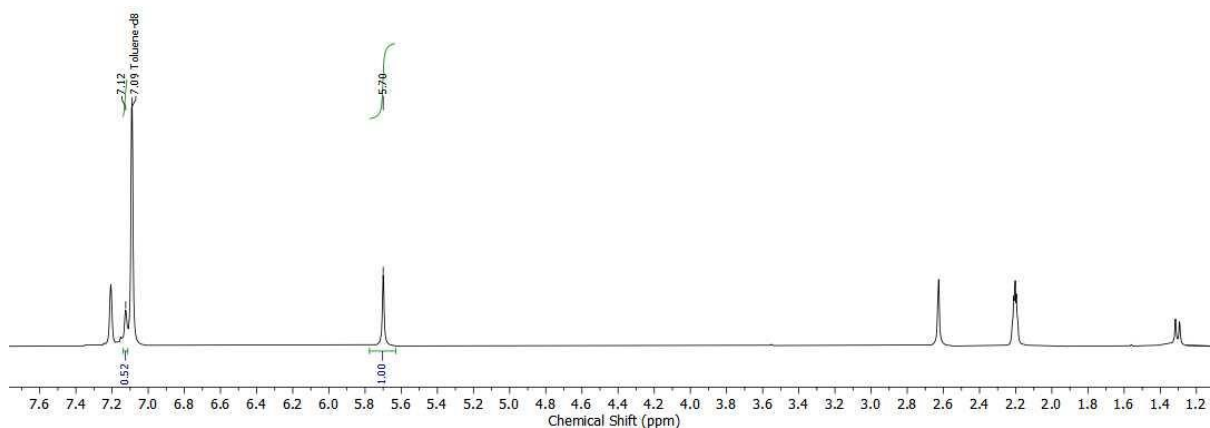


**Figure S18.**  $^1\text{H}$  NMR spectrum of [Fe(NMes)(N{Dipp}SiMe $_3$ ) $_2$ ] ([1]) 24 h after addition of 2 equiv. 1,4-CHD in toluene- $d_8$  (298 K, 300 MHz).

### Reaction of K{crypt.222}[1] with 1-Hydroxy-2,2,6,6-tetramethyl-piperidine (TEMPO-H)

To a solution of 30 mg (0.03 mmol, 1 equiv.) K{crypt.222}[1], dissolved in 0.5 mL THF- $d_8$ , 4 mg (0.03 mmol, 1 equiv.) TEMPO-H were added. The conversion was analysed by  $^1\text{H}$  NMR spectroscopy by calibrating TEMPO-H ( $\delta = 1.08$  ppm) versus the cryptand signal. The conversion amounted to 35% after 24 h (by  $^1\text{H}$  NMR). Attempts for identification or isolation of the presumably formed iron amide or any other iron containing product was not successful.

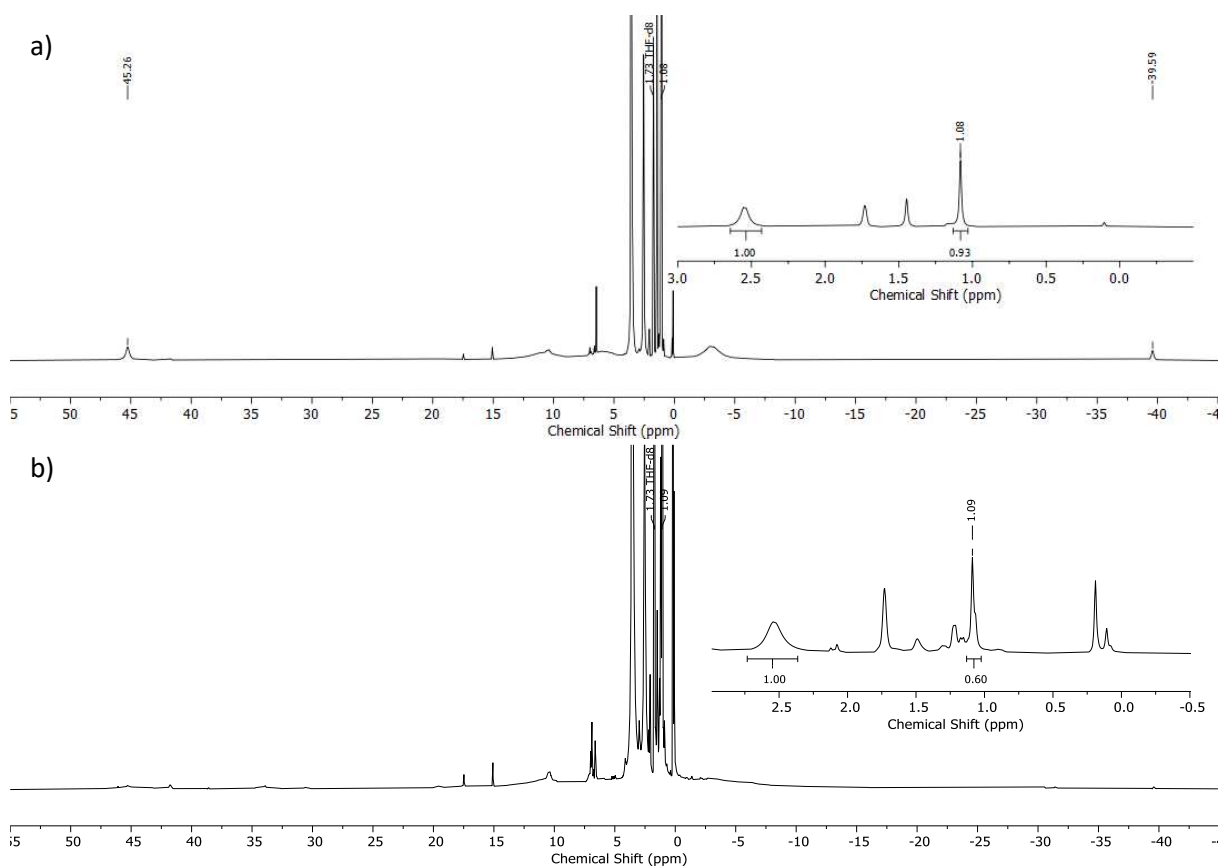


**Figure S19.**  $^1\text{H}$  NMR spectra of K{crypt.222}[Fe(NMes)(N{Dipp}SiMe $_3$ ) $_2$ ] (K{crypt.222}[1]) in addition of 1 equiv. TEMPO-H in THF- $d_8$  after 15 min (a) and 24 h (b) (298 K, 300 MHz).

In addition to the NMR-experiment a mixture of 7 mg (0.01 mmol, 1 equiv.) K{crypt.222}[1] and 1 mg (0.01 mmol, 1 equiv.) of TEMPO-H, dissolved in 0.4 mL THF, was examined via X-Band EPR spectroscopy. The time-dependent graph shows initial formation of minor amounts of the TEMPO radical that vanish over time. Given the significant conversion of TEMPO-H by  $^1\text{H}$  NMR spectroscopy (35% after 24 h) this indicates follow-up/side reactions of either TEMPO or TEMPO-H with either the formed amide or the employed imide.

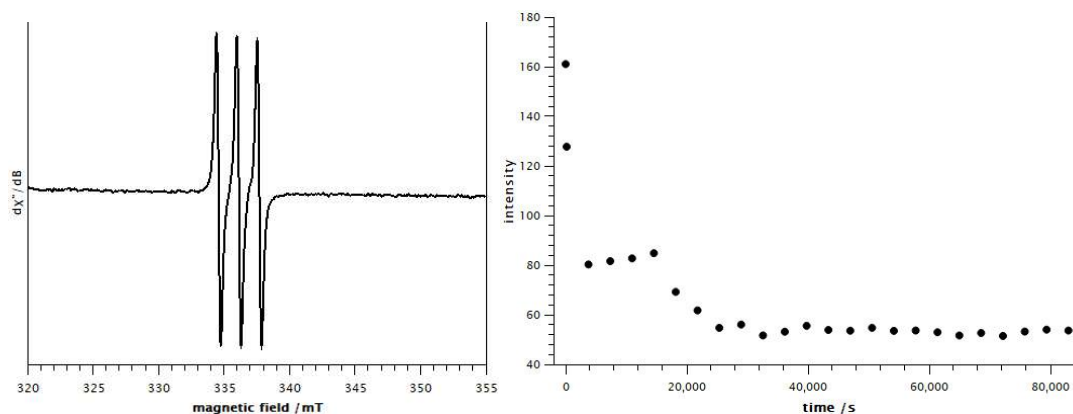


**Figure S20.** Left: X-Band EPR spectrum of  $K\{\text{crypt.222}\}[\text{Fe}(\text{NMe}_2)(\text{N}\{\text{Dipp}\}\text{SiMe}_3)_2]$  ( $K\{\text{crypt.222}\}[\mathbf{1}]$ ) with addition of 1 equiv. TEMPO–H in THF recorded after 10 min at 303.75 K (frequency 9.436407 GHz, 1.0 mW microwave power, 0.5 G modulation amplitude with 100 kHz modulation frequency). Right: Time dependence of the absolute intensity of the the EPR spectroscopic resonance due to the TEMPO radical, generated from the reaction of  $K\{\text{crypt.222}\}[\mathbf{1}]$  with 1 equiv. TEMPO–H.

### Reaction of **[1]** with 1-Hydroxy-2,2,6,6-tetramethyl-piperidine (TEMPO-H)

To a solution of 30 mg (0.04 mmol, 1 equiv.) **[1]**, dissolved in 0.5 mL,  $\text{C}_6\text{D}_6$  7 mg (0.04 mmol, 1 equiv.) TEMPO–H were added. The reaction was monitored by  $^1\text{H}$ -NMR-spectroscopy.

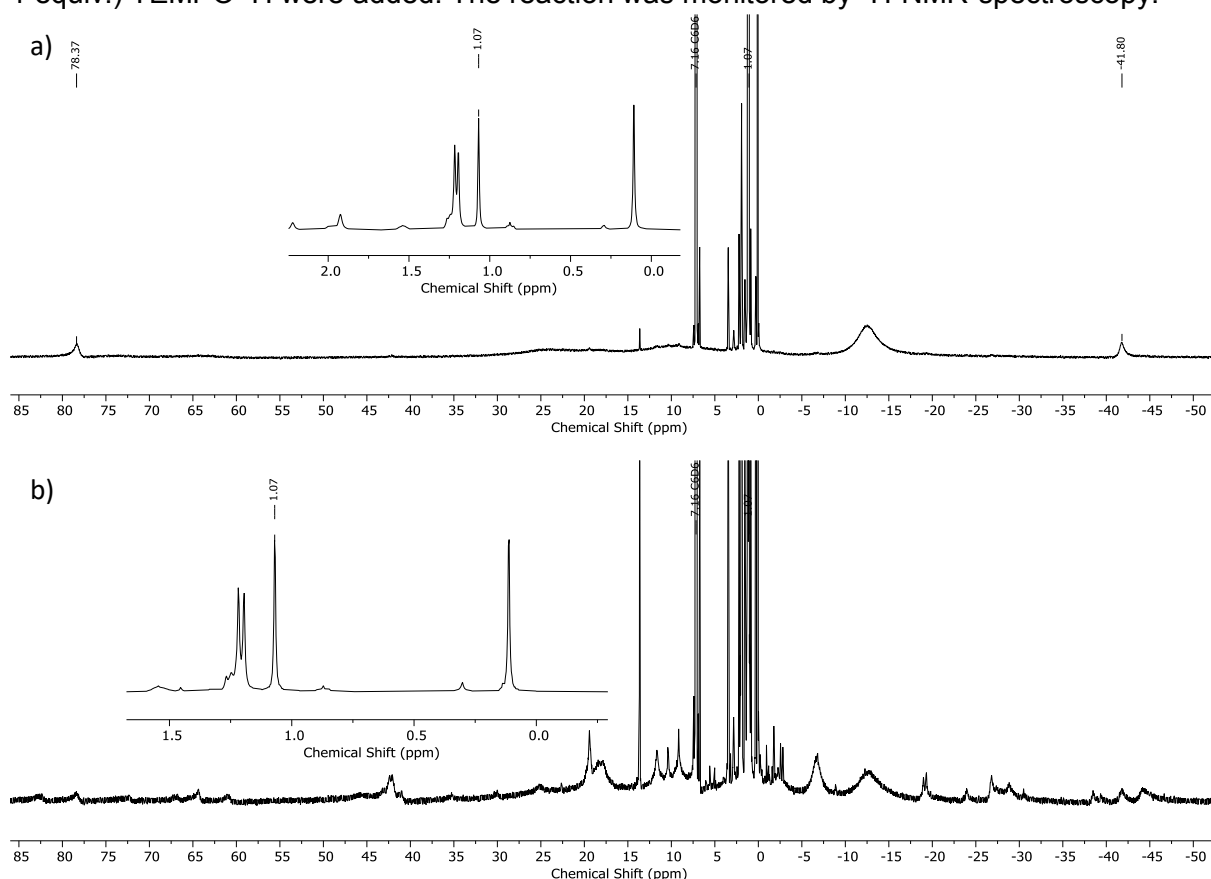


**Figure S21.**  $^1\text{H}$  NMR spectra of  $[\text{Fe}(\text{NMe}_2)(\text{N}\{\text{Dipp}\}\text{SiMe}_3)_2]$  (**[1]**) treated with 1 equiv. TEMPO–H in toluene- $\text{d}_8$ , measured after 15 min (a) and 24 h (b) (298 K, 300 MHz), showing the partial conversion of **[1]** and appearance of a set of signals ascribed to one or more paramagnetic species.

In addition to the NMR-spectroscopic experiments, EPR-spectroscopic examination of a solution of 4 mg (0.01 mmol, 1 equiv.) [1] and 1 mg (0.01 mmol, 1 equiv.) TEMPO–H in 0.4 mL toluene was carried out. The EPR spectroscopic resonance of TEMPO generated in this reaction is shown in Figure S22 (left); a plot showing the intensity of this signal as a function of the reaction time is shown in Figure S22 (right). In order to evaluate the amount of TEMPO generated in this reaction, an EPR spectroscopic calibration curve for the TEMPO radical was recorded, covering the relevant concentration range of the TEMPO radical (Figure S23). Using this calibration, the conversion of TEMPO–H to TEMPO reached 34% after 24 h. Only minor changes were observed after that (conversion of TEMPO–H to TEMPO after 47 h: 36%).

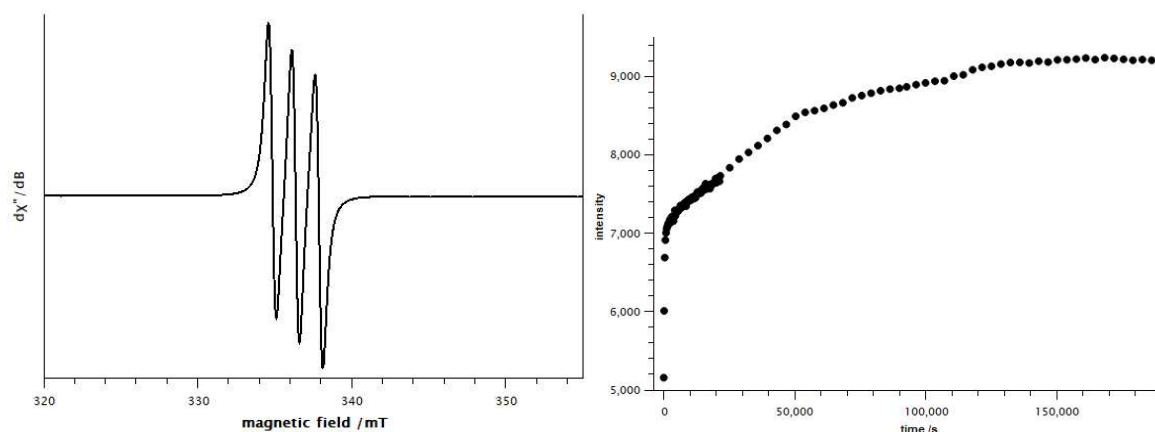


**Figure S22.** Left: X-Band EPR spectrum of  $[\text{Fe}(\text{NMes})(\text{N}\{\text{Dipp}\}\text{SiMe}_3)_2]$  ([1]) 10 minutes after addition of 1 equiv. TEMPO–H in toluene (collected at 303.75 K (frequency 9.436407 GHz, 1.0 mW microwave power, 2 G modulation amplitude with 100 kHz modulation frequency). Right: Time dependence of the absolute EPR intensity of the TEMPO radical formed from the reaction of  $[\text{Fe}(\text{NMes})(\text{N}\{\text{Dipp}\}\text{SiMe}_3)_2]$  ([1]) with 1 equiv. TEMPO–H.

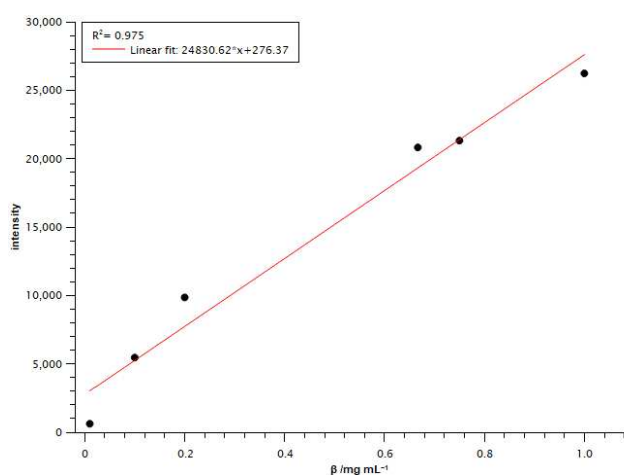


**Figure S23.** Calibration slope of absolute intensity of the EPR spectroscopic signal of TEMPO vs. the concentration of TEMPO in toluene ( $c = 0.01$  mg/mL;  $0.10$  mg/mL;  $0.20$  mg/mL;  $0.667$  mg/mL;  $0.75$  mg/mL;  $1.0$  mg/mL).

## Cyclic voltammetry

The redox behavior of  $K\{\text{crypt.222}\}[1]$  was examined by using a microcell HC “closed” stand (*rhd instruments*) in combination with a temperature controller (*rhd instruments*) and an *AUTOLAB PGSTAT 202* (*Metrohm GmbH*) potentiostat/galvanostat. The measurements were performed at  $25 \pm 0.1$  °C, using a *TSC 1600 Closed* (*rhd instruments*) Pt cell in a three electrode configuration with Pt wires acting as pseudo reference and as working electrode. The redox behaviour of  $[1]$  was examined by using a *TSC 1600 Closed* (*rhd instruments*) glassy carbon cell in a three-electrode configuration with an Ag wire acting as pseudo reference electrode and a glassy carbon working electrode. To secure reproducible conditions the electrodes were freshly polished, rinsed with THF and dried *in vacuo* for 2 hours. 2 mM of analyte and 0.1 M  $n\text{Bu}_4\text{N}[\text{PF}_6]$ , which acted as electrolyte, were used in the default measurement setup. The  $[\text{FcCp}_2] / [\text{FcCp}_2]^+$  ( $\text{Fc}/\text{Fc}^+$ ) redox couple was used as internal standard. The measurements were performed at four different scan rates (50, 100, 200, 500 mV/s), with two full cycles per scan rate. Peak potentials and currents of the second cycle of each measurement were determined using the *NOVA Software* (ver. 2.1.4, *Metrohm GmbH*).

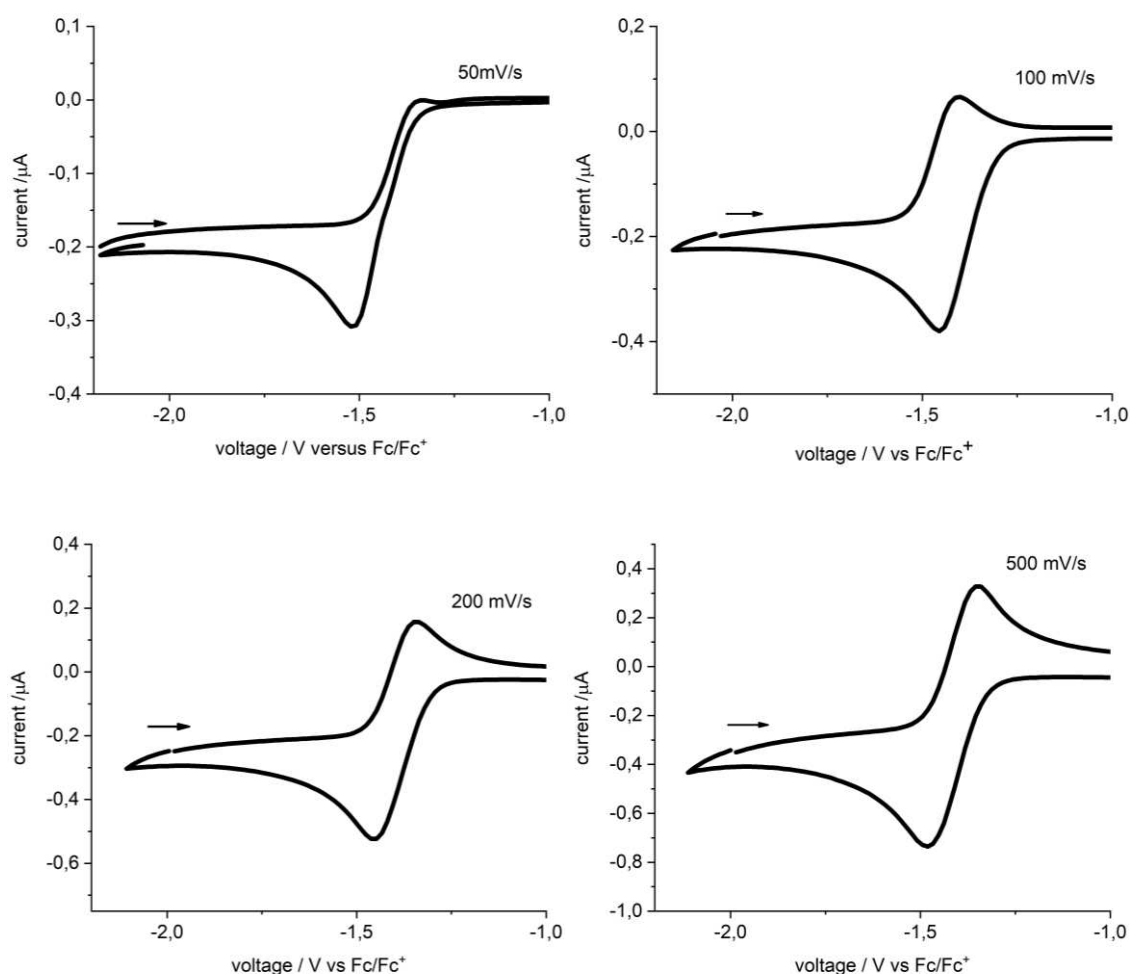


**Figure S24.** Cyclic voltammograms of  $K\{\text{crypt.222}\}[1]$  in THF at depicted scan rates (0.1 M  $n\text{Bu}_4\text{N}[\text{PF}_6]$  vs  $\text{Fc}/\text{Fc}^+$ ). The redox process at  $-1.40$  V is assigned to the  $[1]^- / [1]$  couple.

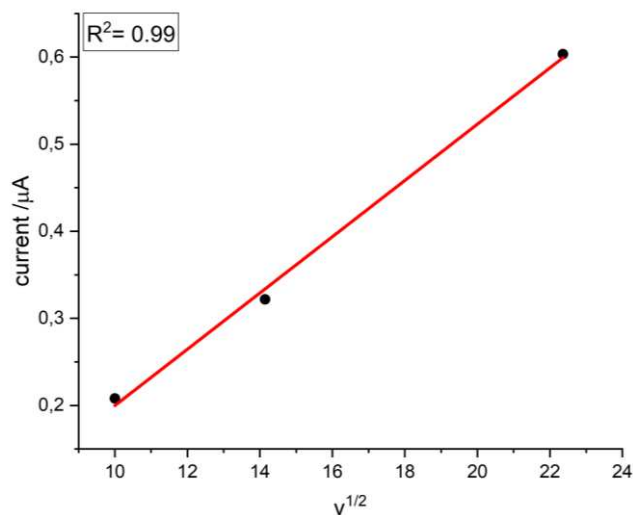


**Figure S25.** Randles-Sevcik fit for the electron transfer at  $E_{1/2} = -1.40$  V of  $\text{K}\{\text{m}\}\{\mathbf{1}\}$  in THF.

**Table S1.** Electrochemical data for the electron transfer at  $E_{1/2} = -1.40$  V of  $\text{K}\{\text{crypt.222}\}\{\mathbf{1}\}$  in THF.

Scan rate / mV/s	$E_{1/2}$ / V	$I_{pa}$ / $\mu\text{A}$	$I_{pc}$ / $\mu\text{A}$	$ I_{pa}/I_{pc} $
50	-1.42	---	-0.25	---
100	-1.41	0.20	-0.31	1.49
200	-1.40	0.32	-0.43	1.33
500	-1.40	0.60	-0.62	1.03

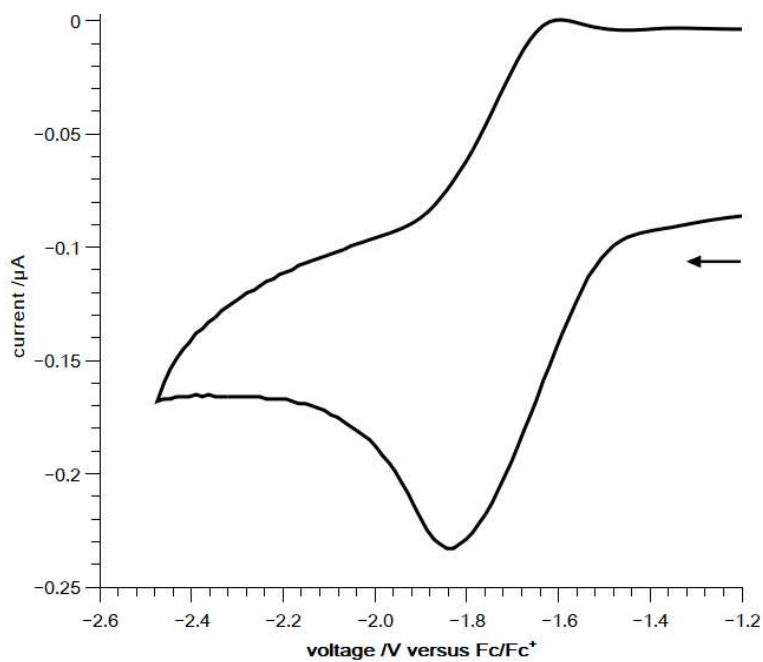


**Figure S26.** Section of the cyclic voltammogram of  $\mathbf{[1]}$  in THF at a scan rate of 200 mV/s (0.1 M  $n\text{Bu}_4\text{N}[\text{PF}_6]$  vs  $\text{Fc}/\text{Fc}^+$ ). The reversible redox process is assigned to the  $[\mathbf{1}]^- / [\mathbf{1}]$  couple.

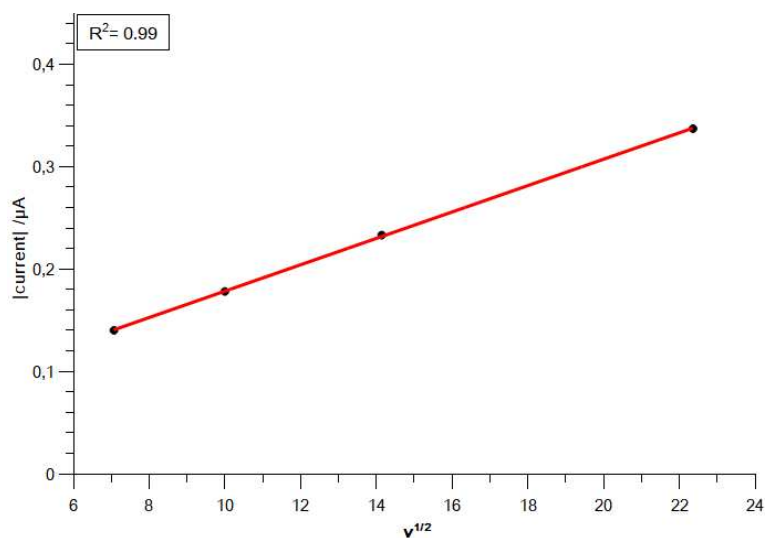


**Figure S27.** Randles-Sevcik fit for the electron transfer at  $E_{1/2} = -1.72$  V of [1] in THF.

**Table S2.** Electrochemical data for the electron transfer at  $E_{1/2} = -1.72$  V of [1] in THF.

Scan rate /mV/s	$E_{1/2}$ /V	$I_{pa}$ / $\mu A$	$I_{pc}$ / $\mu A$	$ I_{pa}/I_{pc} $
50	-1,74	0.053	-0.065	0.82
100	-1.70	0.072	-0.085	0.85
200	-1.72	0.13	-0.12	1.08
500	-1.71	0.21	-0.18	1.17



## Mössbauer spectroscopy

Mössbauer spectra were recorded with a  $^{57}\text{Co}$  source in a Rh matrix using an alternating constant acceleration Wissel Mössbauer spectrometer operated in the transmission mode and equipped with a Janis closed-cycle helium cryostat. Isomer shifts are given relative to iron metal at ambient temperature. Simulation of the experimental data was performed with the Mfit program using Lorentzian line doublets: E. Bill, Max-Planck Institute for Chemical Energy Conversion, Mülheim/Ruhr, Germany.

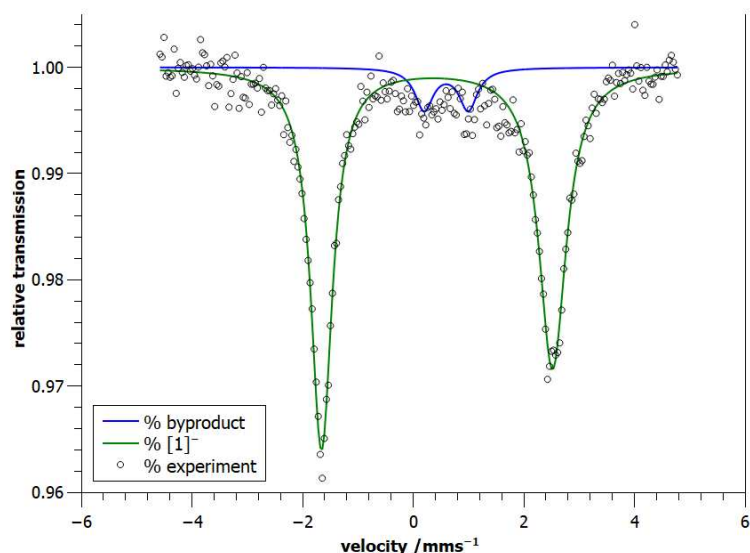


**Figure S28.** Zero field  $^{57}\text{Fe}$  Mössbauer spectrum of solid  $\text{K}\{\text{crypt.222}\}[1]$  at 80 K. The green line represents a fit with  $\delta = 0.43$  mm/s,  $|\Delta E_Q| = 4.18$  mm/s, which can be assigned to  $\text{K}\{\text{crypt.222}\}[1]$  (91.4%). The blue line represents a fit with  $\delta = 0.60$  mm/s,  $|\Delta E_Q| = 0.80$  mm/s, which assigned to an unknown iron(II) byproduct (8.6%).

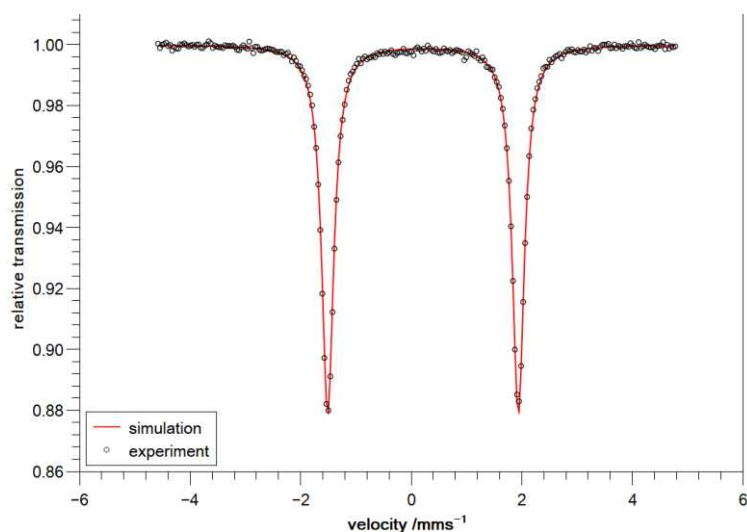


**Figure S29.** Zero field  $^{57}\text{Fe}$  Mössbauer spectrum of solid  $[1]$  at 80 K. The red line represents a fit with  $\delta = 0.21$  mm/s,  $|\Delta E_Q| = 3.45$  mm/s, which can be assigned to  $[1]$ .

## Magnetic measurements

Temperature-dependent magnetic susceptibility measurements were carried out with a Quantum-Design MPMS3 SQUID magnetometer equipped with a 7 Tesla magnet in the range from 210 to 2.0 K at a magnetic field of 0.5 T. The powdered samples were contained in a polycarbonate capsule, covered with a few drops of low viscosity perfluoropolyether based inert oil Fomblin Y45 to fix the crystals, and fixed in a non-magnetic sample holder. Each raw data file for the measured magnetic moment was corrected for the diamagnetic contribution of the sample holder and the polycarbonate capsule. The molar susceptibility data were corrected for the diamagnetic contribution.

Experimental temperature dependent and VTVH (variable temperature – variable field) data were simultaneously modelled by using a fitting procedure to the appropriate Heisenberg-Dirac-van-Vleck (HDvV) spin Hamiltonian for Zeeman splitting and zero-field splitting, equation (1).

$$\hat{H} = g\mu_B\vec{B}\vec{S} + D\left[\hat{S}_z^2 - \frac{1}{3}S(S+1)\right] \quad (1)$$

Simulation of the experimental magnetic data was performed with the julX\_2s program: E. Bill, Max-Planck Institute for Chemical Energy Conversion, Mülheim/Ruhr, Germany.

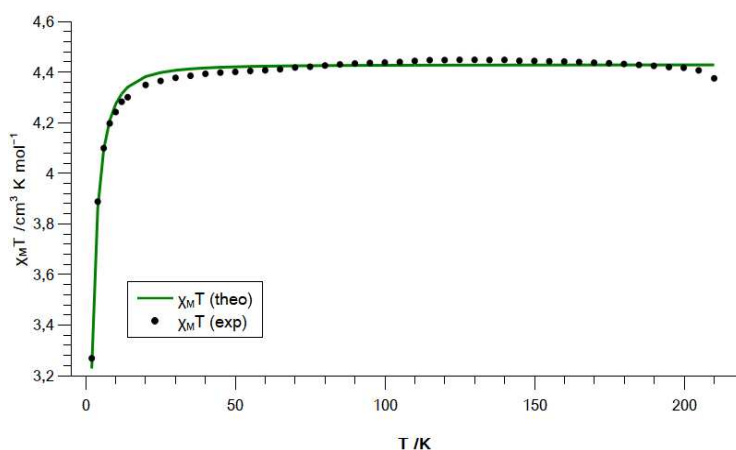


**Figure S30.** Plot of  $\chi_M T$  vs temperature of K{crypt.222}[1] with an applied field  $B = 0.5$  T. The green line represents the best fit with the parameters  $S = 5/2$ ,  $D = 2.5 \text{ cm}^{-1}$ ,  $g = 2.01$ .

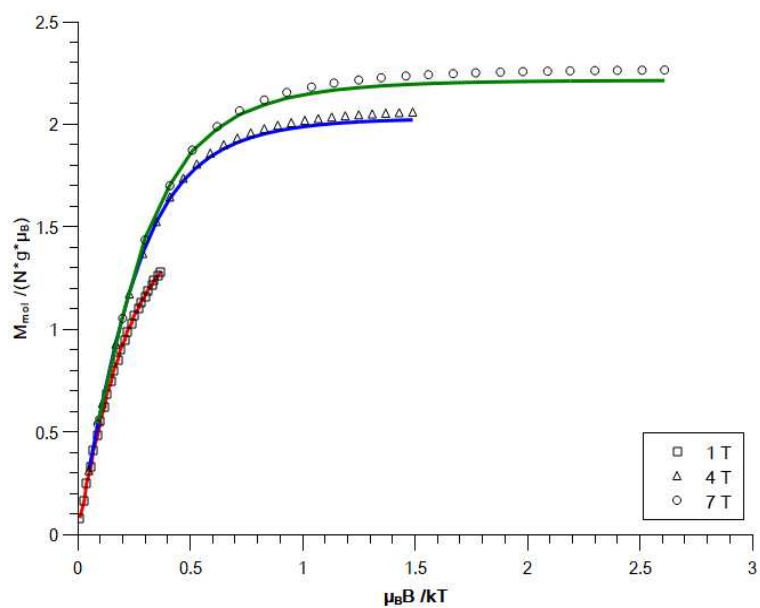


**Figure S31.** Plot of  $M_{mol}$  vs  $\mu_B B$  of K{crypt.222}[1] with an applied field  $B = 1$  T (red), 4 T (blue) 7 T (green). The lines represent the best fit with the parameters  $S = 5/2$ ,  $D = 2.5 \text{ cm}^{-1}$ ,  $g = 2.01$ .

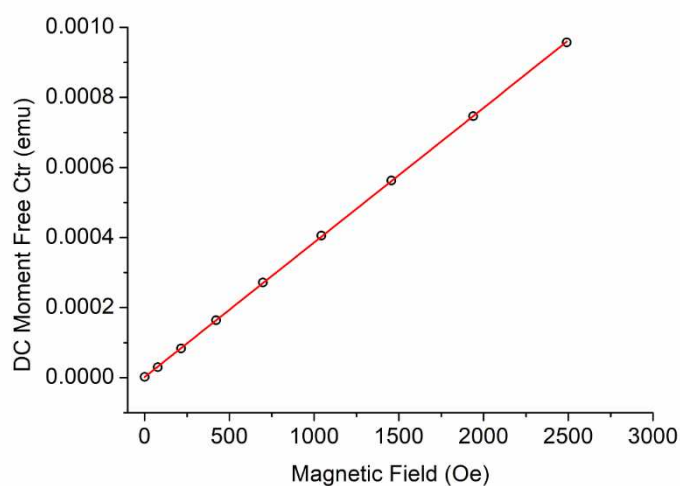


**Figure S32.** Moment vs. field measurement of K{crypt.222}[1] at 100 K. The linear behaviour (red line, goodness of linear correlation: Pearson  $R = 0.99999$ ,  $R^2 = 0.99997$ ) clearly indicates the absence of magnetic impurities/nanoparticles.

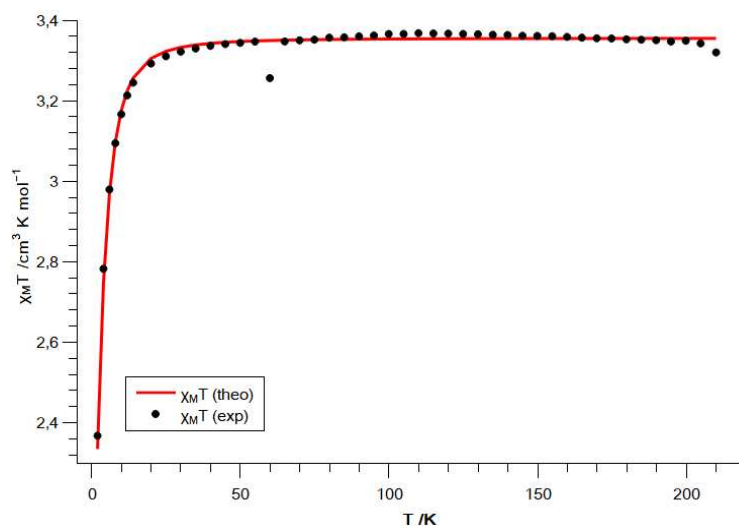


**Figure S33.** Plot of  $\chi_M T$  vs temperature of [1] with an applied field  $B = 0.5$  T. The red line represents the best fit with the parameters  $S = 2$ ,  $D = -3.5$   $\text{cm}^{-1}$ ,  $g = 2.12$ .

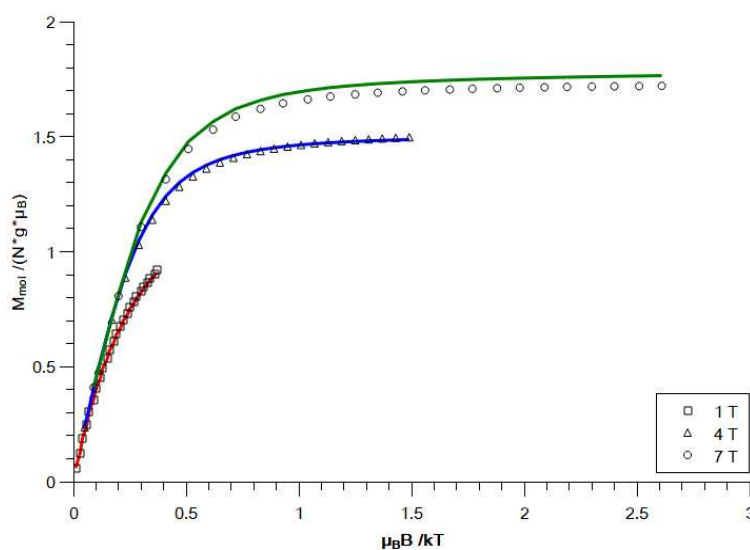


**Figure S34.** Plot of  $M_{mol}$  vs  $\mu_B B$  of [1] with an applied field  $B = 1$  T (red), 4 T (blue) 7 T (green). The lines represent the best fit with the parameters  $S = 2$ ,  $D = -3.5$   $\text{cm}^{-1}$ ,  $g = 2.12$ .

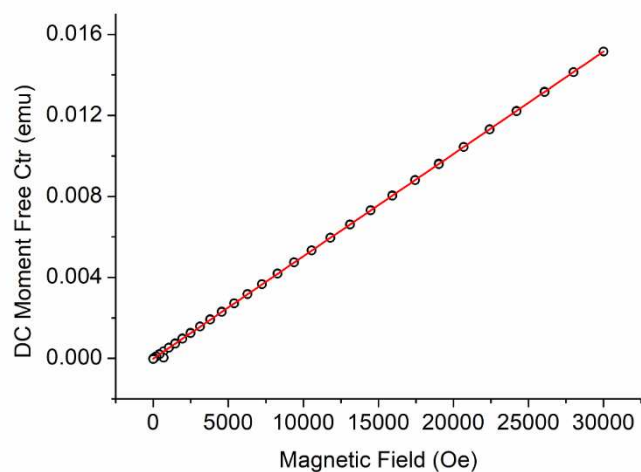


**Figure S35.** Moment vs. field measurement of [1] at 100 K. The linear behaviour (red line, goodness of linear correlation: Pearson  $R = 0.99996$ ,  $R^2 = 0.99993$ ) clearly indicates the absence of magnetic impurities/nanoparticles.

## Electron-paramagnetic-resonance spectroscopy (EPR)

Helium-temperature EPR spectra were performed on a Bruker EMXplus (X-band) EPR spectrometer equipped with the Bruker ER4118X-MD5 probe head. The freshly prepared samples were transferred to J. Young quartz EPR tubes and sealed. The solution in the tube was frozen in liquid nitrogen and kept frozen until measured.

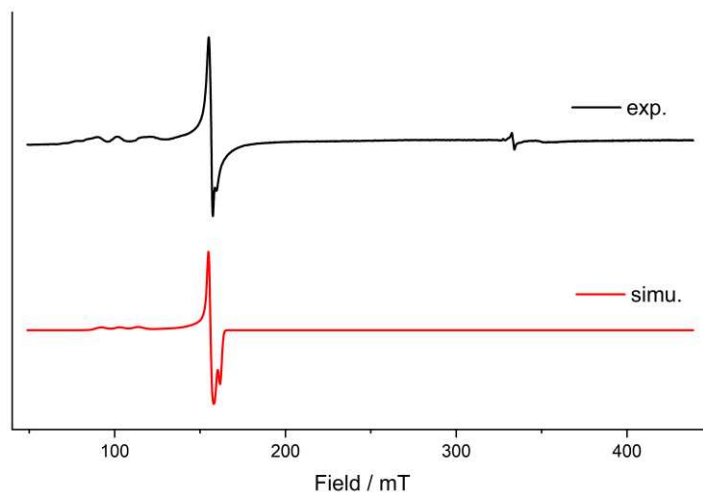


**Figure S36.** X-Band EPR spectrum of K{crypt.222}[1] in frozen THF (frequency 9.354709 GHz, 1.002 mW power, 4.996 G modulation amplitude) collected at 13.0 K (black). Simulation of data using the program EasySpin (red).<sup>[6]</sup> Fitting parameters:  $S = 5/2$ ,  $g_1 = 6.5$ ,  $g_2 = 4.28$ ,  $g_3 = 4.18$ ;  $A_1 = 349.69$  G,  $A_2 = 3.57$  G,  $A_3 = 42.82$  G.

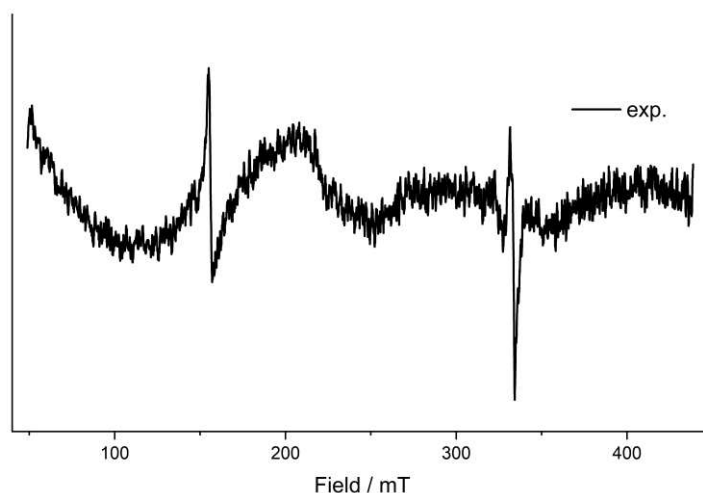


**Figure S37.** X-Band EPR spectrum of [1] in frozen *n*-hexane (frequency 9.359903 GHz, 1.002 mW power, 5 G modulation amplitude) collected at 12.97 K. The weak signals at  $g_1 = 4.3$ ,  $g_2 = 2.0$  are attributed to minimal amounts of an unknown iron(III) impurity.

## Quantum chemical calculations

The calculations were performed with ORCA v. 5.0.1 and v. 5.0.2.<sup>[7]</sup> Three computational strategies were applied, relying either (1.) on the structural parameters from the solid-state structures, or (2) the structural parameters from the solid state in combination with truncation of bulky side-groups, or (3.) optimization of all structural parameters without any constraints. We have applied very similar computational protocols for the analysis of much related compounds.<sup>[8]</sup>

1. The positions of all hydrogen atoms were optimized (*optimizehydrogens true*) using the structural parameters from the solid-state structures and thus constraining the positions of all other atoms (PBE functional). Single point calculations were performed using the PBE,<sup>[9]</sup> PBE0,<sup>[10]</sup> and TPSSh,<sup>[11]</sup> functionals. Scalar relativistic effects were modeled under the Zeroth Order Regular Approximation (ZORA)<sup>[12]</sup> and the ZORA-def2-TZVPP<sup>[13]</sup> basis set. The D4<sup>[14]</sup> dispersion correction was used. The RI approximation with the related auxiliary basis sets (*SARC/J*)<sup>[15]</sup> were used to reduce computation time of calculations using the GGA functionals. For hybrid functionals, the RIJCOSX approximation was applied. Tighter-than-default scf (*tightscf*) criteria were applied. Mössbauer and EPR parameters were calculated following this approach. In case of the EPR calculations, 2<sup>nd</sup> order contribution to the HFCs from spin orbit coupling were considered (*aorb*). The calculation of the Mössbauer parameters followed the procedure developed by Björnsson *et al.* using the “full calibration parameter set” and consequently the functionals TPSSh, BP86 (instead of PBE) and B3LYP (instead of PBE0).<sup>[16]</sup>
2. The positions of all hydrogen atoms were optimized (*optimizehydrogens true*) using the structural parameters from the solid-state structures and thus constraining the positions of all other atoms (PBE functional). Additionally, the two Dipp groups were truncated by methyl groups. CASSCF/NEVPT2 calculations were then carried out at the triple- $\zeta$  level of theory (ZORA-def2-TZVPP, *SARC/J*, *autoaux*, *RIJCOSX*), with active spaces of (10,9) and (11,9) for **[1]** and **[1]<sup>-</sup>**, respectively (Table S15).<sup>[17]</sup> The active space was chosen as to include d-orbitals, ligand centered orbitals and one set of aryl substituent centered  $\pi$  and  $\pi^*$  orbitals (Fig. S76 – S80). Spin-orbit contributions were included by quasi-degenerate perturbation theory (QDPT). The electronic structure analysis in the main part of the manuscript relates to calculations without state averaging, whereas state-averaging was applied to determine the energies of vertically excited states.
3. This approach followed strategy (1), except that the structural parameters were optimized without constraints using the PBE, PBE0 and TPSSh functionals and the ZORA-def2-SVP basis set (def2-TZVP on Fe). All optimized structures were verified as true minima by the absence ( $N^{\text{imag}} = 0$ ) of negative eigenvalues in the harmonic vibrational frequency analysis. Intrinsic bond orbitals (IBOs, Fig. 64)<sup>18</sup> were calculated at the triple- $\zeta$  level of theory and were visualized using Chemcraft and IBOview. The results obtained with PBE, TPSSh, PBE0 were consistent, with each functional giving rise to one strongly covalent orbital between the imido ligand and the metal. Following the amount of exact exchange, PBE slightly favors a  $d^5$ , *i.e.* Fe<sup>III</sup> description for **[1]**, whereas TPSSh and PBE0 slightly favor a  $d^6$ , *i.e.* Fe<sup>II</sup>, electron configuration (*vide infra*).

**Table S3.** Comparison of experimental (XRD) and computed (TPSSh, PBE, PBE0) bond lengths and angles of [1]<sup>-</sup> and [1].

	[1] <sup>-</sup>				[1]			
	XRD	TPSSh	PBE	PBE0	XRD	TPSSh	PBE	PBE0
Fe–N <sub>imido</sub> /Å	1.774	1.767	1.767	1.760	1.741	1.738	1.72	1.764
Fe–N <sub>amido</sub> /Å	1.955	1.944	1.935	1.959	1.900	1.876	1.874	1.882
N–C <sub>Mes</sub> /Å	1.339	1.336	1.335	1.332	1.337	1.331	1.342	1.315
N–Fe–N /°	115.0	113.3	112.4	114.2	114.3	115.8	117.5	114.4
Fe–N <sub>imido</sub> –C /°	173.6	179.5	173.8	179.2	177.5	173.0	173.1	173.5

**Table S4.** Calculated Mössbauer parameters.

	Functional	$\Delta E$ [mm s <sup>-1</sup> ]	$\delta$ [mm s <sup>-1</sup> ]
[1]	Exp.	3.45	0.21
[1] <sup>-</sup>	Exp.	4.17	0.43
[1]	BP86	2.64	0.29
[1] <sup>-</sup>	BP86	3.86	0.38
[1]	TPSSh	2.98	0.78
[1] <sup>-</sup>	TPSSh	3.95	0.88
[1]	B3LYP	3.25	0.26
[1] <sup>-</sup>	B3LYP	4.05	0.37

**Table S5.** Spectroscopic parameters obtained by DFT methods. A-values are given in [MHz].

	$g_x$	$g_y$	$g_z$	$A_x$ (Fe)	$A_y$ (Fe)	$A_z$ (Fe)	$A_x$ (N <sub>imido</sub> )	$A_y$ (N <sub>imido</sub> )	$A_z$ (N <sub>imido</sub> )
<b>TPSSh//Hopt</b>									
[1] <sup>-</sup>	2.01	2.01	2.02	4.8	5	8.1	6.3	16.8	9.1
[1]	2.01	2.02	2.02	10.3	11.1	11.5	20.8	10.6	-3.3
<b>PBE//Hopt</b>									
1] <sup>-</sup>	2.01	2.01	2.02	5.9	6.7	8	6.5	15.4	9
[1]	2.01	2.01	2.02	10	11.7	13.6	21.4	11	2.1
<b>PBE0//Hopt</b>									
1] <sup>-</sup>	2	2.01	2.02	-4.3	-4.6	-0.5	7.3	18	9.8
[1]	2	2.01	2.02	-1	0.5	0.8	19.8	11.6	-5.5
<b>TPSSh//TPSSh</b>									
[1] <sup>-</sup>	2.01	2.01	2.02	3.6	3.7	6.6	6.3	16.7	9.2
[1]	2.01	2.01	2.02	10.3	11.2	11.6	19.7	9.7	11.6
<b>Experimental</b>									
[1] <sup>-</sup>	6.5	4.28	4.18	/	/	/	980	10	120



**Table S6.** Spectroscopic parameters obtained by QDPT/NEVPT2/CASSCF. A-values are given in [MHz], *D*- and *E/D*-values in [cm<sup>-1</sup>].

	$g_x$	$g_y$	$g_z$	$A_x$ (Fe)	$A_y$ (Fe)	$A_z$ (Fe)	$A_x$ (N <sub>imido</sub> )	$A_y$ (N <sub>imido</sub> )	$A_z$ (N <sub>imido</sub> )	<i>D</i>	<i>E/D</i>
[1] <sup>-</sup>	2.00	2.00	2.04	18.1	-10.6	22.5	2.1	10.5	-2.8	-0.7	0.186
[1]	2.00	2.00	2.02	13.0	18.8	7.5	21.2	-7.8	1.8	-1.3	0.168

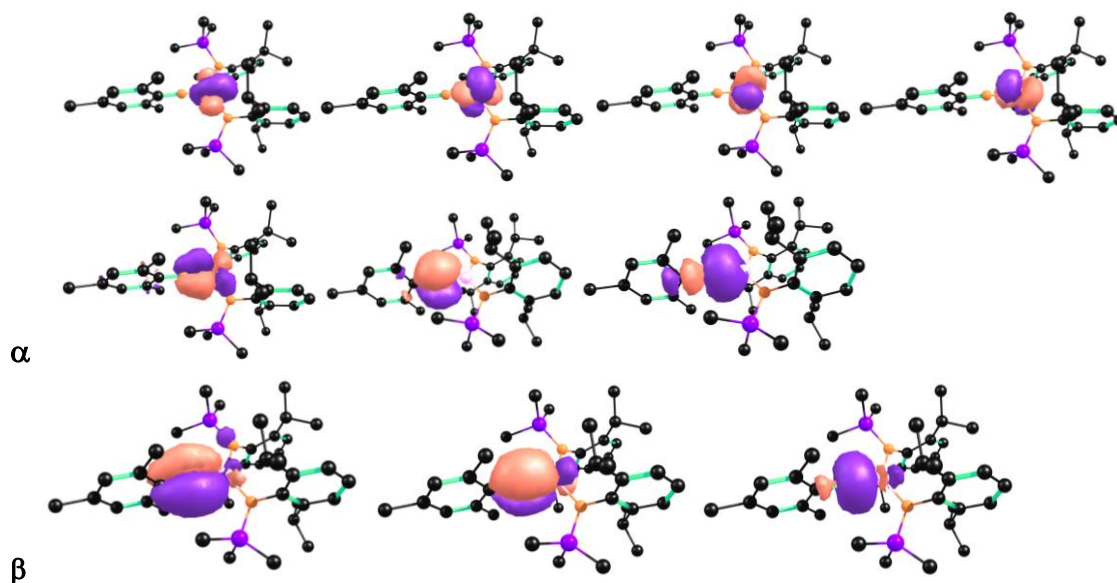


**Figure S38.** Metal-involving IBOs of [1] (TPSSh//TPSSh).

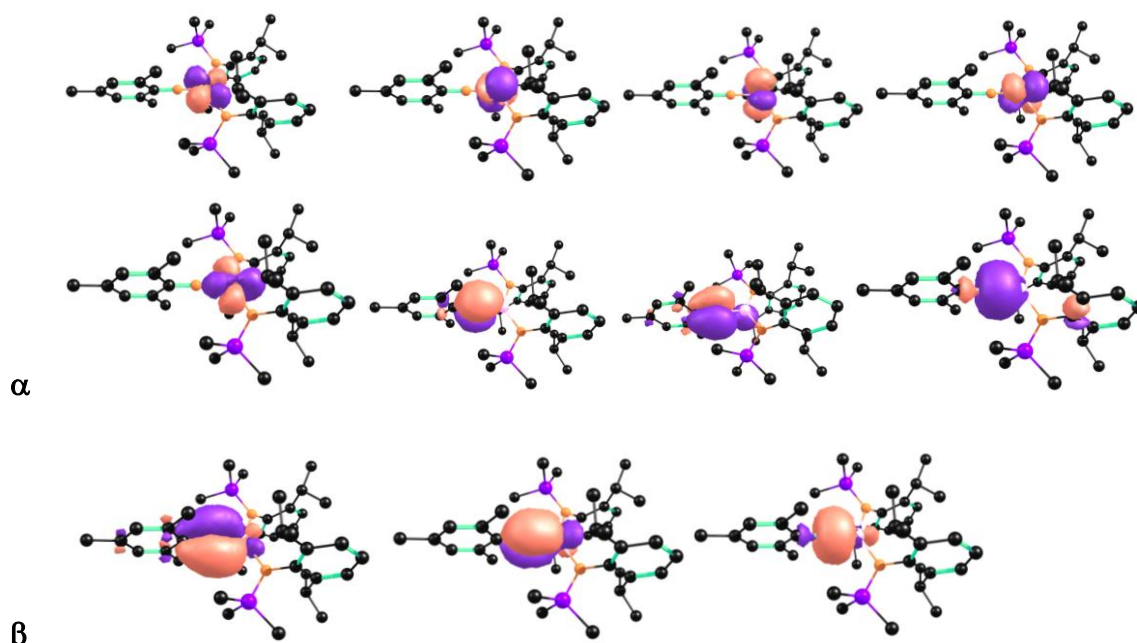


**Figure S39.** Metal-involving IBOs of [1]<sup>-</sup> (TPSSh//TPSSh).

0.62844 [ 1520]: 222111100  
 0.20752 [ 1485]: 221111110  
 0.12910 [ 1425]: 220111120  
 0.01176 [ 967]: 121211110  
 0.01052 [ 1139]: 202111102  
 0.00349 [ 1079]: 201111112  
 0.00274 [ 1282]: 211111111

**Figure S40.** Configuration of ground state of [1] as obtained by CASSCF(10,9).

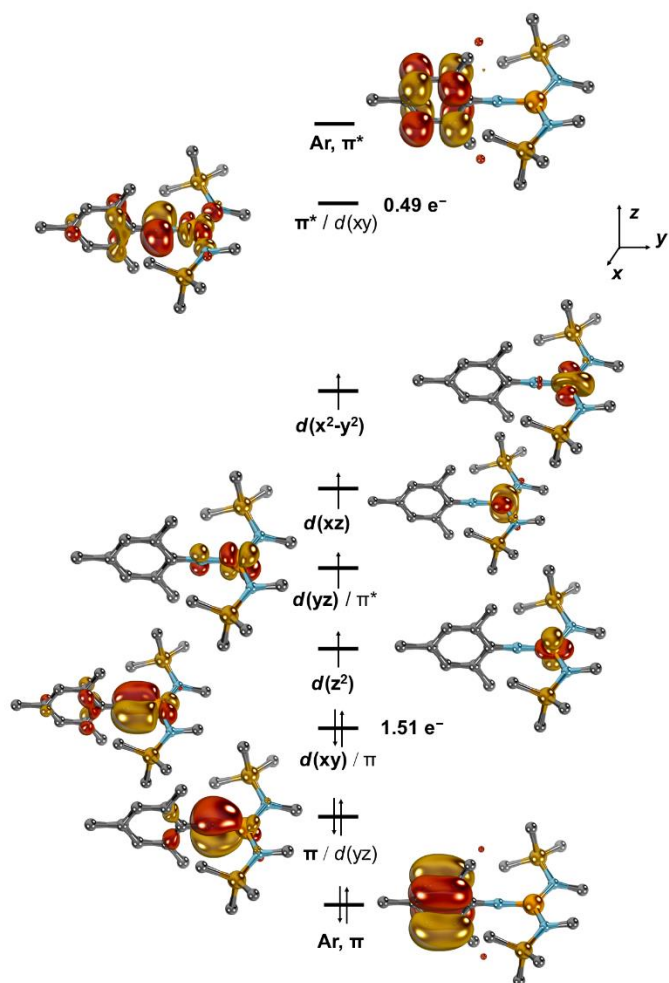


**Figure S41.** Entire active space [CASSCF(10,9)] of [1].

	<b>101</b>	
	-0.42746	
	1.98460	
0 Fe px		2.5
0 Fe dxz	15.2	
0 Fe dxy		0.0
1 Si pz		0.0
3 N px		0.9
4 N px		0.7
4 N py	0.0	
5 N px		65.1
5 N py		0.0
7 C py		0.1
7 C dxz		6.8
8 C py		0.0
11 C py		0.0
12 C py		0.0
14 C py		0.0
18 C pz		0.0
22 C pz		0.0
34 C pz		0.0
34 C py		0.0

	102	103	104	105	106	107
	-0.33435	-0.34266		-0.25877	-0.23660	-0.24808
	1.96387	1.50792		1.01458	1.00012	1.00003
0 Fe dz2	0.0	0.1	0.1	34.4	6.5	49.3
0 Fe dxz	0.0	0.0	89.5	0.0	0.0	0.0
0 Fe dyz	0.0	53.3		0.0	0.1	0.0
0 Fe dx2y2	0.0	0.0	0.0	33.6	15.0	45.1
0 Fe dxy	0.0	0.0	0.0	22.9		71.2
5 N px	0.0	0.0		6.5	0.0	0.0
5 N py	0.0	26.9		0.0	0.0	0.0
6 C py	17.1	2.1		0.0	0.0	0.0
8 C py	20.9	0.0		0.0	0.0	0.0
10 C py	18.1	2.1		0.0	0.0	0.0
12 C py	22.2	0.0		0.0	0.0	0.0

	108	109
	-0.03627	0.17939
	0.49289	0.03612
0 Fe s	0.0	0.0
0 Fe px	0.0	0.0
0 Fe dyz	45.7	0.0
0 Fe dx2y2	0.0	0.0
5 N py	33.4	0.0
6 C py	2.7	17.9
8 C py	0.1	15.4
9 H s	0.0	0.0
10 C py	2.6	19.0
11 C dxy	0.0	5.2
12 C py	0.0	16.7
13 H s	0.0	0.0
47 H s	0.1	0.0
48 H s	0.0	0.0
49 H s	0.0	0.0

**Figure S42.** Reduced Löwdin's population analysis of active space in CASSCF(10,9) of [1].

0.87647 [ 539]: 222111110  
0.08912 [ 465]: 211221110  
0.00964 [ 50]: 022111112  
0.00431 [ 497]: 220111112  
0.00340 [ 455]: 211211111  
0.00268 [ 305]: 121121111

**Figure S43.** Configuration of ground state of [1]<sup>-</sup> as obtained by CASSCF(11,9).

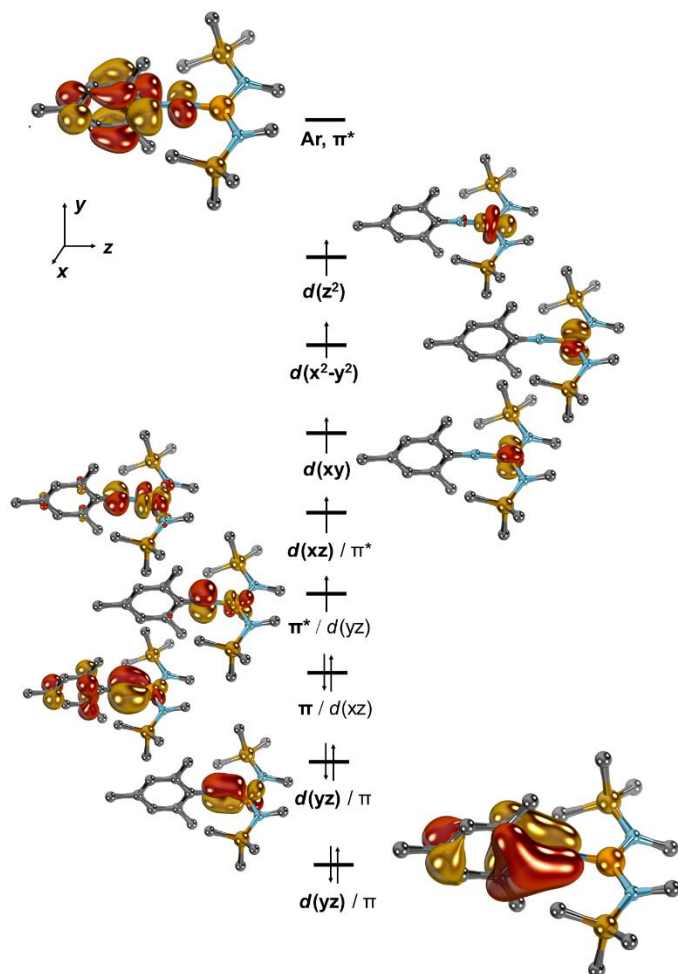


**Fig. S44.** Entire active space [CASSCF(11,9)] of [1]<sup>-</sup>.

	<b>101</b>
	-0.27499
	1.96611
3 N px	5.4
3 N py	0.0
4 N pz	0.2
4 N px	17.4
4 N py	0.0
5 N px	0.1
6 C px	0.0
7 C px	0.0
9 C px	0.0
10 C px	0.0
11 C px	0.0
17 C px	0.0
26 C px	6.1
38 C py	0.6
42 C pz	5.5
46 C px	8.7

	102	103	104		105		106	
	107							
	-0.28652	-0.18343		-0.01719	0.02489		0.02159	0.02643
	1.90056	1.88622		1.09936	1.09658		1.00006	1.00005
0 Fe dxz	0.6	22.0	0.1		73.4		0.0	0.0
0 Fe dyz	67.5	0.3	35.1		0.0		0.0	0.0
0 Fe dx <sup>2</sup> y <sup>2</sup>	0.0	0.0	0.0		0.0	6.7		86.3
0 Fe dxy	0.0	0.0	0.0		0.0	89.2		7.1
5 N px	0.6	40.7		0.3		11.1		0.0
5 N py	24.3	0.5	49.7		0.1		0.0	0.0
6 C dxz	0.1	5.6	0.0		1.9	0.0		0.0
6 C dyz	2.1	0.1	5.6		0.0	0.0		0.0
9 C px	0.0	5.4	0.1		1.2	0.0		0.0
10 C px	0.0	5.7	0.2		1.2	0.0		0.0
17 C px	0.0	5.7	0.1		1.3	0.0		0.0
	108	109						
	0.06099	0.33923						
	1.00000	0.05106						
0 Fe s	0.5	0.0						
0 Fe dz <sup>2</sup>	89.2	0.0						
5 N px	0.0	13.0						
6 C px	0.0	34.2						
7 C px	0.0	2.1						
8 H s	0.0	0.0						
9 C px	0.0	3.9						
10 C px	0.0	4.9						
11 C px	0.0	1.5						
12 H s	0.0	0.0						
17 C px	0.0	11.2						
31 H s	0.0	0.0						
32 H s	0.0	0.1						
33 H s	0.0	0.3						

**Figure S45.** Reduced Löwdin's population analysis of active space in CASSCF(11,9) of [1]<sup>-</sup>.

**Table S7.** Covalency of  $\pi$ -bonds in [1]<sup>-</sup> according to Löwdin's population analysis of the CASSCF(11,9) calculations.

	Fe	N
$d(yz)/\pi$	68	20
$\pi/d(xz)$	22	41
$\pi^*/d(yz)$	35	50
$d(xz)/\pi^*$	73	11

**Table S8.** Energies as obtained by strategy 1. Values are given in [Eh].

	<i>Functional</i>	<i>E</i>	<i>G</i>	<i>E(SP)</i>
[1] <sup>-</sup>	PBE	-3544.58506	-3543.76372	-3546.51764
[1]	PBE	-3544.50905	-3543.68365	-3546.43757
[1] <sup>-</sup>	TPSSh	-3547.59864	-3546.75085	-3549.53167
[1]	TPSSh	-3547.51509	-3546.66455	-3549.44507
[1] <sup>-</sup>	PBE0	-3544.84374	-3543.98957	-3546.77083
[1]	PBE0	-3544.75381	-3543.89704	-3546.67833

**Table S9.** Vertical energy gaps between  $S = 5/2$  (ferromagnetically coupled) and  $S = 3/2$  (antiferromagnetically coupled) states of [1]<sup>-</sup> as obtained by the PBE, TPSSh and PBE0 functionals or CASSCF/NEVPT2 (strategy 1). Negative energy differences  $\Delta E$  indicate ferromagnetic coupling.

	$\Delta E$ in [eV]	<i>Löwdin's spin density on Fe of <math>S = 5/2</math> state in [a.u.]</i>	<i>Löwdin's spin density on imido nitrogen atom of <math>S = 5/2</math> state in [a.u.]</i>	<i>J in [cm<sup>-1</sup>]</i>
PBE	0.05	3.61	0.52	-93
TPSSh	-0.01	3.74	0.54	+13
PBE0	-0.08	3.85	0.54	+151
saCASSCF/NEVPT2	-0.18	3.98	0.66	n.a.

**Table S10.** Electronic structure of broken-symmetry states of [1]<sup>-</sup> as obtained by the PBE, TPSSh and PBE0 functionals or CASSCF/NEVPT2 (strategy 1). Negative energy differences  $\Delta E$  indicate ferromagnetic coupling. UCO = unrestricted corresponding orbitals.

	$\Delta E$ in [eV]	<i>Löwdin's spin density on Fe of "broken symmetry" state in [a.u.]</i>	<i>Löwdin's spin density on imido nitrogen atom of "broken symmetry" state in [a.u.]</i>	<i>UCO overlap</i>	<i>Assignment of "broken symmetry" state</i>
PBE	+0.05	+2.74	+0.06	0.92	Fe <sup>I</sup> nitrene (LMCT state)
TPSSh	-0.01	+3.09	-0.14	0.77	Fe <sup>II</sup> imidyl
PBE0	-0.08	+3.34	-0.28	0.6	Fe <sup>II</sup> imidyl
saCASSCF/NEVPT2	-0.18	+3.37	-0.31	n.a.	Fe <sup>II</sup> imidyl

**Table S11.** Vertical energy gaps between  $S = 5/2$  (ferromagnetically coupled) and  $S = 3/2$  (antiferromagnetically coupled) states of [1]<sup>-</sup> as obtained by the PBE, TPSSh and PBE0 functionals (strategy 3). Negative energy differences  $\Delta E$  indicate ferromagnetic coupling.

	$\Delta E$ in [eV]	<i>Löwdin's Spin Density on Fe of <math>S = 5/2</math> state in [a.u.]</i>	<i>Löwdin's Spin Density on imido nitrogen atom of <math>S = 5/2</math> state in [a.u.]</i>	<i>J in [cm<sup>-1</sup>]</i>
PBE	-0.14	+3.62	+0.51	+230
TPSSh	-0.18	+3.76	+0.54	+311
PBE0	-0.22	+3.87	+0.54	+411

**Table S12.** Electronic structure of broken-symmetry states of [1]<sup>-</sup> as obtained by the PBE, TPSSh and PBE0 functionals (strategy 3). Negative energy differences  $\Delta E$  indicate ferromagnetic coupling. UCO = unrestricted corresponding orbitals.

	$\Delta E$ in [eV]	Löwdin's Spin Density on Fe of "broken symmetry" state in [a.u.]	Löwdin's Spin Density on imido nitrogen atom of "broken symmetry state" in [a.u.]	UCO overlap	Assignment of „broken symmetry“ state
<b>PBE</b>	-0.14	+2.78	+0.05	0.90	Fe <sup>I</sup> nitrene (LMCT state)
<b>TPSSh</b>	-0.18	+3.15	-0.15	0.75	Fe <sup>II</sup> imidyl
<b>PBE0</b>	-0.22	+3.38	-0.28	0.60	Fe <sup>II</sup> imidyl

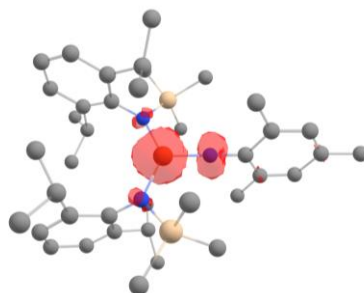


**Figure S46.** Spin-Density Distribution of  $S = 5/2$  ground state of **[1]<sup>-</sup>** according to calculations using the TPSSh functional (strategy 1).

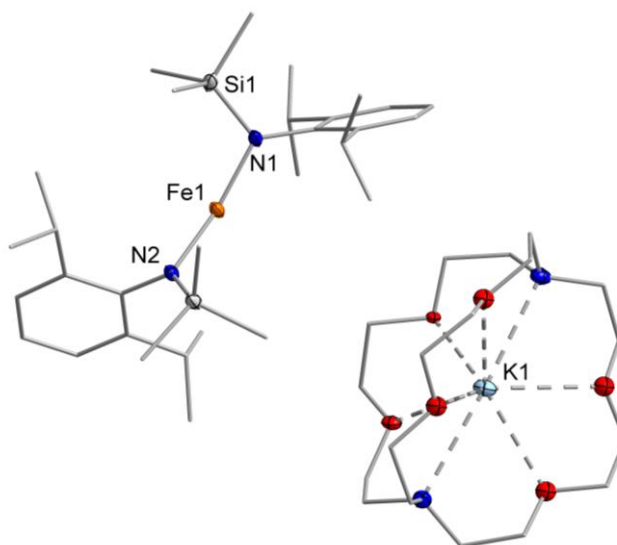
## X-Ray diffraction analysis and molecular structures

Data for K{crypt.222}[Fe(N{Dipp}SiMe<sub>3</sub>)<sub>2</sub>] (CCDC 2130486), K{crypt.222}[**1**] (CCDC 2130485), [**1**] (CCDC 2130488) and K{crypt.222}[**2**] (CCDC 2130487) were collected at 100 K on a Bruker Quest D8 diffractometer using a graphite-monochromated Mo-K  $\lambda$  radiation ( $\lambda = 0.71073\text{\AA}$ ) and equipped with an *Oxford Instrument Cooler Device*. The structures have been solved using either OLEX SHELXT V2014/1 <sup>[xix]</sup> and refined by means of least-squares procedures on a  $F^2$  with the aid of the program SHELXL-2016/6 <sup>[ii]</sup> include in the software package WinGX version 1.63<sup>[xx]</sup> or using CRYSTALS.<sup>[xxi]</sup> The Atomic Scattering Factors were taken from *International Tables for X-Ray Crystallography*.<sup>[xxii]</sup> All non-hydrogen atoms were refined anisotropically. All hydrogens atoms were refined by using a riding model. Absorption corrections were introduced by using the MULTISCAN and X-Red program.<sup>[xxiii, ix]</sup> Drawings of molecules are performed with the programs DIAMOND and POV-Ray with 50% probability displacement ellipsoids for non-H atoms. Depiction of H atoms is generally omitted for clarity.



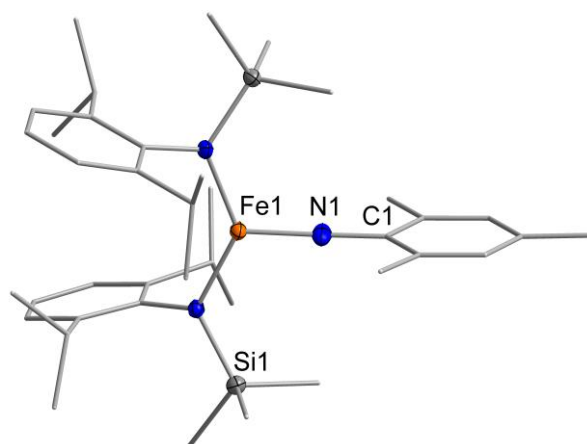
**Table S12.** Crystal data and structure refinement for K{crypt.222}[Fe(N{Dipp}SiMe<sub>3</sub>)<sub>2</sub>].

Identification code	K_crypt_FeNDippTMS
Empirical formula	C <sub>48</sub> H <sub>88</sub> FeKN <sub>4</sub> O <sub>6</sub> Si <sub>2</sub>
Formula weight / g mol <sup>-1</sup>	968.35
Temperature / K	100.0
Crystal system	monoclinic
Space group	<i>P</i> 2 <sub>1</sub> / <i>n</i>
<i>a</i> / Å	18.2810(8)
<i>b</i> / Å	14.0555(6)
<i>c</i> / Å	22.1239(9)
$\alpha$ / °	90
$\beta$ / °	106.2980(10)
$\gamma$ / °	90
<i>V</i> / Å <sup>3</sup>	5456.3(4)
<i>Z</i>	4
$\rho_{\text{calc}}$ / g cm <sup>-3</sup>	1.179
$\mu$ / mm <sup>-1</sup>	0.443
F(000)	2100.0
Crystal size / mm <sup>3</sup>	0.499 × 0.411 × 0.214
Radiation	MoK $\alpha$ ( $\lambda$ = 0.71073)
2 $\theta$ range for data collection / °	4.468 to 53.59
Index ranges	-23 ≤ <i>h</i> ≤ 22, -17 ≤ <i>k</i> ≤ 17, -28 ≤ <i>l</i> ≤ 28
Reflections collected	114411
Independent reflections	11654 [ <i>R</i> <sub>int</sub> = 0.0456, <i>R</i> <sub>sigma</sub> = 0.0232]
Data/restraints/parameters	11654/23/507
Goodness-of-fit on <i>F</i> <sup>2</sup>	1.027
Final <i>R</i> indexes [ <i>I</i> ≥ 2 $\sigma$ ( <i>I</i> )]	<i>R</i> <sub>1</sub> = 0.0422, <i>wR</i> <sub>2</sub> = 0.0955
Final <i>R</i> indexes [all data]	<i>R</i> <sub>1</sub> = 0.0548, <i>wR</i> <sub>2</sub> = 0.1020
Largest diff. peak/hole / e Å <sup>-3</sup>	0.64/-0.53

**Figure S47.** Molecular structure of K{crypt.222}[Fe(N{Dipp}SiMe<sub>3</sub>)<sub>2</sub>] within the crystal.

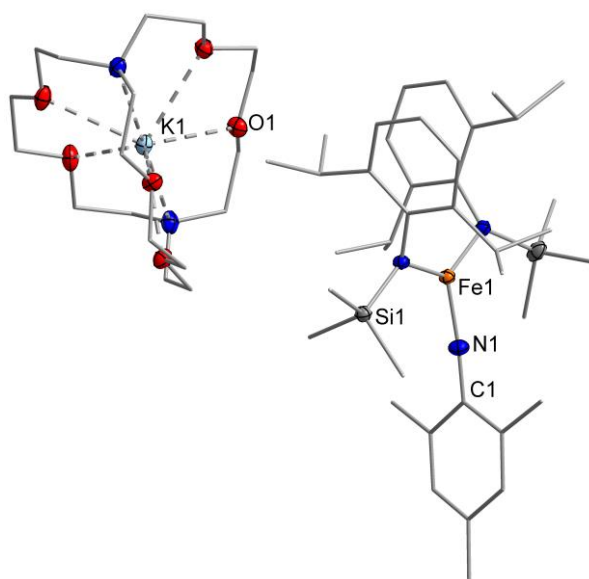
**Table S13.** Crystal data and structure refinement for [1].

Identification code	FeNMes_1
Empirical formula	C <sub>39</sub> H <sub>63</sub> FeN <sub>3</sub> Si <sub>2</sub>
Formula weight / g mol <sup>-1</sup>	685.95
Temperature / K	100
Crystal system	orthorhombic
Space group	<i>Pbca</i>
<i>a</i> / Å	19.2646(7)
<i>b</i> / Å	16.7587(7)
<i>c</i> / Å	24.9520(11)
$\alpha$ / °	90
$\beta$ / °	90
$\gamma$ / °	90
<i>V</i> / Å <sup>3</sup>	8055.7(6)
<i>Z</i>	8
$\rho_{\text{calc}}$ / g cm <sup>-3</sup>	1.131
$\mu$ / mm <sup>-1</sup>	0.462
F(000)	2976.0
Crystal size / mm <sup>3</sup>	0.22 × 0.144 × 0.111
Radiation	MoK $\alpha$ ( $\lambda$ = 0.71073)
2 $\theta$ range for data collection / °	3.89 to 49.994
Index ranges	-22 ≤ <i>h</i> ≤ 22, -19 ≤ <i>k</i> ≤ 19, -29 ≤ <i>l</i> ≤ 29
Reflections collected	76439
Independent reflections	7090 [ $R_{\text{int}}$ = 0.1078, $R_{\text{sigma}}$ = 0.0499]
Data/restraints/parameters	7090/0/423
Goodness-of-fit on $F^2$	1.042
Final <i>R</i> indexes [ $I \geq 2\sigma(I)$ ]	$R_1$ = 0.0464, $wR_2$ = 0.0897
Final <i>R</i> indexes [all data]	$R_1$ = 0.0651, $wR_2$ = 0.0952
Largest diff. peak/hole / e Å <sup>-3</sup>	0.25/-0.29

**Figure S48.** Molecular structure of [1] within the crystal.

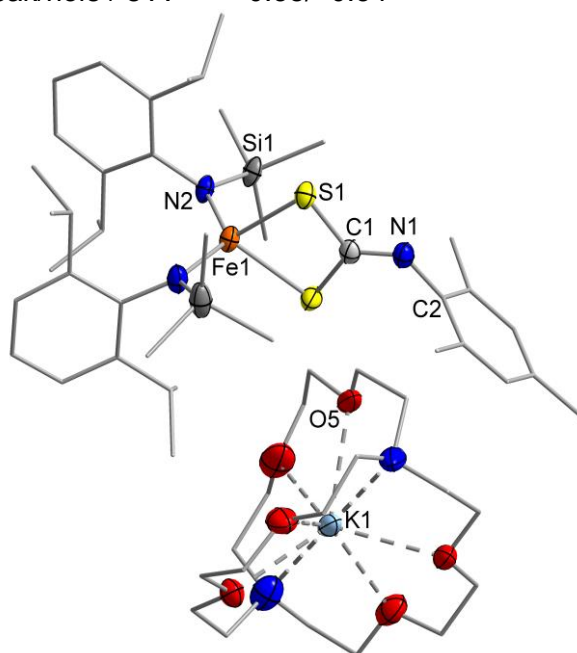
**Table S14.** Crystal data and structure K{crypt.222}[1].

Identification code	K_crypt_1
Empirical formula	C <sub>57</sub> H <sub>99</sub> FeKN <sub>5</sub> O <sub>6</sub> Si <sub>2</sub>
Formula weight / g mol <sup>-1</sup>	1101.54
Temperature / K	100.00
Crystal system	monoclinic
Space group	<i>P</i> 2 <sub>1</sub> / <i>c</i>
<i>a</i> / Å	11.9424(4)
<i>b</i> / Å	24.7899(9)
<i>c</i> / Å	22.9964(9)
$\alpha$ / °	90
$\beta$ / °	95.9740(10)
$\gamma$ / °	90
<i>V</i> / Å <sup>3</sup>	6771.1(4)
<i>Z</i>	4
$\rho_{\text{calc}}$ / g cm <sup>-3</sup>	1.081
$\mu$ / mm <sup>-1</sup>	0.365
F(000)	2388.0
Crystal size / mm <sup>3</sup>	0.21 × 0.14 × 0.13
Radiation	MoK $\alpha$ ( $\lambda$ = 0.71073)
2 $\theta$ range for data collection / °	3.922 to 56.616
Index ranges	-15 ≤ <i>h</i> ≤ 15, -33 ≤ <i>k</i> ≤ 33, -30 ≤ <i>l</i> ≤ 28
Reflections collected	85806
Independent reflections	16789 [ <i>R</i> <sub>int</sub> = 0.0388, <i>R</i> <sub>sigma</sub> = 0.0346]
Data/restraints/parameters	16789/0/666
Goodness-of-fit on <i>F</i> <sup>2</sup>	1.047
Final <i>R</i> indexes [ <i>I</i> ≥ 2 $\sigma$ ( <i>I</i> )]	<i>R</i> <sub>1</sub> = 0.0445, <i>wR</i> <sub>2</sub> = 0.1018
Final <i>R</i> indexes [all data]	<i>R</i> <sub>1</sub> = 0.0571, <i>wR</i> <sub>2</sub> = 0.1072
Largest diff. peak/hole / e Å <sup>-3</sup>	0.38/-0.37

**Figure S49.** Molecular structure of K{crypt.222}[1] within the crystal.

**Table S15.** Crystal data and structure refinement for K{crypt.222}[2].

Identification code	K_crypt_2
Empirical formula	C <sub>58</sub> H <sub>99</sub> FeKN <sub>5</sub> O <sub>6</sub> S <sub>2</sub> Si <sub>2</sub>
Formula weight / g mol <sup>-1</sup>	1177.67
Temperature / K	100.00
Crystal system	monoclinic
Space group	<i>P</i> 2 <sub>1</sub> / <i>c</i>
<i>a</i> / Å	13.8538(8)
<i>b</i> / Å	24.6616(14)
<i>c</i> / Å	23.5229(13)
$\alpha$ / °	90
$\beta$ / °	90.755(2)
$\gamma$ / °	90
<i>V</i> / Å <sup>3</sup>	8036.1(8)
<i>Z</i>	4
$\rho_{\text{calc}}$ / g cm <sup>-3</sup>	0.973
$\mu$ / mm <sup>-1</sup>	0.361
F(000)	2540.0
Crystal size / mm <sup>3</sup>	0.487 × 0.152 × 0.117
Radiation	MoK $\alpha$ ( $\lambda$ = 0.71073)
2 $\theta$ range for data collection / °	3.808 to 50
Index ranges	-16 ≤ <i>h</i> ≤ 16, -29 ≤ <i>k</i> ≤ 29, -27 ≤ <i>l</i> ≤ 27
Reflections collected	237874
Independent reflections	14145 [ <i>R</i> <sub>int</sub> = 0.1409, <i>R</i> <sub>sigma</sub> = 0.0502]
Data/restraints/parameters	14145/0/693
Goodness-of-fit on F <sup>2</sup>	1.048
Final <i>R</i> indexes [ <i>I</i> ≥ 2 $\sigma$ ( <i>I</i> )]	<i>R</i> <sub>1</sub> = 0.0566, <i>wR</i> <sub>2</sub> = 0.1235
Final <i>R</i> indexes [all data]	<i>R</i> <sub>1</sub> = 0.0780, <i>wR</i> <sub>2</sub> = 0.1300
Largest diff. peak/hole / e Å <sup>-3</sup>	0.38/-0.34

**Figure S50.** Molecular structure of K{crypt.222}[2] within the crystal.

---

## References

- [1] a) D. F. Evans *J. Chem. Soc.* **1959**, 2003; b) E. M. Schubert, *J. Chem. Educ.* **1992**, 69, 62.
- [2] J. M. Zadrozny, M. Atanasov, A. M. Bryan, C.-Y. Lin, B. D. Rekker, P. P. Power, F. Neese, J. R. Long, *Chem. Sci.* **2013**, 4, 125.
- [3] L. P. Spencer, R. Altwer, P. Wei, L. Gelmini, J. Gault, D. W. Stephan, *Organometallics* **2003**, 19, 3841.
- [4] N. A. Giffin, M. Makramalla, A. D. Hendsbee, K. N. Robertson, C. Sherren, C. C. Pye, J. D. Masuda, J. A. C. Clyburne, *Org. Biomol. Chem.* **2011**, 9, 3672.
- [5] C. A. Laskowski, G. L. Hillhouse, *Organometallics* **2009**, 28, 6114.
- [6] S. Stoll, A. Schweiger, *J. Magn. Reson.* **2006**, 1, 42.
- [7] a) F. Neese, *Wiley Interdiscip. Rev.: Comput. Mol. Sci.* **2018**, 8, e1327; b) F. Neese, *Wiley Interdiscip. Rev.: Comput. Mol. Sci.* **2012**, 2, 73-78; c) F. Neese, F. Wennmohs, U. Becker, C. Riplinger, *J. Chem. Phys.* **2020**, 152, 224108.
- [8] a) W. Mao, F. W. Heinemann, A. Scheurer, D. Munz, K. Meyer, *Angew. Chem. Int. Ed.* **2021**, 60, 16480-16486; b) A. Grünwald, S. S. Anjana, D. Munz, *Eur. J. Inorg. Chem.* **2021**, 4147 – 4166; c) S. Aghazada, M. Miehlich, J. Messelberger, F. W. Heinemann, D. Munz, K. Meyer, *Angew. Chem. Int. Ed.* **2019**, 58, 18547-18551; d) G. Sieg, Q. Pessemesse, S. Reith, S. Yelin, C. Limberg, D. Munz, C. G. Werncke, *Chem. Eur. J.* **2021**, 27, 16760-16767; e) S. Aghazada, D. Munz, F. W. Heinemann, A. Scheurer, K. Meyer, *J. Am. Chem. Soc.* **2021**, 143, 17219-17225; f) S. Aghazada, D. Fehn, F. W. Heinemann, D. Munz, K. Meyer, *Angew. Chem. Int. Ed.* **2021**, 60, 11138-11142.
- [9] J. P. Perdew, M. Ernzerhof, K. Burke, *J. Chem. Phys.* **1996**, 105, 9982-9985.
- [10] C. Adamo, V. Barone, *J. Chem. Phys.* **1999**, 110, 6158-6170.
- [11] a) J. Tao, J. P. Perdew, V. N. Staroverov, G. E. Scuseria, *Phys. Rev. Lett.* **2003**, 91, 146401; b) V. N. Staroverov, G. E. Scuseria, J. Tao, J. P. Perdew, *J. Chem. Phys.* **2003**, 119, 12129-12137.
- [12] C. van Wüllen, *J. Chem. Phys.* **1998**, 109, 392-399.
- [13] F. Weigend, R. Ahlrichs, *Phys. Chem. Chem. Phys.* **2005**, 7, 3297-3305.
- [14] E. Caldeweyher, S. Ehlert, A. Hansen, H. Neugebauer, S. Spicher, C. Bannwarth, S. Grimme, *J. Chem. Phys.* **2019**, 150, 154122.
- [15] F. Weigend, *Phys. Chem. Chem. Phys.* **2006**, 8, 1057-1065.
- [16] R. Bjornsson, F. Neese, S. DeBeer, *Inorg. Chem.* **2017**, 56, 1470.
- [17] B. O. Roos, P. R. Taylor, P. E. M. Siegbahn, *Chem. Phys.* **1980**, 48, 157-173.
- [18] G. Knizia, *J. Chem. Theory Comput.* **2013**, 9, 4834-4843.
- [xix] G. M. Sheldrick, *Acta Cryst.* **2015**, 71, 3.
- [xx] L. Farrugia, *J. Appl. Crystallogr.* **1999**, 32, 837.
- [xxi] P. W. Betteridge, J. R. Carruthers, R. I. Cooper, K. Prout, D. J. Watkin, *J. Appl. Cryst.* **2003**, 36, 1487.
- [xxii] *International Tables for X-ray crystallography* (Kynoch Press, Birmingham, England, 1974) Vol. IV.
- [xxiii] SADABS-2016/2 (Bruker, **2016**).



